HAL
open science

Geology, tectonics and post-2001 eruptive activity interpreted from high-spatial resolution satellite imagery : the case study of Merapi and Seremu volcanoes, Indonesia

Akhmad Solikhin

To cite this version:

Akhmad Solikhin. Geology, tectonics and post-2001 eruptive activity interpreted from high-spatial resolution satellite imagery : the case study of Merapi and Seremu volcanoes, Indonesia. Earth Sciences. Université Blaise Pascal - Clermont-Ferrand II, 2015. English. NNT : 2015CLF22559 . tel-01555688

HAL Id: tel-01555688

https://theses.hal.science/tel-01555688v1

Submitted on 4 Jul 2017

HAL is a multi-disciplinary open access archive for the deposit and dissemination of scientific research documents, whether they are published or not. The documents may come from teaching and research institutions in France or abroad, or from public or private research centers.

L'archive ouverte pluridisciplinaire **HAL**, est destinée au dépôt et à la diffusion de documents scientifiques de niveau recherche, publiés ou non, émanant des établissements d'enseignement et de recherche français ou étrangers, des laboratoires publics ou privés.

N° D'ORDRE : D.U. 2559

UNIVERSITÉ BLAISE PASCAL
U.F.R. Sciences et Technologies

ÉCOLE DOCTORALE DES SCIENCES FONDAMENTALES
N° 819

THÈSE

Présentée pour obtenir le grade de

DOCTEUR D'UNIVERSITÉ

Spécialité : Volcanologie

par

Akhmad SOLIKHIN

Titulaire d'un Master

Geology, tectonics and post-2001 eruptive activity interpreted from high-spatial resolution satellite imagery: The case study of Merapi and Semeru volcanoes, Indonesia

soutenue publiquement le 16 mars 2015 devant le jury composé de:

Andrew HARRIS	*LMV, Université Blaise Pascal*	*Président*
John PALLISTER	*VDAP, U. S. Geological Survey*	*Rapporteur*
Jean-Louis BOURDIER	*ISTO, Université d'Orléans*	*Rapporteur*
Jean VANDEMEULEBROUCK	*ISTerre, Université de Savoie*	*Examinateur*
Jean-Claude THOURET	*LMV, Université Blaise Pascal*	*Directeur de Thèse*
Virginie PINEL	*ISTerre, Université de Savoie*	*Co-directrice*
SURONO	*Geological Agency, Indonésie*	*Membre invité*

N° D'ORDRE : D.U. 2559

UNIVERSITÉ BLAISE PASCAL
Faculty of Science and Technology

DOCTORAL SCHOOL OF FUNDAMENTAL SCIENCES
N° 819

Geology, tectonics and post-2001 eruptive activity interpreted from high-spatial resolution satellite imagery: The case study of Merapi and Semeru volcanoes, Indonesia

THESIS

by

Akhmad SOLIKHIN

In partial fulfillment of the requirements for degree of

DOCTOR OF PHILOSOPHY

in

Volcanology

Thesis defended on 16 March 2015

Jury:

Andrew HARRIS	*President of jury*	*LMV, Université Blaise Pascal*
John PALLISTER	*Reviewer*	*VDAP, U. S. Geological Survey*
Jean-Louis BOURDIER	*Reviewer*	*ISTO, Université d'Orléans*
Jean VANDEMEULEBROUCK	*Examiner*	*ISTerre, Université de Savoie*
Jean-Claude THOURET	*Thesis director*	*LMV, Université Blaise Pascal*
Virginie PINEL	*Thesis co-director*	*ISTerre, Université de Savoie*
SURONO	*Invited member*	*Indonesian Geological Agency*

Alhamdu lillaahi rabbil 'aalamiin ...

Untuk yang tersayang Abah & Emak

dan yang tercinta istriku, Wening

Acknowledgements

Foremost, I would like to express my deepest thanks to my two supervisors, Professor Jean-Claude Thouret and Dr. Virginie Pinel, for their patience, encouragement, and immense knowledge. They always seemed to believe in my abilities (even when I had grave doubts) and was thus vital in motivating me to finish the work I had started. Jean-Claude has been my supervisor of this PhD research project as well as during my Master 2 Research in 2008-2009. He gave me the opportunity to live in France and work in Singapore, and this thesis may not have been started and ended without his help. I thank him for giving me a big challenge in my thesis so that stimulate me to do better and better. I thank Virginie for allowing me to work at IsTerre Chambéry, well introducing me to InSAR and PolSAR, giving me chances to develop and most of them for the fruitful discussion.

This thesis project would not have been possible without the financial support of the *Bourses du Gouvernement Français* (BGF) from the French Embassy and *Allocations de Recherche pour une Thèse au Sud* (ARTS) from *Institut de Recherche pour le Développement* (IRD). Additional financial support was also received from the City of Clermont-Ferrand (*La Bourse Doctorale Municipale*), the Laboratoire Magmas et Volcans (LMV), LAHARISK project (ANR-09-RISK-005), DOMERAPI project (ANR-12-BS06-0012), and the CNES-TOSCA Project 'Merapi (2012 and 2014).

I would like to thank Dr. Surono, head of Indonesian Geological Agency and former head of the Center for Volcanology and Geological Hazard Mitigation (CVGHM), for giving me permission and great encouragement to conduct PhD thesis in Clermont-Ferrand. He is a chief, mentor and friend, from whom I have learnt the important skill of disciplined critical thinking and volcanic crisis management. I also thank him for assigning and involving me in several "missions" during the volcanic crisis so that improve my experiences and skills.

I am grateful for all the help I received during the fieldwork at Merapi and Semeru, notably from Jean-Claude, Liliane Thouret, Mas Mahjum, and my colleagues from Semeru volcano observatory and BPPTK (Pak Subandrio, Pak Made, Bu Dewi, Bu Sri Sumarti Mbak Naning, Sulis, Radit, Cholic, Pak Sapari and the observers).

Equally I would like to thanks to John Pallister for consultation on Merapi and his wonderful work in reviewing my thesis, Andy Harris for his suggestions and discussions on thermal remote sensing, Liew Soo Chin and Avijit Gupta (CRISP at NUS, Singapore) for providing assistance with satellite imagery, Jean Vandemeulebrouck, Philippe Lesage Svetlana Byrdina and Emmanuel Trouvé for fruitful discussions and advice you have

given me during my "*stage*" in Chambéry, Mas Bro Agus Budi Santoso for the Merapi "lessons", Katie Preece for her encouragement and help in the improvement of English for some part in this thesis, Jean-François Oehler who has taught me the generation of DEM from HSR imagery, and Zaineb Kassouk for her help and useful discussions on image segmentation and classifications.

I am grateful to the members of my thesis committee, John Pallister (VDAP, USGS), Jean-Louis Bourdier (ISTO, Université d'Orléans), Andrew Harris (LMV, Université Blaise Pascal, Clermont-Ferrand), Jean Vandemeulebrouck (ISTerre, Université de Savoie, Chambéry), Jean-Claude Thouret (LMV, Clermont-Ferrand), Virginie Pinel (ISTerre, Chambéry) and Surono (Indonesian Geological Agency) for their useful comments and discussions about this research project.

Je remercie mes amis au LMV. There are too many of you to thank individually, but you know who you are. Thank you very much for help in practical matters, many interesting discussions, the sports as well as lively and always cooperative atmosphere in *our lab*, with all of you *lab* was really fun. Thank you also to all personnel at LMV. *Merci beaucoup pour tout*!

I would like to thanks my colleagues at the CVGHM, including Pak Hendrasto (head of the CVGHM) and Pak Iman Sinulingga for giving me permission and support concerning this thesis, My best friend Devy Syahbana for his encouragement, Sofie Yusmira for helping me in administrations and authorizations, Bu Hetty and Bu Estu for useful discussions on Semeru volcano and remote sensing, and all my friends at the CVGHM for their encouragement.

I would like to say "*terima kasih*" to my family at Clermont-Ferrand, notably to Mbak Upi, Pak Pierre, Erol Ozgur, Pak Dadik, Pak Hendriko, Pak Yusro, Dian, Catia, Annisa, Ines, Andrea, Gisela, Nanda, Demas, Tommy and all others that I could not mention, for their cheerfulness that have been encouraging me.

Lastly (but surely not the least), I would like to thank my family for all their love and encouragement. For my parents, who raised me with a love and supported me in all my pursuits. And most of all for my loving, supportive, encouraging, and patient wife Wening, whose faithful support especially during the final stages of this PhD. Words cannot express how much I have appreciated everything you have done for me, *terima kasih banyak*, I am so lucky to have you by my side.

"Merapi has never broken its promise --
The true key to disaster mitigation is the willingness of mankind to adapt to the will of nature and not to impose his own will against nature" – Surono

Résumé

L'intérêt de la télédétection appliquée aux volcans actifs et potentiellement dangereux a été démontré depuis longtemps dans la mesure où cette technique a participé à l'amélioration de la compréhension des processus éruptifs et des aléas volcaniques, amélioration qui permet une réduction des risques volcaniques. Nous avons entrepris plusieurs études volcanologiques reposant sur l'usage d'images de moyenne et haute résolution spatiale, qu'elles soient optiques (IKONOS, Pléiades, GeoEye, Quickbird and SPOT5), radar (ALOS-PALSAR) ou bien thermiques (ASTER et MODIS «hot spot»). Associées à l'analyse de MNTs et de photographies aériennes acquises par un drone, ces études ont consisté à appliquer des techniques de télédétection sur le Semeru et le Merapi, deux des volcans composites les plus actifs et les plus densément peuplés de l'ile de Java en Indonésie. Cette recherche fondée sur la télédétection a permis de mettre en évidence des structures géologiques et tectoniques, d'identifier, de classer et de cartographier des dépôts éruptifs sur les deux volcans et a servi à améliorer l'évaluation des risques à la suite des grandes éruptions de 2002-2003 au Semeru et de 2010 au Merapi. Nous avons également initié une étude afin de comprendre les interactions entre l'activité eruptive et le contexte sismo-tectonique régional en utilisant l'analyse des données MODIS avec la méthode MODVOLC.

Nous avons remis à jour la carte géologique du volcan Semeru en y associant des données issues de l'interprétation d'images HSR récentes, des photographies aériennes, l'analyse de MNTs et des observations de terrain, notamment dans le réseau hydrograhique qui convoie des lahars. Nous avons décrit l'histoire éruptive postérieure à 2001 au Semeru en incluant la grande eruption à l'origine des écoulements pyroclastiques (EPs) en 2002-2003 et les éruptions effusives de 2012-2014, qui consituent un phénomène rarement observé sur ce volcan. Le Semeru a produit un volume de $2.5 \pm 0.5\ 10^6 m^3$ de coulées de lave provenant du cratère sommital entre 2010 et 2014, ce qui peut annoncer, pour la première fois depuis 1967 ou 1941, une modification profonde du style éruptif de ce volcan. Au moment de terminer cette thèse, le dome-coulée situé dans le cratère Jonggring-Seloko continue à croître et les coulées de lave dépassent 2 km de longueur dans la cicatrice majeure en pente raide sur le flanc SE ; leurs fronts pourraient s'effondrer et produire des EPs dont le volume moyen

pourrait excéder les valeurs de 3 à 6.5 million de m^3 mesurées sur la période 1967-2007. Les écoulements futurs pourront déborder des parois de la cicatrice vers l'aval et se propager vers les vallées des flancs est et sud-ouest.

L'épisode éruptif du 26 octobre au 23 novembre 2010 s'est avéré l'événement majeur de l'activité du Merapi depuis 1872. Notre interprétation des images HSR démontre qu'à l'issue des éruptions explosives, le sommet du Merapi a perdu un volume de 10×10^6 m^3 et la gorge de Gendol orientée SSE a été élargie jusqu'à mesurer 1.3 x 0.3 x 0.2 km. Le nouveau cratère élargi et profond inclut le dome post-2010, qui a été fracturé en 2013, tandis que ses parois verticales instables peuvent être fragilisées par les explosions mineures de 2013 et 2014. Nous avons identifié et cartographié les dépôts pyroclastiques et de lahar de 2010 en appliquant plusieurs méthodes de classification aux images optiques HSR et aux données polarisées de Radar à Synthèse d'Ouverture (RSO). Les résultats démontrent la capacité de l'imagerie satellitaire HSR à capturer l'extension et les impacts de dépôts immédiatement après une grande éruption et avant tout remaniement. Cette technique met en exergue l'utilité de l'imagerie haute resolution et des données radar pour les volcans en activité persistante dont l'accès est souvent rendu impossible. Les dépôts de tephra et EPs de 2010 ont recouvert une surface de 26 km^2 environ dans les deux bassins versants des rivières Gendol et Opak sur le flanc sud le plus affecté, soit 60 à 75% de la surface totale des dépôts pyroclastiques et un volume estimé à 45×10^6 m^3. Les dépôts de retombée ont recouvert une surface de 1300 km^2 environ avec un volume estimé entre 18 et 21 x 10^6 m^3. Le débordement et l'avulsion des lahars constituent les menaces les plus graves le long des cours inférieurs des vallées comme la Kali Putih à l'ouest vers la ville de Magelang et la Gendol-Opak au sud vers le temple de Prambanan. Dans ce but, nous avons analysé une série de paramètres morphométriques des chenaux qui aident à déceler où et comment les lahars peuvent déborder du chenal principal et se propager dans des vallées peuplées adjacentes, qui ne sont pas directement exposées aux effets de ces écoulements. En somme, l'imagerie HSR, qui pour la première fois a été utilisée en Indonésie, les observations de terrain, la cartographie géologique et les mesures géophysiques, ainsi qu'une revue des recherches récentes et des simulations numériques ont aidé à améliorer l'évaluation des risques sur deux des volcans les plus dangereux et les plus peuplés d'Indonésie. Cette méthodologie peut être appliquée, de manière similaire, à d'autres volcans composites dans le monde.

Abstract

Remote sensing has long been recognized as a tool for analysis at active and hazardous volcanoes because it can augment our understanding of the processes that underlie volcanic activity so as enable us to apply this understanding to volcanic risk reduction. This thesis presents a volcanological study using High-Spatial Resolution optical images (IKONOS, Pléiades, GeoEye, Quickbird and SPOT5 satellites), radar data (ALOS-PALSAR sensor) and thermal (ASTER satellite and MODIS hot spot) images. In association with DEMs and low-altitude aerial photographs, remote sensing techniques have been applied for tracing the evolution of activity at Semeru and Merapi, two of the most active and densely populated volcanoes in Java, Indonesia. This remotely sensing-based study has unraveled structures, geological features and erupted deposits of both volcanoes and has improved the existing hazard assessment after their most recent eruptions. The thesis also presents the first advance towards deciphering possible interactions between regional tectonic earthquakes and renewed stages of eruptive activity of Merapi and Semeru volcanoes based on the analysis of volcanic hotspots detected by the MODVOLC technique.

The geological map of Semeru is updated, including additional data derived from the interpretation of the most recent satellite images, aerial photographs, DEM analysis and fieldwork. The post-2001 eruptive activity at Semeru, including the large PDC-forming eruption in 2002-2003 and uncommon lava flow eruptions in 2010-2014 are investigated. The fact that Semeru has produced several lava flows from the central summit vent between 2010 and 2014 may herald a profound change in eruption style for the first time since at least 1967. At the time of writing, a dome-fed coulée in the Jonggring-Seloko crater continues to grow and lava flows are extending to distances of >2 km down Semeru's SE-scar; their fronts may collapse and produce large-volume pyroclastic density currents (PDCs), perhaps exceeding the average (1967-2007) volume range of 3 to 6.5 million m^3. Future dome-collapse PDCs may travel farther down the main SE scar and can spill over its lowermost rims towards the southwest and eastward radiating drainage network.

The 26 October-23 November 2010 eruption was the Merapi's largest event since 1872 (it attained VEI=4). The interpretation of HSR images shows that due to the explosive eruptions, the summit area lost about 10 x 10^6 m^3 and the SSE-trending Gendol Breach enlarged to reach 1.3 x 0.3 x 0.2 km in size. The new, enlarged and deep summit crater including the 2010 lava dome is extremely unstable having been weakened by the post-2010 explosive events. This instability is a result of the steep Gendol Breach below the mouth of the crater and the steep and unstable crater walls. The 2010 Merapi pyroclastic and lahar deposits have been identified by applying several classification methods to HSR optical images and dual-polarization synthetic aperture radar (SAR) data. The results show the ability of remotely sensed data to capture the extent and impacts of pristine deposits shortly after emplacement and before any reworking, and highlight the purpose of using high-spatial resolution imagery and SAR data on persistently active volcanoes where access for field survey is often impossible. The 2010 tephra and PDC deposits covered ca. 26 km^2 in two catchments of Gendol and Opak Rivers on Merapi's south flank, i.e. 60-75% of the total PDC deposit area and a total bulk volume of 45 x 10^6 m^3. The tephra-fall deposit covered an area of ca. 1300 km^2 with a volume range of 18-21 x 10^6 m^3. Volumes of these deposits were estimated using the areas determined from remote sensing data and deposit thickness measured in the field. Lahar overspill and avulsion are the most hazardous processes acting along the lowermost river courses of Kali Putih towards the southwest flank of Merapi, and along the Gendol-Opak Rivers towards the iconic Prambanan temple. To address this problem, a set of morphometric characteristics of river channels has been analyzed, which indicate where and how lahars can spill over the principal river banks and avulse to otherwise unthreatened but populated valleys. Finally, HSR imagery, used here for the first time in Indonesia, in conjunction with field observations, geologic mapping and geophysical measurements, together with a review of recent surveys and flow simulations, have helped to improve hazard assessments at two of the most threatening volcanoes in Indonesia. This methodology can be applied to similar active composite volcanoes worldwide.

Sari

Penginderaan jauh telah lama dikenal sebagai suatu alat untuk analisis di gunungapi aktif dan berbahaya karena dapat meningkatkan pemahaman kita tentang proses yang mendasari aktivitas gunung berapi sehingga memungkinkan kita untuk menerapkan pemahaman ini dalam pengurangan risiko erupsi gunungapi. Disertasi ini menyajikan studi vulkanologi menggunakan citra satelit optik resolusi tinggi (IKONOS, Pléiades, GeoEye, Quickbird dan SPOT5), data radar (ALOS-PALSAR sensor) dan citra termal (satelit ASTER dan *hotspot* MODIS). Dalam kaitannya dengan DEM dan foto udara, teknik penginderaan jauh telah diterapkan untuk melihat evolusi aktivitas di Semeru dan Merapi, dua gunung berapi yang paling aktif dengan kepadatan penduduk yang tinggi terletak di Pulau Jawa, Indonesia. Studi berbasis penginderaan jauh ini telah mengkaji struktur, fitur geologi dan material erupsi dari kedua gunungapi tersebut dan telah mempertajam penilaian bahaya yang ada setelah erupsi terkini. Disertasi ini juga menyajikan kemajuan awal dalam menafsirkan kemungkinan interaksi antara gempa tektonik regional dan aktivitas gunungapi Merapi dan Semeru berdasarkan analisis *hotspot* vulkanik yang terdeteksi oleh MODVOLC.

Peta geologi Semeru telah diperbaharui dengan memasukkan data tambahan yang berasal dari interpretasi citra satelit terbaru, foto udara, analisis DEM dan data lapangan. Aktivitas erupsi pasca-2001 di Semeru, termasuk erupsi dengan aliran pirokastik (*Pyroclastic Density Current*/PDC) besar pada tahun 2002-2003 dan erupsi tidak biasa dengan aliran lava pada 2010-2014, telah dikaji. Fakta bahwa Semeru telah menghasilkan beberapa aliran lava dari kawah di puncak antara tahun 2010 dan 2014, mengindikasikan perubahan besar dalam gaya erupsi untuk pertama kalinya setidaknya sejak 1967. Pada saat penulisan disertasi ini, sebuah kubah lava (*Coulée*) di kawah Jonggring- Seloko terus tumbuj dan aliran lava yang memanjang hingga jarak >2 km arah tenggara Semeru; ujung lava kemungkinan dapat runtuh dan menghasilkan aliran piroklastik yang mungkin melebihi volume rata-rata (tahun 1967 hingga 2007) dalam kisaran 3-6.5 juta m^3. Aliran piroklastik yang akan datang mungkin mengalir sepanjang gawir utama ke arah tenggara dan dapat menyebar melampaui lereng paling bawah ke arah barat daya dan ke arah timur menyebar ke jaringan drainase.

Erupsi yang terjadi pada 26 Oktober-23 November 2010 adalah erupsi terbesar Merapi (mencapai VEI 4) sejak 1872. Interpretasi citra resolusi tinggi menunjukkan bahwa daerah puncak kehilangan batuannya sekitar 10 juta m^3 akibat erupsi eksplosif. Erupsi juga memperbesar "Gendol Breach" dengan orientasi tenggara menjadi berukuran 1.3x0.3x0.2 km. Kawah puncak yang baru, diperbesar dan dalam, termasuk juga kubah lava tahun 2010 sangat tidak stabil dan telah diperlemah oleh beberapa erupsi eksplosif pasca-2010. Ketidakstabilan ini diakibatkan oleh curamnya *Gendol Breach* di bawah mulut kawah dan kondisi dinding kawah yang curam dan tidak stabil. Deposit piroklastik dan lahar diidentifikasi dengan menerapkan beberapa metode klasifikasi terhadap citra optik resolusi tinggi dan data dual-polarisasi *Synthetic Aperture Radar* (SAR). Hasilnya menunjukkan kemampuan data penginderaan jauh untuk merekam jangkauan dan dampak dari deposit murni sesaat setelah pengendapan dan sebelum proses erosi, serta menyoroti tujuan penggunaan citra resolusi tinggi dan data SAR di gunungapi sangat aktif dengan akses untuk survei lapangan sering kali tidak memungkinkan. Endapan tephra dan PDC menutupi area sekitar 26 km^2 di dua DAS, Kali Gendol dan Opak, di sisi selatan Merapi, atau 60-75% dari total luas endapan PDC, dan total volume 45 juta m^3 . Deposit tephra jatuh menutupi area seluas sekitar 1.300 km^2 dengan volume 18-21 juta m^3. Volume endapan vulkanik ini diestimasi menggunakan informasi luas yang ditentukan dari data penginderaan jauh dan ketebalan yang diukur di lapangan. Luapan lahar dan avulsi adalah proses yang paling berbahaya terjadi di sepanjang hilir dari Kali Putih menuju sisi barat daya Merapi, dan sepanjang Gendol-Opak Rivers menuju Candi Prambanan. Untuk mengatasi masalah tersebut, satu set karakteristik morfometrik aliran sungai telah dianalisis, yang menunjukkan di mana dan bagaimana lahar dapat meluap ke tepi sungai dan beravulsi ke lembah yang dinyatakan tak terancam, namun padat penduduk. Terakhir, citra resolusi tinggi, yang digunakan pada studi ini untuk pertama kalinya di Indonesia, dalam hubungannya dengan observasi lapangan, pemetaan geologi dan pengukuran geofisika, bersama-sama dengan ulasan survei terbaru dan simulasi aliran, telah membantu untuk meningkatkan penilaian bahaya di dua gunungapi yang paling mengancam di Indonesia. Metodologi ini dapat diterapkan untuk gunungapi komposit aktif yang serupa di seluruh dunia.

Table of Contents

Acknowledgements i

Résumé iii

Abstract v

Sari vii

Table of Contents ix

Chapter 1: Introduction: Indonesian active volcanoes and remote sensing 1

1.1. Tectonic and volcanic background of Indonesia 1

1.2. Tectonics and volcanism 8

1.3. Remote sensing of volcanoes 10

1.4. Identification of the research problems 15

1.5. Objectives, thesis outline and methodologies 16

1.6. Remote sensing data 19

1.6.1. Optical imagery 19

- GeoEye-1 19
- WorldView-2 20
- Pléiades 20
- IKONOS 20
- SPOT 21

1.6.2. Thermal imagery 22

- ASTER 22
- MODIS 23

1.6.3. Radar imagery 23

- ALOS-PALSAR 23

1.6.4. Digital elevation models 25

Chapter 2: Semeru and Merapi volcanoes: Regional setting, geological structures and historical eruptions 27

2.1. Introduction 27

2.2. Geological, seismotectonic and geophysical contexts of Java Island 28

2.2.1. Geological context 29

2.2.2. Seismotectonic pattern 31
2.2.3. Deep and shallow structures beneath the edifice 34
2.3. Semeru volcano and the Tengger volcanic massif 36
2.3.1. Volcanic features and geology of the massif and edifice 36
- The Bromo-Tengger complex 37
- The Jambangan and Ajek-ajek complex 41
- Mahameru-Semeru volcano 43
2.3.2. Regional tectonic setting of the Semeru-Tengger massif 47
2.3.3. Eruptive history and hazard assessment at Semeru volcano 50
- Eruptive history 50
- Semeru volcanic hazards 52
2.4. Merapi Volcano: geology, tectonic setting, eruptive history and hazards 56
2.4.1. Volcanic features and geology of Merapi volcano 57
2.4.2. Regional tectonic setting of Merapi Volcano 62
2.4.3. Eruptive history and hazard assessment of Merapi volcano 63
- Eruptive history 63
- Merapi volcanic hazards and zonation 68

Chapter 3: Geomorphological evolution and post-2001 eruptive activity of the Semeru Volcano 71
3.1. Introduction 71
3.2. Geology of the Semeru volcano interpreted from high-spatial resolution satellite imagery 74

Geology, tectonics, and the 2002-eruption of the Semeru volcano, Indonesia: Interpreted from high-spatial resolution satellite imagery
Solikhin A, Thouret J-C, Gupta A, Harris AJL, Liew SC
Geomorphology 138 (2012) 364-379

Abstract 75
1. Introduction 75
2. Methodology 77
3. Volcanic features of the massif and of the edifice 77
4. Regional tectonic setting of the Semeru–Tengger massif 81

5. Structures and evolution of the Semeru summit cone 82
5.1. Structures and landforms 82
5.2. Evolution of the summit area: elongated SE-trending scar and deep Vent 84
6. The most recent 2002–2003 (vei 2–3) eruption 85
7. Conclusion 87
Acknowledgments 89
Appendix. Tables 1 and 2 89
References 90
3.3. Evolution of the Semeru summit cone after 2009 91
3.3.1. Structures and landforms of Semeru's summit cone 91
3.3.2. Evolution of the Jonggring Seloko crater and SE scar 94
- The 2002-2009 period 94
- The 2010-2014 period 98
3.4. Geometric characteristics of Kobokan and Lengkong catchments 101
3.5. Discussion 107
3.5.1. The 2009-2014 eruptive activity of Semeru 107
3.5.2. Hazard assessment of recent Semeru eruptive activity 110
3.6. Conclusion 113
Chapter 4: The deposits and impacts of the large (VEI 4) 2010 Merapi eruption 115
4.1. Introduction 115
4.2. High-spatial resolution imagery of the 2010 Merapi volcano eruption 117

High-spatial resolution imagery helps map deposits of the large (VEI 4) 2010 Merapi Volcano eruption and their impact
Solikhin A, Thouret J-C, Liew SC, Gupta A, Sayudi DS, Oehler J-F, Kassouk Z
Bulletin of Volcanology 70 (2015)

Abstract 118
Introduction 119
Data acquisition and processing 120
Remote sensing and field data 120

Supervised and object-oriented classification 121
The 2010 VEI 4 eruption 123
Impact of the 2010 eruption determined from HSR imagery 125
Morphological and structural changes on the volcano summit 125
Extent and behavior of pyroclastic deposits in the Gendol-Opak catchments 126
Post-eruption lahar deposits in 2011 134
Discussion 134
Instability of Merapi's crater rims 134
Behavior of the overbank PDCs and lahars 135
Volumes of the 2010 Merapi deposits 137
Conclusion 138
Acknowledgments 139
References 139

Chapter 5: The 2010 Merapi pyroclastic deposit map based on radar imagery 141

5.1. Introduction 141
5.2. Mapping the 2010 Merapi pyroclastic deposits using SAR data 143

Mapping the 2010 Merapi pyroclastic deposits using dual-polarization radar data
Solikhin A, Pinel V, Vandemeulebrouck J, Thouret J-C, Hendrasto M
Remote Sensing of Environment 158 (2015) 180-192.

Abstract 144
1. Introduction 144
2. Case study: the 2010 Merapi pyroclastic deposits 145
3. Data processing and methods 145
3.1. ALOS PALSAR dataset 145
3.2. Amplitude and coherence extraction 145
3.3. Amplitude evolution 147
3.4. Supervised classification 147
4. Results and discussion 148
4.1. Surface change detection 148
4.1.1. Coherence image 148

4.1.2. Ratio of amplitude image 148
4.2. Deposit classification 150
4.3. Accuracy assessment 152
5. Conclusion 154
Acknowledgments 155
References 155

Chapter 6: Response of Merapi and Semeru eruptive activity to regional tectonic events: first results 157

6.1. Introduction 157
6.2. Method 160
6.3. Seismic and thermal radiance data for Merapi and Semeru 163
6.3.1. Seismicity 163
6.3.2. MODIS-derived radiance data 167
6.4. Results 170
6.4.1. Merapi volcano response to regional earthquake 170
- January-June 2001 170
- 10 May-14 June 2006 173
- January 2009-March 2011 174
- January 2012-May 2014 177
6.4.2. Merapi volcano response to regional earthquake 180
- February 2002-January 2003 180
- January 2004-December 2005 181
- May-July 2006 182
- June-December 2014 184
6.5. Discussion: MODVOLC data for volcano monitoring 187
6.6. Conclusion and perspectives 188

Chapter 7: Conclusion and Perspective 191

7.1. Remote sensing contributions 191
7.1.1. Semeru Volcano 192
7.1.2. Merapi Volcano 193
7.1.3. Remote sensing-based mapping of pyroclastic deposits 195
7.1.4. Earthquake-volcano interactions 197

7.2. Limitation and research perspectives 197
7.3. Hazard assessment 199
Bibliography 203
Appendix A: List of satellite images 225
Appendix B: Supplementary data to Solikhin et al. (2015b) 227
Appendix C: Supplementary data to Solikhin et al. (2015a) 229

Chapter 1 – Introduction: Indonesian active volcanoes and remote sensing

1.1. Tectonic and volcanic background of Indonesia

The vast Indonesian archipelago consists of 17,508 islands located at sub-equatorial latitudes (6°N-11°S) at the boundaries of three major tectonic plates, namely Indo-Australia, Eurasia, and Pacific-Philippine Sea plates (Fig. 1.1A). The present-day geology of Indonesia is broadly the result of Cenozoic subduction and collision at this margin (Hall & Smyth, 2008). Western Indonesia is partly underlain by continental crust whereas Eastern Indonesia has a complex basement (including arc, ophiolites and several young ocean basins) owing to a long period of extension, subduction and collision (Hall, 2009). As a consequence of this complex geodynamic setting, Indonesia is bordered by tectonically active zones characterized by intense seismicity and volcanism (Fig. 1.1).

Present-day volcanic activity in Indonesia has been interpreted as the product of four separate volcanic arcs (in chronological order): Sunda, Banda, Halmahera and Sangihe Arcs (Fig 1.1B). The wide lateral extent of the Sunda Arc, over 3000 km from NW Sumatra to the Banda Sea, includes 78% of Indonesian volcanoes. The Sunda arc has been active since the Eocene (Hamilton, 1979; Hall, 2002) and is the product of subduction of the Indian Ocean crust beneath the margin of Sundaland (the continental core of Southeast Asia). The horseshoe-shaped Banda Arc of eastern Indonesia is due to the subduction of an embayment within the northward-moving Indo-Australian plate (Hamilton, 1979; Hall, 1995, 2002; Charlton, 2000). The Banda volcanic arc has been active only for ~10 Ma (Honthaas et al., 1999) and developed within the collision zone after the Australian margin collided with the former active margin of the Sunda Arc (Hall & Smyth, 2008). North of Banda arc, tectonic complexity increases, with converging plate fragments forming multiple subduction zones, mainly oriented N-S, which in turn produced the Sulawesi-Sangihe volcanoes to the west and Halmahera to the east of the collision zone. The Halmahera and Sangihe Arcs formed during the Neogene and are the only intra-oceanic arcs in the world, which are currently colliding (Hall, 2009).

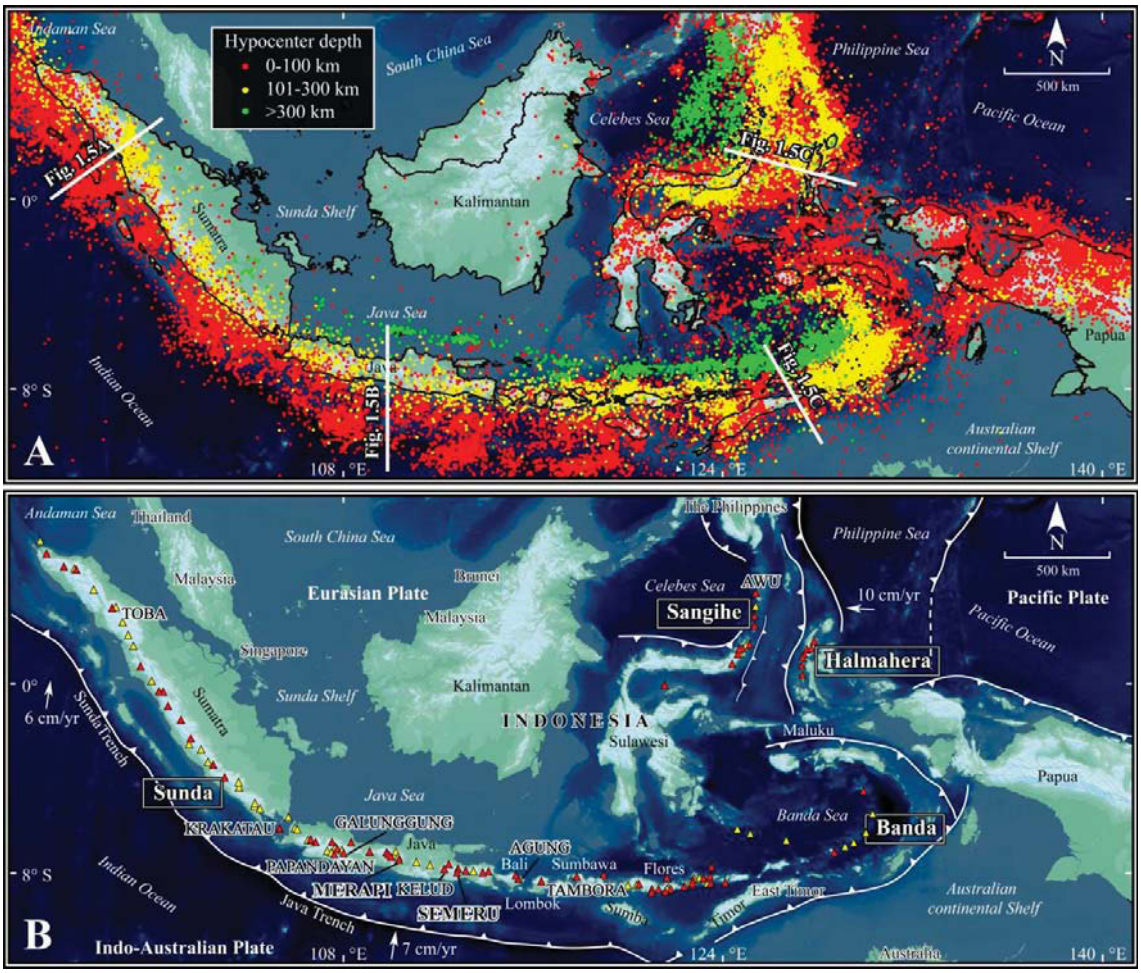

Figure 1.1. A. Seismicity in the Indonesian region between 1964 and 2013 (Source: Bulletin of the International Seismological Centre). The circles with three different colors indicate the earthquake epicenters with three different ranges of depth. **B.** Map of the Indonesian subduction zones showing the present-day tectonic boundaries and distribution of active volcanoes (yellow and red triangles). Red triangles indicate 69 very active volcanoes, which are monitored continuously by CVGHM. Some of the well-known volcano names appear in capital letters. Arrows indicate the direction of plate relative motions with respective convergence rates (Widiyantoro & Van der Hilst, 1997).

The subduction zones are associated with seismicity extending to a depth of about 600 km (Fig. 1.1A) and volcanoes within 250-350 km from the trench axis (Fig. 1.1B). Most volcanoes are located between 100 and 120 km above the descending lithospheric slabs. Indonesian historically active volcanoes, totaling 1250 confirmed eruptions, are second only to Japan with 1469 historical eruptions (Siebert et al., 2010). However, many small eruptions in Indonesia have not been catalogued while historical records of volcanic eruption in Japan are more comprehensive. There are 127 active volcanoes in Indonesia, and at least 77 among them have erupted since 1600. Volcanoes in Indonesia and Japan produce nearly one third of the reported pyroclastic density current (PDC)-producing

eruptions. Among the Indonesian Holocene volcanoes, 32 have records of very large eruptions with a volcanic explosive index (VEI) greater than 4 and 19 of these volcanoes have erupted within the past 200 years. The 1815 eruption of Tambora volcano, Sumbawa Island, caused the historical largest number of fatalities due to a single eruption. This eruption triggered the "year without a summer" in 1816 in the Northern Hemisphere, when crops withered, causing famine and population migrations (Harington, 1992; de Boer & Sanders, 2002). The 1257 eruption of the Samalas volcano, adjacent to Mt. Rinjani on Lombok Island, with an estimated magnitude of VEI 7 is also thought to be one of the largest Holocene eruptions. This eruption formed the 6 x 8.5-km-wide Sagara Anak caldera and the horseshoe-shaped collapse structure that deeply incises the western flank of Rinjani volcano. This eruption has been identified as the source of the great mid-13C "mystery eruption" that is associated with the largest sulfate deposition within polar ice core records from the past 7000 years (Lavigne et al., 2013). The eruption of Toba on Sumatra 74,000 years ago was even more violent (estimated VEI 8) and is the largest known eruption on Earth within the last 2 million years (Chesner, et al., 1991).

Volcanic slopes in Indonesia typically are blessed with fertile soils, abundant amount of water and beautiful landscapes; hence, this country easily leads the world in population density around volcanoes. About 5 million people live on the flanks (within 10 km away from the summit) of 77 Indonesian persistently active volcanoes and many more are at risk on the lower flanks and across ring plains (Siebert et al., 2010). The most densely populated Indonesian volcano within a radius of 30 km (Fig. 1.2A) is Tangkubanparahu (5.7 million people) located in West Java, followed by Merapi (4.3 million people) in Central Java. Indonesia has many major cities that are located within 30 km of any active volcano as shown in Figure 1.2B. Some cities and their populations are potentially exposed to hazards from more than one volcano. For example, Garut in West Java is located within 13, 16 and 21 km away from Guntur, Galunggung and Papandayan volcanoes, respectively. The combination of a densely packed population in a volcano-rich country has led Indonesia to suffer the highest number of eruptions with fatalities and damage to infrastructure.

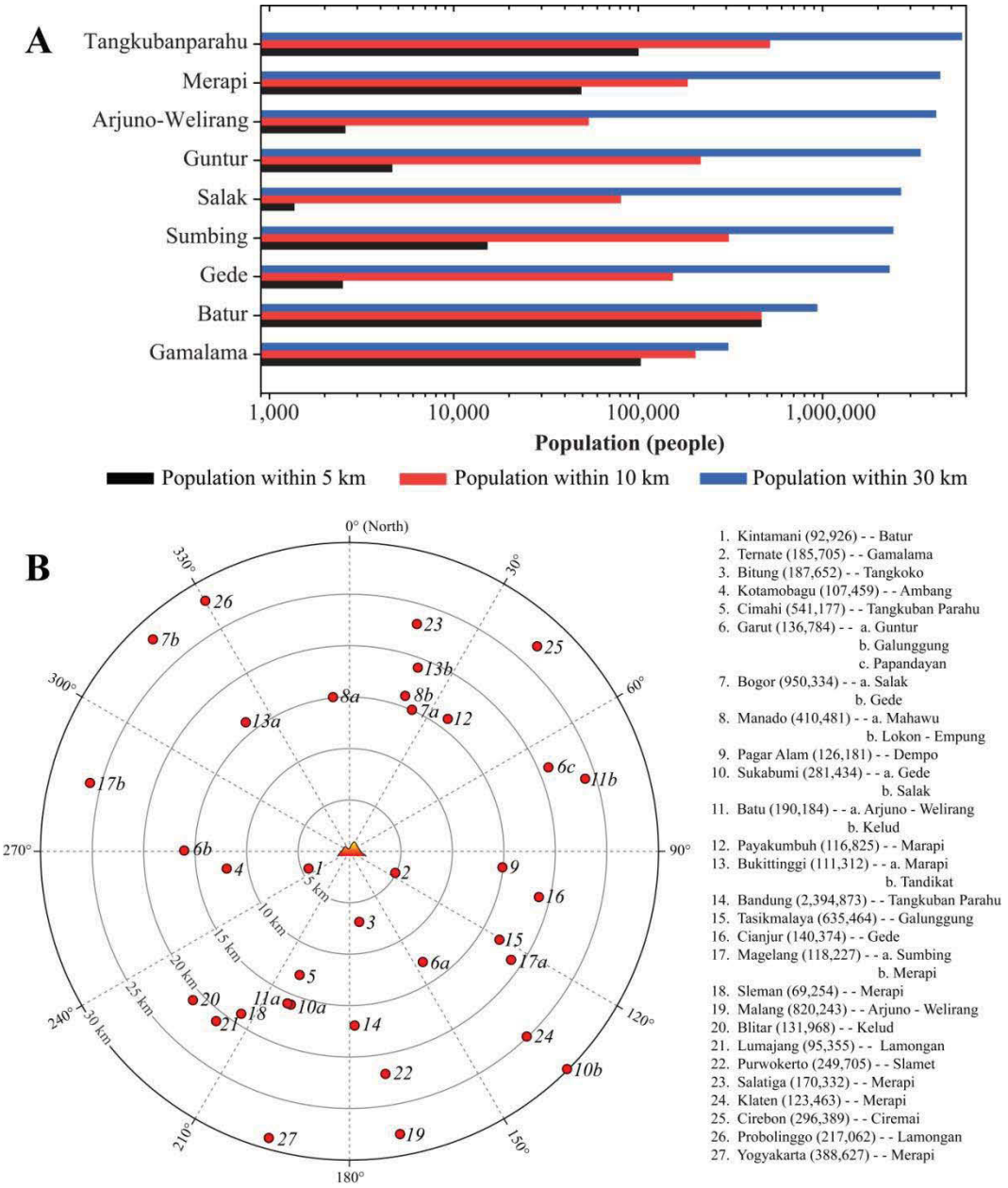

Figure 1.2. A. Chart showing the number of people living in the area within 5, 10 and 30 km of the nine Indonesian most densely populated active volcanoes. B. Virtual target chart showing location and distance of major cities (red circles) in Indonesia from volcanoes, with names and population numbers shown in parentheses. Population data based on the Indonesia 2010 census (BPS, 2011).

In the 1900-2009 period, no less than 70 events occurred in Indonesia, which caused 18,840 fatalities or 18.4% of the worldwide reported volcano mortality (Doocy et al., 2013). Figure 1.3 shows the deadliest volcanoes in Indonesia with their total fatalities and maximum eruption magnitude. Fatalities due to the first two volcanoes are indirect results of eruptions as most of people died from starvation after the 1815 Tambora eruption and in the wake of the 1883 Krakatau volcanogenic tsunami. The probability

that volcanic activity will result in death or injury clearly depends on a variety of factors including the distance from the volcano on which people live, the size of population, the types of relevant volcanic hazards, and the magnitude and frequency of activity. In 1920, the government established the Volcanological Survey of Indonesia (VSI), now known as the Center for Volcanology and Geological Hazard Mitigation (CVGHM), leading to much improved volcano monitoring and recording. In order to monitor continuously 69 very active volcanoes in Indonesia (red triangles in Fig. 1.1B), a network of 76 volcano observatories was installed and is operated by the CVGHM. In recent decades, CVGHM has evacuated people living near volcanoes prior to several large eruptions, avoiding fatalities except for a few eruptions. For example, during the 1982 Galunggung eruption 75,000 people were evacuated, reducing the fatalities to 68, and during the 1990 Kelud eruption, 60,000 people were evacuated, reducing the fatalities to 32. Another example that illustrates the value of carefully monitoring volcanoes is the management of the 2010 Merapi eruption, which led to displacement of almost 400,000 people living within 20 km from the summit for one and a half months. The 2010 Merapi eruption caused about 367 fatalities; however, this number is relatively small compared to the number of people who would have died without the evacuations, estimated to range between 10,000 and 20,000 people (Surono et al., 2012).

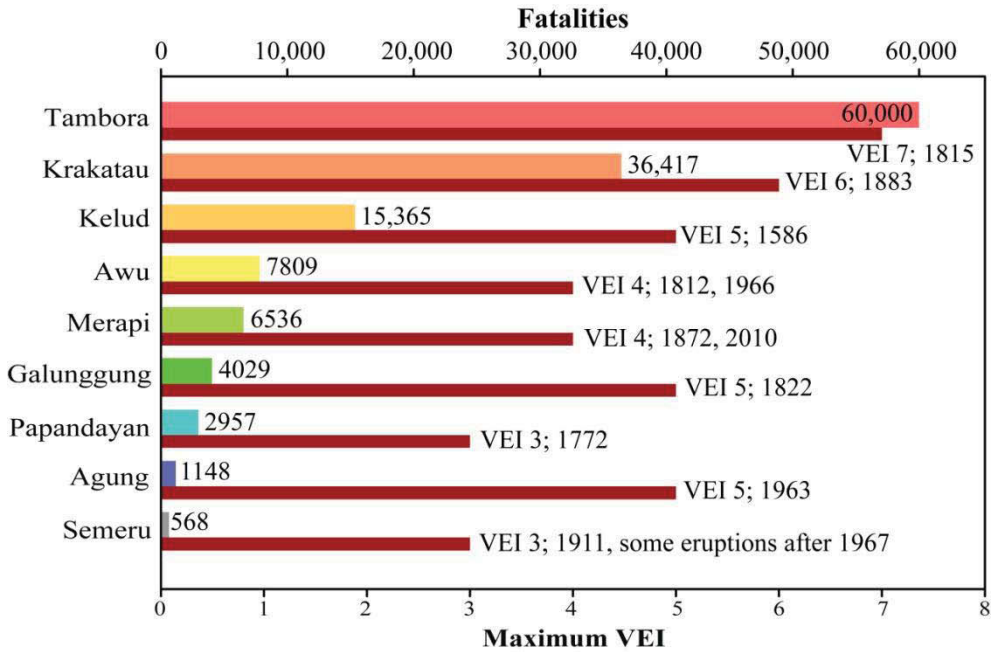

Figure 1.3. Number of fatalities caused by eruptions of nine Indonesian volcanoes and their maximum magnitude in historical records based on Blong (1984), Tanguy et al. (1998) and Siebert et al. (2010).

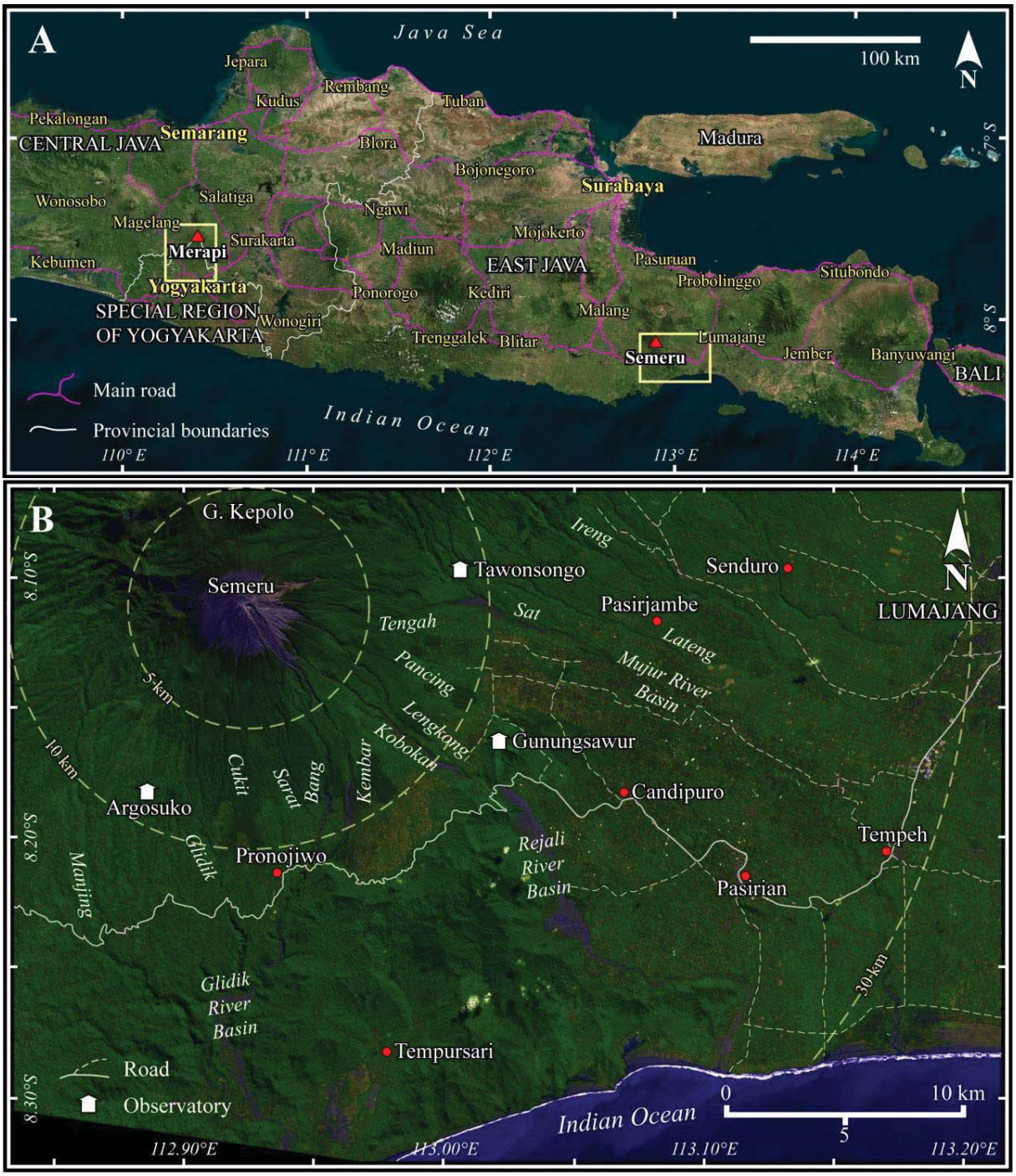

Figure 1.4. A. Geographic map of eastern part of the Java Island showing the location of Semeru and Merapi volcanoes (the base image uses Bing Aerial Maps). **B.** The 15 June 2012 ASTER image shows the Semeru composite cone and principal rivers, cities, towns, roads, and volcano observatories in the south and east ring plain.

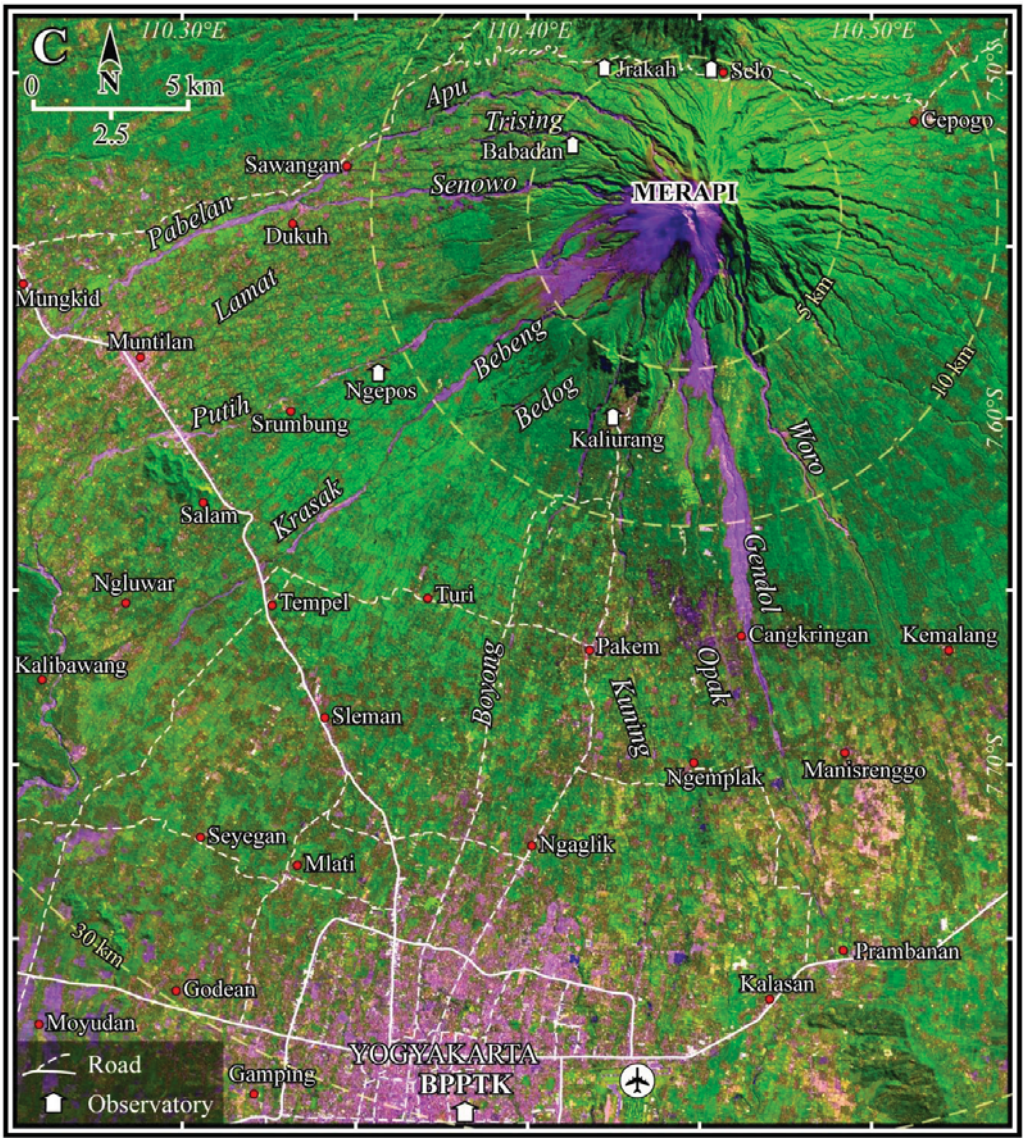

Figure 1.4. (continued) **C.** The 13 June 2012 ASTER image shows the Merapi volcano including the principal rivers, cities, towns, roads, in the south and west ring plain and the six volcano observatories.

This thesis focuses on the active and densely populated Semeru and Merapi volcanoes in Java Island (Fig. 1.4) using remote sensing methods. Semeru is the highest volcano in Java (3676 m asl) and one of the most active volcanoes on Earth. Semeru eruptive activity has been recorded since 1818 and daily eruptive activity has been persistent at least since 1967. Phreatomagmatic or Strombolian eruptions occur almost daily from the Jonggring-Seloko crater. Extrusion, growth and collapse of lava domes in the Jonggring-Seloko Crater have occurred every 5 to 7 years. Ring plain within 5, 10, and 30 km of Semeru (Fig. 1.4B) is home to 2686, 8375 and more than 1 million inhabitants, respectively (Siebert et al., 2010). Another very active volcano in Indonesia is Merapi,

which lies about 30 km north of the major city of Yogyakarta (Fig. 1.4C). More than 74 eruptions were recorded at Merapi since 1548, and at least seventeen of them, including the one in 2010, caused fatalities. About 49,000, 185,000 and more than four million people live on the ring plain of Merapi volcano within a radius of 5, 10 and 30 km, respectively (Fig. 1.4C; Siebert et al., 2010). As Semeru and Merapi are difficult and dangerous to access, remote sensing methods are useful for studying these persistently active volcanoes.

1.2. Tectonics and volcanism

The majority of the most active and dangerous volcanoes in the world are explosive composite volcanoes that are located above subduction zones. Four profiles across the arc-trench systems of Sumatra, Java, Banda and Sangihe-Halmahera are displayed in Figure 1.5 (after Simandjuntak & Barber, 1996). Oblique (50-65°) convergence of the Indian Ocean and Eurasian plates produces the island of Sumatra. The subduction system includes an accretionary complex, exposed in the offshore islands such as Nias and Mentawai and a fore-arc basin (Fig. 1.5A). The Sumatran fore-arc is driven northwards along the Great Sumatran strike-slip fault by the movement of the Indian Ocean plate, and back-arc basins lie to the NE, behind the arc. In the Java region, convergence between the Indian Ocean and SE Asian plates is normal to the subduction trace in the Java Trench (Fig. 1.5B). The subduction system comprises an accretionary complex in the Java fore-arc ridge, fore-arc basin, Java volcanic arc and back-arc basin. Compression across the Java subduction system has resulted in back-arc thrusting. In the Banda arc, the Australian craton has been subducted beneath the accretionary and collision complex in the Timor Ridge (Fig. 1.5C). Subduction has ceased in this segment of the collision zone, but the collision complex has been driven over the volcanic arc, which has in turn been driven over the Banda Sea plate to the north in the earliest stages of subduction reversal. In the Molucca Sea region of northeastern Indonesia, the Sangihe and Halmahera arcs are presently in the process of colliding, the Earth's only example of a collision between facing volcanic arcs (Fig. 1.5D). The Molucca Sea plate is subsiding between the colliding Sangihe and Halmahera fore-arcs. The Sangihe fore-arc has been thrust over the Halmahera fore-arc to form the Talaud Ridge. Subduction of the Sulawesi Sea plate has commenced only recently.

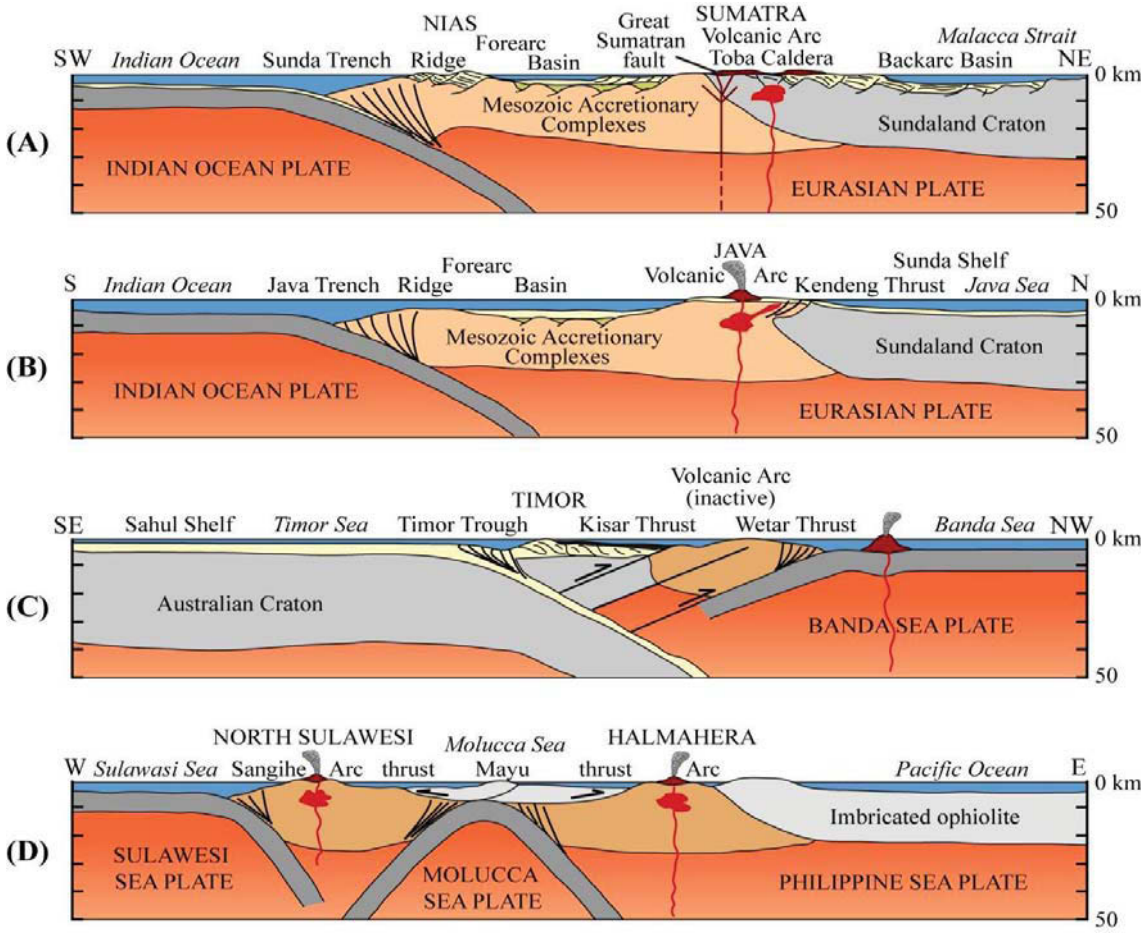

Figure 1.5. Schematic geologic sections across **(A)** Sumatra, **(B)** Java, **(C)** Banda, and **(D)** Sangihe-Halmahera volcanic arcs (after Simandjuntak & Barber, 1996). The cross profiles are indicated in Fig. 1.1A.

Apparent links exist between earthquakes, volcanoes, and plate tectonics as the major seismic and volcanic belts concentrated along the convergent boundaries between plates, for example around the Indo-Pacific rims including Indonesia and the Philippines (Fig. 1.1). A causal relationship between large earthquakes and volcanic eruptions might be expected given that an eruption can be induced by a change in dynamic or static stresses. Seismic waves associated with the dynamic stress are large in magnitude but not permanent, whereas static changes are smaller but permanent (Manga & Brodsky, 2006). Dynamic stress can cause a reduction of co-seismic crustal seismic velocity as it is related to the mechanical weakening of the pressurized crust (Brenguier et al., 2014). The stress change is also the result of the presence of a magma reservoir and/or feeding system-containing gas, such that the effects of a given perturbation might be

complicated by complex processes, among them the rectified diffusion (Brodsky et al., 1998; Walter et al., 2007; Walter & Amelung, 2007). Rectified diffusion is a mechanism by which a strain wave can rapidly pump volatiles into a bubble and therefore increase the pressure in a closed system (Brodsky et al., 1998). Triggered eruptions may occur shortly in time and/or with a delay of days, month, or year after an earthquake. However, many large earthquakes have no immediate effect on volcanoes. Approximately 0.4% of explosive volcanic eruptions occur within a few days of large, distant earthquakes (Manga & Brodsky, 2006). Eruption triggering depends on the initial state of the magmatic system prior to the earthquake, i.e., on magma composition, state of equilibrium of magma and volatiles, magma overpressure, and the strength of the host rocks, and on the type, size, and distance of the earthquake (Hill et al., 2002). Similarly, volcanic processes are able to promote earthquakes along neighboring faults by increasing the Coulomb stress or by increasing fluid pore pressure (e.g. Toda et al., 2002; Feuillet et al., 2006; Albino et al., 2010; White & McCausland, in press). Continued scientific studies in understanding this phenomena are fundamental to providing reliable information on the nature of hazards that large earthquakes and volcanic eruptions pose to the many population centers at risk around the world.

1.3. Remote sensing of volcanoes

A major goal of volcanology is to understand the processes that underlie volcanic activity, and to use this understanding in volcanic risk reduction. Volcanic eruptions are spectacular events and studying these natural phenomena can be a challenging task because of the diversity of activity and remote locations. Volcanoes also have footprints that may extend across many hundreds or thousands of square kilometers, and sometimes their eruption products can be scattered or dispersed over regional or global scales. Consequently, since direct measurements can only provide us with part of the picture of many volcanic processes, remote sensing is now playing an increasingly important role in advancing understanding of the mechanism underlying volcanic behavior (e.g. Mouginis-Mark et al., 2000; Sparks et al., 2012; Pyle et al., 2013, Pinel et al., 2014). Remote sensing also plays an important role when ground-based volcano monitoring and fieldwork are not possible due to meteorological or political conditions (Head et al., 2012). Remote sensing is the measurement or analysis of properties of the

Earth's surface from a distance. Satellite, airborne and ground-based remote sensing are increasingly vital tools for monitoring active or potentially active volcanoes, and assessing their likely real-time or time-averaged impacts (Fig. 1.6). Advances in instruments and techniques mean that scientists can now measure many different aspects of the behavior of restless or active volcanoes, including seismicity, deformation, geomorphic change and emissions of heat and gas. Although measurement of seismicity requires sensitive instruments placed close to the volcano, remote sensing techniques have made major contributions to each of other measurement fields.

Figure 1.6 illustrates remote-sensing approaches using instruments operating at different wavelengths from the ultraviolet to microwave (c. 3 x 10^{-7} to 0.3 m wavelengths) regions of the electromagnetic spectrum, which can be used to monitor volcanoes, volcanic processes and volcanic products throughout an eruption cycle from pre-eruption repose to post-eruption relaxation. New developments in remote-sensing techniques have expanded the capability of scientists worldwide to monitor volcanoes using satellite data. Mouginis-Mark and Domergue-Schmidt (2000) describes six ways satellites are used for monitoring volcanic eruptions: (1) Rapid detection of an eruption plume to mitigate risk for civil aviation (e.g. Schneider et al., 2000); (2) Monitoring thermal energy emitted from a volcano (e.g. Harris et al., 1997 & 2000); 3) Large area mapping of surface deformation of a volcano (e.g. Massonet & Sigmundsson, 2000); (4) Measurement of volcano topography and topographic change to estimate the volume of new material erupted or the magnitude of collapse (e.g. Zebker et al., 2000; Bignami et al., 2013; Pallister et al., 2013); (5) The determination of the spatial distribution of ash, gas and aerosols produced by eruptions (e.g. Krueger et al., 2000; Yu & Rose, 2000), and; (6) The development of a reference remote sensing data set for each volcano for quantifying future changes (Mouginis-Mark et al., 2000). Beside these six ways, remote sensing techniques also enable to delineate and identify fresh erupted material on and around active volcanoes as well as to trace topographic changes due to eruptive activity (Solikhin, et al., 2012, 2015a, 2015b)

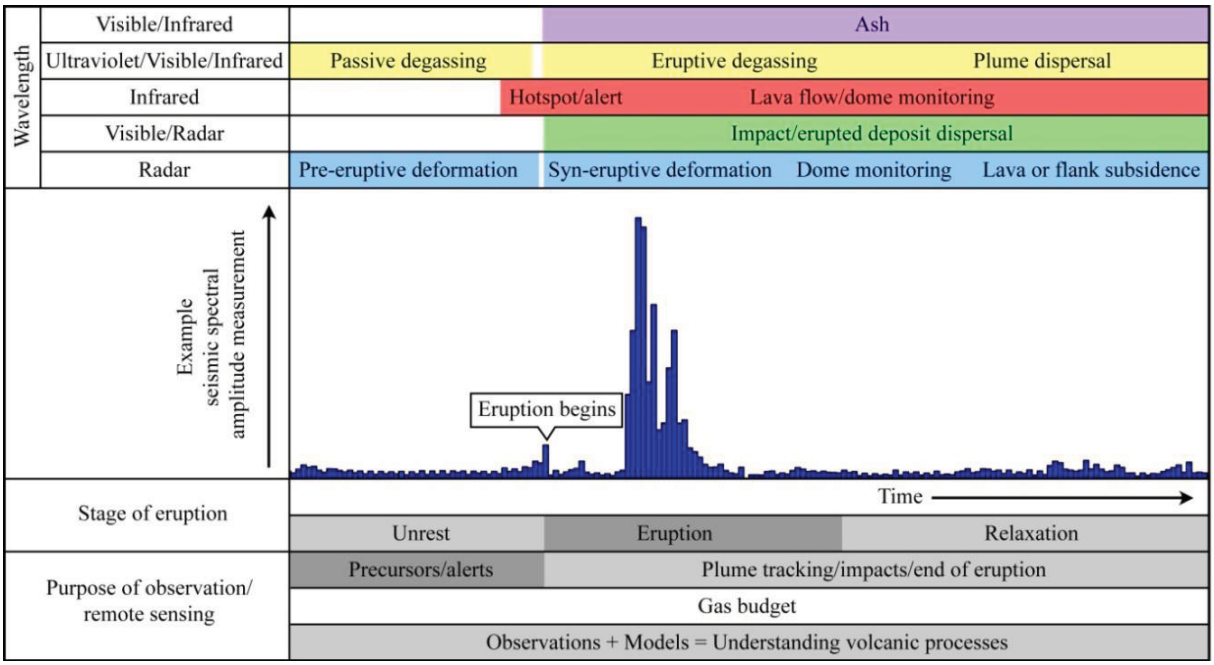

Figure 1.6. An illustration of some of the applications of remote-sensing techniques to a volcano during a hypothetical eruption cycle (after Pyle et al., 2013). The example data of seismic spectral amplitude measurement (SSAM) stems from the recorded seismic energy released at Merapi over the October to December 2010 period including the 2010 eruption episode (26 October-23 November 2010). "Geomorphic change" is included in "deformation" in this figure.

Within the remote sensing community, two categories of satellites (geostationary and low Earth orbit) have evolved due to the diversity in science objectives and the size and precision in areas to be covered. Geostationary satellites are launched in such a way that they follow an orbit parallel to the Equator and travel in the same direction as the Earth's rotation with the same period of 24 hours. A satellite following a geostationary orbit always views the same area of the Earth. Satellites in the geostationary orbits are located at a high altitude of 36,000 km from the Earth's surface and commonly are meteorological satellites. Through their innovation, volcanologists have been able to derive and use meteorological satellite data beyond their original application including the surveillance of volcanic thermal phenomena and eruption plumes, and mapping areas covered by tephra fall deposits (Oppenheimer, 1998). Meteorological satellite data combined with other satellite data and numerical modeling (e.g. Carn et al., 2003; Tupper et al., 2004; 2009) are also very useful in monitoring and forecasting volcanic ash dispersion for aviation safety. Coordination and dissemination information on atmospheric volcanic ash clouds that my endanger aviation is the responsibility of the

Volcanic Ash Advisory Center (VAAC), which has nine Centers located around the world, and each one focusing on a particular geographical region.

A satellite on a low-Earth orbit (<1000 km altitude) is favored to obtain high spatial or spectral resolution data which increases the spatial resolution and signal-to-noise ratio of the data for the similar set of sensor optics and detectors. Earth observation satellites usually follow sun synchronous orbits. A sun synchronous orbit is a near polar orbit whose altitude is such that the satellite will always pass over a location at given latitude and at the same local solar time. In this way, the same solar illumination condition (except for seasonal variation) can be achieved for the images of a given location taken by the satellite. In addition to satellite remote sensing, airborne remote sensing data is also used by volcanologists. In airborne remote sensing, downward or sideward looking sensors are mounted on an aircraft to obtain images of the Earth's surface. An advantage of airborne remote sensing, compared to satellite remote sensing, is the capability of offering very high-spatial resolution images (50 cm or less) and low-atmosphere detection (e.g., of low-altitude gas emissions). The disadvantages are low coverage area and high cost to the end user in cost per unit area of ground coverage. Airborne remote sensing missions are often carried out as one-time operations, whereas Earth observation satellites offer the possibility of continuous monitoring of the Earth.

Each volcano has a unique history of activity and individual eruptions can evolve over periods ranging from hours to more than a decade, so that many volcanic hazards must be studied via a range of techniques. The basic description of the topography of a volcano is one of the most important parts of volcanic hazard evaluation, because most volcanic hazards are controlled by gravity and topography where volcanoes are topographic irregular highs, which threaten their lower surroundings through gravitational potential energy. At all volcanoes, including those in repose, topographic data can be used for the formulation of models predicting which path a pyroclastic density current, debris avalanche or a lahar may follow. In addition, accurate topographic information as Digital Elevation Models (DEMs) are required for ortho-rectification of remotely sensed images, such that quantitative measurement of change is possible. Ground 'truth' or field observations also play a vital role in developing remote sensing capability by allowing verification of models and remotely sensed observations and in ensuring that remote sensing works in the way envisioned. Field

measurement and observations also provide an opportunity to develop more diverse and more precise models by ensuring that direct experience with the volcano occurs, such as determining the past eruptive history and vulnerability of populations as a context for forcasts.

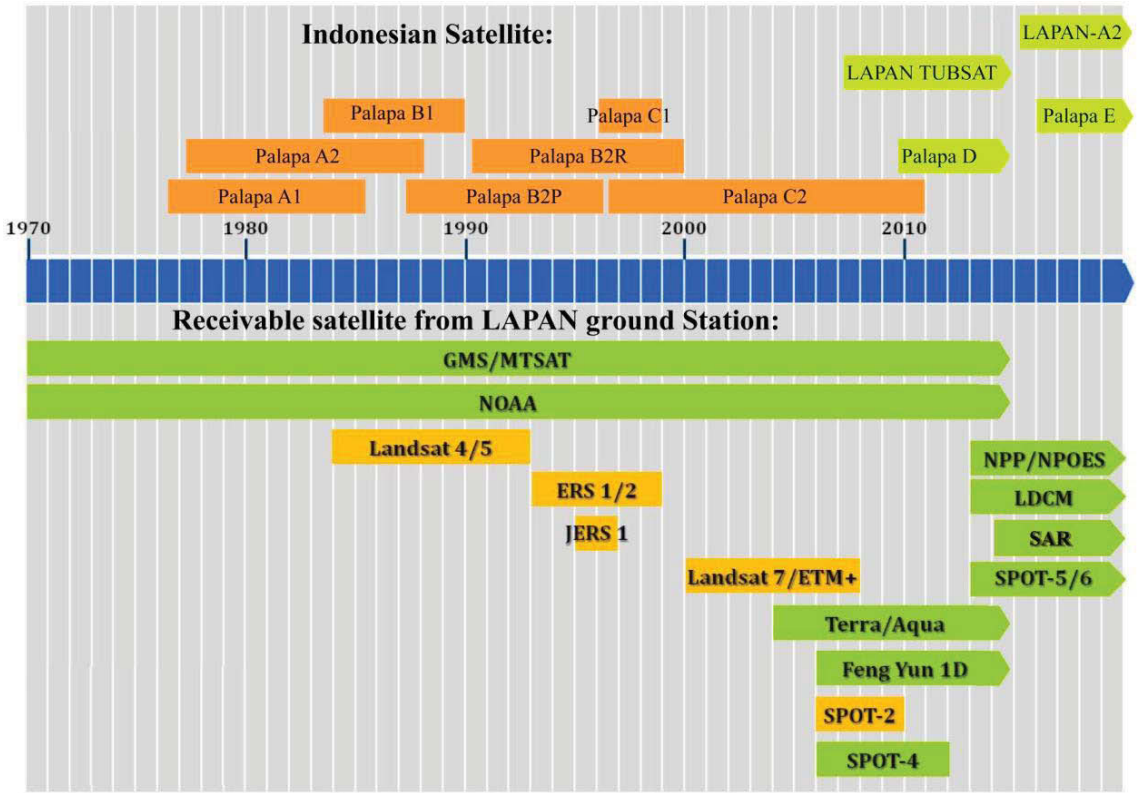

Figure 1.7. List and operation times of Indonesian satellites and remote sensing satellites that can be acquired by LAPAN ground stations.

CVGHM, in charge of monitoring, hazard assessment and warning for all volcanoes in Indonesia, also uses remote sensing in its duties, particularly in research, observation during the volcanic crisis and limited use in monitoring. In using remote sensing, CVGHM collaborates with other institutions both foreign and domestic, one of which is Indonesian National Institute of Aeronautics and Space (*Lembaga Penerbangan dan Antariksa Nasional,* LAPAN). In 1984, LAPAN initiated the use of Earth observation satellite in Indonesia by installing the ground station in Jakarta to acquire Landsat data. Indonesia has launched several satellites and some are still in operation (Fig. 1.7), most are communication satellites except TUBSAT that is also equipped with a video recorder. LAPAN also operates four ground stations (in Jakarta, Bogor, Pare-pare and Biak) to acquire data from remote sensing satellites (Fig. 1.7). LAPAN actively provides information based on remote sensing satellite data related to volcanic eruptions in

Indonesia. Besides LAPAN, the Centre for Remote Imaging, Sensing and Processing (CRISP) of the National University of Singapore (NUS) also operates a satellite ground station that covers western and central part of Indonesia. CRISP satellite ground station is capable to acquire data from SPOT 1, 2, 4, 5, ERS 1, 2, Radarsat 1, SeaWiFS, MODIS, IKONOS, GeoEye-1, Worldview I, II, and XSAT. The U.S. Geological Survey also provides satellite remote sensing data to CVGHM for use in monitoring and crisis response, including assistance with management of the International Charter for Space and Major Disasters.

1.4. Identification of the research problems

The interest of remote sensing has long been emphasized at active volcanoes where ground-based monitoring and fieldwork are hazardous and impossible due to natural conditions (persistent eruptive activity, dense vegetation, rugged relief, etc.). Until recently, volcanological research focused on monitoring active volcanoes or studying a posteriori volcanic events and their deposits. Repose periods between eruptions can be decades to thousands of years long, but not for Semeru and Merapi, two persistently active volcanoes in Indonesia, which are the objects of this research project. For volcanic hazard assessment on active volcanoes, there is an obvious need to map and characterize the range of past deposit types to infer the range of activity that the volcano may exhibit. Prior to geological mapping, the description of the edifice topographic map is also essential for volcanic hazard evaluation. The emergence and improvement of various kinds of satellites that produce high-spatial resolution images (e.g. GeoEye, WorldView, Pléiades and IKONOS) over the first decade of the twentieth century allow volcanologists to conduct more detailed remote sensing studies of active volcanoes. However, there is always the need to assess the accuracy of the quantitative data retrieved from satellite imagery.

Merapi is the best-monitored and studied volcano in Indonesia. Short-lasting return period of Merapi eruptions (between 2 to 8 years) in this modern era (over the past 250 years) have allowed scientists to examine and develop their methods and monitoring tools in order to improve the understanding of the volcano in a wide range of disciplines. Merapi has been long monitored (since 1924) by CVGHM through its observatory and technological center in Yogyakarta (*Balai Penyelidikan dan Pengembangan Teknologi*

Kegunungapian, BPPTK). The surveillance network includes four short-period permanent seismometers and five temporary broadband seismometers, eight continuous geodetic global positioning system (GPS), five tiltmeters and electronic distance measurement (EDM) measuring defomation patterns from five observation posts (Fig. 1.4C). In the first decade of the twentieth century, the ground-based monitoring system together with remote sensing imagery has proven reliable in detecting precursory events of Merapi eruptions, which in turn enabled warnings to the communities living on and around the volcano.

Compared to Merapi, Semeru is less understood and currently monitored by a less complete network of five seismic stations and one tiltmeter. Data from these stations are transmitted to the observatory post at Gunung Sawur on the SE flank (Fig. 1.4B). Semeru has been in almost continuous eruption since 1967, dominated by small- to moderate-volume Vulcanian/phreatomagmatic explosions from the summit crater as well as dome growth and occasional stubby lava flows. This association alternates with episodic but large explosive eruptions that produce pyroclastic density currents that have reached >12 km on the lower flanks of the volcano (Thouret et al., 2007). Semeru has also been reported as one of the most effective lahar producers on Earth (Lavigne & Thouret, 2002; Lavigne & Suwa, 2004; Thouret et al., 2007, 2014).

As the persistently activity of a composite volcano results in rapid evolution of its summit and flanks, hazard assessment for risk prevention and human response must be prepared periodically and/or immediately after the eruption. Thus, remote sensing methods will play a significant role to map and quantitatively study the structure, morphology and texture of volcanic terrains at different scales, in order to gain insights into eruption processes and hence to improve hazard assessment.

1.5. Objectives, thesis outline and methodologies

In the framework of the international collaboration between the Center for Volcanology and Geological Hazard Mitigation (CVGHM) in Indonesia and the Laboratoire Magmas et Volcans (LMV), supported by the Institut de Recherche pour le Développement and the French-Indonesian Institute in France, a PhD research project started in October 2011. The thesis aims to improve the application of remote sensing techniques to study the

Semeru and Merapi volcanoes. The research project has three objectives: (1) to analyze the geological structure of the edifices and their regional tectonic setting; (2) to analyze the most recent, post-2001 eruptions of Semeru and Merapi as well as their products (especially pyroclastic density current (PDC) deposits) in order to assess the associated volcanic hazards, and (3) to examine the response of Merapi and Semeru eruptive activity to the regional tectonic events. Consequently, the thesis encompasses seven chapters as follows:

Chapter 1 (this chapter): **Introduction: "Indonesian active volcanoes and remote sensing"**. The objective of this chapter is to provide a general introduction on the relationship between tectonics and volcanism, between remote sensing and volcanology, and the tools and data availability in remote sensing used for this research project.

Chapter 2: **Semeru and Merapi volcanoes: "Regional setting, geological structures and historical eruptions"**. The second chapter provides updated information on Semeru and Merapi region concerning: (1) the geological structure and geophysical background; (2) the regional tectonic setting; and (3) the geological and hazard-zone maps of the volcanoes. Such information is used to analyze the instability of the volcanic edifice and the ascent of magma, processes that are partially controlled by tectonic structures. In this study, remote sensing techniques using high-spatial resolution optical images combined with digital elevation model (DEMs) are used to define the structural features of the edifices and their surrounding areas.

Chapter 3: **"Geomorphological evolution and post-2001 eruptive activity of Semeru volcano"**. The third chapter illustrates the application of remote sensing techniques using HSR optical (IKONOS, SPOT5 and aerial photograph) and thermal (ASTER) images to the recent evolution of Semeru. The objectives of this chapter are to define: (1) the structure and trace the evolution of the Semeru composite cone; (2) the extent of deposits that result from different style of emplacement and their impact during the period between 2001 and 2014; and (3) the characteristics of two selected catchments, Kobokan and Lengkong Rivers, on the southeast slopes of the volcano, which currently is the most threatened flank in terms of pyroclastic flows and lahars.

Chapter 4: **"The deposits and impacts of the large (VEI 4) 2010 Merapi eruption"**. The objective of the fourth chapter is to assess the extent and effects of the 2010 Merapi

PDCs, tephra fall and subsequent lahars based on remote sensing techniques using HSR imagery from GeoEye1, Pléiades, IKONOS, and SPOT5 satellites and aerial photographs. This chapter encompasses several studies of the 2010 Merapi eruption to determine: (1) a new estimate of volumes of tephra fall deposits using three empirical calculation methods (exponential, power-law and Weibull thinning); (2) the effect of the eruption and structural changes on the volcano summit; (3) the extent of pyroclastic deposits in the Gendol-Opak catchment; (4) the origin of post-eruption lahar deposits; and (5) behavior of the overbank PDCs and lahars based on the analysis of geomorphometric indices in the river channels.

Chapter 5: "**The 2010 Merapi pyroclastic deposits map based on satellite radar data**". Radar remote sensing provides imagery that characterizes the physical properties of the terrain surface and its observations are independent of cloud cover, light rain, smoke haze and solar illumination. Thus, it has a large potential for eruptive-deposit-mapping at volcano in the tropics such as Merapi. The objective of chapter 5 is to examine the utilization of direct- and cross-polarized L-band SAR data using the combination of amplitude evolution with temporal decorrelation information, to characterize the 2010 Merapi pyroclastic deposits. This study is performed using a set of L-Band ALOS-PALSAR images acquired before, during and after the 2010 eruption. The pyroclastic deposits are classified and mapped based on (1) surface change detection from coherence and amplitude ratio images, and (2) supervised classification based on Maximum Likelihood Classification (MLC) and Support Vector Machine (SVM) methods.

Chapter 6: "**Response of Merapi and Semeru eruptive activity to regional tectonic events: first results**". The objective of this chapter is to examine the relationships between the pulses of eruptive activity and the seismotectonic context of the two volcanoes as expressed by the recent (post-2000) earthquakes. We use the earthquake catalogues from the US Geological Survey National Earthquake Information Center (NEIC) and Indonesian *Badan Meteorologi, Klimatologi dan Geofisika* (BMKG). We have approached the volcanic activity by estimating the heat and volume fluxes using volcanic hot spots from the Moderate Resolution Imaging Spectrometer (MODIS) data (Harris & Ripepe, 2007). In order to overcome the lack or absence of MODIS data due to cloud cover, as this was the case in October-November 2010, we have used the seismic data of volcanic events.

Chapter 7: "**Concluding remarks**". In this chapter, the overall conclusions of our studies have been summarized as follows: (1) contributions of remote sensing applied in this thesis to understanding two persistently active volcanoes, Semeru and Merapi; (2) the limitations and methods that still need to be improved and perspectives for future research projects; and (3) an updated hazard assessment for the Semeru and Merapi volcanoes.

1.6. Remote sensing data

This PhD project applies remote sensing techniques using high-spatial resolution (HSR) optical (GeoEye, WorldView, Pléiades, IKONOS, and SPOT5), radar (ALOS-PALSAR) and thermal (ASTER and MODIS hot spot) images combined with digital elevation models (DEMs) and aerial photographs. Satellite images were acquired through the financial support of several research projects including the STIC ASIA « *Imager le Risk* » research and exchange project (2009-2011) and CNES projects (2010-2014) for optical and ASTER images, as well as Japan (RESTEC) and Indonesia (LAPAN and Geological Agency) collaboration and JAXA project n°1188 for ALOS-PALSAR images. Some HSR optical images are also provided by CRISP, National University of Singapore in the framework of collaborative program between LMV and CRISP. This PhD project was also partially supported by DOMERAPI (ANR-12-BS06-0012). The main technical specifications of satellite optical imagery used for this PhD project are summarized in Table 1.1. The list of images used in this thesis is provided in Appendix A.

1.6.1. Optical imagery

The following descriptions of optical satellite sensors are extracted from publications by the satellite data providers that are summarized on the website of Satellite Imaging Corporation (*http://www.satimagingcorp.com/satellite-sensors*)

GeoEye-1

The GeoEye-1 satellite sensor, launched on September 6, 2008, is able to provide an image resolution of 0.46 meter. GeoEye-1 flies in a sun-synchronous orbit with 98° inclination at an altitude of about 681 km and has an average revisit less than 3 days. During the summer of 2013, the orbit altitude of the GeoEye-1 Satellite sensor was

raised to 770 km. As of 29 January 2013, GeoEye was merged into the Digital Globe Corporation. Digital Globe plans to launch GeoEye-2 that will be capable of discerning objects as small as 34 cm on the Earth's surface in the panchromatic mode.

WorldView-2

DigitalGlobe's WorldView-2 satellite sensor, launched 8 October 2009, provides 0.46 m panchromatic mono and stereo satellite image data. The WorldView-2 sensor also provides eight multispectral bands: four standard colors (red, green, blue, and near-infrared 1) and four new bands (coastal, yellow, red edge, and near-infrared 2), full-color images for enhanced spectral analysis, mapping and monitoring applications, land-use planning, disaster relief, exploration, defense and intelligence, and visualization and simulation environments. With its improved agility, WorldView-2 is able to collect very large areas of multispectral imagery in a single pass of nearly 1 million km^2 every day. The combination of WorldView-2's increased agility and high altitude (770 km) enables it to typically revisit any place on earth in 1.1 days, revisit time drops below one day and never exceeds two days, providing the most same-day passes of any commercial high resolution satellite.

Pléiades

The Pléiades constellation is operated by the French Centre National d'Etudes Spatiales (CNES), and is composed of two very high-spatial resolution optical Earth-imaging satellites traveling in a sun-synchronous orbit at 694 km of altitude. Pléiades 1A (launched on 17 December 2011) and Pléiades 1B (launched on 2 December 2012) provide the coverage of the Earth's surface with a repeat cycle of 26 days. The Pléiades have a maximum theoretical acquisition capacity of one million square kilometers per day and per satellite with a resolution of 0.5 meter in panchromatic mode and 2 meters in multispectral mode.

IKONOS

IKONOS is the world's first commercial satellite providing very high-spatial resolution (1 m) imagery of the Earth. Space Imaging Inc. in Denver, Colorado, USA operates the IKONOS satellite, which simultaneously collects one-meter resolution black-and-white (panchromatic) images and four-meter resolution color (multispectral) images. The

IKONOS satellite was launched on 24 September 1999 and travels in a sun-synchronous orbit with 98.1° inclination at 681 km altitude. This satellite has 1.5 to 2.9 days of off-nadir revisit frequency at 40° latitude.

SPOT

The SPOT satellites are operated by the French Space Agency, Centre National d'Etudes Spatiales (CNES). Since 1986, SPOT satellite have acquired images of the Earth from SPOT 1 (22 February 1986 to 31 December 1990), SPOT 2 (22 January 1990 to July 2009), SPOT 3 (26 September 1993 to 14 November 1997), SPOT 4 (24 March 1998 to July 2013), SPOT 5 (since 4 May 2002), SPOT 6 (since 9 September 2012) and SPOT 7 (since 30 June 2014). The SPOT 1 to 5 satellites orbit is sun-synchronous with an inclination of 98.7° at an altitude of 832 km, and has 1 to 3 days of off-nadir revisit time. SPOT 1, 2 and 3 are identical as they have a scene size of 3600 km^2 with resolutions of 10 meters for panchromatic band and 20 meters for multispectral bands. The SPOT 4 satellite carries on-board a low-resolution wide-coverage instrument for monitoring the continental biosphere and crops. The SPOT 5 satellite offers a higher resolution of 2.5 to 5 meters in panchromatic mode and 10 meters in multispectral mode. The SPOT 6 and 7 are more precise with image resolutions of 1.5 meter in panchromatic mode and 6 meters in multispectral mode.

Table 1.1. Technical characteristics of satellite sensors and images (for visible to infrared wavelengths) used in this PhD research project.

Satellite sensor; Provider	Spectral range*	Spatial resolution/ swath width (at nadir)
GeoEye1; DigitalGlobe	Pan: 450-800 nm	0.46 m / 15.2 km
	B1 (blue): 450-510 nm	1.65 m
	B2 (green): 510-580 nm	1.65 m
	B3 (red): 655-690 nm	1.65 m
	B4 (NIR): 780-920 nm	1.65 m
WorldView-2; DigitalGlobe	Pan: 450-800 nm	0.46 m / 16.4 km
	B1 (coastal): 400-450 nm	1.85 m
	B2 (blue): 450-510 nm	1.85 m
	B3 (green): 510-580 nm	1.85 m
	B4 (yellow): 585-625 nm	1.85 m
	B5 (red): 630-690 nm	1.85 m
	B6 (red edge): 705-745 nm	1.85 m
	B7 (NIR1): 770-895 nm	1.85 m
	B8 (NIR2): 860-1040 nm	1.85 m

Table 1.1. (Continued)

Satellite sensor; Provider	Spectral range*	Spatial resolution/ swath width (at nadir)
Pléiades; CNES	Pan: 450-800 nm	0.5 m / 20 km
	B1 (blue): 450-510 nm	2 m
	B2 (green): 510-580 nm	2 m
	B3 (red): 655-690 nm	2 m
	B4 (NIR): 780-920 nm	2 m
IKONOS; DigitalGlobe	Pan: 450-800 nm	0.82 m / 11 km
	B1 (blue): 450-510 nm	3.28 m
	B2 (green): 510-580 nm	3.28 m
	B3 (red): 655-690 nm	3.28 m
	B4 (NIR): 780-920 nm	3.28 m
SPOT 5; CNES	Pan: 480-710 nm	2.5-5 m / 60 km
	B1 (green): 500-590 nm	10 m
	B2 (red): 610-680 nm	10 m
	B3 (NIR): 780-890 nm	10 m
	B4 (SWIR): 1580-1750 nm	20 m
SPOT 1 & 2; CNES	Pan: 500-730 nm	10 m / 60 km
	B1 (green): 500-590 nm	20 m
	B2 (red): 610-680 nm	20 m
	B3 (NIR): 780-890 nm	20 m
ASTER TIR; NASA's EOS	B10: 8125-8475 nm	90 m
	B11: 8475-8825 nm	90 m
	B12: 8925-9275 nm	90 m
	B13: 10250-10950 nm	90 m
	B14: 10950-11650 nm	90 m

* B: Band; Pan: Panchromatic; NIR: Near Infrared; SWIR: Short Wave Infrared; TIR: Thermal Infrared

1.6.2. Thermal imagery

ASTER

The Advanced Spaceborne Thermal Emission and Reflection Radiometer (ASTER) sensor is part of the National Atmospheric and Space Administration (NASA) Earth Observing System (EOS) Terra satellite platform that was launched on 18 December 1999. ASTER represents a high level of sophisticated imaging instrument science to provide global multispectral imaging data at relatively high-spatial resolution (15– 90 m/pixel). ASTER has the unique ability to collect multispectral data in the thermal infrared (TIR) region of the spectrum, with five bands in the TIR region of the spectrum (Table 1.1). The TIR subsystem operates in five bands in the thermal infrared region

using a single, fixed-position, nadir-looking telescope with a resolution of 90 m. For our research project, we used ASTER TIR Surface Kinetic Temperature, which is an on-demand product of ASTER and is generated from the five thermal infrared (TIR) bands (acquired during either day or nighttime), between 8 and 12 μm spectral range. It contains surface temperatures at 90 m spatial resolution for the land areas only. The above description is extracted from publications by the ASTER data provider (*http://asterweb.jpl.nasa.gov*).

MODIS

Moderate Resolution Imaging Spectroradiometer (MODIS) is one of four instruments carried on-board NASA's first Earth observing System (EOS) satellite 'Terra', which was launched in December 1999. Another MODIS sensor was launched on the second EOS satellite 'Aqua' in May 2002. Terra and Aqua MODIS orbit is sun-synchronous and viewing the entire Earth surface every 1 to 2 days. Terra orbit around the Earth is timed so that is passed from north to south across the Equator in the morning, while Aqua passes south to north over the Equator in the afternoon. The instrument captures data in 36 spectral bands ranging in wavelength from 0.4 μm to 14.4 μm and at varying spatial resolutions (2 bands at 250 m, 5 bands at 500 m and 29 bands at 1 km). The description of MODIS is extracted from *http://modis.gsfc.nasa.gov*.

For our research project, we used output from the MODIS volcanic hot spot detection algorithm (MODVOLC) as given on http://hotspot.higp.hawaii.edu (Wright et al., 2002). MODVOLC is a non-interactive algorithm that uses low spatial resolution (1 km pixel) satellite data acquired by MODIS sensor to detect and map global thermal anomalies. MODVOLC scans the MODIS data stream searching for evidence of sub-pixel hot spots. These data can be used to determine the presence, radiant intensity and heat flux of volcano-related hot spots (e.g., Wright & Flynn, 2004; Harris & Ripepe, 2007).

1.6.3. Radar imagery

ALOS-PALSAR

The Phased Array L-Band Synthetic Aperture Radar (PALSAR), a remote sensing instrument, belongs to the Japanese Advanced Land Observing Satellite (ALOS), and has been developed by a joint project between the Japan Aerospace Exploration Agency

(JAXA) and the Japan Resources Observation System Organization (JAROS). ALOS-PALSAR is an active microwave sensor using L-band frequency to achieve cloud-free and day-and-night land observation. ALOS, also called Daichi, was launched on 24 January 2006 with the multiple purposes of mapping, regional observation, disaster monitoring, and resource surveying. Besides PALSAR, ALOS has two other remote sensing instruments: the Panchromatic Remote-sensing Instrument for Stereo Mapping (PRISM) for digital elevation mapping and the Advanced Visible and Near Infrared Radiometer type2 (AVNIR-2) for precise land coverage observation. The ALOS orbit is sun-synchronous with an inclination of 98.16° at an altitude of 691.65 km, and has a 46 days repeat cycle. ALOS-PALSAR has three observation modes (fine, scanSAR and polarimetric) with main characteristics summarized in Table 1.2. The above description is extracted from publications by the ALOS-PALSAR data provider (*http://www.eorc.jaxa.jp/ALOS/en/about/palsar.htm*).

Data used in this study are ascending track 431 acquired with an incidence angle of 34.3°. We utilized five dual polarization (dual-pol, Fine Beam Double Polarization termed FBD) data in horizontal transmit-horizontal receive (HH) and horizontal transmit-vertical receive (HV) polarization mode. These datasets were acquired before (on 13 September 2009, 16 June 2010 and 16 September 2010), during (on 1 November 2010) and after (on 1 February 2011) the 2010 Merapi eruption. We also utilized one single polarization (Fine Beam Single Polarization termed FBS) data (HH) acquired after the eruption on 17 December 2010.

Table 1.2. Main characteristics of ALOS PALSAR images.

Mode	Fine		ScanSAR	Polarimetric
Center Frequency	1270 MHz (L-band)			
Chirp Bandwidth	28MHz (FBS)	14MHz (FBD)	14MHz,28MHz	14MHz
Polarization	HH or VV	HH+HV or VV+VH	HH or VV	HH+HV+VH+VV
Incident angle	8 to 60°	8 to 60°	18 to 43°	8 to 30°
Range Resolution	7 to 44 m	14 to 88 m	100 m (multi-look)	24 to 89 m
Observation Swath	40 to 70 km	40 to 70 km	250 to 350 km	20 to 65 km
Bit Length	5 bits	5 bits	5 bits	3 or 5bits
Data rate	240 Mbps	240 Mbps	120 Mbps, 240Mbps	240 Mbps

1.6.4. Digital elevation models

We utilized three types of digital elevation models (DEMs) as basic topographic data. The first DEM, called SRTM-DEM, was derived from the third Shuttle Radar Topography Mission (SRTM3, produced by NASA), computed at 3-arc-second (ca. 90 m) resolution. Accuracy of SRTM3 is mainly dependent on the altitude and the slope angles, for example in areas around Merapi the SRTM data satisfy a 90% confidence level for an elevation up to 1000 m (Gerstenecker et al., 2005). The second DEM termed TOPO-DEM with 15x15 m horizontal resolution and 1 m vertical resolution was produced by digitizing digital topographic maps that were printed at 1:25000 scale and have 12.5 m contour intervals. The topographic maps were published by the Indonesian agency for geospatial information (*BIG*) between 1998 and 2001. The third DEM called Airphoto-DEM with 1x1 m horizontal and 1 m vertical resolution was generated by J.-F. Oehler (Altran Ouest Atlantide) from low altitude aerial photographs (taken from an ultralight aviation) using photogrammetric and stereo-matching techniques with an average accuracy of 0.2 m. The Airphoto-DEM is only available for the southern flank of Merapi volcano. We have also used a high resolution DEM of the south flank based on orthophotos taken from a drone by C. Aris (Faculty of Geodesy, UGM) in 2011. In 2014, we calculated a new and very high resolution (2 m pixel) by using stereo-photogrammetry techniques (J.-F. Oehler, Altran Ouest Atlantide) applied to a stereo pair of Pléiades images acquired in 2012.

Chapter 2 – Semeru and Merapi volcanoes: Regional setting, geological structures and historical eruptions

2.1. Introduction

Semeru and Merapi are two persistently active volcanoes located in Java (Fig. 2.1), the most densely populated (1071 people/km^2) island in Indonesia hosting 56% of the total population of the country (BPS, 2011). The detailed record of volcano past eruptions and the wide variety of studies at these two volcanoes (especially on Merapi) have started since the Dutch colony (1800's) and have continuously been developed by CVGHM over the past five decades in the effort of providing the scientific rationale for assessing likely future hazards, thus contributing to reduce volcanic risk. One of the critical studies towards this effort consists in recognizing the geological structures of volcanoes and their regional tectonic setting as well as delineating the past erupted deposits. "*What are the relationships between the geological structures of the volcano and the regional tectonic setting?*" is an important question to address as a basis to our study.

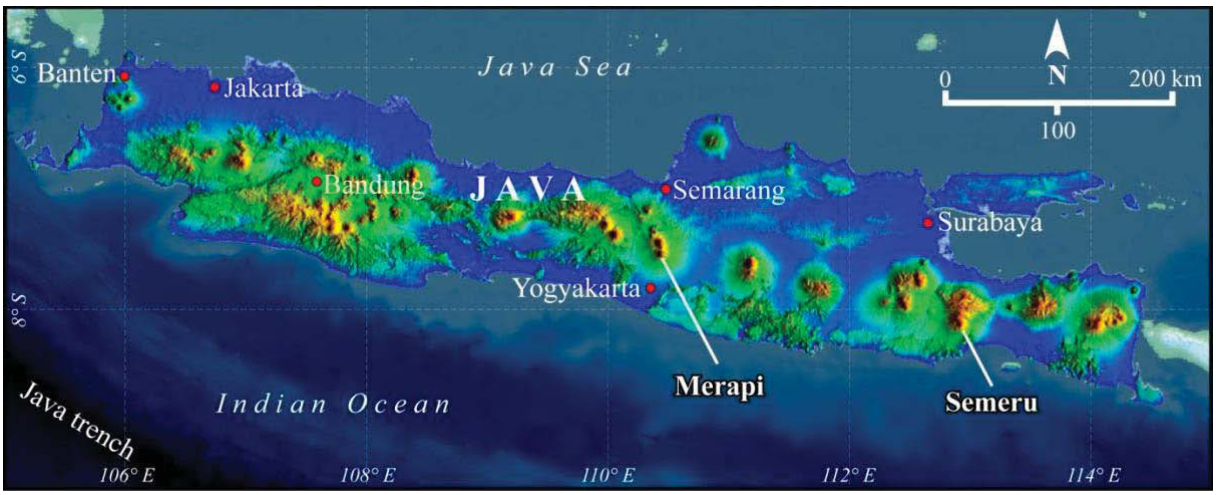

Figure 2.1. Geography of Java island showing the location of Merapi and Semeru volcanoes.

The objective of the second chapter is to provide updated information concerning the geophysical, geological and tectonic setting, the structure of the edifices as well as historical activity of Semeru and Merapi volcanoes. Such information may be useful to answer the above question especially related to instability of volcanic edifices and magma ascent, which are partially controlled by their tectonic features and to

implementation of methodologies for mapping and assessing volcanic hazards. In this chapter, we start our study by evaluating the geological, tectonic and geophysical backgrounds as well as the source of volcanism in Java Island based on literature and a synthesis of seismic data. Remote sensing techniques using high-spatial resolution optical images combined with digital elevation model (DEM) are applied to define the structural features of the edifices and their surrounding areas. The geological maps and volcanic hazard assessment of the volcanoes are also discussed to obtain a general context of eruptive activity of Semeru and Merapi volcanoes and to characterize how activity has evolved over time.

In order to derive a structural map from remote sensing images, first we define the cumulative deformation associated with growth structures and tectonically-controlled topographic highs characterized by clear borders and linear, trapezoidal or irregular shapes at surface. A useful tool to recognize cumulative deformations consists of two DEMs images that highlight topographic variations. For this purpose we used SRTM- and TOPO- DEMs (see Chapter 1) that have a large coverage. We recognize the faults from optical satellite images and aerial photographs based on a series of criteria: juwtaposition of layers of different rock units, abrupt topographic discontinuities of landforms, depressions along the fault trace (sheared rock may be more easily eroded), scarps or cliffs, abrupt changes in vegetation patterns, and sudden shifts (at least 1 km long) of drainage reaches. Multiple drainage shifts along one river can be associated with faults. The drainage network map and the visible/optical images are used to distinguish and to classify inferred features as geological structures.

2.2. Geological, seismotectonic and geophysical context of Java Island

The island of Java is part of the Sunda Arc that outlines the subduction of the Indo-Australian plate beneath the Eurasian plate, which extends from northwestern Sumatra to Flores (Fig. 1.1B in Chapter 1). The subduction is highly oblique along Sumatra, while it is almost perpendicular to the arc (N10°E) on the eastern part of the Sunda Arc (i.e. Java and small islands east of it). The convergence rate of the Indo-Australian and Eurasian plates in general increases from Sumatra to the easternmost part of the Sunda arc (Minster & Jordan, 1978). Convergence rates across the Java trench between areas southwest of Java and west Java in a direction of N11°E and are about 6.7 cm/year

(DeMets et al., 1994; Tregoning et al., 1994). The age of the subducted plate varies laterally, ranging from 40 Ma beneath northern Sumatra to 110 Ma south of Java (Müller et al., 1997). Most of Indonesian volcanoes (about 77%) are part of the Sunda Arc, which represents a region with strong seismic and volcanic activity. Java itself is host to 34 active volcanoes and 19 among them have erupted at least once since 1600.

2.2.1. Geological context

Java, with a backbone composed a subduction-produced volcano-plutonic arc (Fig. 2.2), is an example of the relationship of calc-alkaline magmatism to subduction. Subduction of the Indian Ocean beneath the Sunda Arc has been active since the Eocene (e.g., Van Bemmelen, 1970; Hamilton, 1979; Hall, 2002; Garwin et al., 2005). The western part of the Java Sea is a continuation of the Paleozoic to Early Mesozoic continental basement complexes of Sumatra and Borneo (Kalimantan). Most of Java Island appears to be underlaid by Late Cretaceous-Eocene age accretionary complexes and Paleogene volcanic arc. Outcrops of the oldest 'basement' are found in only three relatively small areas in central and southwest Java. It has been suggested from the composition of Quaternary volcanic rocks that parts of East Java may be underlain by oceanic crust (Verbeek & Fennema, 1896). The backbone of Java is a series of relatively young active volcanoes, most of them about 3000 m high and spaced about 80 km apart. An earlier volcanic arc in the Southern Mountains that runs the length of Java was active from the middle Eocene (ca. 45 Ma) to the early Miocene (ca. 20 Ma), and its activity included significant felsic volcanism (Hall & Smyth, 2008; Smyth et al., 2008). Subsequently arc volcanism resumed in the late Miocene (ca. 12–10 Ma) in the modern Sunda Arc, but in a position 50 km north of the older arc (Smyth et al., 2008). The more recent and active volcanoes of Java often overlie volcanic and/or intrusive rock units. Volcanic rock units are intercalated with Neogene sediments, and intrusive rocks cut these sediments. The non-volcanic products are represented by Lower-Middle Pleistocene sediments with only small amount of marine sediments. The volcanic deposits are mainly the results of Middle Pleistocene to Recent volcanic activities. The Quaternary sediments are exposed almost in all regions in Java, particularly in the middle and northern parts of the island (Fig 2.2).

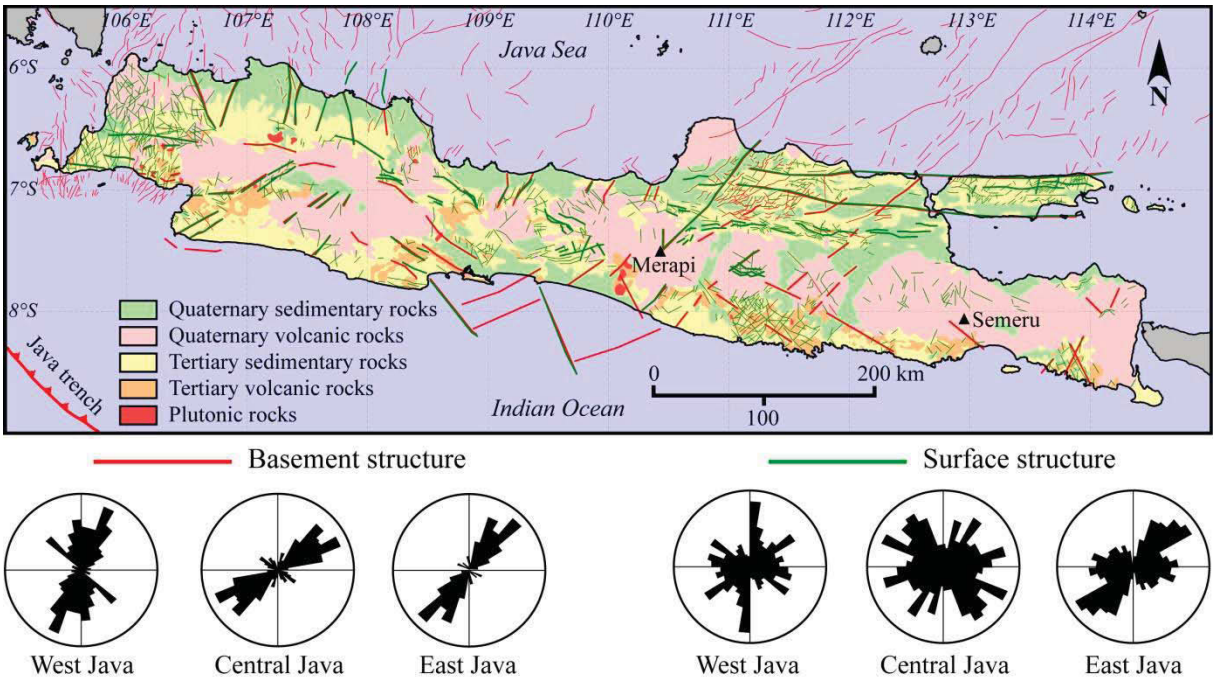

Figure 2.2. The simplified geological map of Java provides the general distribution of geological units based on rock association and their age (Sukamto & Sukarna, 2001) as well as the distribution of basement and surface structures (Sribudiyani et al., 2003).

Hall et al. (2007) delivered a new interpretation of Java's structure, in which Java has an apparently simple structure in which the east-west physiographic zones broadly correspond to structural zones. In the north is the margin of the Sunda Shelf and to the south of the shelf are Cenozoic volcanic arc rocks. The structural simplicity is complicated by structures inherited from Cretaceous subduction beneath Java, extension and subsidence related to development of subsequent volcanic arcs, late Cenozoic contraction, and by cross-arc extensional faults, which are active today. Java can be separated into three structural sectors of West, Central and East Java (Fig. 2.2; Sribudiyani et al., 2003; Hall et al., 2007). Central Java displays the deepest structural levels of thrusting and exposures of Cretaceous basement; in these areas the over-thrust volcanic arc has been largely removed by erosion. In West and East Java, the over-thrust volcanic arc rocks are still preserved. In West Java, the arc rocks are also thrust onto shelf sedimentary sequences that formed on the Sundaland continental margin. In East Java, the volcanic arc is thrust onto a thick volcanic/sedimentary sequence formed north of the arc in a flexural basin that is interpreted to have resulted mainly from volcanic arc loading (Hall et al., 2007; Smyth et al., 2008).

2.2.2. Seismotectonic pattern

Several authors have conducted studies of seismotectonic pattern as a means to investigate the morphology and internal structure of the Wadati-Benioff zone (Hanuš et al., 1996), the active tectonic structure of lithospheric wedge (Špičák et al., 2002), and also the relationship of tectonism to volcanic activity (Hill et al., 2002). The Wadati-Benioff zone is understood as a dipping planar zone of earthquakes that is produced by subduction of one oceanic crustal plate beneath another or the subduction of an oceanic plate beneath a continental plate. The Wadati-Benioff zone along the Java Island dips approximately 50° and extends to depths of about 600 km and a deep aseismic gap exists between 300 and 500 km depth. Seismic gaps are commonly identified in the Wadati-Beniof zone that is directly situated beneath active volcanoes. These gap likely represent a partially melted medium, which constitutes the main source storage areas of magmas that feed overlying active volcanoes (Hanuš & Vaněk, 1988; Hanuš et al., 1996). Here, we study the seismotectonic pattern of Java, focusing on the investigation of the intermediate-depth aseismic gap within the Wadati-Benioff zones beneath Merapi and Semeru volcanoes to constrain the source region of magma generation beneath these volcanoes. We have used the earthquake hypocenter catalogue of Java region for the period 1964-2011 (Fig. 2.3A), which we retrieved from the International Seismological Centre (ISC On-line Bulletin; http://www.isc.ac.uk). We relocated earthquakes from the catalogue using the procedure of Engdahl et al. (1998). We also used the earthquake source parameters including hypocenters and centroid-moment tensor (CMT) solutions (Fig. 2.3B) provided by the Global CMT catalogue (www.globalcmt.org; Dziewonski et al., 1981; Ekström et al., 2012).

We used the narrow vertical cross-sections perpendicular to the Java trench (azimuth 10°) to analyze regional seismic activity across Merapi and Semeru (Figs. 2.4) and to distinguish between events belonging to the Wadati-Benioff zone and those located in the overlying wedge. The problem of deep seismicity is beyond the scope of this study, thus we are not considering the earthquake located below 350 km depth. Figure 2.4 shows the vertical sections of seismicity that confirm the presence of a region without strong (m > 4.0) intermediate-depth earthquakes in the Wadati-Beniof zone beneath Merapi and Semeru volcanoes. The region that is aseismic with respect to strong earthquakes, is defined as a gap in the Wadati-Benioff zone (pink box in Figs. 2.4) and

interpreted as the location of the source region of primary magma at 150-190 km depth beneath Merapi volcano, and at 150-240 km depth beneath Semeru volcano.

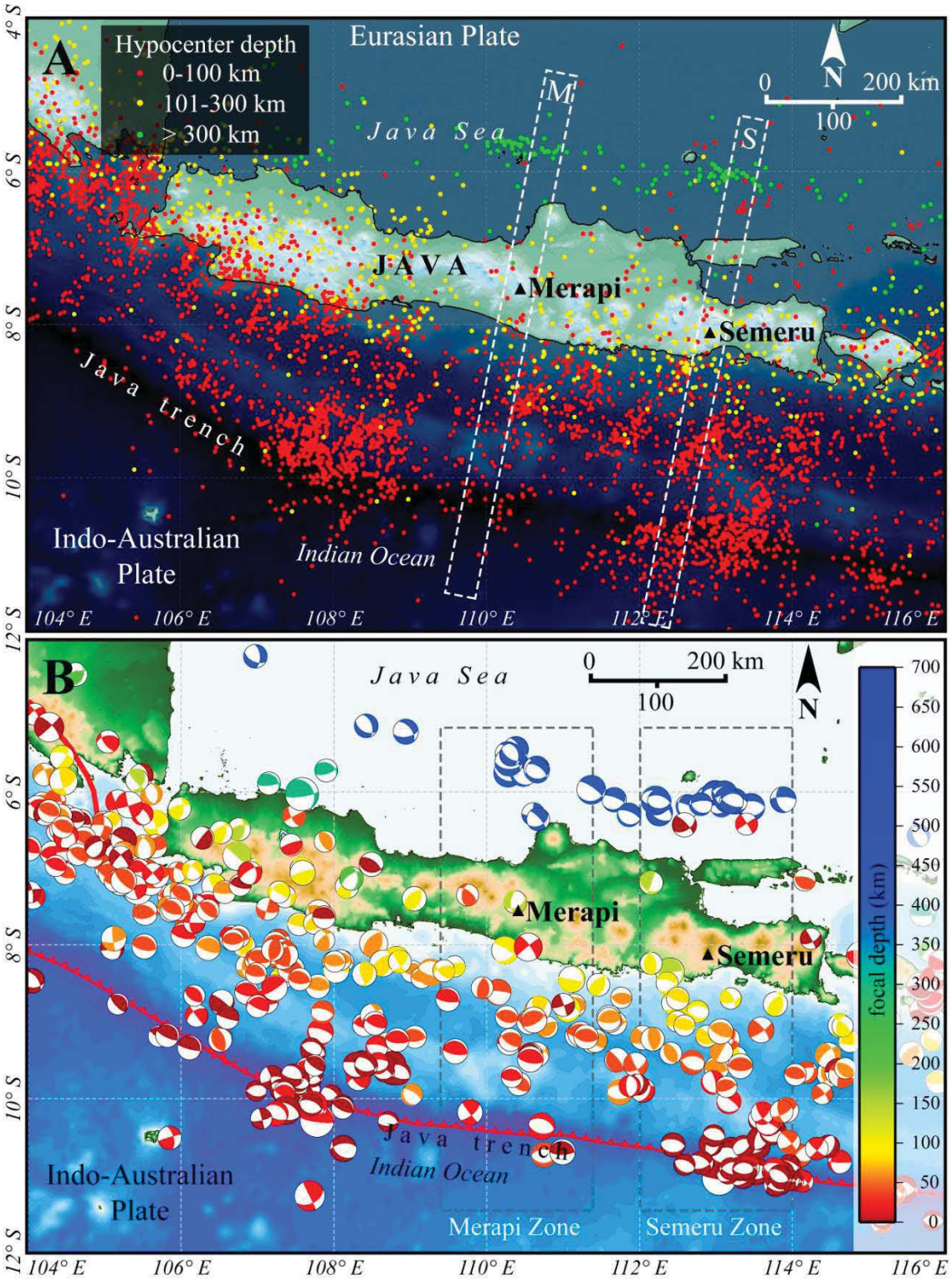

Figure 2.3. Map of **(A)** seismicity around Java Island based on earthquake hypocenter catalogue of International Seismological Centre (ISC), and **(B)** centroid-moment tensor solutions collected from Global CMT catalogue from the period 1964-2011. Dashed rectangle boxes are the reference areas for vertical cross-sections across Merapi (M) and Semeru (S) volcanoes.

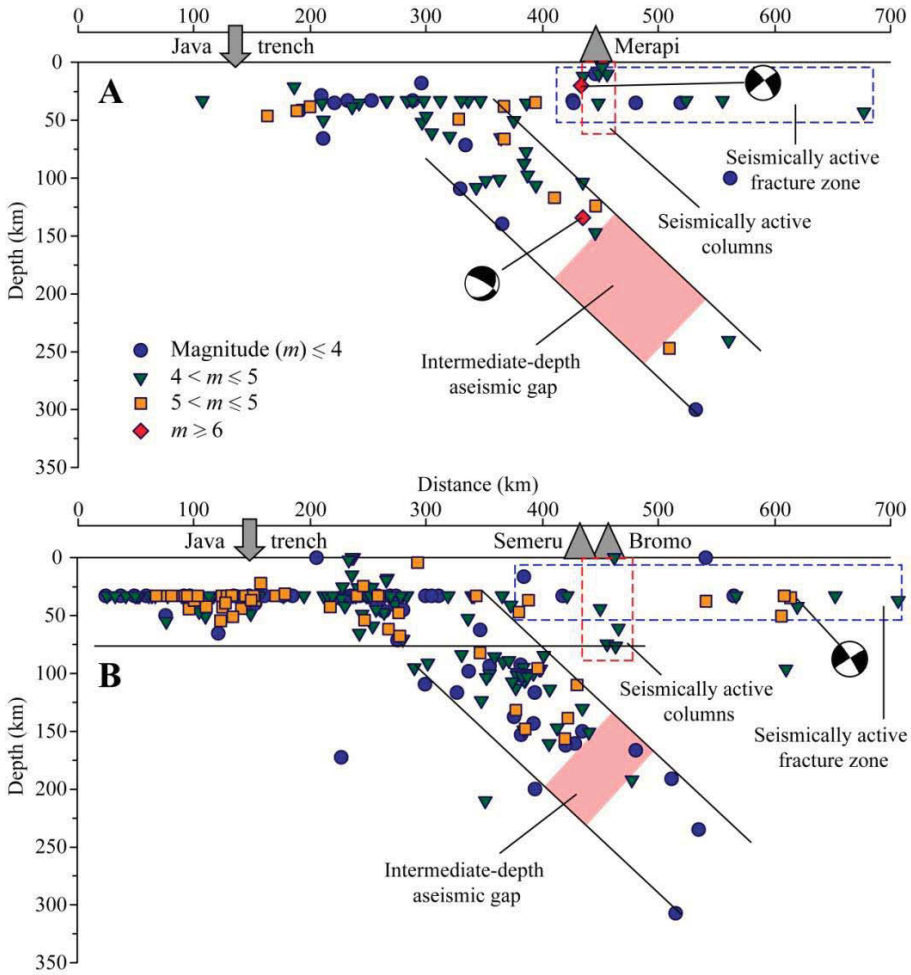

Figure 2.4. Vertical cross-sections perpendicular to the trench giving the depth distribution of earthquake foci in relation to the trench for Merapi **(A)** and Semeru **(B)** volcanic domains. The reference areas are outlined by dashed white boxes in Figure 2.3.

More detailed distributions of hypocenter locations in the lithospheric wedge above the Wadati-Benioff based on local volcano monitoring networks reveal the presence of seismically active columns and fractures zones in the two regions of Merapi and Semeru (dashed blue boxes in Fig. 2.4). A CMT solution in the zone near Merapi indicates that one of the active faults in the zone has a strike-slip mechanism and a southwest-northeast orientation. In the Semeru region, the most seismically active fractures are located north of the volcano, as indicated by several relative large (magnitude >4) shallow earthquakes in Fig. 2.4. The seismically active columns (blue dashed rectangle in Fig. 2.4) are distributed beneath and slightly north of Merapi and Semeru (and Bromo) volcanoes. The earthquake events in the column are mostly at a shallow depth (< 50 km) beneath Merapi and at deeper depths (up to 80 km) beneath Semeru and Bromo. The earthquake in these columns can be interpreted as events induced by magma transport

through the medium of the lithospheric wedge that has been subcritically pre-stressed by the process of plate convergence (Špičák et al., 2002).

2.2.3. Deep and shallow structures beneath the edifice

The geophysical background for the area around Merapi and Semeru volcanoes is summarized from several studies, including gravimetry (Untung & Sato, 1978) and seismic tomography (Koulakov et al., 2007; Widiyantoro et al., 2011, Luehr et al., 2013). A Bouger gravity anomaly map (Fig. 2.5A) of the eastern part of Java (Untung & Sato, 1978) covers the areas of Merapi and Semeru volcanoes. A negative anomaly lies directly behind and north of the Southern Mountains and modern-day volcanic arcs. The negative anomaly is interpreted as an east-west oriented basin, at least 400 km long, called Kendeng Basin. At the west end of the Kendeng Basin a relatively abrupt change in the character of the anomaly is observed around the modern volcanoes of Merapi and the Dieng Plateau (Fig. 2.5A). The Southern Mountains Arc is marked by a strong positive Bouguer gravity anomaly of more than 1000 μms^{-2}. The modern volcanic arc section is characterized by a positive Bouguer anomaly of gravity up to 800 μms^{-2}. Based on regional scale gravity anomaly (Fig. 2.5A), Semeru region has stronger positive anomaly (~750 μms^{-2}) than Merapi region (~250 μms^{-2}), which could suggest that the crustacl section at Semeru is denser or older than at Merapi.

Widiyantoro et al. (2011) applied a non-linear approach to seismic tomography in order to image detailed P- and S-wave speed velocity structures beneath the Sunda arc. The dip angle of the slab from the trench to the arc is at 10°-30° and then increase gradually at c. 60°-70° down to the transition zone. There is a discontinuity of the subducted slab in the mid upper mantle (between 250 and 450 km depth) below eastern Java, where Merapi and Semeru are located (Fig. 2.5B). This discontinuity or gap may be related to the subduction of a relatively buoyant oceanic plateau near this region at c. 8 Ma (Hall et al., 2009; Widiyantoro et al., 2011). Koulakov et al. (2007) and Luehr et al. (2013) provided a more detailed image of processes beneath the volcanic chain in central Java and present lines of evidence for a very strong low-velocity anomaly (Merapi Lawu Anomaly, MLA) in the crust just north of Sumbing, Merapi and Lawu volcanoes (Fig. 2.5C). This anomaly is related to an area with high content of fluids and melts in the crust, which can play a role in feeding the active volcanoes in central Java. The migration

paths of fluids and partial melts from slab are also detected beneath the MLA as reflected by an inclined low-velocity zone.

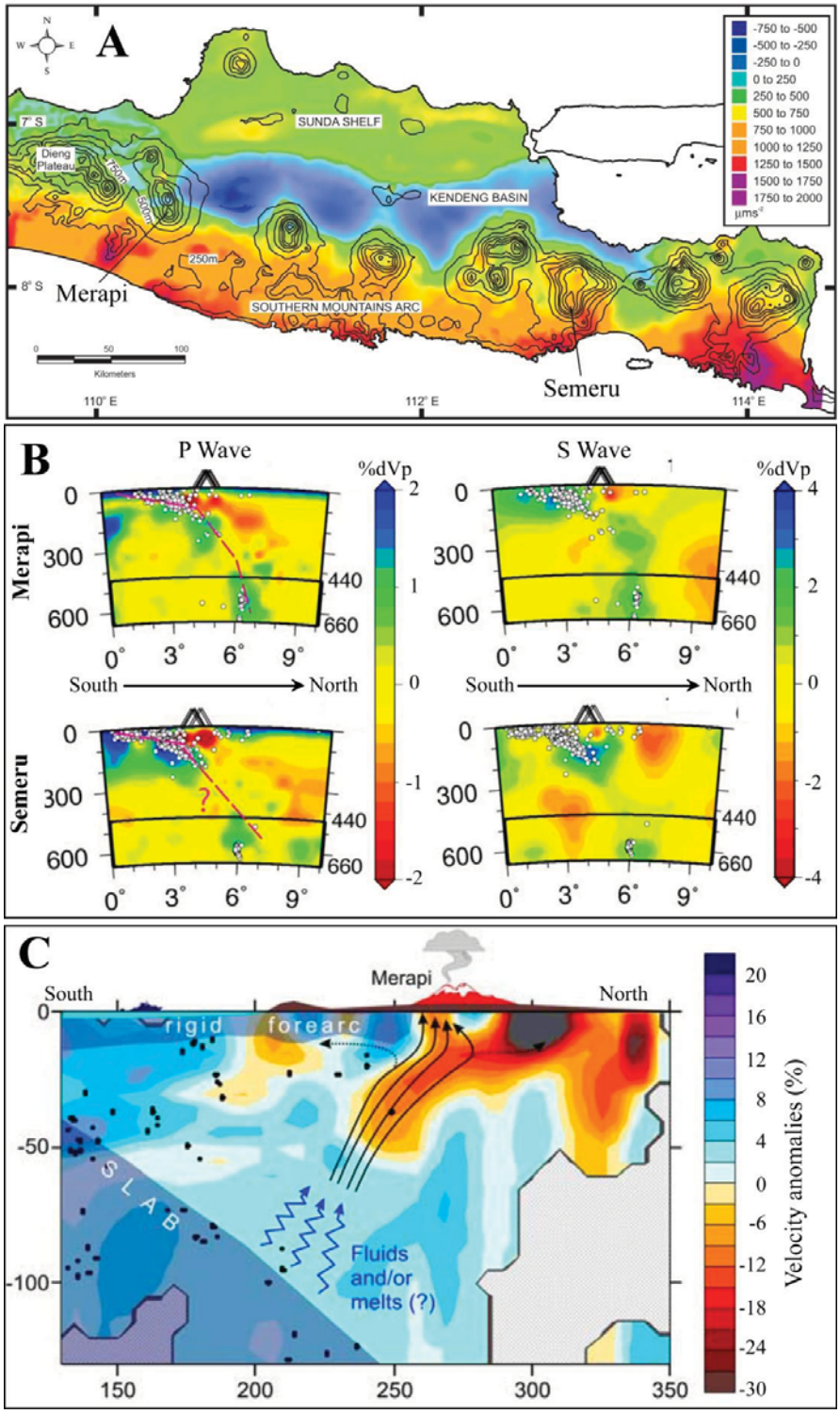

Fig 2.5. A. Bouguer gravity anomaly map of East Java (Untung & Sato, 1978) with topographic contours at 250 m intervals. **B.** Vertical section across the convergent margin and the Merapi and Semeru volcanoes through the P- and S-wave models plotted as velocity perturbations (Widiyantoro et al., 2011). **C.** S-wave velocity anomaly distribution beneath Merapi and the interpretation of the velocity structure (Koulakov et al., 2007).

2.3. Semeru volcano and the Tengger volcanic massif

Semeru volcano (8°06′05″S, 112°55′E) at 3676 m, the highest mountain in Java, is the southernmost edifice of the Semeru–Tengger volcanic massif (Fig. 2.6). The massif area belongs to the Bromo-Tengger-Semeru (BTS) National Park, which is a favorite mountain trekking destination and the most visited tourist attraction in East Java, Indonesia.

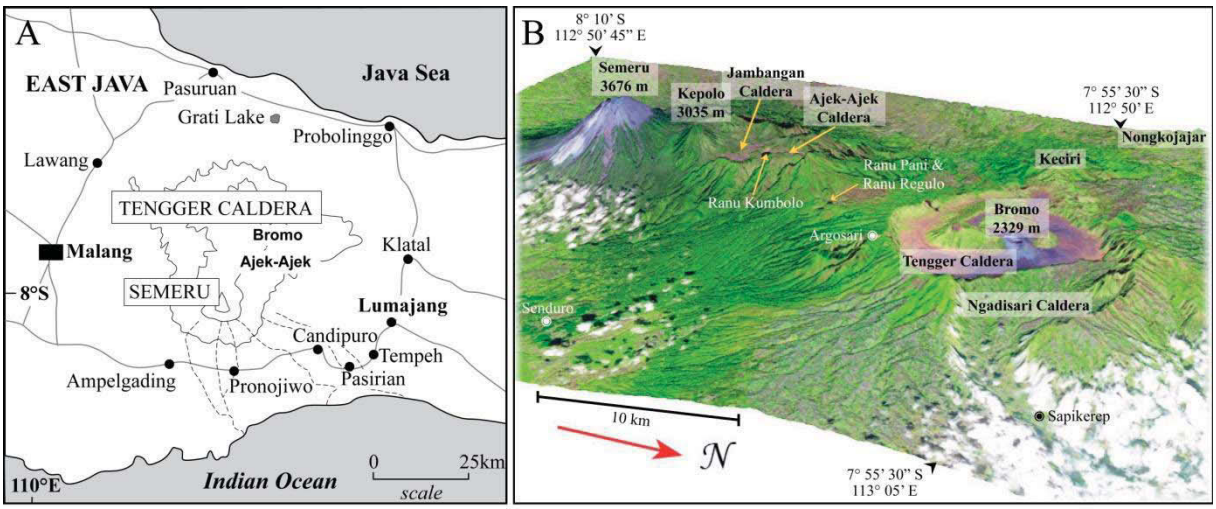

Figure 2.6. A. Sketch maps showing the location of the Semeru composite cone south of the Semeru–Tengger volcanic complex. **B.** The 11/08/2003 SPOT5 image, looking southwest and draped on a SRTM-DEM, shows the Semeru-Tengger massif.

2.3.1. Volcanic features and geology of the massif and edifice

The Semeru-Tengger volcanic massif with an area of about 900 km^2 comprises a cluster of calderas and strato-cones aligned from north to south over 25 km, including: the Bromo-Tengger (7.942°S, 112.95°E), Jambangan (8.065°S, 112.92°E) and Ajek-Ajek (8.042°S, 112.92°E) calderas; the Mt. Kepolo (8.077°S, 112.92°E) lava cone; and the composite cone of Mt. Mahameru-Semeru (Figs. 2.6 and 2.7). The calderas formed and the edifices were constructed over a deeply eroded volcanic arc of Oligocene–Miocene age. The eruptive centers of the Semeru-Tengger massif lie on a roughly north-south-trend that is slightly concave towards the east. The trend continues northward to Lake Grati (Fig. 2.6A), a maar at the foot of the Tengger massif (Van Bemmelen, 1949; Situmorang, 1989; Sutawidjaja et al., 1996; Carn, 1999). Van Bemmelen (1949) and Wahyudin (1991) contend that volcanic activity of Semeru-Jambangan-Tengger massif was initiated by the Jambangan, followed by the old Tengger and then Ajek-Ajek. Later,

the activity moved to the south crater rim of Jambangan caldera, then resumed at Mt. Kepolo and Mt. Mahameru, and ended with the youngest activity forming the Jonggring-Seloko crater. The main geological features of the Semeru–Tengger massif are presented in Figure 2.7, based on the combined 2008 SPOT5 image and the shaded relief SRTM-DEM at a regional scale. In this sub-section we divided the Semeru-Tengger massif into three parts: Bromo-Tengger complex (Fig. 2.7B), Jambangan-Ajek-ajek complex (Fig. 2.7C) and Mahameru-Semeru volcano (Fig. 2.7D).

The Bromo-Tengger complex

The Tengger massif was considered as a stratovolcano whose north flank slid towards the Madura Strait inducing a "growing rift". This rift is a 25 km of lateral amplitude vast structure corresponding to area of the slide, and a northwest slipped block, an anticlinorium affecting Pliocene-Pleistocene marine lands corresponding to the frontal area of the slide (Van Bemmelen, 1949). Mulyadi (1992) explains that the "growing rift" described by Van Bemmelen is a polygenetic structure corresponding to a curved alignment of eruptive centers that have occurred over time. These eruptive centers (in chronological order) are Nongkojajar located ~15 km west of the Tengger "Sand-Sea" caldera (Figs. 2.6B & 2.7A), Kundi-Baruklinting-Sapikerep, Ngadisari, Keciri and Tengger. Based on K/Ar-data, Mulyadi (1992) suggested the following chronology of major events: (1) formation of the Nongkojajar volcano at ca. 1.4 Ma; (2) the Ngadisari volcano at ca. 820 ka; (3) the Tengger volcano at ca. 265 ka; (4) the Nongkojajar caldera at ca. 204 ka; (5) the Ngadisari caldera at ca. 152 ka; (6) the Cemorolawang strato-cone at ca. 144-100 ka; and (7) the Tengger caldera > 45 ka. The post-caldera volcanism, which started prior to about 1800 yr BP, is represented by six edifices arranged centripetally according to their age: the phreatomagmatic (andesitic) tuff rings of Widodaren, Kursi, Segarawedi Kidul, Segarawedi Lor, Bromo, and the Strombolian (basaltic) cone of Batok (Fig. 2.7B).

The Bromo-Tengger complex consists of two main units, the pre-caldera and post-caldera formations (van Gerven & Pichler, 1995), which was formed by at least two calderas, Ngadisari and Tengger (also named Sand-Sea caldera). Based on satellite imagery and geochemical data, Zaennudin (1990) suggests the existence of a third caldera (Argowulan/Cemorolawang; Fig. 2.7B) that probably formed at about 100 ka.

The pre-caldera formation exposed in the steep caldera walls shows a decrease in height above the caldera floor from 650 m in the northeast and southeast to about 400 m at the western flank of the pre-caldera volcano. The eastern wall of Tengger caldera (Cemorolawang) is the lowest part, with a height of only 100 m above the caldera floor. The post-caldera formation is dominated by a volcanic complex within the caldera, including the active crater of Bromo volcano.

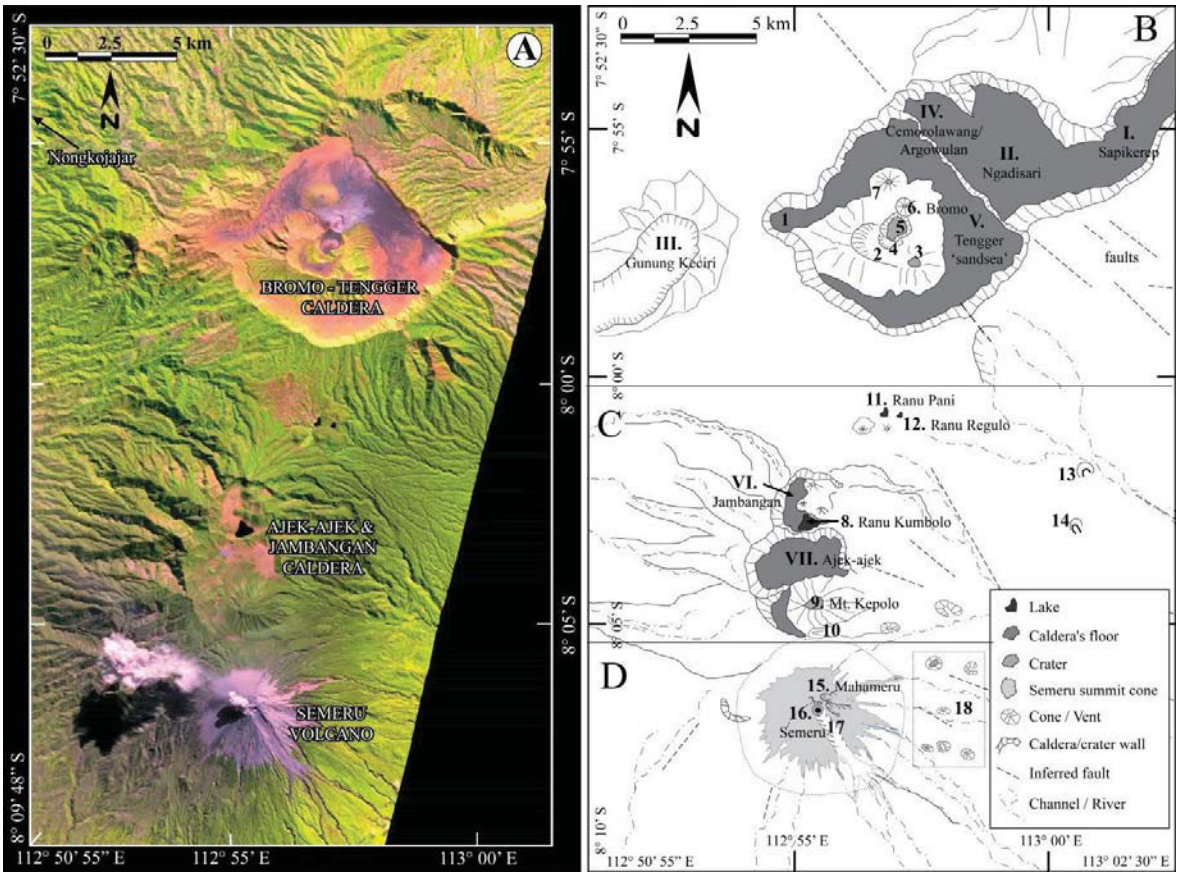

Figure 2.7. A. The 26/07/2008 SPOT5 image portrays the Semeru–Tengger volcanic massif, which comprises from north to south: **B.** the Bromo–Tengger complex with remarkable landforms: the Sapikerep outlet valley (I); the Ngadisari caldera (II); Mt. Keciri truncated by an amphitheater valley open to the SW (III); the Cemorolawang/Argowulan caldera (IV); and the Tengger 'sand-sea' caldera (IV) with a parasite cone, Mt. Ijo (1). The post-caldera volcanism has formed: the phreatomagmatic tuff rings of Widodaren (2), Kursi (3), Segarawedi Kidul (4), Segarawedi Lor (5), Bromo (6), and a cinder cone Mt. Batok (7). **C.** The Jambangan (VI) and Ajek-Ajek (VII) calderas extend about 6 km in a northern direction. Several intra-caldera vents include the maar of Ranu Kumbolo (8). Mt. Kepolo strato-cone (9) is lined up with Tawonsongo, a youthful lava cone and flow (10). Ranu Pani (11) and Ranu Regulo (12) are maars in the northern part, and two small vents (13 and 14) are located on the east flank. **D.** The youngest volcano in Semeru–Tengger massif, Mahameru-Semeru volcano (15-16), including the currently active Jonggring-Seloko vent at the top of the principal SE-trending scar (17) in the edifice. Several flank vents are visible on the eastern flanks (18).

The Tengger caldera has a volume of about 28 km^3 (Mulyadi, 1992) and a roughly circular shape except the northeast part where the straight wall of Cemorolawang is located (Fig. 2.7B). The caldera diameter is 10 km from east to west and 9 km from north to south. A sub-circular basin of Mt. Ijo (1.75 km in diameter) is located to the west of the caldera. The older Ngadisari caldera has been identified to the Northeast of Tengger caldera bounded by a NW-SE morphologic feature, which reflects an overlapping caldera structure. Ngadisari caldera continues to the east through the 2 km-wide Sapikerep valley, which formed from the collapse of an edifice (Kundi-Baruklinting-Sapikerep). This collapse occurred prior to the formation of Ngadisari caldera (Mulyadi, 1992). Mt. Keciri to the west of Tengger caldera is a large parasitic cone also truncated by a summit caldera 2 km in diameter, which forms an amphitheater valley open to the SW.

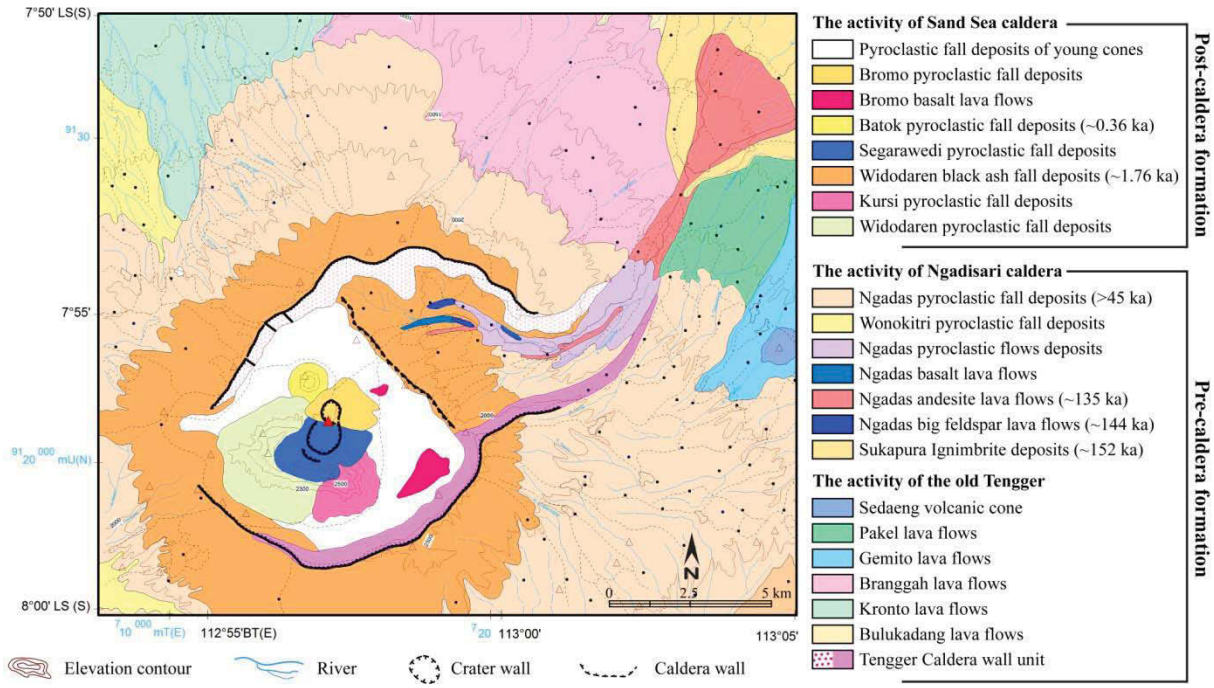

Figure 2.8. Geological map of Bromo-Tengger complex published by CVGHM (Zaennudin et al., 1995). The deposit units are divided into three groups, the activity of Sand-Sea caldera for post-caldera formation, and the activity of Ngadisari caldera and the old Tengger for pre-caldera formation.

The geological map of the Bromo-Tengger complex (Zaennudin et al., 1995; Fig. 2.8) divides the deposit units into three groups, namely those produced by activity of Sand-Sea caldera, deposits from Ngadisari caldera and those from the old Tengger caldera and pre-caldera volcanic complex. The lithology of the old Tengger caldera walls consists of

alternating layers of lava flows, pyroclastic-flow, massive ash-fall, phreatic deposits, cut by some dykes. Three main lava types of the pre-caldera formation are basaltic, basaltic andesite and scarce scoriaceous basalt types (van Gerven & Pichler, 1995). The geological map (Fig. 2.8) shows only one partially welded ignimbrite named Sukapura and associated with the formation of Ngadisari caldera (Hadisantono, 1990; Zaennudin, 1990). However, Mulyadi (1992) suggests two additional ignimbrites, which are associated with the formation of Tengger caldera, the Tosari and Ngadas ignimbrites. Both ignimbrites correspond to the Wonokitri tephra fall, Ngadas pyroclastic-flow and tephra fall deposits in the geological map proposed by Zaennudin et al. (1995).

The Post-Sand-Sea caldera formation is dominated by the activity of six intra-caldera edifices; four are aligned in a south-north direction and apparently younger from south to north. These are respectively Widodaren, Segarawedi Kidul, Segarawedi Lor and Bromo. The other two, Kursi and Batok, lie outside the alignment. All these edifices, except Mt. Batok (a cinder cone), are tuff cones, essentially phreatomagmatic in origin with a small proportion of magmatic products of basic andesite to andesite composition. This tuff cones have characteristic low relief morphology with a perfectly horizontal crater. The largest crater and first to be generated at the caldera floor is the Widodaren crater with a diameter of about 1.5 km and a total ejecta volume of about 4.5 km^3 (van Gerven, 1990). This was partly destroyed by the eruption of the Segarawedi Kidul, Segarawedi Lor craters and the development of Mt. Kursi. The black ash-fall deposits (dated at 1.81 to 1.62 ka; Zaennudin, 1990) were associated with phreatomagmatic deposits and with the formation of Widodaren Crater. These ash-fall deposits have a widespread extent outside the caldera (Fig. 2.8; Zaennudin et al., 1995). The two youngest eruption craters are Mt. Bromo and the Batok scoria cone, the latter likely being the youngest (van Gerven, 1990). This indicates that the eruption focus shifted back to the Bromo crater after the formation of Mt. Batok. A young lava flow is exposed on the caldera floor at the base between Bromo and Batok. Post-caldera formation is dominated by ash and lapilli-fall deposits (van Gerven and Pichler, 1995). The lava flows of the post-caldera formation are vesicle-rich, dark colored rocks containing large (up to 0.5 cm) plagioclase phenocrysts.

Since the first recorded activity of Bromo volcano in 1804, its eruptive activity was dominated by explosive eruptions from the central vent ejecting ash, sand, lapilli and

lava bombs, except the 1980 activity, which formed a lava plug at the bottom of the crater. During the last four decades, Bromo volcano has erupted nine times with rest periods between four months to eleven years. The latest eruption took place over an extended period (26 November 2010 – 13 June 2012) that was dominated by ash explosions that produced 300 to 3000 m-high columns and deposits of fine grained volcanic material. The 2010-2012 Bromo eruptions initiated as phreatic events, followed by phreatomagmatic eruptions and then by magmatic eruptions. These sequences and extended duration are attributed to a repeatedly supply of new basaltic andesite magma (Zaennudin et al., 2012).

The Jambangan and Ajek-ajek complex

South of Bromo-Tengger complex, the Jambangan-Ajek-ajek complex is clearly visible in the SPOT-5 images (Figs. 2.6B and 2.7A). The complex comprises of two calderas (Jambangan and Ajek-ajek), three maars (Ranu Kumbolo, Ranu Pani and Ranu Regolo) and a stratocone (Mt. Kepolo) (Fig. 2.7C). There is no currently active volcano in this complex. The nested Jambangan and Ajek-ajek calderas (VI and VII in Fig. 2.7C) extend about 6 km in a northern direction and are characterized by a caldera floor, caldera rims and older volcanic landforms (Fig. 2.7C). These calderas opened to the east are thought to have produced debris avalanches, which may or may not have been accompanied by an eruption (Carn, 1999). The southern and southeastern walls of the Jambangan caldera have been buried by the composite volcanoes of Mt. Mahameru and Mt. Kepolo (16 and 9 in Fig 2.7C). The caldera floor is covered by lava flows, pyroclastic-flow deposits and ash-fall deposits (Wahyudin, 1991). The Jambangan caldera rim is cut by the Ajek-ajek caldera, proving that the Jambangan caldera is older. Several intra-caldera vents were constructed including the crater lake of Ranu Kumbolo (8 in Fig 2.7C) with a diameter of 600 m and a deep crater that may indicate a third explosive eruption from the complex. The Holocene Mt. Kepolo strato-cone, located near the south rim of Jambangan caldera, is lined up with a youthful Tawonsongo lava cone and flow at the northern foot of Semeru summit. Two other maars, Ranu Pani and Ranu Legolo, are located in the north of Jambangan caldera. Several northwest-trending amphitheaters of flank erosion were formed to the west of Jambangan and Ajek-ajek calderas.

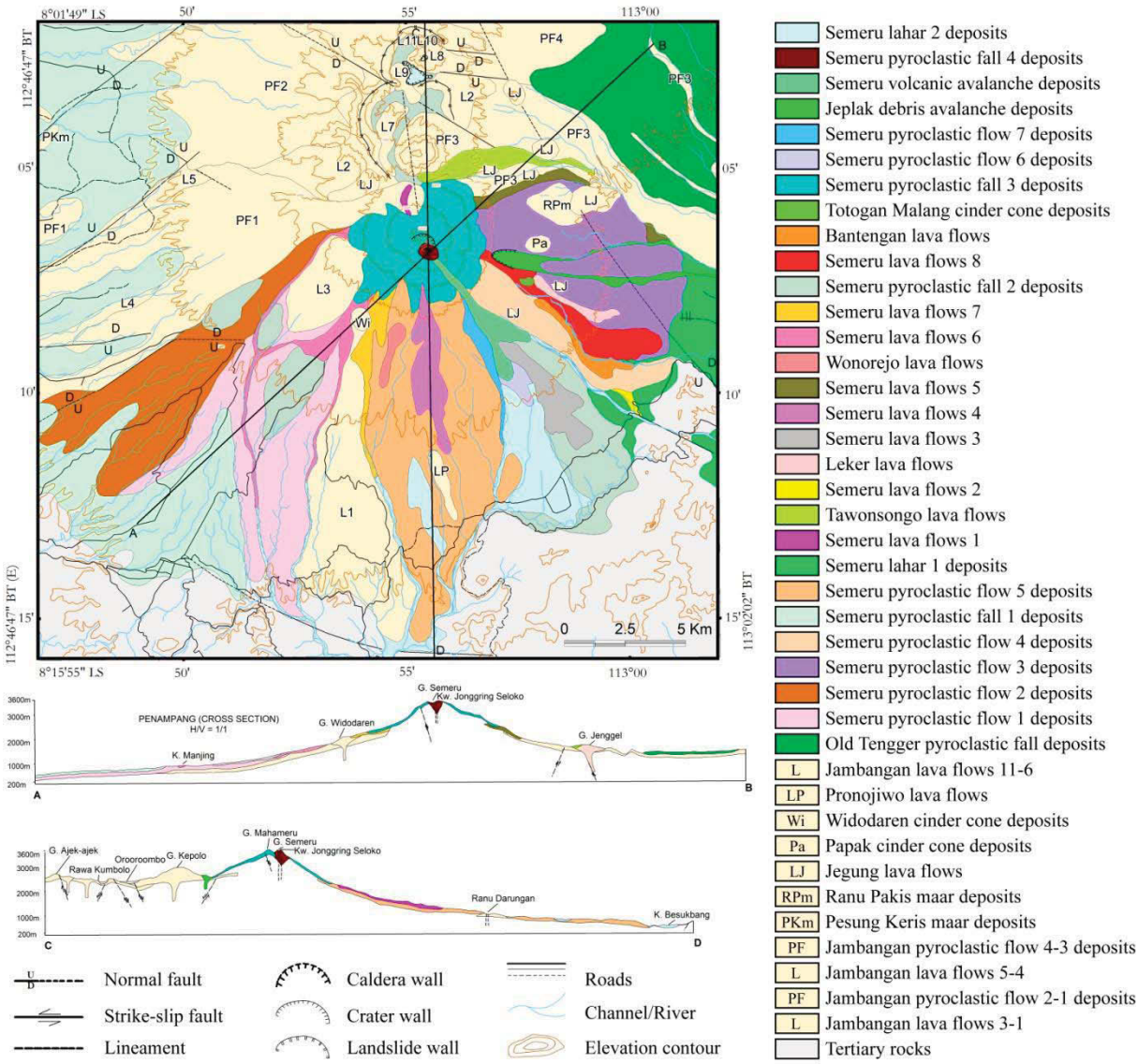

Figure 2.9. The geological map of the Semeru-Jambangan complex published by CVGHM (Sutawidjaja et al., 1996) including Jambangan, Old Tengger, Ajek-ajek, Kepolo, Mahameru and Semeru volcanic deposits.

The geological map of Jambangan-Ajek-ajek complex, together with Mahameru-Semeru volcano (Sutawidjaja et al., 1996) is shown in Figure 2.9. Based on the lithologic characteristics, stratigraphic succession and eruptive source, the volcanic products of Semeru-Jambangan complex comprise Jambangan, Old Tengger, Ajek-ajek, Kepolo, Mahameru and Semeru volcanic deposits. In this map, the volcanic products are divided into primary deposits (pyroclastic flows, lava flows, scoria cone and pyroclastic fall) and secondary deposits (volcanic debris avalanches and lahars). According to Wahyudin (1991), the volcanic products in the Jambangan-Ajek-ajek complex are: (1) medium-K basalt, mafic andesite, andesite, and dacite; (2) remnants of composit cones that consist

of basalt, basic andesite, acid andesite lavas and pyroclastic-flow deposits; (3) the Old Tengger volcanic deposits, which here consist of a series of tephra fall deposits; (4) Ajek-ajek mafic andesite, andesite and dacite lavas; and (5) Kepolo mafic andesite lavas.

Mahameru-Semeru volcano

Semeru, the youngest volcano in the Semeru-Tengger massif, hosts the currently active Jongring Seloko vent, and has been built on, and is buttressed against the Mahameru (or old Semeru) to the west, and against the Jambangan caldera to the north. The Semeru summit cone has grown on the older edifice of Mahameru (Fig. 2.10). The Mahameru summit area shows three arcuate scarps, probably crater rims, suggesting that vents have migrated from northwest to southeast (Thouret et al., 2007). The Jonggring-Seloko crater with a hexagonal shape of the vent area, 500 m southeast from Mahameru summit, reportedly initiated in 1913 (Van Padang, 1951). The recent active vent sits at the top of the conspicuous SE-trending scar that cuts the steep-sided SE flank of the edifice. This elongated horseshoe-shaped scar, about 1.8 km long and 490 m at its widest point, channels rock-falls and pyroclastic flows during phases of heightened activity.

Wahyudin (1991) and Sutawidjaja et al. (1996) outlined the lithological succession of the Semeru volcanic complex. Primary deposits of Semeru consist of lava flows and pyroclastic (fall and flow) deposits. Mount Semeru is composed of two cones, Mahameru (the old Semeru) and Semeru (young). The Mahameru volcanic deposits consist of basalt, basic andesite lavas, pyroclastic-flow and pyroclastic fall deposits, and lahar deposits. In the geological map (Fig. 2.8), deposit units of Semeru pyroclastic-flows 1-5, Semeru pyroclastic-fall 1, Semeru lahar 1, and Semeru lava flows 1 are the product of Mahameru ('old' Semeru) cone. Young Semeru products comprise all deposit units after Semeru lava flows 1. Semeru volcanic deposits are composed mainly of Strombolian-Vulcanian fall deposits, pyroclastic-flow deposits, basalt, mafic andesite, andesite lava flows and secondary volcanic deposits such as lahars and debris avalanches. Non magmatic debris avalanches with more than 6 million m^3 volume were emplaced on the east flank of Semeru in 1909 and 1981 (Siswowidjoyo et al., 1997). The rocks of young Semeru erupted from the central vent at the summit and at least five flank vents. The products generated from flank eruptions are the lava flows of Tawonsongo, Leker,

Wonorejo and Bantengan (1941 lava), and the Totogan Malang cinder cone deposit (Sutawidjaja et al., 1996).

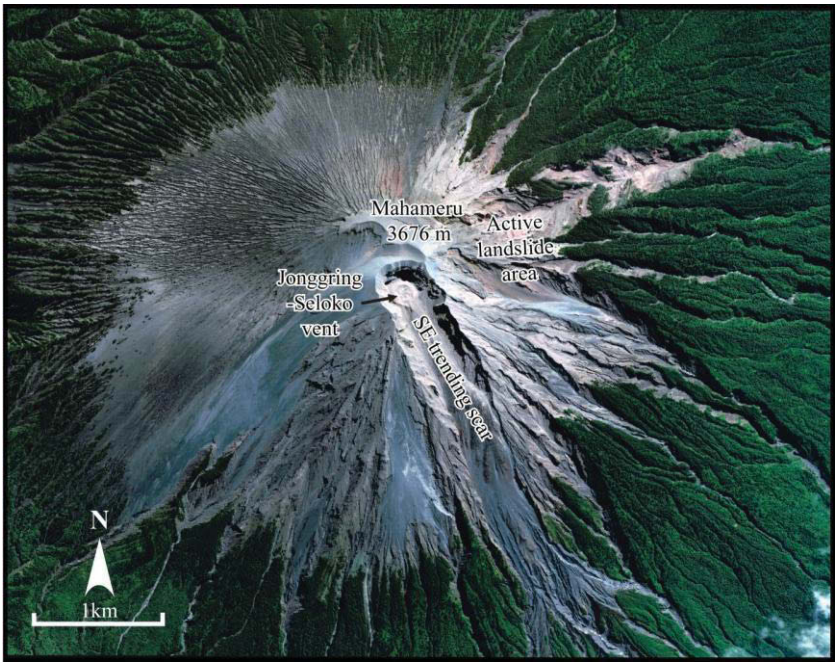

Figure 2.10. The 8 June 2011 WorldView image of Semeru summit cone shows the Mahameru summit area, the Jonggring-Seloko vent and the SE-trending principal scar.

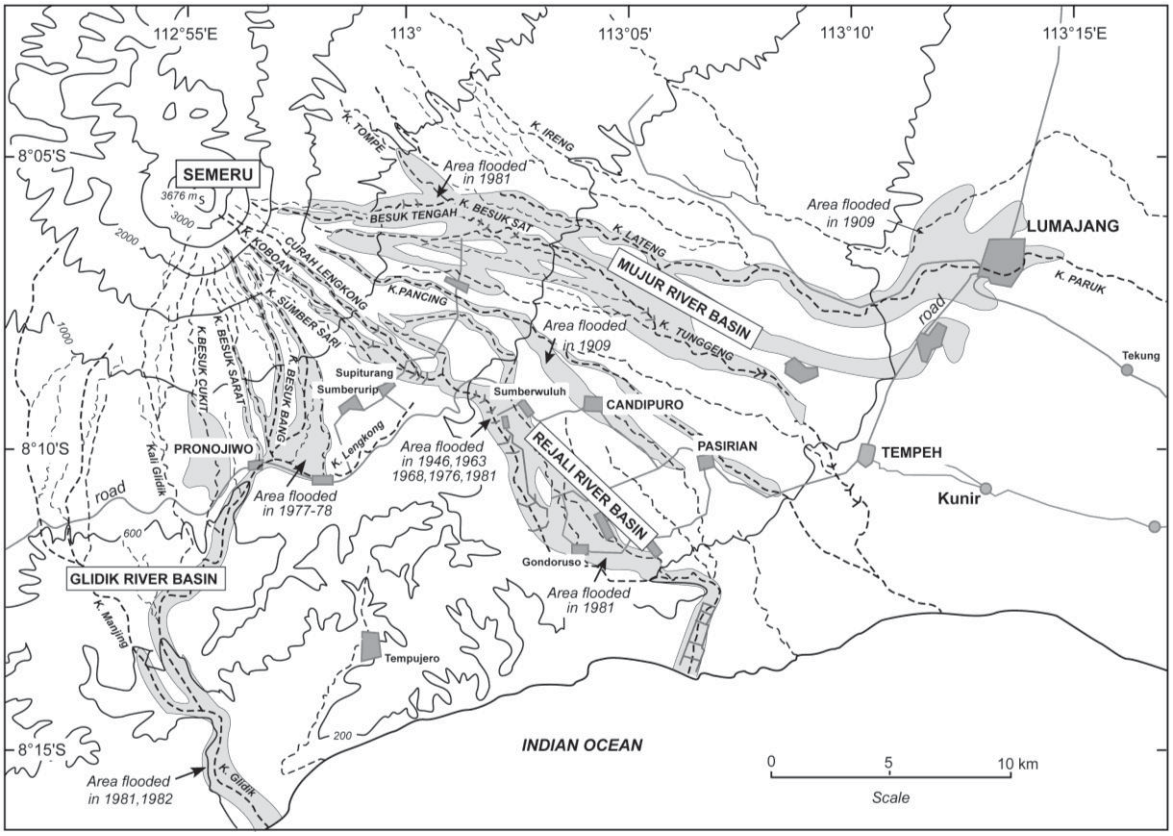

Figure 2.11. Map of Semeru valleys and plains flooded by lahars (grey areas) during the twentieth century (Thouret et al., 2007).

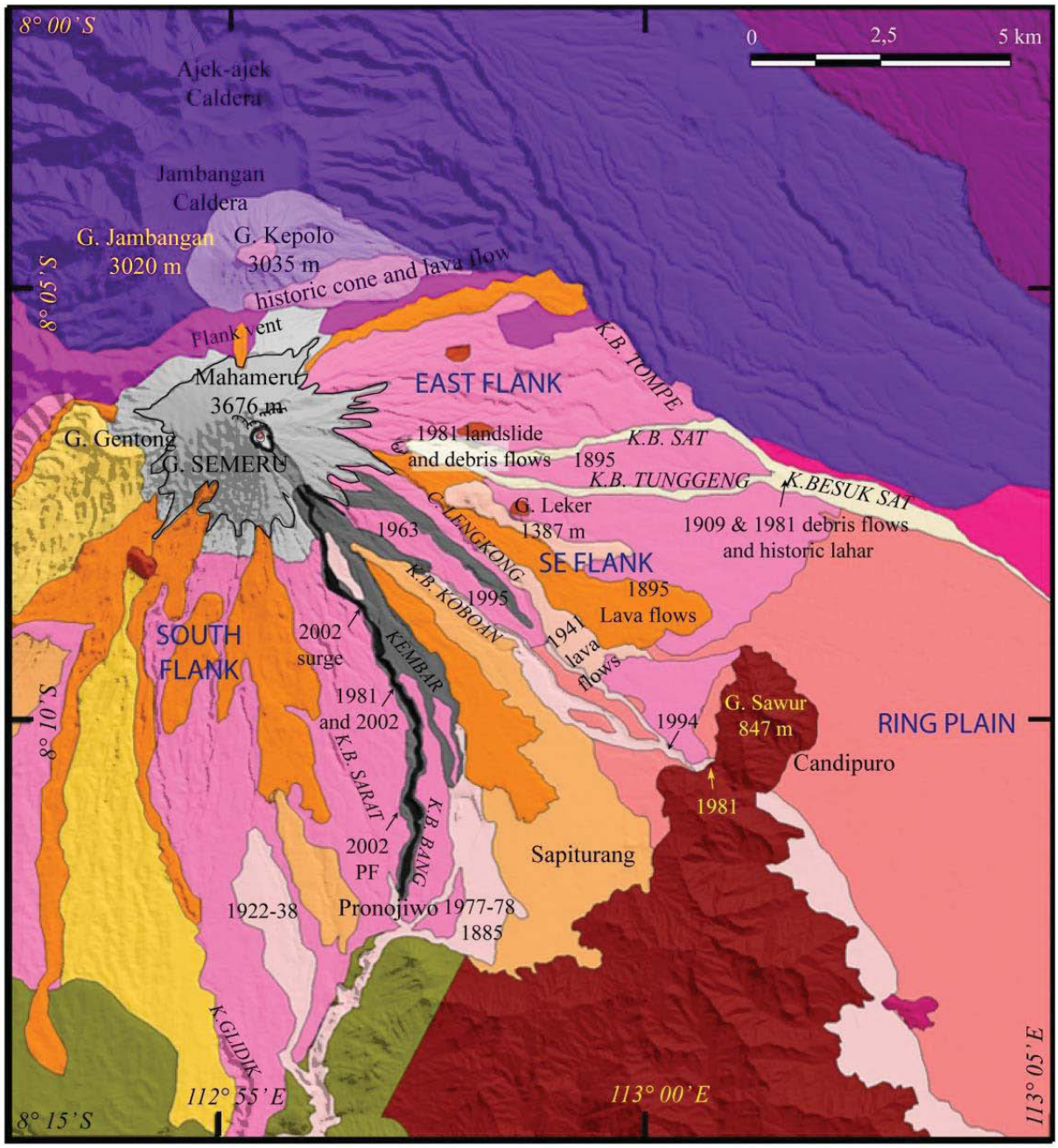

Figure 2.12. Geological map of Semeru composite cone and ring plain map overlain on the TOPO-DEM (Solikhin, 2009).

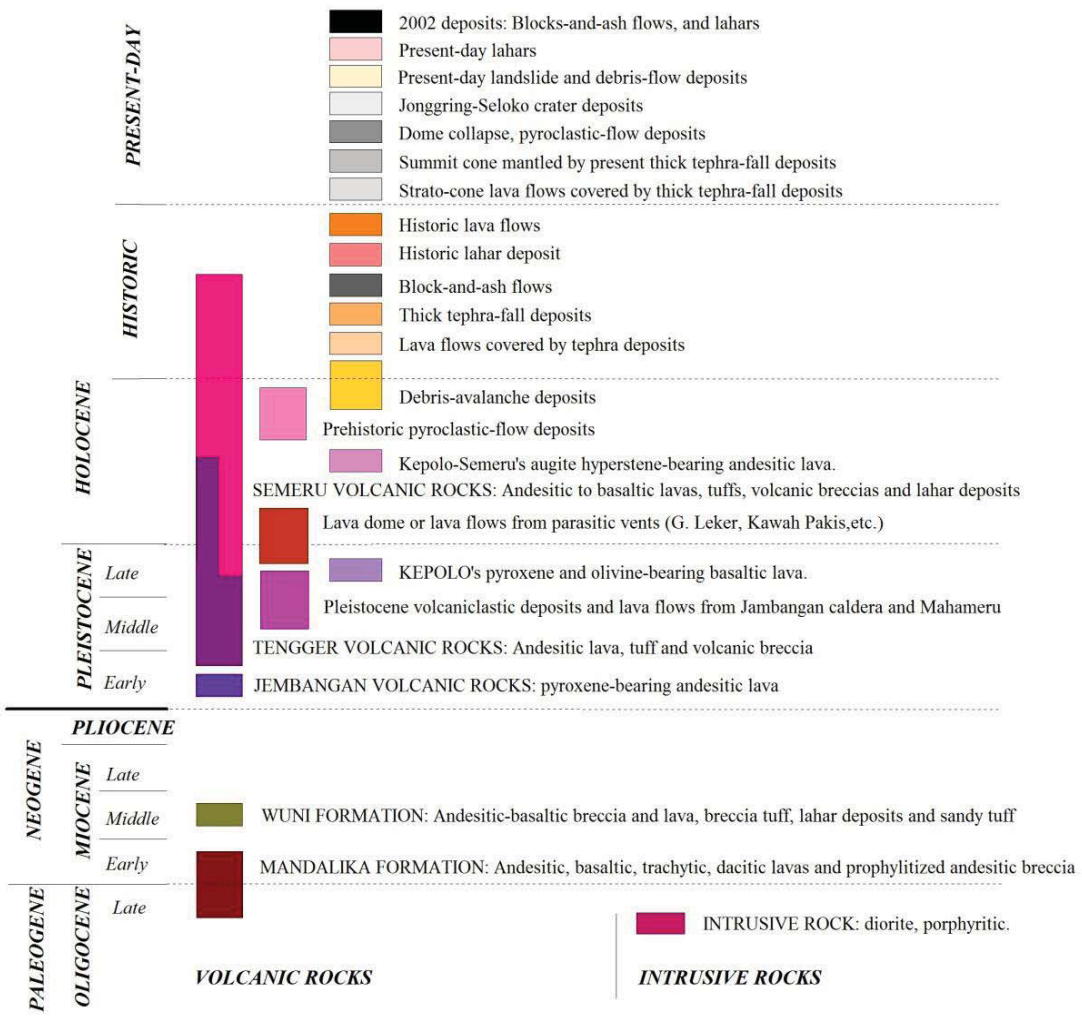

Figure 2.12. (continued) Caption of the geological map of Semeru shows the stratigraphy of deposit units.

Remote sensing methods using high-spatial resolution satellite imagery, aerial photographs and DEM analysis have been applied to map the geology of Semeru volcano. Thouret et al. (2007) have updated and simplified the geological map of Semeru composite cone and ring plain based on previous work (Situmorang, 1989; Wahyudin, 1991; Simkin & Siebert, 1994; Sutawidjaja et al., 1996; Siswowidjoyo et al., 1997; Carn, 1999), aerial photographs 1990-1991, and three SPOT 4 and 5 scenes. The map outlines the extent of the 29 December 2002 pyroclastic-flow and surge deposits in the Bang valley (see Fig. 1.4B in Chapter 1) and the scar of 1981 landslides on the east flank of Semeru. Thouret et al. (2007) provides a map of twentieth century lahar deposition in Semeru's valley and plains (Fig. 2.11). Hyperconcentrated flows are more frequent in Semeru drainages than large debris flows, but the latter, including primary (hot) lahars, are not unusual during and after pyroclastic flows (Thouret et al., 2007).

Solikhin (2009) and Solikhin et al. (2012), following Thouret et al. (2007), have updated the geological map of Semeru with additional data from interpretation of later satellite images, aerial photos, DEM analysis and fieldwork (Fig. 2.12). The DEM analysis and interpretation of satellite images help to better distinguish each group of deposits. Geology and landforms of Semeru volcano and ring plain have also been mapped semi-automatically by Kassouk et al. (2014), who used the object-oriented classification (OOC) of high-spatial resolution (HSR) satellite imagery. This technique provides a map with more detail for geomorphic features.

2.3.2. Regional tectonic setting of the Semeru-Tengger massif

As previously noted, the eruption centers of the Semeru-Tengger complex occur along a N-S lineament that is slightly concave to the east. This N-S line probably represents a transverse fault or flexure. Wahyudin (1991) has defined at least four normal faults or structural trends in the Jambangan-Semeru complex, namely the Gunungsawur fault, Jambangan fault, Butak graben and Rejosari fault (Fig. 2.13). The NW-SE trending fault of Gunungsawur, aligned from Gunungsawur to Ranu Pani, suggests a reactivation after the emplacement of Jambangan lava in Ranu Pani. The NW-SE trending fault of Jambangan is located across Jambangan caldera, which was reactivated after formation of the Ajek-ajek caldera. The Butak graben is a fault collapse which crosses Mt. Ajek-ajek, and consists of two parallel E-W trending faults. The graben is younger than Jambangan lava, and it is marked by an escarpment in the lava. The NE-SW-trending Rejosari fault is located in the western part of Semeru volcano. It is identified by uplift, escarpment and crushed rock along fault line where it traverses basement (Tertiary) rocks of the Semeru-Tengger complex.

The structural map of Semeru-Tengger volcanic massif (Fig. 2.13) is based on the interpretation of digital elevation models (DEMs) as well as of IKONOS and SPOT5 satellite images combined with the drainage network map and the CVGHM geological map. This map updates the structural map of Semeru-Tengger massif in Solikhin et al. (2012) with a new interpretation of fault mechanism. The map in Figure 2.13 shows the relationship between the regional tectonic setting and the principal structures of the edifices. A rose diagram of faults or structural trends and a sketch portraying fault kinematics summarize the regional tectonic setting of the massif (Fig. 2.13). Widespread

and thick vegetation prevented many of these faults from being identified in the field. The linear features comprise long (more than 1 km), rectilinear topographic alignments and sharp, systematic changes in river directions.

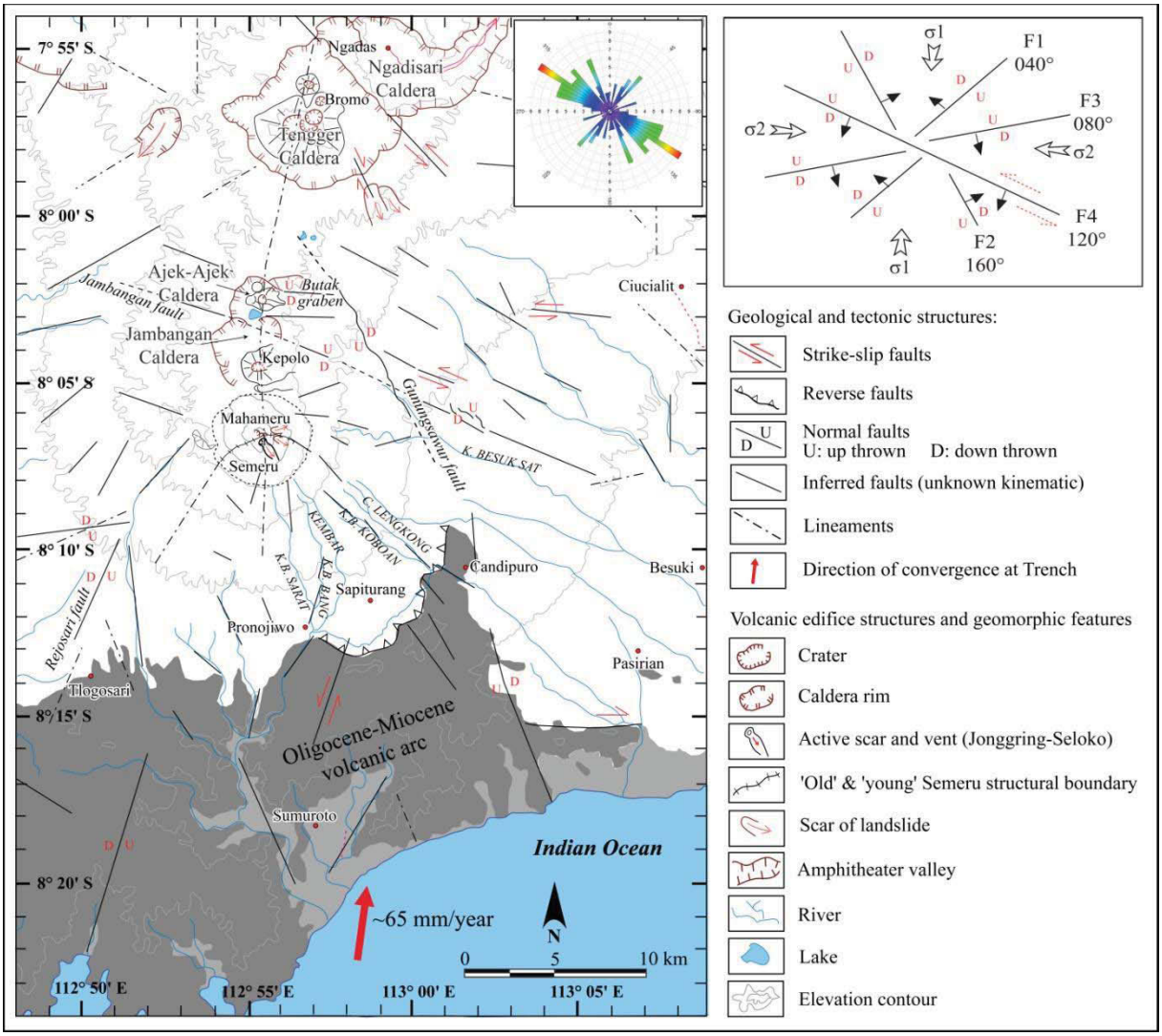

Figure 2.13. Structural map of the Semeru-Tengger volcanic massif, inferred from DEMs and satellite images. Rose diagram of lineaments showing the dominant NW-trending alignment and the sketch diagram depict the regional setting around Semeru consist four groups of faults, F1 to F4. The four faults defined by Wahyudin (1991) are also included in this map.

The rose diagram of all identified linear topographic segments shows a dominant NW–SE structure trend. Based on the rose diagram, we have identified four groups of faults F1 to F4: (F1) A 040°-trending group, including the Rejosari fault corresponds to normal faults observed on the S and the SW flank and ring plain of Semeru as well as in the 'old' (Oligocene–Miocene) volcaniclastic rocks (Fig. 2.13). (F2) A 160°-trending group matches the normal fault in the Tertiary volcanic deposit area SE and S of Semeru. The

Gunungsawur fault is part of this group. NNW–SSE trending features on the eastern part of Semeru and a NW–SE sinistral strike–slip fault delineate the northern limit of pyroclastic deposits from Semeru, as deduced from the texture of these deposits on the images. (F3) A 080° group contains the faults that guide the E and NNE alignments of the Tengger post-caldera vents and Butak graben. (F4) The last group of 105° to 140° faults with a prevailing trend of 120°, occur on the western side of the Semeru–Tengger volcanic massif including the Jembangan fault across Jembangan Caldera. Several amphitheaters caused by flank erosion and opened to the west are probably controlled by the NW–SE trending faults. This group of faults (F4) probably has two fault mechanisms, normal and sinistral strike-slip faults. This 120°-trending structure has also been mapped by Sribudiyani at al. (2003) as a basement structure in the south of Semeru. However, this group also offsets other groups of faults, which suggests that the NW–SE trending fault is probably the old fault structure that has been reactivated in the recent time. The structural map of the Semeru–Tengger volcanic massif shows that the southern area is dominated by the NNE–SSW compressional stress regime (σ1) due to subduction process at the trench <50 km to the south. This produces the first and second groups of faults. The third group, located in the north sector, shares the same direction as the Madura basin and magmatic intrusions from older (Pleistocene) volcanoes such as Jambangan and Ajek-ajek.

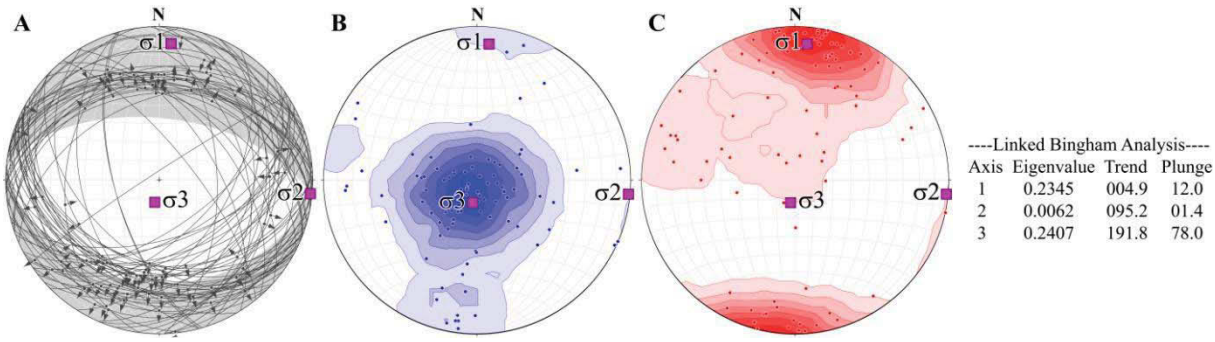

Figure 2.14. Kinematic analysis of faults at the Semeru zone (Fig. 2.3B). **A.** Fault planes and striae (n=90) showing that most of faults are vertical and follow to ESE direction. Contour diagram of shortening axes **(B)** and extension axes **(C)**. The direction of stress axes based on Linked Bingham analysis are shown with the 005° principal striking axes.

A kinematic analysis of fault data was performed using the "Faultkin" algorithm, which calculates P and T axes for each fault based on fault orientation, striae orientation and the sense of motion (Marret & Allmendinger, 1990; Allmendinger et al., 2012). As the

input we used the faults mechanism data from the Global CMT catalogue on the selected area (Semeru zone indicated in Fig. 2.3B). The diagram in Figure 2.14 helps distinguish three major stresses: σ1 parallels the convergence trend, σ2 favors opening and strike slip and σ3 as vertical stress. The mean P and T axes approximate the infinitesimal shortening (σ3) and extension (σ1) directions, respectively, for a population of faults (Fig. 2.14). The principal stress axis is the N-S (005°) direction, which is related to the stress from the movement of Indo-Australian plate south of the Semeru Zone (Fig. 2.3B). The contour diagram shows the faults in the population trending along the E-W direction with a normal fault mechanism.

2.3.3. Eruptive history and hazard assessment at Semeru volcano

Semeru volcano is a very active and hazardous volcano in Indonesia. Since at least 1967, phreatomagmatic or Strombolian eruptions have occurred almost daily in the Jonggring-Seloko crater. In addition, every 5 to 7 years on average, extrusion, growth and collapse of lava domes in Jonggring-Seloko crater feed PDCs that travel along the SE-trending scar and then down river valleys towards south and southeast flanks. The ring plain to a distance of 30 km from Semeru is home to more than one million inhabitants (Siebert et al., 2010).

Eruptive history

Data on Semeru activity have been assembled and summarized from a variety of sources by Wahyudin (1991) for 1818 to 1989 period, and Siebert et al., 2010 for 1818 to recent time. Thouret et al. (2007) provide more information of Semeru activity over the 1884-2003 period, whereas Solikhin et al. (2012) summarized the 2002 to 2003 seismic and eruptive activity. Prehistoric eruptions of Semeru-Mahameru volcano took place at the summit (central) and five flank vents located along a lineament on the south-southeastern and northern slopes of the Semeru cone. This Holocene activity has included Strombolian explosive eruptions, lava flows from the summit or from three flank vents and production of large lahars whose deposits extended about 34 km southeast from the volcano. Historical activity of Semeru volcano has been reported since 1818 and the present unrest period started in 1967.

Table 2.1. Semeru eruptive activity since March 2003 summarized from Siebert et al. (2010) and CVGHM reports.

Reported date	Valley, flank, direction and distance	Event and deposits*	Observed activity, magnitude and aftermath
24 March - 11 May 2003	Vent area and scar; Bang and Kembar SSE, 1.5-3.75 km	Aval., Pf, Lh	Explosive activity; dome growth and collapse
24 January 2004	Vent area and scar; Bang SSE, 2.5 km	Aval., Pf	Explosive activity; dome growth and collapse
7 October - December 2004	Vent area and scar; Bang SSE, 1-3 km	Aval., Pf	Explosive activity; dome growth and collapse
22 December 2005	Vent area and scar; Bang SSE, 1-2.5 km	Aval., Pf	Explosive activity; dome growth and collapse
15 November 2007	Vent area and scar; Bang SSE, 1 km	Aval., Pf	Explosive activity;
15-22 May 2008	Vent area and scar; Bang and Kembar SSE, 0.5-3 km; Kobokan SE, 1-3 km	Aval., Pf	Explosive activity; dome growth and collapse
25-28 February 2010	Vent area and scar; Bang and Kembar SSE, 1.7 km	Aval., Lf	Explosive activity; 1.5 km lava flow toward SE-trending scar and 50-200 m rock-falls from lava flow front.
September - November 2010	Vent area and scar; Bang SSE, 4 km	Aval., Pf	Explosive activity: 4.6 km high columns; 400-600 m incandescent avalanche; dome growth and collapse
1-28 February 2012	Vent area and scar; Kembar SSE, 0.5 km; Kobokan SE, 3.2 km	Aval., Lf, Pf	Explosive activity; lava dome started to extrude in late 2011; 400-600 m incandescent avalanche since January 2012; 2.5 km incandescent material on 2 February 2012; two lava flows (1.9 km-long) avalanches and rock-falls from lava flow fronts.

* Aval: Rock avalanches; Lf: Lava flow; Pf: pyroclastic flow; Lh: Lahar

Semeru eruptive activity since 2003 to 2012 is summarized in Table 2.1. Since March 2003 the activity with short-lived eruption columns dominated Semeru activity but at least 9 events of heightened activity produced larger explosions, lava flows, rock avalanches and pyroclastic flows associated with explosions or dome growth and collapse. The last episode of increased activity occurred in the beginning of 2012 and resulted in lava and pyroclastic flows (Wunderman, 2012). This activity began earlier

with the extrusion of a new lava dome in late 2011 directly over the 2010 dome. The 2011 dome was drained by two subsequent lava flows towards the SE-trending scar, the longer of which extended about 1.9 km from the summit vent. Pyroclastic flows were generated by collapse of the steep termini of the lava flows, and their deposits extended to 3.2 km from the summit or 0.7 km from the lava front. In addition, the collapsing lava-flow fronts resulted in high levels of avalanche and rockfall activity.

Semeru volcanic hazards

Based on the historical record of eruptive activity, hazard at and around Semeru may be induced by four possible forms of activity:

1) Strombolian to Vulcanian and phreatomagmatic explosions. Since 1967, when the persistent activity started, the short-lived eruption columns from phreatic (300-1000 m-high above the crater), "cannon-like" (1-3 km-high Vulcanian columns) and small phreatomagmatic explosions that occurred several times a day, are the Semeru 'background' activity (Thouret et al., 2007). During the increased activity every 5 to 7 years, Vulcanian explosions with 3 to 7 km-high columns produce ballistic bombs and disperse ash fall. These explosive activities sometime coexist with incandescent rock avalanches from a dome plug, which are followed by small-scale pyroclastic flows mostly towards the SE-trending scar. These explosions produced ejected deposits dispersed from Jonggring Seloko vent that consist of volcanic bombs, lapili and ash. Due to the high summit elevation, volcanic bombs can reach a distance as far as 8 km from the summit, whereas the dispersion of lapilli and ash depends on the explosion magnitude and the wind speed.
2) Lava dome extrusion, growth and collapse in the Jonggring-Seloko crater. These activities occur during the increased activity related to accelerated extrusion rates. Hazard during dome growth is confined to the summit area but increases to higher level during dome disruptions as a result of partial dome collapse accompanied by incandescent rock avalanches and pyroclastic flows. Block-and-ash flows induced by dome collapse sweep the SE-trending scar and are channeled as far as 5 to 12 km downstream Bang, Kembar and Kobokan valleys at about 5 years interval (e.g. 1972, 1977, 1981, 1994, 1995, and 2002) (Thouret et al., 2007). The 3 February 1994 pyroclastic flows with a volume of 6.8×10^6 m^3 swept the Koboan and Lengkong

valleys as far as 11.5 km from the vent on the SE flank (Sadjiman et al., 1995). On 20 July 1995, pyroclastic flows traveled 9.5 km downstream the Koboan valley (Dana et al., 1996). On 29 December 2002, fine-ash rich pyroclastic surges swept across the forest and agricultural land at the southwest edge of the Bang Valley at a distance between 5 and 8 km from the crater (Venzke, 2003). The 2002 block-and-ash flows, with a volume of 5.45 million m^3, caused the evacuation of 500 people and damaged the forest and tilled land on the west side of the Bang Valley (Solikhin et al., 2012).

3) Extrusion of lava flow and formation a new parasitic vent. The eruptions of Semeru volcano throughout prehistoric times have been dominated by the summit extrusion of lava flows (Wahyudin, 1991) and have formed a lobate topography on the SW, SE, and east flanks of Semeru. Several parasitic cones are found on the Semeru flanks, and most modern flank eruptions are andesite in composition. Future parasitic eruptions can be controlled by lineaments or structural trends on the south-southeastern sector of the volcano at a distance of less than 7 km from the central vent (Wahyudin, 1991). Lava flows at Semeru have been reported since 1832, then in 1895 and 1941-1942 along >1 km long fissures on the cone's flank. For example, the 1941-1942 lava flow issued from a NW-SE fissure 1.3 km in length, which opened at the southeastern foot of the Semeru cone. Its volume amounted to 3 million m^3 in about one month. The latest lava flows in 2012 towards the SE-trending scar extended about 1.9 km from the summit vent and was followed by pyroclastic flows generated by collapse of the lava-flow fronts. Although lava flows and parasitic eruptions are minor hazards due to relatively slow movement, renewed extrusion of lava flows from both summit and flank would be a higher threat because of the presence of villages in the probable flow path. Lava flow on higher and steeper slope also can collapse and produce rock avalanches and pyroclastic flows.

4) Lahars and debris flows. Semeru is known as one of the most effective lahar producers on Earth (Lavigne and Thouret, 2002; Thouret et al., 2007, 2014). Although lahar and debris flow from Semeru are secondary volcanic hazards, these are the most likely serious hazards. Lahars at Semeru caused more than 1000 casualties during the 20th century, devastating more than 40 villages and 110 km^2 of tilled land since 1884 (Thouret et al., 2007). Large-scale lahars exceeding 5 million m^3 in volume have occurred at least five times since 1884. During the rainy season,

Semeru produces small to medium-scale lahars (≤0.1 million m^3) every week, which are triggered by the remobilization of pyroclastic debris. Semeru's lahars can travel runout distances 15 to 35 km as debris flows onto the ring plain below 600 m elevation. In the south, they end up in the coastal area after passing through several villages. Historical lahars occurred most frequently in the Sat and Kembar valleys (Fig. 2.11), where pyroclastic deposits from the summit were concentrated. Debris flows are even more deadly than pyroclastic flows at Semeru because they can occur in any year, even in the absence of an eruption. Large-volume debris flows took place in 1909 and 1981 sourced from the east and northeastern slopes of Semeru. Landslide-induced debris flows occurred in particular on the east flank drained by the Tengah and Tompe Rivers (Fig. 2.11).

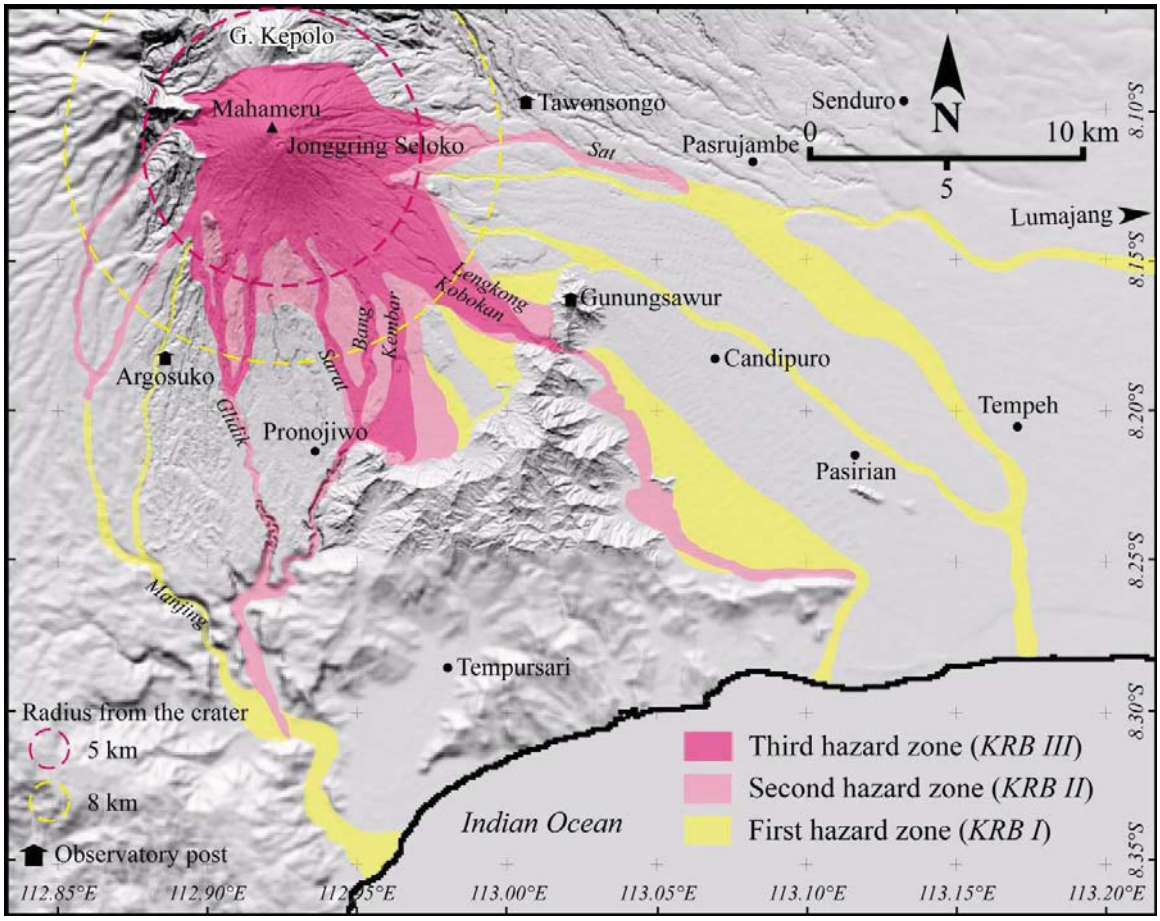

Figure 2.15. Hazard zonation map of Semeru showing three hazard zones (KRB I-III) as redefined after Bronto (1996). This map is used by CVGHM and local government as a guide for volcano disaster management.

To assist in the planning of mitigation measures against the volcanic hazards, the CVGHM published a volcanic hazard map in 1986 (Surjo, 1986), revised in 1992

(Situmorang, 1992) and 1996 (Fig. 2.15; Bronto et al., 1996). The 1996 map has not been revised and is still used by CVGHM and local government. In this map, the hazardous areas have been divided in three hazard zones termed *Kawasan Rawan Bencana* (KRB), namely first, second and third hazard zones (KRB I, II and III).

The first hazard zone (KRB I) is potentially affected by lahars, possible extension of pyroclastic and lava flows, and tephra fall. The lahar-prone zones are adjacent to the river channels as lahars can spill over channel banks. The area prone to heavy ballistics and tephra fall lies in the radius of 8 km from the Jonggring-Seloko crater. People living in the first hazard zone should increase their alertness during a large eruption and in case of heavy rainfall in the summit area.

The second hazard zone (KRB II) is potentially affected by pyroclastic flows, lava flows, rockfall, rock avalanche, heavy tephra fall, ejected hot mud (from phreatic eruption), lahars and toxic gas. This hazard zone is located 5 km around the Jonggring-Seloko crater and extends as far as 20 km to several river valleys. Inhabitants in this zone must be alerted when there is an indication of increased activity and would be recommended to evacuate by CVGHM when there is an imminent threat of eruption.

The third hazard zone (KRB II), also called forbidden zone, is the area most likely to be affected by pyroclastic flows, lava flows, incandescent rock avalanche and toxic gas. This zone lies within a radius of 5 km around the crater and along river channels as far as 12 km from the summit. This zone is forbidden for permanent settlements or human activity, and will be totally closed in case of high level of activity.

The Semeru hazard-zone map has been suggested to be revised by Siswowidjoyo et al. (1997) and Thouret et al. (2007). Siswowidjoyo et al. (1997) did not propose changes to the hazard zone related to volcanic activity, but stressed on the assessment of hazardous debris flows in the Tompe-Sat catchment. Some dikes were constructed after the 1909 event to prevent any possibility of overflow into the Sat and Patuk Rivers which run to Lumajang city. Additional training dikes, consolidation dams and check dams were also constructed since the 1980's to 2000's along the lahar and debris flow-prone catchments. These dike and dam constructions can minimize and control the impact of debris flows or lahars. Thouret et al. (2007) suggested two additional hazard prone areas: an area to the east that would be affected by a debris avalanche in case of failure of the upper east flank of Semeru, and the Mujur River drainage network that is likely to be flooded by voluminous debris flows triggered by landslide, heavy rainfall and

possibly earthquakes. Related to the landslide hazard mitigation, CVGHM provided the landslide susceptibility zone map of Lumajang Regency (Fig. 2.16). This map consists of four level of susceptibility to landslide, namely very low, low, moderate and high landslide susceptibility zone. Noteworthy, the landslide susceptibility map also indicates potential areas for debris flows derived from the eastern slopes of Semeru volcano, Jembangan and Ajek-ajek calderas.

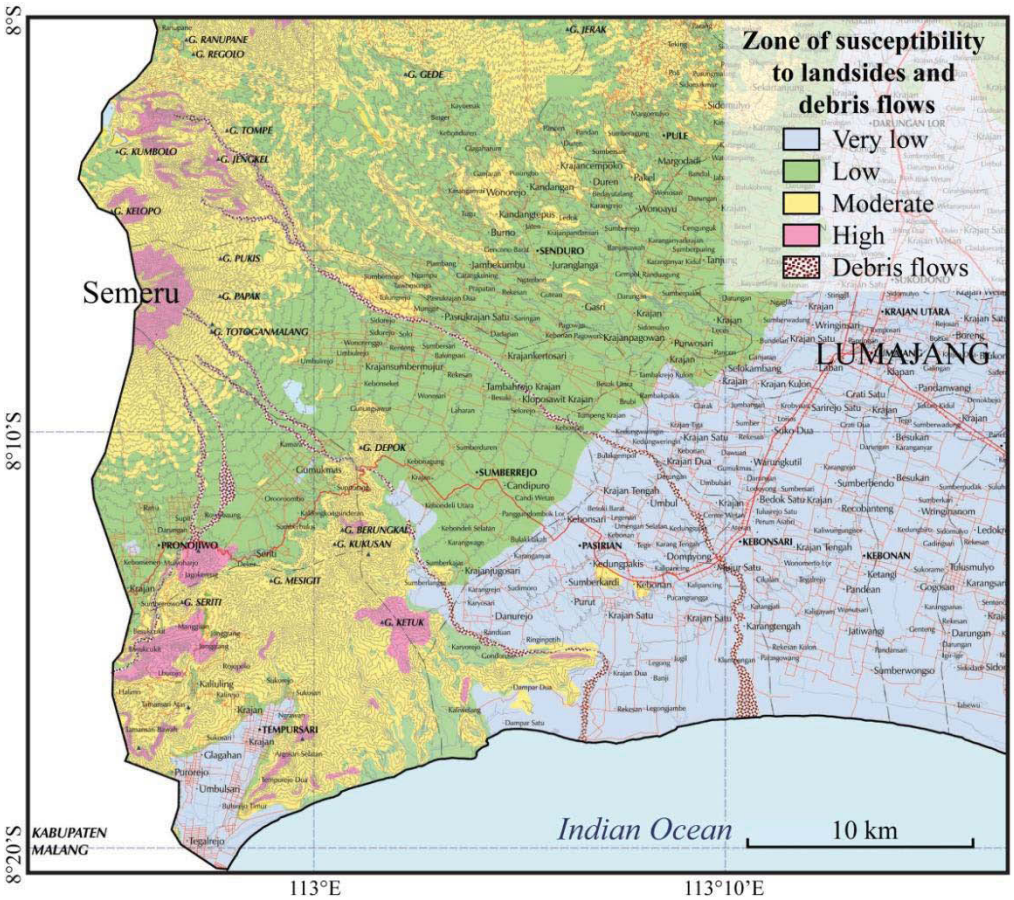

Figure 2.16. Susceptibility to landslide zone map of Lumajang Regency, East Java Province, provided by CVGHM.

2.4. Merapi volcano: geology, tectonic setting, eruptive history and hazards

Mount Merapi or *Gunung Merapi* (literally "Mountain of Fire" in Indonesian/ Javanese), is a very active stratovolcano located on the border between Central Java and Yogyakarta Provinces, approximately 28 km north of the large Yogyakarta city (Fig. 2.17). It erupts every 2 to 6 years on average (in the last 100 years; see Voight et al., 2000 for a detailed summary) and is feared for its deadly block-and-ash flows (BAFs) - avalanches of hot rocks and gas that are generated when parts of lava domes constructed during recent eruptions in the summit crater collapse and slide down the

mountain's steep flanks. Like most of andesitic composite volcanoes, the history of Merapi has been marked by alternating episodes of effusive and explosive activity. Beyond the threat of disaster that can occur at any time, iconic Merapi has social and economic aspects which are important for more than 4 million people in the surrounding region. Mining erupted material support the structural development in Yogyakarta and Central Java Provinces, as well as the agricultural products from the slopes of Merapi and the development of tourism that support the growth of the local economy.

2.4.1. Volcanic features and geology of Merapi volcano

Merapi volcano is part of the volcanic front of the Sunda Arc (Fig. 1.1B in Chapter 1) and belongs to a cross-island range of four composite volcanoes comprising, from north to south, Ungaran, Telemoyo, Merbabu and Merapi, which is a regional alignment with 165° direction (Hamilton, 1979; Fig. 2.17). These volcanoes are young from north to south and Merapi is the most active among them. The main structures of Merapi as shown in Figure 2.18 consist of several features (Camus et al., 2000) and several hills around Merapi summit cone (Mt. Bibi, Mt. Turgo, and Mt. Plawangan).

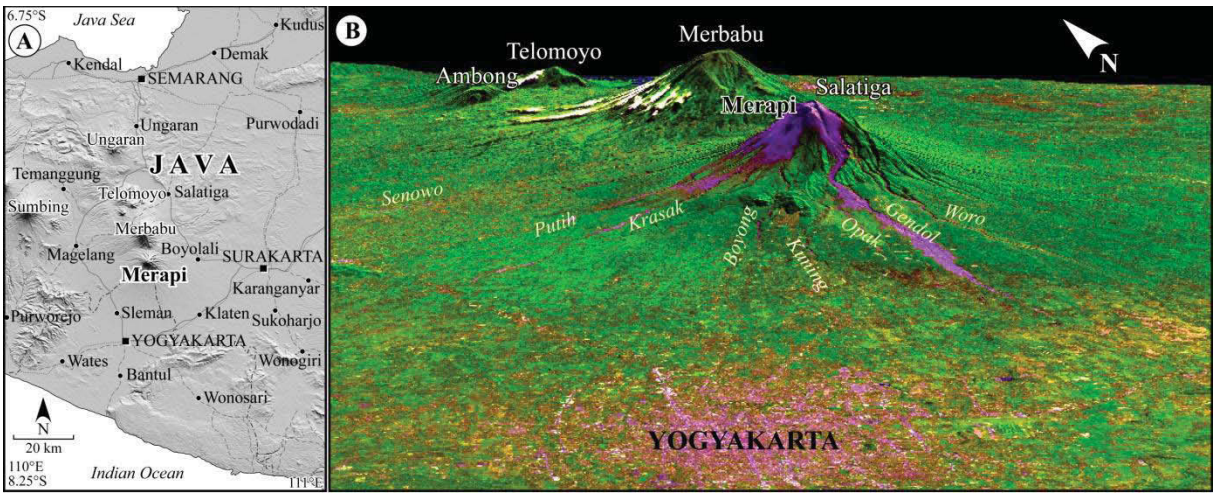

Figure 2.17. A. Location of Merapi volcano 28 km north of the Yogyakarta City. **B.** ASTER image of the Merapi and surrounding area acquired on 13 June 2012, looking northeast and draped on a SRTM-DEM. Several rivers that source at Merapi are outlined.

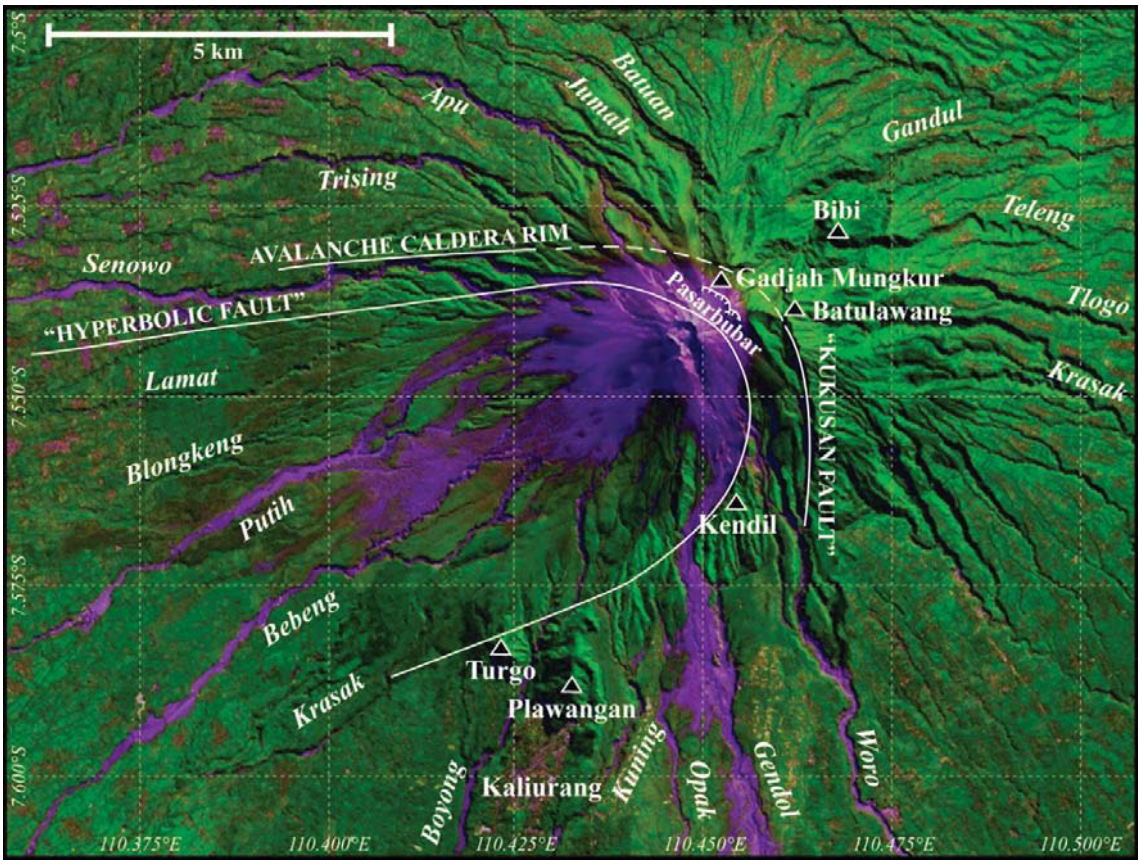

Figure 2.18. Main structural features of Merapi volcano (after Camus et al., 2000) outlined on the 13 June 2012 ASTER image.

Detailed stratigraphic and geochronological studies have defined the history and evolution of the Merapi composite cone (Bahar, 1984; del Marmol, 1989; Berthommier, 1990; Andreastuti, 1999; Andreastuti et al., 2000; Camus et al., 2000; Newhall et al., 2000; Gertisser et al., 2012). These studies have shown that Merapi is a very young volcanic complex, but age information on the older Merapi units has remained scarce and many aspects of the overall volcanological and structural evolution of Merapi continue to be controversial (Camus et al. 2000; Newhall et al. 2000). Several authors have published different hypotheses and age information particularly for the older Merapi units. Berthommier (1990) and Camus et al. (2000) suggested that the growth of Merapi has included four stages, termed 'Ancient Merapi' (40,000–14,000 yr BP), 'Middle Merapi' (14,000–2200 yr BP), 'Recent Merapi' (2200 yr BP–1786 AD), and 'Modern Merapi' (after 1786 AD). In a more simple way, Newhall et al. (2000) distinguished three evolutionary stages, namely 'Proto Merapi' (older than 9630 yr BP), 'Old Merapi' (9630 yr BP – 50 AD) and 'New Merapi' (after 50 AD). More recently, Gertisser et al. (2012) suggested that the construction of the basaltic andesite composite

cone of Merapi began after 170 ka and retained the three Merapi stages of Newhall et al. (2000), but with different ages: 170 – 30 ka for 'Proto Merapi', 30 – 4.8 ka for 'Old Merapi' and less than 4.8 ka for 'New Merapi'.

In addition to differences in Merapi's stage numbers and chronology, discrepancies in interpretations stem from the significance attributed by authors to geologic archives from Merapi growth, flank failure(s), and blast deposits. Newhall et al. (2000) suggested that Gunung Turgo and Plawangan, two basaltic hills in the southern sector of the volcano, represent the erosional remnants of a Proto Merapi cone and interpret G. Bibi to be a vent that erupted through the upper flank of Old Merapi. Berthommier (1990) and Camus et al. (2000) considered Gunung Turgo and Plawangan to be a basaltic flank vent of 'Ancient Merapi' with an age of 40±18 ka whereas the 67 ka-old Gunung Bibi was interpreted as an old, pre-Merapi edifice. In contrast, Gertisser et al. (2012) suggested that Gunung Turgo and Plawangan (138 and 135±3 ka) including Gunung Bibi (109±60 ka) are the two earliest, Proto-Merapi volcanic edifices.

Although all authors recognize the occurrence of at least one flank failure at Merapi, their interpretation of deposits, chronology and significance widely differ. Berthommier (1990) and Camus et al. (2000) claim that a debris-avalanche deposit to the west reflects a flank failure linked to an eruption between 6700 and 2200 yr BP. Newhall et al. (2000) suggest that Old Merapi collapsed once or several times producing debris avalanche(s) and leaving a somma rim high on Merapi's eastern slope between 1600 and 1100 yr BP. Gertisser et al. (2012) consider the possibility of several flank failures, the latest of which occurred after 4.8±1.5 ka and marked the end of the 'Old Merapi' stage. The extent of pyroclastic flows, surges and blasts also became the subject of debates. A series of deposits record the 'recent Merapi' growth, such as ash- and scoria-flow deposits and thick Plinian and/or phreato-Plinian tephra fall deposits that mantle an area in excess of 800 km^2, especially to the south. Additional pyroclastic-surge deposits are possibly related to phreatomagmatic eruptions that produced the Gumuk ashfall deposit (2200–1470 yr BP) and Sambisari ashfall deposit (600–470 yr BP) as far as 30 km from the Merapi summit (Berthommier, 1990; Camus et al., 2000). These authors argue that Sambisari ash and lahar deposits 8 m thick, which extend about 30 km on the Yogyakarta plain, buried the Sambisari temple at 20 km distance from the source (Fig. 2.19A) at the start of the 15th century. Newhall et al. (2000) assume that large explosive

eruptions followed shortly the Old Merapi collapse, based on the occurrence of pyroclastic flows to the south and west on the Yogyakarta plain and in the Kaliurang vicinity. Newhall et al. (2000) suspect, without direct evidence, that large explosive eruptions followed the c. 928 AD cultural change in Central Java and may have led to the decentralization of the Mataram civilization (Djumarma et al., 1986; Boechair, 1976).

The geological map of Merapi volcano and its ring plain (Fig. 2.19A) is adapted from previous studies (Thaden et al., 1975; Wirakusumah et al., 1989; Rahardjo et al., 1995; Gertisser et al., 2012) and combined with interpretation from DEMs and satellite imagery. This map depicts the lithological units and tectonic structures of the Merapi region. The basement of this area is composed of metamorphic rocks and igneous rocks that formed between the Late Cretaceous and Early Paleogene (Sribudiyani et al., 2003). In the south-eastern part, Gunung Kidul (Fig. 3A), steep mountains of volcanic rocks and limestone with karst landforms, are exposed. Volcanism in the Gunung Kidul area took place between the middle Eocene (c.45 Ma) and the early Miocene (c.20 Ma), and its activity included significant felsic volcanism (Smyth et al, 2008).

The Tertiary volcanic arc in the Merapi region has been characterized by extensive explosive activity, and its deposits including ash, tuff, breccias, and lava flow range from andesite to rhyolite in composition. Our geological map of Merapi (Fig. 2.19A) is adapting and simplifying the geological map in Gertisser et al. (2012), which presented an adapted version of the geological map of Merapi (Wirakusumah et al., 1989), and considering stratigraphic data from Bahar (1984), del Marmol (1989), Berthommier (1990), Andreastuti et al. (2000), Camus et al. (2000), and Newhall et al. (2000). Deposits of Merapi simply divided in three units: Proto- (Late Pleistocene to 30 ka), Old (30 to 1.7 ka) and Young Merapi deposits (<1.7 ka). The Proto-Merapi deposits comprised of lava flows from Mt. Bibi, Mt. Turgo and Mt. Plawangan (Fig. 2.18). Mt. Bibi (109±60 ka) is a small basaltic andesite volcanic structure on Merapi's north-east flank. Mt. Turgo and Mt. Plawangan (138±3 ka; 135±3 ka), two basaltic hills in the southern sector of the volcano, predate the Merapi cone sensu stricto. The Old Merapi deposits encompass the lava flows from Somma-Merapi and tephra, pyroclastic-flow and lahar deposits. The Young deposits include post-Somma-Merapi lava flows, recent (younger than 1.7 ka) tephra and PDC deposits, lahar deposits, and lava domes.

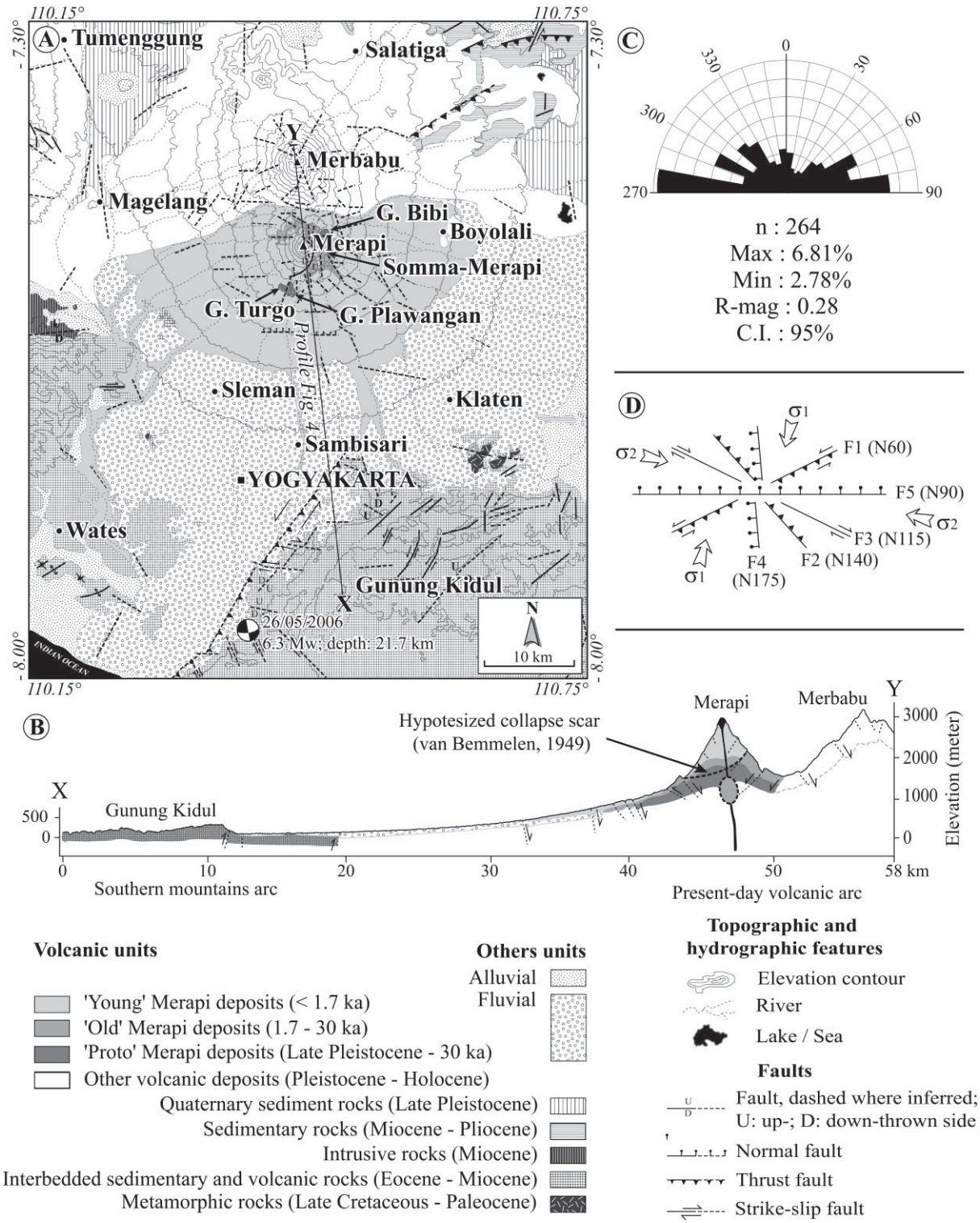

Figure 2.19. A. Geological and tectonic map of Merapi and surroundings including (**B**) a N-S cross section (X-Y), inferred from SRTM3, TOPO-DEM and optical satellites images; **C.** Rose diagram showing five groups of faults with N60, N90, N115, N140, and N175 orientations (n: population; Max: Maximum percentage; Min: Minimum percentage; R-Mag: Resultant of the vector mean; C.I.: Confidence Interval); **D.** The sketch diagram depicts the regional tectonic setting around Merapi.

2.4.2. Regional tectonic setting of Merapi volcano

We have mapped tectonic lineaments and inferred faults from the DEM analysis and based on anomalies in drainage networks from HSR satellite images (e.g. Fig. 2.18). A rose diagram of inferred faults (Fig. 2.19C-D) shows five groups with trends that cluster at 060°, 090°, 115°, 140°, and 175°. We suggest that the NE-SW trending faults are the oldest because they parallel basement structures (Fig. 2.2). They have been recently reactivated as inverse and sinistral strike-slip faults. The NW-SE-trending basement structures also appear to control the orientation of 115° dextral strike-slip and 140° trending reverse faults at the surface. Both structural orientations in the basement may be associated with the compressional stress regime that produced subduction at the Java trench (Sribudiyani et al., 2003). The 175° and the 090° trending faults appear to be normal faults. The 175° trending fault appear to have formed from crustal extension, and may act as the weak zone in which the Unggaran-Merapi volcanic range has been formed. The 090° trending normal faults are located mainly in the central part of the present volcanic arc and are interpreted as the products of N-S-directed crustal extension. Such extension is indicated by the presence of a deep flexural basin in Central Java, generated (at least in part) by the load imposed by the volcanoes in west and east Java (Hall et al., 2007).

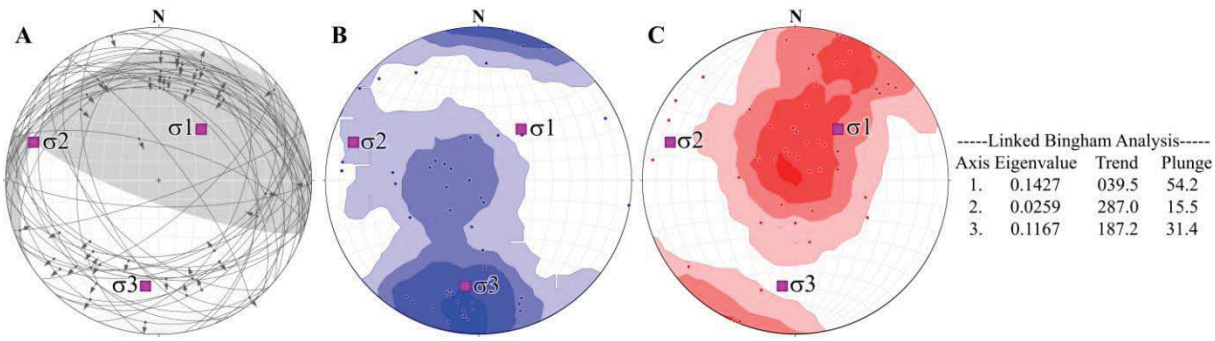

Figure 2.20. Kinematic analysis of fault data from Merapi zone. **A.** Fault planes and striae (n=90) showing that most of faults are vertical and strike to ESE direction. Contour diagram of shortening axes (**B**) and extension axes (**C**). The directions of stress axis based on Linked Bingham analysis are shown in figure with the principal axes following 040° direction.

A kinematic analysis was also performed to the fault data in Merapi zone (Fig. 2.3B). The mean P and T axes approximate the infinitesimal shortening (σ3) and extension (σ1) directions, respectively, for a population of faults (Fig. 2.20). The diagram in Figure 2.20

helps distinguish the three major stresses: σ1 parallels 040°-060° strike-slip faults, σ2 explains ESE-WNW thrust faults perpendicular to convergence trend, and σ3 as vertical stress. The principal stress axis is the NE-SW (040°) direction. The contour diagram shows that the faults in the population are not homogenous in orientation, but many faults point to a prevailing ESE-WNW direction with thrust fault mechanism.

2.4.3. Eruptive history and hazard assessment of Merapi volcano

Eruptive history

Tephrostratigraphic evidence (Andreastuti et al., 2000; Voight et al., 2000; Newhall et al., 2000) suggest that eruptions of Merapi during the 19th century were larger than those of the 20th century. Four large-magnitude eruptions (VEI ≥ 3) occurred during the 19th century, as in 1672, 1822, 1849 and 1872. The 1872 event was the largest (VEI 4), which created a large crater and produced pyroclastic flows from column-collapse that travelled over 20 km from the summit of Merapi and dispersed tephra fall tens of km towards northeast. During the 20th century, there are only two VEI 3 eruptions that occurred in 1930-1931 and 1961. The 1930 VEI 3 event generated a pyroclastic flow over a distance of 12 km that caused 1369 casualties and displaced more than 13,000 people. Another VEI 3 in 1961 also generated a 12 km pyroclastic flow that caused six casualties and resulted in the evacuation of about 6000 people. During the 20th century, Merapi eruptions are known for frequent, small to moderate eruptions and scores of mostly small pyroclastic flows produced by lava dome collapse. In the 21st century, Merapi volcano produced its largest and most explosive eruptions in more than a century in 2010. This eruption abruptly changed the usual behavior of Merapi over past seven decades.

Since the beginning of the 20th century, Merapi volcano has been intensively studied and monitored, and its eruptive history after the 20th century was recorded in detail. More than 74 eruptions have been recorded at Merapi since 1548 and at least seventeen of them have caused fatalities. Based on the historical eruption record of Siebert et al., (2010), the average time interval between two eruptions is 2-6 years. Most events fall in the VEI 2 range, at least once per decade since 1861 (Fig. 2.21). Dome collapse events (VEI<3) that commonly produce 1 to 10 million m^3 of deposits (Voight et al., 2000) and have prevailed among the past 80 year-long eruption record. Figure 2.22 shows the map

of observed pyroclastic flows of Merapi since 1911 together with the distance and direction from the summit. The figure shows a predominance of flows towards the western half of Merapi flank (NNW to SSE flanks). It is also clear that PDCs generated by the 2010 event were considerably larger than all other flows.

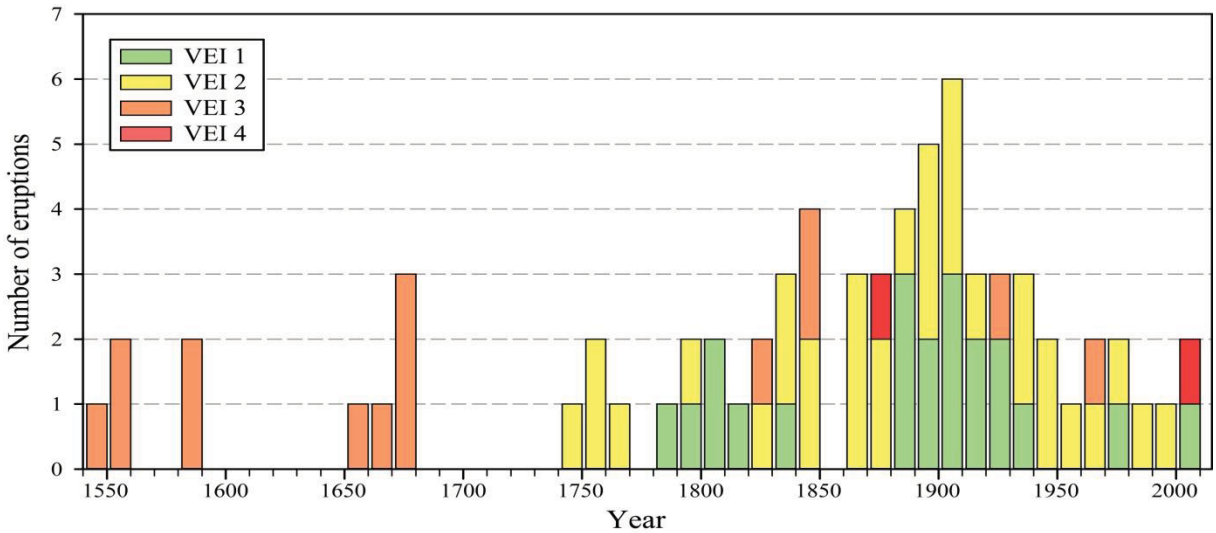

Figure 2.21. Historical eruptions of Merapi since 1548 shown as frequency histograms of Volcanic Explosivity Index (VEI) divided by 10-year time intervals. Note that before AD 1700, the number of large eruptions is undoubtedly biased with respect to unreported small eruptions.

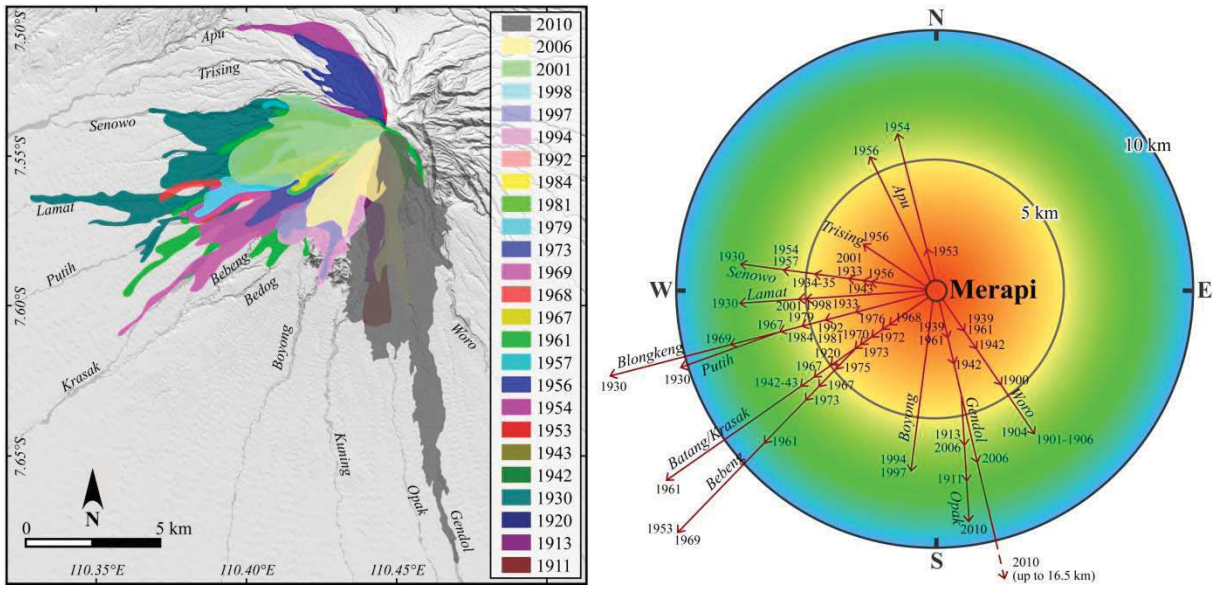

Figure 2.22. Map of observed pyroclastic flows of Merapi volcano since 1911 (after CVGHM) and diagram of distance and directions of flows from the summit (after Wilson et al., 2007).

Merapi eruptions in 1994, 1997, 2001, and 2006 were associated with small- to modest-sized dome growth and collapse. In 1994, BAFs driven by dome collapse travelled 6.5 km to the SSW flank (Fig. 2.22) producing about 2.5-3 million m³ of complex deposits

due to the accumulation of dozens of 'nuées ardentes' (Abdurachman et al., 2000). The 1994 Merapi eruption was responsible for 95 casualties in the vicinity of the Boyong valley, at the edges of Kaliurang and Turgo villages (Shelley & Voight, 1995). Prior 1994, the pyroclastic flow and rockfalls had been exclusively travelled down to the southwest, but afterwards, some rockfalls had shifted toward the Boyong River (southern flank) as in 1996, 1997, and 1998. In contrast to the 1994 eruption, the 1997 pyroclastic flow was generated by fountain collapse and the 1998 events also suggest an explosive component influenced by gas-pressurization of the lava dome (Voight et al., 2000). The 2001 eruption produced pyroclastic flows generated from a collapse of the 1998 lava dome and they extended 7 km in the direction of the Sat River (West flank).

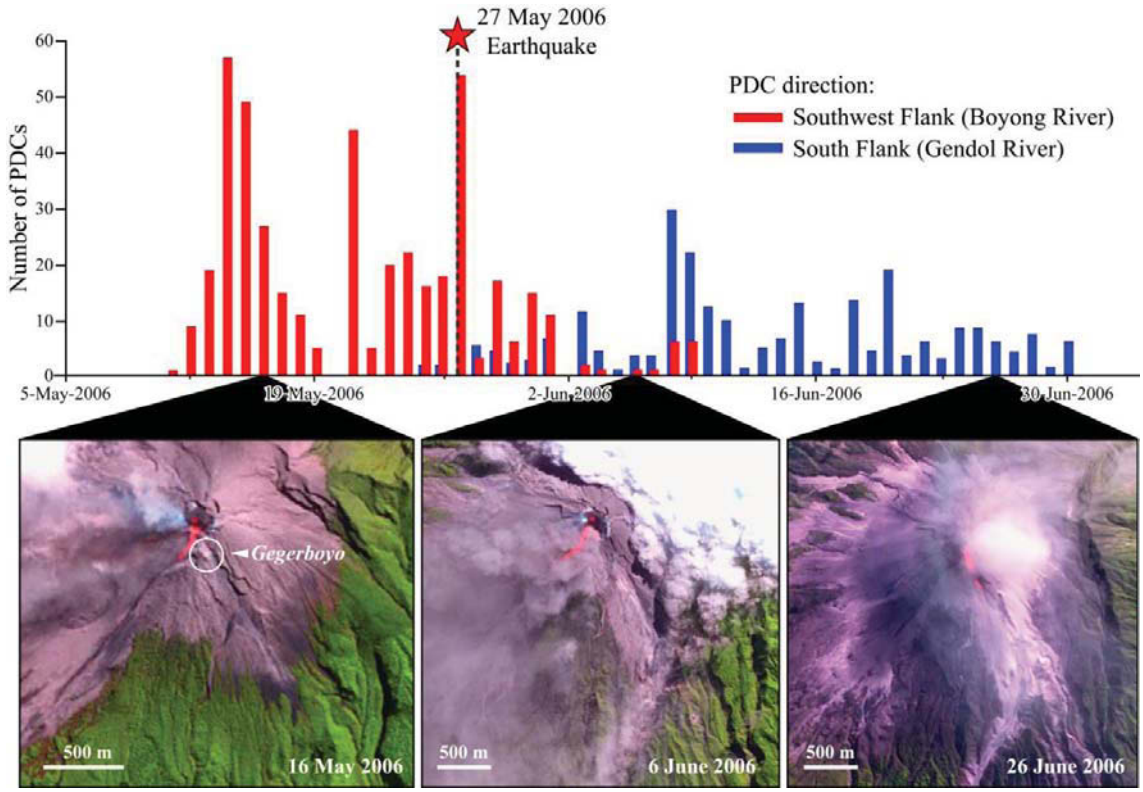

Figure 2.23. Graph of number of 2006 PDCs in the Boyong river drainage in the southwest flank and Gendol river drainage in the south flank accompanied by three SPOT5 images showing the shift in PDC direction from the southwest flank to the south flank.

Although small in magnitude (VEI 2), the 2006 eruption (Fig. 2.23) contributed to the instability of the southern flank of Merapi, which was then affected by the larger event in 2010. The two month-long 2006 Merapi crisis consisted of a series of block-and-ash flows and associated surges, generated by dome collapses, which produced a total of 13.3 million m^3 of deposits (Charbonnier and Gertisser, 2008; Lube et al., 2011). The

"*Gegerboyo*" rim wall, which formed during the 1911 eruption (Wunderman, 2007) and protected the south flank of Merapi for the past 100 years, failed as a result of the 27 May 2006 Bantul earthquake (Charbonnier & Gertisser, 2008), henceforth exposing these areas to PDCs (Fig. 2.23). However, Ratdomopurbo et al. (2013) stated that the "*Gegerboyo"* rim was progressively eroded by repeated pyroclastic flows and block and ash flows, preceding and after the Bantul earthquake. The shift from SW to SE overlapped the time of the earthquake on 27 May, but collapse of the rim did not take place until 4 June when the main passage to the Gendol was created.

Larger in magnitude (VEI 4) and more explosive (large Vulcanian to sub-Plinian), the 2010 eruption of Merapi differs from previous eruptions in 1994, 1997, 2001, and 2006. The 2010 eruption was the Merapi's largest event (VEI 4) since 1872. Results of detailed studies of this eruption have been discussed in the special issue of the Journal of Volcanology and Geothermal Research (JVGR 261: Jousset et al., 2013) and in other publications such as Solikhin et al. (2015a & 2015b) or in chapters 4 and 5 of this thesis. The 26 October-23 November 2010 crisis encompassed several episodes of PDC emplacement with deposits that covered an area about 26 km^2 and a bulk volume of about 45 million m^3 in the Gendol-Opak catchment on the south flank. The most voluminous PDC was deposited in the Gendol valley during the peak stage of the eruption on 4-5 November 2010. The tephra fall deposit covered an area of about 1300 km^2 with a volume of 18-21 million m^3 (Solikhin et al., 2015b). About 2300 houses were destroyed and severely damaged, 376 people lost their lives and hundreds of thousands of people were displaced due to the 2010 Merapi event. This eruption also has an impact to the morphological and structural character of the volcano summit. The eruption formed a large (400 m x 350 m) summit crater with a 23,000 m^2 lava dome in the middle and has lengthened and deepened the 'Gendol Breach' (Camus et al., 2000), a major southeast-trending, elongated, deep canyon towards the headwaters of Gendol River. Lahars also generated at Merapi during and just after the end of the eruption, and endangered people living close to river banks to the west, southwest and south of the volcano.

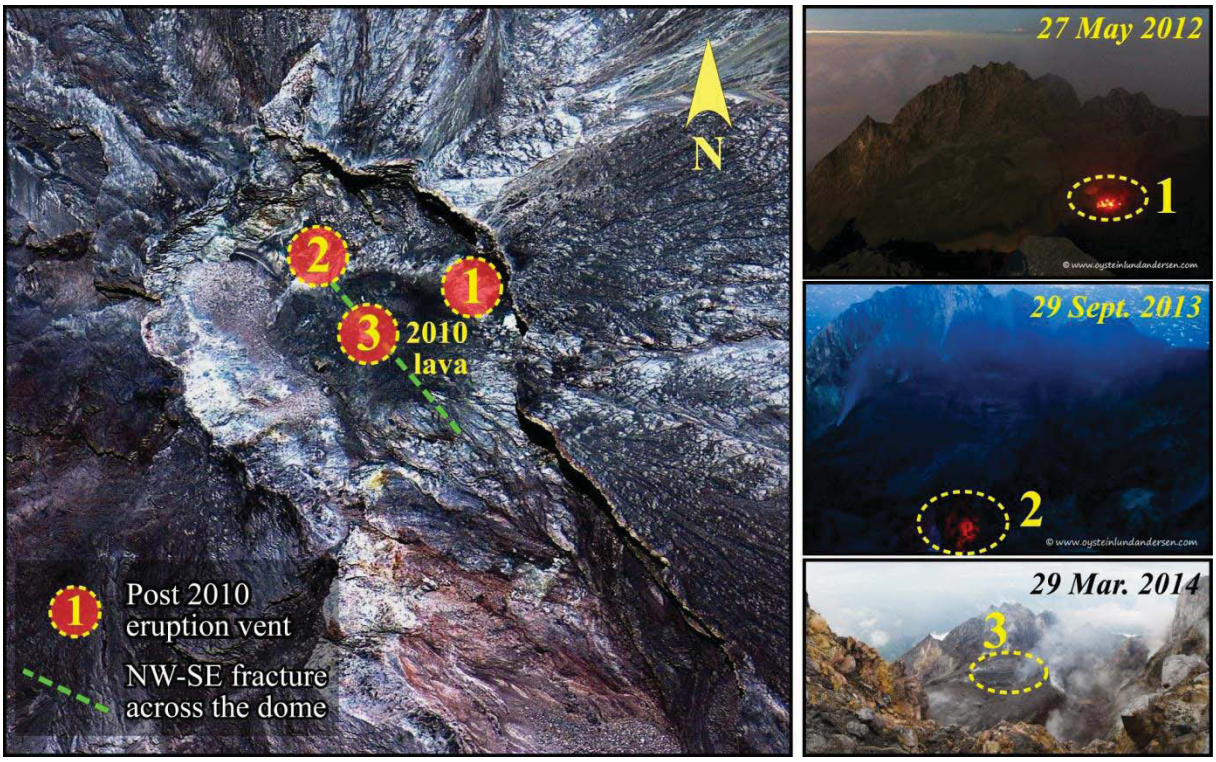

Figure 2.24. 4 September 2011 GeoEye image (left) and three photographs (right) of the Merapi summit crater showing the 2010 lava dome and the location of post-2010 eruption vents.The top and middle photographs are taken from www.oysteinlundanderson.com and the bottom photo is courtesy of DOMERAPI project.

Merapi eruptions after 2010 were characterized by short explosive events that produced several km-high ash plumes. Eight events may be sourced from three different vents inside the 2010 summit crater (Fig. 2.24). The first vent, located in the northeast part of the crater, may be acted as a vent of the explosions on 15 July 2012 and 20 August 2012. The vent moved 150 m to the west of the first vent during the 22 July 2013 explosion. The third vent is located in the middle of the crater and the lava dome which was formed during the 2010 eruption. However, it is also possible that the first (and possibly second) vents are deeper level exposure of the former high-temperature near-summit fumarole fields; whereas, the third is the main magmatic conduit. Five explosive events on 18 November 2013, 12 December 2013, 10 March 2014, 27 March 2014 and 20 April 2014, were generated from the third vent. The explosions on 18 November 2013 has broken up the 2010 dome into two main parts and left a major NW-SE trending fracture (Fig. 2.24). After the last eruption on 20 April 2014, this NW-SE fracture in the dome had widened 70 m to the west, and new material had been

deposited in the western part of the crater. This fracture may affect the dynamics and the stability of the post-2010 Merapi dome (Walter et al., 2015)

Merapi volcanic hazards and zonation

Merapi volcano is one of the most dangerous volcanoes of the world due to its persistent activity and location in a densely populated area (>4 million people within 30 km). Thouret et al. (2000) identified three major threats at Merapi comprising: (1) the collapse of the summit dome complex in the short-to mid-term, which can release large-volume BAFs and high-energy surges towards the south–southwest sector of the volcano; (2) an explosive eruption, larger than any since 1930, which can produce PDCs that sweep all the flanks of Merapi at least once every century; and, (3) a potential collapse of the entire summit area, involving the fumarolic field of Gendol and part of the southern flank; in addition to PDCs such a collapse would result in a moderate-scale debris avalanche and related debris flows. Another threat, both during and after eruptions, stems from rain-triggered lahars. Merapi lahars have average measured velocities of 5–7 m/s at 1000 m elevation and they are known to inundate areas of the extensive ring plain below 600 m elevation as far as 30-40 km from the summit along each of the thirteen rivers that drain the volcano (Lavigne et al., 2000).

A volcanic hazard map (Fig. 2.25; Sayudi et al., 2010) was created after the 2010 eruption to update the previous hazard map (Hadisantono et al., 2002). This map was used by local authorities as an input for contingency. The Merapi hazard zone map displays three danger zones (KRB) ranked from I (low) to III (highest).
The first hazard zone (KRB I) is potentially affected by lahars (yellow zone), heavy tephra fall and incandescent ejected rock fragment (the latter only within the red circle at a radius of 10 km from the crater). The lahar-prone zones follow river valleys that have sources near Merapi's upper flanks, and they extend to include downstream river reaches and bends, and low river banks with frequent lahar overflows. People living in the first hazard zone should increase their alertness during a large eruption and/or heavy rainfall on the summit area.

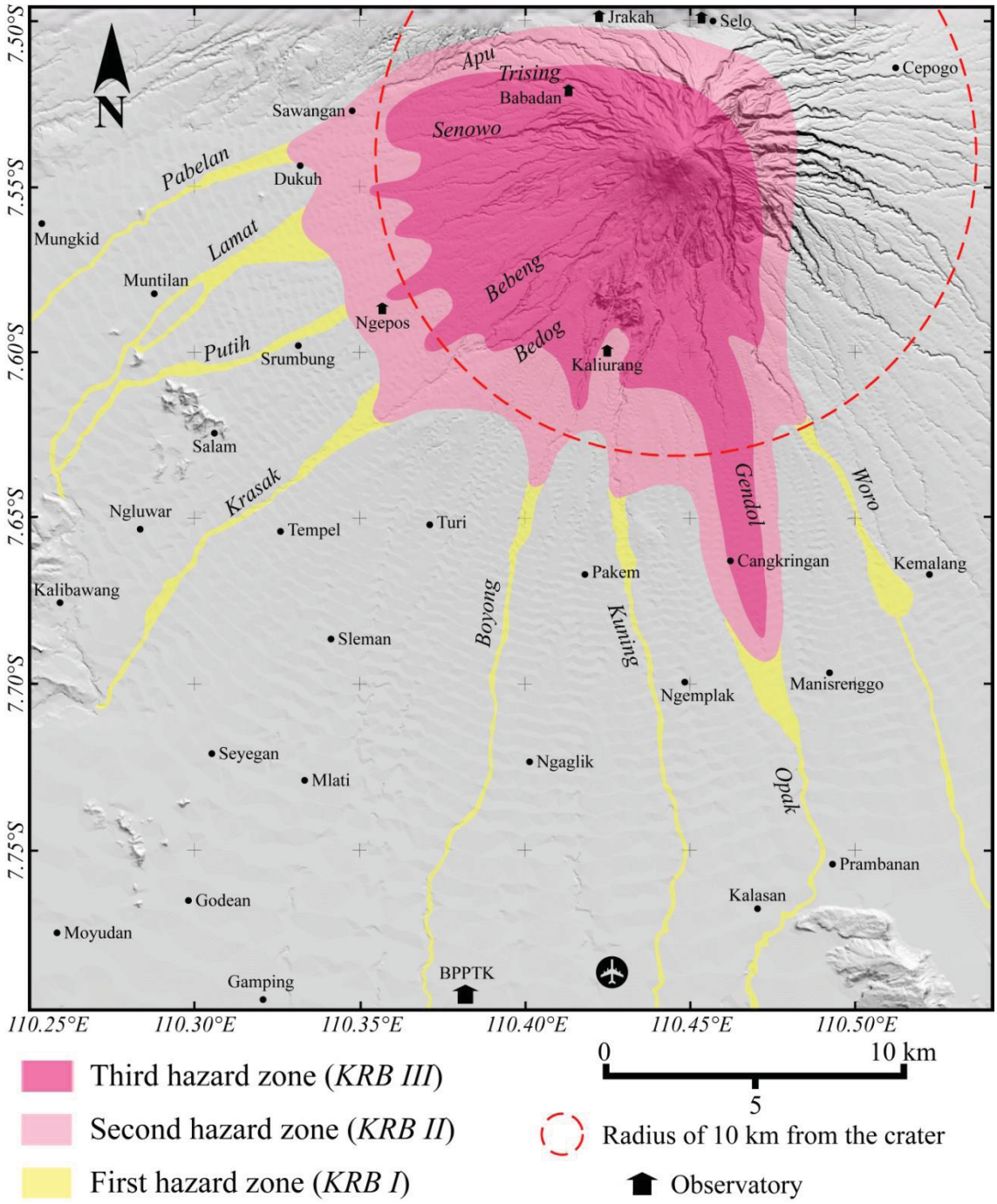

Figure 2.25. Map of Merapi hazard zone (KRB) (Sayudi et al., 2010), which is used by CVGHM and local government as a guidence for volcano disaster management.

The second hazard zone (KRB II) is potentially affected by pyroclastic flows, lava flows, lahars, ash fall, volcanic bombs and other ejected volcanic materials. The outer boundary of this hazard zone is determined based on historical eruptions older than a hundred years with VEI 3-4. Inhabitants in the second hazard zone should prepare for evacuation when there is an indication of increased activity in accordance with the CVGHM recommendation.

The third hazard zone (KRB III) encompasses the area most likely to be affected by pyroclastic flows, lava flows, rock falls and ballistics. This zone is determined based on study of the impacts of eruptions that occurred throughout the 20th century and take into account the distribution of small-volume dome-collapse driven pyroclastic flows together with morphological changes in the summit area that influence the direction of dome collapse. The hazard zones also take into account geologic structures and unstable sectors of the summit and the locations of the most recent eruptive activity. The third hazard zone is forbidden for a permanent settlement or human activity, and will be totally closed in case of a high level of activity.

Chapter 3 - Geomorphological evolution and post-2001 eruptive activity of the Semeru volcano

3.1. Introduction

Remote sensing techniques can be applied to improve understanding of volcanic processes, to detect precursory activity to volcanic hazards and to provide key monitoring data during an eruptive crisis (for example in October-November 2010 at Merapi). Chapter 3 of the thesis illustrates the application of remote sensing techniques using high-spatial resolution (HSR) optical and thermal images together with digital elevation models (DEMs) in interpreting volcanic structures of the Tengger-Semeru massif and the recent evolution of Semeru volcano. So far, volcanological studies that have applied remote sensing and GIS techniques for mapping the Tengger-Semeru massif complex are limited. Recent studies include: monitoring volcanic ash cloud (Situmorang & Modjo, 1991; Jenkins et al., 2012), geology and landforms interpretation (Wahyudin, 1991; Mulyadi, 1992; Carn, 1999; Thouret et al., 2007; Solikhin et al., 2012; Kassouk et al., 2014), lahar behavior and erosion process (Gomez & Lavigne, 2010; Starheim et al., 2013; Thouret et al., 2014) and hazard mapping and assessment (Sutawidjaja et al., 1996; Thouret et al. 2007).

The first objective of this chapter is to define the structure and evolution of Semeru's composite cone. Composite cones commonly grow in spurts (>1-2.5 km^3/kyr) and remain active over relative short periods (<200 ka) whereas degradation processes during and after eruptive activity are very fast (minutes to years): e.g. Hildreth and Lanphere (1994); Hora et al. (2007); Thouret (1999). The Semeru volcano is one of the few composite volcanoes worldwide that are persistently active. Semeru volcano and its summit cone are evolving rapidly (almost annually) due to continuous eruptive activity at least since 1967, very much like Sakurajima in Kyushu, Japan. In addition, the rapid alternations between effusive and explosive regimes seen at Semeru are uncommon and its eruptive styles are variable. The typical, daily activity encompasses phreatomagmatic and Vulcanian events or Strombolian eruptions, but this alternates with short episodes (1-3 years in durations) of lava flow production and longer episodes of lava dome

growth and collapse (every 5 to 7 years) that feed pyroclastic density currents (PDCs). The mechanism for such uncommon, persistent and alternating activity points to a rapid shift from open to close system at the summit cone and vent area, has not been determined despite limited geophysical monitoring (Nishi et al., 2007; Iguchi et al., 2008; Nishimura et al., 2012).

The restricted access to the Semeru summit cone requires remote sensing imagery and DEM analysis in order to study and follow the evolution of its volcanic landforms. Application of DEM analysis to volcanic terrains has been widely used to decipher geomorphic and structural features, especially at large-scale edifices and freshly erupted deposits, which cannot be readily studied or identified in the field (e.g., Socompa, Chile: Wadge et al., 1995; Börzsöny Mountains, Hungary: Székely & Karátson, 2004; Semeru, Indonesia: Thouret et al., 2007, 2014; Solikhin et al., 2012; Kassouk et al., 2014, to name just a few example). In this chapter, we highlight the use of optical and thermal imagery together with DEM analysis to pursue three objectives as outlined below.

1) The first objective of Chapter 3 is to define the structures and trace the evolution of the Semeru composite cone. Structures and volcanic landforms are interpreted based on DEM computing and analysis, HSR satellite images and aerial photographs along with analysis of river channel network. DEM analysis includes landform analysis from two- or three- dimensional relief images, elevation and slope distribution analysis, and cross sections. Spectral analysis of selected channels (e.g., Wadge et al., 1995) and availability of high-resolution data at different times enabled us to obtain unprecedented spatial resolution, which allows for mapping and following the landform evolution of the Semeru composite cone.

2) The second objective of this chapter is to map the extent of deposits that result from different styles of emplacement and their impacts during the period 2001-2014. HSR images enable us to map fresh volcanic deposits and geomorphic changes that occur on the volcano flanks after a major volcanic eruption (Rowland et al., 1999; Mazzarani & Armienti, 2001; Charbonnier et al., 2013; Kassouk et al., 2014; Solikhin et al., 2015b). The activity of Semeru over the period of 2001 to the end of 2014 has been dominated by short-lived, almost daily, Vulcanian columns from the Jonggring-Seloko crater. The activity increased several times to produce larger explosions (VEI 3), lava flows, rock avalanches and PDCs associated with explosions or dome growth and collapse (see

Chapter 2). The last major PDC-forming eruption occurred between December 2002 and January 2003, where PDCs travelled down the south flank as far as 12 km away from the summit. Smaller PDCs were produced in 2008 and 2009-2011, while a substantial volume of lava flows was erupted in February 2010, January-March 2012 and July 2014. We mapped eruption deposits based on HSR optical images and thermal images.

3) The third objective of Chapter 3 is to define the characteristics of two selected catchments, Kobokan and Lengkong Rivers, on the southeast slopes of Semeru volcano, which currently is the most threatened flank in terms of pyroclastic flows and lahars. Under certain conditions, heavy rainfall (2000 to 2800 mm per year), unconsolidated deposits and steep slopes all contribute to the formation and mobilization of lahars at the expenses of pyroclastic deposits. As the channel morphology is a governing factor in the formation of lahars, geometric characteristics of the river basin are useful information to compute the aggradation and degradation rates and sediment yields in the channels (e.g. Thouret et al., 2014). In order to characterize and analyze the geometry of the Kobokan and Lengkong catchments, we measured morphometric parameters of the river basins and then computed their hypsometric curves. Geometric characteristics of river basins are interpreted and measured based on DEM analysis along with interpretation of HSR satellite imagery and field-based geologic mapping.

3.2. Geology of the Semeru volcano interpreted from high-spatial resolution satellite imagery

This section contains an article published in Geomorphology in 2012.

Geology, tectonics, and the 2002–2003 eruption of the Semeru volcano, Indonesia: Interpreted from high-spatial resolution satellite imagery

Akhmad Solikhin[1,2], Jean-Claude Thouret[2], Avijit Gupta[3], Andy J.L. Harris[2] and Soo Chin Liew[3]

[1] *Center for Volcanology and Geological Hazard Mitigation, Jalan Diponegoro 57 Bandung 40122, Indonesia*

[2] *Clermont Université, Université Blaise Pascal, Laboratorium Magmas et Volcans, UMR 6524 CNRS et IRD R163, 5 rue Kessler, 63038 Clermont-Ferrand cedex, France*

[3] *Centre for Remote Imaging, Sensing and Processing, National University of Singapore, Lower Kent Ridge Road, 119076, Singapore*

Highlights:

- High-spatial resolution images have been used to analyze the Semeru–Tengger volcanoes.
- High resolution satellite images have tracked changes on the active Semeru's summit.
- SPOT5 images have contributed to map faults and landslide scars on the edifice.
- A map of deposits and impacts from the 2003 eruption is based on thermal ASTER images.
- The effects of the 2003 pyroclastic flows are evaluated in terms of hazard assessment.

Published in Geomorphology, Volume 138, Issue 1, February 2012, Pages 364-379

Geomorphology 138 (2012) 364–379

Contents lists available at SciVerse ScienceDirect

Geomorphology

journal homepage: www.elsevier.com/locate/geomorph

Geology, tectonics, and the 2002–2003 eruption of the Semeru volcano, Indonesia: Interpreted from high-spatial resolution satellite imagery

Akhmad Solikhin [a], Jean-Claude Thouret [b,*], Avijit Gupta [c], Andy J.L. Harris [b], Soo Chin Liew [c]

[a] Center for Volcanology and Geological Hazard Mitigation, Jalan Diponegoro 57, Bandung, Java, Indonesia
[b] Clermont Université, Université Blaise Pascal, Laboratoire Magmas et Volcans, UMR 6524 CNRS et IRD R163, 5 rue Kessler, 63038 Clermont-Ferrand cedex, France
[c] Centre for Remote Imaging, Sensing and Processing, National University of Singapore, Lower Kent Ridge Road, 119076, Singapore

ARTICLE INFO

Article history:
Received 29 March 2011
Received in revised form 29 September 2011
Accepted 2 October 2011
Available online 15 October 2011

Keywords:
IKONOS
SPOT5
ASTER TIR
Semeru volcano
Tectonics
Eruption

ABSTRACT

The paper illustrates the application of high-spatial resolution satellite images in interpreting volcanic structures and eruption impacts in the Tengger–Semeru massif in east Java, Indonesia. We use high-spatial resolution images (IKONOS and SPOT 5) and aerial photos in order to analyze the structures of Semeru volcano and map the deposits. Geological and tectonic mapping is based on two DEMs and on the interpretation of aerial photos and four SPOT and IKONOS optical satellite images acquired between 1996 and 2002. We also compared two thermal Surface Kinetic Temperature ASTER images before and after the 2002–2003 eruption in order to delineate and evaluate the impacts of the pyroclastic density currents. Semeru's principal structural features are probably due to the tectonic setting of the volcano. A structural map of the Tengger–Semeru massif shows four groups of faults orientated N40, N160, N75, and N105 to N140. Conspicuous structures, such as the SE-trending horseshoe-shaped scar on Semeru's summit cone, coincide with the N160-trending faults. The direction of minor scars on the east flank parallels the first and second groups of faults. The Semeru composite cone hosts the currently active Jonggring-Seloko vent. This is located on, and buttressed against, the Mahameru edifice at the head of a large scar that may reflect a failure plane at shallow depth. Dipping 35° towards the SE, this failure plane may correspond to a weak basal layer of weathered volcaniclastic rocks of Tertiary age. We suggest that the deformation pattern of Semeru and its large scar may be induced by flank spreading over the weak basal layer of the volcano. It is therefore necessary to consider the potential for flank and summit collapse in the future. The last major eruption took place in December 2002–January 2003, and involved emplacement of block-and-ash flows. We have used the 2003 ASTER Surface Kinetic Temperature image to map the 2002–2003 pyroclastic density current deposits. We have also compared two 10 m-pixel images acquired before and after the event to describe the extent and impact of an estimated volume of 5.45×10^6 m^3 of block-and-ash flow deposits. An ash-rich pyroclastic surge escaped from one of the valley-confined block-and ash flows at 5 to 8 km distance from the crater and swept across the forest and tilled land on the SW side of the Bang River Valley. Downvalley, the temperature of the pyroclastic surge decreased and a mud-rich deposit coated the banks of the Bang River Valley. Thus, hazard mitigation at Semeru should combine: (1) continuous monitoring of the eruptive activity through an early-warning system, and (2) continuous remote sensing of the morphological changes in the drainage system due to the impact of frequent pyroclastic density currents and lahars.

© 2011 Elsevier B.V. All rights reserved.

1. Introduction

Remote sensing techniques provide the opportunity to study active and dangerous volcanoes, allowing us to safely observe morphological and structural details over a large area. This is particularly true for Semeru, an extremely active volcano in Indonesia, where the access to the summit cone is difficult and dangerous. Standard remote sensing techniques using high-spatial resolution images from IKONOS (1 m) and SPOT5 (2.5 m), as well as thermal ASTER images thus offer a fruitful means with which to characterize the volcano's structural features and to recognize the extent and effects of the eruptive processes. Aerial photographs were also combined with satellite images for tracking the morphological evolution of a persistently active volcano. This study illustrates the application of such remote sensing techniques to define: (1) structures, faults and scars of the edifice, (2) the evolution of a persistently active composite cone, and (3) the emplacement of deposits from pyroclastic density currents and the morphological effects of the 2002–2003 eruption.

Semeru volcano (8°06′05″S, 112°55′E) at 3676 m the highest mountain in Java, Indonesia, is the southernmost edifice of the

* Corresponding author.
E-mail address: thouret@opgc.univ-bpclermont.fr (J.-C. Thouret).

0169-555X/$ – see front matter © 2011 Elsevier B.V. All rights reserved.
doi:10.1016/j.geomorph.2011.10.001

Semeru–Tengger volcanic massif (Fig. 1). The recent composite cone of about 60 km^3 (Thouret et al., 2007) has not been dated, but maybe Late Pleistocene to Holocene in age. The twofold edifice (Mahameru and Young Semeru) has been superimposed on, and buttressed to the N, by the Jambangan complex. To the S and SE Semeru overlies weathered volcaniclastic sediments and lava flows of the Oligocene–Miocene 'Tuff and Old Andesite formation' (Sutawidjaja et al., 1996). Its ring plain below 400 m of about 1790 km^2 supports more than one million people including the cities of Lumajang (85,000 inhabitants) to the E and 600,000 people living in or near the city of Malang to the W. The cone-shaped summit is bare and covered by tephra but the volcano flanks are home to dense, evergreen forest between 900 and 2800 m in elevation. The equatorial monsoon climate produces as much as 2000 to 3700 mm per year on the E and SE flanks of Semeru while 200 mm of rain can fall in 24 h every 5 years on average (Siswowidjoyo et al., 1997).

Semeru's eruptive activity has been recorded since 1818 and eruptions have been persistent since 1967, probably even earlier. Its activity consists of vulcanian and phreatomagmatic eruptions, which produce short-lived eruption columns several times a day (Thouret et al., 2007). Strombolian eruptions also occur based on the presence of scoriae and bombs on the upper slopes. Extrusion of lava domes take place during more intense eruptive episodes that occur every 5–7 years. Pyroclastic flows occur once every five years on average, mostly as block-and-ash flows. Block-and-ash flows triggered by dome collapse have travelled as far as 12 km to the SE and S directions, following drainage networks (e.g. in 1994, 1995, and 2003). Lava flows from flank fissures or vents (e.g. in 1895 and 1941) have also been recognized as far as 9 km from the summit on the SE flank. Semeru is known as one of the most effective lahar producers on Earth (Lavigne and Thouret, 2002; Thouret et al., 2007). Large-scale lahars exceeding 5 million m^3 in volume have occurred at least five times since 1884. During the rainy season, Semeru produces small to medium-scale lahars ($\leq$0.1 million m^3) every week, which are triggered by the remobilization of pyroclastic debris. Daily explosions deposit pyroclastic debris as far as 3 km from the vent area.

Prior to 1999, SPOT's panchromatic band represented the highest spatial resolution available at 10 m. These data had been shown of utility in identifying and mapping volcanic products (e.g. Chorowicz et al., 1992). In 1999, IKONOS was launched and provided 1 m panchromatic images of the Earth surface (e.g. Zanoni and Goward, 2003). With the launch of Quick-Bird2 in 2001 (60 cm resolution) and of SPOT5 in 2002 (2.5 m resolution), three very high-spatial-resolution satellite datasets were available for the analysis of volcanic terrains and eruptive phenomena. However, a limited number of studies with such a very high-spatial-resolution have examined the products of volcanic eruptions (e.g., Mouginis-Mark and Garbeil, 2005; Thouret et al., 2007; 2010; Miller et al., 2008; Joyce et al., 2009).

This paper will (1) review the methods used in remote sensing and in mapping based on DEMs, (2) describe the volcanic features of the Tengger–Semeru massif and of the Semeru edifice, (3) analyze

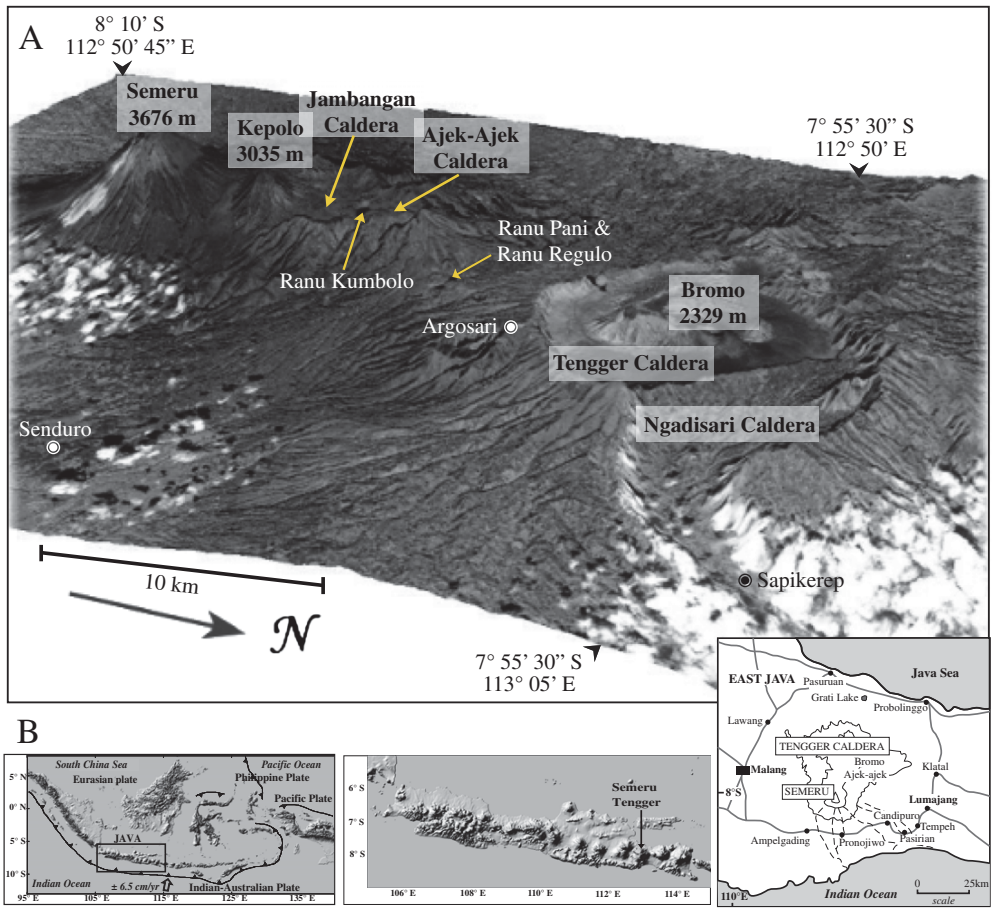

Fig. 1. A. The 11/08/2003 SPOT5 image, looking SW and draped on a SRTM-derived Digital Elevation Model, shows the Tengger–Semeru massif. The Semeru–Tengger volcanic massif comprises a cluster of calderas and composite cones including, from N to S: the Ngadisari, Bromo–Tengger, Jambangan and Ajek-Ajek calderas, Mt. Kepolo, and Mt. Semeru; B. Sketch maps showing the geodynamical setting of Indonesia, the Island of Java, and the location of the Semeru composite cone south of the Semeru–Tengger volcanic complex. Courtesy of CRISP Centre for Imaging, Sensing and Processing, National University of Singapore.

the tectonic setting of the Tengger–Semeru massif, (4) examine the evolution of the Semeru summit cone since 1923, and (5) analyze the pyroclastic deposits emplaced by the 2002–2003 eruption and their related effects.

2. Methodology

This study is based on combined methods: remote sensing of optical and thermal imagery, field observations and measurements, geologic mapping based on aerial photos, DEM computing and analysis for interpreting landforms and structures, and ^{14}C of charcoal for dating recent deposits.

The satellite images used in this study are: (1) five high-spatial resolution (1 m) IKONOS satellite images dated 14-11-2002, 25-09-2004, 16-06-2006, 10-04-2008 and 20-08-2009; (2) two SPOT5 images including one panchromatic (2.5 m) dated 24-10-2003 and one multispectral (5 m) dated 26-07-2008; (3) one SPOT2 image (10 m) dated 11-05-1996 and one SPOT1 scene (10 m) dated 08-08-1997, both at 10 m; and (4) three AST08 or ASTER TIR Surface Kinetic Temperature products (90 m) dated 16-08-2002, 12-03-2003 and 25-09-2005. These images have their technical specifications summarized in Table 1. The procedure is based on visual image interpretation and on image processing techniques. The images have been locally checked during field work and mapping carried out on the S and SE flanks and the SE ring plain of the Semeru volcano. The IKONOS and SPOT images were first used for mapping the structures and landforms of Semeru, and the tectonic setting of the volcanic massif. The ASTER images were secondly used for tracking the thermal anomalies linked to the deposits from the 2002–2003 eruption and for mapping the impacts and changes in the S drainage of Semeru.

Aerial photographs used in this study were acquired during 1981, 1990, 2005 and 2008 aerial surveys. Furthermore, two Digital Elevation Models (DEMs) were also generated. The first DEM was derived from the 30-m resolution Shuttle Radar Topography Mission (SRTM), here called SRTM-DEM, and the second DEM from four quadrangles (Ranu Pane, Senduro, Pronojiwo and Pasirian) digital maps (at a scale of 1:25,000 with a 12.5 m contour interval). It is referred to as TOPO-DEM in the paper.

The IKONOS satellite is a high-resolution satellite operated by GeoEye, which collects high-resolution images at 1 m (panchromatic) and 4 m (color) spatial resolution. Its capabilities include capturing a 3.2 m multispectral, Near-Infrared (NIR)/0.82 m panchromatic spatial resolution at nadir. SPOT satellites have acquired images of the Earth since 1986. Except for SPOT3 that stopped acquisition on November 1996, SPOT1, 2 and 4 formed a constellation, which was reinforced by the launching of SPOT5 in early 2002. SPOT satellites are designed to acquire images in such a way that the scenes acquired on different dates can be compared with each other. The SPOT satellites (SPOT 1, 2, 4 and 5) travel in a sun-synchronous orbit with 98.7° inclination at 832 km altitude, taking 26 days to complete one orbital cycle. The orbital plane intersects the equatorial plane at two points along a straight line known as the line of nodes. The SPOT satellites acquire data during the day with a north–south descending path.

The Advanced Spaceborne Thermal Emission and Reflection Radiometer (ASTER) sensor is part of NASA's Earth Observing System (EOS) Terra satellite platform, which was launched on 18 December 1999 (Pieri and Abrams, 2004). ASTER allows multispectral imaging at high to moderate spatial resolution (15–90 m/pixel). The ASTER TIR Surface Kinetic Temperature product is an on-demand ASTER product, generated from the five thermal infrared (TIR) bands (acquired either during the day or night) within 8 and 12 μm wavelength. It contains surface temperatures at 90 m spatial resolution for land areas only. In this product, surface kinetic temperature is determined by applying Planck's Law using the emissivity values from the Temperature-Emissivity Separation (TES) algorithm, which uses atmospherically corrected ASTER Surface Radiance (TIR) data (Gillespie et al., 1998). The TES algorithm first estimates emissivity in the TIR channels using the Normalized Emissivity Method (NEM). These estimates are then used along with Kirchoff's Law to account for the land-leaving TIR radiance that is due to sky irradiance. This result is subtracted from TIR radiance iteratively to estimate the emitted radiance from which temperature is calculated using the NEM module.

Processing of the images is required to improve their quality and the interpretation of the content of the image digital data. Several processing functions have been applied to the images, such as contrast stretching, filtering and band-ratio using the ENVI 4.7 software in order to enhance contrasts between features. Band ratio between Near-Infra-red (NIR) and Red Bands and the Normalized Difference Vegetation Index ($NDVI = (NIR - Red)/(NIR + Red)$) are especially used on IKONOS and SPOT images to enhance contrasts between vegetation and rocks or deposits, as well as to reduce the variation of topographic illumination. Most common enhancement, contrast stretching, was applied to produce sharper and clearer images. This expands the range of DN values to the full limits determined by byte size in the digital data. In order to enhance contrasts locally in the spatial domain, spatial filtering with a non-directional filter was applied to some images. This technique explores the distribution of pixels of varying brightness across an image. It is especially good at detecting and sharpening boundary discontinuities between adjacent pixels.

We have thus used seven sets of images and aerial photographs (1981, 1990, 1996, 2002, 2003, 2004 and 2008) spread over 27 years, as a time series to track the evolution of the Semeru's summit cone. A long scar open to the SE and radial valleys on the S and SE flanks was especially observed. Geo-referencing from satellite images or geo-referencing based on Global Positioning System (GPS) Ground Control Points (GCP) was used so that the images can be directly compared with each other.

3. Volcanic features of the massif and of the edifice

The main geological features of the Semeru–Tengger massif are presented, based on the combined 2008 SPOT5 image (Fig. 2A) and the shaded relief SRTM-DEM (Fig. 2B) at a regional scale. The analysis of the Semeru composite cone and its ring plain is based on the enhanced TOPO-DEM (box area in Fig. 2C) and on the high-spatial resolution images.

The Semeru–Tengger volcanic massif with an area of about 900 km^2 comprises a cluster of calderas and strato-cones including, from north to south: the Bromo–Tengger (7.942°S, 112.95°E), Jambangan (8.065°S, 112.92°E) and Ajek-Ajek (8.042°S, 112.92°E) calderas; the Mt. Kepolo (Figs. 1A and 3B) (8.077°S, 112.92°E) lava cone; and the composite cone of Mt. Mahameru–Semeru. The calderas have formed and the edifices have grown over a deeply eroded volcanic arc of Oligocene–Miocene age in south Java. The eruptive centers of the Semeru–Tengger massif lie on a roughly north–south-trending direction, slightly concave towards the east, which continues northward to Lake Grati (Fig. 1B), a maar at the foot of the Tengger massif (Van Bemmelen, 1949; Situmorang, 1989; Sutawidjaja et al., 1996; Carn, 1999).

The 16-km-wide Bromo–Tengger caldera in eastern Java is located at the north of the volcanic massif and at the other end from Semeru volcano. The massive Tengger volcanic complex consists of five overlapping composite volcanoes, each truncated by a caldera. The most recent is the 9 × 10 km-wide Sandsea caldera, which formed incrementally during the late Pleistocene and early Holocene (> 45 ka and ca. 33 ka: Mulyadi, 1992). An overlapping cluster of post-caldera cones was constructed on the floor of the 'Sandsea' caldera (V in Fig. 3A) within the past several thousand years. The youngest of these is the Bromo tuff cone (Fig. 3B), one of Java's most frequently visited and most active volcanoes, whose eruptive activity resumed

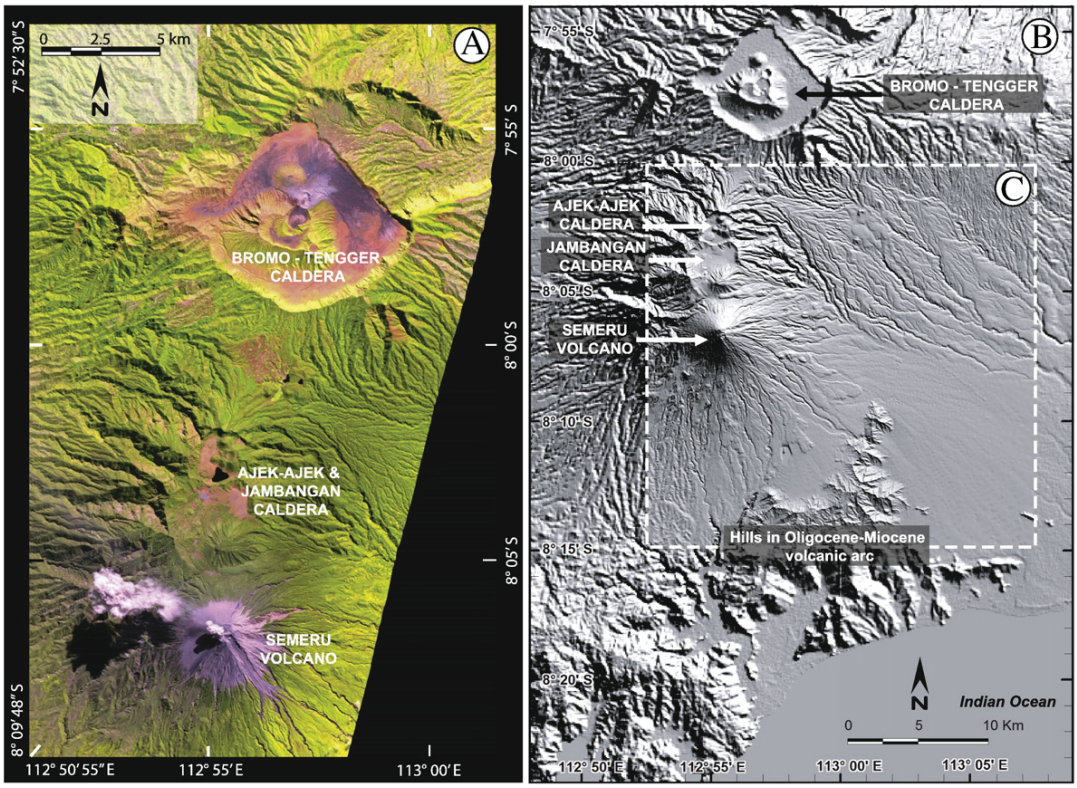

Fig. 2. A. The 26/07/2008 SPOT5 image portrays the Semeru–Tengger volcanic massif. Band combination displayed in this color composite image includes R: Short-wave Infrared, G: Near-Infrared and B: Red. The distinct colors of the image in the Bromo–Tengger caldera encompass: green for vegetation, purple for loose volcanic deposit (tephra, ash and sand), darker for 'old' deposits and lighter for recent deposits. B. Shaded relief image including much of the same area generated from the 90 m/pixel SRTM-based DEM. C. Shaded relief image of enhanced DEM (enclosed in box) obtained from 1:25,000 scale topographical maps with elevation contour interval of 12.5 m. The even surface of the N and NW summit cone flanks due to a thick tephra cover contrasts with the rough surface and landslide scars of the eroded S, SE and SW flanks. Several topographic and geomorphic features are indicated by arrows in C: lava cones and domes on the S and E flanks; smooth, slightly elevated surface of lava flows above the SE flank slope; regular and smooth surface of the fans forming the SE ring plain. North of Semeru: rugged topography carved by deep ravines in the area of Ajek-Ajek and Jambangan calderas; to the NE and N of the Semeru ring plain, the smooth topography of aprons suggests thick pyroclastic and/or lahar deposits.

on 26th November 2010. More than 50 mild-to-moderate explosive eruptions have occurred since 1804, as recorded in the Global Volcanic Network (GVN) data base and by Sjarifudin (1990). South of Tengger the older, nested Jambangan and Ajek-Ajek calderas (VI and VII in Fig. 3B), which are open to the east, are thought to have produced debris avalanches, which may or may not have been accompanied by an eruption (Carn, 1999). No hummock related to debris-avalanche deposits has been observed on the eastern flank of these calderas but we have identified at least two parasitic lava or tephra cones in the area in the SPOT image and the DEM. Several intra-caldera vents were formed, including the deep crater lake of Ranu Kumbolo (8 in Fig. 3B) that may indicate the presence of a third eruption vent from the Ajek Ajek caldera. The Holocene Mt. Kepolo strato-cone (9 in Fig. 3B), located near the southern rim of Jambangan caldera, is aligned up N–S with a youthful lava cone and lava flow at the foot of the Semeru's north flank. The NE-trending eruption centers form an oblique, low angle alignment and are cut by NNE-oriented faults. Both are offset by NW-trending faults that cut through the two groups of nested calderas: Tengger with Ngadisari and Jambangan with Ajek-Ajek.

Although thick vegetation mantles large areas of the massif, the combined 2008 SPOT5 image (Fig. 2A) and the shaded relief SRTM-DEM (Fig. 2B) enables us to visualize the topography and interpret the geology and landforms of the Semeru–Tengger massif on a regional scale. The better spatial resolution TOPO-DEM (box area in Fig. 2C) highlights the topography and morphology of the Semeru composite cone and its ring plain.

Semeru, the youngest volcano in this volcanic massif, hosts the currently active Jonggring-Seloko vent, and has been built on, and is buttressed against the Mahameru (or old Semeru) to the West, and against the Jambangan caldera to the North. To the south and south-east, Semeru's eruptive deposits and associated lahars rest against extensive outcrops of the Oligocene–Miocene 'Tuff and Old Andesite formation' (Sutawidjaja et al., 1996; Thouret et al., 2007). We suggest that the boundary between Semeru deposits and the outcrops of the Oligocene–Miocene 'Tuff and Old Andesite formation' to the east and south of Semeru is a reverse fault formed by compression and uplift linked to the subduction process south of the volcano. This sharp boundary may also be interpreted as a thrust fault overriding the Tertiary formation towards the SE as a response to lateral spreading of the south flank of Semeru. Several NW-trending faults can be inferred from the 2008 SPOT5 image on the east and southeast flanks, whereas on the south and west flanks the orientation of the faults shifts to NE (Fig. 4).

We divided Semeru into four parts based on geologic and geomorphological criteria and on the visual interpretation of landforms and deposits: (1) the cone-shaped summit covered by thick tephra fallout above about 2500 m, (2) the steep flanks between 2500 m and 900 m, (3) the volcaniclastic fans between 900 and 400 m, and (4) the ring plain below 400 m (Sutawidjaja et al., 1996; Thouret et al., 2007). Overlying the large Late Pleistocene 'old' Semeru (Mahameru) composite volcano, the bulk of the 'young' Semeru cone (about 60 km^3 of mafic medium-K andesites with 55–57 wt.% SiO_2) is probably

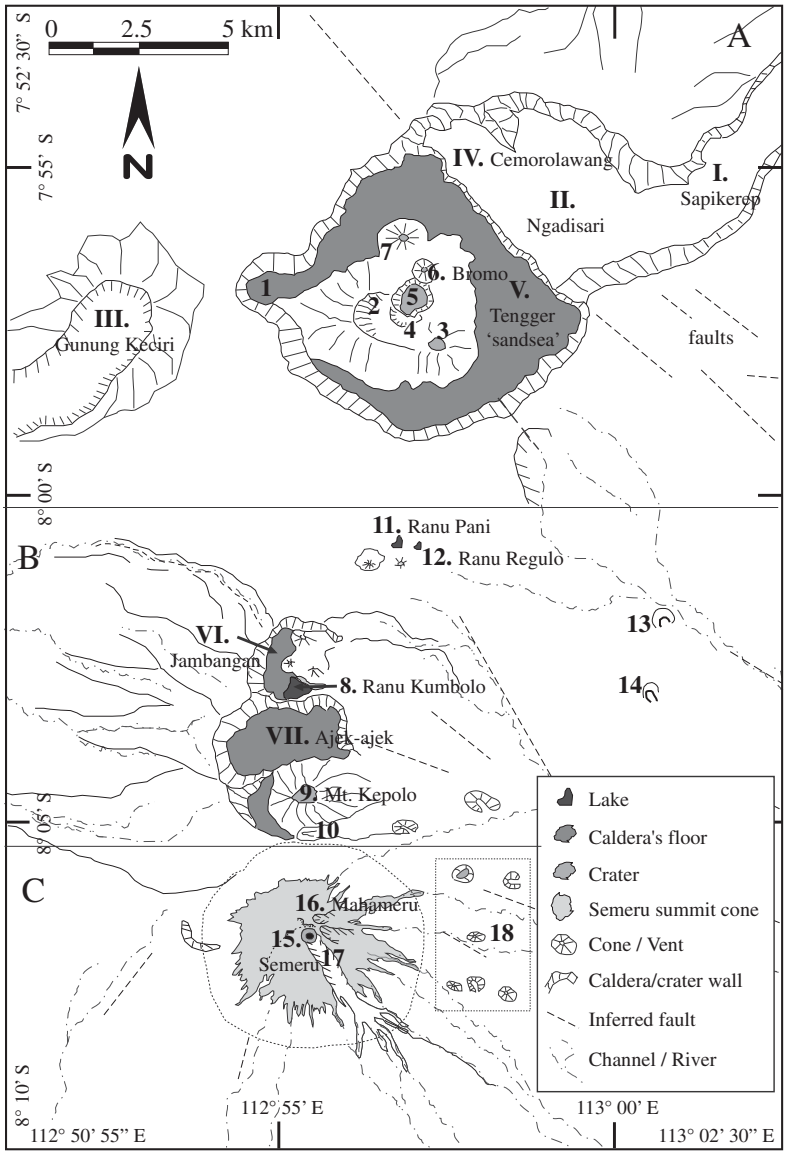

Fig. 3. (Interpreted map from Fig. 2). A. The Bromo–Tengger caldera with remarkable landforms: I the 2 km-wide Sapikerep outlet valley; II the Ngadisari caldera; III the large flank cone Gunung Keciri truncated by an amphitheater valley 2 km-wide, open to the SW; IV Cemorolawang caldera; and V Tengger 'sand-sea' (= ash-covered floor) caldera with a parasite cone, Gunung Ijo (1), located in the west corner. The post-caldera volcanism has formed six edifices inside the Tengger caldera: phreatomagmatic tuff rings of Gunung Widodaren (2), Gunung Kursi (3), Segarawedi Kidul (4), Segarawedi Lor (5), Gunung Bromo (6) and a strombolian cone, Gunung Batok (7). B. The older nested Jambangan (VI) and Ajek-Ajek (VII) calderas extend about 6 km in a northern direction. Several intra-caldera vents were formed including the maar of Ranu Kumbolo (8) in a deep crater. The Holocene Mt. Kepolo strato-cone (9) is lined up with a youthful lava cone and flow (10). Ranu Pani (11) and Ranu Regulo (12) are maars in the northern part, and two small vents (13 and 14) are located on the east flank. C. The youngest volcano in Semeru–Tengger massif, Semeru (15), including the currently active Jonggring-Seloko vent, has been built on, and buttressed against the Old Semeru, Mahameru (16) and Jambangan caldera to the north. The active vent sits at the top of the principal SE-trending scar (17) in the edifice. Several flank vents are visible on the eastern flanks (18).

Holocene in age (Sutawidjaja et al., 1996). Volcanic deposits of Mahameru–Semeru consist of lava flows, pyroclastic-flow deposits and tephra-fall deposits, debris-avalanche, and lahar deposits (Fig. 5). Based on our ^{14}C dating and on chronicles, the volcaniclastic deposits in the radial valleys of the S and SE flanks of Semeru are middle–Late Holocene and historical. The radial valleys such as Koboan and Lengkong Rivers contain up to three terrace systems, the highest 8–10 m thick, the second ca.5 m thick, and the lowest 2–3 m thick. We have used the ^{14}C method to date volcanic deposits forming the terraces. The pyroclastic-flow units forming the base of the uppermost terrace <10 m thick in the Bang River Valley near Pronojiwo yield ^{14}C ages of 1500 ± 30 yr BP (Gif-12358/SacA-11577 : $\partial^{13}C = -30‰$), i.e. 1351–1406 cal BP (with 95.2% confidence interval). The youngest age indicates an eruption during the 6th or 7th Century AD. The pyroclastic-flow units forming the top of the uppermost terrace 10 m thick in the Lengkong Valley yield 3770 ± 40 yr ^{14}C BP (Gif 12290, $\partial^{13}C = -26.39‰$), i.e. 3986–4283 cal yr BP (with 95.2% confidence interval). In these valleys, while the middle terrace is ca.5 m thick and has a mid- to Late Holocene age, the lower terrace is 2–3 m thick and is historical in age (<2000 years).

Our geologic map (Fig. 5) depicts the historic and present-day deposits of Semeru's composite cone and ring plain based on previous works (see references in Thouret et al., 2007) and on our interpretation of satellite images, aerial photos, and on fieldwork. The prehistoric activity of Semeru is poorly known, the oldest reported eruption dating back to just 1818 (references in Thouret et al., 2007). The current active period began in 1967 (Wahyudin, 1991;

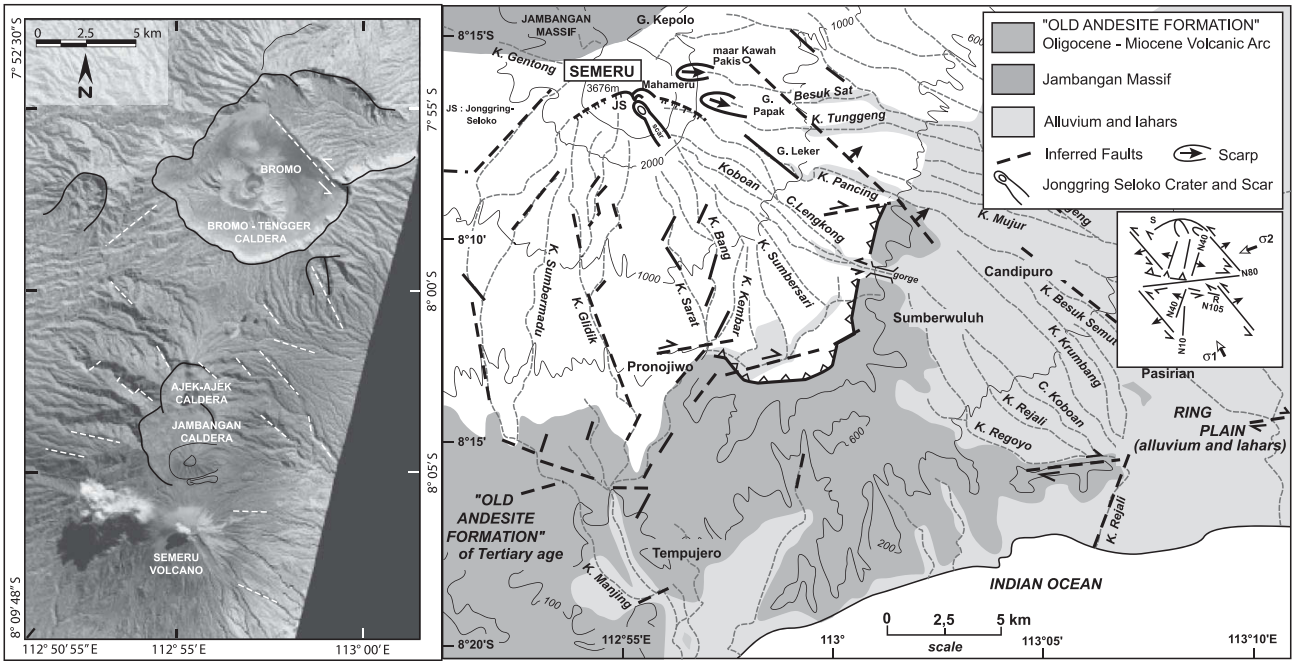

Fig. 4. The 2008 SPOT5 image (left) and the interpreted map (right) portray the regional tectonic setting of Semeru Volcano and its surrounding. The faults (dashed line) were inferred from the interpretation of SPOT-4 satellite images and drainage network map. Note the prevailing N130- and N15-trending faults in this area.

Simkin and Siebert, 1994). Since 1967, cycles of dome growth and collapse have occurred every 5 to 7 years in the Jonggring-Seloko crater, feeding pyroclastic flows that travelled up to 12 km along the SE-trending scar and then the drainage network towards the SE formed by the Kembar–Bang and Koboan–Lengkong Rivers and their tributaries. The last major pyroclastic-flow producing eruption occurred

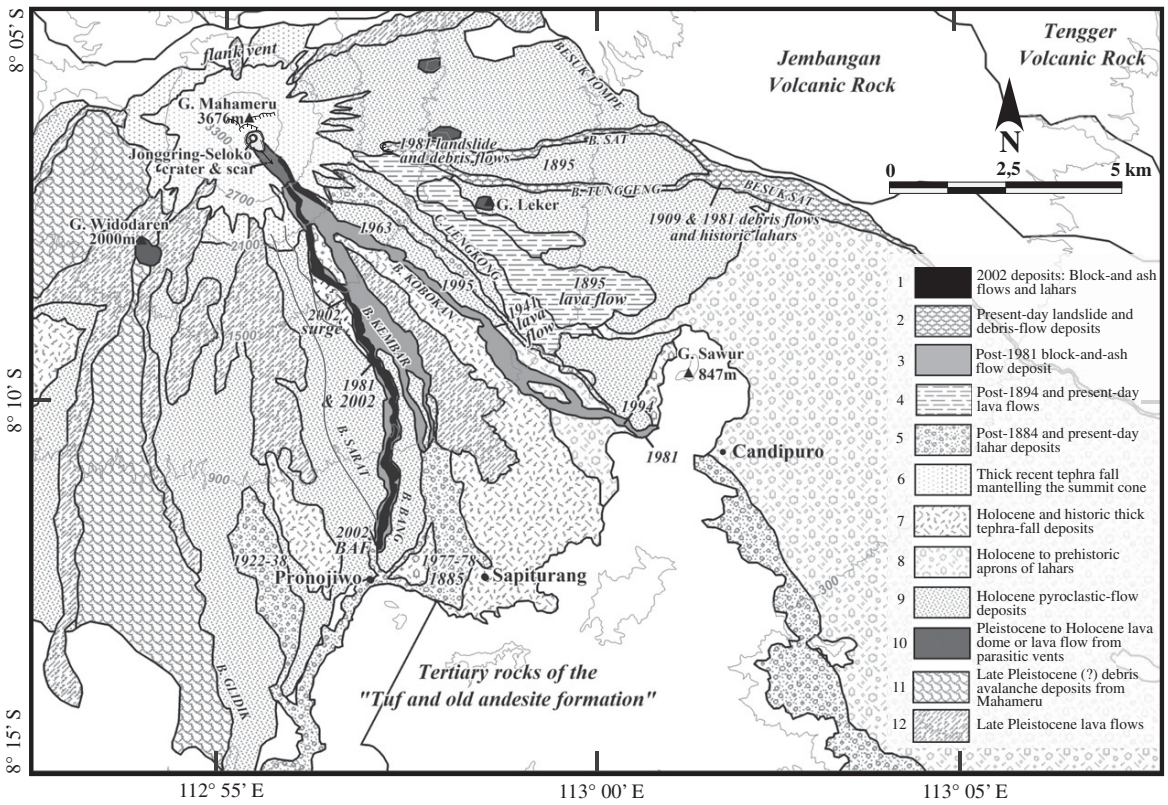

Fig. 5. Geological map of the Semeru's composite cone and ring plain (based on Situmorang, 1989; Wahyudin, 1991; Simkin and Siebert, 1994; VSI geological map by Sutawidjaja et al., 1996; Siswowidjoyo et al., 1997; Carn, 1999; Thouret et al., 2007, and TOPO-DEM). Stratigraphic units 1 to 12 are keyed to symbols in map caption.

in December 2002 to January 2003. On 30th December 2002, pyroclastic flows travelled 12 km down the Kembar and Bang Valleys (GVN, 2003, 2004, and unpublished VSI reports, Bandung).

4. Regional tectonic setting of the Semeru–Tengger massif

Our structural map of Semeru–Tengger volcanic massif (Fig. 6A) is based on the interpretation of our SRTM-DEM and TOPO-DEM as well as of optical satellite images combined with the drainage network map. This map shows the relationships between the regional tectonic setting and the principal structures of the edifices. To obtain a map of geological structures from satellite imagery, we specify the geometric features at surface that reflects the topography, which is controlled by tectonic and deformation associated with the growth structure. The most useful tool with which to recognize cumulative deformations consists of two merged DEMs that highlight topographic variations. SRTM and TOPO DEMs are automatically overlaid by using georeferenced mosaicing procedure on ENVI software.

A rose diagram of lineaments and faults and a sketch portraying fault kinematics summarize the regional tectonic setting of the massif (Fig. 6A–C). Widespread and thick vegetation prevented many of these faults from being identified in the field. The linear features comprise long, rectilinear topographic alignments and sudden, systematic changes in river directions. The rose diagram of all identified linear topographic segments (Fig. 6B) shows a prevailing NW–SE trend. Based on the second rose diagram (Fig. 6C) in which only the long (>1 km), rectilinear topographic segments have been selected, we have identified four groups of faults F1 to F4: (F1) a N40-trending group corresponding to sinistral strike–slip faults observed on the S and the SW flank and ring plain of Semeru as well as in the 'old'

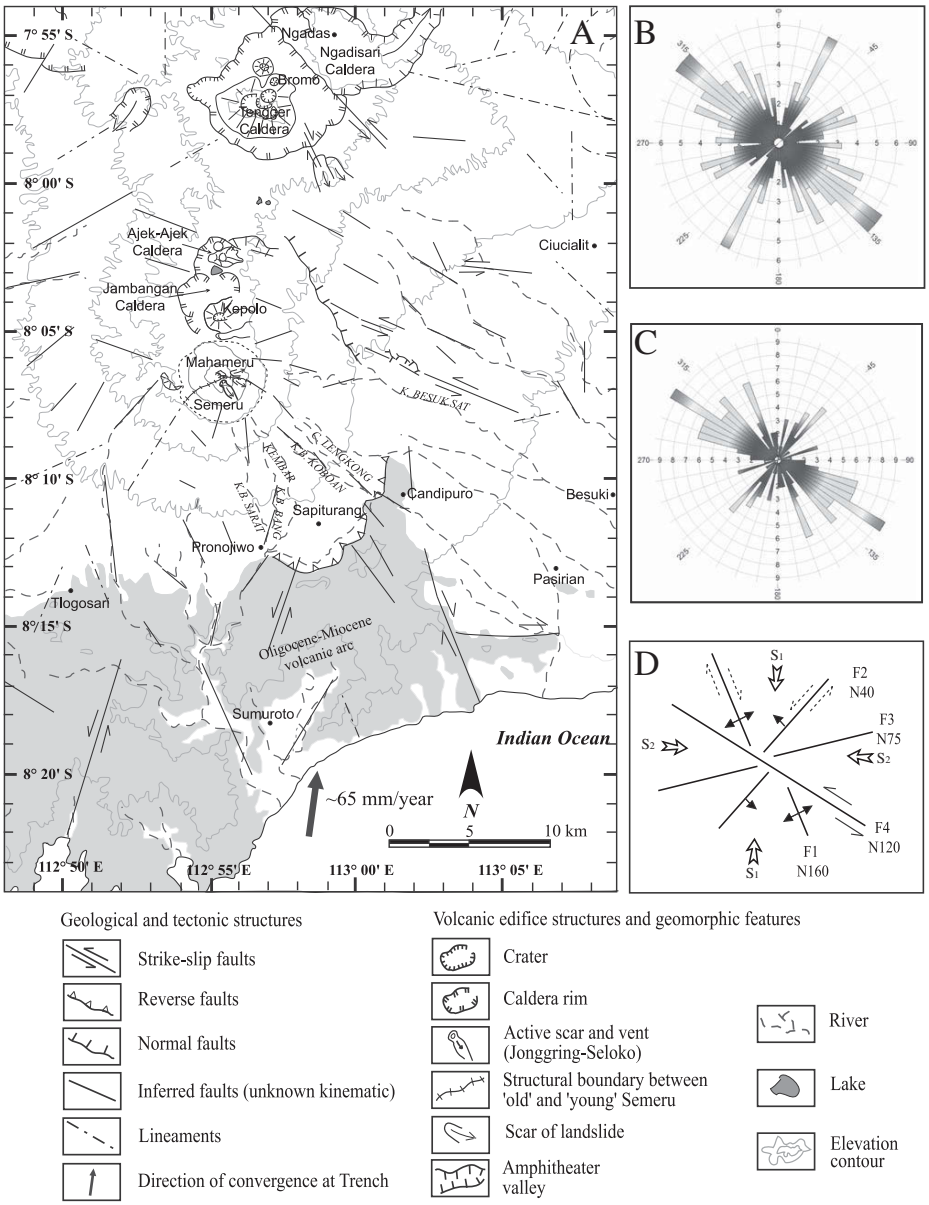

Fig. 6. A. Structural map of the Semeru–Tengger volcanic massif, inferred from SRTM-DEM, TOPO-DEM and optical satellite images. B. Rose diagram of lineaments showing the dominant NW-trending alignment. C. Rose diagram of faults showing four groups of faults, F1 to F4. F4 is the youngest because offsets faults of other groups. D. The sketch diagram depicts the regional tectonic setting around Semeru.

(Oligocene–Miocene) volcaniclastic rocks; (F2) a N160-trending group matching the dextral strike–slip fault in the Tertiary volcanic deposit area SE and S of Semeru (NNW–SSE trending features on the eastern part of Semeru and a NW–SE sinistral strike–slip fault delineate the northern limit of pyroclastic deposits from Semeru, as deduced from the texture of these deposits on the images); (F3) a N75 group containing the faults that guide the E and NNE alignments of the Tengger post-caldera vents ; and (F4) the last group of N105 to N140 faults with a prevailing trend of N120, occurring on the western side of the Semeru–Tengger volcanic massif. Several amphitheaters caused by flank erosion and open to the west are probably controlled by these NW–SE trending faults. The fourth group of faults offsets faults of other groups, and is obviously the youngest.

Our working hypothesis on the fault kinematics and, hence, the tectonic fault regime is summarized in Fig. 6D. The structural map of the Semeru–Tengger volcanic massif shows that the southern area is dominated by the NNE–SSW compressional stress regime due to subduction process at the trench <50 km to the south. This produces the first and second groups of faults. The third group, located in the north sector, shares the same direction as the Madura basin and magmatic intrusions from older (Pleistocene) volcanoes such as Jambangan.

5. Structures and evolution of the Semeru summit cone

Based on two IKONOS images and on the TOPO-DEM, we analyze the structural features of the Semeru composite cone, which lead us to highlight the relationships between deformations and the structural edifice growth. The evolution of the summit cone and its SE-trending scar stems from the comparison of a time series of drawings and photographs since 1923, completed by satellite images since 2003.

5.1. Structures and landforms

The 10th April 2008 and 20th August 2009 IKONOS images (Fig. 7A–C) show the Mahameru summit area, Semeru's active Jonggring-Seloko vent in the youngest SE crater, and a SE-trending scar. Based on the interpretation of both IKONOS images (Fig. 7C), we divide the summit of the Semeru composite cone into three zones:

(1) The Semeru summit cone has grown on the older edifice of Mahameru. A structural boundary is indicated between 'old' Semeru (Mahameru) and 'young' Semeru (Jonggring-Seloko). Together these edifices have formed the Semeru composite volcano. The north to southwest part of the Mahameru cone and the northwest slope of the Semeru summit cone are covered by thick tephra fallout. The Mahameru summit area shows three arcuate scarps, probably vent rims, suggesting that vents have migrated from NW to SE (Thouret et al., 2007). The three crater rims are located at the intersection of the N40-, N70- and N130-trending fractures.

(2) The upper northeastern flank of the summit cone appears more weathered, comprising reddish brown, unconsolidated deposits. To the NE of Jonggring-Seloko are the scars of the 1909 and 1981 landslides and gullies. These form the catchment headwall of the Besuk Sat river valley. These landslides are still active today. The 2008 and 2009 IKONOS images (Fig. 7 A,B) and SPOT5 image (Fig. 8C) show landslides and gullies that cut in reddish brown deposits high on the NE flank. We suggest that the unconsolidated, weathered deposits are related to a previously active hydrothermal system beneath this area.

(3) The southwestern to east part of the young Semeru cone (Fig. 8D,E) is fractured and deeply cut by a dense network of gullies. The summit area consists of thick ash layers that

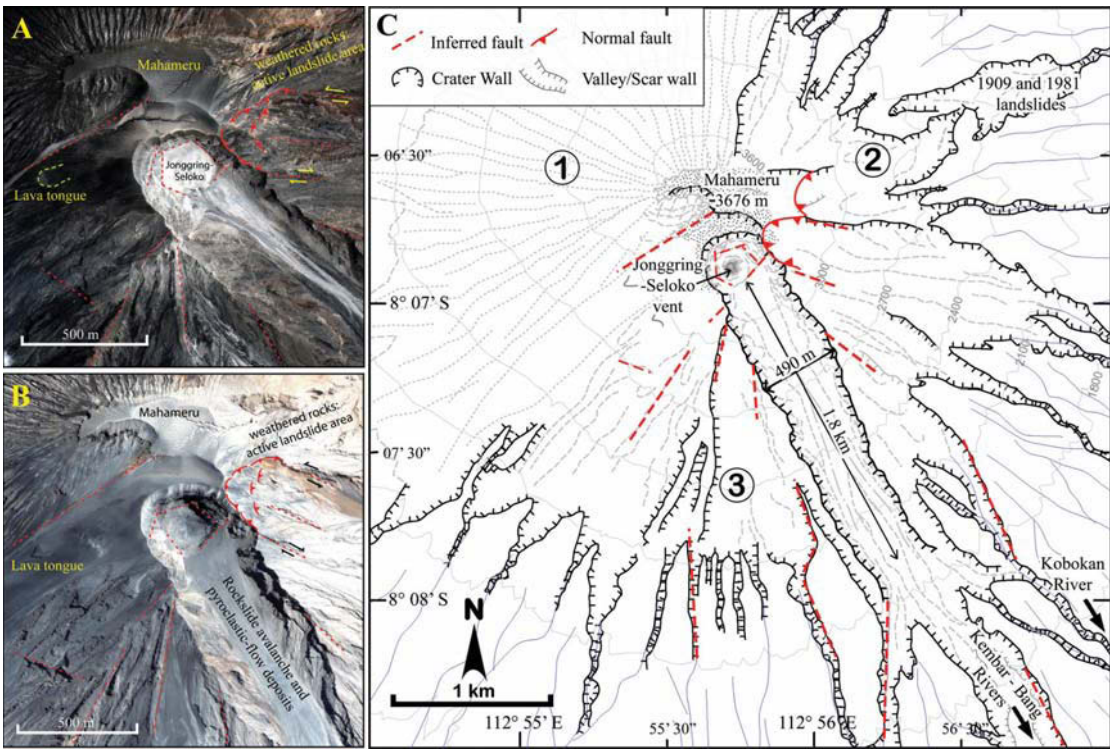

Fig. 7. A. The 10th April 2008 IKONOS image and B. 20th August 2009 IKONOS image show the Mahameru summit area, Jonggring-Seloko and the SE-trending principal scar. Stratification on the wall of the crater shows a pile of lava flows separated by pyroclastic-fall and flow deposits. Crater ring faults are visible in this image. B. Sketch map based on the 20th August IKONOS image showing the structure and geomorphic features of the Semeru summit cone.

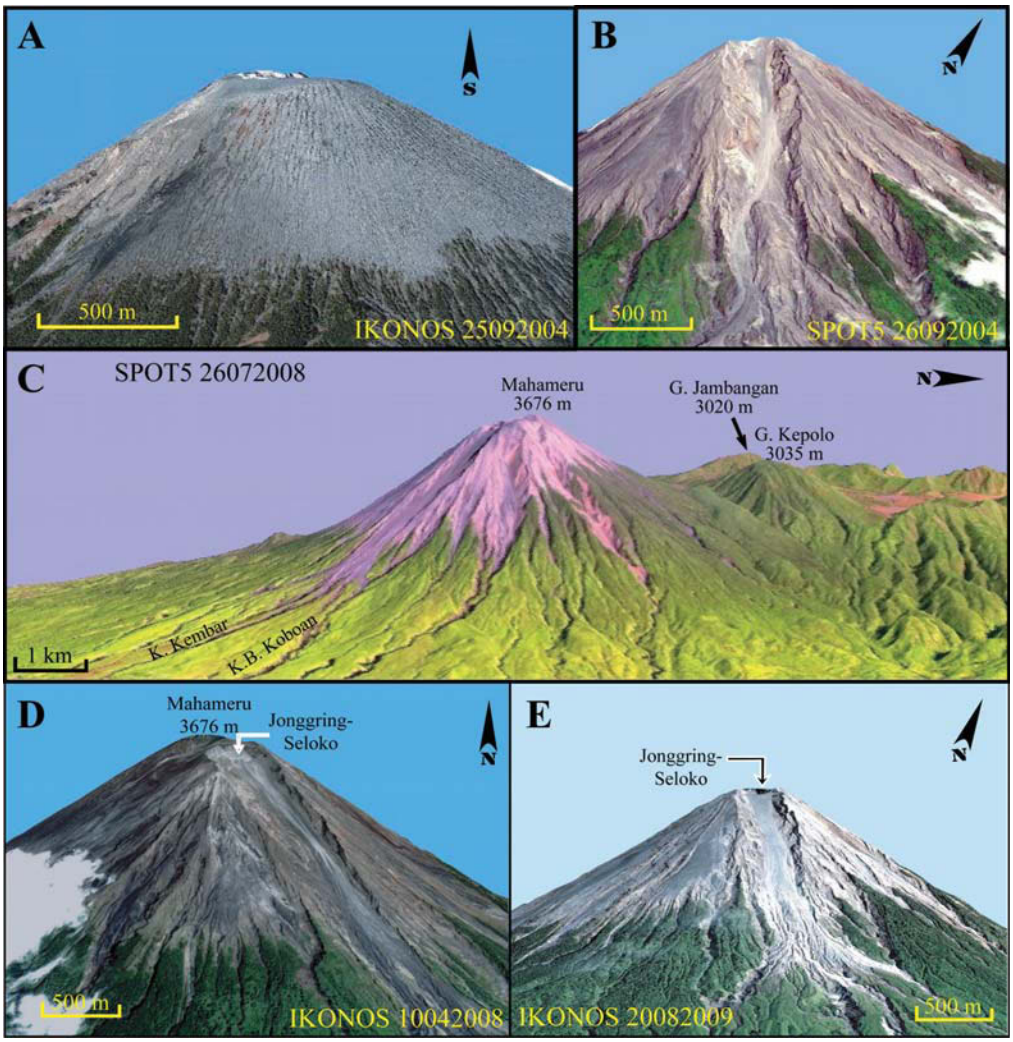

Fig. 8. Three IKONOS images (25-09-2004, 10-04-2008 and 20-08-2009) and two SPOT-5 images (26-09-2004 and 26-07-2008) draped on the TOPO-DEM show the Semeru edifice, including the Jonggring-Seloko vent and SE-trending scar, and landslide scars on the East flank.

cover lava flows, which crop out outside the crater and scar area. The Jonggring-Seloko crater, 500 m SE from Mahameru summit, reportedly initiated in 1913 (Van Padang, 1951). The 2008 and 2009 IKONOS images (Fig. 7A,B) display the hexagonal shape of the vent area, a shape guided by N60–75 and N150–160-trending fractures. The stratigraphy of the active crater wall consists of a ≤500 m-thick pile of lava flows with intercalated pyroclastic-fall and flow deposits. To the west of Jonggring-Seloko crater, a lava tongue from a lateral flank eruption is possibly linked to one of lava flows cropping out in the crater wall. To the south of the vent, a lava flow is found that originates from the crater itself. The recent active vent sits at the top of the principal SE-trending scar that cuts the steep-sided SE flank of the edifice. This elongated horseshoe-shaped scar, about 1.8 km long and 490 m at its widest point, channels rock-falls and pyroclastic flows during phases of heightened activity. The orientation of the scar coincides with a N160-trending fault, which is related to the second group of faults (Fig. 6). Minor scars cutting the west flank are probably controlled by NW and NNE-trending faults or the first and second group of faults.

Our flank profiles of Semeru's summit cone are extracted from the TOPO-DEM (Fig. 9A) and show the slope and morphology of three zones. The slope map of the Semeru summit cone between 1800 and 3500 m (Fig. 9B) shows average slopes of 30.6° for the WNW flank, 36.3° for the S flank, and 32.5° for the E flank. While no significant convexity is observed in the WNW flank, the S zone and E flanks show convex–concave profiles that suggest deformation of these flanks. The difference in slope segments and convexity in profiles may be due to material eroded from the elongated SE-trending scar, which accumulates mid-slope on the SE flank between 1500 and 2000 m. Slope segment and profile differences observed on the S and SE flanks are linked to normal faults mid-slope, and thrust faults are inferred to be the influence at the base of the summit cone flank (Fig. 9B). These structures suggest that deformation has resulted from the structural growth of the Semeru edifice. The Semeru composite cone has been built on, and is buttressed against, the Mahameru edifice along a structural unconformity. This unconformity probably acts as a semi-circular failure plane (Fig. 9C) but no geophysical data are available to allow us test this hypothesis. Inferred structures such as a bulge and thrust faults at the base of the SE summit cone flank (Fig. 9C) can also result from flank spreading of the weak-cored volcano with asymmetric deformation (e.g. Cecchi et al., 2004). Factors that could induce volcano spreading are a weak basal layer and a sufficiently high mass and magma influx (Borgia, 1994). A weak basal layer is known at Semeru. Reddish brown, weathered deposits seen in the 2008 IKONOS image crop out in the vicinity of

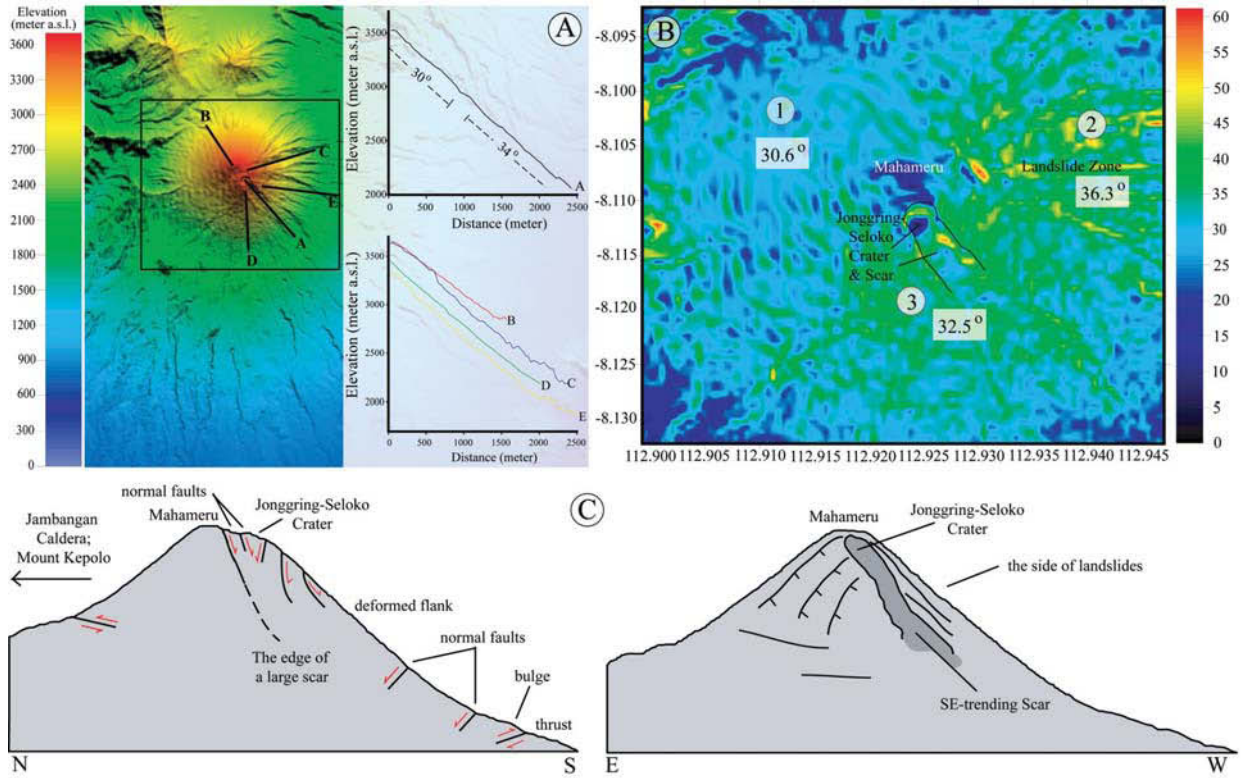

Fig. 9. A. TOPO-DEM of Semeru with blue-red color code for elevation values and flank section profiles showing convex–concave slopes. B. Slope map of Semeru analyzed from TOPO-DEM, showing the different slope values between each segment described in Fig. 8. C. North–south and east–west cross section sketches of Semeru edifice illustrating that the younger Semeru composite cone has been built on and is buttressed against the Mahameru edifice along an unconformity that may act as a failure plane.

the volcaniclastic sediment of Tertiary age (below 1000 m asl in the Koboan Valley on the SE flank, Figs. 4, 5). Because repeated daily explosions eject magma from an open conduit at short time intervals (Nishi et al., 2007; Iguchi et al., 2008), and because Semeru has a relatively shallow, narrow and pressurized conduit, the magma influx and mass may be large enough to induce significant deformation especially in the summit cone of the edifice.

5.2. Evolution of the summit area: elongated SE-trending scar and deep vent

A series of drawings and photographs shows the morphological changes observed on the Semeru's summit since 1923 (Fig. 10). The evolution of Semeru's summit resulted from a combination of eruption processes: growth and collapse of domes in the Jonggring-Seloko vent area, dome collapse-driven pyroclastic flows, and dome growth- or gravity-driven rockslides. Between the intervals of heightened eruptive activity, the vent area remains open with a crater up to 400 m in width and at least 200 m in depth. High vulcanian columns or violent strombolian activity produces persistent tephra fallout. Fig. 11B shows the morphological evolution of the Jonggring-Seloko vent area and the SE-trending scar. Although two aerial photos (1981 and 1990) and two satellite images only are shown in Fig. 11A, the resulting map in Fig. 11B results from the interpretation of the two aerial photos and all SPOT5 and IKONOS satellite images available between 2003 and 2009. Two main scarps are located to the east and the west of the Jonggring-Seloko crater. To the west is the remnant of an older crater, which has been modified by a landslide, and to the east is a landslide scar where weathered rocks have been removed. The crater has enlarged by about 100 m from 1981 to 1990, up to a scarp towards the north, as shown on the 1981 aerial photograph (Fig. 11). This scarp results from a large collapse within the crater formerly occupied by a lava dome. From 1990 to 2009, the crater has also expanded but only by a few meters to reach a width of 400 m by 2009. The crater was filled by a lava dome in 1981 but it re-opened in 1990 with a deeper vent conduit. The 1990 aerial photograph shows that the Jonggring-Seloko crater at the base of its headwall was roughly 200 m deep at that point, comparable to the depth of the 2009 vent.

According to a 1923 aerial photograph, the SE-trending scar was not yet established although a small channel may have been concealed between two lava flows. In 1963, pyroclastic-flow deposits along the Besuk Semut Valley on the SE flank were the result of dome collapse. After 1977, the summit has been eroded and a horseshoe-shaped amphitheater valley was formed, which acted as a channel for eruption-related flows. In 1994, this structure extended downstream and into three river heads: Besuk Kembar and Besuk Bang towards the south and Besuk Koboan toward the SSE (Figs. 4, 5). This SE course was used again on 3rd February 1994 and 20th July 1995 by large (5–7 million m^3 each) pyroclastic flows, which were channeled 11.5 km and 9.5 km, along the Koboan Valley and in the upper course of Lengkong Valley respectively (Figs. 4, 5). On 29th December 2002, pyroclastic flows were channeled along the principal SE-trending scar towards the Bang and Kembar Valleys and traveled 11 km to the south as far as Supit, a suburb of the district capital Pronojiwo.

The persistent eruptive activity of Semeru that began in 1967 started with continuous emission of gas from a vent in the southern part of the Jonggring-Seloko crater. This was followed by lava extrusion which formed a stream-like lava flow that moved towards the south slope. Eruptive activity continued until 1974 and was characterized by extrusion of lava, which created a lava dome that grew in the west and south area of the summit. The extrusion later shifted to the SE but remained in the summit area. This eruptive activity

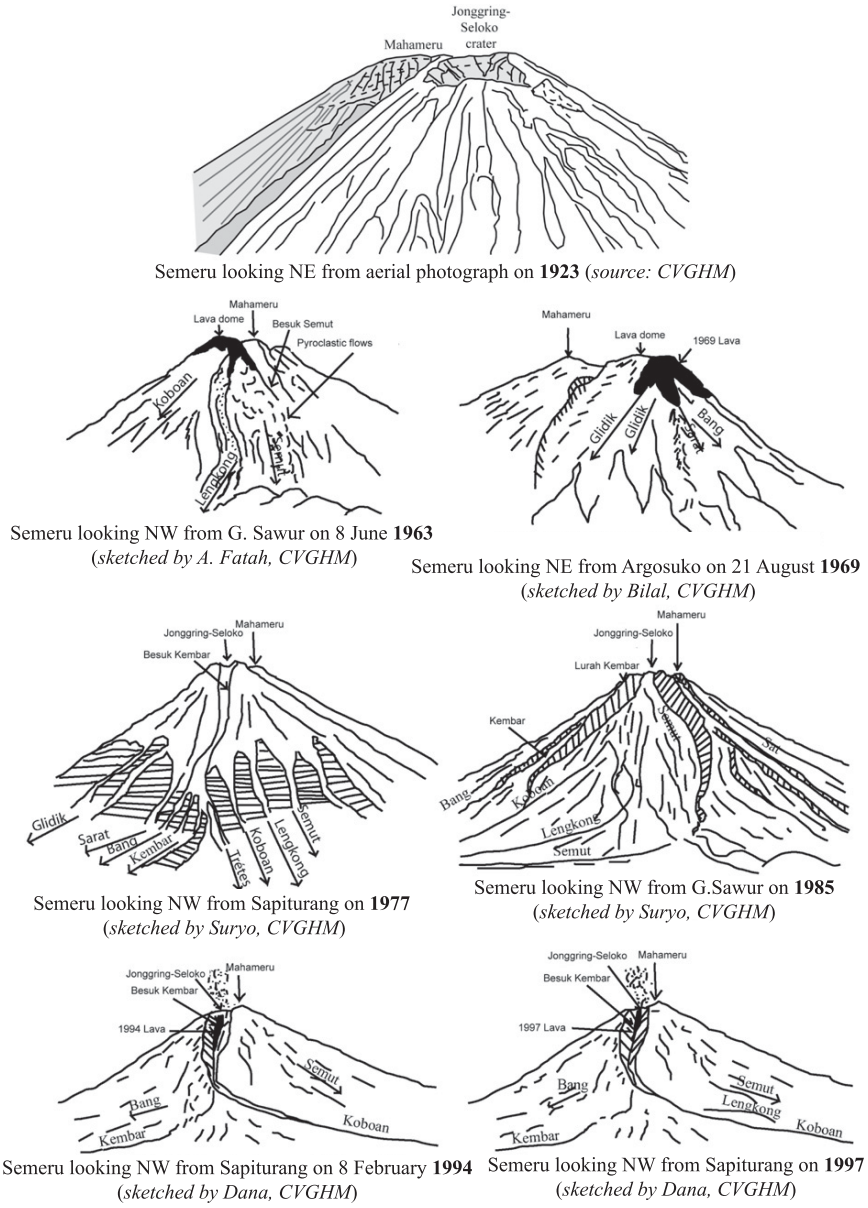

Fig. 10. Sketches of the Semeru edifice from 1923 to 1997 portray the morphological changes of the summit cone. The SE scar was not visible in 1923. The 1963 lava dome and pyroclastic flows are located on the SE flank between Koboan and Semut River Valleys. The 1969 lava dome and pyroclastic flows are located on the south flank. The 1977 sketch shows a horseshoe-shaped scar towards Kembar River, which expanded much in 1985. The 1994 and 1997 sketches show the 1997 lava tongue, lava dome and an eruption column. Sapiturang is located 12 km to the SSE, G. Sawur 12 km to the SE, and Argosuko 22, 5 km to the NW of the Jonggring-Seloko crater.

was accompanied by ash-producing explosions, lava avalanches, and block-and-ash flows that widened the SE-trending channel. Since 1979, the rate of dome growth decreased, but the activity continued with lava avalanches from the dome, occurrence of dome collapse-driven block-and-ash flows, and explosions (GVN, 1980).

After 1979, the SE-trending principal scar widened rapidly. The 1981 and 1990 aerial photographs (Fig. 11) show the SE-trending wide scar from the upstream crater rim at c.3300 m descending to c.2600 m, over a distance of more than 1.5 km. The scar narrowed through the upper course of the Kembar River Valley, partly branching into the Koboan River. The maximum scar width in 1981 was about 290 m and 350 m in 1990. The eruptive 1994 activity resulted in extension of the scar downvalley, and it extended into the Bang River Valley. The scar width of about 490 m at its widest point in 2009 is almost twice the 1981 width (about 290 m). The SE-trending scar has thus expanded at a rate of about 8 m/year over the period 1981–2009. Such an evolutionary history is difficult to reconstruct for a dangerous volcano without satellite images.

6. The most recent 2002–2003 (vei 2–3) eruption

Semeru is one of the few persistently active composite volcanoes on Earth erupting on a daily basis. Based on chronicles, Thouret et al. (2007) identified three eruptive styles for Semeru since 1818: (1) persistent vulcanian and phreatomagmatic regime of short-lived eruption columns, which occur several times a day; (2) increased activity levels every five to seven years to produce pyroclastic density currents (block-and-ash flows, and associated surges) from domes growing in the Jonggring-Seloko vent; and (3) flank lava flows of andesitic composition and aa type, stem from parasitic lava cones and

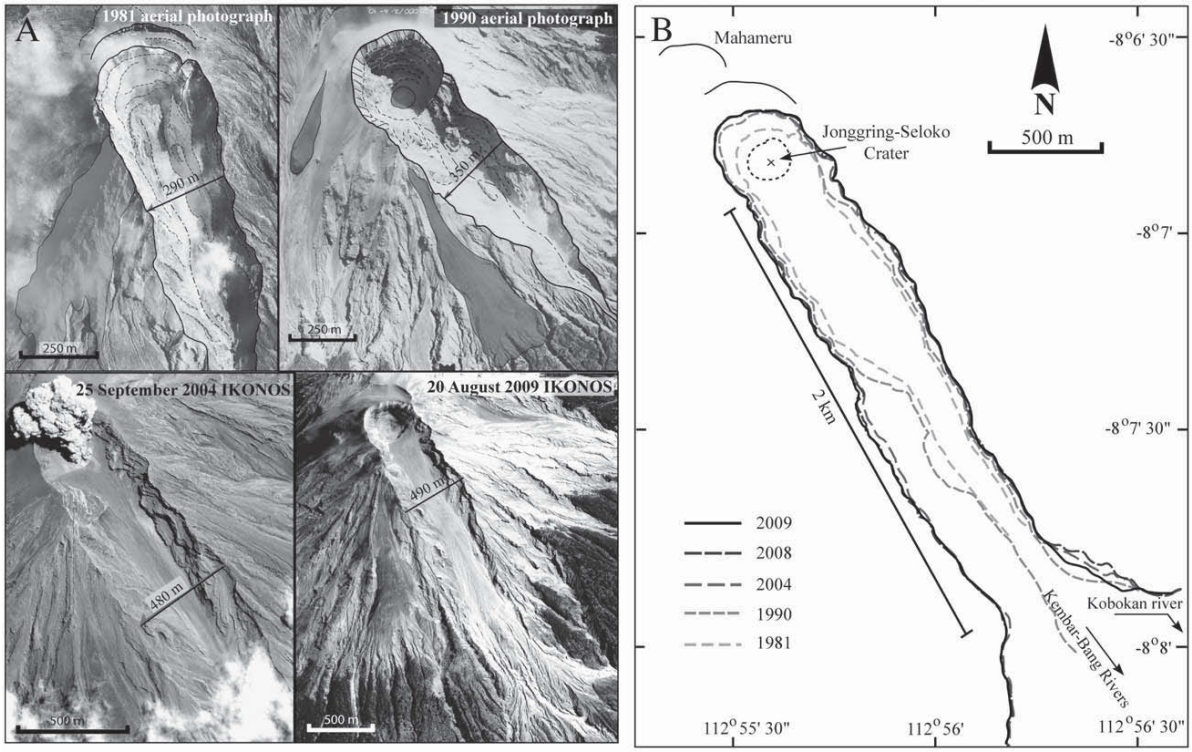

Fig. 11. A. Aerial photographs of 1981 and 1990 and satellite images of 25/09/2004 and 20/08/2009 reveal morphological changes of the Jonggring-Seloko vent and SE-trending scar. B. Sketch showing the evolution of the Jonggring-Seloko vent and the SE-trending scar whose width has increased from 290 m in 1981 to 490 m in 2009.

flank eruptive vents and reached 5 to 8 km in length on the S and SE flanks (Fig. 5). The two most recent lava flows of Semeru were emplaced on the SE flank: the 1895 lava flow reached c.10.5 km from the Jonggring Seloko vent area, covering an area of ~7 km^2, while the 1941–1942 lava flow from a parasitic lava cone reached c.6.5 km and covered an area of ~2.5 km^2.

Seven to eight years after the two 1994 and 1995 explosive episodes the eruptive activity moved towards the second eruptive style, characterized by a high number of explosions and pyroclastic flows at the end of December 2002 (GVN, 2002). The peak of the eruptive episode occurred on 29th December 2002 when block-and-ash flows with a total volume of 3.5 to 5 million m^3 traveled ~11 km from the summit down the Besuk Bang Valley. About 500 people were evacuated from the hamlet of Supit to the district capital Pronojiwo for about one week but no casualties were recorded.

The 2002–2003 activity, as summarized in Appendix Table 2, was initiated by an increase in seismic activity in March 2002. This was followed by emission of a gray plume that rose 300–400 m above the summit. Several lava avalanches traveled 750 m down Kembar Valley and several pyroclastic flows traveled downvalley (black area in Fig. 5). The eruptive activity increased until August 2002, when a slight decrease was perceived between September and December 2002 but the eruptive activity remained at a level higher than normal, categorized at alert level 2 on a scale of 4 (Center of Volcanology and Geologic Hazard Mitigation, CVGHM). Between 30th November and 28th December 2002, block-and-ash flows occurred several times, extended down the Bang River Valley, and attained a 5 km maximum distance. Other flows were channeled along the Kembar Valley. Voluminous block-and-ash flows and hot lahars occurred on 29th and 30th December 2002 on the SSE flank. Block-and-ash flows of a volume of 3.25×10^6 m^3 were channelled 11 km down the Bang Valley, extending as far as the Supit suburb of Pronojiwo (Fig. 5). On 29th December 2002 trees were singed and land was covered by a muddy ash over an area 2.2 km long and 0.5 km wide: located along the west side (right bank) of the Bang Valley between 1250 m and 1400 m asl (Fig. 5; GVN, 2003). The deposit was attributed to a 'wet' pyroclastic surge that decoupled from one of the flows moving down the valley and which then swept across the Bang Valley to damage the forest and agricultural land. The 29th December 2002 light brownish, block-and-ash flow deposits of andesitic composition contain lithic blocks of dome and lava blocks up to 12.5 m in diameter with a matrix of coarse ash. The eruptive activity continued after this event but at a lower intensity until the end of January 2003 when the eruptive episode ended (GVN, 2004).

The 2002 block-and-ash flow and lahar deposits are shown in Fig. 5 and also in the 12th March 2003 ASTER image as color-coded pixels indicating a thermal anomaly with respect to the image background (Fig. 12A, C). Based on the ASTER image, the thermal anomaly occupies the 11.36-km-long channel of Bang Valley and covers an area of about 1.65×10^6 m^2. Based on field investigation by researchers of the Volcanological Survey of Indonesia (VSI, now CVGHM), block-and-ash flow deposits in the Bang Valley at 750 m asl had a thickness of 4–7 m. By using these data and assuming a variable thickness of deposits, depending on local topography (minimum of 1 m and maximum of 9 m), we calculate the volume of the 2002 block-and-ash flows deposits to be about 5.45×10^6 m^3.

Remote sensing of two ASTER thermal images provides details on eruptive activity and related deposits that have not been identified so far. The 16th August 2002 thermal image (Fig. 12B) shows thermal anomaly on the SE-trending scar extending 1.4 km from the Jonggring-Seloko Crater with the high temperature occurring in the crater and a higher temperature hotspot being located at a distance of 500 m from the crater. This can be related to the eruptive activity before 16th August 2002 when most lava avalanches or pyroclastic flows travelled about 500 m from the crater and occasionally as far as 1.4 km. The hot spot was caused by accumulation of hot materials (lava rockslide or pyroclastic-flow fronts) within the scar. The location of the hot spot is related to the morphology of the SE-trending

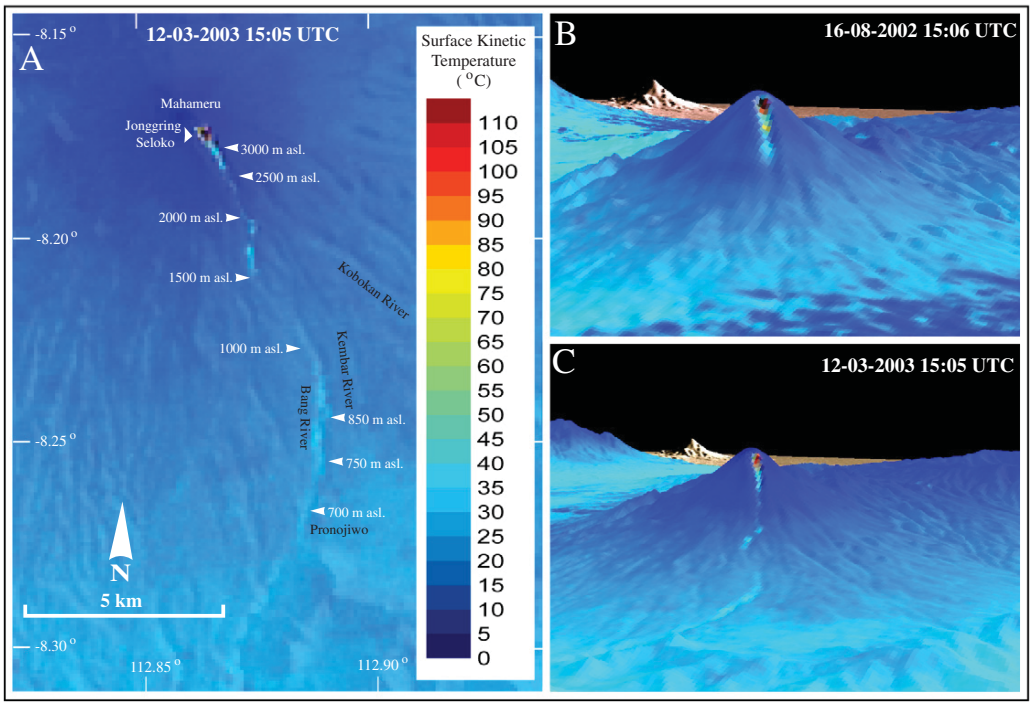

Fig. 12. A. The ASTER TIR surface kinetic temperature image taken on 12th March 2003 with a blue-red color code shows thermal anomalies induced by the 2002 block-and-ash flows on Semeru along the SE-trending scar and into the Bang River Valley as far as Supit, a suburb of Pronojiwo. B. and C. 3D surface view of 16th August 2002 and 12th March 2003 ASTER TIR surface kinetic temperature images on TOPO-DEM, showing thermal anomalies on Semeru before and after 29th December 2002.

scar (Fig. 9), where it occurs at a break in slope where deposition may be expected. The 12th March 2003 thermal image (Fig. 12C) reveals that the block-and-ash flows deposits retained a higher temperature than its background for two months after deposition: this may be due to slow cooling or the thermal characteristics of the block-and-ash flow deposits that may absorb heat more effectively during the day to heat up to a greater degree in the sun than the background surfaces. The thermal anomaly on Jonggring-Seloko Crater and its SE-trending scar, due to persistent explosions, lava avalanches and pyroclastic flows, was again observed.

If we compare the 24th October 2003 SPOT 5 (Panchromatic) image and the 14th November 2002 IKONOS image, we can recognize four impacted areas. (1) The first area is characterized by a dark gray, smooth surface which caps the thick block-and-ash flow deposits, which extend 11.36 km from the SE-trending scar to Pronojiwo in the Bang River Valley (Fig. 13A). Within weeks of the eruption end, the top surface was already incised by small, shallow and active channels cut by runoff. The valley-confined block-and-ash flow deposits also widened, by two- to three-fold, the pre-eruption channel bed (Fig. 13A–C). (2) While the second area appears brownish in the 2002 IKONOS scene, it is marked by a light-grey to whitish color in the 2003 SPOT5 images. This scorched or singed forested area between 1200 and 1500 m asl was swept by the wet pyroclastic surge that extended 0.5–1 km from the Bang Valley channel at distances of 5 to 7 km from the crater (Fig. 13A). (3) Along the sinuous channel between 750 m and 1100 m, large, grey patches of deposits on banks and valley terraces across convex and concave bends indicate overbank deposits of the block-and-ash flows (Fig. 13C). (4) Below 1000 m, the down-valley banks of the Bang Valley are dusted by a thin, brownish muddy deposit. The thin, mud-rich, fine ash layer may be due to an increase in water vapor at the time of the eruption in rainy season and to a decrease in flow temperature at ≥11 km runout distance. The temperature of the dry ash-rich flow front at Supit was measured about 120 °C two days after the emplacement.

Based on Semeru's historical eruptive activity, the dome collapse-driven block-and-ash flows witnessed in 2002–2003 occur every five to seven years, so that the same event is likely to happen again. The area potentially affected by avalanches and block-and-ash flows is defined as a triangle-shaped area opening at 45° toward the SE with a width of ~15 km at 12 km from the vent. At least 100,000 people live in the lower part of this triangle-shaped area (Thouret et al., 2007). This hazardous area and the E, SE and S valleys are also threatened by syn-eruption and post-eruption lahars, which can reach the sea 25 km away. To assess the hazard of eruptions in the future, volcano monitoring is the main tool capable of providing an early warning to people who live or conduct their activities in the Semeru's hazard zones. Other work that can be done to predict the direction of pyroclastic flows is to monitor the evolution of the morphology of the SE-trending scar and of the drainage network. Additional prediction may be based on simulation runs of pyroclastic flows extent and runout using numerical codes such as TITAN2D or VOLCFLOW over up-to-date DEMs. This is one of the objectives of our ongoing research project.

7. Conclusion

The objective of our work was to use high-spatial resolution images (IKONOS and SPOT5) to analyze the structures developing across a persistently active volcanic complex and to map the deposits and impact of the 2002–2003 eruptive activity of Semeru volcano. Based on our results, we reach five main conclusions.

(1) The high-spatial resolution imagery enabled us to safely study a persistently active, yet dangerous composite volcano such as Semeru. A single SPOT5 image also allowed us to study structural and geomorphic objects a few tens of meters over 1800 km^2 in the Tengger–Semeru volcanic massif. SPOT5 and IKONOS images were merged with ASTER thermal imagery

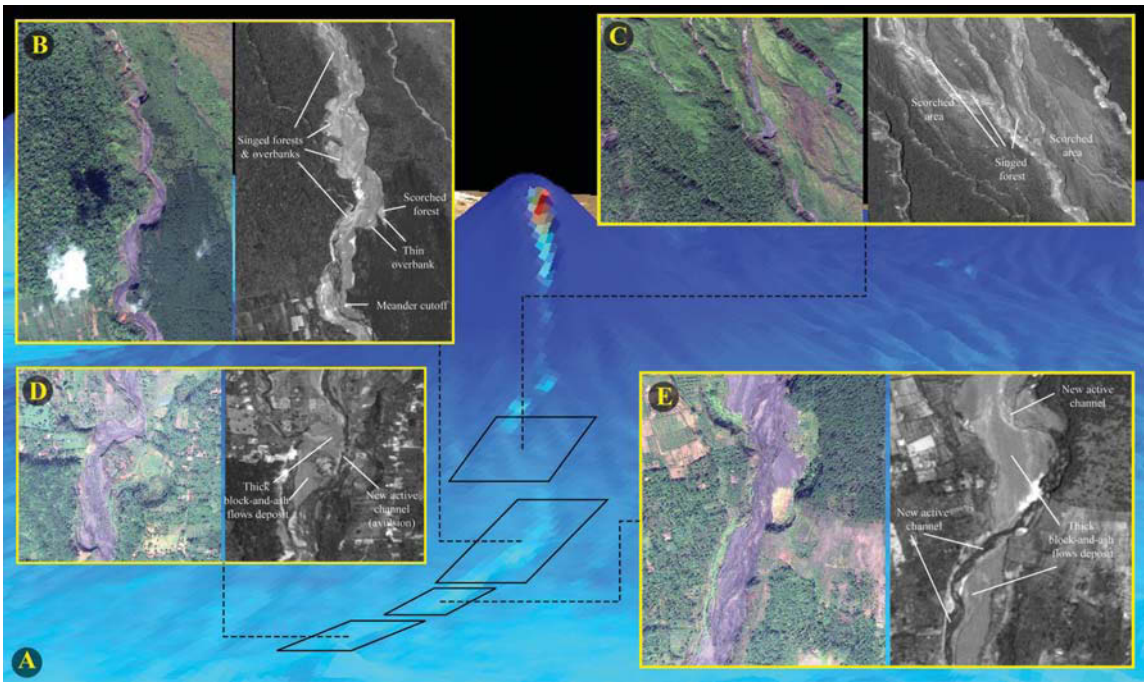

Fig. 13. The 14th November 2002 IKONOS image compared with 24th October 2003 SPOT-5 (panchromatic) image shows the Bang River Valley prior to and after the 29th December 2002 block-and-ash flows. The figure shows scorched and singed forests due to pyroclastic surge (B top right) and overbank (C top left). Thick block-and-ash flow deposits are characterized by smooth, dark grey surface (bottom left D and right E) and by new, shallow active channels formed by runoff and lahars.

and Digital Elevation Models to improve the interpretation of structures, deposits and effects of volcanic flows. Despite limitations such as cloud and vegetation cover, the reliable return period of the satellite orbit makes satellite time series a powerful tool for mapping geological and geomorphological changes at an active volcano when combined with ground-based observations (Thouret et al., 2010). Each of the data used in this study was useful for the distinct purposes of structural and geomorphic analysis. The two SRTM-DEM and TOPO-DEM were useful for recognizing structural features and describe the relationships between fault groups and the drainage network. The IKONOS images helped to determine structures and deposits in the summit vent area with unprecedented detail. The SPOT5 image enabled us to outline deposits and structures at the regional scale of the volcanic massif. The ASTER TIR images were useful in tracking thermal anomalies linked to recent pyroclastic deposits to be mapped during and shortly after an eruption. In addition, the high-resolution images can be used for detailed mapping and interpretating the summit cone and the vent area without compromising the safety of geologists. Safety is a constant issue at a persistently active volcano such as Semeru, which has killed several volcanologists in the recent past.

(2) Four groups of faults trending N40, N160, N75 and N120 occur on the Semeru–Tengger volcanic massif. The first and second groups, located mostly to the south of the massif, are related to the compressional stress regime due to convergence at the subduction zone >50 km south of Semeru. The third group, which is dominant in the northern area of the Tengger–Semeru massif, may be related to extension in the Madura basin. The young N120 faults, which offset all other fault families, may be related to crustal spreading caused by magmatic intrusions from 'older' volcanoes such as Jambangan.

(3) Structures visible on the Semeru's summit cone may be related to the regional tectonic setting. The SE-trending scar is partly controlled by the N160-trending fault, which belongs to the second tectonic group. This scar, which channels eruption-related flows and dome-growth related rockfalls, appeared between 1969 and 1979 and widened rapidly until 2009 at a rate of about 8 m/year. Besides the main scar, minor scars that cut down the west flank of Semeru are likely to be controlled by NW- and NNE-trending faults.

(4) The Semeru composite cone has been built on and is buttressed against the Mahameru edifice. Some structures, such as summit normal faults, and thrust faults at the base of the SW to E flank of Semeru, indicate an asymmetric deformation pattern possibly induced by flank spreading of the weak-cored volcano. The existence of the weak basal layer of weathered volcaniclastic deposits of Tertiary age beneath Semeru is a working hypothesis to be tested. In addition, the large mass of the edifice (about 60 km^3) and the constant magma influx (at least since 1967) are expected to create a significant deformation especially in the upper part of the edifice. Deformation measurements and geophysical methods should be applied, and the possibility of flank collapse must be considered in the future.

(5) An example of the hazards of Semeru is the 2002 block-and-ash flows, with a volume of $5.45\times10^6\ m^3$, that caused the evacuation of 500 people and damaged the forest and tilled land on the west side of the Bang Valley. A wet, fine-ash rich pyroclastic surge swept across the forest and agricultural land at the edge of the Bang Valley at a distance between 5 and 8 km from the crater. The pyroclastic-flow and surge deposits marked easily detectable morphological changes to the volcano surface. Detected morphological changes return to our first point that time series of high-spatial resolution data can be of great utility in tracking the rapid changes that occur in the structures and morphology of a persistently active volcanic complex.

Acknowledgments

This work was supported by ICT-ASIE "ImagerLeRisk" and VELI (*Volcanisme Explosif Laboratoire Indonésien*) programs funded by the *Ministère des affaires étrangères et européennes* (MAEE) — *Agence Française pour le développement* (AFD). Remote sensing, processing and interpretation have been carried out at the Laboratoire Magmas et Volcans, UMR 6524 CNRS et IRD, Université Blaise Pascal in Clermont-Ferrand, France. Our collaborators abroad are: the Center for Volcanology and Geological Hazard Mitigation (CVGHM) of the Geological Agency, Ministry of Energy and Mineral Resources, Indonesia; and the Center for Remote Imaging, Sensing and Processing (CRISP), National University of Singapore.

Appendix. Tables 1 and 2

Table 1

Technical characteristics of satellite sensors and images used for this study.

Satellite sensor; provider	Spectral range	Spatial resolution/ swath width (at nadir)	Average revisiting time; off-track viewing angle
IKONOS Space Imaging GeoEye	Panchromatic: 450–900 nm	0.81 m/11 km	2–3 days ±30°
	B1 (blue): 445–516 nm	3.2 m	
	B2 (green): 506–595 nm	3.2 m	
	B3 (red): 632–698 nm	3.2 m	
	B4 (NIR): 757–853 nm	3.2 m	
SPOT-5 SPOT Image	Panchromatic: 480–710 nm	2.5 or 5 m/60 km	2–3 days ±27°
	B1 (green): 500–590 nm	10 m	
	B2 (red): 610–680 nm	10 m	
	B3 (NIR): 780–890 nm	10 m	
	B4 (SWIR): 1580–1750 nm	20 m	
SPOT-4 SPOT Image	Monospectral: 610–680 nm	10 m/60 km	2–3 days ±27°
	B1 (green): 500–590 nm	20 m	
	B2 (red): 610–680 nm	20 m	
	B3 (NIR): 780–890 nm	20 m	
	B4 (SWIR): 1580–1750 nm	20 m	
SPOT-1 SPOT-2 SPOT image	Panchromatic: 500–730 nm	10 m/60 km	2–3 days ±27°
	B1 (green): 500–590 nm	20 m	
	B2 (red): 610–680 nm	20 m	
	B3 (NIR): 780–890 nm	20	
ASTER Thermal Infra-Red (TIR)	TIR Band10: 8125–8475 nm	90 m	16 days ±8.55°
	TIR Band11: 8475–8825 nm		
	TIR Band12: 8925–9275 nm		
	TIR Band13: 10,250–10,950 nm		
	TIR Band14: 10,950–11,650 nm		

Table 2

The 2002–2003 Semeru seismic and eruptive activity summarized from Smithsonian Institute/USGS weekly volcanic activity reports (GVN, 2002; 2003).

Date	Semeru volcano activities	Source
2002		
3–10 March	An increase in volcanic and seismic activity at Semeru	VSI
8 March	An emission rise ~400 m above the volcano, and two pyroclastic flows travel S as far as 2.5 km down the Kembar River.	VSI
11–17 March	Volcanic and seismic activity remained high at Semeru; Observations on 12, 14, and 17 March revealed that a gray plume rose 300–400 m above the summit.	VSI
15–21 April	Volcanic activity remained higher than normal at Semeru . A small plume rose ~400 m above the summit and a "red reflection" was occasionally visible 25 m above the crater rim. Lava avalanches traveled 750 m to the E down Besuk Kembar River.	VSI
17–23 June	Seismic and volcanic activity were higher than normal at Semeru. Lava avalanches were observed traveling 750 m E to the Besuk Kembar River	VSI
1–7 July	Lava avalanches were sometimes observed traveling 750 m from Semeru's crater rim E toward Besuk Kembar River.	VSI
8–14 July	Lava avalanches were sometimes observed traveling 750 m from Semeru's crater rim E toward Besuk Kembar River. Low-level ash plumes rose above the crater	VSI
15–21 July	Lava avalanches were observed traveling ~750 m from Semeru's crater rim E toward Besuk Kembar River. Explosions produced ash plumes reaching 300–500 m above the crater	VSI
31 July–6 August	Activity at Semeru remained at a higher level than normal, but thick fog obscured the view.	VSI
5–18 August	Volcanic and seismic activity at Semeru remained at higher-than-normal levels. On 6 August a lava avalanche traveled ~750 m E toward Besuk Kembar River.	VSI
2–8 September	Seismicity was dominated by explosion earthquakes; on 8 September at 7:47 pm an ash explosion at Semeru was accompanied by ejected incandescent material. The material traveled 150 m E to the upper portion of the Kembar River.	VSI
22–23 September	Ash clouds were observed at Semeru rising to ~7.6 km a.s.l. on 22 September at 1453 and on 23 September at 1700. The September 23rd cloud drifted SW. Neither cloud was visible on satellite imagery due to meteorological clouds in the area.	Darwin VAAC
9–22 December	Volcanic and seismic activity remained above normal levels at Semeru. Ash columns rose 400–500 m above the volcano, and lava avalanches and pyroclastic flows were seismically recorded.	VSI
17–30 December	Volcanic and seismic activity were relatively high at Semeru. 49 lava avalanches, 6 pyroclastic flows, and 3 floods/lahars. Explosions sent ash plumes to 400 m above Jonggring Seloko crater.	VSI
25 December	A pyroclastic flow traveled 2.5 km into the Besuk Kembar River	VSI
29 December	Pyroclastic flow at Besuk Bang traveled ~9 km from the summit. At 5 pm–8:15 pm, a lahar traveled along the Besuk Kembar River relatively close to Supit village. Early that morning the residents of Supit were evacuated.	VSI
30 December	A pyroclastic flows traveled 2 km toward the Besuk Kembar River at 7:20 am, and at 10 am, one traveled 4 km toward Supit village.	VSI
2003		
1–12 January	Relatively high volcanic and seismic activity continued at Semeru; several explosions sent ash columns to 700 m above the crater. Lava avalanches sent material up to 750 m from the crater rim and a pyroclastic flow traveled 1.5 km E to the Besuk Kembar River.	VSI
13–26 January	Volcanic activity remained at relatively high levels at Semeru, with ash plumes rising 400–600 m above the summit. On 19 and 23–24 January incandescent lava avalanches traveled ~500 m down Besuk Kembar River.	VSI

Table 2 (*continued*)

Date	Semeru volcano activities	Source
3–9 February	Volcanic activity remained at high levels at Semeru, with ash plumes rising 300–400 m above the summit. On 7 February a pyroclastic flow traveled 2–4 km into the Besuk Bang River.	VSI
24 February–2 March	Volcanism at Semeru remained at high levels. "White-gray ash plumes" were observed rising 300–400 m above the summit.	VSI
3–9 March	Volcanism at Semeru remained at high levels. "White-gray ash plume[s]" rose to low levels above the summit and several "pyroclastic avalanches" traveled 200–2000 m into Besuk Kembar River.	VSI
10–16 March	"White-gray ash plumes" rose to low levels and several pyroclastic flows traveled 1.5–4 km down Bang River.	VSI
17–23 March	Seismic and volcanic activity continued at relatively high levels at Semeru, with "gray ash plumes" rising 300–400 m above the summit, and several pyroclastic flows traveling toward Bang River to runout distances of around 500 m.	VSI
24–30 March	Seismic and volcanic activity continued at relatively high levels at Semeru, with "gray ash plumes" rising to low levels, pyroclastic-flow activity, and several explosions.	VSI
27 March	A pyroclastic flow travelled around 3750 m toward Bang River.	VSI
31 March–6 April	Volcanic activity remained at relatively high levels at Semeru; "White-gray ash plumes" rose 400–600 m above the summit.	VSI
15 April	At 10:38 am, a pilot reported seeing ash ~2.5 km above Semeru. No ash was visible on satellite imagery.	Darwin VAAC
12–18 May	Volcanic and seismic activity at Semeru continued at relatively high levels. Several small ash explosions rose to low levels above the summit.	VSI
29 May	At 08:38 am, plumes emitted from Semeru were visible on satellite imagery at a height of ~6 km a.s.l. drifting NW.	Darwin VAAC
2 June	At 0625 am, plumes emitted from Semeru were visible on satellite imagery at a height of ~6 km a.s.l. drifting SSE.	Darwin VAAC
2–29 June	Activity continued at high levels at Semeru. Several explosions occurred with the highest ash plumes rising to a height of ~600 m.	VSI
21 July	At 11:16 pm, an ash cloud from Semeru was visible on satellite imagery extending ~75 km to the WSW	Darwin VAAC
31 July	Based on information from an aircraft report, the Darwin VAAC reported that an ash plume emitted from Semeru rose to ~4.5 km a.s.l. at 11:20 am. No ash was visible on satellite imagery.	Darwin VAAC
8–9 August	Thin ash plumes from Semeru were visible on satellite imagery on 8 and 9 August. On 9 August the plume extended ~40 km SW of the volcano.	Darwin VAAC
13 August	A faint ash plume from Semeru was visible on satellite imagery extending ~75 km E of the summit.	Darwin VAAC
11–17 August	Volcanic activity at Semeru continued at relatively high levels. Explosions produced ash columns that rose to 400 m above the summit.	VSI
9 September	An ash plume emitted from Semeru, rose to ~7.3 km a.s.l. and drifted S. Ash was not visible on satellite imagery.	Darwin VAAC
1–28 September	Volcanic activity at Semeru continued at relatively high levels. Several ash explosions produced plumes to 400–500 m above the volcano.	DVGHM (VSI)
October	Ash explosions at Semeru continued to produce low-level plumes and seismicity was dominated by hundreds of explosion earthquakes.	DVGHM (VSI)
2 December	At 5:28 pm, satellite imagery showed an ash plume from Semeru at ~4 km a.s.l. that extended ~55 km WSW.	Darwin VAAC

References

Borgia, A., 1994. Dynamic basis of volcanic spreading. Journal of Geophysical Research 99, 17791–17804.

Carn, S.A., 1999. Application of synthetic aperture radar (SAR) imagery to volcano mapping in the humid tropics: a case study in East Java. Indonesia Bulletin of Volcanology 61, 92–105.

Cecchi, E., van Wyk de Vries, B., Lavest, J.-M., 2004. Flank spreading and collapse of weak-cord volcanoes. Bulletin of Volcanology 67, 72–91.

Chorowicz, J., Deffontaines, B., Huaman-Rodrigo, D., Guillande, R., Le Guern, F., Thouret, J.C., 1992. SPOT Satellite monitoring of the eruption of Sabancaya volcano. Remote Sensing of Environment 42, 43–49.

Gillespie, A.R., Matsunaga, T., Rokugawa, S., Hook, S.J., 1998. Temperature and Emissivity Separation from Advanced Spaceborne Thermal Emission and Reflection Radiometer (ASTER) images. IEEE Transactions on Geoscience and Remote Sensing 36, 1113–1126.

GVN, 1980. Scientific Event Alert Network Bulletin. Semeru 5 (1).

GVN, 2002. Bulletin of the Global Volcanism Network. Semeru 27 (6), 7 2; (9), 7–8; (12).

GVN, 2003. Bulletin of the Global Volcanism Network. Semeru 28 (4), 11–13 (7), 5; (9), 7–8; (10), 12; (12), 7.

GVN, 2004. Bulletin of the Global Volcanism Network. Semeru 29 (6), 12–13.

Iguchi, M., Yakiwara, H., Tameguri, T., Hendrasto, M., Hirabayashi, J.-I., 2008. Mechanism of explosive eruption revealed by geophysical observations at the Sakurajima, Suwanosejima and Semeru volcanoes. Journal of Volcanology and Geothermal Research 178, 1–9.

Joyce, K.E., Samsonov, S., Manville, V., Jongens, R., Graettinger, A., Cronin, S.J., 2009. Remote sensing data types and techniques for lahar path detection: a case study at Mt Ruapehu. New Zealand Remote Sensing of Environment 113 (8), 1778–1786.

Lavigne, F., Thouret, J.-C., 2002. Erosion, sédimentation et lahars sur le volcan Semeru, Java-est, Indonésie. Geomorphology, from expert opinion to modelling. A tribute to Prof. J.-C. Flageollet, Strasbourg: Centre Européen Recherches Géomorphologiques, pp. 193–202.

Miller, V., Ammon, Ch., Voight, B., De Angelis, S., 2008. A moving block-and-ash flow of Merapi Volcano (Indonesia) and deposit facies as imaged by IKONOS on 16 June 2006. IAVCEI General Assembly, 18–22 August 2008, Reykjavik (Abstract).

Mouginis-Mark, P., Garbeil, H., 2005. Quality of TOPSAR topographic data for volcanology studies at Kilauea volcano, Hawaï: an assessment using airborne lidar data. Remote Sensing of Environment 96, 149–164.

Mulyadi, E. (1992). Le complexe de Bromo-Tengger, Est Java, Indonésie. Etude structurale et volcanologique. (Unpublished) PhD thesis, département de géologie, université Blaise Pascal, Clermont-Ferrand, pp 136.

Nishi, K., Hendrasto, M., Mulyana, I., Rosadi, U., Purbawinata, M.A., 2007. Micro-tilt changes preceding summit explosions at Semeru volcano, Indonesia. Earth Planets Space 59, 151–156.

Pieri, D., Abrams, M., 2004. ASTER watches the world's volcanoes: a new paradigm for volcanological observations from orbit. Journal of Volcanology and Geothermal Research 135, 13–28.

Simkin, T., Siebert, L., 1994. Volcanoes of the world, Smithsonian Institution, 2nd edition. Geoscience Press, Tucson, Arizona, p. 349.

Siswowidjoyo, S., Sudarsono, U., Wirakusumah, A.D., 1997. The threat of hazards in the Semeru volcano region in East Java. Indonesia Journal of Asian Earth Sciences 15, 185–194.

Situmorang, T., 1989. Lahar and pyroclastic flow hazards zoning of Semeru volcano, East Java, Indonesia (using aerial photograph). International Symposium on Erosion and Volcanic Debris Flow Technology. Yogyakarta, Indonesia, p. 12. July–August 1989.

Sjarifudin, M.Z., 1990. Berita Berkala Vulkanologi, Edisi Khusus No. 127 (in Indonesian). G. Bromo, Bandung, Indonesia.

Sutawidjaja, I.S., Wahyudin, D., Kusdinar, E., 1996. Geological Map of Semeru Volcano, East Java (1:50,000 Scale). Direktorat Vulkanologi, VSI, Bandung, Indonesia.

Thouret, J.-C., Lavigne, F., Suwa, H., Sukatja, B., Surono, 2007. Volcanic hazard at Mount Semeru, East Java (Indonesia), with emphasis on lahars. Bulletin of Volcanology 70, 221–244.

Thouret, J.-C., Gupta, A., Lube, G., Cronin, S.J., Surono, 2010. Analysis of the 2006 eruption deposits of Merapi Volcano, Java, Indonesia, using high-resolution IKONOS images and complementary ground based observations. Remote Sensing of Environment 114, 1949–1967. doi:10.1016/j.rse.2010.03.016.

Van Bemmelen, R.W., 1949. The Geology of Indonesia and Adjacent Archipelago. Government Printing Office, The Hague, pp. 1–150.

Van Padang, N.M., 1951. Semeru. Catalogue of the Active Volcanoes of the World Including Solfatara Fields. Part 1. Indonesia. International Association of Volcanology, Napoli, p. 271.

Wahyudin, D., 1991. Volcanology and petrology of Mt. Semeru volcanic complex, East Java, Indonesia. Diploma of Applied Science (Volcanology), Victoria University of Wellington, New Zealand, p. 126.

Zanoni, V.M., Goward, S.N., 2003. A new direction in Earth Observations from space: IKONOS. Remote Sensing of Environment 88 (1–2), 1–2.

3.3. Evolution of the Semeru summit cone after 2009

Structures and landforms of the Semeru composite cone, interpreted from IKONOS images acquired on 10 April 2008 and 20 August 2009, have been discussed in section 3.2. An updated geologic and geomorphological map of Semeru volcano and its ring plain was proposed by Kassouk et al. (2014) based on the object-oriented classification (OOC) of one HSR satellite panchromatic SPOT5 image (2003) and our TOPO-DEM. The OOC involves segmenting image into objects or groups of pixels, and then the objects were classified based on their attributes. On Semeru, the objects were classified on the basis of spectral (panchromatic hue and textures), topographic (slope, elevation) information and geologic/geomorphic processes. The result has been compared to the previous geologic maps of Semeru and its surroundings (Sutawidjaja et al., 1996; Thouret et al., 2007; Solikhin et al., 2012). The new geologic and geomorphologic map delineates 20 geologic and geomorphic units and 47 sub-units across seven volcanic and non-volcanic domains (Semeru and Mahameru summit cone, transitional slopes and volcano flanks, volcano piedmont, ring plain, drainage valleys, Tertiary hills and coastal areas). In this section, we provide a new interpretation and follow the evolution of the Semeru summit cone based on Kassouk et al. (2014) to which we have added the interpretation of three recent HSR (50 cm) images of WorldView-2 (8 June 2011), GeoEye (16 April 2012) and Pléiades (22 October 2012) satellites, as shown in Figure 3.1. We have also used ASTER multispectral images (2002-2014) and low-altitude or ground photographs (2010-2014) from various sources to support the interpretation.

3.3.1. Structures and landforms of Semeru's summit cone

In section 3.2 (Solikhin et al., 2012), the Semeru summit cone is divided into three zones based on interpretation of HSR images and DEM analysis. The Semeru summit cone is defined by Kassouk et al. (2014) as a domain that consists of two geologic and geomorphic units, based on remote sensing criteria, such as high altitude (> 2600 m), steep slopes (between 13% and 27%) mantled by tephra and devoid of vegetation (Fig. 3.1), high panchromatic hue, and contrast enhancement of the 2003 panchromatic image. This domain has been divided into two geologic and geomorphic units, namely Semeru and Mahameru summit cones and the steep summit flanks. The first unit, Semeru and Mahameru summit cones, consists of: (i) present-day Semeru crater

(Jonggring-Seloko) where the current vent is located, (ii) arcuate crater rims of Mahameru that probably formed during historical eruptive activity of Mahameru, (iii) the presumed boundary of Mahameru flank failure, (iv) a scar open to the southeast (SE scar) including its bottom and walls, and (v) eroded vents of Mahameru filled by collapse deposits and covered by tephra from Semeru (Fig. 3.1B). The second unit, Semeru summit flanks, is divided into five sectors (termed F1 to F5 in Fig. 3.1A). In the Semeru summit cone classification defined by Solikhin et al. (2012), F1-F2 and F3-F4 are part of the first and the second zones, respectively, and F5 corresponds to the third zone.

F1 is the Semeru west flank with Holocene to Late Pleistocene lava flows, now mantled by tephra cover except the recent, rugged and steep lava flows of Semeru to the southwest. F2 sector is the northwest summit incised flank where the uppermost slopes (between 2950 and 3650 m) are covered by thick (>10 m) recent tephra deposit. However, the distribution of tephra mantle deposits, which are incised by a dense, ribbon-like radial network of rills, shows that tephra dispersal does not occur often towards north and northwest. Contrasting F1 and F2 surface landforms show that the Semeru composite volcano has been built by two edifices, Mahameru ('old' Semeru) and Jonggring-Seloko ('young' Semeru). F3 sector corresponds to the northeast summit flank where 20-30 m thick tephra and 'old', weathered lava flows are cut by dense and deep gullies (> 50% of total area). Downhill slopes are incised by deep gullies that are partly vegetated. Gullies and two >100 m-deep ravine headwalls (Besuk Sat and Besuk Semut) are formed in hydrothermally altered deposits (reddish color) and may correspond to the location of the probable Mahameru failure scar(s). F4 sector extends on the east summit flank more dissected in hydrothermally altered deposits. This area consists of vegetation stripped ridges, locally covered by patchy ash cover, and narrow and steep catchment headwalls scoured by active landslides in weathered lava flows. F5 encompasses the steepest and most unstable south and southeast summit flanks filled by volcanic products of past (mostly effusive) and recent (mostly explosive) Semeru activity. This sector shows relatively thick (>5 m) tephra deposits from recent activity (to the southwest), slightly dissected recent lava flows covered by tephra (<5 m, to the south), and old lava flows covered by thin tephra deposits (<2 m, to the southeast). The most conspicuous feature is the SE scar (see section 3.2) that channels lava flows (2010-2014) and most of the PDCs towards the lowermost flanks. Based on a comparison of the 2009 image (Fig. 7B in section 3.2) with three most recent HSR images (Fig. 3.1), no

significant changes occurred on the Semeru summit cone after 2009 except in the Jonggring-Seloko crater and SE scar. Observed changes in the Jonggring-Seloko crater and SE scar are likely due to eruptive activity during the period from 2009 to 2014.

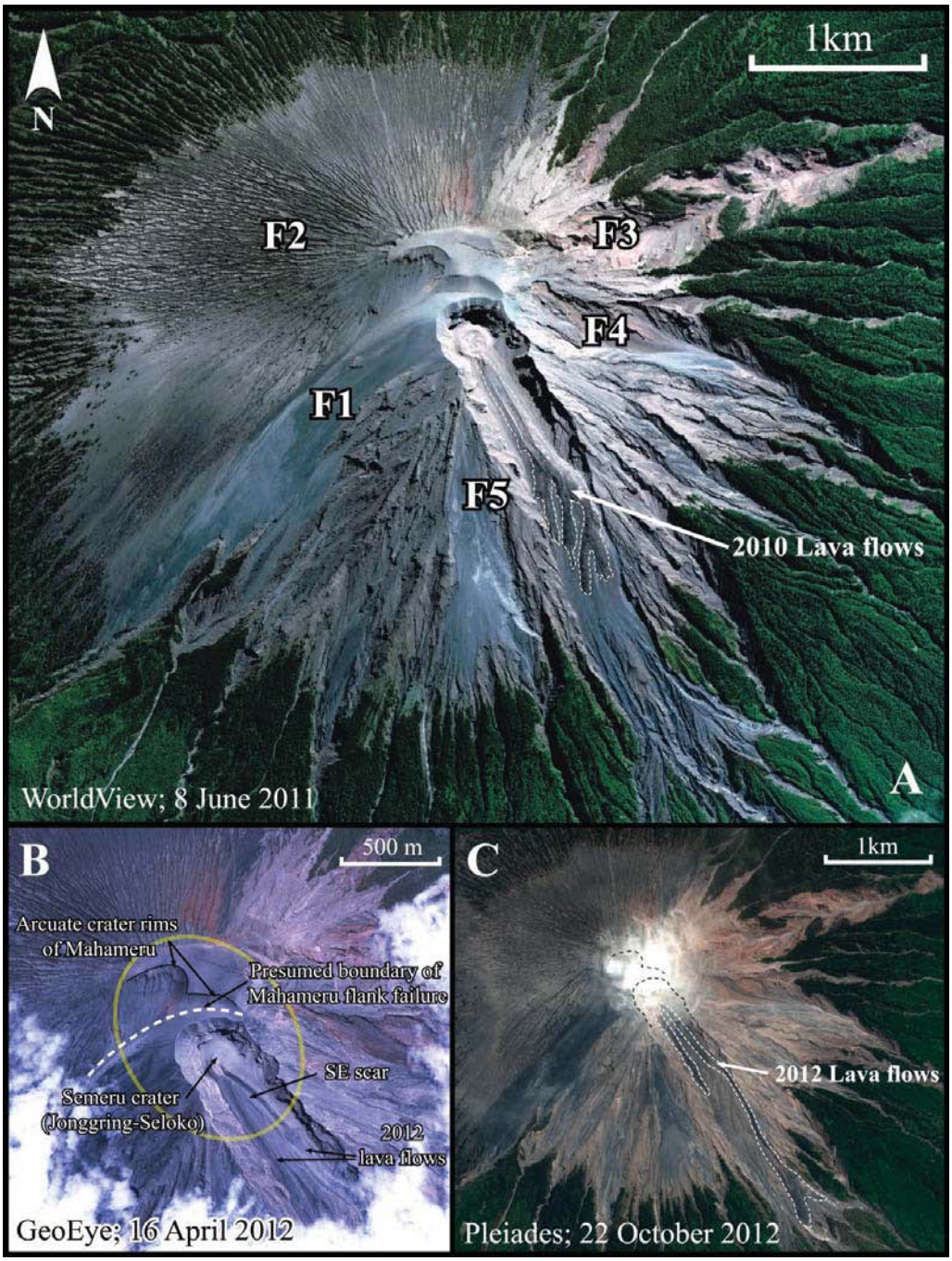

Figure 3.1. The Mahameru-Semeru summit area. **A.** 8 June 2011 WorldView image shows five flank sectors: the west flank with Holocene to Late Pleistocene lava flows of Mahameru (F1), the northwest summit incised flank (F2), the northeast summit flank (F3), the east summit flank with hydrothermally altered deposits (F4), and the south to southeast summit flank on steep lava flows deeply incised by gullies (F5). **B.** The 16 April 2012 GeoEye image shows the geomorphic units of Mahameru-Semeru summit cone (yellow circle). **C.** The 22 October 2012 image shows the2012 lava flows.

3.3.2. Evolution of the Jonggring Seloko crater and SE scar

We trace the evolution of the Jonggring-Seloko crater and SE scar by using the 15 meter resolution of ASTER multispectral imagery acquired between 2002 and 2014 (Fig. 3.2). The ASTER visual images are provided by the ASTER Volcano Archive (AVA) of U.S. Jet Propulsion Laboratory (JPL) and freely available at http://ava.jpl.nasa.gov. ASTER visual image is a false-color composite image generated from three ASTER Visible and Near Infra-Red bands (VNIR), where band 1 (520-600 nm), band 2 (630-690 nm), and band 3N (780-860 nm) are set in the red, green and blue channels, respectively. Figure 3.2 shows 12 ASTER visual images with less than 30% cloud cover on Semeru's summit cone in 2002 to 2014, one image each year except for 2007.

The 2002-2009 period

The first image in Figure 3.2 was acquired on 26 October 2002 or two months before the main eruptive activity in December 2002–January 2003. The Jonggring-Seloko crater was partly filled by lava dome and accumulation of unconsolidated PDC deposits. PDC deposits produced from the previous June-September 2002 eruptive activity filled the SE scar, but most of deposits were accumulated within a distance of no more than 750 meters from the headwall of the scar. Almost all pyroclastic deposits in the crater and scar were subsequently swept away and/or slid down during the December 2002 to January 2003 eruptions. This is reflected by a greater depth for the crater (50-100 m) and scar (10-30 m) as observed in the 23 June 2003 image (Fig. 3.2). In January 2004, PDCs flowed down through the SE scar and Bang River reaching distances of 2.5 km from the crater. This dome collapse and PDC episode was followed by low to moderate daily short-lived Vulcanian columns until September 2004. The 28 August 2004 image clearly shows one vent 60-80 m in diameter in the middle of the scar headwall, while the SE scar has been partly re-filled by PDC deposits. PDCs became more frequent in November and December 2004 with flow distances in the range of 1 to 3 km towards Bang River. Subsequently, no sizeable eruption occurred at Semeru until November 2005. No significant change can be detected in the 3 November 2005 image compared to the 28 August 2004 image, except the vent that is no longer visible in the later image. PDC-forming eruptions then occurred on 22 December 2005 when PDCs travelled down toward Bang River as far as 2.5 km from the crater. A steady inflation was detected from

tilt measurement during a period of nearly two weeks preceded the occurrence of these PDCs (Nishi et al., 2007).

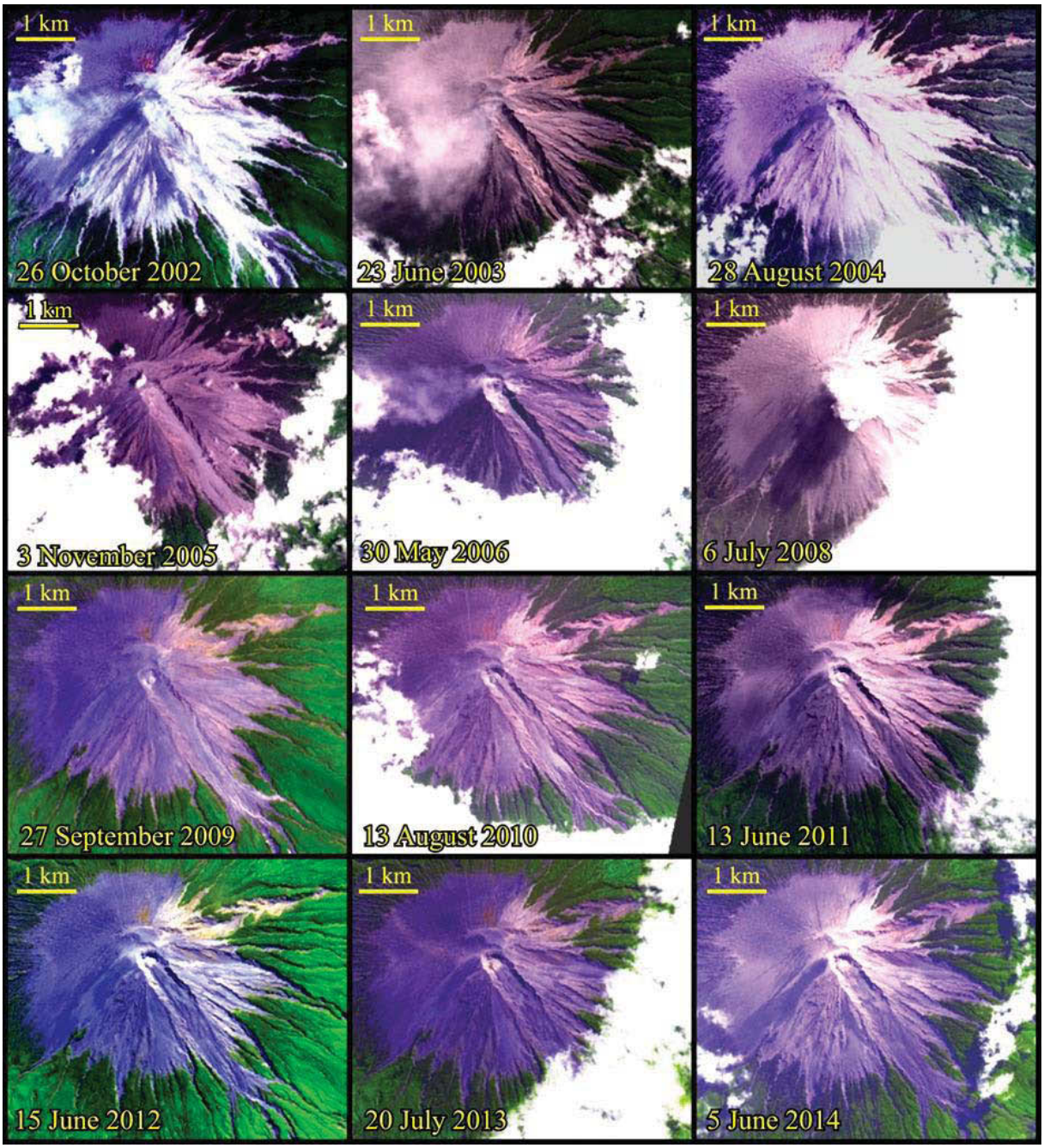

Figure 3.2. ASTER visual images of the Semeru summit cone between 2002 and 2014 provided by the ASTER Volcano Archive of U.S. Jet Propulsion Laboratory (http://ava.jpl.nasa.gov). Image acquisition date is indicated on each image.

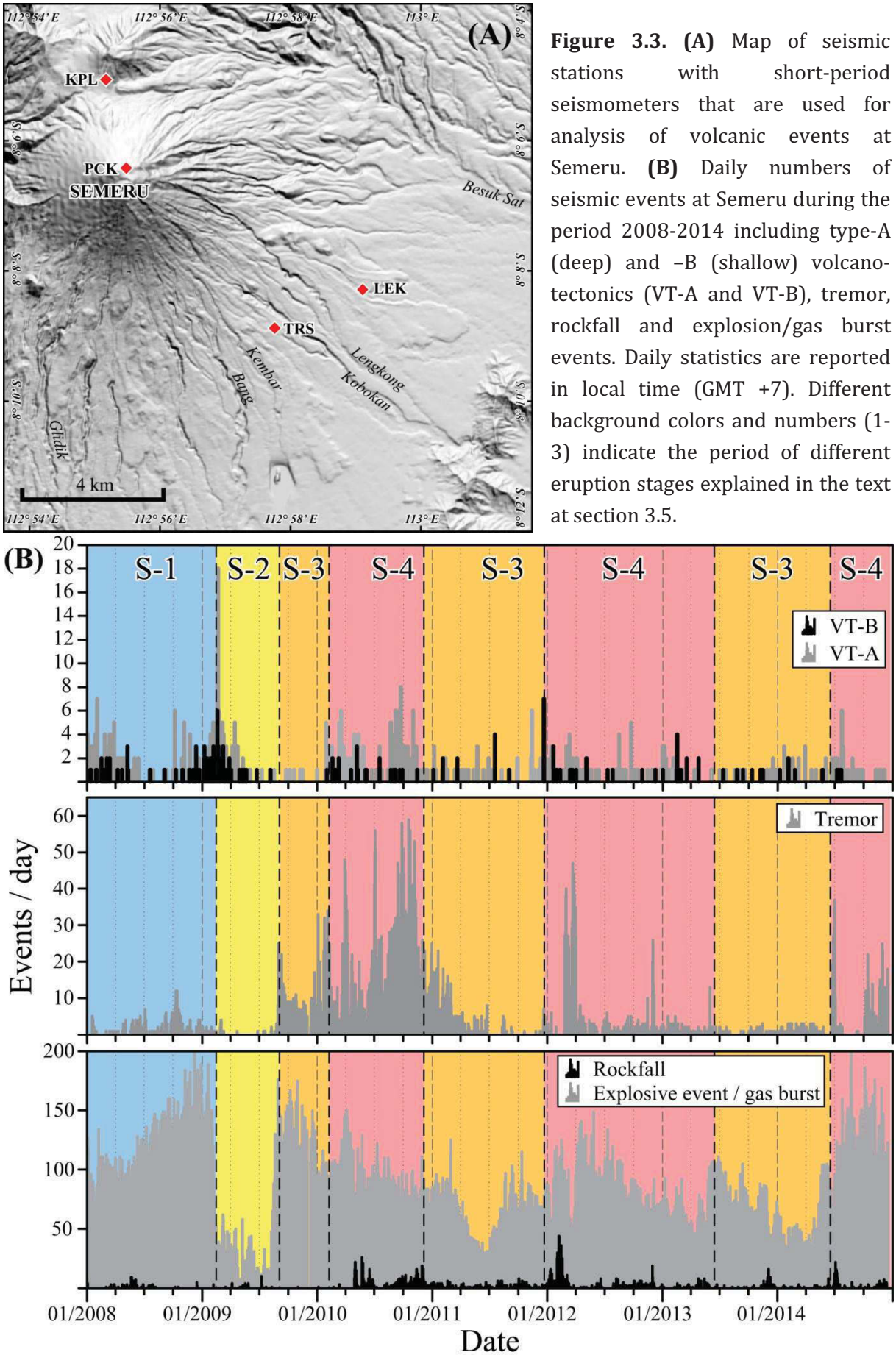

Figure 3.3. (A) Map of seismic stations with short-period seismometers that are used for analysis of volcanic events at Semeru. **(B)** Daily numbers of seismic events at Semeru during the period 2008-2014 including type-A (deep) and –B (shallow) volcano-tectonics (VT-A and VT-B), tremor, rockfall and explosion/gas burst events. Daily statistics are reported in local time (GMT +7). Different background colors and numbers (1-3) indicate the period of different eruption stages explained in the text at section 3.5.

Semeru eruptive activity between 2006 and early 2009 has been more explosive (Vulcanian) with significant variation in magnitude and sometime accompanied by dome-coulée collapse PDCs (deposits are commonly 2.5 km long, 100-200 m wide and a few tens of meters thick). Unfortunately, there is no clear ASTER image of the Semeru summit cone in 2007 to 2008 due to cloud cover. A prominent collapse event occurred on 15-22 May 2008 and produced a series of PDCs that travelled down the SE scar as far as 3 km. Effusive and collapse activity, with short repose times interspersed with repeated Vulcanian ash columns, stopped suddenly in March 2009, while only small magnitude ash puffs occurred sporadically for the following five months (Nishimura et al., 2012). More vigorous eruptive activity resumed in August 2009 as characterized by an increasing number of volcanic earthquakes recorded from four seismic stations (Fig. 3.3A). Figure 3.3B shows daily numbers of seismic events at Semeru during the period 2008-2014 and the period of four eruptive stages (S-1 to S-4) inferred from seismic events and CVGHM reports (e.g., Triastuty et al., 2012). The seismic events at Semeru including type-A or deep (1-20 km beneath the volcanic crater) volcano-tectonic (VT-A), type-B or shallow (<1 km) volcano-tectonic (VT-B), tremor, rockfall, and explosion together with gas burst (*hembusan* in Indonesian). Volcano-tectonic (VT-A and VT-B) events are related to brittle failure in volcanic rocks triggered by fluid movement while tremor event have been interpreted as due to the resonance of a fluid-filled resonator excited by a pressure disturbance (Kumagai, 2009).

Changes in the characteristics of Semeru activity in between 2009 and 2011 have been observed by Triastuty et al. (2012) on the basis of spectral analysis of harmonic tremor events. We have defined four eruptive stages of Semeru the period 2008-2014 and discuss it in sub-section 3.5.1. Five months of low activity in 2009 (March-August) are referred to as the transition stage (stage 2 in Fig. 3.3B) from 'normal' activity characterized by frequent Vulcanian to Strombolian eruptions (stage 1) to more effusive activity or open system (stage 1). During the transition stage, seismic cata suggest that magma migrated from a deep reservoir to a shallow magma chamber. The transition stage is followed by the third stage of magma intrusion and onset of the dome growth, accompanied by intensive gas burst events in the period between August 2009 and January 2010. The clear image on 27 September 2009 (Fig. 3.2) shows that the SE scar was half filled by PDC deposits and a lava dome with a diameter of 120 meters observed in the Jonggring-Seloko crater. Starting in late February 2010, Semeru activity was

characterized by lava extrusion and flows (whose front collapses generated PDCs). These events were also accompanied by gas burst events (stage 4). The gas that generated gas burst event is not the result of interactions between magma and groundwater, but is probably derived from the separation of water vapor from magma in the conduit (Nishimura et al., 2012).

The 2010-2014 period

Prominent lava flows towards the SE scar occurred in February 2010 and February 2012 (Figs. 3.4 & 3.5). On 25 February 2010, lava started to flow towards the SE scar and was accompanied by rock avalanches. Small PDCs were also generated by repeated collapses of the high and steep termini of the lava flow. Based on HSR images, the 2010 lava flows reached 1.5 km, covering an area of 0.24 km^2 with a volume of 1.8 ± 0.6 million m^3 (assuming the thickness of lava to reach 5 to 10 meters). A lava dome with a diameter of about 120 m is also observed in the 13 August 2010 ASTER visual image (Fig. 3.2). The lava dome and flows partially collapsed on 4 November 2010 and generated PDCs that travelled down as far as 4 km towards Bang River (Fig. 3.4). The 4 November event has brought down approximately 40% of the 2010 lava, or about 0.7 million m^3, as the remnant of the 2010 lava is visible in the 12 November 2010 photograph (Fig. 3.4). The lava dome in the Jonggring-Seloko crater kept growing thereafter. The lava dome grew to 200 m diameter and 10-15 m in height, as observed in ASTER visual image (Fig. 3.2) and photographs (Fig. 3.6) in June and August 2011, respectively.

A new lava dome started to extrude in late 2011 directly over the dome formed since 2010. In February 2012, the dome was being drained by two lava flows, both flowing the SE scar alongside the 2010 lava (Fig. 3.5). The first lava flow travelled down on the western edge of the scar as far as 1 km from the summit vent, while the second one on the eastern edge extended farther down to 2.7 km. The February-October 2012 lava flows covered an area of 0.38 km^2 and we obtained an estimated volume of 2.8 ± 0.9 million m^3 by assuming the thickness of lava to be between 5 and 10 meters. This volume may have changed due to the additional subsequent lava flows or reduction due to collapse of the flow front. Lava dome in the crater continues to grow so that in October 2012 the volume reached 1.3 ± 0.3 million m^3 (Table 3.1). Since October 2012,

Semeru activity has included gas bursts or small explosions and interspersed small rock avalanches and PDCs. However, in the Jonggring-Seloko crater, the lava dome has kept growing such that volume estimate had reached 2.3 million m^3 by the end of May 2014. The weathered northeastern part of lava dome is characterized by reddish rocks (oxidized scoria) that appear on the May 2014 photograph (Fig. 3.6). Semeru activity increased at the end of June 2014 and then a new lava flow began draining the dome and again flowed down the eastern edge of the SE scar in July 2014 (Fig. 3.7). The lava flows travelled 2.7 km towards Kobokan River and 2.4 km towards Bang River. These flows have an area of 0.25 km^2 and an estimated volume of c. 1.9 million m^3. Since July 2014, the daily number of gas bursts increased and since September Strombolian activity was frequently observed in the Jonggring-Seloko crater. Estimated volumes of lava flows and lava domes since 2010 are summarized in Table 3.1.

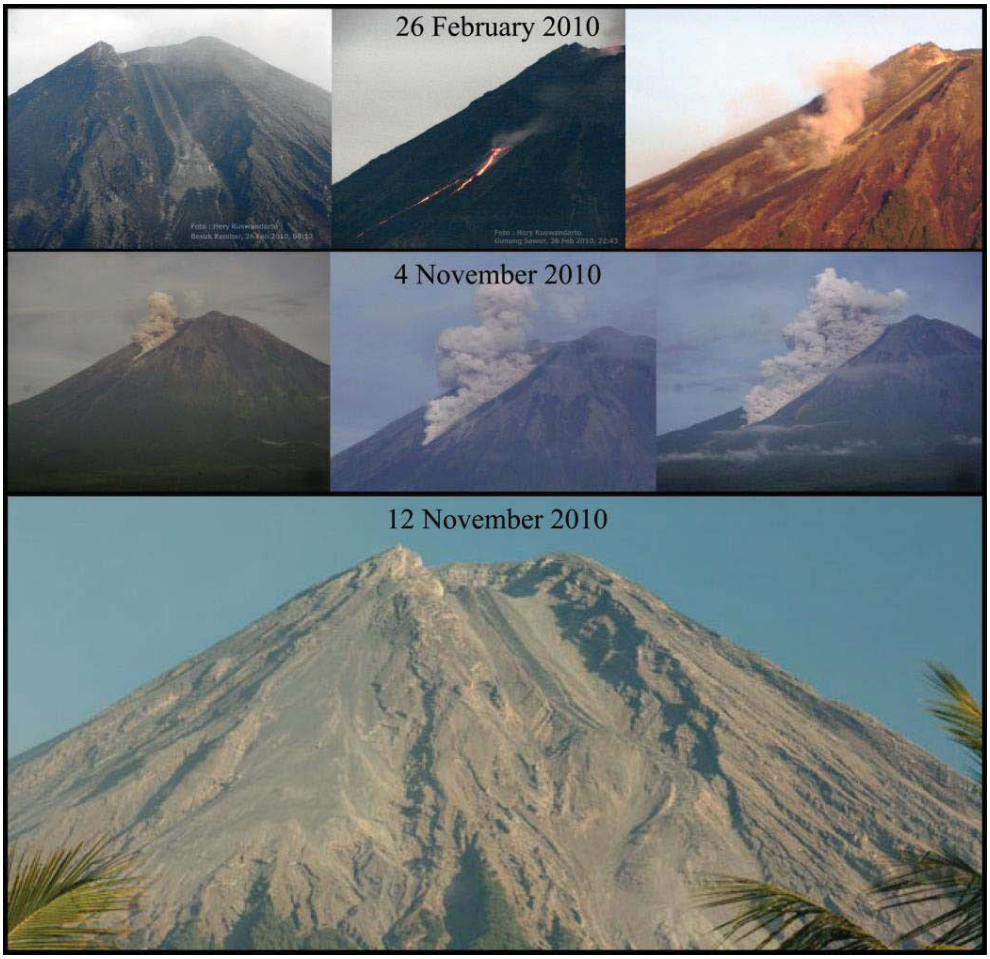

Figure 3.4. Photograph of volcanic activity of Semeru in 2010 showing the initial lava flows on 26 February 2010, and PDCs generated from lava front collapses on 4 November 2010, which left 60% only of the lava deposit in the scar (shown in 12 November 2010 photograph). Photographs: courtesy of CVGHM (Hery Kuswandarto).

Figure 3.5. Photograph of the Semeru summit cone on 7 and 9 February 2012 showing the two lava flows from Jonggring-Seloko vent travelling down the SE scar. Photographs: courtesy of ANTARA (Indonesian news agency).

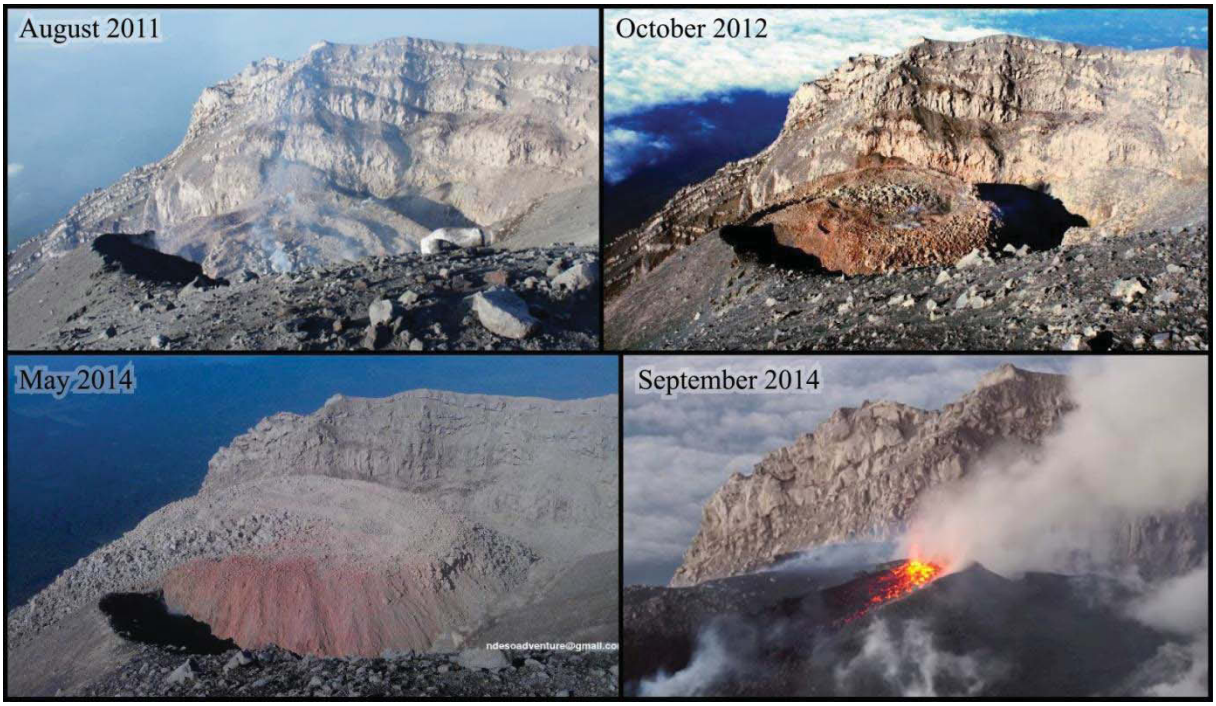

Figure 3.6. Photograph of Jonggring-Seloko crater in August 2011, October 2012, May and September 2014, showing the growth of a lava dome. Photographs: courtesy of Aris Yanto, Ndeso Adventure (www.exploredesa.com).

Table 3.1. Geometry and volume of lava flows in the SE scar and lava domes in the Jonggring-Seloko crater since 2010, estimated from satellite images and photographs.

Lava flows			
Period	Area (km^2)	Thickness (m)*	Volume (m^3)**
February-November 2010	0.24	5 - 10	$1.8 \pm 0.6 \times 10^6$
February-October 2012	0.38	5 - 10	$2.8 \pm 0.9 \times 10^6$
July-October 2014	0.25	5 - 10	$1.9 \pm 0.6 \times 10^6$

Lava domes				
Time	Diameter (m)	Area (km^2)	Thickness (m)	Volume (m^3)
August 2011	180	0.025	~ 10	$0.3 \pm 0.05 \times 10^6$
October 2012	220	0.038	~ 35	$1.3 \pm 0.3 \times 10^6$
May 2014	240	0.045	~ 50	$2.3 \pm 0.5 \times 10^6$
September 2014	240	0.045	~ 55	$2.5 \pm 0.5 \times 10^6$

* *Thickness of the lava flows and height of domes are estimates based on interpretation of satellite images and photographs.*

** *Volume of lava flow in the SE scar may change due to additional, subsequent lava flows or reduction due to partial collapse.*

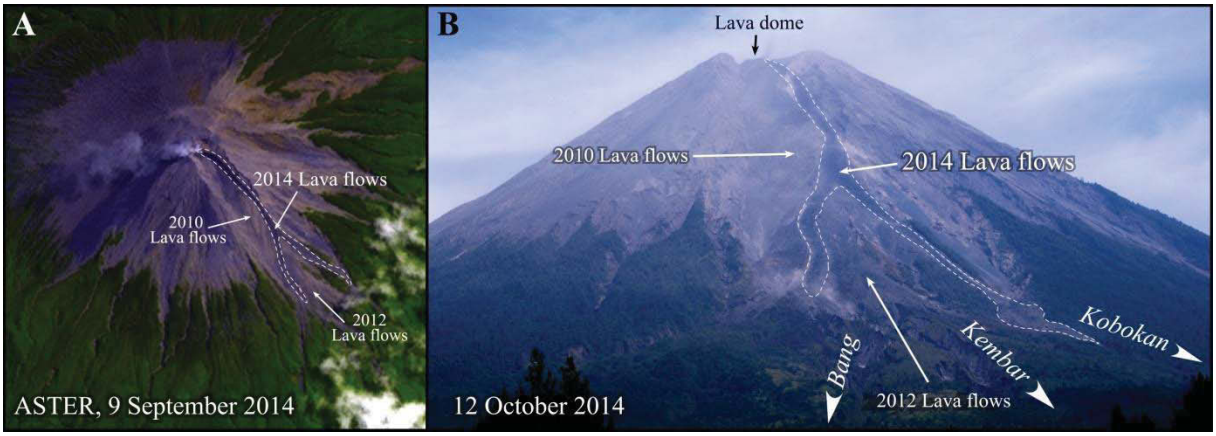

Figure 3.7. A. The 9 September 2014 ASTER visual image. **B.** The 12 October 2014 photograph of the Semeru summit cone showing the new lava flows since July 2014. Photograph: courtesy of CVGHM (Mukdas and Parno).

3.4. Geometric characteristics of Kobokan and Lengkong catchments

Semeru is one of the few persistently active composite volcanoes worldwide with a nearly continuous production of tephra fall and PDC deposits. Its persistent and rapidly alternating eruptive activity supplies steady but relatively small amounts of sediment to

rivers, but their cumulative effects may be greater than that of sediment produced by episodic large- or medium-sized eruptions. Recently, as described in the section 3.3, the 2014 lava flows have filled the Kobokan head valley over a distance of 2.7 km from the Jonggring-Seloko crater (Fig. 3.7). As a result, the valley channel will become an area of aggradation due to PDC deposits or lava debris produced by lava front collapses, which will be remobilized by rain-triggered lahars during the next rainy seasons. In addition, Semeru is located in a low-latitude equatorial climate with a long rainy season, thus posing significant hazards and making it an excellent site for studying sediment storage and transfer.

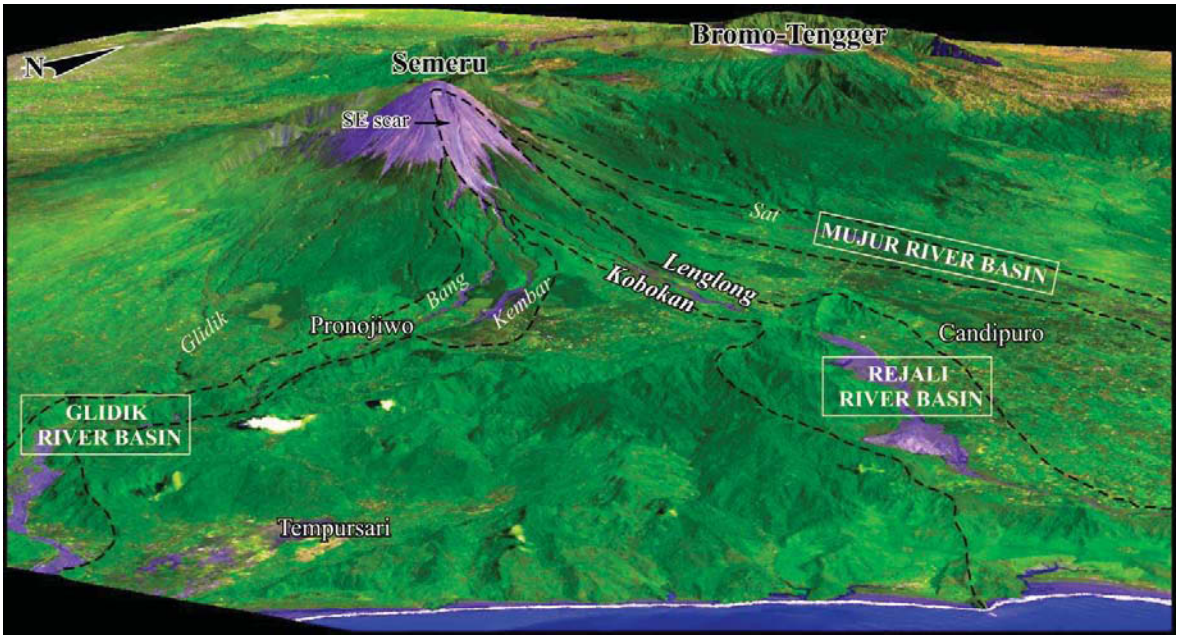

Figure 3.8. The 27 September 2009 ASTER visual image draped on a DEM showing the Semeru volcano-Tengger massif looking northwest, three major watersheds across the south (Glidik and Rejali river basins) and east (Mujur river basin) flanks of the volcano.

Semeru flanks are drained by three major watersheds, two to the south: Glidik and Rejali River valleys, and one to the east: Mujur River Valley (Fig. 3.8). The east drainage system conveys voluminous lahars induced by landslides during the 20th Century (1909, 1981) and many debris flows triggered by rainfall. The south and southeast valleys, fed by the Jonggring-Seloko vent and SE scar, carry lahars almost on a weekly basis during rainy seasons as far as 35 km to the sea across the ring plain. The Kobokan valley and its tributary, the Lengkong River, belong to the Rejali catchment (108.9 km^2 in area; Fig. 3.8 & 3.9). Kobokan and Lengkong Rivers, where fresh PDC deposits are located, transport very large volumes of sediment with an average annual sediment yield of 2.7 x 10^5 m^3

km^{-2} (Lavigne & Suwa, 2004). In the recent past, the Kobokan valley and to a lesser extent, the Lengkong valley have been partly filled by volumes of c. 6.3 and 5.5 million m^3 of BAF deposits emplaced during the 1994 and 1995 eruptions (Thouret et al., 2007). We have described and measured the geometric characteristics of both Kobokan and Lengkong catchments based on the analysis of Topo-DEM (Fig. 3.9), interpretation of HSR SPOT5 satellite images and field-based geologic mapping. This information has been used to trace the processes of aggradation (PDC deposits and tephra) and degradation (erosion due to lahars and streamflows) on Semeru volcano (e.g. Thouret et al., 2014). Besides studies on aggradation/degradation processes following large eruptions (Mount St. Helens and Pinatubo, e.g. Pierson & Major, 2014), the Semeru case study documents one of rare examples of aggradation/degradation processes acting on a persistently active volcano.

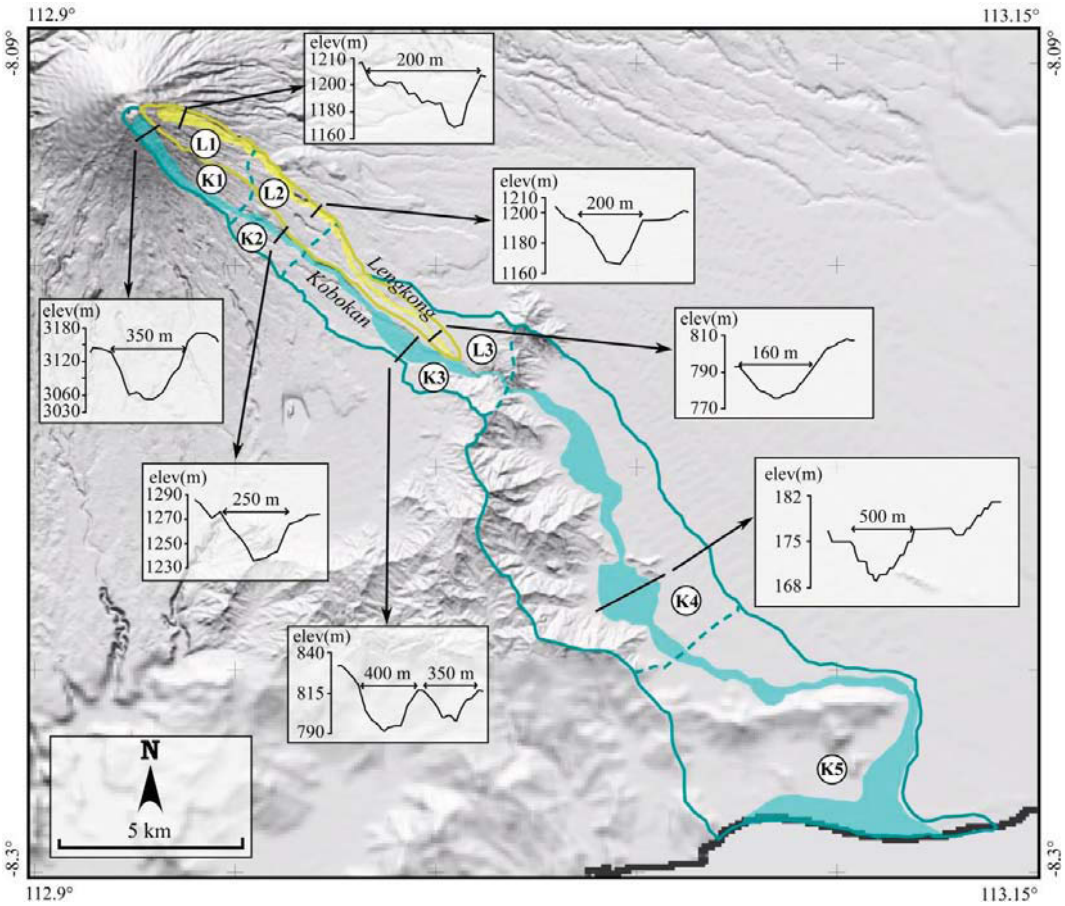

Figure 3.9. Catchment of the Kobokan River and sub-catchment of the Lengkong River on the Semeru Topo-DEM (Solikhin et al., 2012) including valley cross sections at specific locations. The Kobokan and the Lengkong catchments can be divided into five and three reaches, respectively: proximal source (K1 and L1), two middle reaches (K2-K3 and L2-L3), and two depositional reaches (K4-K5).

Table 3.2. Geometric characteristics of the catchments and reaches of the Kobokan and the Lengkong Rivers. Breakdown in five reaches for the Kobokan and three reaches for the Lengkong (Thouret et al., 2014).

Basin	Surface area (km^2)	Length (km)	Slope (°)	Gradient	Perimeter (km)
Kobokan (K)	108.9	37.03	5.42	Source 3472 m	72.91
Lengkong (L)	8.23	12.61	10.2	Source 3142 m	24.09

Reach	Surface area (km^2) | (%)		Length (km) | (%)		Slope (°)		Gradient		Perimeter (km)	
	K	L	K	L	K	L	K	L	K	L
Source 1 Proximal	6.67 | 6.13	2.46 | 29.44	4.94 | 13.33	3.51 | 9.51	24.20	26.13	0.449	0.491	11.08	7.31
Medial 2 Storage and byp	5.68 | 5.21	2.88 | 34.96	2.22 | 6.00	4.43 | 11.98	9.33	7.73	0.164	0.136	10.43	8.63
Medial 2 Storage and byp	13.3 | 12.21	2.89 | 35.10	8.04 | 21.71	4.67 | 19.43	3.87	3.93	0.068	0.069	19.01	12.29
Deposition and bypassing 4	44.1 | 40.51	-	10.5 | 28.25	-	1.98	-	0.035	-	27.50	-
Deposition 5 Distal delta	39.1 | 35.93	-	11.4 | 30.71	-	0.77	-	0.013	-	28.45	-

K Kobokan, *L* Lengkong, *byp* bypassing

Tables 3.2 and 3.3 display the characteristics of the Kobokan and the Lengkong catchments based on analysis of DEM (Fig. 3.9 and Thouret et al., 2014). The Kobokan catchment (109 km^2) is 13 times larger and three times longer than its steep Lengkong tributary (8.2 km^2). Based on geomorphic and hydrological parameters (Figs. 3.8-3.10; Tables 3.2 & 3.3) the catchment of Kobokan can be divided into five reaches: the steep source reach, K1; two middle reaches, K2 and K3, with the gradient decreasing below the southeast flank break-in-slope; and two gently sloping depositional reaches, K4 and K5, including the low delta on the coast. The Lengkong sub-catchment is 12.61-km long between its source at 3150 m msl. and its confluence with the Kobokan at c. 700 m msl. The Lengkong can be divided in three reaches: a narrow gully scouring the steep volcano's summit slope, the source of the debris source reach L1; a wider bypassing reach L2 across the relatively steep lower SE flank and below the break-in-slope at c.

1000 m msl.; and a narrow, lower bypassing reach L3 on the moderately sloping volcaniclastic apron above the confluence. A large fan with changing geometry since 1981 has formed at the confluence of the two rivers. The "bypassing" term is used after Manville et al. (2009) to describe the middle reaches, where sediment is stored temporarily between the upper erosional and lower depositional reaches before being transferred towards the confluence or the sea.

Table 3.3. Morphometric indices of the Koboan and the Lengkong catchments. These indices were used to compute the hypsometric curves and break down the valley reaches (Thouret et al., 2014).

Morphometric parameter	Kobokan	Lengkong
Area (A)	108.9 km^2	8.23 km^2
Height of basin (H)	3635 m	3610 m – 725 m = 2885 m
Height of river (h)	3472 m	3142 m – 725 m = 2417 m
Basin length (L)	33,653.6 m	11,421.4 m
Perimeter (P)	72.91 km	24.09 km
Relief ratio ($Rh=H/L_n$)	0.108	0.253
Relative relief ($Rhp=H/p$)	0.05	0.12
Relative basin height ($v=h/H$)	0.955	0.838
Relative basin area ($x=a/A$)	1/3 of east and southeast catchments	0.076
Length area ($L=1.4\ A^{0.6}$)	23.35 km	4.96 km
Basin shape ($Rf=A/Lb^2$)	0.1	0.06
Basin area ratio ($Ra=A_n/A_{n-1}$)	13.23	
ΣL sum of channel lengths	~290 km	37.02 km
Drainage density ($D=\Sigma L/A$)	2.66	4.49
Number of drains (N)	~120	18
Stream frequency ($Fs=N/A$)	1.10	2.18
Average stream length $avL=avL_1R_{L\ 0\text{-}1}$	37,032.42 m	12,612.43 m
Length ratio ($R_L=avL_n/L_{n+1}$)		0.341

Breaks in the Kobokan slope appear first at 2000-2100 m between the bare steep summit and the forested flanks, then at ~1200 m between the volcano flanks and the volcaniclastic aprons, and finally at ~600 m between the aprons, hills, and low-relief plain surrounding the volcano. Predominant geomorphic processes are the best method

for identifying different reaches. Proximal reach 1 coincides with daily debris supply and removal on the highly dissected, bare uppermost slopes >24°. In the middle reach 2, lahars pass through a dense network of steep gullies on >7° of slope. In the middle reach 3, sediment waves are stored and/or bypass through less entrenched channels across slopes ~3°. The distal reaches 4 and 5 are fan-like depositional areas created by wide, braided river floodplains. Usually, reaches upstream of reach 2 are dry outside the rainy seasons, whereas springs related to aquifers feed perennial streams below 1200-1000 m msl. between reaches 2 and 3.

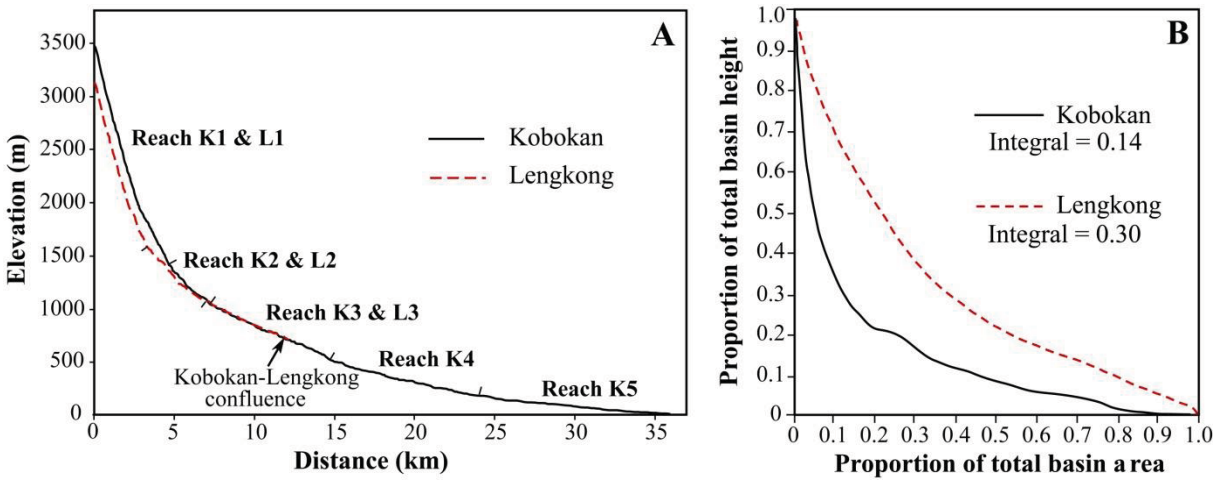

Figure 3.10. A. Breakdown of the longitudinal profiles of the Kobokan (K) and the Lengkong (L) rivers per reach, whose areas and slopes are displayed in Table 3.2. **B.** Hypsometric curves and hypsometric integral HI for the more "mature" Kobokan's catchment (0.14) and the steeper Lengkong's sub-catchment (0.3).

Hypsometric curves (Fig. 3.10B) suggest that the Kobokan's catchment (hypsometric index, HI, 0.14) is more "mature" or closer to equilibrium than the Lengkong's sub-catchment (HI 0.3) (Thouret et al., 2014). The Kobokan's hypsometric curve, however, exhibits two convex segments (Fig. 3.10B): the upper one is the gorge between reaches K3 and K4, suggesting the effect of recent uplift and faulting of the Tertiary hills (Figs. 3 & 6 in section 3.2.); the second one reflects the large and thick depositional area upstream of the delta. The knickpoint k is now located between the confluence and the wide Kobokan check dam. The steep and straight Lengkong channel responds faster to both large and modest sediment supply events than the long, meandering Kobokan. However, the Lengkong response can be complex and lahars can overlap in the middle reaches owing to the interference between the two tributaries at their headwall valleys as shown in Figure 3.8.

Aggradation and degradation processes at Semeru volcano, particularly in the Kobokan and the Lengkong catchments, have been discussed in detail by Thouret et al. (2014). Their computation of the linear aggradation and degradation rates and sediment yields takes into account the geometric characteristics of each reach as summarized in Table 3.2. The geomorphic response of the Kobokan and the Lengkong rivers to volcanic sediment migration indicates that each river experiences alternating aggradation and degradation cycles following PDC-producing eruptions. The degradation rate in the Kobokan (area 109 km^2) is three to eight times that measured in the Lengkong (area 8.2 km^2), suggesting that size of catchments affects how they integrate rainfall and runoff. Spatial patterns of aggradation and degradation are governed by geomorphic characteristics in all reaches. Degradation is stronger in middle reaches K2 and L2, and K3 and L3. Aggradation predominates in the Kobokan reaches K1, K3, and K5. In between these two reaches, deposition occurs at a low rate in the Kobokan reach K4 which has been artificially modified. Aggradation apparently continues at a high rate in the Lengkong reach L1.

3.5. Discussion

3.5.1. The 2009-2014 eruptive activity of Semeru

Semeru eruptive activity during the period 2010-2014, which produced several lava flows from the central vent, shows a different style of eruption for the first time least since 1967 or possibly since 1941, when the near-continuous eruption period began. A lava tongue (a few hundred meters long) derived from the central vent has been observed several times in the SE scar, e.g. in 1994 and 1997 (Fig. 10 in Section 3.2). However, the 1994 and 1997 lavas were stubby flows that can be interpreted as dome-coulées or lava flow-domes, a hybrid form between lava flow and lava dome (Blake, 1999; see examples at Santiaguito volcano). Historical flank lava flows have been erupted on the lower southeast and east flanks in 1895 and in 1941-1942 (Fig. 3.11; Thouret et al., 2007). The 1941 Semeru eruption occurred after 28 years of repose, following the previous explosive eruption in 1913. The 1941 lava flow issued from a NW-SE fissure 1.3 km in length, which opened at the southeastern foot of the Semeru cone after an initial explosion on 21 September (Van Bemmelen, 1949). The lava flow came to a complete standstill in February 1942 with a length of 6.9 km, covering an area

of 3 km^2, and its volume amounted to 3 million m^3 (Van Bemmelen, 1949). The lava was andesite in composition with 57.6-57.7 wt. % SiO_2 and 1.3 wt. % K_2O (Wahyudin, 1991). The 2010-2014 lava flows are narrow and shorter compared to the 1941 and 1895 lava flows. At the time of this writing (January 2015), lava flows have occupied the head of Kobokan River valley down to 2.7 km from the summit and the head of Kembar valley and Bang river down to 2.4 km from the summit. Unfortunately, the access to the current lava flows has prevented anyone from sampling the lava to be analyzed and compared with previous lava flows in order to understand whether or not the 2014 lava may be more mafic and less vesicular andesite.

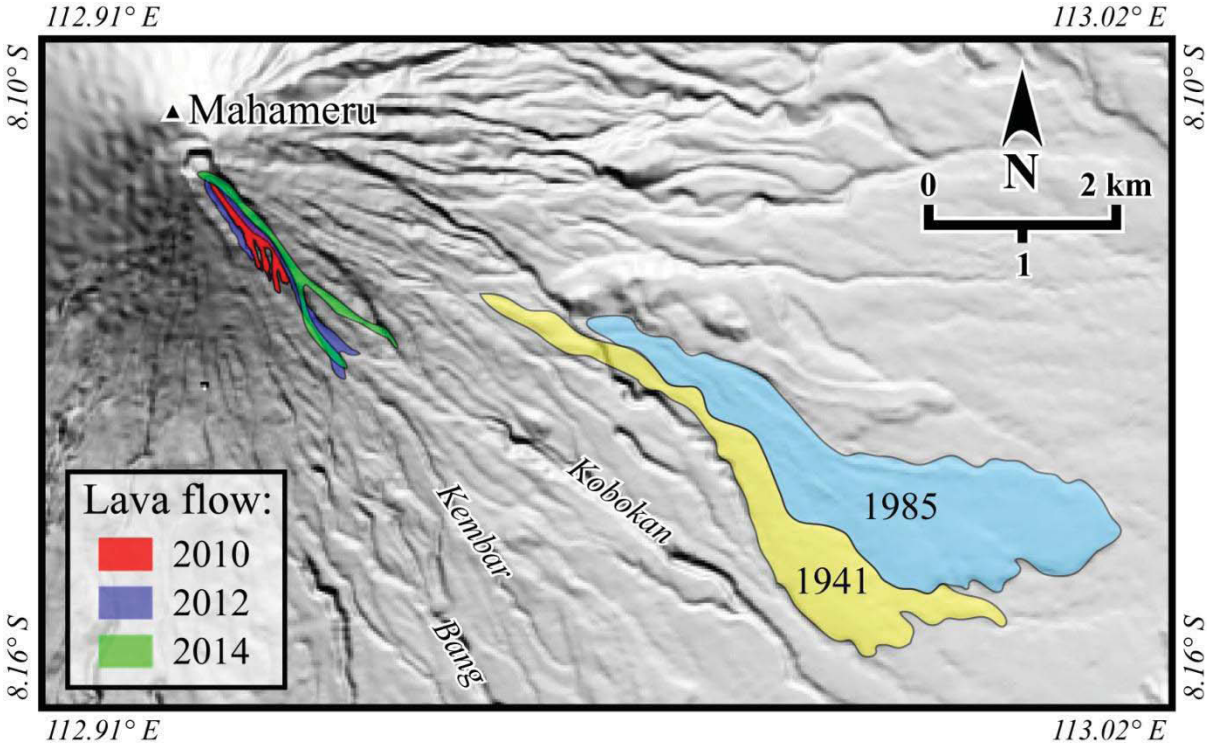

Figure 3.11. Map of Semeru lava flows erupted in 1941, 1985 and 2010-2014.

We have defined four stages of eruptive activity at Semeru during the period from 2008 to 2014 based on spectral analysis of the 2009-2011 harmonic tremor events (Triastuty et al., 2012) and is associated with statistical seismic data (Figs. 3.3 & 3.12) as follows:

1) The first stage (S-1) of eruptive activity before March 2009 is defined by a persistent Vulcanian and phreatomagmatic regime with short-lived eruption columns several times a day. During the explosions, the volcanic plug at the top of conduit is disrupted by expansion of bubbles and gas pockets, resulting in an air shock and

ejection of volcanic bombs and ash. During this stage, the dominant frequency of volcanic tremor tends to decrease, indicating less supply from the depth.

2) The second stage (S-2) is the transition period initiated by a high number of VT events that indicates new supply of magma to the reservoir. Siswowidjojo et al. (1995) suggested two magma reservoirs as indicated by a-seismic zones, depths of 5 km and 20 km. During this stage, the dominant frequency of volcanic tremor was stable suggesting an open volcanic system. The number of explosive events had decreased but the magnitude for single events had increased. The transition period lasted for 6 months from March to August 2009.
3) Eruptive activity during the third stage (S-3) comprises lava dome extrusion accompanied by gas bursts, Strombolian and sometimes small Vulcanian eruptions. This stage is characterized by a wide-range frequency of volcanic tremor but less VT-A events indicating a relatively low rate of magma intrusion. Since September 2009 (first S-3), Semeru was in the state of an open volcanic system, which we define as astate which the magma within the system is free to ascend the conduit towards the vent.
4) Lava flows occurred during the fourth stage (S-4), when dominant frequency of volcanic tremor and number of VT-A tended to increase. At this stage, the rate of magma intrusion was increasing due probably to additional supply to the upper magma chamber. Besides gas bursts and Strombolian eruptions, incandescent rock avalanches and PDC-forming eruptions also occurred during the fourth stage. PDCs were mostly generated from the collapse of lava fronts. Three episodes of lava flows during S-4 (the period of 2008-2014) occurred in February-November 2010, January 2012-May 2013, and July-December 2014 (Fig. 3.3).

Given the current circumstances, at least three possibilities can lead to a significant change in eruptive style at Semeru. The first factor is a change in magma viscosity (e.g., due to a changes in composition, vesicularity and/or gas content). If the magma viscosity did not change, then a second possibility would be a change in conduit geometry. Supporting this view, Triastuty et al. (2012) suggests that the variations in dominant frequency of volcanic tremor are likely due to changes in the conduit width. A third possibility is a combination between changes in magma viscosity and conduit geometry.

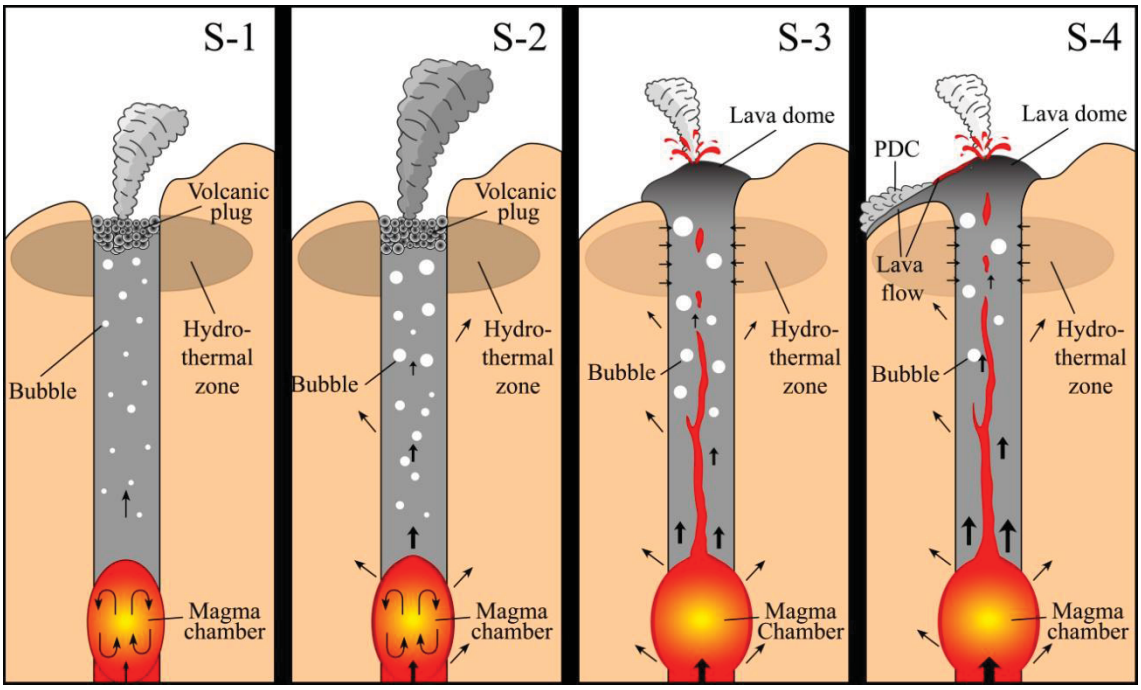

Figure 3.12. Illustration of four eruption stages (S-1 to S-4) at Semeru during the period 2008-2014 based on the statistical seimic data and spectral analysis of the 2009-2011 harmonic tremor events (Triastuty et al., 2012). This scheme adapted from the January-February 1994 eruptions (Siswowidjojo et al., 1995). The duration of each stage is shown in Fig. 3.3. The illustration is not drawn to scale.

3.5.2. Hazard assessment of recent Semeru eruptive activity

One of the common Semeru eruption styles is lava dome collapse to produce PDCs. This style of eruption takes place every 5-7 years on average (Thouret et al., 2007). PDCs may also be generated from the collapse of lava front down the SE scar, but their magnitude and volume is typically smaller than PDCs generated from summit lava-dome collapse. Since 1884 at least six eruptions produced relatively large (>1 to 6 million m^3) PDC events (mostly BAFs) that traveled down more than 7 km distance from the summit crater in 1885, 1977, 1981, 1994, 1995 and 2002-2003 (Fig. 3.13). Eruptions in 1977, 1981, 1994 and 1995 emplaced PDC deposits with an approximate volume of c. 6.4, 6.2 and 6.3 million m^3 (references in Thouret et al. 2007; VSI reports). The most recent large PDC event (BAFs and wet surge) occurred on 30 December 2002, when PDCs travelled down the Kembar and Bang Valleys as far as 12 km distance from the crater and emplaced 5.5 million m^3 of BAF deposits (Venzke, 2003; report by VSI, 2003; Thouret et al., 2007; Solikhin et al. 2012).

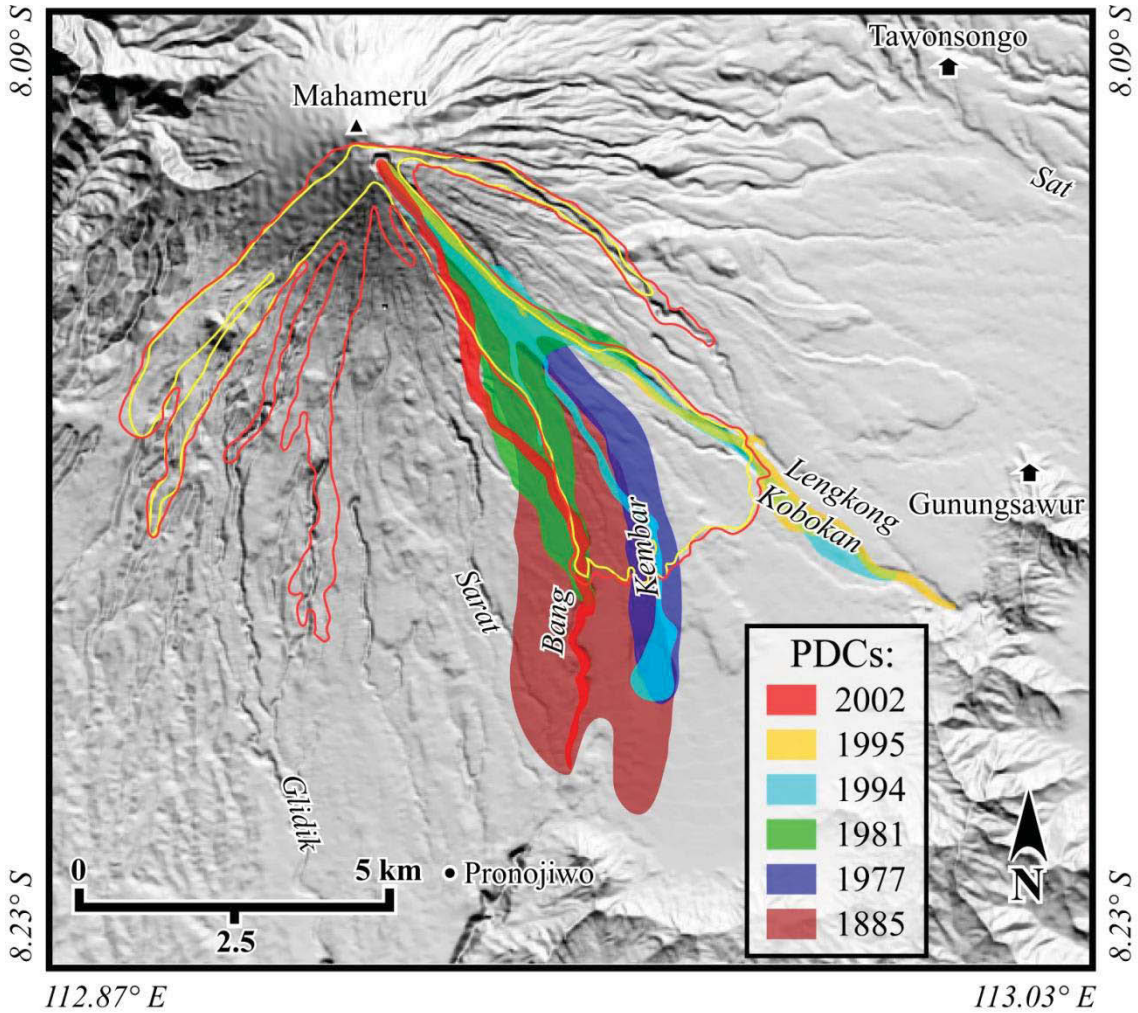

Figure 3.13. Map of PDC deposits since 1885 with a distance in excess of 7 km away from the summit crater. Yellow and red lines indicate the outline of PDC inundated areas based on Titan2D simulations show potential inundation areas for input volumes greated than those of the deposits shown, i.e., 5 (yellow) and 10 (red) million m^3 (Weningsulistri et al., 2014). The Titan2D simulations used the Topo-DEM as topographic base.

We calculated the mobility parameter of the PDC-forming events at Semeru in 1885, 1977, 1981, 1994, 1995 and 2002-2003, to be compared with other flows (Fig. 3.14). The mobility parameter (ΔH/L) is the ratio of height difference between summit crater and distal limit of flow deposit (ΔH) to the flow length or runout distance (L). This parameter captures the ability of gravity driven mass flows to move downslope (e.g., Hayashi & Self, 1992; Iverson, 1997). ΔH/L ratios for Semeru PDCs are similar within a narrow range between 0.23 and 0.26, except the 1981 PDCs that traveled shorter distances (higher ΔH/L ratio) than the others. We obtained ΔH/L ratios of 0.33 and 0.43 for the 1981 PDCs that traveled towards Bang and Kobokan Rivers, respectively. In fact, all Semeru PDCs resemble those of the small-volume PFs of Fisher and Schmincke

(1984), the Unzen 1991 dome-collapse PFs (Yamamoto et al., 1993) and the Merapi 2010 channeled PFs and surges (Charbonnier et al., 2013). The ΔH/L ratios of Semeru PDCs are relatively high, which suggest that the basal friction of flows flowing on Semeru bedrock may be high.

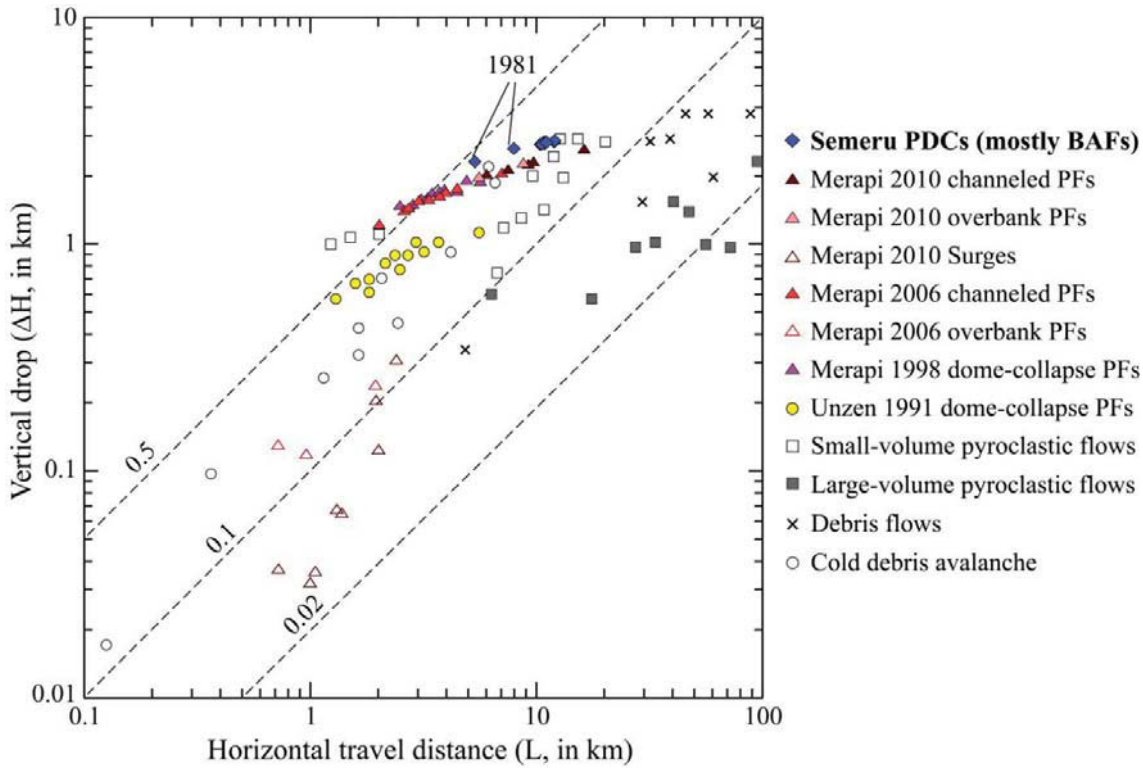

Figure 3.14. Vertical drop (ΔH) and horizontal travel distance (L) ratios for the 1885, 1977, 1981, 1994, 1995 and 2002-2003 PDCs of Semeru in comparison with those from Merapi, 2013 (Charbonnier et al., 2013), 2006 (Charbonnier & Gertisser, 2011) and 1998 (Schwarzkopf et al., 2005); Unzen, 1991 (Yamamoto et al., 1993); and other flow types (Fisher & Schmincke, 1984).

Taking account of the current conditions, dome-coulées continue to grow and will probably collapse to produce large volume of PDCs (in the range of 5 to 10 million m^3). PDC simulations using the Titan2D numerical models have been carried out by CVGHM (Weningsulistri et al., 2014) as a part of hazard assessment. The simulation was run under various scenarios, including source volumes of 5 and 10 million m^3, as shown in Fig. 3.13. Simulation results suggest that when source volume exceed the recent PDC volume (in the range of 3 to 6.5 million m^3), PDCs not only travel toward the southeast flank but also to the southwest and east flanks. We can consider that the SE scar is partially filled by the 2010-2014 lava flows and the fact that the dome-coulee continues to grow and flow at the time of writing, so the geometry of the scar has changed to a point that PDCs will be deflected or will spill over the scar rims. Alternatively, the

eruption behavior of Semeru can change and return to Vulcanian explosions. However, we caution that the topographic base for these simulations is the Topo-DEM, which has a low horizontal resolution of 15 m, thus the rough geometry of the SE scar and head valleys should be taken into account.

3.6. Conclusion

We outline the changes of Semeru eruptive behavior during the period 2009-2014 as concluding remarks for Chapter 3. The transition stage between March and August 2009 was characterized by an increase in magma intrusion rate likely due to additional supply to the magma chamber. This stage was followed by lava extrusion and the onset of dome-coulee growth. For the first time since 1967 or perhaps since 1941, lava flows emitted from the central vent flowed down more than 1.5 km in February 2010. A series of lava flows were emplaced in 2012 and 2014. This significant change in Semeru eruptive behavior may have been caused by the changes in magma viscosity (composition, vesicularity and gas content) and/or in conduit geometry. At the time of writing (January 2015), dome-coulée in the Jonggring-Seloko crater keeps growing. The most recent estimated volume of the summit dome-coulee is 2.5 ± 0.5 million m^3 as of September 2014.

Lava-dome collapse producing large volume of PDCs (3 to 6.5 million m^3) is a common Semeru hazards. Semeru PDC events in 1885, 1977, 1981, 1994, 1995 and 2002-2003 have relatively high $\Delta H/L$ ratio and are comparable with the previous small volume PFs, which may suggests high basal friction of flow on Semeru bedrock. However, some of these PDCs travelled down as far as 12 km from the crater towards the southeast flank. Future dome-collapse PDCs may travel farther down the SE scar and can spill over the rims of the scar towards southwest and east. Four eruptive scenarios may be accounted for the upcoming major eruption: (1) Common PDCs generated from lava dome and lava front collapse are channeled towards the SE scar and have a heavy impact on the southeast and south flanks of Semeru. (2) Unusually large PDCs may flow in and outside the SE scar due to the fact that the lava flows have partially filled the scar; thus the PDCs may be deflected or may spill over the scar rims down valley. (3) Large PDCs may flow in any direction if large Vulcanian occur in the upcoming eruption. (4) Lava flows may continue as dome coulee deposits and completely fill the SE scar. If this is the case, other

simulations of PDCs using a new or artificial/adapted topographic base are needed to determine the potentially affected areas.

Chapter 4 - The deposits and impacts of the large (VEI 4) 2010 Merapi eruption

4.1. Introduction

The October-November 2010 eruption of Merapi volcano was the largest eruption (VEI 4) over the past 140 years. Previously, Merapi volcano was better known for smaller dome-collapse eruptions every 2-6 years on average, and 'large' explosive episodes every 8-15 year (Thouret et al., 2000). The 20th Century Merapi eruptions typically produced summit lava domes, which collapsed to generate block-and-ash pyroclastic flows (BAFs), previously known as "Merapi type" "nuées ardentes", a category of pyroclastic density currents (PDCs). In addition to lava domes extrusions, the 2010 eruption also produced several powerful explosions, vertical eruption columns up to 17 km altitude and numerous PDCs that extended into populated areas at distances as far as 16 km from the summit (Surono et al., 2012). On the other hand, this remarkable event demonstrated the effective crisis management by Indonesian authorities together with the involvement of international scientific cooperation. Between 26 October and 8 November 2010, the eruptive events around Merapi caused 376 people were lost their lives and about 400,000 people were displaced (Mei et al. 2013), but timely forecasts delivered by the Center for Volcanology and Geological Hazard Mitigation (CVGHM) and prompt evacuations of many tens of thousands of people saved as many as 10,000-20,000 lives (Surono et al., 2012). The role of international collaborators was also critical in delivering near-real-time data and advice that complemented the extensive experience of CVGHM in interpreting the eruptive activity of Merapi.

Continuous research efforts inverted on Merapi for decades have been directed at understanding the mechanisms of dome extrusion and subsequent collapse "Merapi-type" eruptions and at improving eruption forecasting. In addition, the 2010 Merapi eruption has offered a rich set of scientific data to be analyzed and interpreted in order to advance in the understanding of, and ability to forecast, explosive volcanism. Such research studies have been carried out and published, for example in the special issue of the Journal of Volcanology and Geothermal Research, volume 261, in 2013 (Jousset et al.,

2013). Published studies have covered a wide range of research fields and volcanological topics including the application of satellite remote sensing. During the 2010 Merapi crisis, satellite remote sensing data have been integrated with seismic data for near-real time monitoring of the eruption to a point that interpretation did play role in decision support, especially with respect to the deleniation of exclusion zones (Surono et al., 2012). Measurements of SO_2 emissions and maps of volcanic cloud dispersal from satellite remote sensing were available and useful during the most explosive phases of eruption. Synthetic Aperture Radar (SAR) imagery, capable of providing information during day or night and independent of the meteorological conditions, has been shown to be useful for recurrent monitoring of Merapi volcano during the crisis (Pallister et al., 2013), defining ground surface displacement (Saepuloh et al., 2013), evaluating the extent of impacts (Yulianto et al., 2013; Solikhin et al., 2015a) and estimating deposit volume (Bignami et al., 2013). Satellite multispectral (optical) imagery has been used to support the field investigations and to estimate their volume (Cronin, et al., 2013; Komorowski et al., 2013; Charbonnier et al., 2013; Jenkins et al., 2013; Solikhin et al., 2015b).

The methodological work of analysis of PDCs and other erupted materials using satellite imagery has a clear potential for helping the volcanological community to contribute to decision making process during a volcano crisis. Our study, presented in the fourth chapter, aims to assess the extent and effects of the 2010 Merapi PDCs, tephra-fall and subsequent lahars based on remote sensing techniques using HSR optical imagery. We used the most recent HSR imagery data sets from Pléiades, GeoEye, QuickBird and SPOT5 satellites and aerial photographs, acquired before and after the eruption. Among them Pléiades sensor has been used for the first time to identify and map pyroclastic deposit immediately after a large eruption. Pléiades, GeoEye, QuickBird and other HSR images offers unprecedented detail for mapping pyroclastic deposit on otherwise unaccessible active volcanoes. These data sets have enabled us to provide additional insight into the chronology, dynamics, and impacts of the volcanic eruption, which are complementary to previous detailed studies. This chapter encompasses several studies of the 2010 Merapi eruption including: (1) a new estimate of volumes of tephra-fall deposits using three empirical calculation methods (exponential, power-law and Weibull thinning); (2) the effects of the eruption and structural changes on the volcano summit; (3) the extent of pyroclastic deposits in the Gendol-Opak catchments; (4) the origin of

post-eruption lahar deposits; and (5) the behavior of the overbank PDCs and lahars based on the analysis of geomorphometric indices related to river channels.

4.2. High-spatial resolution imagery of the 2010 Merapi Volcano eruption

This section corresponds to an article that has been accepted for publication in the Bulletin of Volcanology on 6 Feburary 2015.

High-spatial resolution imagery helps map deposits of the large (VEI 4) 2010 Merapi Volcano eruption and their impact

Akhmad Solikhin[1, 2], Jean-Claude Thouret[2], Soo Chin Liew[3], Avijit Gupta[3, 4], Dewi Sri Sayudi[1], Jean-François Oehler[5], Zeineb Kassouk[2]

[1] *Center for Volcanology and Geological Hazard Mitigation, Jalan Diponegoro 57, Bandung Indonesia*

[2] *Clermont Université, Université Blaise Pascal, Laboratoire Magmas et Volcans UMR 6524 CNRS, IRD-R163 and CLERVOLC, 5 rue Kessler, 63038, Clermont Ferrand cedex, France*

[3] *Center for Remote Imaging, Sensing and Processing, National University of Singapore, Singapore*

[4] *School of Earth and Environmental Sciences, University of Wallongong, Australia*

[5] *Altran Ouest, Technopôle Brest Iroise, Site du Vernis CS 23866, 29238 Brest cedex 3, France*

Published in Bulletin of Volcanology, Volume 77, Issue 3, March 2015, Article 20

Supplementary data to this article can be found in Appendix B

Bull Volcanol (2015) 77:20
DOI 10.1007/s00445-015-0908-0

RESEARCH ARTICLE

High-spatial-resolution imagery helps map deposits of the large (VEI 4) 2010 Merapi Volcano eruption and their impact

Akhmad Solikhin · Jean-Claude Thouret · Soo Chin Liew · Avijit Gupta · Dewi Sri Sayudi · Jean-François Oehler · Zeineb Kassouk

Received: 22 February 2013 / Accepted: 7 February 2015
© Springer-Verlag Berlin Heidelberg 2015

Abstract The 26 October–23 November 2010 eruption is Merapi's largest event (VEI 4) over the past 140 years. We used high-spatial-resolution (HSR) imagery from GeoEye, Pléiades, IKONOS, and SPOT5 satellites to assess the extent and effects of the pyroclastic density currents (PDCs) and subsequent lahars. We have tracked the geomorphic and structural (fracturing) changes of Merapi's summit crater and dome between 2008 and 2012. The 4 September 2011 GeoEye image shows that due to the explosive eruption, the summit area lost about 10×10^6 m^3. The eruption enlarged the SSE-trending Gendol breach to be $1.3\times0.3\times0.2$ km. The 2010 tephra and PDC deposits covered about 26 km^2 in the two catchments of Gendol and Opak Rivers on Merapi's south flank, i.e., 60–75 % of the total PDC deposit area, with a total bulk volume of 45×10^6 m^3. The tephra-fall deposit covered an area of about 1300 km^2 with a range in volume of 18–21$\times$ 10^6 m^3. Supervised and object-oriented classification on HSR imagery enables us to map in detail the PDC deposits across the Gendol-Opak catchment. We delineated 16 spectrally and/or texturally distinct units of PDC deposits and compared them with previously published results. They encompass high-energy surge deposits within ca. 8 km of the summit, valley-confined PDC deposits channeled as far as 16.5 km in the Gendol River, and widespread overbank PDC with ash-cloud surge deposits on valley margins.

Additional high-resolution data are provided to map and analyze flooded areas due to lahar activity in 2011–2012 on the south and west flanks. Subsequent overbank lahars

Editorial responsibility: S. A. Fagents

Electronic supplementary material The online version of this article (doi:10.1007/s00445-015-0908-0) contains supplementary material, which is available to authorized users.

A. Solikhin · D. S. Sayudi
Center for Volcanology and Geological Hazard Mitigation, Geological Agency, Ministry of Energy and Mineral Resources, Jalan Diponegoro 57, Bandung 40122, Indonesia

A. Solikhin (✉) · J.-C. Thouret · Z. Kassouk
Laboratoire Magmas et Volcans, Clermont Université, Université Blaise Pascal, UMR 6524 CNRS, IRD-R163 and CLERVOLC, 5 rue Kessler, 63038 Clermont Ferrand Cedex, France
e-mail: aksolikhin@vsi.esdm.go.id

A. Solikhin
e-mail: A.Solikhin@opgc.univ-bpclermont.fr

J.-C. Thouret
e-mail: J.C.Thouret@opgc.univ-bpclermont.fr

S. C. Liew · A. Gupta
Center for Remote Imaging, Sensing and Processing, National University of Singapore, Singapore, Singapore

S. C. Liew
e-mail: scliew@nus.edu.sg

A. Gupta
e-mail: agupta@uow.edu.au

A. Gupta
School of Earth and Environmental Sciences, University of Wollongong, Wollongong, Australia

J.-F. Oehler
Altran Ouest, Technopôle Brest Iroise, Site du Vernis CS 23866, 29238 Brest Cedex 3, France
e-mail: jeanfrancois.oehler@altran.com

impacted selective small areas in the populated ring plain, devastating villages along the Putih River on the southeast flank and the Gendol River. We have analyzed the morphometric parameters (channel cross-sectional capacity, longitudinal rate of channel confinement, and channel sinuosity) of the Gendol-Opak River channels that govern overbank and avulsion of lahars in the ring plain. The paper demonstrates the potential of HSR satellite imagery to outline tephra, PDC, and lahar deposits; map the geomorphic and structural evolution of the summit area of persistently active composite cones; and thus improve hazard assessment for Merapi, a volcano whose summit, slopes, and drainages have changed more since October 2010 than at any other time since 1931.

Keywords Remote sensing · Merapi · Eruption · Pyroclastic density current · Tephra · Lahar · Hazard

Introduction

Merapi (7° 32.5′ S and 110° 26.5′ E), located in the densely populated province of Yogyakarta in central Java, is one of Indonesia's most active volcanoes (Fig. 1). More than a million people live on its slopes and the ring plain, within a radius of 20 km from the volcano. As many as 227,000 people live in the three official hazard zones termed *Kawasan Rawan Bencana* (KRB) I, II, and III (Fig. 1c; BAPPENAS and BNPB 2011) among which about 23 % live in the third and the most dangerous hazard zone (KRB III; BPS 2010). More than 74 eruptions have been recorded at Merapi since 1548, and at least 17 of them, including the one in 2010, have caused fatalities. Based on the historical eruption record of Siebert et al. (2010), the average time interval between eruptions is 1–6 years. Most events fall in the VEI 2 range, at least one per decade since 1861 (Appendix Fig. 1). Several have been categorized as large-magnitude eruptions (VEI ≥3), as in 1672, 1822, 1846, 1849, 1872, 1930–1931, and 1961 (Voight et al. 2000; Siebert et al. 2010; Gertisser et al. 2012). Dome collapse events (VEI <3) that commonly produce 1 to 10 million m^3 of deposits (Voight et al. 2000) have prevailed during the past 80 years.

Merapi's summit (2978 masl prior to the 2010 eruption) has been built up by andesitic lava domes. The volcano is well known for its block-and-ash flows (BAF), composed of large fraction of juvenile volcanic blocks in a matrix of volcanic ash produced by the collapse of summit lava domes. They are often referred to as the "Merapi-type nuées ardentes" or glowing avalanches (Voight et al. 2000). These are a type of pyroclastic density current (PDC), a more general term that refers to fast-moving mixtures of hot gas, rock fragments, and ash, and include dense pyroclastic flows (PFs) and dilute pyroclastic surges (Branney and Kokelaar 2002).

Thouret et al. (2000) identified three major hazardous eruption scenarios at Merapi: (1) the common collapse of the summit dome complex leading to the emplacement of large-volume BAFs and high-energy surges toward a sector of the volcano, (2) an explosive eruption larger than any since 1930

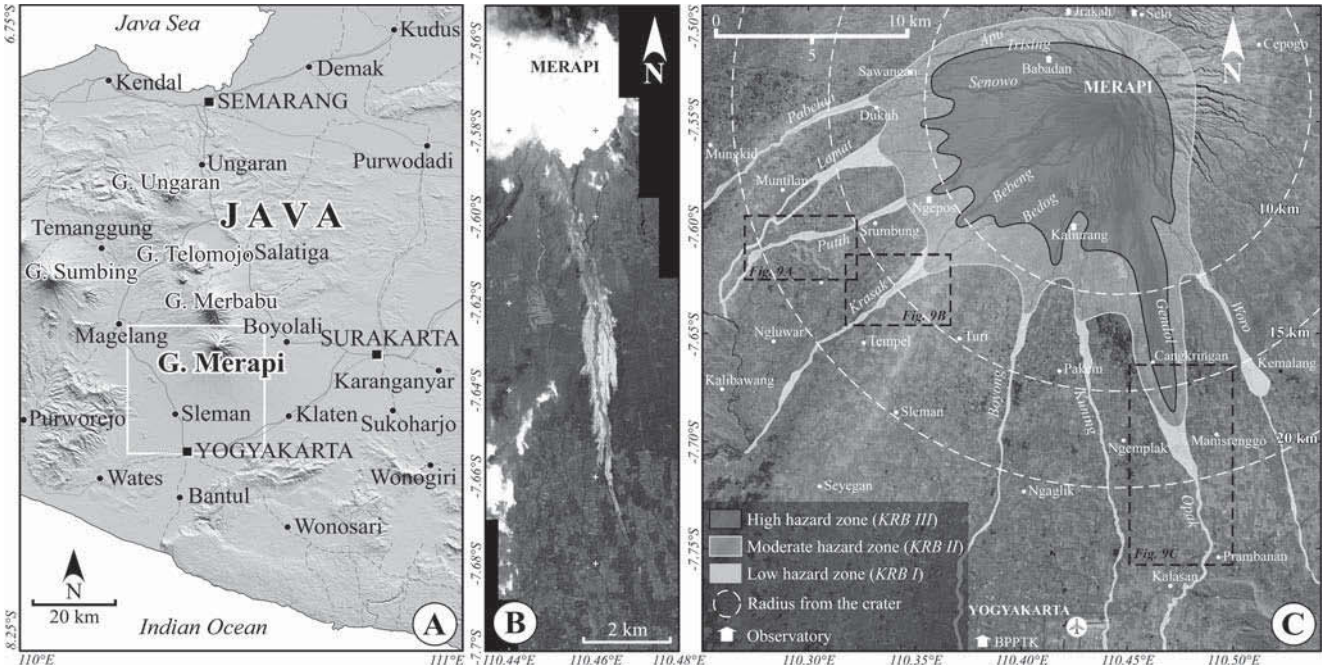

Fig. 1 **a** Location of Merapi volcano. **b** November 15, 2010, GeoEye panchromatic image of Merapi and its south flank. **c** SPOT5 image of the Merapi-Merbabu area from 10 June 2011 draped over a SRTM-DEM. View is to the northwest. The three Merapi hazard zones (KRB) as redefined after the 2010 eruption (Sayudi et al. 2010) are outlined. *Black dashed line boxes* indicate the locations of Fig. 9

that would produce PDCs which can spread over all flanks of Merapi similar to eruptions that have occurred once every century, and (3) a potential collapse of the entire summit area, involving the fumarolic field of Gendol and part of the south flank, which would result in the emplacement of a moderate volume debris avalanches and related debris flows as well as PDCs. The "100-year" eruption (Surono et al. 2012) in 2010 included aspects of the first (toward the south sector) and second scenarios, but its characteristics are also reminiscent of both the 1930–1931 explosive eruption (VEI 3) and the explosive large vulcanian to subplinian event (VEI 4) of 1872 (Voight et al. 2000).

Rain-triggered lahars constitute an additional hazard both during and following eruptions. Lahar is an Indonesian term that refers to water-saturated flows originating from a volcano and involving a mixture of rock debris and water other than normal stream flow (Smith and Fritz 1989). Merapi lahars can flow with average velocities of 5–7 ms^{-1} at 1000-m elevation and inundate areas of the extensive ring plain below 600-m elevation, reaching as far as 30–40 km from the summit along each of the 13 rivers that drain the volcano (Lavigne et al. 2000). Each year, lahars with discharges between 200 and 2000 m^3 s^{-1} are triggered during the rainy season in several rivers that drain the west, southwest, and south flanks. In the 1900s, 17 lahars related to the eruptions killed at least 100 people, destroyed about 80 villages and 1500 houses, and flooded several thousand hectares of tilled land (Thouret et al. 2000).

Images of Merapi volcano and its ring plain before and after the 2010 crisis were recorded by satellite-borne high-spatial-resolution (HSR) optical instruments. For this study, we have used images from the SPOT5, IKONOS, Pléiades, and GeoEye-1 satellites (Table 1), as well as low-altitude photographs and three different digital elevation models (DEMs). Field observations of structural damage and deposit mapping provide ground truthing for interpretations based on remote sensing (Thouret et al. 2010; Lube et al. 2011; Charbonnier and Gertisser 2011; Solikhin et al. 2012). These tools have enabled us to provide additional insights into the chronology, dynamics, and impacts of the volcanic eruption, which are complementary to detailed field-based study of Cronin et al. (2013), Komorowski et al. (2013), Charbonnier et al. (2013), and Jenkins et al. (2013). Our study illustrates the ability of HSR optical imagery for identifying a wide range of pyroclastic deposits at an active volcano immediately after a paroxysmal event and therefore removes the need for scientists to perform ground surveys in unsafe conditions. We found remote sensing extremely useful and effective for assessing PDC and subsequent lahar deposits. HSR images have allowed us to (1) map and evaluate the area covered by fresh volcanic deposits, (2) analyze the structural setting of the summit and flank areas prior to and after the eruption with implications for better understanding the eruption processes, and (3) analyze the effects and behavior of PDCs and subsequent lahars on the volcano flanks travelling down to the ring plain of the volcano.

We traced the spatial and temporal patterns of deposit aggradation by the emplacement of the October–November 2010 PDCs and the subsequent remobilization by lahars in the subsequent year and a half. Geomorphic and structural changes on Merapi's summit were interpreted based on the comparison of HSR images before and after the 2010 eruption. Finally, based on this investigation, we identified new hazard-prone areas that have resulted from the eruption and subsequent lahars.

Data acquisition and processing

Remote sensing and field data

This study is based on HSR optical imagery, DEM analysis, and geomorphic interpretation of landforms and structures and some ground-truth field data (deposit map and Global Positioning System survey for ground control points) in selected key areas. The satellite images used in this study are as follows: (1) two multispectral GeoEye-1 satellite images dated 15 November 2010 (Fig. 1b) and 04 September 2011; (2) one multispectral Pléiades satellite image dated 29 September 2012; (3) one multispectral IKONOS satellite image dated 7 July 2008; and (4) three multispectral SPOT5 images of 18 May 2008, 15 November 2010, and 10 June 2011. Table 1 summarizes the technical specifications of the images. We applied contrast stretching, filtering, band ratio, and the Normalized Difference Vegetation Index (NDVI) to the HSR images in order to enhance contrasts between features, as well as to reduce the variations in topographic illumination. These processing techniques have been previously applied to IKONOS and Spot images of Semeru, another persistently active Indonesian volcano (Solikhin et al. 2012; Kassouk et al. 2014).

Tephra isopachs used in this study are based on field observations carried out during the period November 2010 to May 2011 by joint teams of scientists from the Indonesian Center for Volcanology and Geological Hazard Mitigation (CVGHM) and the US Geological Survey's Volcanic Disaster Assistance Program (USGS/VDAP). The volume of tephra deposit from Merapi has been determined using empirical volume calculation methods based on exponential (Pyle 1989; Fierstein and Nathenson 1992), power-law (Bonadonna and Houghton 2005), and Weibull thinning (Bonadonna and Costa 2012).

We have used DEMs and carried out differential Global Navigation Satellite System (GNSS) surveys to establish ground control points and derive sediment thickness. We utilized three different digital elevation models (DEMs) in combination with optical satellite images and a drainage network map in order to delineate the geomorphic features and deposits

Table 1 Technical characteristics of satellite sensor and images used for this study

Satellite sensor; provider	Spectral range (nm)	Spatial resolution/swath width (at nadir)	Average revisiting time; off-track viewing angle	Acquisition date of the imagery used
GeoEye-1; DigitalGlobe	Panchromatic 450–800	0.41 m/15.2 km	1–3 days	November 15, 2010; 4 September 2011
	B1 (blue) 450–510	1.65 m	Max±30°	
	B2 (green) 510–580	1.65 m		
	B3 (red) 655–690	1.65 m		
	B4 (NIR) 780–920	1.65 m		
Pléiades; Spot Image (CNES)	Panchromatic 470–830	0.5/20 km	1 day	29 September 2012
	B1 (blue) 430–550	2 m	Max±45°	
	B2 (green) 500–620	2 m		
	B3 (red) 590–710	2 m		
	B4 (NIR) 740–940	2 m		
IKONOS; DigitalGlobe	Panchromatic 445-900	0.82 m/11 km	1–3 days	07 July 2008
	B1 (blue) 445–516	3.28 m	Max±30°	
	B2 (green) 506–595	3.28 m		
	B3 (red) 632–698	3.28 m		
	B4 (NIR) 757–853	3.28 m		
SPOT-5; Spot Image (CNES)	Panchromatic 480–710	2.5 or 5 m/60 km	1–4 days	18 May 2008; 15 November 2010; 10 June 2011
	B1 (green) 500–590	10 m	Max±27°	
	B2 (red) 610–680	10 m		
	B3 (NIR) 780–890	10 m		
	B4 (SWIR) 1580–1750	20 m		

of the study area. The first DEM was derived from the third Shuttle Radar Topography Mission (SRTM3, produced by NASA), computed at 3-arc-second (ca. 90 m) resolution. Accuracy of SRTM3 is mainly dependent on the elevation and the slope angles. In areas around Merapi, the SRTM data satisfy a 90 % confidence level for an elevation up to 1000 m (Gerstenecker et al. 2005). The second DEM called TOPO-DEM with 15×15-m horizontal resolution and 1-m vertical resolution was generated from 12 digital topographic quadrangles at 1:25,000 scale and 12.5-m contour intervals. The topographic maps were produced by the Indonesian Agency for Geospatial Information (BIG) between 1998 and 2001. The Merapi TOPO-DEM has height inaccuracies due to an average shift of 5±14 m, on average, with respect to ground control points. The third DEM called Airphoto DEM, with 1×1-m horizontal and 1-m vertical resolution, was generated from low-altitude aerial photographs using photogrammetric and stereo matching techniques with an average accuracy of 0.2 m. The Airphoto DEM covers only the southern flank of Merapi volcano along the Opak-Gendol Valley at distances between 15 and 25 km from the summit.

Supervised and object-oriented classification

Identification of the deposits benefited from the high resolution of the images (50 cm), and mapping was conducted by using two supervised and object-oriented methods for classification (Fig. 2). The object-oriented method comprises five steps.

1. We utilize intensity, hue, and saturation (IHS) and geomorphic parameters to divide the catchment into five reaches (Appendix Fig. 2). We then compute three

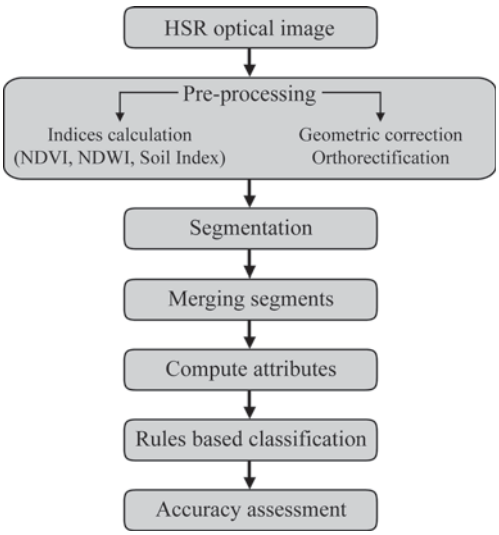

Fig. 2 Flow chart showing the classification stages of HSR satellite images based on the object-oriented method

spectral indices: NDVI related to vegetation, Normalized Difference Water Index (NDWI), and Normalized Difference Soil Redness Index (NDSRI) in order to distinguish areal units (e.g., Kassouk et al. 2014).

2. Deposit segmentation begins with the edge detection by identifying potential boundaries between segments, based on the assumption that two neighboring pixels with large differences in their spectral value are members of different segments. Then, we merge adjacent segments that have similarities in their spatial spectral characteristics.
3. Several attributes representing both geometric characteristics and average pixel information for each segment were computed to create objects.
4. A supervised classification of these objects according to attributes (form, texture, and mean spectrum) was carried out in order to infer the deposit units.
5. Finally, we evaluate the segmentation quality by measuring both topological and geometric similarities between segmented polygons (objects) and reference polygons.

Four different issues commonly observed in HSR analysis can lead to false identification of deposits. (1) The presence of shadows. However, our images have no clouds except for the summit on the 15 November 2010 GeoEye scene (Fig. 1b), so we avoided this difficulty by using the cloud-free 4 September 2011 GeoEye image with 0.5 m pixel resolution and relatively high incidence angle. (2) The surface of PDC deposits of the same type can be either hot/dry or wet/water saturated depending on weather conditions, which produces different reflectance characteristics and which may lead to the potentially false interpretation that different spectral units are present. However, very little rain fell on the pristine pyroclastic deposits during the waning eruptive stage before 15 November 2010. In the lower course of the Gendol River, we identified springs or resurgence of water, ponded water, and newly formed rills in the rectilinear valley bottom. (3) Runoff on, and early incision of, pristine deposits can lead to misinterpretation of the texture and spectral indices used for object classification. The 15 November 2010 image acquired during the waning phase allowed recognition of pristine surface of deposits before runoff and the incision by rill networks and remobilization by later lahars. We could even map small mudflows that occurred as a consequence of the 4–5 November 2010 PDC overspills across the engineered dikes and onto the rice fields down valley. (4) Vegetation cover can mask deposit surfaces or lead to a misinterpretation of bedrock mantled by new deposits. The high resolution of satellite images helped to outline and differentiate the different types of vegetation types (grass, bush, trees) according to density, strata, and canopy height. For example, an un-impacted forest could be identified from the narrow strips of singed (still standing) and burnt (blown down or snapped) forest affected by the ash-cloud surges in the valley margins.

Identifying and mapping pyroclastic deposits from the HSR images needs a cautionary approach because of three factors. (1) The 0.50- to 2.50-m resolution of the satellite images does not prevent us from misinterpreting in some circumstances the nature of deposit in complex successions or on rugged topography for which the resolution is too low. (2) The pyroclastic deposits were mined in the Gendol valley channel soon after the eruption. We resolved the problem by interpreting the pyroclastic deposits mostly from the two 15 November 2010 images, and we mapped the summit area unaffected by human activities based on the 4 September 2011 GeoEye image. (3) Despite the high spatial resolution, the images cannot be used to recognize the spatio-temporal variation of lithostratigraphy that is inherent to the complex succession of pyroclastic deposits produced by the 26-day-long eruption over a rugged topography (Cronin et al. 2013; Komorowski et al. 2013; Charbonnier et al. 2013). It is difficult to separate veneer PDC deposit units from reworked PDC deposits when interpreting the image after 10 November 2010. Veneer PDC deposits consist mostly of pyroclastic surge deposits and thin, dense PF deposits that mantle interfluves with variable thicknesses. It is also impossible to distinguish spatial-temporal variations of lithofacies due to topographic obstacles in the rugged proximal zone near the summit. Komorowski et al. (2013) have described this issue in detail. Instead, we show how the HSR imagery can complement field studies of the deposits by encompassing wide and inaccessible areas on the volcano. We also present a methodology for delineating the areal extent of deposits after a large eruption and before any erosion. Interpreting deposits from damage on vegetation can be misleading, but we distinguished (1) the uppermost catchment swept by high-energy surges, showing trees that were uprooted, knocked, and blown down with preferential directions; (2) the narrow margins of the valley/catchment affected by ash-cloud surges and characterized by broken, burnt, or singed trees without preferential directions; and (3) ash-covered forest. The 0.5 m pixel resolution thus allows for the distinction of categories of damage in forest, on vegetation cover, and on tilled land.

Our interpretation from the satellite images was verified by our selective field mapping of the south flank of the Merapi volcano, low-altitude aerial photographs with 0.2-m resolution taken in January 2011 over the Gendol Valley, and other field-based studies already published (Cronin et al. 2013; Komorowski et al. 2013; Charbonnier et al. 2013; and Jenkins et al. 2013). Geologic mapping based on HSR images cannot identify the complex stratigraphic succession of the deposits that were determined by Cronin et al. (2013); Komorowski et al. (2013), and Charbonnier et al. (2013). However, our maps provide a more complete spatial distribution of pyroclastic (PDC and tephra) and lahar deposits from the summit to the ring plain on the south and west flanks of the volcano (Fig. 3). Our methodology (object-oriented and supervised

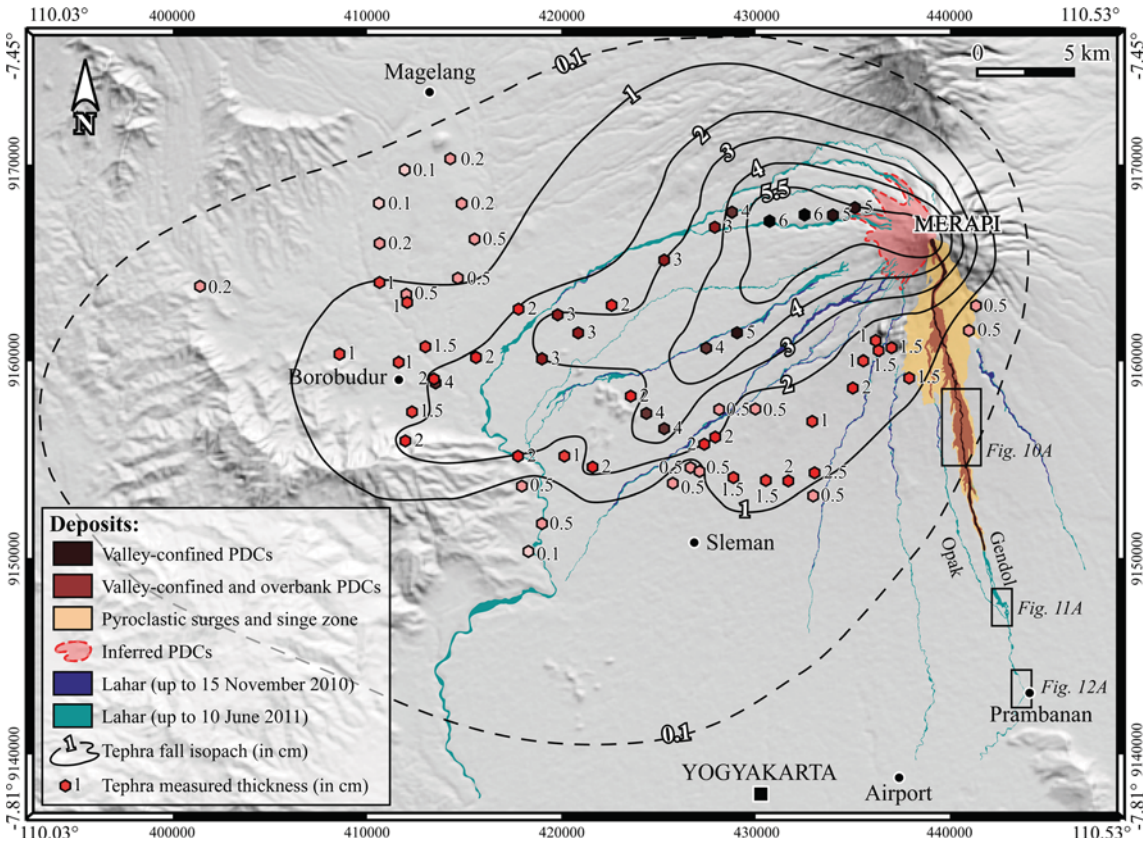

Fig. 3 Map showing the 2010 PDC deposits on the southern flank of Merapi and the tephra-fall and lahar deposits around Merapi. PDCs were mapped using our interpretation of the 15 November 2010 GeoEye and 10 June 2011 SPOT5 images and checked at 50 localities with field observations and GNSS ground control points. The tephra isopach map is based on field observations carried out by a joint Indonesia (CVGHM)-US (USGS/VDAP) team. The map of lahar deposits is based on our interpretation of the 15 November 2010 and 10 June 2011 SPOT5 images. *Black line boxes* indicate the locations of Figs. 10, 11, and 12

classification), based on HSR images acquired on multiple dates, helps to address four important issues.

1. Identification of the different types of pyroclastic and lahar deposits on the entire volcano, in order to better understand the spatial patterns of damage and infer the processes of emplacement and remobilization
2. Mapping volcanic deposits in inaccessible locations
3. Recording the remobilization processes of the pristine deposits by runoff and lahars in all catchments
4. Assessing the evolution of the new vent and dome structures in the summit area, which was disrupted during the eruption, as well as the fractures detected across summit lava flows and along crater rims

The 2010 VEI 4 eruption

Although small in magnitude (VEI 2), the 2006 eruption contributed to the instability of the southern flank of Merapi affected by the larger event in 2010. The analysis of the 2006 eruption contributed to our understanding of the behavior of PDCs during the 2010 eruption in several ways. First, the "*Gegerboyo*" rim wall, which formed during the 1911 eruption (Global Volcanism Program 2007) and protected the south flank of Merapi for the past 100 years, failed as a result of the 27 May 2006 Bantul earthquake (Charbonnier and Gertisser 2008), henceforth exposing these areas to PDCs. Second, overbank and avulsion processes due to the construction of new check dams and dikes and the presence of narrow bends in the Gendol river channel and subsequent flowage in the hitherto protected tributaries were recognized for the first time after this eruption (Charbonnier and Gertisser 2008, 2011; Lube et al. 2011) as the most severe hazard.

A summary of the 2010 eruption is given in Table 2 and Fig. 4. Hundreds of thousands of people were displaced, 2300 houses were destroyed or severely damaged, and 376 people lost their lives. Between 26 October and 8 November 2010, the eruptive events around Merapi caused about 400,000 people to be displaced for one and a half months (Mei et al. 2013). The 2010 Merapi eruption was characterized by several phases that produced numerous and voluminous PDCs at the beginning of the rainy season (October–November). Various

Table 2 Characteristics of the four 2010 eruption phases based on Surono et al. (2012), Pallister et al. (2013), Cronin et al. (2013), Komorowski et al. (2013), Charbonnier et al. (2013), CVGHM reports, and our observations

Parameter	Phase I intrusion	Phase II initial explosive	Phase III magmatic	Phase IV waning
Date	31 October 2009–26 October 2010	26 October–1 November	1–7 November	8–23 November
Activity	I, Sp	De, Dd, PDC, Ex, Apf, Sp, L	De, Dd, PDC, Fc, Ex, Apf, Sp, L	Ex, PDC, Apf, L
Deformation (EDM)	Inflation rate (south Flank) <10 to >500 mmd^{-1}	Not detected (reflector destroyed at summit)	Not detected Ibid	Not detected Ibid
Seismicity	(maximum events/day)	(maximum events/day)	(maximum events/day)	(maximum events/day)
	MP 624	MP 223	MP 84	MP 49
	VT 227	VT 67	VT 31	VT 57
	RF 454	RF 354	RF ∞	RF 38
Maximum distance of PDCs (from summit crater)	–	7 km toward Gendol River (south flank)	15.5 km along Gendol River (south flank)	~4 km toward Gendol River (south flank)
Maximum ash plume height	–	18 km	>15 km	7.6 km
Estimated area covered by PDC deposits	–	ca. 11 km^2	ca. 37 km^2	ca. 3 km^2
Victims	0	35 people	341 people	0

I inflation, *De* dome growth, *Dd* dome destruction, *PDC* pyroclastic density current, *Fc* fountain-collapse pyroclastic flow, *Ex* explosion, *Sp* steam plume, *Apf* ash plume and tephra fall, *L* lahar, *MP* multiphase event, *VT* volcano-tectonic event, *RF* rockfall event

aspects of the eruption were discussed in detail by Surono et al. (2012); Cronin et al. (2013); Komorowski et al. (2013); Charbonnier et al. (2013), and Jenkins et al. (2013). Surono et al. (2012) divided the 2010 eruption into four phases based on radar remote sensing data combined with seismic monitoring and ground-based observations. These are the following: (1) the intrusive phase (31 October 2009–26 October 2010), (2) the initial phreatomagmatic explosive phase (26 October–1 November), (3) the magmatic phase (1–7 November), and (4) the waning phase (8–23 November 2010).

Komorowski et al. (2013) provided additional data supporting the breakdown of the eruption into eight main stages as follows (Fig. 4): stage 1, unrest and intrusion (31 October 2009–26 October 2010); stage 2, initial phreatomagmatic explosions (26–29 October 2010); stage 3, recurrent, rapid dome growth, and destruction (29 October 2010–04 November 2010); stage 4, paroxysmal dome explosion and collapse (05 November 2010); stage 5, retrogressive summit collapse (05 November 2010); stage 6, subplinian convective fountain collapse (05 November 2010); stage 7, rapid dome growth with alternating effusive and explosive activity (05–08 November 2010); and stage 8, declining ash venting and degassing (08–23 November 2010).

The 2010 Merapi crisis produces PDCs that flowed down the south and west flanks of the volcano. The deposits covered an area of about 26 km^2 in the Gendol-Opak catchment on the south flank, which comprises 75 % of the total PDC deposit area (Fig. 3). Charbonnier et al. (2013) have identified a total of 23 PDC events in the Gendol-Opak catchment including five main channeled flows, 15 overbank flows, and two main surge events whose deposits totaled a bulk volume of approximately 36.3 million m^3. CVGHM volcano observation posts reported PDC events on the west flank on 1, 4, 6, 7 and 8 November 2010. The PDCs traveled as far as 3–4 km toward the Apu (northwest flank), Senowo, Lamat, Trising (west flank), and Boyong-Bebeng Rivers (southwest flank). The areal extent of PDC deposits in the northwest, south, and southwest flanks (i.e., 6 km^2) was inferred from the interpretation of HSR images (Fig. 3), but the thickness of the deposits remains unknown due to the lack of field measurements on the inaccessible west summit flank. Intense rainfall events on thick and poorly consolidated pyroclastic deposits covering the slopes of Merapi generated lahars during and just after the end of the eruption and endangered people living on and close to riverbanks to the west, southwest, and south of the volcano. The first lahars occurred on 27 October 2010 and were channeled through the Boyong and Kuning Rivers draining the southwest and south flanks (de Bélizal et al. 2013). Many of the lahars were confined to the channel, but overflow breakouts 10–20 km downstream from the head waters of several large rivers damaged several villages and continue to threaten other villages near river channels more than 20 km from of the summit.

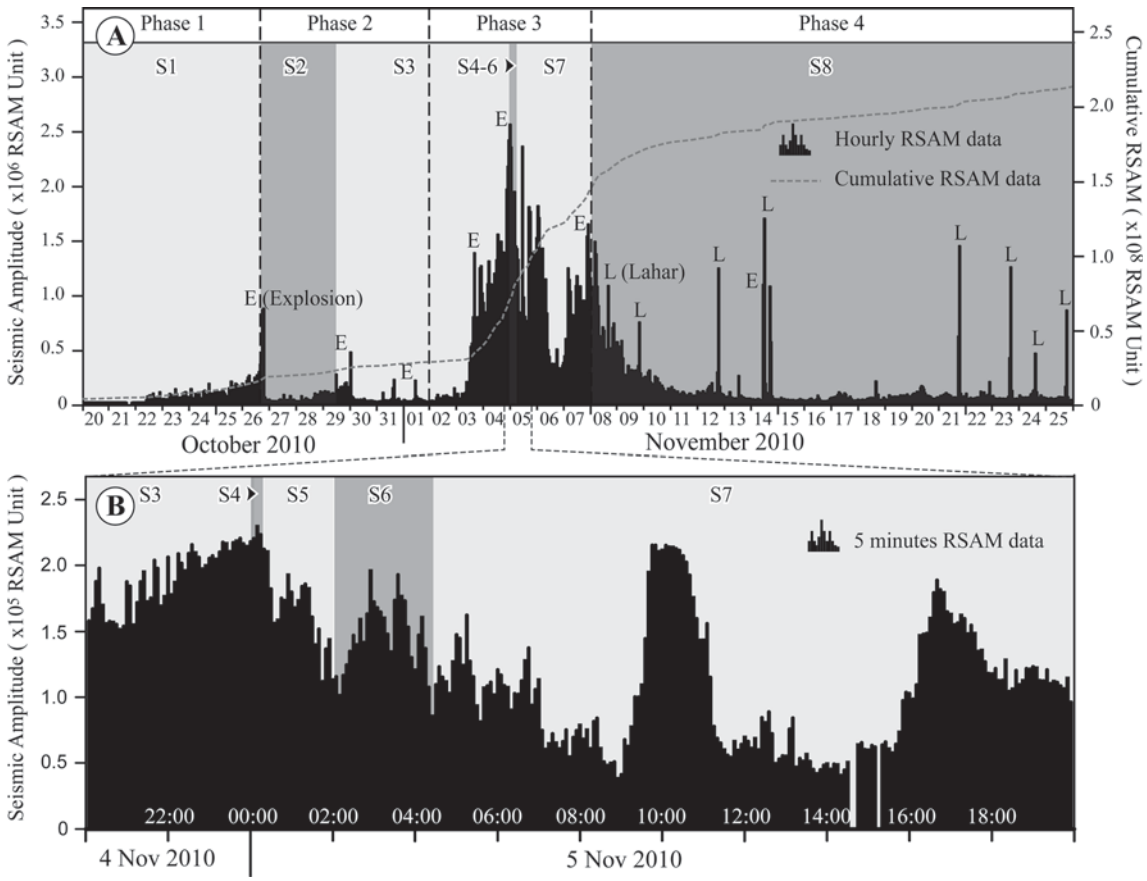

Fig. 4 Real-time seismic amplitude measurement (RSAM) data from Merapi in October–November 2010. **a** Hourly and **b** 5-min RSAM data (black histograms expanded below) associated with four phases (phases 1–4; Surono et al. 2012) and eight stages (S1–S8; Komorowski et al. 2013) of the 2010 Merapi seismic and eruptive crisis starting on 20 October and ending on 23 November. All times are in local time (UTC +7 h)

Ash dispersed by the wind affected mostly the west flank of the volcano. The total thickness of tephra from several events (among them, at least three that reached Yogyakarta) during the 2010 eruption was plotted on a map (Fig. 3) where five isopachs in the range 1 to 5.5 cm were contoured and one additional 0.1-cm contour was inferred from reported ashfall in the most distal area. A plot of the tephra thickness in a logarithmic scale (T) against the square root of isopach area ($A^{1/2}$) shows deposit thinning rate fitted by an exponential function with breaks-in-slope (two segments), a power-law function, and a Weibull function (Fig. 5). The calculated bulk volume of the tephra, derived by integrating the different functions over given intervals, is shown in the inset table in Fig. 5. Using the exponential method, we obtained a volume of $16\pm2\times10^6$ m^3 for single segment and $18\pm2\times10^6$ m^3 for one and two breaks-in-slope (two and three segments) curves. The Weibull method yielded a tephra volume of $22\pm4\times10^6$ m^3. The power-law method yields both a larger volume and error, as its integration is sensitive to the choice of the integration limits due to a relatively low power-law coefficient (i.e., 1.553). We used several variations with proximal and distal boundaries to obtain volumes of $23\pm12\times10^6$ m^3 (for integration limit of 0.3–50 km), $32\pm13\times10^6$ m^3 (0.3–100 km), $22\pm9\times10^6$ m^3 (0.5–50 km), $32\pm10\times10^6$ m^3 (0.5–100 km), $21\pm7\times10^6$ m^3 (1–50 km), and $31\pm8\times10^6$ m^3 (1–100 km).

Impact of the 2010 eruption determined from HSR imagery

Morphological and structural changes on the volcano summit

A comparative analysis of HSR satellite images of Merapi before (IKONOS image of 7 July 2008; Fig. 6a, b) and after (GeoEye-1 image as of 4 September 2011, Fig. 6c, and Pleiades image as of 29 September 2012, Fig. 6d) the eruption allowed us to recognize and quantify the striking changes in the summit morphology. The post-2010 evolution of Merapi's summit has not previously been imaged and interpreted in detail, but the syn-eruptive morphological changes, eruption deposits, and processes were discussed in detail by Komorowski et al. (2013) and Charbonnier et al. (2013).

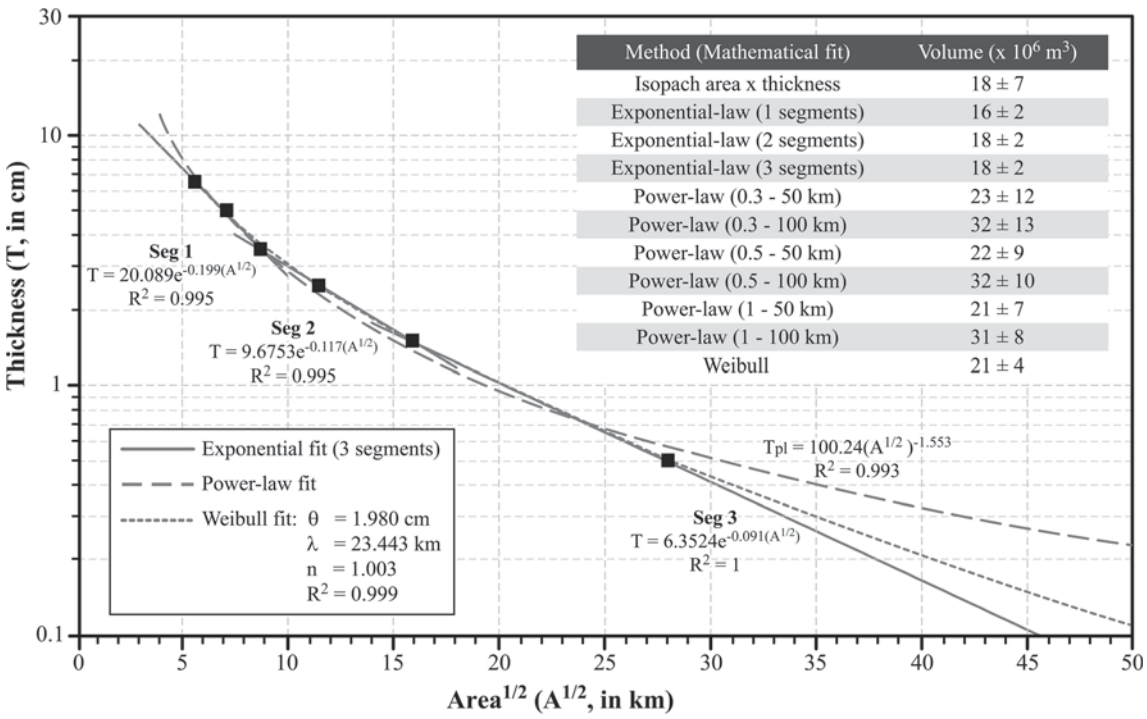

Fig. 5 Semilog plot of thickness against the square root of isopach area for the tephra fall of the 2010 Merapi eruption based on the following: a two-segment exponential fit (Fierstein and Nathenson 1992), power-law (Bonadonna and Houghton 2005), and Weibull (Bonadonna and Costa 2012) methods. The volume ranges of tephra-fall deposit are shown in the *inset table*

The eruption formed a large (400 m east–west × 350 north–south) summit crater that replaced the pre-2010 dome area and the former remnant of the 2006 lava dome and removed the 1940 lava flows and parts of the 1954, 1956, 1957, 1992, 1997, and 1998 lava flows. The rectangular-shaped crater walls cut down deeply (>100 m) in the thick lava dome lobes and stubby flows that were emplaced during the twentieth century. The south rim of the 2010 crater coincides with the 1961 crater, although the 2010 crater area is 40 % larger than the 1961 vent. Inside the crater, a high rate (35 m^3/s over 12 h) of lava extrusion on 6 November 2010 (Pallister et al. 2013) formed a lava dome 200 m in diameter with an area of 23, 000 m^2 and a 15-m-wide central vent (Fig. 6c, d). The volume of the lava dome may have been reduced, and the central vent may have been enlarged, by the short explosive events taking place since 2010 (e.g., on 18 November 2013 and 9 March 2014). The subsiding block, which might have acted as a vent during the eruption (Pallister et al. 2013), is located on the northwest and south of the 2010 dome (Fig. 6c, d). The north side of the dome is occupied by a fumarolic area (Fig. 6c–e), which acted as a source of the moderate phreatic and/or vulcanian explosions on 22 July and 18 November 2013.

The "Gendol breach" (Camus et al. 2000), a major southeast-trending elongated deep canyon that incises the SE flank of Merapi toward the headwaters of the Gendol River, was significantly lengthened (ca. 1.75 km) and deepened (ca. 250 m) (Fig. 6c–e). The Gendol breach is an unstable area likely to be enlarged by mass wasting, given that the northeast-facing wall, the longest and highest of the structure, is composed of unconsolidated and hydrothermally altered material. Moreover, the southeast portion of the crater wall immediately above the Gendol River is formed by a prominent 250-m-wide sliding lava dome that has lowered the crater rim by at least 100 m. The extensive fracturing and loose composition of the vertical crater walls engenders frequent rockfalls, landslides, and undercutting.

Vegetation and soil were stripped by the 2010 PDCs down to 1300-m elevation on the southwest, south, and southeast flanks below the summit lava domes, which, prior to the eruption, were bare only above 1800-m elevation. The lava flows on the northeast, east, south, and southwest flanks show a closely spaced pattern of furrows (e.g., across the 1888–1909 and 1900 lavas, Fig. 6b, e) formed by erosive PDCs descending from the summit area. Older pyroclastic sequences that mantled the upper southwest and west flanks show a pattern of closely spaced and deep gullies. This pattern most likely resulted from scouring by surface runoff, which remobilized tephra from the eruption during the first rainy season.

Extent and behavior of pyroclastic deposits in the Gendol-Opak catchments

The interpretation of the 15 November 2010 GeoEye image reveals a complex distribution of pyroclastic deposits below the summit, as discussed in previously published stratigraphic

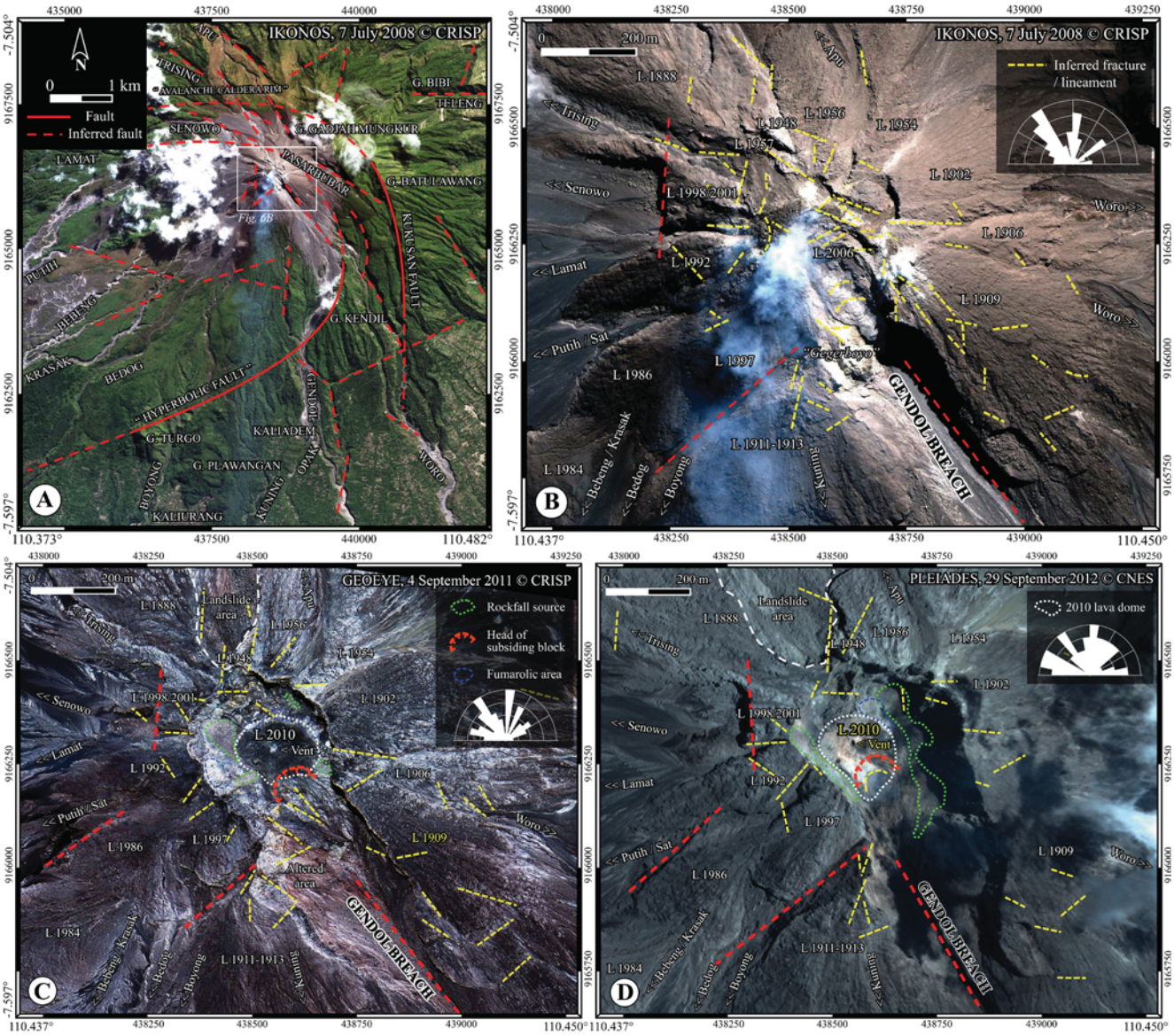

Fig. 6 Merapi's summit as interpreted from HSR images. **a** July 07, 2008, IKONOS image showing the structure and faults of the Merapi summit cone and **b** the distribution of summit lava domes and flows before the 2010 eruption. **c** September 04, 2011, GeoEye, and **d** September 29, 2012, Pléiades images showing the impact of the 2010 eruption for comparison with the image in **b**. These images are not georectified. **e** Sketch map of the Merapi summit indicating the location of the successive crater rims since 1822 (Voight et al. 2000; Camus et al. 2000), the Gendol breach enlarged in 2010, and the dates of their formation.

reports (Cronin et al. 2013; Komorowski et al. 2013; Charbonnier et al. 2013). The 50-cm resolution of the 2010 GeoEye image allowed the identification of 16 spectrally or texturally distinct areal units of PDC and tephra-fall deposits and recorded modification of landforms and impacts to settlements. In addition, we mapped lahar deposits that were emplaced during the 10 days after the paroxysmal phase and until a year and a half after the eruption. The geologic map does not include all lithofacies and the complex stratigraphic succession of the deposits as established by Cronin et al. (2013), Komorowski et al. (2013), and Charbonnier et al. (2013). Compared to maps published by Cronin et al. (2013), Komorowski et al. (2013), and Charbonnier et al. (2013), our geologic map provides a new detailed areal delineation and a synthetic view of the spatial distribution of PDC, tephra-fall, and lahar deposits from the summit to the ring plain on the southern and western flanks of Merapi. The exception to these is the more detailed distribution of high-energy surge deposits in the proximal area mapped by Komorowski et al. (2013). The geologic map shows how PDC and other deposits are distributed in five reaches along the Gendol-Opak Valley from the summit to the ring plain

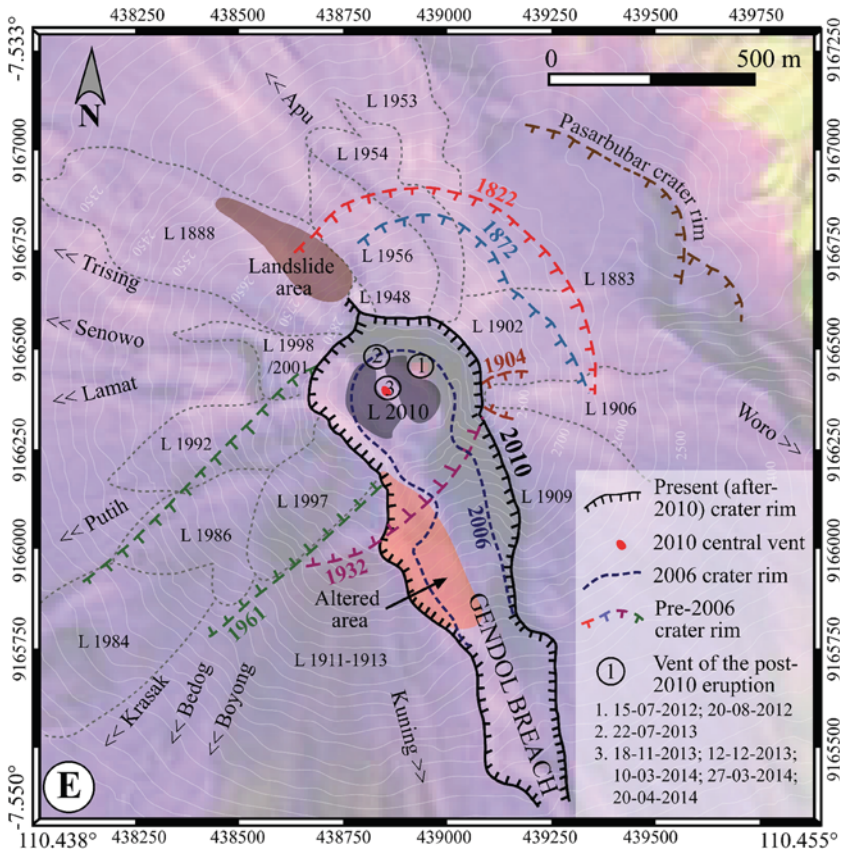

Fig. 6 (continued)

(Figs. 7 and 8). Reach boundaries were determined on the basis of differences in geomorphic and depositional characteristics: slope angle and breaks-in-slope as well as landform types including valley channel and terraces or banks, scarps, and fans, together with drainage density and hierarchy. Another distinction was based onto the location of PDC deposits, either confined to the valley channel or unconfined on valley banks and interfluves (Fig. 7; e.g., Kassouk et al. 2014). The topographic and geomorphic characteristics of the catchment played a role in the emplacement processes of PDCs. The areal extent of confined and unconfined PDC deposits apparently parallels radial valleys extending SSE in the Gendol-Opak catchment from proximal to distal sites, but the distribution pattern of PDC deposits is also transverse to the Gendol-Opak catchment. The uppermost catchment (reach 1) best illustrates the transverse areal extent of PDC deposits, while the geological map from the interpreted image shows how interfluves and valleys influenced the emplacement of PDCs across the catchment. Depositional changes are related to the breaks in slope (among other factors linked to the PDC behavior) that support the division of the valley into five reaches (Fig. 7). We have subdivided the first three reaches into two segments, each according to variation in the axial, transverse, and longitudinal distribution of deposits with respect to the Gendol River. The deposit types are categorized as HSR mapped geologic units and distinguished by color and number (see the map caption in Fig. 8e). Under this classification scheme (Fig. 8e), the deposits fall in four categories based on depositional processes and facies: (1) valley-confined PDCs, mostly BAFs; (2) overbank PDCs, produced by valley-confined PDCs (mostly BAFs and pumice or scoria-rich PFs) that spill over the valley banks and mantled interfluves; (3) high-energy surges, in the complex, proximal uppermost area; and (4) lahar deposits. Other non-PDC elements have been added (Fig. 8). We use the map unit numbers from Fig. 8 to describe selected deposits of special interest in five reaches.

Reach 1: southeast scar, Gendol breach, and head valley

Reach 1 encompasses the proximal summit slopes within 4 km from the vent, between ca. 2200 and ca. 1400 masl and with an area of ca. 5 km^2 (Fig. 7b). This reach was devastated by high-energy surges (Komorowski et al. 2013), which destroyed the forest and left the slopes almost bare over an area of 1.5 km^2. Important erosional features were well

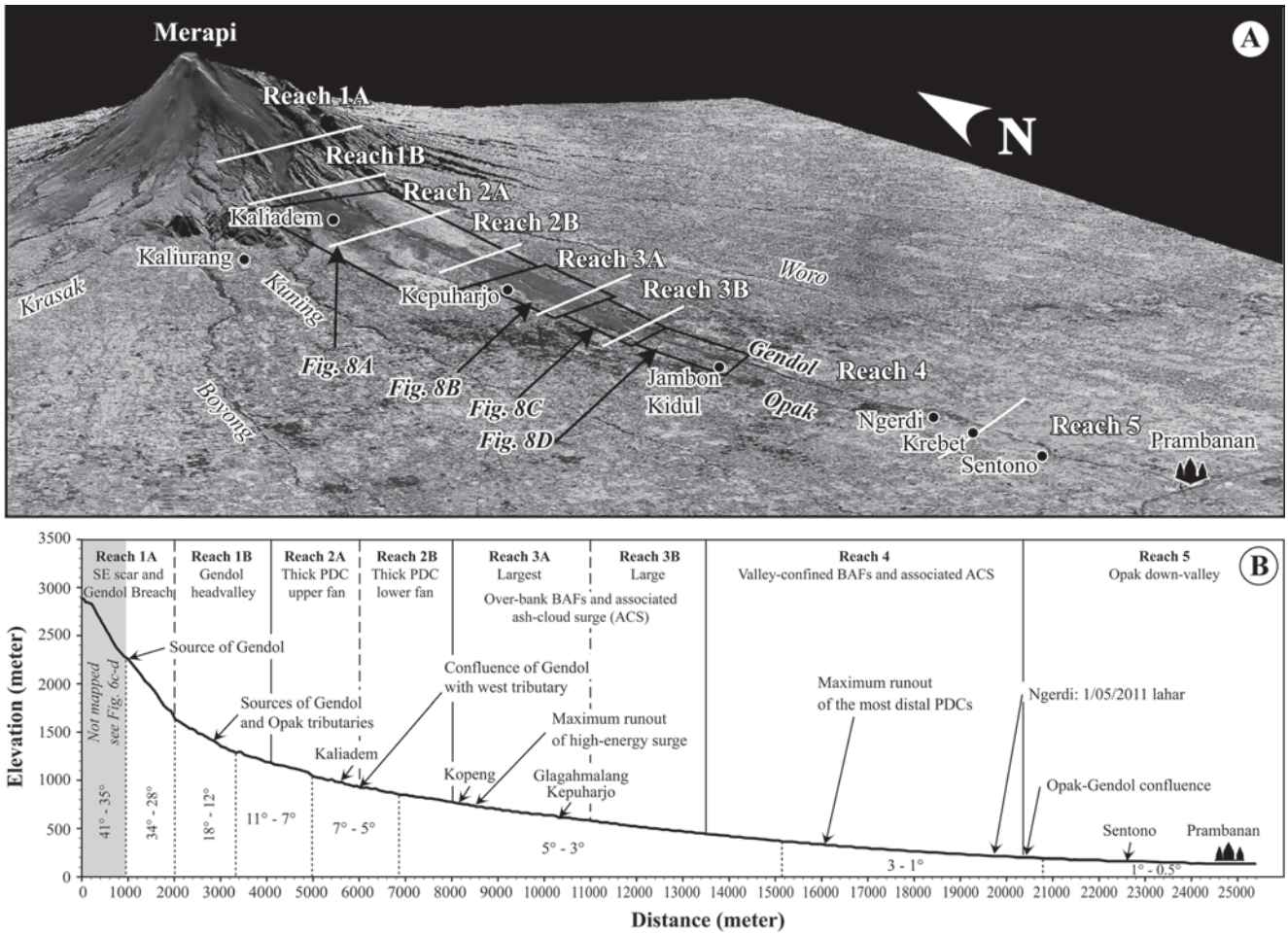

Fig. 7 **a** Oblique view of the Gendol valley from the Merapi summit to the distal ring plain near Prambanan temple shown by the 10 June 2011 SPOT5 image draped over a SRTM-DEM. **b** Longitudinal profile showing reaches 1–5 with average slope values, keyed to the text, and depicting the principal areas of PDC and lahar deposits, keyed to the captions of Fig. 8

displayed on the 4 September 2011 GeoEye image (Fig. 6c). Reach 1a consists of the steep (28°–34°) summit cone and the steeply sloping (35°–41°) 5-km-long Gendol breach between ~2250 m (source) and ~1600 masl. This erosional area is covered by 1–4-m-thick PDC deposits, which thicken in small tributaries of the Gendol breach. Reach 1B includes unconfined pyroclastic flow and high-energy surge deposits (unit 11 and part of unit 14, Fig. 8a, e), located within 4.5 km from the summit, which have destroyed forests and settlements on the steep uppermost slopes (18°–21°) above 950 masl. The dense forest was severely devastated, suggesting that these slopes were swept by high-energy surges (units 11 and 14 of Fig. 8) on 26 October and 6 November, as described in detail by Komorowski et al. (2013). Channeled flows in the deep valley of reach 1B consist of complex stacked piles of BAFs (units 2, 3, 12, and 13, Fig. 8a). Only the late (5–6 November) pumice and scoria-rich PDCs (Komorowski et al. 2013) were confined to valleys and are represented by deposits with wet top surface in the 15 November 2010 image in the uppermost course of the Gendol and Opak River courses (units 12 and 13). A small fraction of the 4–5 November 2010 PDCs was rerouted upon emplacement in the Opak valley and tributary (unit 3), into which these PDCs extended as far as 8.75 km from summit (Fig. 8a).

Reach 2: thick PDC fan

Reach 2 is a thick, triangle-shaped PDC fan covering ca. 7.5 km^2 between ca. 1200 m and 750 masl. The upper part of this reach, reach 2A, is the extensive (7.5 km^2), thick, uppermost pyroclastic fan (unit 11) that extends below the first major break-in-slope at 1150–1200 masl between the summit cone and the upper flanks. This 3 km×2.5 km fan extends downslope 8 km from the summit to ~750 m in elevation (Fig. 8a). Extensive, 1–3-m-thick PDC deposits forming this fan have been interpreted as the products of high-energy surges (unit 11) that covered earlier and thicker BAF deposits on the 5 November 2010 (Komorowski et al. 2013; Charbonnier et al. 2013). The PDC deposits (mostly high-energy surges of the late eruption stage as seen on the 15

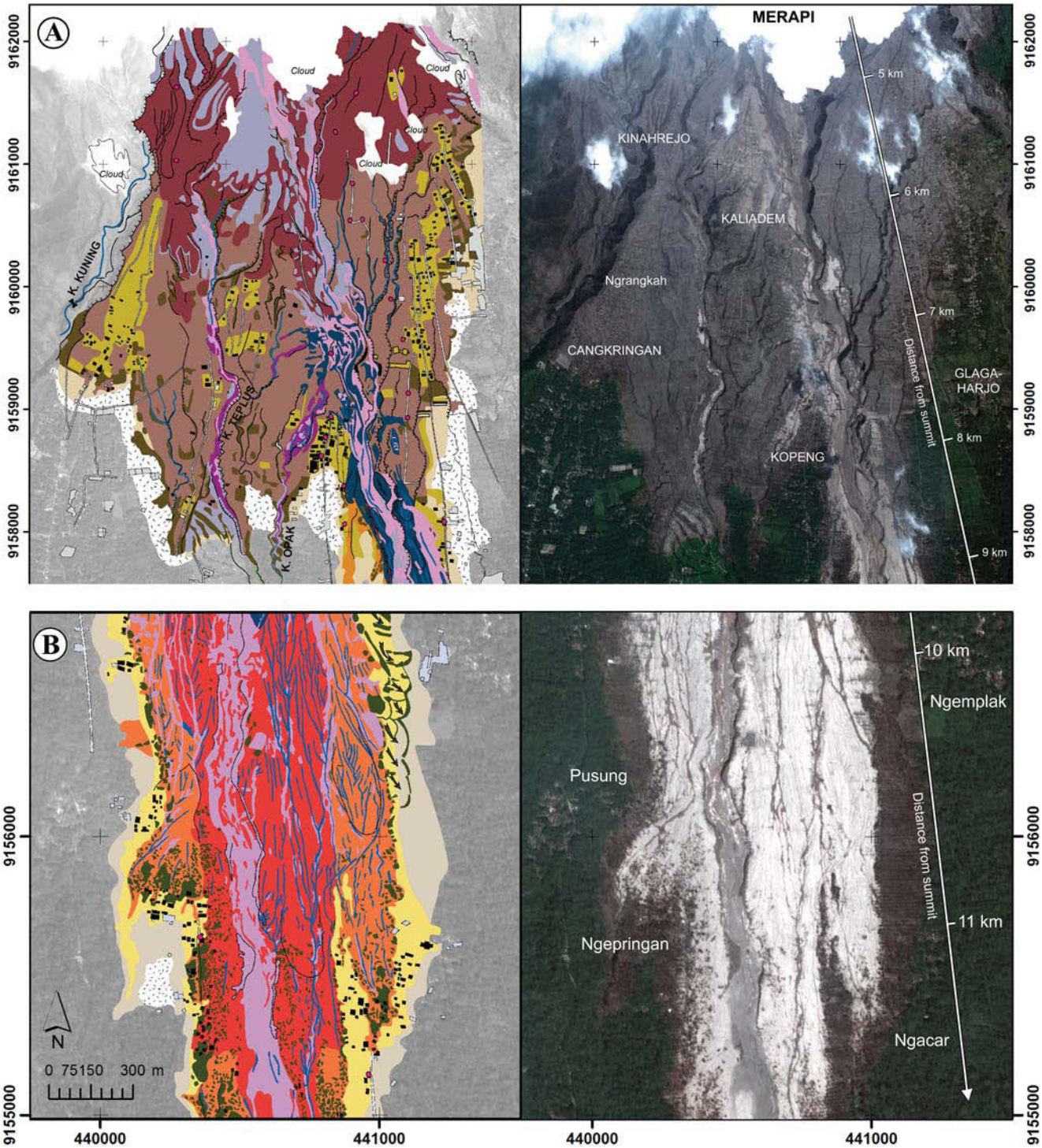

Fig. 8 Geologic map of the pyroclastic and lahar deposits from the 2010 eruption in the Gendol catchment based on our compilation from the 15 November 2010 GeoEye image and field observations. The GeoEye image is shown separately in the *panels on the right side*. Location of the area is shown in Fig. 7. **a** Thick PDC fan in reach 2 located in the upper catchment. **b** Largest overbank BAF and associated ash-cloud surge (ACS) deposits forming reach 3A in the upper middle river course. **c** Largest overbank BAF and associated ACS deposits forming reach 3B in the lower middle river course. **d** Distal valley-confined BAF deposits and associated ACS deposits forming the reach 4 in the lowermost river course. **e** Description of the mapped units

November 2010 image) devastated villages and cultivated areas on the ~8° sloping interfluves above 750–850 masl (unit 14). Blown-down trees, devastated houses, concrete power poles, bridges, and damaged agricultural terraces reflect the effects of high-energy surges emplaced by the climactic 5 November 2010 eruption (Jenkins et al. 2013). Undulating

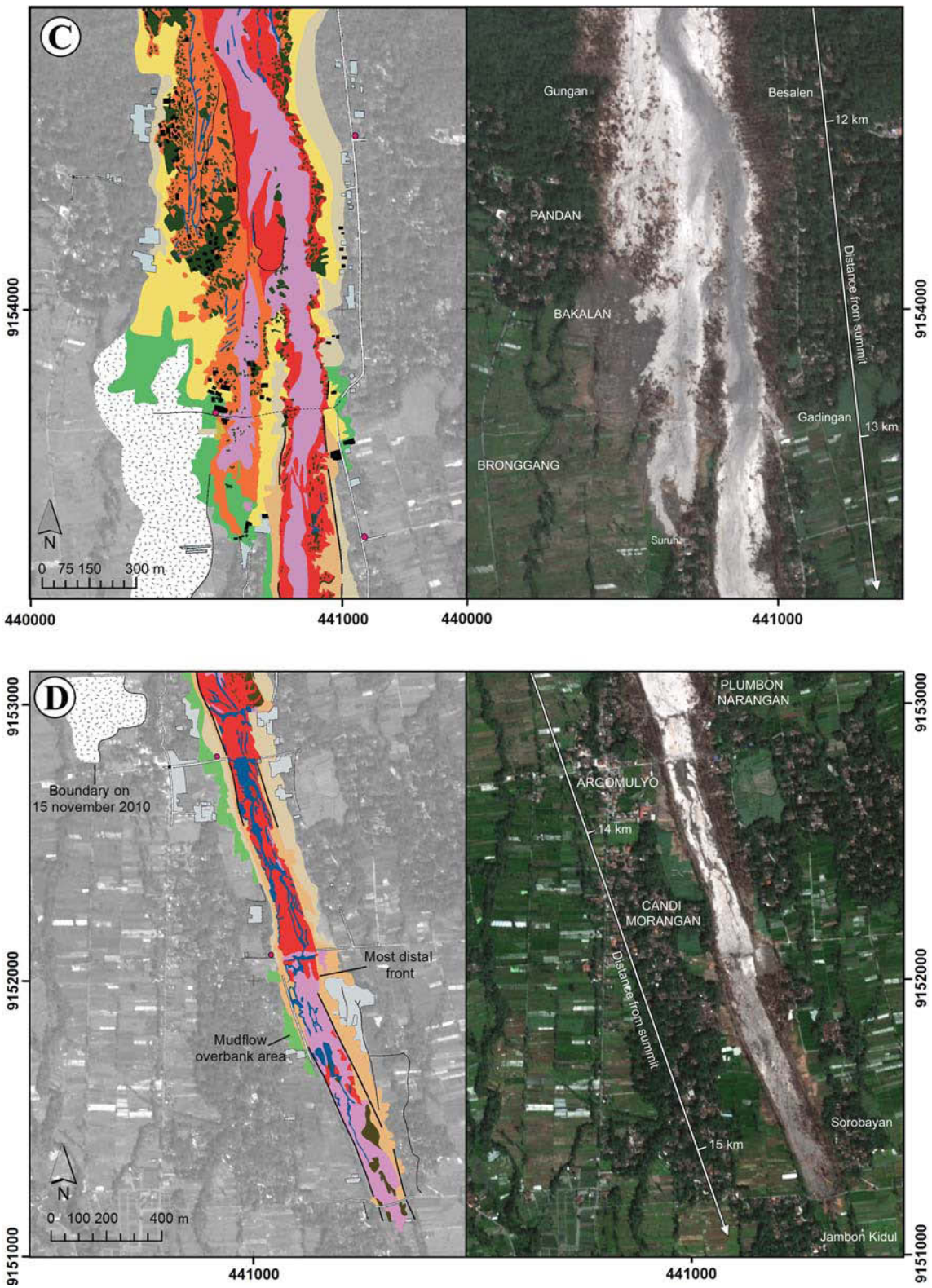

Fig. 8 (continued)

beds of gray ash deposited on the surface in this area suggest sandwave surge bedforms. The upper fan (units 3 and 12) has been eroded in 2011–2012 by the currently 50–60-m-deep Gendol River and its east tributary, which coalesce downslope at about 950-m elevation, and also by the Opak and Tepus valleys (Fig. 8a).

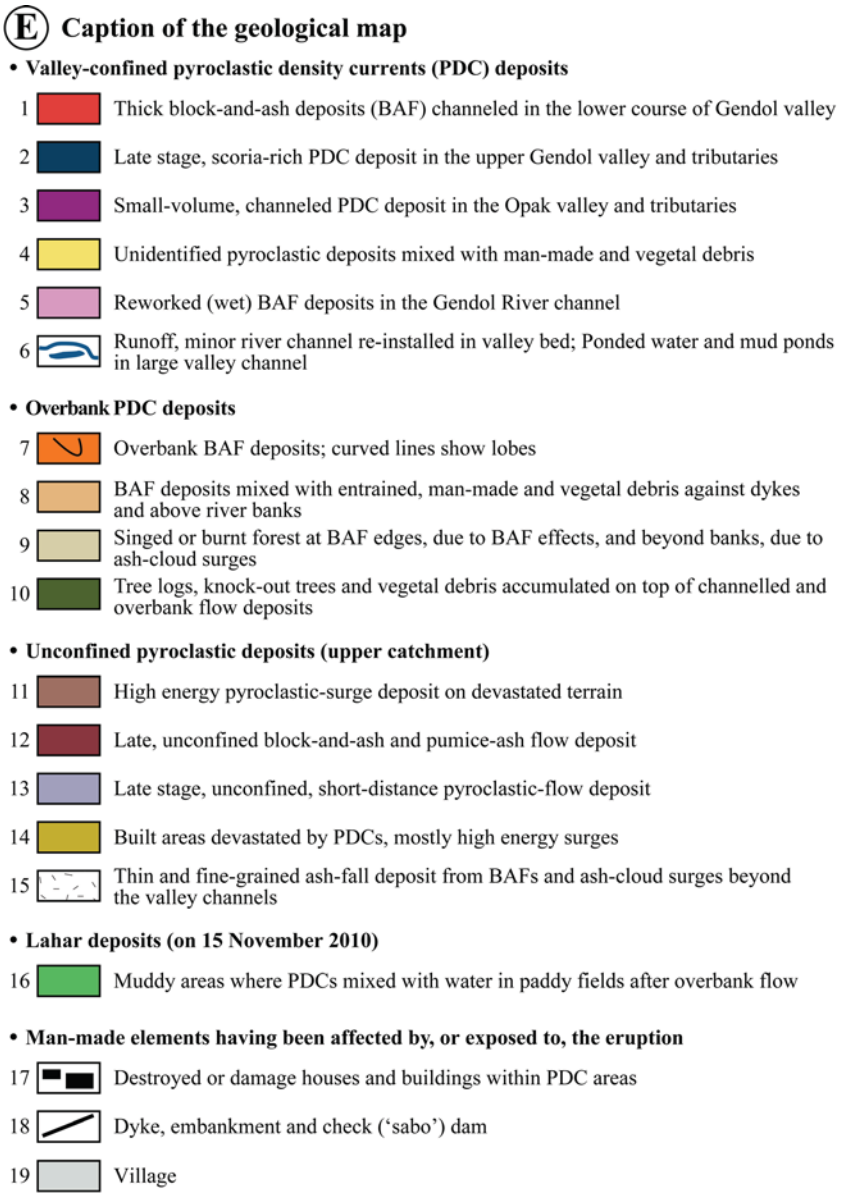

Fig. 8 (continued)

Reach 2B, the lower part of reach 2, is a wider (2.5–3 km), 20–30-m-thick pyroclastic fan (maximum thickness observed in the valley banks on top of the pre-2010 eruption soil) whose central axis changes from north–south to south-southeast. Its apex is located at the confluence of Gendol River and the east tributary near Kaliadem at 950 masl while the present-day Gendol River has cut down its eastern edge (Fig. 8a). The fan, 1.625 km wide near Kali Opak to the west to 1.25 km near Kali Kuning to the east, consists of extensive, thick lobes of overbank or veneer flows and surge deposits. Starting at the confluence at 9 km from the summit, the 120–190-m-wide and 50-m-deep winding Gendol channel was filled with thick (20–50 m) PDC deposits in 2010. However, in 2011, the channel has already cut as much as 20–30 m into the deposits and the pre-2010 bedrock. Lobes of darker, scoria-rich BAF deposits (unit 2) were also mapped in the Gendol channel below the confluence with the east tributary. The dark scoria-rich deposits were identified on the basis of the NDRSI and exhibit broad lobes with darker hues and higher roughness than other BAF deposits (Fig. 8a). These lobes adjacent to the main channel are clearly different from the later lahar material that cuts and fills the pristine overbank deposits after their emplacement.

Reach 3: large overbank BAF and associated ash-cloud surge deposits

Reach 3 covers a 0.5–1.2-km-wide fan with an area of ca. 3.6 km^2 that was formed on the Gendol valley margins and the interfluves between Opak and Kuning Rivers by thick overbank BAFs and companion ash-cloud surges between ca. 750 m and ca. 540 masl (Figs. 7 and 8a–c). Reach 3A consists of a 30-m-thick (observed in previous valley) and 1.2-km-wide PDC fan that begins at the second break in slope at ~750-m elevation (SE of Kopeng village) between 7 and 11 km from the summit (Fig. 8b). This largest PDC fan on the south flank includes a >30-m-thick pile of BAF deposits (unit 7) and darker scoria-rich flow deposits (unit 2) that spilled out from the Gendol channel over a 3°–5° slope. The overbank flows (unit 7) occurred where the slope angle declined from 7° to 5° (Fig. 8b) and the channel becomes rectilinear and shallower (30 m) and changes its orientation from SSE to south at ~780 masl. The apex of the largest BAF fan between Kepuharjo and Kopeng (~715 masl, Fig. 8a) starts at the lower end of a train of meanders. From the exit of the deep (50 m) Gendol valley near Kepuharjo, the BAFs spilled over the banks of the 20–30-m-deep former valley and produced veneer deposits (Fig. 8b). These are thicker and wider (750 m) toward the east than the west (500 m) due to the prevailing slope of this interfluve between Gendol and Opak Rivers toward the SSE.

Reach 3B corresponds to a large (1.2 km wide) fan of PDC deposits that becomes narrower (750 m) between 11 and 13 km down valley from Ngepringan (Fig. 8b). In the middle course of the Gendol Valley, BAFs spilled over the margins and left 1–3-m-thick overbank deposits (unit 7) at a change in slope angle from 3° to 2° (gradient from 0.1 to 0.06 m/m). This is the transition from the cone to the ring plain at elevations between 720 m and 540 masl. At a distance of about 11.5 km from the summit, overbank flows spread out from another meander in the Gendol River, where the orientation changes from north–south to NNW-SSE toward Bakalan (Fig. 8c). Upstream of Bakalan at 10 km from the summit, channeled deposits spread out toward the west 0.5 km beyond the former Gendol River where a sinuous gorge (50 m deep and 50–75 m wide) had a higher topographic gradient in this area prior to the 2010 eruption.

A damaged forest (unit 9) is present along both sides of the devastated valley between 8 and 13 km from the summit downstream from Kopeng (800 masl) and is associated in particular with overbank BAF deposits (Fig. 8a–c). HSR images identify both burnt and singed forest in two narrow (50–100 m), pinch-and-swell strips beyond the edges of the valley. The outer strip of singed forest, adjacent to the pristine forest, is distinguishable from the inner strip, adjacent to the bare overbank deposits, in which unidentified pyroclastic deposits are thoroughly mixed with entrained anthropogenic and organic debris on gentle slopes (unit 4). Accumulation of logs and organic debris mixed with construction debris and garbage is distinguished as a separate map unit 10. This unit is present in areas of devastated villages and their cultivated terraces (e.g., Bakalan, Fig. 8c). Numerous houses and some damaged buildings (black rectangles) are still standing in this area, although some that were almost buried cannot be recognized. Beyond the devastated areas, the mapped unit 15 depicts paddy fields or pristine forest mantled by a veil of fine-grained ash that settled from ash-cloud surges blown toward the west valley edge. This thin ash veil was mapped on the 15 November 2010 image before any heavy rainfall. This would not have been possible without the HSR image.

Reach 4: valley-confined BAF deposits and associated ash-cloud surge deposits

Reach 4 corresponds to the rectilinear lower reach of the Gendol valley extending from 13 to 16.5 km from the summit, which channeled the 2010 confined BAFs and 2011 lahars on a slope of ca. 3° (Fig. 8d). The longest confined BAF deposits (unit 1) occurred on 4–5 November 2010 (two main BAF units according to Komorowski et al. 2013). The nearly 4-m-thick BAF deposits extend for 14.5 km down the Gendol valley. The decreasing width (200–250 m) of overbank deposits on each valley edge in reach 4 is attributed to decelerating flows on a wider, coarser riverbed and higher topographic gradient valley. In addition, it appears that check dams, road bridges, and stonewalls contributed to constricting and obstructing the flows, leading to deposition. Between 13.5 and 16.5 km from the summit, the BAF deposits, which are mixed with anthropogenic and organic debris, form distinct narrow bands that coated the dikes on the riverbanks and small areas of overbank spill outs (unit 8). Extensive embankment walls, 4 m high and up to 2.5 km long, were erected before the eruption in the lower reach of the river valley below 450-m elevation as far as 13 km from the summit. The BAF deposits spilled over these embankments to mix with water from paddy fields and to produce mud ponds and short-runout breakout mudflows, inundating villages and additional paddy fields, mostly along the west valley margin (unit 16, e.g., Bakalan or Bronggang, Fig. 8c) and the lowermost river channel. Such breakout lahars occurred during the waning phase of the eruption between 6 and 15 November 2010 as inferred from the GeoEye image of 15 November 2010. These small mudflows are distinguishable from later lahars that formed in the Gendol and Opak River valley bottoms after the eruption (Fig. 8d compared to Fig. 9).

Wet block-and-ash deposits were produced as a result of limited reworking by runoff following rainfall after 6 November 2010. Based on the 15 November 2010 image, they are not mapped as lahar deposits, but PDC deposits reworked by runoff (unit 5) as observed in the Gendol River bed. Ponded water typically occupied ca. 20 % of the lower reach of the Gendol River on 15 November, and areas of flowing water correspond

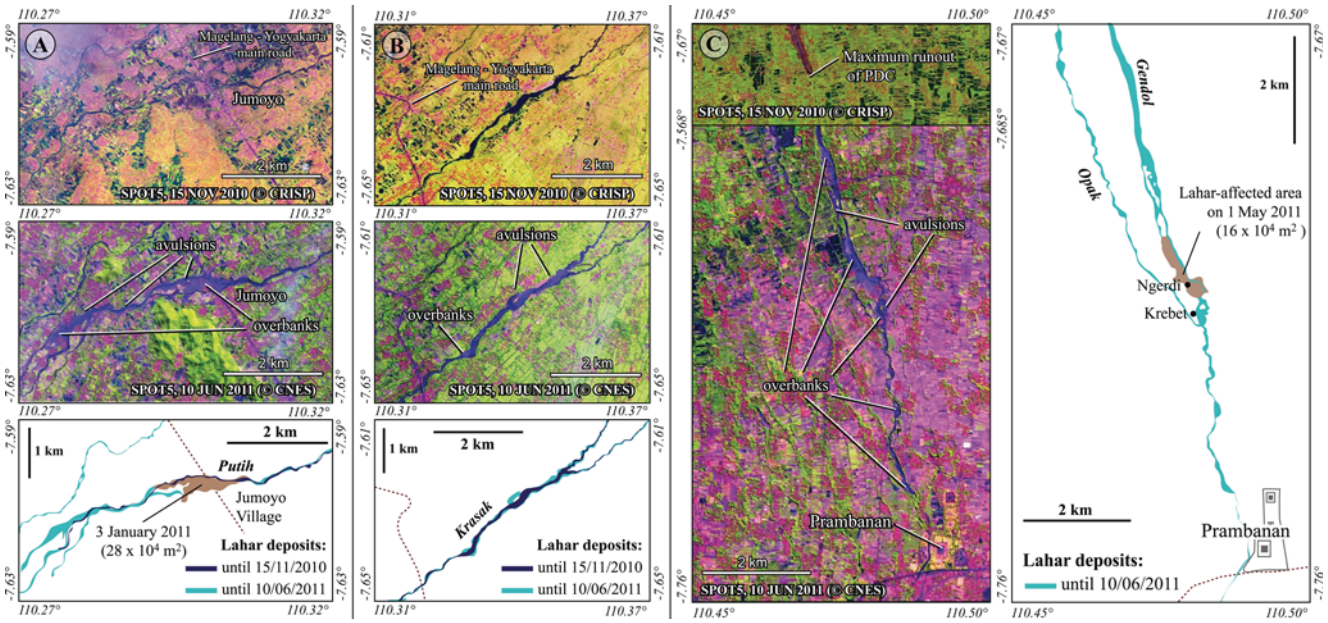

Fig. 9 Comparison between enlarged excerpts from the 15 November 2010 and 10 June 2011 SPOT5 images shows the extent of lahar deposits and highlights the effects of the 2011 lahar events along **a** Putih, **b** Krasak, and **c** Opak-Gendol Rivers

to springs and to resurgent river runoff at the interface between the PDC deposits and the former river bed (unit 6, Fig. 8e). This was observed as soon as the down-valley deposits were thoroughly mined in 2011.

Reach 5: Opak-Gendol down valley and lahar deposits beyond the BAF front

Reach 5 downslope of the Gendol valley is the lowermost valley reach that we mapped beyond the 2010 BAF front between 275 and 200 masl and at a distance of 16.25 to 20 km from the summit (Fig. 9c). After the eruption, lahars deposited sediment within the enlarged river bed of the Gendol behind check dams between Jambon Kidul and the confluence of Gendol and Opak rivers at 20.5 km down valley (Figs. 7 and 9c). At this distance, the Gendol river valley was able to channel hyperconcentrated stream flows and floods toward the area of the Prambanan temples another 5 km away. In May 2011, such flows reached the area of Sentono and Prambanan temples 25 km away from the summit (Figs. 7 and 9c).

Post-eruption lahar deposits in 2011

Voluminous lahars were frequent and voluminous on the west flank during the first two rainy seasons after the eruption, as the watersheds were covered by extensive, loose PDC, and ashfall deposits (Fig. 3). As many as 240 lahars occurred during the 2010–2011 rainy season (October 2010–May 2011), damaging 860 houses and 14 check dams and destroying 21 bridges (de Bélizal et al. 2013). A voluminous lahar (about 1.5 million m^3) occurred on 3 January 2011 and inundated an area of ca. 0.28 km^2. BNPB (the Indonesian National Board for Disaster Management) reported that the lahar destroyed 65 houses and damaged 118 houses in Jumoyo and four neighboring villages as well as two bridges on the main Magelang-Yogyakarta highway (Fig. 9a). More than 2000 people were evacuated from the villages located on the banks of the Kali Putih River while minor damage also occurred along the Kali Krasak River (Fig. 9b).

Large but less frequent lahars also occurred on the south flank. On 1 May 2011, additional lahars (about 1 million m^3) spilled out from the lowermost, narrow, and winding Gendol River, inundated ~0.16 km^2 on the west bank of the valley (Fig. 9c). This lahar buried Ngerdi with approximately 2 m of mud, destroyed 40,000 m^2 of crops, and damaged 51 houses (de Bélizal et al. 2013). These overbank lahars occurred along the most sinuous part of the river course where tributaries of the Gendol river cross low-relief slopes (<2 %) down valley from the confluence with the Opak river. These inundation areas are shown in maps derived from the 15 November 2010 and 10 June 2011 SPOT5 images along the Kali Putih and Kali Krasak Rivers (at distances of 18 and 15 km, respectively) on the southwestern flank and the Gendol River (19 km) on the southern flank of Merapi (Fig. 9).

Discussion

Instability of Merapi's crater rims

Any given dome growth, especially if associated with intense shallow volcanic seismicity, a regional earthquake, or

endogenous deformation of the summit area, can exert important strain on the fragile WSW walls of the summit crater. This could lead to the formation of another breached crater to the WSW, which could focus future PDCs toward the numerous valleys at the base of the west and southwest flanks of the volcano from Senowo to Boyong Rivers (Fig. 6). Northwest of the crater rim, landslides occurred in eroded and hydrothermally altered 1888 lava flows (Fig. 6c–e). If this activity continues, the landslide growth may breach the northwest rim of the crater. However, the most important threat for the population is linked to the Gendol breach (Fig. 6c–e), which is likely to act as a favored passage for future lava flows or PDCs, although the PDCs may shift toward the southwest, west, or northwest. The Gendol breach parallels a N140-trending fracture and a SE-trending fault group that cuts the southwest and northeast rims of the crater. In addition, a N230-trending fracture parallels the 1931 and 1961 scars. The crater rims with thin peaks and marked notches owe their very craggy shape to the explosive eruption processes. As the older dome rocks were destroyed by the crater, the walls showed extensive large-scale fracturing, fumarolic activity, and hydrothermal alterations, particularly to the west and southwest (Fig. 6c, d).

Behavior of the overbank PDCs and lahars

The complex phenomenon of overbank PDCs and lahars involves many parameters, such as flow depth, volume and dynamics, flow grain size, source mechanism, and the topography and geometry of the flow-confining valley (Lavigne et al. 2000; Lube et al. 2011; Andrews and Manga 2011; Charbonnier et al. 2013; de Bélizal et al. 2013). On Merapi's slopes, the construction of check dams and dikes also plays a role, especially concerning overbank PDCs (Lube et al. 2011; Andrews and Manga 2011). Overbank flows strongly depend on the geometry of the confining valley. The changes in channel capacity, channel geometry, and river gradient are critical

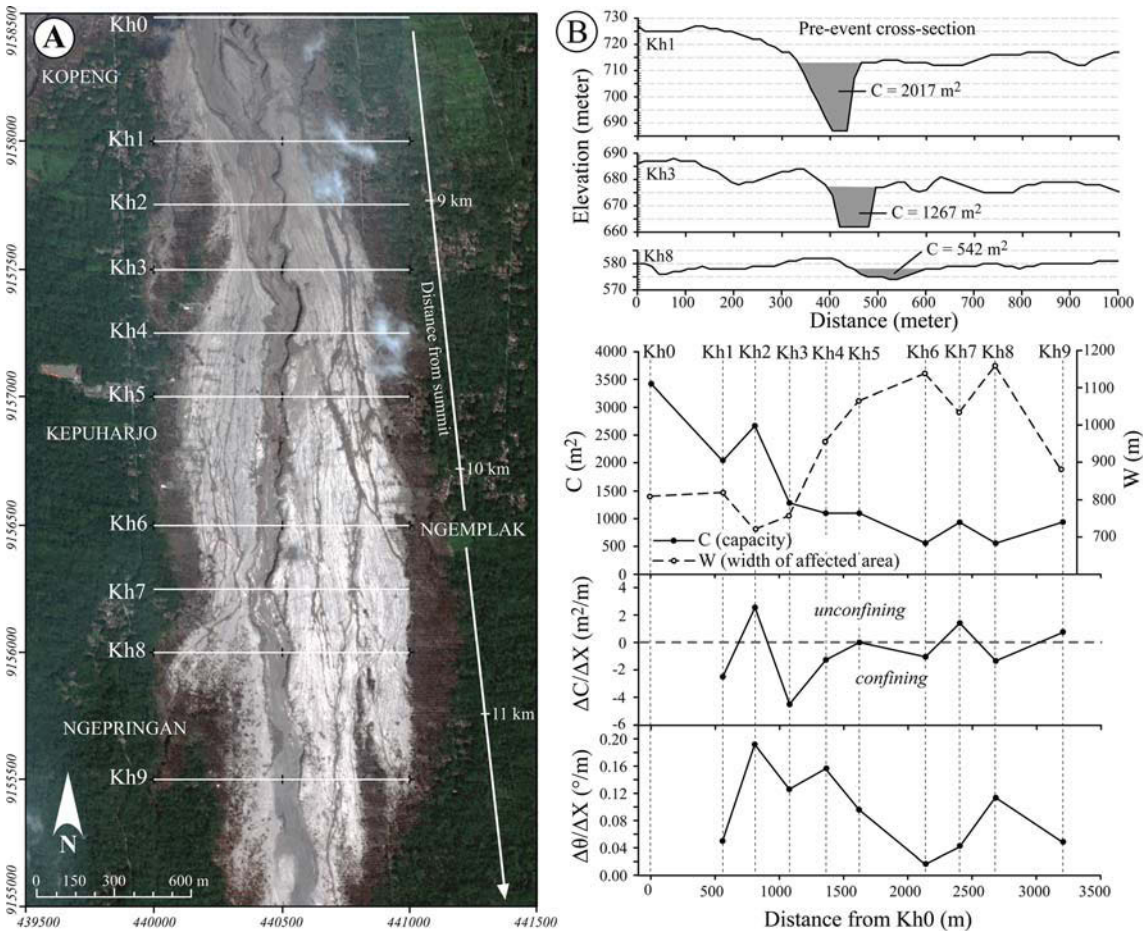

Fig. 10 Morphometric parameters of the Gendol River channel. **a** November 15, 2010, GeoEye image of the upper middle course of the Gendol Valley near the village of Kepuharjo showing a series of cross-sectional profiles of Kh0–Kh9. **b** One example of pre-event channel cross sections Kh1, Kh3, and Kh8 used to determine three morphometric indices: channel capacity (C in m^2; w, width of affected area, in m, longitudinal change in channel confinement ($\Delta C/\Delta X$ in m^2/m), and channel sinuosity ($\Delta\theta/\Delta X$ in deg/m). See Lube et al. (2011) for calculation technique

in terms of hazard assessment for people and villages near the river banks and down valley. We have investigated the relationships between the topography of the Gendol Valley, the morphology of the river channel, and the overbank process of PDCs and lahars using the deposit map (Figs. 3 and 8), the longitudinal profile (Figs. 10, 11, and 12), and the TOPO-DEM. Factors that favor flow overspill from the river channel include the channel cross-sectional area or capacity (C), the longitudinal rate of channel confinement ($\Delta C/\Delta x$), and the channel sinuosity ($\Delta\theta/\Delta x$) where x is the travel distance (Fig. 10b; Lube et al. 2011).

We have analyzed major changes through ten transects (Kh0–Kh9; Fig. 10) at distances of 8 to 11 km from the summit (near the villages of Kopeng and Kepuharjo), where PDC deposits formed a large apron of overbank and veneer deposits in reach 3A (Fig. 10). The Kh0–Kh9 cross-sectional profiles display deposits mostly from the 4–5 November PDCs (Komorowski et al. 2013; Charbonnier et al. 2013). Before the 4–5 November 2010 events, the channel between Kh0 and Kh3 was partly filled by the 3 November 2010 valley-confined PDCs (Charbonnier et al. 2013), which reduced the channel capacity by 5–8 % compared to the pre-event capacity if we assume the thickness of valley-confined PDCs to be 3 m. A clear correlation exists between the channel capacity and the width of areas characterized by overbank deposits (Fig. 10b) for which any reduction in channel capacity would lead to wider affected areas. The Kh3 section, where the PDC deposits expand laterally beyond the valley, exhibits the most negative value of longitudinal channel confinement (−4.5 m^2/m), together with the relatively high value of longitudinal change in channel sinuosity (0.13 deg/m). Kh3 is located at the end of the reach having both the largest channel capacity and the most meandering river channel.

Computation of channel geomorphic parameters from the HSR images and DEM is also useful to anticipate sites of future lahar overspills (e.g., Fig. 9), which can be enhanced by a decrease in channel capacity and the existence of sharp river bends. The case study of the May 2011 lahar that moved overbank at the village of Ngerdi for a distance of 1400 m down the Gendol Valley (Figs. 9c and 11) allowed us to compute geometric parameters for the river channel where lahars inundated about 0.16 km^2 mostly on the west bank (Fig. 11a). Figure 11 illustrates the pre-eruption valley cross sections with longitudinal distance at a 20-m spacing between the upper check dam in Bangsan Village (zero point, 19 km from the summit) and the lower check dam (end point) 100 m

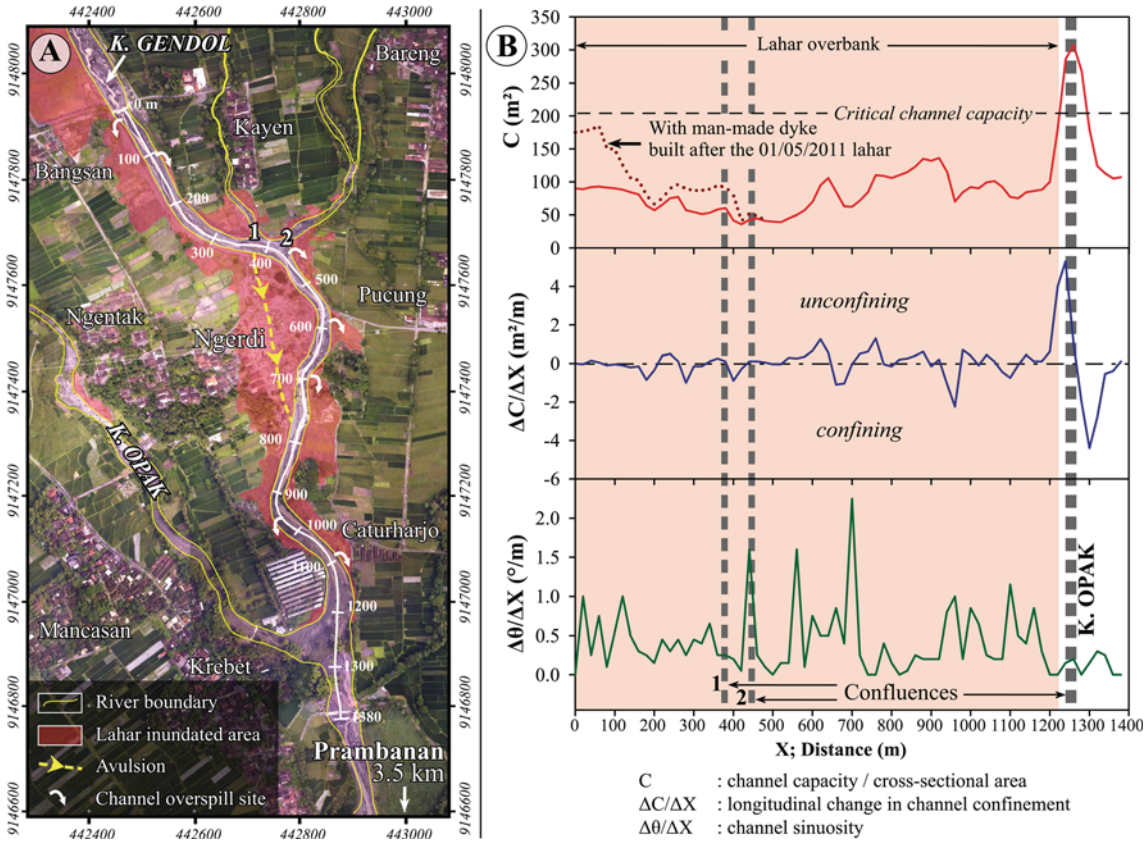

Fig. 11 **a** Low-altitude photograph of the Gendol Valley near the village of Ngerdi (19.5 km from Merapi summit) showing the 1 May 2011 lahar deposits. **b** Three morphometric indices have been computed: channel capacity (C in m^2), longitudinal change in channel confinement ($\Delta C/\Delta X$ in m^2/m), and channel sinuosity ($\Delta\theta/\Delta X$ in deg/m). Channel overspill sites (*white arrow*) occur where the channel sinuosity is high (>1 deg/m)

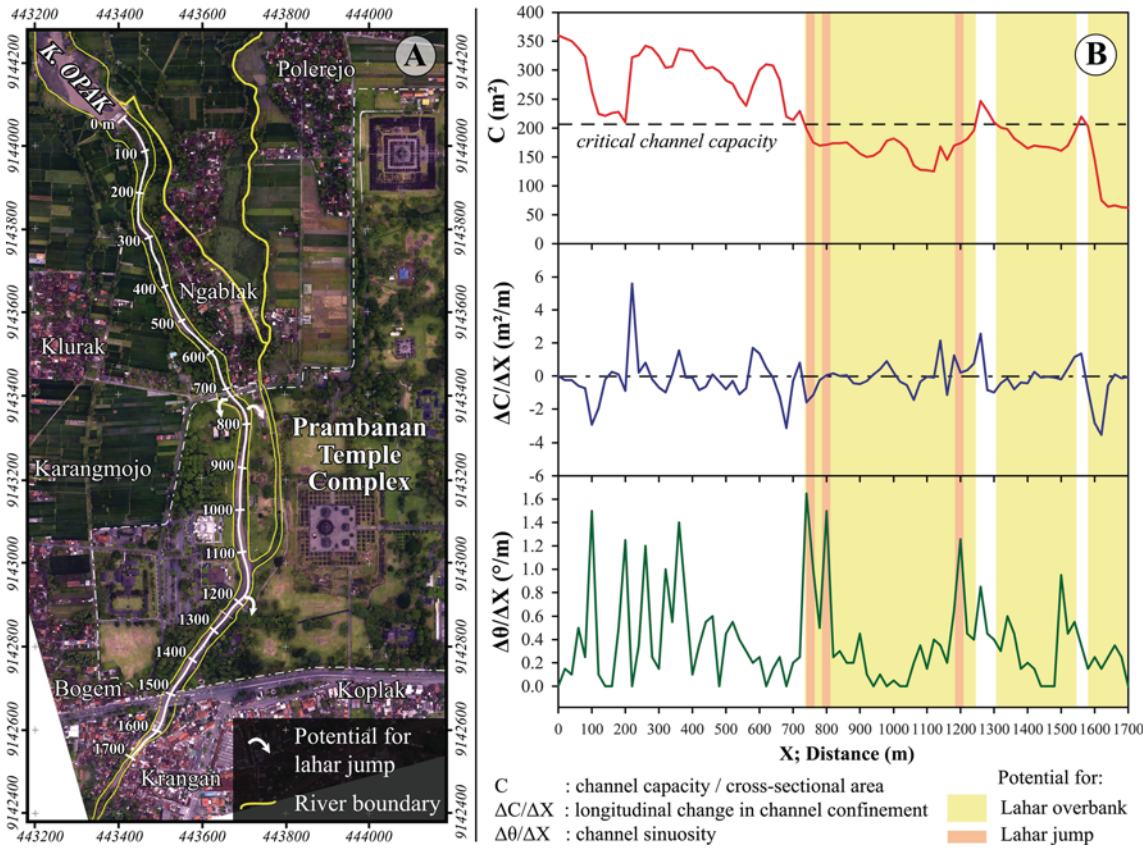

Fig. 12 **a** Low-altitude photograph of the Opak-Gendol Valley near the Prambanan temple (25 km from Merapi summit) with the outlined profile of **b** the three morphometric indices: channel capacity (C in m^2), longitudinal change in channel confinement ($\Delta C/\Delta X$ in m^2/m), and channel sinuosity ($\Delta\theta/\Delta X$ in deg/m)

downstream the confluence of Gendol and Opak Rivers (20 km from the summit). Figure 11a shows the mapped extent of the lahar overbank at a distance of 1210 m from the zero point. In the lahar inundation areas (red zone in Fig. 11a), the wetted channel cross section is always less than 210 m^2, which is defined as the critical channel capacity. However, no overbank lahar occurred 1300 m downstream from the zero point although the channel capacity drops below 210 m^2 (Fig. 11b). This may be due to the distance factor and capacity expansion in the upper stream that result in a decrease in lahar volume and velocity.

Dikes were built using lahar deposits along the riverbank from the zero point up to 450 m in distance, in order to protect the villages. Although up to 100 m^2 has been added to the channel cross section, the engineered dikes are ineffective as the capacity of the channel remains lower than the 210-m^2 critical wetted cross section of the 1 of May 2011 lahar. The capacity curve C (Fig. 11b) reaches its minimum at the distance of 350–450 m, where the lahar avulsion occurred (Fig. 11a). For the channel segment with capacities less than 210 m^2, the longitudinal change in channel confinement, $\Delta C/\Delta X$, with distance (Fig. 11b) is less than 4 m^2/m and mostly less than 1 m^2/m, with no significant negative minima. The curve for $\Delta\theta/\Delta X$ (Fig. 11b) has seven maxima where channel sinuosity increases above 1 deg/m, three of which exceed 1.5 deg/m at distances of 450, 550, and 700 m from the zero point. High channel sinuosity, and hence potential for flow acceleration, in outer bends may lead to overbank/avulsion processes. Lahars currently threaten the area of the iconic Prambanan temple farther down the Opak River. Future lahars may travel farther downslope getting closer to the Prambanan temples and the Yogyakarta airport. We applied geomorphometric indices analyzed in the May 2011 Ngerdi village case study to the area near the Prambanan temples. In this area, we found three spots where channel sinuosity exceeds 1 deg/m and channel capacity is below 210 m^2 (Fig. 12). These spots are potential sites for future lahar overbank flows if the lahar volume and velocity are equal to or greater than the May 2011 Ngerdi event.

Volumes of the 2010 Merapi deposits

Previous studies have estimated the volumes of the Merapi 2010 erupted material, particularly the deposits in the Gendol-Opak catchment on the south flank. Estimating the PDC bulk volume is difficult owing to the lack of any high-resolution pre-eruption DEM. Charbonnier et al. (2013) estimated a bulk volume of about 36.3×10^6 m^3 of PDC deposits based on field data and HSR satellite imagery, while Bignami

Table 3 Areal and volumetric characteristics of the 2010 PDC and tephra-fall deposits from Merapi in the Gendol-Opak catchment

Location	Deposit	Surface ($\times 10^6$ m^2)	Mean thickness (m)	Bulk volume ($\times 10^6$ m^3)
Reach 1	PFs	0.36	4–6	1.8
	VOB	0.46	2–3	1.15
	Surges	4.39	0.05–0.15	0.44
Reach 2	PFs	0.52	25–35	15.6
	VOB	2.76	2–4	8.28
	Surges	13.04	0.1–0.4	3.26
Reach 3	PFs	0.39	10–20	5.85
	VOB	2.68	2–4	8.04
	Surges	1.3	0.01–0.1	0.07
Reach 4	PFs	0.28	3–5	1.12
	VOB	0.15	0.1–1	0.08
	Surges	0.4	0.01–0.1	0.02
Gendol–Opak catchment Total	PFs	1.55	3–35	24.37
	VOB	6.05	0.1–4	17.55
	Surges	6.55	0.01–0.1	3.79
	PDCs	26.33		45.71±10[a]
NW, W, and SW flanks	PDCs	8.93	0.1–3[b]	7.08±4[b]
All	T-fall	~1300		21±4[c]

PF valley-confined pyroclastic flow, *VOB* veneer and/or overbank pyroclastic flow, *surges* high-energy and ash-cloud surges, *T-fall* tephra fall

[a] PDC volume by previous study: 20–40×10^6 m^3 (Surono et al. 2012), 36.3×10^6 m^3 (Charbonnier et al. 2013), 40×10^6 m^3 (Bignami et al. 2013), at least 41–50×10^6 m^3 (Komorowski et al. 2013), and 48.62×10^6 m^3 (Cronin et al. 2013)

[b] Underestimated or overestimated due to the lack of thickness measurements

[c] Weibull method

et al. (2013) determined a volume of ca. 40×10^6 m^3 using synthetic aperture radar (SAR) data. Komorowski et al. (2013) estimated using field data and HSR satellite imagery a bulk volume of ca. 41×10^6 m^3 for PDC deposits from stages 3 to 6 in the Gendol-Opak Rivers system to which the bulk volume of PDC deposits of stage 2 must be added that are included in the 6×10^6 m^3 DRE volume of the crater formed during stage 2 on 26 October 2010. Surono et al. (2012) determined a range of bulk volumes between 20 and 40×10^6 m^3 for the PDC deposits and between 10 and 20×10^6 m^3 for the tephra-fall deposits.

We calculated areas of each category of the PDC and tephra-fall deposits on the basis of CVGHM data and our image interpretation and field surveys, as we were not able to measure deposit volume for each of the eight stages of the eruption (Table 3). Using HSR (50 cm) imagery, we measured the total area covered by PDCs as 26±2×10^6 m^2 in the south flank and 9±2×10^6 m^2 for areas on the northwest, west, and southwest flanks combined. Based on our maps and GNSS measurements and the CVGHM estimates of thicknesses, PDC deposits (including valley-confined, overbank, veneer PFs, and high-energy and ash-cloud pyroclastic surge deposits) total a bulk volume of 45±10×10^6 m^3 (Table 3). The large uncertainty takes into account that the full thickness of the valley-confined 2010 deposits is not yet exposed in all valley reaches and considerable variations in thickness can be observed in thin veneer or thick overbank PDC deposits beyond the valley edges. The tephra-fall deposit covered an area of about 1300 km^2 with volumes of 18±2×10^6 m^3, 21±7×10^6 m^3, and 21±4×10^6 m^3 based on exponential (two and three segments), power-law (1–50-km integration limit), and Weibull methods, respectively (Fig. 5 and Table 3). However, our calculation is biased by the lack of tephra measurements on the summit. Overall, the Gendol-Opak catchment, which is located SE of the tephra dispersal lobes (Figs. 3 and 6), contains about 10–15 % of the total volume of the tephra-fall deposit but encompasses as much as 65–70 % of the total PDC bulk volume.

Conclusion

The 26 October–23 November 2010 eruption is Merapi's largest event (VEI 4) over the past 140 years. HSR images from the GeoEye satellite, collected on 15 November 2010, allowed us to test the capability of remote sensing in identifying and differentiating a complex spectrum of pyroclastic deposits and also interpreting the effects of the 2010 PDCs on Merapi's landforms, vegetation, and settlements. We chose the Gendol-Opak Rivers on the south flank for intensive study because the available GeoEye images with 0.5-m resolution show considerable detail in this region. This area of Merapi was the most affected by the eruption and contained 60–75 % (bulk volume) of the total volume of the 2010 PDC deposits. The channeled PDC deposits reached a significant distance of 16.5 km and were associated with ash-cloud surges, while unconfined PDCs and high-energy surge deposits formed a 3- to 5-km-wide apron of deposits on the upper slopes. The 15 November 2010 GeoEye image provided a snapshot during the waning phase of the eruption, allowing us to recognize (1) fresh landforms and deposits associated with valley-confined and unconfined PDCs; (2) severe PDC impacts on devastated villages and housing, cultivated terraces, and forests; (3) mudflows fed by water from rice fields beyond the river banks overrun by PDC deposits; and (4) small features such as flow lobes, levees, tree logs, and debris strewn on the top surface of pyroclastic flow deposits. Additional SPOT5 and GeoEye images enabled us to map lahars that travelled down three drainages on the west and south flanks a year and half after the eruption.

We reappraise the hazard assessment for the south flank of Merapi (Thouret et al. 2000). The 2006 Yogyakarta

earthquake and emplacement of the 2006 PDCs led to the collapse of the buttressing southern rim of the summit and deep incision of the upper part of the Gendol River (Gendol breach) directed to the SE. However, the exceptional run-out of PDCs in 2010 to 16.5 km was unexpected. Our new hazard assessment indicates the following issues (areas, deposits, and processes) at stake in the near future.

1. The new, enlarged, and deep summit crater is unstable. Rockslides originate from either the steep inward or outward facing rims. Phreatic, phreatomagmatic, or small vulcanian events such as the 22 July 2013, 18 November 2013, and 9 March 2014 eruptions (BPPTK/Merapi Volcano Observatory reports) will pose threats to visitors and scientists around the summit area and can weaken the already unstable rims of the summit crater.
2. The enlarged summit scar and the Gendol breach may act as a pathway for future flows, and the high, steep, fractured, and hydrothermally altered walls of the breach are subject to rockfalls and earthquake-triggered landslides. The voluminous unconsolidated 2010 deposits in the breach and in the gorge down valley (reach 1A), together with the newly exposed hydrothermally altered rocks, will continue to feed lahars in the future.
3. Unlike the thick PDC fans on the upper slopes, where half of the surface has been colonized by vegetation, a large amount of sediment accumulated in all valleys is still bare and being remobilized by lahars. In particular, the PDC deposits channeled in the Gendol River between 8 and 11.5 km from the summit and the upper PDC fan in the vicinity of Kaliadem (Fig. 7) and the Gendol gorge currently supply lahars to the ring plain as far as 20 km from the summit.
4. The drainage network may transfer lahars beyond our study area until the pyroclastic deposits have been entirely removed within a few years. Field evidence shows that such reworking is developing at a fast rate. Lahars derived from the remobilization of ~45 million m^3 of PDC deposits are less frequent on the south flank but typically larger in volume than those on other flanks (de Bélizal et al. 2013). However, mining extraction since 2011 has already removed the majority of the PDC deposits within the Gendol channel ranging from a distance of 7 km from the summit (upstream of Kopeng, Fig. 7) to the 2010 PDC front down valley (Jambon Kidul, Fig. 7).
5. Lahar overspill is the most hazardous process acting along the lowermost river courses of Kali Putih toward the city of Magelang and along the Gendol-Opak Rivers which transport material toward the Prambanan temples and toward the Yogyakarta airport. Long stretches of narrow channels were inundated by sand-size sediment between 16.5 (Jambon Kidul) and 19.5 km (Krebet, Fig. 7) in 2011 and 2012. Lahar disasters in 2011 can be attributed to the low topographic valley gradient (0.04 m/m) of meandering rivers across the <2° ring plain and the limited capacity (200–300 m^2) of river channels. Lahars currently threaten the area of the iconic Prambanan temple farther down the Opak River. Future lahars may travel farther downslope getting closer to the Prambanan temples and the Yogyakarta airport. By applying geomorphometric indices analyzed in the May 2011 Ngerdi village case study, we found that three spots near the Prambanan temples are potential sites for future lahars overbank processes.

The 50-cm resolution of the satellite images allowed identification of 16 areal units of tephra and PDC deposits, modifications of the summit area, impacts on settlements, and mapping lahar deposits within a year and half of the eruption. Although the remotely sensed geologic maps cannot include the complex stratigraphic succession of the deposits (see Charbonnier et al. 2013; Komorowski et al. 2013), the technique allows us to determine a more complete spatial distribution of PDC, tephra, and lahar deposits on the entire volcano from the summit to the ring plain of Merapi. Remotely sensed data enable us to trace the temporal evolution of a pyroclastic eruptive sequence as a result of erosion, removal, and recolonization by vegetation. Moreover, its ability to capture fresh, pristine features and extent of deposits shortly after emplacement and before any reworking highlight the purpose of using HSR imagery on persistently active volcanoes where access for field surveys is often impossible.

Acknowledgments We would like to thank the reviewers (J-C. Komorowski and S. Charbonnier) for their comments and suggestions, which greatly improved the quality of the paper. The support from several partner institutions is acknowledged: the French Embassy for A. Solikhin's PhD grant, the ANR RiskNat project for J-C, Thouret fieldwork, CNES for the SPOT5 images, and CRISP-NUS and ICT Asia for the GeoEye images. J. Pallister and J. Griswold (VDAP, USGS) are thanked for consultation and L. Thouret for artwork. This article received the support of the French National Research Agency within the project "Laharisk" (ANR-09-RISK-005), DOMERAPI (ANR-12-BS06-0012), and the CNES-TOSCA Project "Merapi" (2012 and 2014).

References

Andrews BJ, Manga M (2011) Effects of topography on pyroclastic density current runout and formation of coignimbrites. Geology 39(12): 1099–1102

BAPPENAS, BNPB (2011) Rencana aksi rehabilitasi dan rekonstruksi wilayah pasca bencana erupsi Gunung Merapi di Provinsi D.I. Yogyakarta dan Provinsi Jawa Tengah 2011–2013 (The action plan of post-disaster rehabilitation and reconstruction of Merapi volcano eruption in Yogyakarta and Central Java Provinces, 2011–2013). BAPPENAS and BNPB, Jakarta, p 205

Bignami C, Ruch J, Chini M, Neri M, Buongiorno MF, Hidayati S, Sayudi DS, Surono (2013) Pyroclastic density current volume estimation after the 2010 Merapi volcano eruption using X-band SAR. J Volcanol Geotherm Res 261:236–243

Bonadonna C, Costa A (2012) Estimating the volume of tephra deposits: a new simple strategy. Geology 40:415–418

Bonadonna C, Houghton BF (2005) Total grain-sized distribution and volume of tephra-fall deposits. Bull Volcanol 67:441–456

BPS (2010) Daerah Istimewa Yogyakarta Dalam Angka, 2010 (Daerah Istimewa Yogyakarta in Figures, 2010). Biro Pusat Statistik (Statistics Bureau) of DI Yogyakarta Province, Yogyakarta, Indonesia, p 560

Branney MJ, Kokelaar BP (2002) Pyroclastic density currents and the sedimentation of ignimbrites. Geol Soc Lond Mem 27:143

Camus G, Gourgaud A, Mossand-Berthommier PC, Vincent PM (2000) Merapi (Central Java, Indonesia): an outline of the structural and magmatological evolution, with a special emphasis to the major pyroclastic events. J Volcanol Geotherm Res 100:139–163

Charbonnier S, Gertisser R (2008) Field observations and surface characteristics of pristine block-and-ash flow deposits from the 2006 eruption of Merapi Volcano, Java, Indonesia. J Volcanol Geotherm Res 177:971–982

Charbonnier SJ, Gertisser R (2011) Deposit architecture and dynamics of the 2006 block-and-ash flows of Merapi Volcano, Java, Indonesia. Sedimentology 58:1573–1612

Charbonnier SJ, Germa A, Connor CB, Gertisser R, Preece K, Komorowski J-C, Lavigne F, Dixon T, Connor L (2013) Evaluation of the impact of the 2020 pyroclastic density currents at Merapi volcano from high-resolution satellite imagery, field investigation and numerical simulations. J Volcanol Geotherm Res 261:295–315

Cronin SJ, Lube G, Sayudi DS, Sumarti S, Surono, Subandriyo (2013) Insights into the October–November 2010 Gunung Merapi eruption (Central Java, Indonesia) from the stratigraphy, volume and characteristics of its pyroclastic deposits. J Volcanol Geotherm Res 261: 244–259

de Bélizal E, Lavigne F, Hadmoko DS, Degeai J-P, Dipayana GA, Mutaqin BW, Marfai MA, Coquet M, Mauff BL, Robin A-K, Vidal C, Cholik N, Aisyah N (2013) Rain-triggered lahars following the 2010 eruption of Merapi volcano, Indonesia: a major risk. J Volcanol Geotherm Res 261:330–347

Fierstein J, Nathenson M (1992) Another look at the calculation of fallout tephra volumes. Bull Volcanol 54:156–167

Gerstenecker C, Läufer G, Steineck D, Tiede C, Wrobel B (2005) Validation of digital elevation models around Merapi Volcano, Java, Indonesia. Nat Hazards Earth Syst Sci 5(6):863–876

Gertisser R, Charbonnier SJ, Keller J, Quidelleur X (2012) The geological evolution of Merapi volcano, Central Java, Indonesia. Bull Volcanol 74(5):1213–1233

Global Volcanism Program (2007) Report on Merapi (Indonesia). In: Wunderman R (ed) Bulletin of the Global Volcanism Network, 32: 2. Smithsonian Institution, pp 3–8

Jenkins S, Komorowski J-C, Baxter PJ, Spence R, Picquout A, Lavigne F, Surono (2013) The Merapi 2010 eruption: an interdisciplinary impact assessment methodology for studying pyroclastic density current dynamics. J Volcanol Geotherm Res 261:316–329

Kassouk Z, Thouret J-C, Solikhin A, Gupta A, Liew SC (2014) Object-oriented classification of very high resolution panchromatic imagery for geologic mapping of an active volcano: Semeru volcano, Indonesia. Geomorphology 221:18–33

Komorowski J-C, Jenkins S, Baxter PJ, Picquout A, Lavigne F, Charbonnier S, Gertisser R, Preece K, Cholik N, Budi-Santoso A, Surono (2013) Paroxysmal dome explosion during the Merapi 2010 eruption: processes and facies relationships of associated high-energy pyroclastic density currents. J Volcanol Geotherm Res 261: 260–294

Lavigne F, Thouret J-C, Suwa H (2000) Lahars at Merapi: an overview. J Volcanol Geotherm Res 100:423–456

Lube G, Cronin SJ, Thouret J-C, Surono (2011) Kinematic characteristics of pyroclastic density currents at Merapi and controls on their avulsion from natural and engineered channels. Geol Soc Amer Bull 123(5–6):1127–1140

Mei ETW, Lavigne F, de Bélizal E, Brunstein D, Picquout A, Grancher D, Sartohadi J, Cholik N, Vidal C (2013) Lesson learned from the 2010 evacuation at Merapi Volcano. J Volcanol Geotherm Res 261:348–365

Pallister JS, Schneider DJ, Griswold JP, Keeler RH, Burton WC, Noyles C, Newhall CG, Ratdomopurbo A (2013) Merapi 2010 eruption—chronology and extrusion rates monitored with satellite radar and used in eruption forecasting. J Volcanol Geotherm Res 261:144–152

Pyle DM (1989) The thickness, volume and grainsize of tephra fall deposits. Bull Volcanol 51(1):1–15

Sayudi DS, Aisyah N, Juliani Dj, Muzani M (2010) Peta Kawasan Rawan Bencana Gunungapi Merapi, Jawa Tengah dan Daerah Istimewa Yogyakarta 2010 (Merapi Hazard Map, Central Java and Yogyakarta Special Region Provinces). Center for Volcanology and Geological Hazard Mitigation (CVGHM), Bandung

Siebert L, Simkin T, Kimberly P (2010) Volcanoes of the world, 3rd edn. University of California Press, Berkeley, p 568

Smith GA, Fritz WJ (1989) Volcanic influences on terrestrial sedimentation. Geology 17:375–376

Solikhin A, Thouret J-C, Gupta A, Harris AJL, Liew SC (2012) Geology, tectonics, and the 2002–2003 eruption of the Semeru volcano, Indonesia: interpreted from high-spatial resolution satellite imagery. Geomorphology 138:364–379

Surono, Jousset P, Pallister J, Boichu M, Buongiorno MF, Budisantoso A, Costa F, Andreastuti S, Prata F, Schneider D, Clarisse L, Humaida H, Sumarti S, Bignami C, Griswold J, Oppenheimer C, Lavigne F (2012) The 2010 explosive eruption of Java's merapi volcano—a '100-year' event. J Volcanol Geotherm Res 241–242:121–135

Thouret J-C, Lavigne F, Kelfoun K, Bronto S (2000) Toward a revised hazard assessment at Merapi volcano, Central Java. J Volcanol Geotherm Res 100:479–502

Thouret J-C, Gupta A, Lube G, Liew SC, Cronin SJ, Surono (2010) The 2006 pyroclastic deposits of Merapi Volcano, Java, Indonesia: high-spatial resolution IKONOS images and complementary ground based observations. Remote Sens Environ 114:1949–1967

Voight B, Constantine EK, Siswowidjoyo S, Torley R (2000) Historical eruptions of Merapi Volcano, Central Java, Indonesia, 1768–1998. J Volcanol Geotherm Res 100:69–138

Chapter 5 - The 2010 Merapi pyroclastic deposits map based on satellite radar data

5.1. Introduction

The volcanology community has long recognized the advantages of synthetic aperture radar (SAR), a technique that allows high-resolution radar images to be created from data acquired by side-looking radar instruments, carried by aircraft or spacecraft (Curlander & McDonough, 1991). A great advantage of radar remote sensing is that its observations are independent of cloud cover, light rain, smoke haze and solar illumination due to active measurement and longer wavelength. SAR system provides imagery that characterizes the physical properties of the terrain surface. A SAR image has both an amplitude and a phase assigned to each resolution element on the ground illuminated by the radar. The amplitude of a SAR image can be interpreted in terms of backscattering properties of the Earth's surface. The phase is not informative on its own, as it contains a pseudo-random phase contribution from the configuration of scatterers within a resolution element on the ground. However, if two observations of the same terrain from very similar position are available, the difference in phase between two images can be interpreted in terms of the change in range from the radar instrument to the ground. This technique is called Interferometric SAR or InSAR with a capability to measure signals from eruption-related surface deformation (Massonnet et al., 1995; Zebker et al., 1996).

Earth observation by satellite SAR have resulted in numerous new insights into active volcanism, including a better understanding of subsurface magma storage and transport, deposition of volcanic material on the surface, and the structure and development of volcanic edifices (Pinel et al., 2014). During the 2010 Merapi crisis, SAR amplitude data have proven their interest by providing frequent and detailed images of the volcano to document and track changes at the summit, quantify lava dome discharge rate and extent of pyroclastic density currents (PDCs) (Pallister et al., 2013). This information was used to assist and facilitate hazard mitigation efforts that probably prevented extensive loss of life during the crisis (Surono et al., 2012; Pallister et al., 2013). SAR

interferometry was also used to define a time-series of ground surface displacement at Merapi (Saepuloh et al., 2013) and estimate the volume of 2010 Merapi PDC deposits along the Gendol River (Bignami et al., 2013). Yulianto et al. (2013) generated a map of 2010 Merapi pyroclastic deposits and their impact based on change detection using SAR data.

Our study, presented in Chapter 5, aims to characterize the 2010 Merapi pyroclastic deposits based on the combination of the amplitude evolution with temporal decorrelation information from SAR data. The most important surface characteristics that control the strength of SAR backscatter are moisture content, roughness, and slope. Surfaces that are oriented toward the radar, roughness on the scale of radar wavelength, and/or moisture will generally have stronger reflected returns than those that are not. On volcanoes, roughness and slope tend to be the most important of these factors, and they define much of the variation in amplitude within a radar image (Gaddis et al., 1989). The reflected signal received by a SAR sensor is a function of the characteristics of the scatterers within a resolution cell on the ground. If the geometry of the scatterers changes between the times of two SAR acquisitions, the reflection from that resolution cell will not be correlated between the two images (incoherence). Changes in amplitude and incoherence may provide evidence of volcanic activity, including emplacement of new deposits and destruction of pre-existing landforms.

Previous SAR studies on eruptive deposits were restricted so far to the use of one polarization and only based on the variation of the amplitude in the SAR images. Most of the studies utilising polarized data have dealt with lava flows; however, Saepuloh et al. (2012) used full polarimetric L-band ALOS data to map volcanic deposits resulting from explosions at Sakurajima, Japan. Therefore, the principal objective of this study is to examine the utilization of direct- and cross-polarized SAR data in order to identify and map pyroclastic deposits. This study is achieved by using a set of L-Band ALOS-PALSAR images acquired before, during and after the event. The pyroclastic deposits maps are generated based on surface change detection from coherence and amplitude ratio images, and supervised classification based on Maximum Likelihood Classification (MLC) and Support Vector Machine (SVM) methods.

5.2. Mapping the 2010 Merapi pyroclastic deposits using SAR data

This section corresponds to an article published in Remote Sensing of Environment in 2015.

Mapping the 2010 Merapi pyroclastic deposits using dual-polarization Synthetic Aperture Radar (SAR) data

Akhmad Solikhin[1, 3], Virginie Pinel[2], Jean Vandemeulebrouck[2], Jean-Claude Thouret[3], Muhamad Hendrasto[1]

[1] *Center for Volcanology and Geological Hazard Mitigation, Jalan Diponegoro 57, Bandung Indonesia*

[2] *ISTerre, Université de Savoie, IRD, CNRS, 73376 Le Bourget du Lac cedex, France*

[3] *PRES Clermont, Université Blaise Pascal, Laboratoire Magmas et Volcans UMR 6524 CNRS, IRD-R163 and CLERVOLC, 5 rue Kessler, 63038, Clermont Ferrand cedex, France*

Highlights:

- We characterize pyroclastic deposits using co- and cross-polarized L-band SAR data.
- We use L-band ALOS-PALSAR images to classify the 2010 Merapi pyroclastic deposits.
- Changes in radar amplitude efficiently enable us to map the pyroclastic deposits.
- Maximum likelihood classification helps to map 4 main pyroclastic deposit units.
- Temporal decorrelation information has improved the classification results.

Remote Sensing of Environment 158 (2015) 180-192

Supplementary data to this article can be found in Appendix C

Remote Sensing of Environment 158 (2015) 180–192

Contents lists available at ScienceDirect

Remote Sensing of Environment

journal homepage: www.elsevier.com/locate/rse

Mapping the 2010 Merapi pyroclastic deposits using dual-polarization Synthetic Aperture Radar (SAR) data

Akhmad Solikhin [a,c,*], Virginie Pinel [b], Jean Vandemeulebrouck [b], Jean-Claude Thouret [c], Muhamad Hendrasto [a]

[a] Center for Volcanology and Geological Hazard Mitigation, Geological Agency, Ministry of Energy and Mineral Resources, Jalan Diponegoro 57, Bandung 40122, Indonesia
[b] ISTerre, Université de Savoie, IRD, CNRS, 73376 Le Bourget du Lac cedex, France
[c] PRES Clermont, Université Blaise Pascal, Laboratoire Magmas et Volcans UMR 6524 CNRS, IRD-UR163 and CLERVOLC, 5 rue Kessler, 63038 Clermont Ferrand cedex, France

ARTICLE INFO

Article history:
Received 27 June 2014
Received in revised form 6 November 2014
Accepted 7 November 2014
Available online xxxx

Keywords:
Merapi
2010 eruption
Pyroclastic deposits
ALOS-PALSAR
Dual polarization
Classification
Mapping

ABSTRACT

L-band ALOS-PALSAR images acquired before, during and after the 2010 Merapi eruption have been used to classify and map the pyroclastic deposits emplaced during this VEI-4 event. We characterize the deposits using direct-polarized and cross-polarized L-band SAR data and by combining the information of amplitude evolution with temporal decorrelation. Changes in amplitude of the radar signal enable us to map the pyroclastic density currents (PDCs) and tephra-fall deposits. Radar amplitudes in direct (HH) and cross (HV) polarizations decrease where the valley-confined and overbank block-and-ash flow (BAF) deposits (D1) are emplaced. Rainfall- and runoff-reworked PDC deposits (D2) are characterized by an increase in ground backscattering for HH polarization and a decrease for HV polarization. Ground backscattering transiently increases in both polarizations after pyroclastic surge (D3) and tephra fall (D4) deposition. We use a supervised classification method based on maximum likelihood to map the deposits D1–D4. The temporal decorrelation of the radar signal and the amplitude evolution improve the quality of classification results. Classification derived from ALOS-PALSAR images using the maximum likelihood classification provides a result with 70% classification accuracy for deposits overall. The estimated areas of valley-confined and overbank PDC deposits (either primary or reworked by rainfall and runoff) are consistent with the areas measured by other studies, while the large discrepancy in area estimated for pyroclastic-surge deposits can be partly explained by the strong erosion due to intense rainfall that removed a large part of these thin deposits.

© 2014 Elsevier Inc. All rights reserved.

1. Introduction

Remote sensing has long been recognized as an essential tool to study volcanoes and the benefit of these new techniques to modern volcanology was recently highlighted (Pyle, Mather, & Biggs, 2013; Sparks, Biggs, & Neuberg, 2012). Optical, radar and thermal satellite imageries can be used to map structural features and eruptive deposits thus contributing to the information required to produce hazard maps and forecast the impact of future eruptions (e.g., Hooper, Sigmundsson, & Prata, 2012). The interest of remote sensing is emphasized at volcanoes where ground based monitoring and field work are hazardous or impossible, due to natural (eruptive activity, dense vegetation, rugged relief, etc.) or political conditions (Head, Maclean, & Carn, 2012). Most studies are based on optical data taking advantage of the high resolution of GeoEye, WorldView, Quickbird and Pléaides sensors now available with sub-metric image pixels (Solikhin, Thouret, Gupta, Harris, & Liew, 2012; Thouret et al., 2010). In contrast to optical sensors, Synthetic Aperture Radar (SAR) data may provide information during day or night, independent of the meteorological conditions, and may penetrate the vegetation canopy for long wavelengths (Saepuloh, Koike, & Omura, 2012). SAR data therefore provide useful information in humid tropical environments where volcanoes are often densely vegetated and covered by clouds (Carn, 1999; Lu & Dzurisin, 2014).

The application of radar data to volcano deformation measurements has been described in detail by Massonnet and Sigmundsson (2000). Zebker, Amelung, and Jonsson (2000) show that, in addition to deformation measurements, Interferometric SAR (InSAR) is a suitable tool to map deposits and track changes in topography. The radar echo is sensitive to any change in the distribution of scatterers within a resolution cell at the ground. As a result, if scatterers are moved or replaced by a new set, as in the case of the emplacement of new lava flows, this can easily be detected through multi-temporal SAR images. Detection can be based, either on evolution of reflectivity, i.e. the amplitude of the radar images, or on the temporal decorrelation of the signal. Decorrelation of the signal has been successfully used by Zebker, Rosen, Hensley, and Mouginis-Mark (1996) to estimate the surface changes of an active pahoehoe lava flow at Kilauea, Hawaii and, with

* Corresponding author at: PRES Clermont, Université Blaise Pascal, Laboratoire Magmas et Volcans UMR 6524 CNRS, IRD-UR163 and CLERVOLC, 5 rue Kessler, 63038 Clermont Ferrand cedex, France.
E-mail address: aksolikhin@vsi.esdm.go.id (A. Solikhin).

http://dx.doi.org/10.1016/j.rse.2014.11.002
0034-4257/© 2014 Elsevier Inc. All rights reserved.

the estimated lava flow thickness, to quantify the mean effusion rate. Dietterich et al. (2012) use the same method to map lava flows over a period of seven years. Coherence has been also used by Wadge, Scheuchl, and Stevens (2002) to map pyroclastic-flow deposits using two images acquired within a 24-hour time interval, and by McAlpin and Meyer (2013) to map lahar deposits emplaced during the 2009 eruption of Redoubt volcano, Alaska. Changes in radar amplitude have also been largely used for mapping new erupted products and deposits from volcanoes (Cracknell & Reading, 2014; Saepuloh, Koike, Omura, Iguchi, & Setiawan, 2010). The changes are usually quantified by calculating the difference or the ratio between amplitudes of successive acquisitions (Wadge et al., 2002, 2011). High-resolution amplitude images (with ground resolution of one meter) can also be used to estimate the eruptive deposit thickness using the radar shadowing (Wadge et al., 2011), resulting in improved estimates of the eruption rate and its temporal evolution (Wadge, Saunders, & Itikarai, 2012).

Ground backscattering depends on the local topography, soil roughness and surface moisture. However, ground backscattering is also a function of the radar wavelength and, for a given wavelength, it depends on the polarization of the radar emission and reception. Surfaces oriented towards the radar, rough at the scale of the radar wavelength and/or moist, will have stronger reflected returns than those that are not oriented towards the radar. Several airborne SAR systems and the Spaceborne Imaging Radar-C/X-band Synthetic Aperture Radar (SIR-C/X-SAR) acquired polarized data in L, C and X bands over a few active volcanoes. These data sets have shown that the L-band yields the best results to map lava flows and distinguish several units (Gaddis, 1992; MacKay & Mouginis-Mark, 1997; Schaber, Elachi, & Farr, 1980) and the use of various polarizations significantly improves lava flow characterization (Dellwig & Moore, 1966; Zebker, van Zyl, & Held, 1987). However, no general agreement exists on the most adequate polarization for classification of volcanic deposits between direct-polarized (same polarization direction for transmitting and receiving) and cross-polarized (orthogonal polarization directions for transmitting and receiving) (Blom, Schenck, & Alley, 1987; Gaddis, 1992). Most of the studies performed with polarized data deal with lava flows, however Saepuloh et al. (2012) used full polarimetric L-band ALOS data to map volcanic deposits resulting from explosions at Sakurajima, Japan.

The objective of this study is to identify and map volcanic (pyroclastic) deposits using direct-polarized and cross-polarized L-band SAR data and to combine the information gained from amplitude evolution with temporal decorrelation. The 2010 eruption of Merapi volcano, as described in the Section 2 of this paper, is used as a case study. Section 3 describes ALOS-PALSAR datasets processing and methodology followed in this study. Section 4 presents the results and discussion while the last section provides the conclusions of the study.

2. Case study: the 2010 Merapi pyroclastic deposits

Merapi (7°32.5′ S and 110°26.5′ E) is one of the most active volcanoes in Indonesia and located in the densely populated Province of Yogyakarta in Central Java (Fig. 1a–b). The volcano is well known for its block-and-ash flows (BAFs) produced by repeated collapses of summit lava domes, a specific type of pyroclastic density current (PDC) commonly associated with dome growth and collapse. BAFs refer to ground-hugging hot avalanches and flowing mixtures of volcanic particles and gas (Branney & Kokelaar, 2002). More than 74 eruptions have been recorded at Merapi since 1548 A.D. and at least seventeen of them, including the 2010 one, have caused fatalities.

The 26 October–23 November 2010 eruption was the Merapi's largest event (Volcanic Explosivity Index 4) of the last 140 years. In order to relate the collection times of the different images to chronology of this eruptive sequence, we use the daily seismic spectral amplitude measurement (SSAM, Budi-Santoso et al., 2013; Syahbana, 2013) as a representative parameter of the eruptive activity (Fig. 2). The 2010 Merapi crisis encompassed several episodes of PDCs, channeled mostly towards the Gendol–Opak catchment on the southern flank, where they reached a distance of 16.5 km from the summit (Fig. 1c). The most voluminous PDC was deposited during the peak phase of the eruption on 4–5 November 2010 (Fig. 2). PDC deposits cover an area of ~22.3 km^2, are composed of valley-confined and overbank deposits (29.3% area) and surge and associated tephra-fall deposits (70.7%) (Charbonnier et al., 2013). During the eruption, tephra fall dispersed by the wind affected mostly the west flank of the volcano, totaling a volume of $21 \pm 4 \times 10^6$ m^3 (Solikhin et al., in revision). Since the eruption, much of the PDC deposits have been partly transformed into lahars (volcanic mud flows) and another large part have been mined for construction material.

Remote sensing has been largely applied to characterize the deposits of the 2010 Merapi eruption, either based on optical data (Charbonnier et al., 2013; Komorowski et al., 2013; Solikhin et al., in revision) or SAR images using X-band (Bignami et al., 2013) or L-band (Saepuloh et al., 2013; Yulianto, Sofan, Khomarudin, & Haidar, 2013). As SAR images can be used to track lava extrusion and dome growth at highly explosive andesitic volcanoes, they were essential for managing the 2010 eruptive crisis of Merapi (Pallister et al., 2013). However, previous SAR studies on eruptive deposits were restricted to the use of one polarization and only based on the variation of the amplitude in the SAR images.

3. Data processing and methods

3.1. ALOS PALSAR dataset

We used L-band SAR data acquired by the Phased Array L-band Synthetic Aperture Radar (PALSAR) on board of the Japanese Advanced Land Observing Satellite (ALOS). Table 1 summarizes the details of ALOS-PALSAR images used for this study. Data are from ascending track 431 acquired with an incidence angle of 34.3°. We utilized five dual polarization (dual-pol, Fine Beam Double Polarization, termed FBD) datasets in horizontal transmit-horizontal receive (HH) and horizontal transmit-vertical receive (HV) polarization mode. These datasets were acquired before (on 13 September 2009, 16 June 2010 and 16 September 2010; Fig. S1a), during (on 1 November 2010), and after (on 1 February 2011) the 2010 eruption (Fig. 2). We also utilized one single polarization (Fine Beam Single Polarization, termed FBS) dataset (HH) acquired after the eruption (on 17 December 2010).

3.2. Amplitude and coherence extraction

First, all raw data (Level 1.0) were transformed into arrays of complex numbers or Single Look Complex (SLC) data, which retains the phase and amplitude information of the original SAR data. SLC images were then co-registered and amplitude images were multi-looked (eight looks in azimuth and four in range) ending with a pixel resolution of 28.4 m in azimuth and 33.2 m in ground range. Amplitude images contain variations in brightness (the amplitude of the signal), which reflects spatial variations of the physical characteristics of the ground surface (the reflector). Georeferenced amplitude images after pyroclastic deposit emplacement are shown on Fig. 3a–d for the direct (HH) and cross-polarization (HV) data. The phase information from SAR images is extracted by differencing two images that are separated in time. An image map of coherence or the constancy of phase information is generated from standard practices that are part of the interferometric processing. Our coherence image (Fig. 3e) is obtained when forming the interferogram between the two HH polarization images acquired on 1 November 2010 and 17 December 2010, this pair of images having the best baseline (temporal baseline = 45 days, perpendicular baseline = 15 m) of all pairs in our dataset. Areas with a good coherence (value close to 1) appear as bright, whereas dark areas indicate a poor coherence (value close to 0). ALOS-PALSAR data processing was performed using ROI_PAC software (Rosen, Henley, Peltzer, & Simons, 2004). Amplitude and coherence images were geocoded using the Shuttle

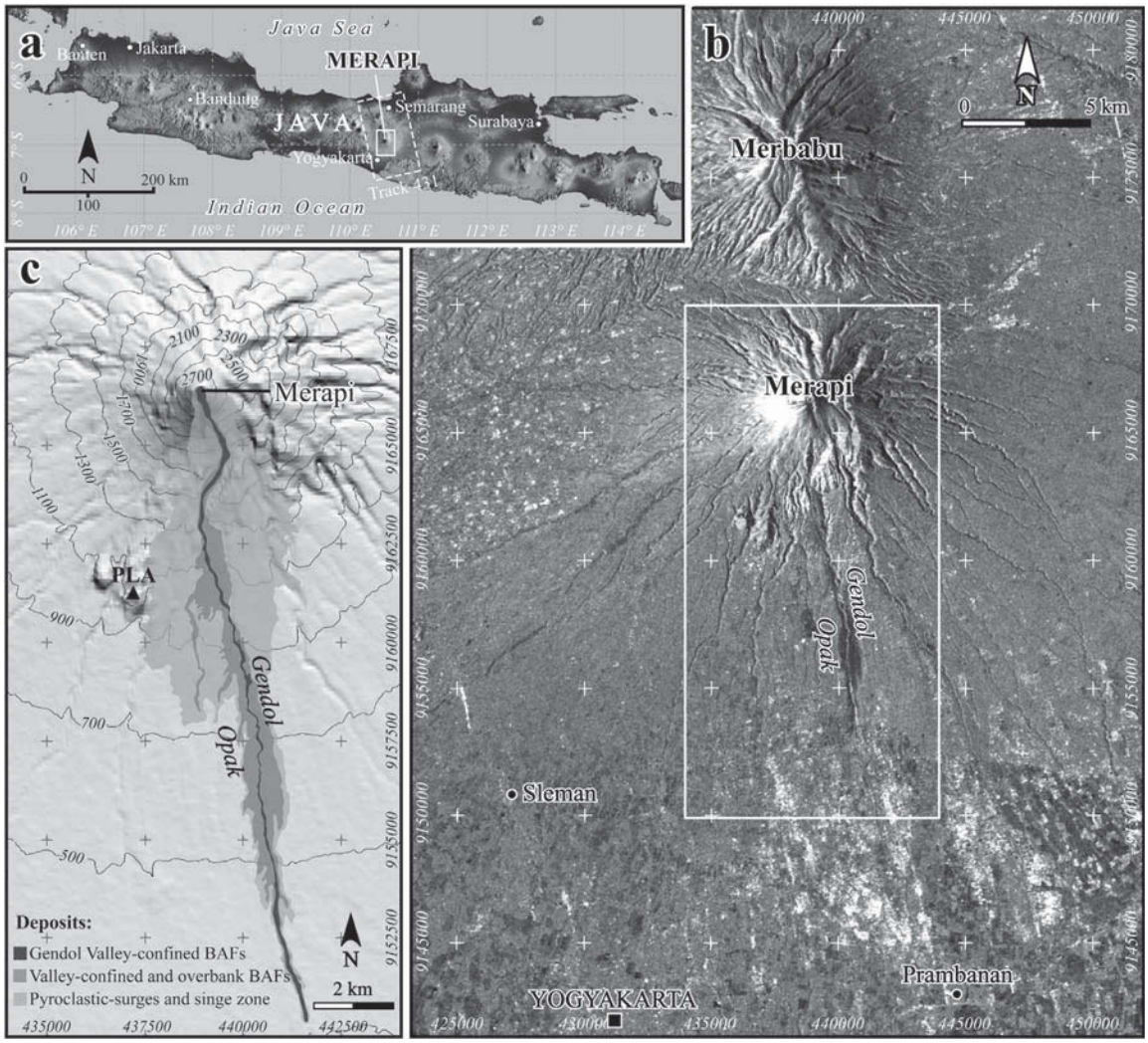

Fig. 1. (a) Location of Merapi volcano (Java Island) including the coverage of track 431 ALOS-PALSAR images (dashed white box). The Merapi summit lies 30 km north of Yogyakarta city. (b) ALOS-PALSAR amplitude image of 1 February 2011 showing Merapi and Merbabu volcanoes and the study area (white box) (c) Shuttle Radar Topography Mission (SRTM) digital elevation model (DEM) used to geocode the amplitude image, overlain by a map of the 2010 PDC deposits on the Merapi southern flank (Solikhin et al., in revision).

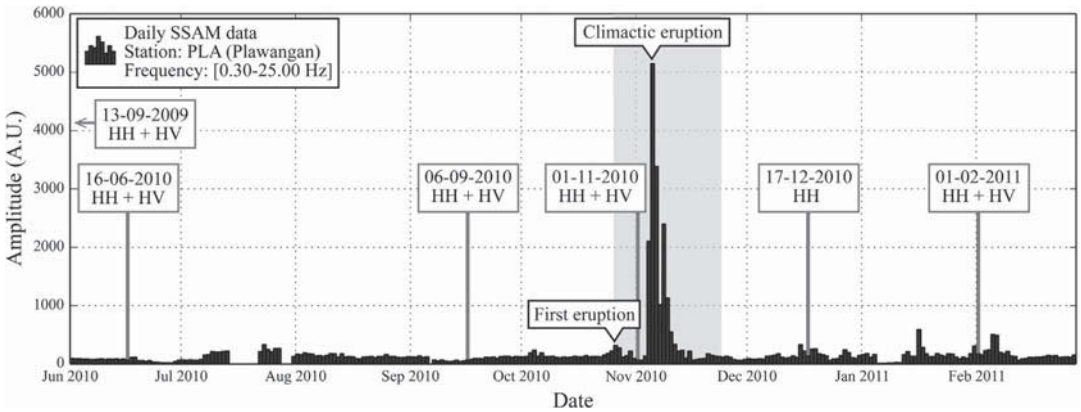

Fig. 2. Daily data of seismic spectral amplitude measurement (SSAM) of Merapi as recorded at the Plawangan (PLA) seismic station on the southern flank of Merapi (Fig. 1c) overlain by the acquisition date of ALOS-PALSAR images. This SSAM data shows the seismic energy release of Merapi activity for the June 2010 to February 2011 period that comprises the 2010 eruption episode (26 October–23 November 2010; gray box).

Table 1
Characteristics of ALOS-PALSAR images used for this study.

Acquisition date	Time (UTC)	Polarization
13–06–2009	15:31	HH + HV
16–06–2010	15:30	HH + HV
16–09–2010	15:29	HH + HV
01–11–2010	15:28	HH + HV
17–12–2010	15:28	HH
01–02–2011	15:27	HH + HV

Data are from ascending track 431 (Fig. 1a) acquired with an incidence angle of 34.3°.

Radar Topography Mission (SRTM) digital elevation model (DEM; Fig. 1c) oversampled four times, and having a pixel resolution of around 23 m. The topography may have changed in the period between the SRTM and ALOS-PALSAR data acquisitions (2000 to 2010 respectively) but, we think, not sufficient to affect the geocoding.

3.3. Amplitude evolution

Prominent changes in the topography or radar scatterer properties, distribution or orientation, can be detected by comparing two SAR images, either through the phase information using the coherence image or using the temporal evolution of amplitude. Surface changes occurring between the two SAR acquisitions induce a temporal decorrelation, such that areas marked by these surface modifications appear as dark pixels (low coherency) in the coherence image, whereas the bright pixels characterize non-modified areas. Local slope, dielectric constant of the terrain and surface roughness are the dominant factors that influence the amplitude of the return signal in radar imagery. Some ground features appear similar in either HH or HV images, but rough surface and inhomogeneous sub-surfaces appear brighter on HV than on HH images due to depolarization that occurs mainly over vegetation (black rectangles in Fig. 3a–b). Changes in amplitude can be quantified by taking the ratio between the two amplitude images. The bright pixels in the ratio image have stronger backscatter in the numerator (later) scene than the denominator (earlier) scene and vice versa. When the amplitude variation is due to surface roughness evolution, a smoother surface will lead to a decrease in backscattering whereas a rougher one will lead to an increase. Pyroclastic deposits mainly affect the topography and surface roughness inducing changes in amplitude images. However, some changes in amplitude images are also expected in areas not affected by the eruptive activity due to surface temperature and water content modifications especially over paddy fields.

3.4. Supervised classification

From a variety of algorithms that were developed for supervised classifications, we apply the Maximum Likelihood Classification (MLC) and the Support Vector Machine (SVM) classification techniques (Tupin, Inglada, & Mercier, 2014) in order to discriminate the 2010 Merapi pyroclastic deposits. MLC is the most common parametric classifier, which assumes normal or near normal spectral distribution for each class in each band. This classifier calculates the probability that a given pixel belongs to a class specified by a mean vector and a covariance matrix (Richards & Jia, 2006). We define training samples (Fig. S1b) as inputs to the supervised classification and control samples (Fig. S1c) in order to assess the classification performance. Training and control data have been manually extracted based on visual interpretation of optical views and the radar image in the false-color composite representation by referring to field-based data by Charbonnier et al. (2013), Komorowski et al. (2013) and Solikhin et al. (in revision).

The training data for each class have to be well separated spectrally in order to determine higher classification accuracies. We used the Jeffries–Matusita (J–M) distance (Richards & Jia, 2006) to compute the separability value between a pair of training classes before performing the classification. The J–M distance output value ranges between 0 and 2; two classes are considered well separated when the J–M distance is above 1.90 and very poorly separated when the J–M distance is below 1.0 (Richards & Jia, 2006). Majority filtering with 3 × 3-kernel size was applied in post-classification analysis in order to change spurious pixels within a large single class to that class. Another post-classification analysis used to measure accuracy is derived from the confusion matrix with control data as the validation site.

The distribution of amplitude or coherence in radar data is not Gaussian, even after noise reduction by multi-look processing; subsequently the MLC is theoretically not well adapted to these data. Thus we also used the SVM classification method that often yields good classification results from complex and noisy data (Tupin et al., 2014). SVM is a supervised classification method derived from statistical learning theory that discriminates the classes with a decision surface (hyperplane) that maximizes the margin between the classes. The training data used are in a multidimensional feature space and these closest to

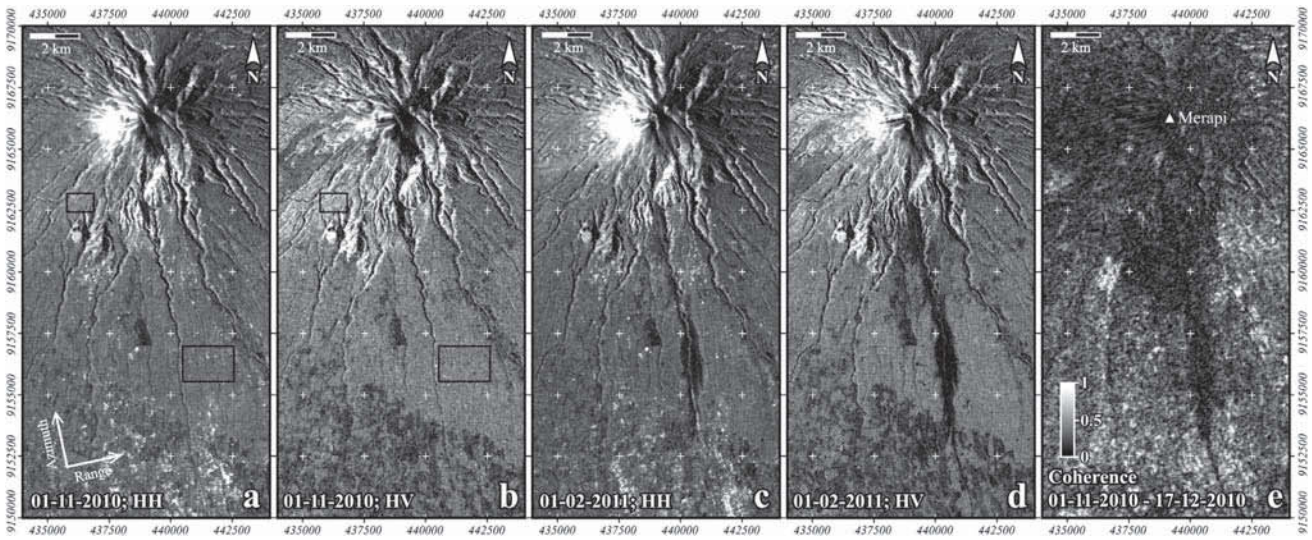

Fig. 3. Georeferenced ALOS-PALSAR amplitude image (four-looks) of (a) HH polarization on 1 November 2010 (HH syn-eruption); (b) HV syn-eruption; (c) HH post-eruption (1 February 2011) and (d) HV post-eruption. (e) Coherence image obtained when forming the interferogram between the 1 November 2010 and 17 December 2010 images. Black rectangles in a and b show similar ground features that appear brighter on HV than on HH images due to depolarization that occurs mainly over vegetation.

the hyper plane are the so-called support vectors (Vapnik, 1998). In this work, the SVM is applied using the radial basis kernel. Results obtained are then compared with the results derived from MLC.

4. Results and discussion

4.1. Surface change detection

4.1.1. Coherence image

Fig. 3e shows the coherence image for the interferogram obtained with images acquired on 1 November and 17 December 2010 over Merapi volcano. As the vegetation quickly recolonizes devastated areas on the slopes of Merapi, a rapid decorrelation occurs. This pair of images is the only one for which the coherence is fairly good, such that the decorrelation due to the pyroclastic deposits emplaced after 1 November 2010, can be clearly identified. The acquisition obtained on 17 December 2010 is the first one available after the eruptive period. Despite being noisy, this coherence image can help in distinguishing the areas covered by pyroclastic deposits, which are characterized by a strong decorrelation (dark pixels). The dark areas of low phase coherence at the summit and on the western and the southern flanks of the volcano correspond to pyroclastic deposits emplaced during the eruption after 1 November 2010. The bright (white) areas of high phase coherence indicate infrastructure (houses, building, road, etc.), which did not change between the acquisition dates. The unstable natural elements like vegetation or fields appear as gray areas in the coherence image.

4.1.2. Ratio of amplitude image

Fig. 3 shows georeferenced amplitude images of Merapi acquired from an ascending pass during the eruptive crisis on 1 November 2010 (a and b) and two months after the end of the eruption on 1 February 2011 (c and d) with HH and HV polarizations respectively. Due to the radar acquisition geometry, the west-facing slope of Merapi volcano is affected by foreshortening effects, whereas some parts of the east-facing slope are in the shadow. Visually, we can distinguish the areas covered by eruption deposits when we compare the amplitude image of syn- or post-eruption (i.e. 1 November 2010 and 1 February 2011) with the pre-eruption image (Fig. S1a). However, this visual estimation is not sufficient due to a large amount of dark and bright pixels, which are not associated with pyroclastic deposits. In the following paragraphs, we discuss the changes in a qualitative manner and illustrate some of them through images created by combining post- and pre-eruption images. A view of change detection involving ratio images is shown in Fig. 4.

Fig. 4e shows an image ratio of the amplitude image acquired on 17 December 2010 (post-eruption) divided by the amplitude image acquired on 16 September 2010 (pre-eruption), both with HH polarization. In this figure, the changes indicated by dark pixels along the Gendol catchment are due to the emplacement of valley-confined and overbank PDC deposits with thickness varying from a few meters to a few tens of meters from field surveys (Charbonnier et al., 2013; Komorowski et al., 2013). The bright-tone change occurring on the Gendol channel is due to the PDC deposits remobilized by runoff and incised by the new drainage, termed reworked PDC. The bright-tone change in the southern flank that envelops the dark area is due to the emplacement of dilute PDCs (pyroclastic-surge deposits) and associated impact zones (singe zone). Other bright-tone change scattered in the western flank of Merapi corresponds to tephra-fall deposits. The false-color composite images in Fig. 4a–d and f are obtained using pairs of ALOS-PALSAR amplitude images for HH (a, b and c) and HV (d and f) polarizations. In these images, red color indicates the surface where amplitude decreased in the post-eruption image (smoother if the change can be attributed to roughness decrease), blue color indicates the surface where amplitude increased in the post-eruption image (rougher if the change can be attributed to roughness increase) and yellow color for the surfaces where amplitude did not change.

Changes observed in Fig. 4a and d are due to eruptive activity of the Merapi Volcano between 26 October and 1 November 2010, which correspond to the initial explosive phase and the beginning of the magmatic phase as defined by Surono et al. (2012). During this period, several explosive eruptions occurred on 26 and 31 October, removing the 2006 lava dome, enlarging and deepening the summit crater (Pallister et al., 2013; Surono et al., 2012) while several PDC events were recognized. Valley-confined and overbank PDCs reached ~7 km down-valley towards Gendol River as well as associated ash-cloud surges forming the singe zone (Charbonnier et al., 2013). Merapi eruptions after 1 November 2010, including the climactic eruption on 5 November 2010, produced ash columns up to 17 km in height and BAFs that traveled as far as 16 km down Gendol River valley (Surono et al., 2012). Changes due to eruption including pyroclastic deposits are also shown in the false-color composite images of 17 December 2010 (HH only, Fig. 4b) and 1 February 2011 (HH and HV, Fig. 4c and f) as post-eruption images. Changes in the summit crater and southeast-trending Gendol breach are recognized in Fig. 4, not only in HH polarization but also in HV polarization. During this eruption, the summit crater expanded from 0.048 km^2 (on 1 November 2010) to 0.093 km^2 (on 1 February 2011), which is similar to the result based on optical satellite images (0.11 km^2; Solikhin et al., in revision). Crater expansion was also followed by geomorphological changes of the dome surface, from an area of 0.0135 km^2 on 1 November 2010 to 0.0432 km^2 on 1 February 2011 (Saepuloh et al., 2013).

The 2010 Merapi pyroclastic deposits were emplaced over the south flank of volcano (mostly vegetation and village on slopes >5°) that was previously characterized by small-scale topographic variations (10–20 m range) and can be considered as rough on amplitude images. Tens of meter-thick valley-confined and overbank BAF deposits have buried forest and villages resulting in a smoother surface on the scale of the L-band wavelength of red areas in false-color composite images. Radar backscattering decreases by about 6 decibels (dB) in both polarizations after valley-confined and overbank BAF deposit emplacement. Pyroclastic-surge deposits are much thinner (a few centimeters to decimeters; Charbonnier et al., 2013; Komorowski et al., 2013) than valley-confined and overbank BAF deposits, therefore the effects of these pyroclastic deposits did not greatly alter the surface roughness but resulted in destruction and burning of forests and villages. Such pyroclastic-surge deposits appear as light blue areas in false-color composite images of HH polarization. In HV polarization, these deposits are represented as red areas with the color intensity lower than the red color of valley-confined and overbank BAF deposits (Fig. 4f). An interpretation is that the destruction of vegetation increased the backscattering by about 3 dB for HH polarization and by about 1 dB for HV polarization. Explosive eruptions produced 2–7 cm-thick tephra-fall deposits in the southwest flank of Merapi, which are identified by light blue areas but with lower color intensity than the light blue of pyroclastic-surge deposits. Radar amplitude of tephra-fall deposits increased by about 2 and 1 dB for HH and HV polarizations respectively. We observe that this is not related to deposit type but surface texture (roughness) as tephra-fall and pyroclastic-surge deposits are both fine-grained (ash-rich) and relatively thin (<1 m), whereas BAFs are coarser boulder-rich and thicker (m to tens m).

The post-eruption images used in Fig. 4c and f were acquired about 46 days after the one used in Fig. 4b and three months after deposit emplacement. As a result, pyroclastic deposits have undergone changes due to remobilization or transformation into PDC deposits reworked by runoff and lahars and to surface erosion by rain and runoff. Beside changes observed in surface roughness and topography, reworked PDC deposits have a higher water content, which consequently increases radar backscatter amplitude of about 4.5 dB for HH polarization and decrease that of about 3 dB for HV polarization. Reworked PDC deposits appear in HH polarization indicated by blue areas inside the

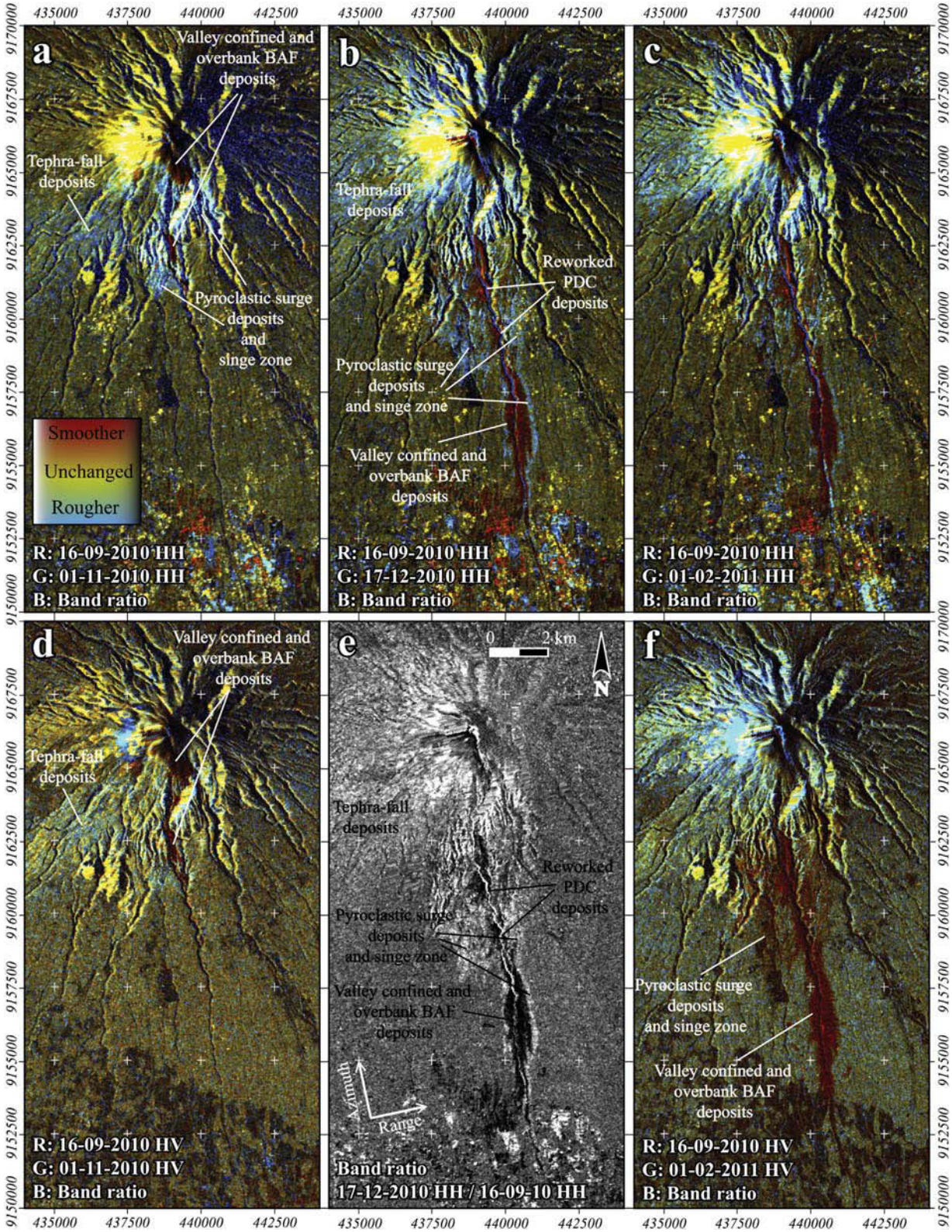

Fig. 4. ALOS-PALSAR amplitude change images of the Merapi area and its south flank. The false-color composite (R: first/earlier image; G: second/later image; B: ratio of the second image divided by the first image) images are obtained using pairs of amplitude images of (a) 16 September 2010 and 1 November 2010 for HH polarization; (b) 16 September 2010 and 17 December 2010 for HH polarization; (c) 16 September 2010 and 1 February 2011 for HH polarization; (d) 16 September 2010 and 1 November 2010 for HV polarization (f) 16 September 2010 and 1 February 2011 for HV polarization. (e) Ratio image of the amplitude image on 17 December 2010 divided by the amplitude image acquired on16 September 2010 for HH polarization. Annotations of deposit type are defined based on our field data and observations and previous studies (e.g. Charbonnier et al., 2013; Komorowski et al., 2013) on Merapi.

channel while in HV polarization they are indicated by dark red areas. The erosion induces a slight decrease in amplitude of HH-polarized radar for pyroclastic-surge (and singe zone), valley-confined and overbank BAF deposits and a decrease in amplitude for tephra-fall deposits. The change over time of tephra-fall deposits is more significant than that of the pyroclastic-surge deposits because the tephra-fall deposits are thinner and their emplacement did not result in significant destruction of the vegetation. The change over time of pyroclastic-surge deposits is due to vegetation that quickly recolonized the forest margins near the valley channel. This evolution is clearly shown by the comparison of Fig. 4b–c obtained for post-eruption images acquired with a 46 daytime interval.

Changes are also detected in areas that were not affected by the 2010 Merapi eruptions (e.g. the southern part in Fig. 4). These areas include bare soil and dynamic areas of agricultural land, which have changed over time depending on the plants, soil moisture and weather conditions. Radar backscatter amplitude of dry bare soils is lower than that of cultivated land or vegetation, but the amplitude can increase when the surfaces change from dry to wet.

4.2. Deposit classification

The supervised classification based on MLC and SVM has been applied to ALOS-PALSAR data in order to create a map of the 2010 Merapi pyroclastic deposits in a semi-automatic way. This classification aims to categorize all pixels in the radar image into one of several pre-defined deposit or land cover classes. We define a set of training samples (Fig. S1b) characterizing seven deposit classes (D1 to D7) and five 'non-deposit' classes (O1 to O5). Four classes of valley-confined and overbank BAF (D1), reworked PDC (D2), pyroclastic-surge (D3) and tephra-fall (D4) deposits are defined from the post-eruption image acquired on the 1 February 2011. D2 are limited to tephra-fall deposits that cover vegetation, whereas tephra-fall deposits that cover bare soil or older deposits will resemble pyroclastic-surge deposit in the amplitude image. D5, D6 and D7 classes, the early stages of D1, D3 and D4 respectively, are defined from the syn-eruption image acquired on the 1 November 2010. Early stage deposits (D5 to D7) were emplaced between 26 October to 1 November 2010, while D1 to D4 are deposits produced during the entire eruption episode (26 October to 23 November 2010). We have combined the valley-confined and overbank PDC deposits into one class (D1) as both have a similar pattern in the amplitude image and are therefore difficult to distinguish. The 'non deposit' classes consist of vegetation (O1), agriculture/farm (O2), settlements and villages (O3), bright pixels corresponding to foreshortening effect (O4) and shadowed areas (O5).

Fig. 5 shows the evolution of the average backscattering amplitude of D1–D7 and O1 training samples over six different acquisition times on 13 June 2009, 16 June 2010, 16 September 2010, 1 November 2010, 17 December 2013 (HH polarization only) and 1 February 2011. The average amplitudes of all classes were normalized by dividing them by the mean amplitude of class O1, as a reference area that did not change significantly. This normalization aims to avoid or reduce the variation of calibration coefficients that are expected to occur through space and time. Before the eruption, there was no significant change for all classes in HH polarization, while in HV polarization changes only occur for D2 class. Such changes before the eruption can be explained by the location of these deposits, generally inside the river valley, where deposit morphology was constantly evolving due to lahars and mining. After the eruption, radar amplitude of D1 and D5 decreased in both polarizations. D2 deposits are characterized by increasing radar amplitude for HH polarization and decreasing amplitude for HV polarization. Radar amplitude is increasing transiently in both HH and HV polarizations for D3, D4, D6 and D7. The transient increase in the amplitude of D3 for HV polarization is not apparent in

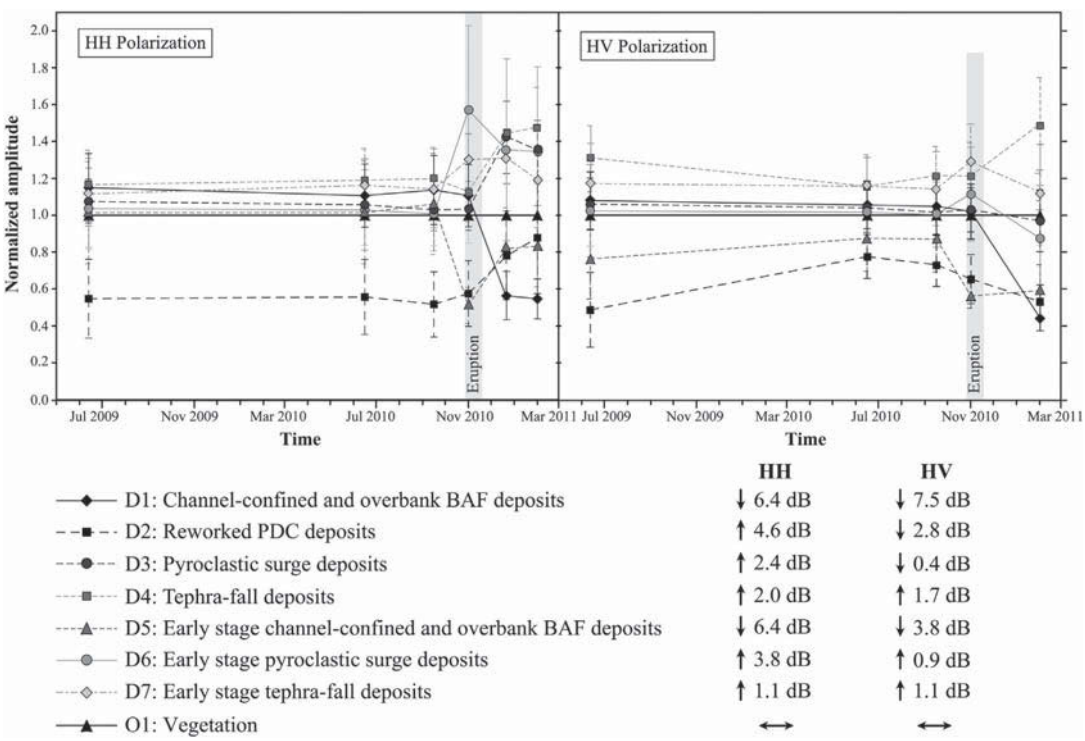

Fig. 5. The plot of normalized average amplitude and its standard deviation (error bar) of D1–D7 and O1 training samples over seven different times of acquisition as of 13 June 2009, 16 June 2010, 16 September 2010, 1 November 2010, 17 December 2011 (only for HH polarization) and 1 February 2011. The average amplitude was normalized by dividing by the mean amplitude of class O1. For each class, the backscattering evolution corresponding to products deposition is indicated in decibels (20 $\log_{10}$ (amplitude after deposition/amplitude before deposition)).

Fig. 5 as it was followed by an erosion process that resulted in a rapid decrease of the amplitude. This analysis is consistent with the statements given in the change detection section (Section 4.1).

Separability values between pairs of training classes were computed using J–M distance with varying inputs from two to seven bands (Table 2). The deposit classes (D1–D4) are generally well separated (>1.9), but some have moderate (1.5–1.9), low (1–1.5) and very low (<1) separability. The D3–D4 pair shows a very low separability between two bands of HH polarization, but a low separability between two bands of HV polarization. Low separability (1–1.5) of deposit classes is also observed for the D1–D2 pair when using two bands of HV polarization as input. By using four bands or more as input, we always obtain an acceptable separability (>1) either for deposit classes or 'non-deposit' classes. The separability between different deposit classes and between deposit classes and other classes always increases when a larger number of bands are used, that is when information is added by taking advantage of both polarization and using the coherence information (Table 2).

Table 2
Separability of Jeffries–Matusita distance (J–M) calculated using a various sets of amplitude images and one coherence image with two to seven bands of inputs.

Input	Training class	D1	D2	D3	D4	D5	D6	D7	O1	O2	O3	O4	O5
2 bands	D1	–	1.916	1.983	1.949	–	–	–	1.729	1.134	1.824	1.994	1.943
(HH polarization)	D2	hs	–	1.598	1.7	–	–	–	1.555	1.262	1.789	1.975	1.334
	D3	hs	ms	–	0.381	–	–	–	1.074	1.469	1.724	1.973	1.999
	D4	hs	ms	ps	–	–	–	–	1.06	1.427	1.562	1.955	1.996
	O1	ms	ms	ls	ls	–	–	–	–	0.832	1.689	1.983	1.917
	O2	ls	ls	ls	ls	–	–	–	ps	–	1.511	1.972	1.873
	O3	ms	ms	ms	ms	–	–	–	ms	ms	–	1.594	1.936
	O4	hs	hs	hs	hs	–	–	–	hs	hs	ms	–	1.997
	O5	hs	ls	hs	hs	–	–	–	hs	ms	hs	hs	–
2 bands	D1	–	1.167	1.81	1.964	–	–	–	1.889	1.232	1.636	1.978	1.528
(HV polarization)	D2	ls	–	1.721	1.936	–	–	–	1.693	0.362	1.311	1.978	0.311
	D3	ms	ms	–	1.054	–	–	–	0.04	1.013	0.186	1.836	1.862
	D4	hs	hs	ls	–	–	–	–	0.963	1.755	0.835	1.309	1.962
	O1	ms	ms	ps	ps	–	–	–	–	1.035	0.151	1.818	1.817
	O2	ls	ps	ls	ms	–	–	–	ls	–	0.747	1.948	0.747
	O3	ms	ls	ps	ps	–	–	–	ps	ps	–	1.743	1.506
	O4	hs	hs	ms	ls	–	–	–	ms	hs	ms	–	1.985
	O5	ms	ps	ms	hs	–	–	–	ms	ps	ms	hs	–
4 bands	D1	–	1.937	1.994	1.994	–	–	–	1.963	1.644	1.95	1.999	1.976
(HH and HV polarizations)	D2	hs	–	1.916	1.973	–	–	–	1.905	1.451	1.904	1.997	1.459
	D3	hs	hs	–	1.139	–	–	–	1.184	1.629	1.762	1.989	1.999
	D4	hs	hs	ls	–	–	–	–	1.281	1.856	1.83	1.974	1.998
	O1	hs	hs	ls	ls	–	–	–	–	1.449	1.76	1.993	1.952
	O2	ms	ms	ms	ms	–	–	–	ls	–	1.625	1.993	1.899
	O3	hs	hs	ms	ms	–	–	–	ms	ms	–	1.867	1.977
	O4	hs	hs	hs	hs	–	–	–	hs	hs	ms	–	1.999
	O5	hs	ls	hs	hs	–	–	–	hs	ms	hs	hs	–
5 bands	D1	–	1.938	1.994	1.994	–	–	–	1.967	1.813	1.991	1.999	1.977
(HH and HV polarizations + coherence image)	D2	hs	–	1.919	1.974	–	–	–	1.913	1.683	1.978	1.997	1.473
	D3	hs	hs	–	1.227	–	–	–	1.272	1.738	1.941	1.991	1.999
	D4	hs	hs	ls	–	–	–	–	1.404	1.901	1.963	1.974	1.998
	O1	hs	hs	ls	ls	–	–	–	–	1.502	1.897	1.994	1.954
	O2	ms	ms	ms	hs	–	–	–	ms	–	1.737	1.996	1.933
	O3	hs	hs	hs	hs	–	–	–	ms	ms	–	1.992	1.993
	O4	hs	hs	hs	hs	–	–	–	hs	hs	hs	–	1.999
	O5	hs	ls	hs	hs	–	–	–	hs	hs	hs	hs	–
6 bands	D1	–	1.965	1.995	1.996	1.989	1.791	1.99	1.97	1.852	1.972	1.999	1.994
(HH and HV polarization)	D2	hs	–	1.944	1.979	1.786	1.801	1.994	1.933	1.64	1.957	1.999	1.535
	D3	hs	hs	–	1.191	1.999	1.55	1.533	1.212	1.727	1.883	1.998	1.999
	D4	hs	hs	ls	–	1.995	1.79	1.478	1.356	1.895	1.913	1.995	1.999
	D5	hs	ms	hs	hs	–	1.939	1.999	1.989	1.653	1.952	1.999	1.931
	D6	ms	ms	ms	ms	hs	–	1.497	1.559	1.561	1.722	1.984	1.963
	D7	hs	hs	ms	ls	hs	ls	–	1.157	1.561	1.876	1.998	1.999
	O1	hs	hs	ls	ls	hs	ms	ls	–	1.525	1.864	1.999	1.975
	O2	ms	ms	ms	ms	ms	ms	ms	ms	–	1.76	1.998	1.942
	O3	hs	hs	ms	hs	hs	ms	ms	ms	ms	–	1.923	1.993
	O4	hs	hs	hs	hs	hs	hs	hs	hs	hs	hs	–	1.999
	O5	hs	ms	hs	hs	hs	hs	hs	hs	hs	hs	hs	–
7 bands	D1	–	1.966	1.995	1.996	1.99	1.833	1.99	1.975	1.933	1.996	1.999	1.995
(HH and HV polarization + coherence image)	D2	hs	–	1.945	1.979	1.791	1.847	1.994	1.938	1.771	1.99	1.999	1.548
	D3	hs	hs	–	1.275	1.999	1.666	1.546	1.295	1.8	1.968	1.999	1.999
	D4	hs	hs	ls	–	1.995	1.873	1.485	1.447	1.923	1.979	1.995	1.999
	D5	hs	ms	hs	hs	–	1.955	1.999	1.99	1.8	1.991	1.999	1.933
	D6	ms	ms	ms	ms	hs	–	1.583	1.594	1.625	1.859	1.993	1.97
	D7	hs	hs	ms	ls	hs	ms	–	1.271	1.879	1.967	1.998	1.999
	O1	hs	hs	ls	ls	hs	ms	ls	–	1.57	1.94	1.999	1.976
	O2	hs	ms	ms	hs	ms	ms	ms	ms	–	1.827	1.999	1.96
	O3	hs	hs	hs	hs	hs	ms	hs	hs	ms	–	1.996	1.998
	O4	hs	hs	hs	hs	hs	hs	hs	hs	hs	hs	–	1.999
	O5	hs	ms	hs	hs	hs	hs	hs	hs	hs	hs	hs	–

The 2 and 4 band inputs are using amplitude images acquired on 16 September 2010 and 1 February 2011, the 6 band input coupled with the images acquired on 1 November 2010, and the coherence image is added for the 5 and 7 band inputs. Separability value is shown in the upper right half of the table and the ranges of separability in the lower left half of the table. hs: high (good) separability (>1.9); ms: moderate separability (1.5–1.9); ls: low separability (1–1.5); ps: very low (poor) separability (<1).

The map of 2010 Merapi deposits based on MLC using various sets of 16 September 2010 and 1 February 2011 images and nine classes (D1–D4 and O1-O5) of training data is shown in Fig. 6. The corresponding result obtained with the SVM classification is presented in Fig. S2. Classification using only two images (acquired before and after the eruption) of HH polarization (Fig. 6a) produces better results than using HV polarization images (Fig. 6b), whatever the MLC and SVM methods used. However, the pyroclastic deposits on the south flank, as well as tephra-fall deposits on the west flank of the volcano seem slightly better imaged using HV polarization. We have also performed a classification using seven images: six amplitude images for three different dates of acquisition (16 September 2010, 1 November 2010 and 1 February 2011) with HH and HV polarizations and one coherence image (Fig. 7). The false-color composite images (Fig. 7a–b) and classification result (Fig. 7c) can be used as a map of the 2010 Merapi deposits at various times, which compares the 26 October to 1 November 2010 deposits with the deposits of the entire eruption episode. The classification always produces better results when combining both HH and HV images (Fig. 6c) and even better when adding the coherence image (Figs. 6d and 7c) as input. The quality of the resulting classification can be directly related to the separability between the training classes as expressed in Table 2.

4.3. Accuracy assessment

We compared the results obtained on the radar images by MLC classification (Fig. 8b and d) with the GeoEye-1 optical image acquired just before the end of the eruption on the 15 November 2010 (Fig. 8a and c). Comparison was also made between the deposit map produced from high-resolution satellite imagery and field-based data by Charbonnier et al. (2013), Komorowski et al. (2013) and Solikhin et al. (in revision). The results derived from radar data are in good agreement with optical and field information obtained on the south flank of Merapi characterized by a gentle slope at elevations less than 1300 m asl (Fig. 1c) particularly for D1 and D2. The deposit classes D3 and D4 correspond to thin and easily eroded deposits, whose texture is expected to have changed between the time of emplacement and that of radar image acquisition. Field conditions after emplacement of 4-5 November 2010 PDCs, in the Gendol valley at a distance of 10.5 km from Merapi summit, are schematically illustrated in Fig. 8e. At this location in the valley alongside the channel, D1 deposits (1–3 meter thick) containing boulders, smaller clasts and coarse tephra have progressively smoothed the irregular pre-event topography. D2 deposits are mostly located inside the channel, where they were transported from the upper reaches of the valley by lahars that occurred immediately after the eruption. D3 deposits, which represent the ash-cloud surge associated with overbank flows that burned the surrounding vegetation and deposited a few cm-thick layer of ash, are located on both edges of BAF area away from the channel.

Accuracy assessment of the classification has been quantitatively performed by comparing the results of MLC and SVM classification obtained using five input images with control data (Fig. S1c) from four deposit classes (D1–D4). This comparison is summarized in a confusion matrix (Tables 3 and S1). MLC provides better overall classification accuracy (70.03%) than SVM (63.97%). SVM is less accurate than MLC in classifying D3 (27.29%), where most of its control data (52.84%) are classified into O1. Despite the low separabitily between D3, D4 and O1 (1.2–1.4; see Table 2), MLC is still capable of classifying them with fairly good accuracy (55%–58%). We measured the area of the deposits from the MLC classification results and compared it with the area measured

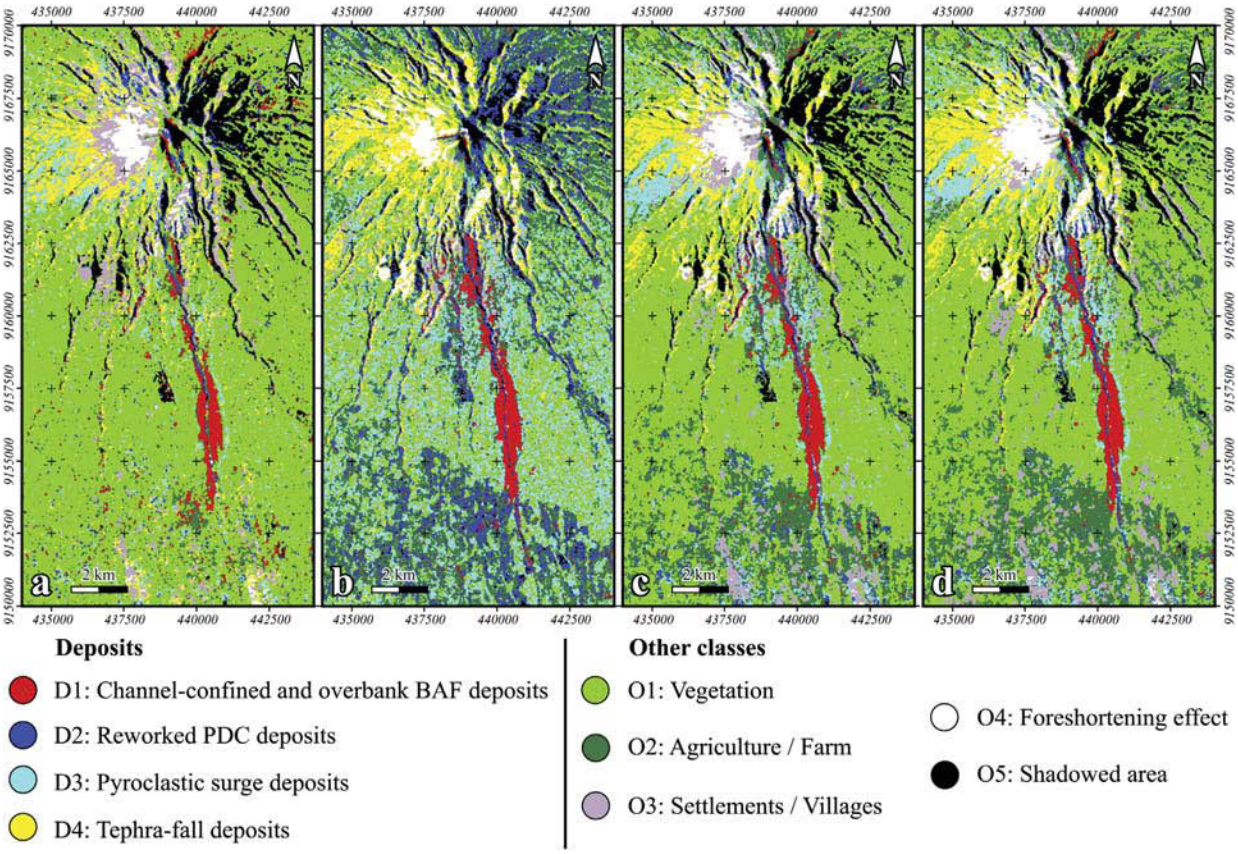

Fig. 6. The map of 2010 Merapi pyroclastic deposits based on the maximum likelihood classification (MLC) using images acquired on 16 September 2010 (before the eruption) and on the 1 February 2011 (after the eruption) for (a) HH polarization only (two images have been used for this purpose); (b) HV polarization only (two images); (c) HH and HV polarizations (four images); and (d) HH and HV polarizations and additional coherence image (five images).

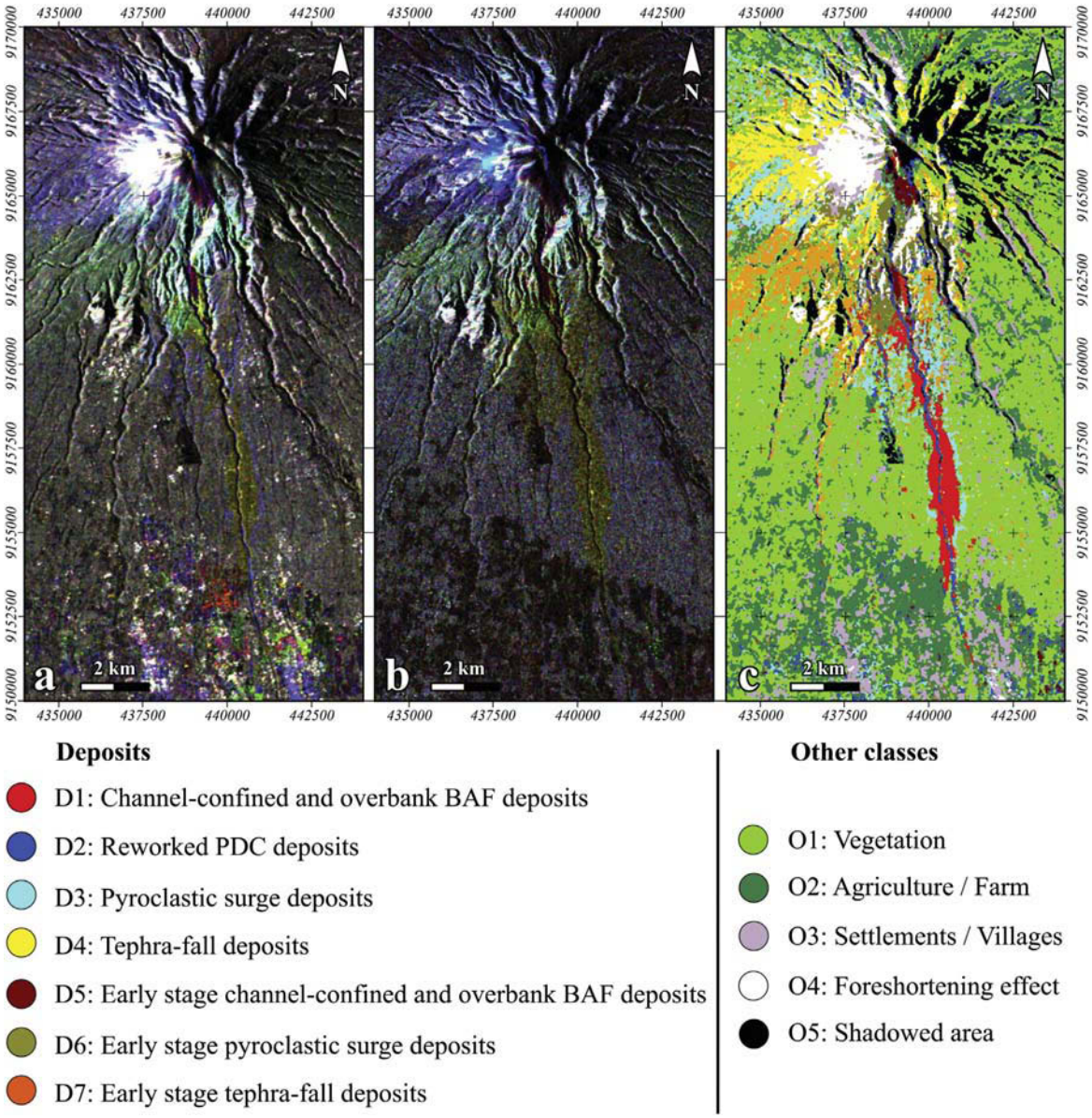

Fig. 7. False-color composite images obtained using amplitude images at three different dates, before (in the red channel), during (green channel) and after (blue channel) the eruption, on 16 September 2010, 1 November 2010 and 1 February 2011 for (a) HH polarization and (b) HV polarization. (c) Map of the 2010 Merapi pyroclastic deposits based on MLC using amplitude for HH and HV polarizations at these three acquisition dates together with the coherence image represented on Fig. 3e (seven images have been used for this purpose).

by Charbonnier et al. (2013). We obtained an area of 4.44 km^2 for D1, 2.22 km^2 for D2 and 4.92 km^2 for D3, while Charbonnier et al. (2013) provided an area of 6.53 km^2 for D1 + D2 and 15.77 km^2 for D3. The estimate of D1 + D2 is consistent with previous results, while the large discrepancy in area estimation for D3 can be partly explained by strong erosion having affected the thin deposits after rainfall and runoff.

The change in amplitude images due to PDC deposition observed in L-band radar images (ALOS-PALSAR, used here) is now compared to the change detected in X-band radar image (TerraSAR-X) used at Soufriere Hills Volcano (SHV) Montserrat by Wadge et al. (2011) as summarized in Table 4. At SHV, for HH polarized data only, the fresh BAF deposits increase X-band backscattering, which is in contrast with the pattern observed on the L-band radar image at Merapi in the summit area at early stage, i.e. less than 7 km from the summit (see Fig. 4a) and then at larger distances further downstream of the Gendol River (Fig. 4b–c). In addition, the 2010 Merapi eruption produced high-energy surges that severely devastated the dense forest, increasing L-band backscattering while the pyroclastic-surge deposits at SHV tend to reduce it.

At SHV (Wadge et al., 2011), the effect of erosion has led to a decrease of the radar backscattering in the central incised part (BAF deposits) and to a relative increase on the valley flank (pyroclastic-surge deposits), which was interpreted as a reversal change in roughness. On the contrary, at Merapi erosion of the surge deposits tend to decrease the radar backscattering (Fig. 4b–c). Additionally, when BAF deposits are reworked by lahars the radar backscattering tends to increase. This comparison has to be taken with caution as the nature and structure of deposits, and the characteristics of erosion processes might be different on these two volcanoes. For example, the 2010 Merapi pyroclastic-flow deposits are observed to be coarser and more poorly sorted than the SHV deposits (Charbonnier et al., 2013), which may lead to differences in the pattern of the radar image. However, the different behavior observed by X-band radar at SHV and L-band

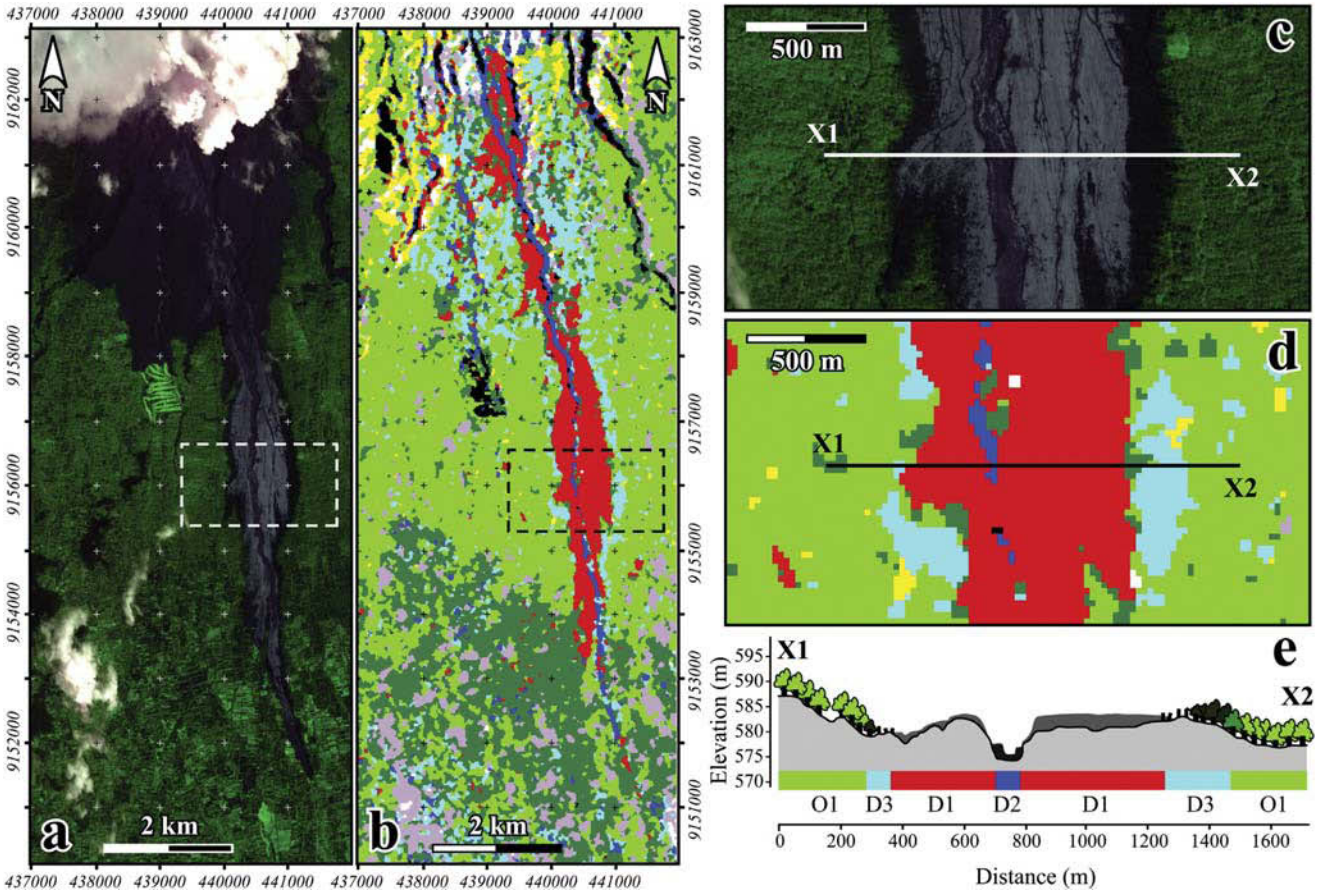

Fig. 8. (a) The 15 November 2010 GeoEye-1 image in false-color composite (R: band 3; G: band 4; B: band 1); (b) MLC results as shown in Fig. 7d for the same area with (a). (c) Zoom in view of the dashed white box in (a) and (d) of the dashed black box in (b). (e) Schematic cross section through X1-X2 transect in (c) and (d) to illustrate the field condition in the Gendol valley, which was partly covered by PDC deposits.

radar at Merapi, may be due to the different wavelengths of the radar data.

5. Conclusion

The 2010 Merapi eruption produced numerous and voluminous pyroclastic density currents (PDCs) at the beginning of the rainy season (26 October–23 November). The ability of L-band radar data of ALOS-PALSAR to classify and map the pyroclastic deposits emplaced during this event has been highlighted by the use of direct-polarized and cross-polarized radar data, and by the combination of amplitude evolution with temporal decorrelation. Changes in amplitude quantified by taking the ratio between the two amplitude images are useful to map pyroclastic deposits. The deposition of valley-confined and overbank BAF products reduces the radar amplitude in direct (HH) and cross (HV) polarizations. This is likely due to a decrease in ground roughness at the scale of the L-band wavelength. PDC deposits reworked and remobilized by runoff are characterized by an increase in ground-backscattering for HH polarization, probably related to an increase in the ground moisture. Deposits of pyroclastic-surge and tephra-fall result in a transient amplitude increase in HH polarization due to the increasingly rough surface, and in HV polarization due to the increasing depolarization over partially damaged vegetation. The increase in the amplitude after pyroclastic-surge deposits in HH polarization is higher than after tephra-fall deposits, but is lower in HV polarization.

Seven deposit classes and five 'non-deposit' classes have been successfully defined from radar data with acceptable separability between each class. The classification produces better outcomes when combining both HH and HV images and when adding the coherence image as input. The resulting classification based on MLC and SVM, using only two images

Table 3
Cross-validated confusion matrix for Maximum Likelihood Classification (SVM) method.The bold font indicates the percentage of correctly classified pixels of each deposit class.

Class	Control data (%)			
	D1	D2	D3	D4
D1	**86.43**	10.38	1.87	0.13
D2	1.79	**76.77**	1.87	0.40
D3	1.62	3.42	**58.48**	30.61
D4	0.00	0.12	2.85	**55.47**
O1	0.67	0.24	26.33	10.72
O2	9.14	4.48	6.93	0.68
O3	0.08	0.00	1.50	1.31
O4	0.27	0.47	0.17	0.45
O5	0.02	4.13	0.00	0.23

Table 4
Comparison of the change due to PDC deposition observed in L-band radar images (ALOS-PALSAR, used here at Merapi volcano) and in X-band radar image (TerraSAR-X) used at Soufriere Hills Volcano (SHV) Montserrat (Wadge et al., 2011).

Deposit	L-band in Merapi	X-band in SHV
Block-and-ash flow	Decrease	Increase
Pyroclastic-surge	Increase	Decrease

(acquired before and after the eruption) of HH polarization is better than using the HV polarization images. However, the pyroclastic deposits mantling the Merapi southern flank, and the 2 to 7 cm thick tephra-fall deposits on the western flank are better imaged using HV polarization. When comparing the classification results with control samples based on high-spatial-resolution satellite imagery and field-based studies, MLC provides a better classification accuracy (70%) than SVM (64%).

Our classification of the 2010 Merapi deposits is based on change detection and semi-automated (supervised) classification methods applied to ALOS-PALSAR dual polarization data. It can also be utilized for other active volcanoes with new pyroclastic deposits. Moreover, the ability of SAR data to possibly provide information during day or night, independently from the meteorological conditions, and penetrate the vegetation canopy, highlights the value of using ALOS-PALSAR dual polarization data at the active volcanoes during or shortly after eruption for hazard mitigation.

Acknowledgments

The support from several partner institutions is acknowledged: the French Embassy for A. Solikhin's PhD grant, the cooperation between RESTEC Japan with Indonesian LAPAN and Geological Agency as well as JAXA project no. 1188 for ALOS-PALSAR images, CRISP-NUS and ICT Asia for the GeoEye image, the CNES project on Merapi remote sensing (JCT). This work is part of the DOMERAPI project funded by the French National Research Agency (ANR-12-BS06-0012) and supported by the French Institute of Research for Development (IRD). The authors are grateful to Emmanuel Trouvé for fruitful discussions and advice, as well as to Katie Preece for English improvement. We also thank the reviewers for their relevant comments and suggestions, which served to improve the overall quality of the paper.

Appendix A. Supplementary data

Supplementary data to this article can be found online at http://dx.doi.org/10.1016/j.rse.2014.11.002.

References

Bignami, C., Ruch, J., Chini, M., Buongiorno, M.F., Hidayati, S., Sayudi, D.S., et al. (2013). Pyroclastic density current volume estimation after the 2010 Merapi volcano eruption using X-band SAR. *Journal of Volcanology and Geothermal Research*, *261*, 236–243, http://dx.doi.org/10.1016/j.jvolgeores.2013.03.023.

Blom, R.G., Schenck, L.R., & Alley, R.E. (1987). What are the best radar wavelengths, incidence angles, and polarizations for discrimination among lava flows and sedimentary rocks? A statistical approach. *IEEE Transactions on Geoscience and Remote Sensing, GE-25*, 208–213.

Branney, M.J., & Kokelaar, B.P. (2002). Pyroclastic density currents and the sedimentation of ignimbrites. *Memoirs. Geological Society of London*, *27*, 143.

Budi-Santoso, A., Lesage, P., Dwiyono, S., Sumarti, S., Subandriyo, Surono, Jousset, P., et al. (2013). Analysis of the seismic activity associated with the 2010 eruption of Merapi Volcano, Java. *Journal of Volcanology and Geothermal Research*, *261*, 153–170, http://dx.doi.org/10.1016/j.jvolgeores.2013.03.024.

Carn, S.A. (1999). Application of synthetic aperture radar (SAR) imagery to volcano mapping in the humid tropics: A case study in East Java, Indonesia. *Bulletin of Volcanology*, *61*, 92–105, http://dx.doi.org/10.1007/s004450050265.

Charbonnier, S.J., Germa, A., Connor, C.B., Gertisser, R., Preece, K., Komorowski, J. -C., et al. (2013). Evaluation of the impact of the 2010 pyroclastic density currents at Merapi volcano from high-resolution satellite imagery, field investigations and numerical simulations. *Journal of Volcanology and Geothermal Research*, *261*, 295–315, http://dx.doi.org/10.1016/j.jvolgeores.2012.12.021.

Cracknell, M.J., & Reading, A.M. (2014). Geological mapping using remote sensing data: A comparison of five machine learning algorithms, their response to variations in the spatial distribution of training data and the use of explicit spatial information. *Computers and Geosciences*, *63*, 22–33, http://dx.doi.org/10.1016/j.cageo.2013.10.008.

Dellwig, L.F., & Moore, R.K. (1966). The geological value of simultaneously produced like- and cross-polarized radar imagery. *Journal of Geophysical Research*, *71*, 3597–3601, http://dx.doi.org/10.1029/JZ071i014p03597.

Dietterich, H.R., Poland, M.P., Schmidt, D.A., Cashman, K.V., Sherrod, D.R., & Espinosa, A.T. (2012). Tracking lava flow emplacement on the east rift zone of Kīlauea, Hawai'i, with synthetic aperture radar coherence. *Geochemistry, Geophysics, Geosystems*, *13*, http://dx.doi.org/10.1029/2011gc004016 (17 pp.).

Gaddis, L.R. (1992). Lava-flow characterization at Pisgah volcanic field, California, with multiparameter imaging radar. *Geological Society of America Bulletin*, *104*, 695–703, http://dx.doi.org/10.1130/0016-7606(1992)104<0695:lfcapv>2.3.co;2.

Head, E.N., Maclean, A.L., & Carn, S.A. (2012). Mapping lava flows from Nyamuragira volcano (1967–2011) with satellite data and automated classification methods. *Geomatics, Natural Hazards and Risk*, *4*(2), 119–144, http://dx.doi.org/10.1080/19475705.2012.680503.

Hooper, A., Sigmundsson, F., & Prata, F. (2012). Remote sensing of volcanic hazards and their precursors. *Proceedings of the IEEE*, *100*(10), 2908–2930.

Komorowski, J. -C., Jenkins, S., Baxter, P.J., Picquout, A., Lavigne, F., Charbonnier, S., et al. (2013). Paroxysmal dome explosion during the Merapi 2010 eruption: Processes and facies relationships of associated high-energy pyroclastic density currents. *Journal of Volcanology and Geothermal Research*, *261*, 260–294, http://dx.doi.org/10.1016/j.jvolgeores.2013.01.007.

Lu, Z., & Dzurisin, D. (2014). *InSAR Imaging of Aleutian Volcanoes: Monitoring a Volcanic Arc from Space*. Springer Praxi (ISBN 978-3-642-00347-9, 390 pp.).

MacKay, M.E., & Mouginis-Mark, P.J. (1997). The effect of varying acquisition parameters on the interpretation of SIR-C radar data: The Virunga volcanic chain. *Remote Sensing of Environment*, *59*(2), 321–336, http://dx.doi.org/10.1016/s0034-4257(96)00144-7.

Massonnet, D., & Sigmundsson, F. (2000). Remote sensing of volcano deformation by radar interferometry from various satellites. *Remote Sensing of Active Volcanism. 116*. (pp. 207–221). Washington, DC: AGU.

McAlpin, D., & Meyer, F.J. (2013). Multi-sensor data fusion for remote sensing of post-eruptive deformation and depositional features at Redoubt Volcano. *Journal of Volcanology and Geothermal Research*, *259*, 414–423, http://dx.doi.org/10.1016/j.jvolgeores.2012.08.006.

Pallister, J.S., Schneider, D.J., Griswold, J.P., Keeler, R.H., Burton, W.C., Noyles, C., et al. (2013). Merapi 2010 eruption—Chronology and extrusion rates monitored with satellite radar and used in eruption forecasting. *Journal of Volcanology and Geothermal Research*, *261*, 144–152, http://dx.doi.org/10.1016/j.jvolgeores.2012.07.012.

Pyle, D.M., Mather, T.A., & Biggs, J. (2013). Remote sensing of volcanoes and volcanic processes: Integrating observation and modeling—Introduction. *Geological Society, London, Special Publications*, *380*(1), 1–13, http://dx.doi.org/10.1144/sp380.14.

Richards, J.A., & Jia, X. (2006). *Remote sensing digital image analysis: An introduction* (4th ed.). Berlin: Springer-Verlag978-3-540-29711-6 (439 pp.).

Rosen, P.A., Henley, S., Peltzer, G., & Simons, M. (2004). Updated repeat orbit interferometry package released. *Eos, Transactions of the American Geophysical Union*, *85*(5), 47, http://dx.doi.org/10.1029/2004eo050004.

Saepuloh, A., Koike, K., & Omura, M. (2012). Applying Bayesian decision classification to Pi-SAR polarimetric data for detailed extraction of the geomorphologic and structural features of an active volcano. *IEEE Geoscience and Remote Sensing Letters*, *99*(4), 554–558, http://dx.doi.org/10.1109/lgrs.2011.2174611.

Saepuloh, A., Koike, K., Omura, M., Iguchi, M., & Setiawan, A. (2010). SAR- and gravity change-based characterization of the distribution pattern of pyroclastic flow deposits at Mt. Merapi during the past 10 years. *Bulletin of Volcanology*, *72*(2), 221–232, http://dx.doi.org/10.1007/s00445-009-0310-x.

Saepuloh, A., Urai, M., Aisyah, N., Sunarta, Widiwijayanti, C., Subandriyo, et al. (2013). Interpretation of ground surface changes prior to the 2010 large eruption of Merapi volcano using ALOS/PALSAR, ASTER TIR and gas emission data. *Journal of Volcanology and Geothermal Research*, *261*, 130–143, http://dx.doi.org/10.1016/j.jvolgeores.2013.05.001.

Schaber, G.G., Elachi, C., & Farr, T.G. (1980). Remote sensing data of SP Mountain and SP lava flow in North-Central Arizona. *Remote Sensing of Environment*, *9*, 149–170, http://dx.doi.org/10.1016/0034-4257(80)90005-x.

Solikhin, A., Thouret, J. -C., Gupta, A., Harris, A.J., & Liew, S.C. (2012). Geology, tectonics, and the 2002–2003 eruption of the Semeru volcano, Indonesia: Interpreted from high-spatial resolution satellite imagery. *Geomorphology*, *138*, 364–379, http://dx.doi.org/10.1016/J.geomorph.2011.10.001.

Solikhin, A., Thouret, J. -C., Liew, S.C., Gupta, A., Sayudi, D.S., Oehler, J. -F., et al. (2014n). High-spatial resolution imagery helps track the effects and deposits of the large (VEI 4) 2010 Merapi Volcano eruption. *Bulletin of Volcanology* (in revision).

Sparks, R.S.J., Biggs, J., & Neuberg, J.W. (2012). Monitoring volcanoes. *Science*, *335*, 1310–1311, http://dx.doi.org/10.1126/science.1219485.

Surono, Jousset, P., Pallister, J., Boichu, M., Buongiorno, M.F., Budisantoso, A., et al. (2012). The 2010 explosive eruption of Java's Merapi volcano—A '100-year' event. *Journal of Volcanology and Geothermal Research*, *241-242*, 121–135, http://dx.doi.org/10.1016/j.jvolgeores.2012.06.018.

Syahbana, D.K. (2013). *Seismological study of volcanic activity at Papandayan volcano, West Java, Indonesia.* (PhD thesis). Brussels: Universite Libre de Bruxelles.

Thouret, J. -C., Gupta, A., Lube, G., Liew, S.C., Cronin, S.J., & Surono (2010). The 2006 pyroclastic deposits of Merapi Volcano, Java, Indonesia: High-spatial resolution IKONOS images and complementary ground based observations. *Remote Sensing of Environment*, *114*, 1949–1967, http://dx.doi.org/10.1016/j.rse.2010.03.016.

Tupin, F., Inglada, J., & Mercier, G. (2014). Image processing techniques for remote sensing. In F. Tupin, J. -M. Nicolas, & J. Inglada (Eds.), *Remote Sensing Imagery*. ISTE Ltd, Wiley, John & Sons, Incorporated9781848215085.

Vapnik, V.N. (1998). *Statistical Learning Theory*. New York: Wiley-Interscience.

Wadge, G., Cole, P., Stinton, A., Komorowski, J. -C., Stewart, R., Toombs, A.C., et al. (2011). Rapid topographic change measured by high-resolution satellite radar at Soufriere Hills Volcano, Montserrat, 2008–2010. *Journal of Volcanology and Geothermal Research*, *199*, 142–152, http://dx.doi.org/10.1016/j.jvolgeores.2010.10.011.

Wadge, G., Saunders, S., & Itikarai, I. (2012). Pulsatory andesite lava flow at Bagana Volcano. *Geochemistry, Geophysics, Geosystems*, *13*, Q11011, http://dx.doi.org/10.1029/2012GC004336.

Wadge, G., Scheuchl, B., & Stevens, N.F. (2002). Spaceborne radar measurements of the eruption of Soufriere Hills Volcano, Montserrat. In T.H. Druitt, & B.P. Kokelaar (Eds.), *The eruption of Soufriere Hills Volcano, Montserrat, from 1995 to 1999. Geological Society, London, Memoir*, *21*. (pp. 583–594).

Yulianto, F., Sofan, P., Khomarudin, M.R., & Haidar, M. (2013). Extracting the damaging effects of the 2010 eruption of Merapi volcano in Central Java, Indonesia. *Natural Hazards*, *66*, 229–247, http://dx.doi.org/10.1007/s11069-012-0438-4.

Zebker, H., Amelung, F., & Jonsson, S. (2000). Remote sensing of volcano surface and internal processes using radar interferometry. In P.J. Mouginis-Mark, J.A. Crisp, & J.H. Finks (Eds.), *Remote Sensing of Active Volcanism. Vol. 116*. (pp. 179–205). Washington, DC: AGU.

Zebker, H.A., Rosen, P.A., Hensley, S., & Mouginis-Mark, P.J. (1996). Analysis of active lava flows on Kilauea volcano, Hawaii, using SIR-C radar correlation measurements. *Geology*, *24*, 495–498, http://dx.doi.org/10.1130/0091-7613(1996)024<0495:aoalfo>2.3.co;2.

Zebker, H.A., van Zyl, J.J., & Held, D.N. (1987). Imaging radar polarimetry from wave synthesis. *Journal of Geophysical Research*, *92*, 683–701, http://dx.doi.org/10.1029/JB092iB01p00683.

Chapter 6 - Responses of Merapi and Semeru eruptive activity to regional tectonic events: first results

6.1. Introduction

The initiating mechanisms of volcanic eruptions commonly include magma influx from deeper reservoirs and an increase in the magma/gas pressure in the plumbing system towards the edifice. The main importance in understanding how and why a volcano erupts is to determine factors that drive changes in volcanic activity. Volcanoes are systems that may interact with their environment at different scales, and with different modes and processes. Fluctuations in volcanic activity may be influenced by external factors such as Earth tides (e.g., Johnston & Mauk, 1972; Sparks, 1981), daily variations in atmospheric pressure and temperature (e.g., Neuberg, 2000), changes in sea level (e.g., McGuire et al., 1997), and surface load variations (e.g., Pinel & Jaupart, 2000, 2005; Albino et al., 2010). In addition, seismotectonic activities have been widely discussed as a key process and event external to volcanoes that are able to affect volcanic activity.

Stress changes associated with a large (above magnitude 7) earthquake are capable of triggering volcanic unrest and possibly even triggering eruptions in special situations. Triggering of volcanic unrest (e.g., as earthquake swarms) may take place over a wide range of distances (a few kilometers to several hundreds of kilometers). Times delays depend on the mechanism and range from a few minutes for dynamic triggering to several days, weeks, months or years for static triggering. Such eruption triggering occurs under the right circumstances, which depends on the earthquake parameters (magnitude, distance to the epicenter, and orientation of the earthquake focal mechanism), as well as on the initial state of the magmatic system prior to the earthquake, i.e. on state of equilibrium of magma and volatiles, magma overpressure, and the strength of the host rocks (Hill et al., 2002). Interaction between earthquake and eruptive activity may occur at short distances by static stress diffusion (Walter & Amelung, 2007) and at distance of several hundred kilometers or more by dynamic stress transfer (Hill et al., 2002; Manga & Brodsky, 2006). Static stress change is the difference in the stress field from just before an earthquake to shortly after the seismic

waves have decayed, while dynamic stresses are induced by the seismic waves from a large earthquake (Hill et al., 2002). Volcano response to the earthquake depends on the magnitude and distance of the earthquake as well as the fault orientation in relation to the location of the volcano (Delle Donne et al., 2010). Triggering of volcanic eruptions by regional earthquakes has been observed or proposed for both effusive and explosive eruptions, for example the November 1975 Kilauea eruption was a small basalt eruption that took place along a local fault that transected intersected shallow magma (Tilling et al., 1976), the 1991 Pinatubo eruption is thought by some workers to have been favored by static stress changes from an earthquake in northern Luzon a year before (Bautista et al., 1996), and the 1960 Cordón Caulle rift eruption (Lara et al., 2004) is one of the few clear cases of eruption triggering. This eruption took place 38 hours after the M 9.5 Chile earthquake and is clearly related to the tensional response of the crust to the earthquake. A global study found a statistically significant increase in the number of eruptions following large earthquakes (e.g., Linde & Sacks, 1998). However, regional earthquake events are not always able to trigger an eruption itself, but do have sufficient influence to modify the rhythm of activity at on-going eruptions (Harris & Ripepe, 2007; Walter et al., 2007; Delle Donne et al., 2010).

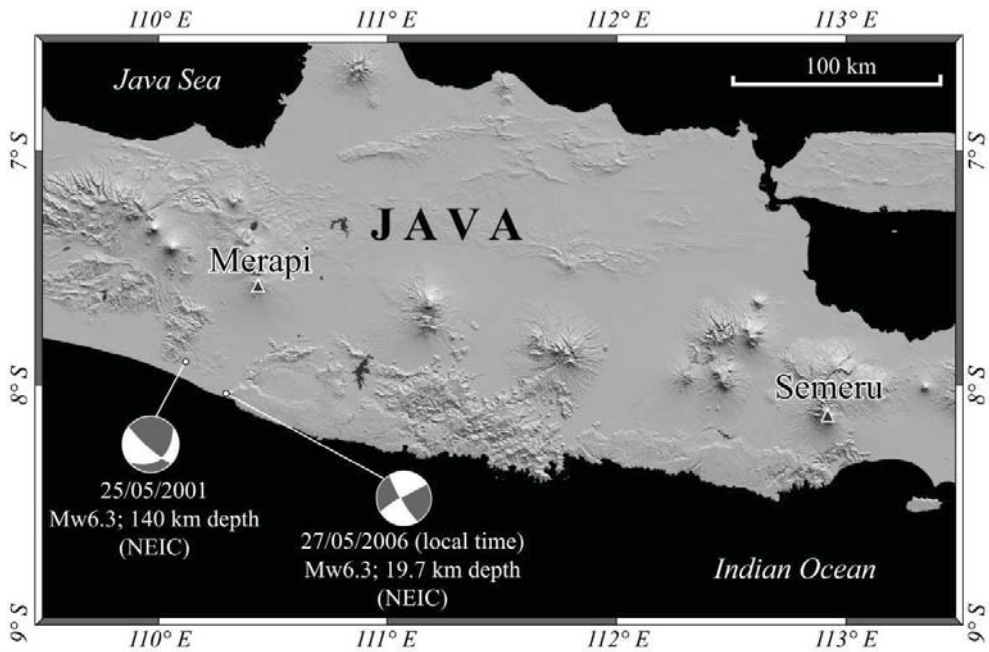

Figure 6.1. Shaded relief map of central and eastern part of Java showing Merapi and Semeru volcanoes (triangles) with epicenters of the 2001 and 2006 earthquakes (circles). Earthquake data and focal mechanisms after the global Centroid-Moment-Tensor (CMT) catalogue (www.globalcmt.org). Regional structural map of Semeru and Merapi volcano can be seen in Chapter 2 (Fig. 2.13 and 2.19)

Geology and structural maps of Semeru and Merapi volcanoes show that the structural features of the edifices are linked to its regional tectonic setting (see Figs. 2.13 and 2.19 in Chapter 2). The structural pattern of the edifice and its surroundings raises the possibility that Semeru and Merapi will respond to tectonic events with a potentially increased activity due to additional stress under the volcano. In this chapter, we discuss the interactions between regional tectonic earthquakes in Java and the volcanic activity of two persistently active volcanoes, Semeru and Merapi. Past evidence lies with two Mw 6.3 Java earthquakes in 2001 and 2006, which Walter et al. (2007) suggested led to an increase in activity at Merapi. Moreover, it has been suggested that the 2006 earthquake not only affected the Merapi activity but also activity at Semeru, ~260 km from Merapi (Harris & Ripepe, 2007). One of the earthquakes took place at a horizontal distance of ~50 km southwest of Merapi (Fig. 6.1), and at ~130 km in depth associated with the activity of the subducting slab under the region. Merapi was already in a phase of higher activity when the tectonic earthquake struck, and a sudden increase of about 30° C in fumarole temperature at a site about 200 m southeast of the Merapi crater coincided with the 25 May 2001 earthquake (Walter et al., 2007). Merapi and Semeru volcanoes were also in a phase of higher activity when the 27 May 2006 (local time) earthquake took place. The earthquake was produced by motion on a crustal fault located ~50 km south of Merapi and ~280 km west of Semeru (Fig. 6.1). Both volcanoes experienced an increase in thermal and eruptive volume flux beginning 3 days after the earthquake while this response lasted 9 days at both volcanoes (Harris & Ripepe, 2007).

The objective of this chapter is to show some insight in the interactions between regional earthquakes and volcanic activity of Merapi and Semeru, over the period 2000-2014. Then, the results can be followed up in further study in order to find a clear correlation between the response of persistently active volcano to the occurrence of regional earthquakes. This chapter also aims to examine the advantage of satellite infrared data to approach the eruptive activity of the two volcanoes. In this case, we used infrared data from the Moderate Resolution Imaging Spectroradiometer (MODIS) sensors.

6.2. Method

Infrared observations have particular utility in the study of active volcanoes by virtue the very nature of volcanism, which is associated with the transfer of heat to the surface (Oppenheimer, 1998). The thermal emittance of a volcanic surface relates to its activity at a specific time, which may consist of an active lava flow, lava lake or lava dome, a system of fumaroles or a more subtly radiant surface heated by shallow magma intrusions. As a result, infrared observations may indicate impending changes in activity, or may simply provide information as to a particular volcano activity status. Various satellite instruments, which have infrared observational functionality and are able to provide global and regional volcanic hotspots on an hourly to daily basis, have been widely used for monitoring the eruptive state of active volcanoes (e.g., Harris et al, 2000; Wright et al., 2004; Blackett, 2013; Jay et al., 2013).

We followed Harris and Ripepe (2007) methodology in estimating the heat and volume fluxes to approach the activity of Merapi and Semeru volcanoes. The fluxes are estimated by using the radiance data from MODVOLC, the MODIS volcanic hot spot detection algorithm (Wright et al., 2002). The MODIS sensors are onboard the Terra and Aqua satellites platforms that belong to the US National Aeronautic and Space Administration (NASA). The sensors on these two satellites pass over every point on the planet four times a day. MODVOLC is a non-interactive algorithm that allows automated global hotspot detection in MODIS data and provides a global inventory for volcanic hotspots dating back to February 2000 and available at http://hotspot.higp.hawaii.edu (Wright et al., 2004). This algorithm computes a normalized thermal index to detect the volcanic hot spots, which are calculated on the basis of the middle infrared and thermal infrared radiances measured in the MODIS bands 21 or 22, and 32, respectively (Wright et al., 2002; 2004). However, MODVOLC is not intended to detect low intensity activity (open vent degassing, fumarolic activity and Strombolian activity) and is unable to quantify the influence of clouds and eruption plume, thus its database does not provide complete information for all aspects of volcanic activity. Therefore we use seismic data to be compared with available heat and volume fluxes data as well as to cover the lack of MODVOLC data due to the limitations described above.

We combined thermal infrared data with seismic data to evaluate the activity of Merapi and Semeru volcanoes and potential relationships to regional earthquakes. The use of

seismological observations in the monitoring and forecasting of volcanic eruptions is justified because almost all volcanic eruptions have been accompanied by some sort of seismic anomaly. Seismic activity on volcanoes is generally considered to be an indication of their internal state of activity. When magma and volcanic gases or fluids move, they will either cause rocks to break or cracks to vibrate. Then, crack vibration may trigger a continuous shaking associated with the resonance of a fluid-filled resonator called volcanic tremor. In addition, superficial volcanic activities such as explosive events, pyroclastic density currents (PDCs) and rockfalls also can be detected by seismometers. For this study, our seismic dataset consists of the daily and monthly number of classified volcanic events at Merapi and Semeru volcanoes, for a period spanning 2000 to the end of 2014. This statistical data of seismic events are taken from several seismic stations with short-period seismometer around each of the two volcanoes (Fig. 6.2), and the signals are recorded continuously in digital as well as in analog on paper drums at the observatories. Paper seismograms are examined every day to record the number and the magnitude of various seismic events. It relies on routine manual counting and classification of events based on waveform shape. In addition, up to six broadband seismometers were installed on Merapi, but they were only operated temporarily between July 2009 and February 2010 (Budi-Santoso et al., 2013). Therefore, we use only the short-period seismic data, which continuously and consistently covers the period of our study. In addition, due to limited seismic data, our study only applied a simple analysis based on the number of volcanic events and an estimation of the energy of events.

The classification of seismic signal types and other events at Merapi includes deep (>2 km beneath the summit) volcano-tectonic (VT-A or "type A"), shallow (<2 km) volcano-tectonic (VT-B or "type-B"), multiphase (MP), low frequency (LF), rockfall, pyroclastic density current (PDC), and gas burst events (Ratdomopurbo & Poupinet, 2000). At Semeru, seismically expressed volcanic events are classified into five types of events: deep (1-20 km beneath the volcanic crater) volcano-tectonic (VT-A or "type-A"), shallow (<1 km) volcano-tectonic (VT-B or "type-B"), tremor, rockfall, and explosion with associated gas burst (*hembusan* in Indonesian). The LF and MV events are not classified at Semeru. The classification refers to, and adopts the terminology of seismic events proposed by Minakami (1974). Volcano-tectonic (VT-A and VT-B) events are related to brittle failure in volcanic rocks triggered by fluid movement while LF and tremor events

have been interpreted as due to the resonance of a fluid-filled resonator excited by a pressure disturbance (Kumagai, 2009). A multiphase (MP) event is related to magma flow in the upper conduit and to dome growth (Ratdomopurbo & Poupinet, 2000). Rockfall and PDC events have a similar seismic signal pattern to MP events, but PDC signals have a longer duration (up to tens of minutes) and larger amplitude (Budi-Santoso et al., 2013). Gas burst and explosive (vulcanian or phreatic) events that have a similar signal pattern are differentiated by their amplitude and range frequency, after which explosive events have a larger amplitude and wider range of frequency (the explosive events tend to include higher frequencies). Seismic energy for volcanic events is calculated using the Guttenberg-Richter equation

$$\log E = 11.8 + 1.5M \quad \text{(Gutenberg \& Richter, 1956)}, \qquad (1)$$

where E is energy (in ergs.) and M is the magnitude calculated using the local magnitude definition of Richter (1958). In addition, real-time seismic amplitude measurement (RSAM) and seismic spectral amplitude measurement (SSAM) are applied to digital seismic data recorded from the stations Plawangan (PLA) at Merapi and Leker (LEK) at Semeru (Fig. 6.2). RSAM is a robust tool for monitoring volcanic activity that provides a simple indicator of the level of released seismic energy (Endo & Murray, 1991).

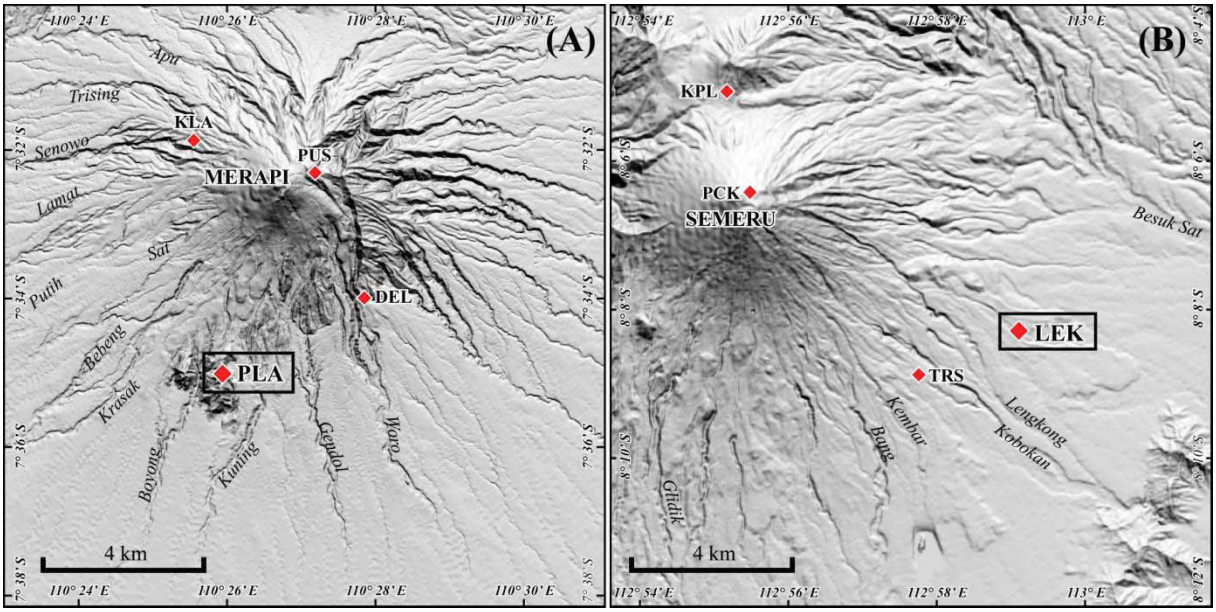

Figure 6.2. Map of seismic stations with short-period seismometer that are used for analysis of volcanic event at (A) Merapi and (B) Semeru volcanoes. The real-time seismic amplitude measurement (RSAM) and seismic spectral amplitude measurement (SSAM) are performed using seismic data recorded from two stations, Plawangan (PLA) at Merapi and Leker (LEK) at Semeru.

In this chapter we have inventoried earthquake events that might be expected to alter the volcanic activity at Semeru and Merapi during the period 2000-2014. We limited our study to the earthquakes occurring at less than 1000 km from the volcanoes. The reported earthquakes can be derived from activities of subduction zone (Java megathrust), deep intraplate, and crustal faulting. However, we do not restrict this study to the large tectonic earthquakes (magnitude ≥ 6) but also include relatively small events (magnitude 3 to 5) occurring closer to the volcanoes. We used two earthquake catalogues, i.e. the US Geological Survey National Earthquake Information Center (NEIC) and Indonesian *Badan Meteorologi, Klimatologi dan Geofisika* (BMKG). NEIC provides earthquakes with a magnitude greater than 4 and uses the moment magnitude (Mw) for each earthquake. BMKG provides earthquakes that are not recorded by NEIC, mostly small magnitude events. However, BMKG uses the local magnitude (M_L) or sometimes the body-wave magnitude (mb) for each recorded earthquake. We homogenize the earthquake magnitude into Mw by converting mb based on the formula of Scordilis (2006) and M_L based on Irsyam et al. (2010). Several earthquakes (mostly greater than Mw 5) have focal mechanism information, as given by the Harvard Centroid Moment Tensor Project (http://www.globalcmt.org), which helped us to determine the earthquake focal mechanism. Each earthquake was cross-checked with the time series of volcanic heat flux and seismic events searching for a change in volcanic activity immediately following each event.

6.3. Seismic and thermal radiance data for Merapi and Semeru

6.3.1. Seismicity

History of the seismic activity at Merapi and Semeru volcanoes during the period 2000-2014 is shown in Figures 6.3 and 6.4, respectively. During this period of 15 years, Merapi has erupted in 2001, 2006 and 2010. Eruptions at Merapi are generally preceded by VT and MP seismicity varying in time scale from weeks to months as a manifestation of magma intrusion and formation of lava domes (Ratdomopurbo & Poupinet, 2000; Budi-Santoso et al., 2013). PDCs and/or glowing rock avalanches are generated from lava dome collapse due to gravitational instability or lava dome destruction due to an explosion. After dome collapse and PDC-producing eruptions, the unstable volcanic rocks of the dome and vertical crater rims trigger rockfalls for as long as one or two

years. The general pattern of seismic activity mentioned above occurred during the 2001 and 2006 eruptions of Merapi, as shown in seismic event number on a daily basis in Figure 6.3. Compared with the previous two eruptions based on seismic data, the 2010 eruption had a larger magnitude and a different pattern of eruption stages (Surono et al., 2012; Budi-Santoso et al., 2013). VT and MV seismicity started to increase 6, 10 and 12 months before the 2001, 2006 and 2010 eruptions, respectively (Fig. 6.3). However in 2010, a significant increase in VT and MP events occurred 1.5 months only prior to the eruption. The number of PDC events in 2010 was smaller than in 2006 but these flows had larger magnitude and were preceded by more VT and MP events. After the 2010 eruption, explosion events associated with phreatic eruptions and gas bursts were frequently observed at Merapi and had relatively small magnitudes seismic signatures.

Volcanic-related seismicity at Semeru is dominated by explosive (gas burst, Strombolian and vulcanian) events with 2500 events per month or 90-100 events per day on average. Each eruption produces volcanic plumes rising a few hundred to a few thousand meters (Nishi et al. 2007; Thouret et al., 2007). Since 1967, small Strombolian-vulcanian eruptions have occurred at intervals of 5–60 min, accompanied by ash clouds rising to less than 1 km (Iguchi et al., 2008). At Semeru, rockfalls are generated mostly from the unconsolidated ejected and tephra products in the Jonggring Seloko crater and pyroclastic deposits in the scar. This is different from Merapi, where rockfalls are generated mostly from dome collapse. Since at least 1990, VT-A events in Semeru show a long-term variation every 7 to 8 years with maxima at the ends of 2000 and 2008 (Fig. 6.4). This apparent 'cycle' may be followed by an increase in Semeru activity that produced several kilometer-high eruption columns, ballistic bombs and thick tephra fall as described by Thouret et al. (2007). In addition, one to two years after the intensive VT-A events, PDC-producing eruptions occurred at Semeru, such as during the December 2002-January 2003 and November 2010 eruptions. Since early 2009, eruption behavior of Semeru has changed. This change began with a gradual decrease in number of explosions over about six months. Since 2010, Semeru explosions have been dominated by gas burst events in which the rapid effusion of steam is accompanied by explosive sounds and white plumes (Nishimura et al., 2012). This activity is typically followed by intensive volcanic tremor, thought to be related to magma migration from

depth to the upper part of conduit. Since 2010, Semeru eruptions have become mainly effusive with lava flows and dome-coulées erupted from a central vent.

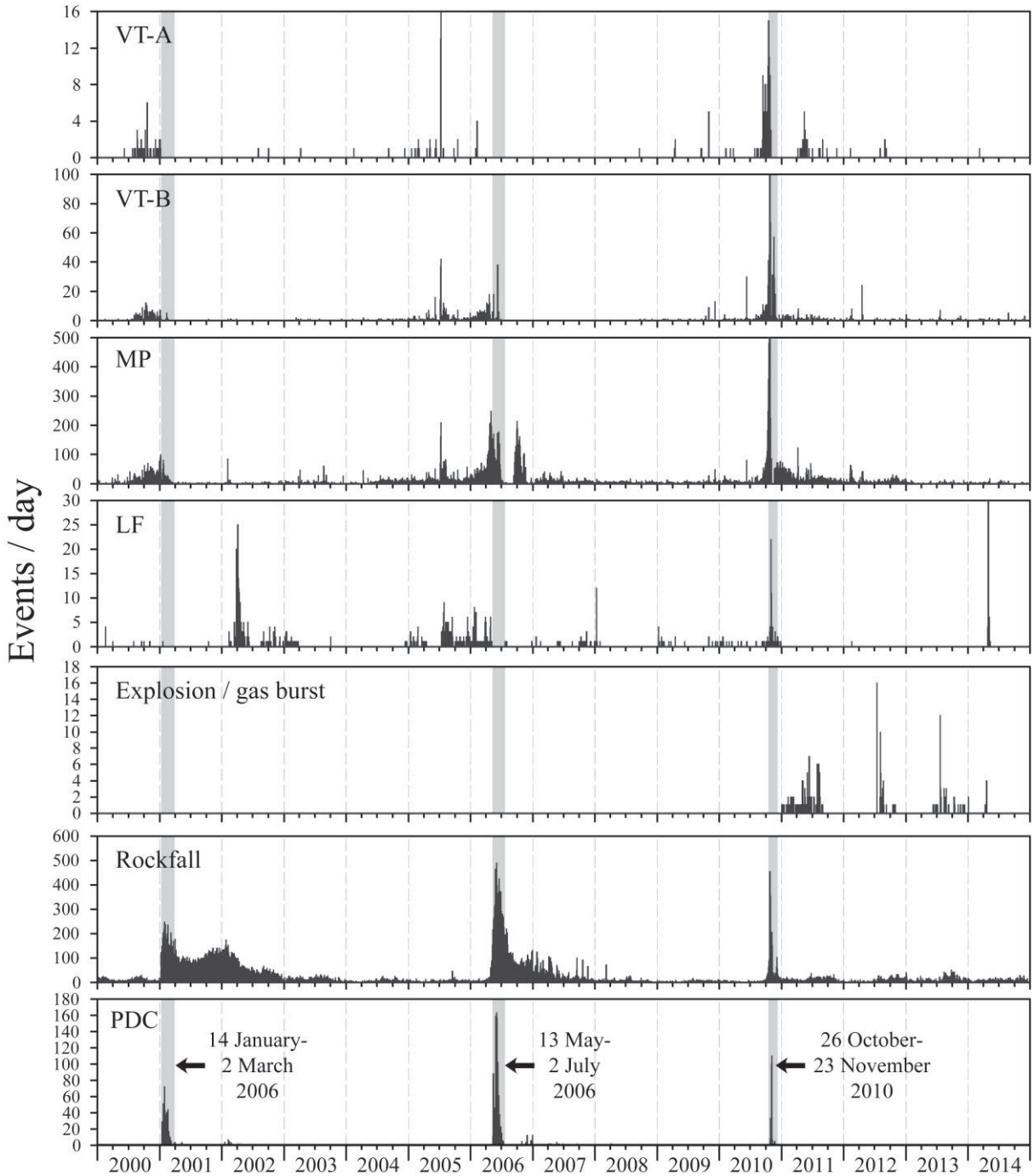

Figure 6.3. Daily numbers of seismic events at Merapi during the period 2000-2014 including type-A and -B volcano-tectonics (VT-A and VT-B), multiphase (MP), low frequency (LF), explosion / gas burst, rockfall and PDC events. Daily seismic events are reported in local time (GMT +7). Gray boxes indicate the period of major eruptions in 2001, 2006 and 2010.

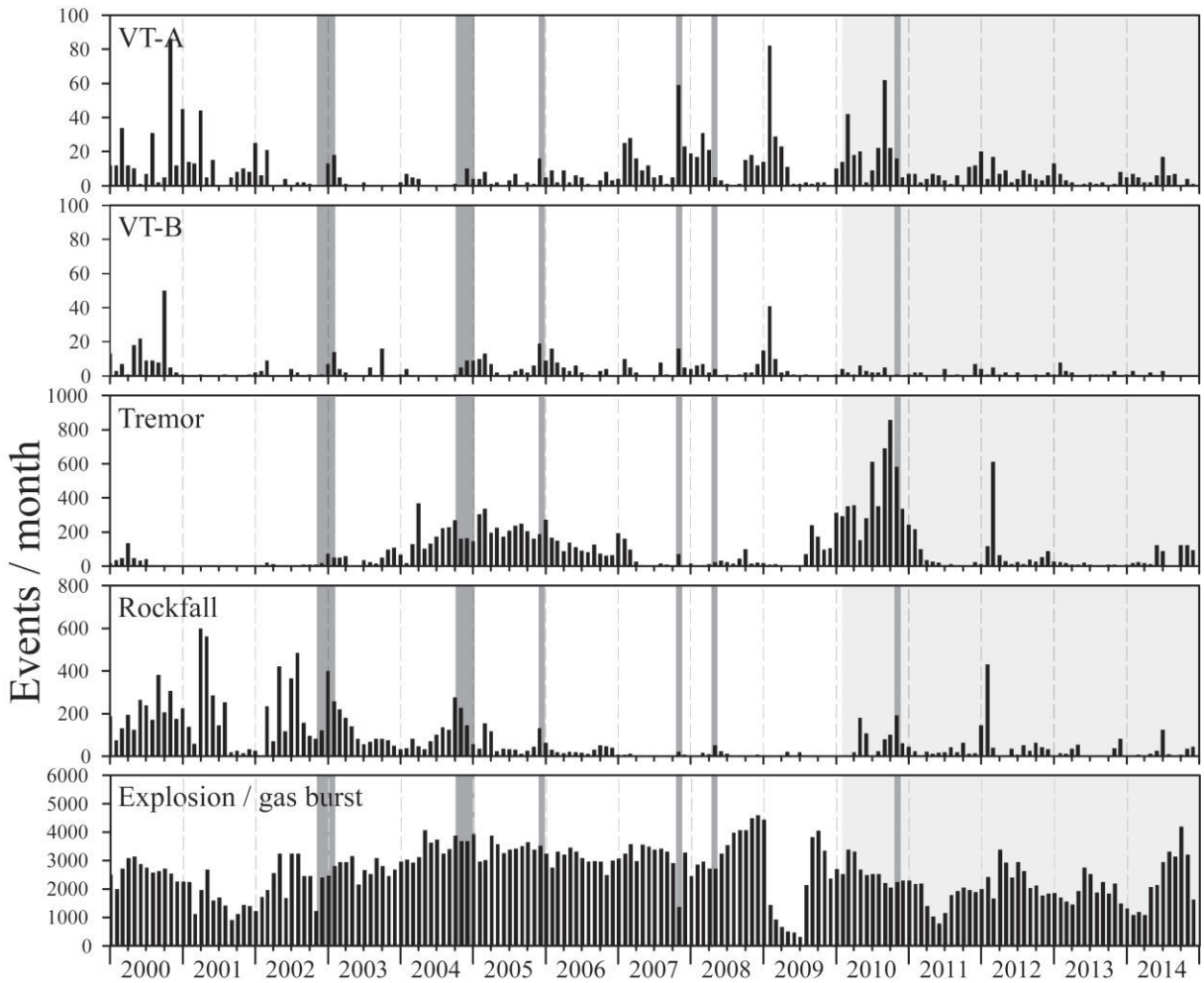

Figure 6.4. Monthly numbers of seismic events at Semeru during the period 2000-2014 include type A and B volcano-tectonics (VT-A and VT-B), tremor, rockfall, explosions/gas burst events. Dark gray boxes indicate the period of PDC-producing eruption and light gray box (2010-2014) indicate period of lava flow production and dome-coulée growth.

Monthly number of VT events in Semeru show seasonal variations, with frequency increasing during rainy seasons (October to March) compared to dry seasons (Fig. 6.4). This variation not only occurred during the period 2000-2014, but also in previous years since at least 1990, as reported by the Indonesia Center for Volcanology and Geological Hazard Mitigation (CVGHM). In addition, during the period 1997-2007, explosive events at Semeru also show seasonal variations with enhanced activity between September and January (Mason et al., 2004). However, explosive events do not always show seasonal variations during the later period of 2000-2014 (Fig. 6.4). The seasonality in seismicity may be correlated with environmental fluctuations associated with deformation of the Earth in response to the annual hydrological cycle including falls in sea level and regional atmospheric pressure (Mason et al., 2004), and

groundwater recharge (Saar & Manga, 2003). The annual rainfall on Semeru varies temporally and spatially but ranges between 2000 and 2800 mm, while monthly rainfall during the rainy season (in 2000) ranged from 350 to 570 mm (Lavigne & Suwa, 2004). The most likely cause of seasonality in VT events is stress changes caused by changes in groundwater recharge rate, which can be the result of variations in precipitation. The stress changes caused by hydrological loading are typically 10^{-3}-10^{-1} MPa, which may be larger than stress changes caused by solid Earth (10^{-3}) and Ocean (10^{-2}) tides (Manga & Brodsky, 2006). Unfortunately, information on subsurface volcanic structures as well as the location of VT events at Semeru is poorly known. In addition, the availability of continuous long-term data on rainfall and hydrology at Semeru and its surroundings is also poor. Therefore, the relationship between the variations of VT events with seasonal effect was not studied in detail in this thesis, except to the degree that it constitutes the background variation for analysis of potential effects of tectonic earthquakes on volcanic unrest and eruption rates.

6.3.2. MODIS-derived radiance data

During 2000-2014, MODVOLC detected hot spots at Merapi during 217 Terra and Aqua overpasses and at Semeru during 1644 overpasses (Fig. 6.5). One overpass could detect more than one hot spot (pixel). The maximum pixel counts are 4 and 6 pixels for Merapi and Semeru, respectively (Fig. 6.5A). Given a total of 21,552 overpasses by Terra and Aqua during the 5388-day-long period (1 March 2000 to 30 November 2014), 1% and 8% of the overpasses detected hot spots at Merapi and Semeru, respectively. Fewer hot spots were detected by MODVOLC due to low intensity of volcanic activity and/or cloud cover that prevented hot spot detection. Impact of cloud cover on hot spot detection is well illustrated by the 26 October-23 November 2010 Merapi eruption, when only one overpass could detect hotspot during this one month-long VEI-4 eruption (Fig. 6.5). Cloud cover also affected seasonal variations in detection of hot spots at Semeru, as more hot spots were detected during the dry season than during the rainy season (Fig. 6.5). MODIS detected thermal anomalies are associated with surface volcanic activity and seismic signals associated with PDC events (mostly at Merapi), and explosion events (vulcanian and strombolian eruption at Semeru), and probably glowing rock avalanches at both volcanoes.

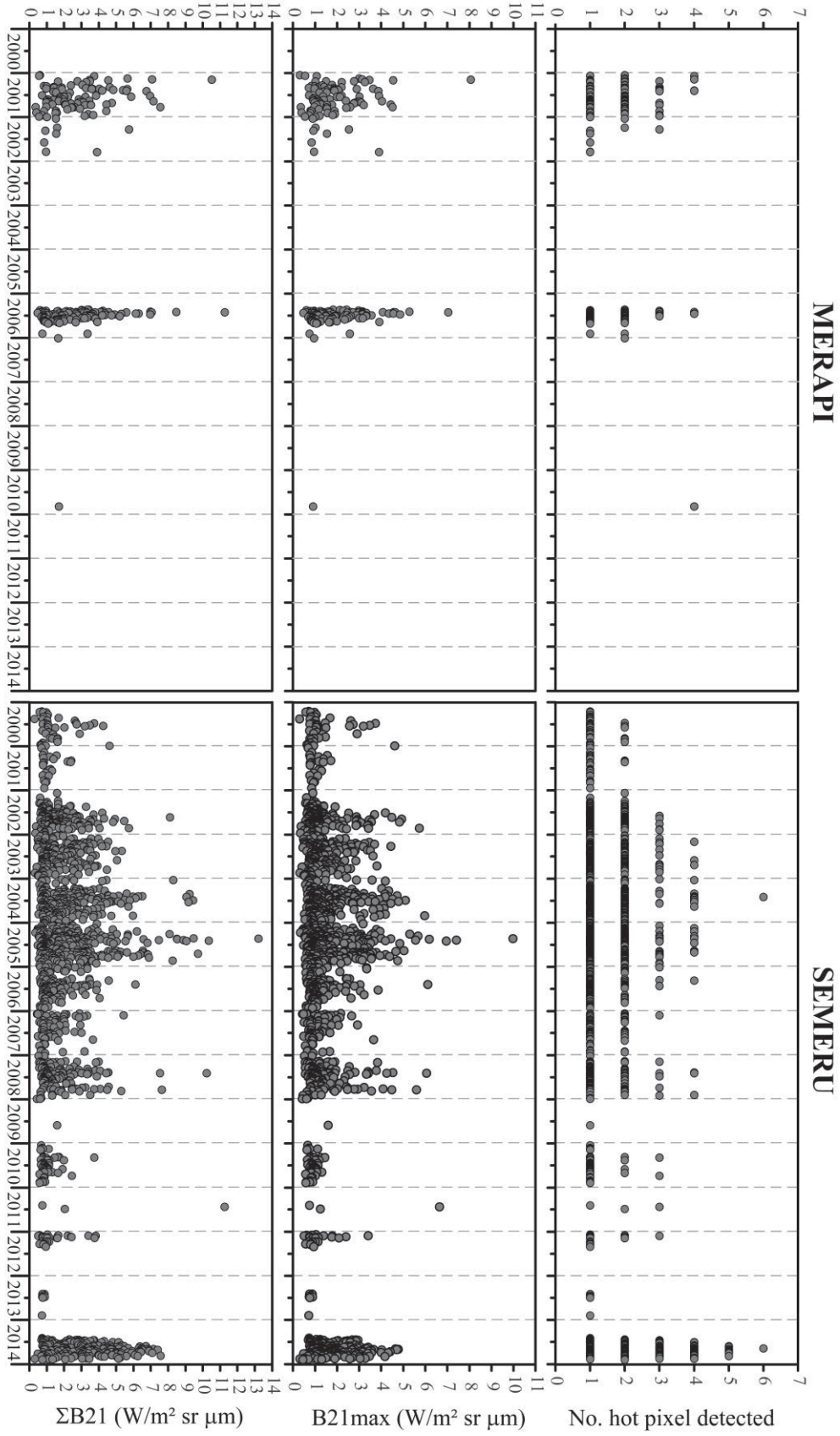

Figure 6.5. MODVOLC data of Merapi and Semeru volcanoes over the period 2000-2014 consists of: **(A)** number of thermally anomalous pixels; **(B)** maximum band 21 radiance ($B21_{max}$) for detected pixels; and **(C)** sum of all band 21 pixel radiances (ΣB21).

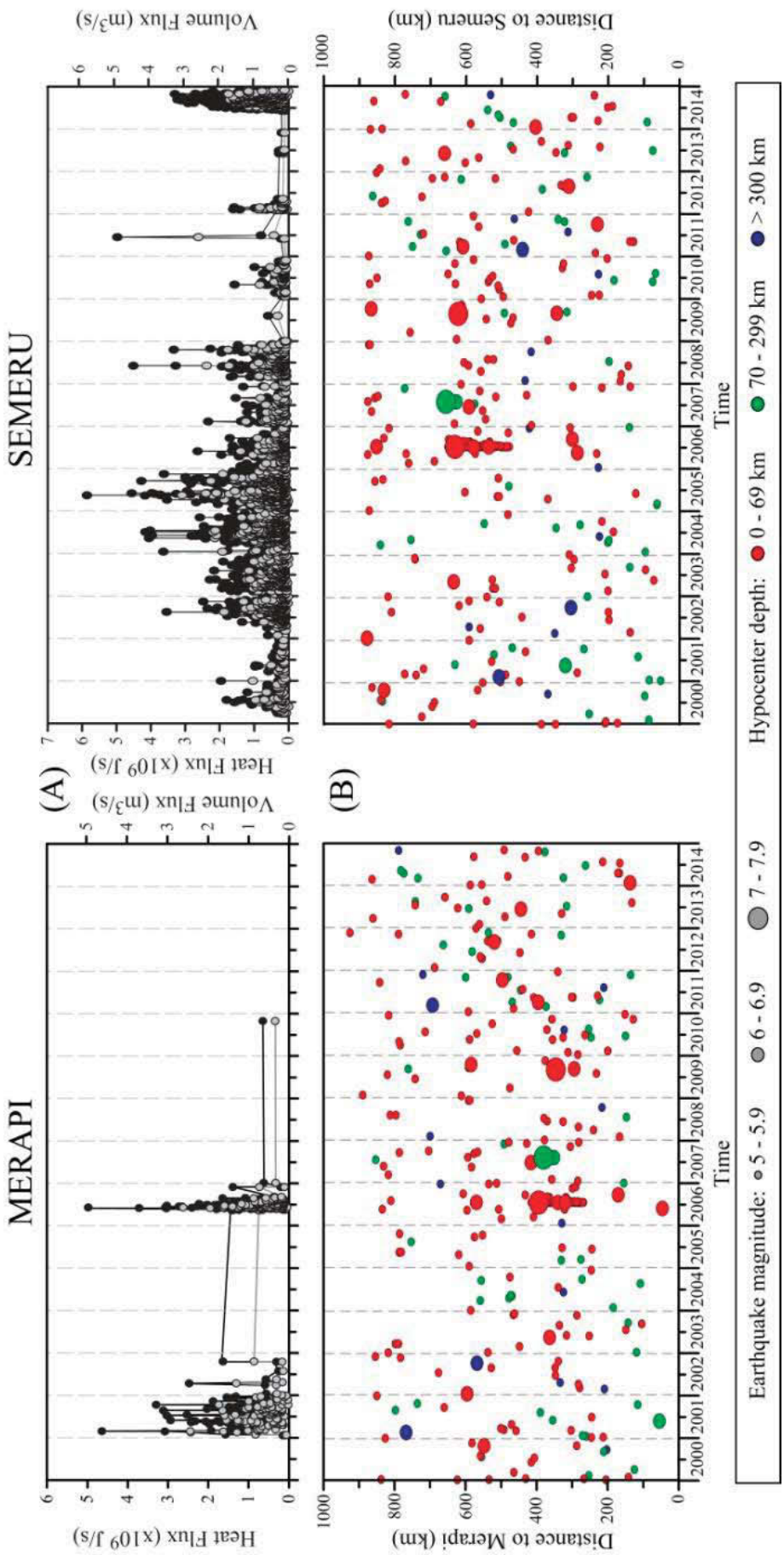

Figure 6.6. A. Heat and volume flux ranges calculated using MODVOLC data. Maximum (black circle) and minimum (gray circle) bounds are placed on the heat or volume flux through application of cold and hot models. See Harris and Ripepe (2007) for detail computing technique and methodology. **B.** Tectonic earthquakes (≥ 5Mw) time distribution and their distance to volcanoes. All data is for Merapi (left) and Semeru (right) during the period 2000-2014.

Thermal radiance data for each detected hot spot were converted to heat flux (in units of joules per second) and volume flux (in m^3 per second), following the method and computing technique of Harris and Ripepe (2007) (Fig. 6.6A). During the period 2000-2014, we obtain heat fluxes from detected hot spots for Merapi in the range of 0.3 to 49.8 x 10^8 J/s. These convert to volume fluxes in the range 0.03 to 4.9 m^3/s, with a mean of 1.1 m^3/s. While at Semeru, we obtain heat fluxes in the range 0.04 to 58.6 x 10^8 J/s and volume fluxes in the range 0.004 to 5.8 m^3/s, with a mean of 0.8 m^3/s. Total power and volume for a certain period of time during high volcanic activity can be obtained by integrating the heat and volume flux through the time interval.

6.4. Results

In this section, we express the heat and volume fluxes data within a shorter period for a better and more detailed view of variations in the activity of Merapi and Semeru based on thermal satellite data. Related seismic data are also displayed to be compared with the heat and volume fluxes data or to substitute them when not available. We record every earthquake that may drive changes in activity of each volcano, either an increase or decrease in activity, and summarize them in Table 6.1 for Merapi and Table 6.2 for Semeru.

6.4.1. Merapi volcano response to regional earthquakes

January – June 2001

In early 2001, Merapi shows a high level of activity with lava dome onset and growth following by dome collapse resulting in PDCs and hot lava avalanches starting on 14 January 2001. Over the period from18 January to 18 February 2001, approximately 25 PDCs occurred daily (Fig. 6.7A) and moved down to the flanks to the Sat, Bebeng, and Senowo Rivers (Fig. 6.2) to the southwest, southwest and west of Merapi, respectively. Larger eruptions occurred on 28 January 2001 with 72 PDCs per day and pyroclastic flows reached a maximum runout distance of 4.5 km from the crater in the Sat River drainage (Fig. 6.2). A major eruptive episode on 10 February 2001 generated PDCs that extended as far as 7 km from Merapi in the direction of the Sat River and 4.5 km in the direction of the Lamat River (Fig. 6.2), and an ash plume that spread out 60 km towards the east. After the 18 February eruption, volcanic activity, including lava avalanches and

PDCs, continued but decreased in number and intensity. Earthquakes related to rockfall, ash emissions and fumaroles dominated the seismicity, though they continued to decrease in number and amplitude over time. Activity at Merapi increased during 23-29 April and 2-8 May to produce several medium-sized of PDCs (Wunderman, 2001).

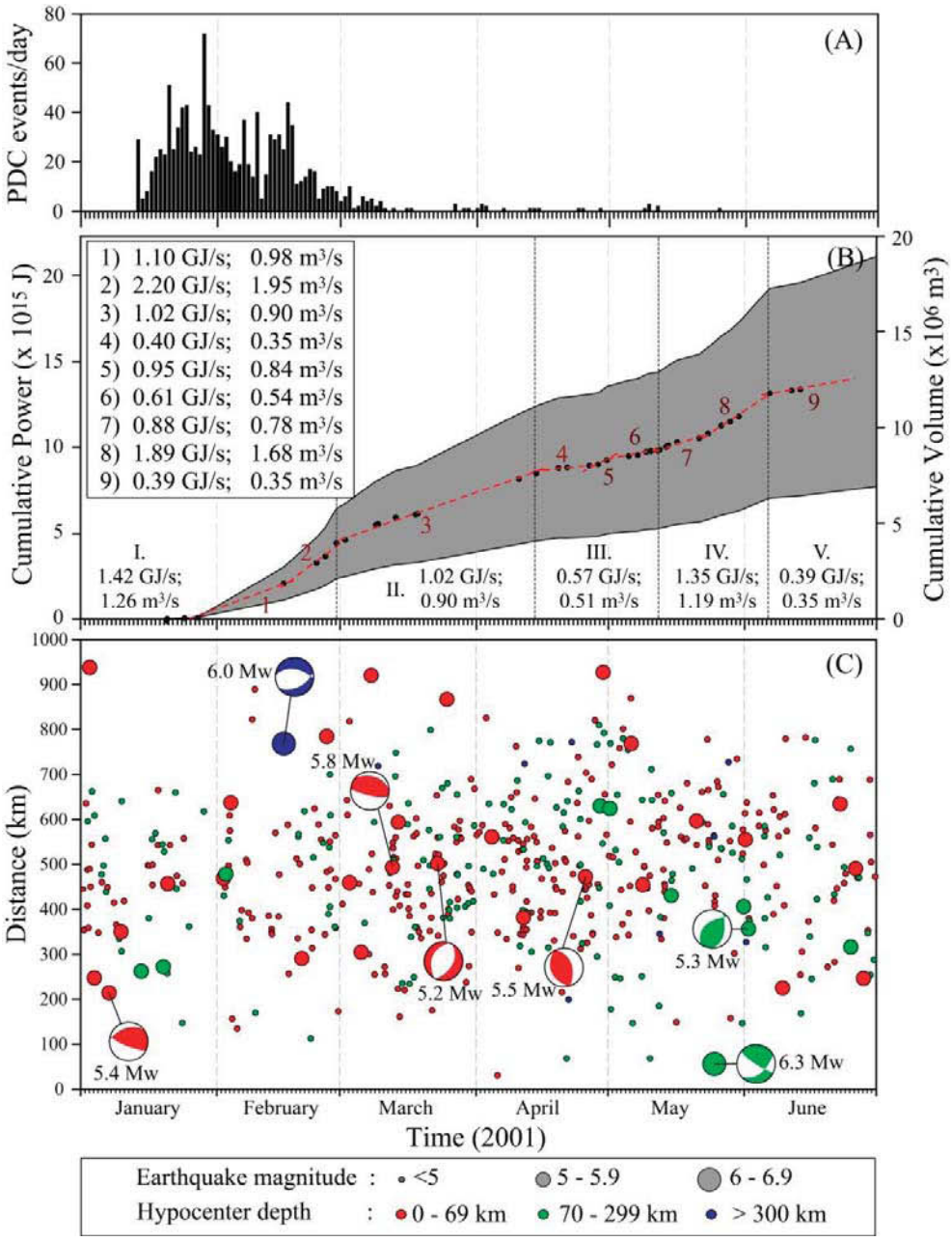

Figure 6.7. Merapi activity and regional tectonic earthquakes during the period from January to June 2001 are shown in: **(A)** daily numbers of PDC events, **(B)** envelope of cumulative power and volume (gray zone) from the integration of heat and volume fluxes given in Figure 6.6. Black dots indicate the mean values for cumulative power and volume. The mean values for heat and volume fluxes for the certain periods (dashed red lines and numbers 1 to 9) are indicated in the inset box. **(C)** Regional tectonic earthquakes time distribution and their distance to Merapi.

Figure 6.7 shows Merapi activity represented by PDC-related seismic events and cumulated power and volume based on MODVOLC data, as well as the distribution of regional tectonic earthquakes during the period January to June 2001. Unfortunately, cloud cover prevented hot spot detection for about 98% of the Terra and Aqua overpasses during this period, and most of hot spots were detected in May 2001 (Fig. 6.7B). We compute heat fluxes for Merapi during the period between January and May 2001 in the range of 0.6 to 46.4 x 10^8 J/s or equivalent to volume fluxes in the range of 0.05 to 4.6 m^3/s. The total power during the high activity of Merapi (14 January to 13 March 2001) was 5.96 ± 1.8 x 10^{15} J or equivalent to a total extruded volume of 5.3 ± 2.4 x 10^6 m^3. This volume is overestimated when compared to a ground-based estimation of the 2001 lava dome, which amounted to a volume of 1.4 x 10^6 m^3 (Wunderman, 2001). However, the 2001 PDC-producing eruption of Merapi was not only derived from the fresh (2001) lava dome but also involved the collapse of the 1998 lava dome (Wunderman, 2001).

Several regional earthquakes during the period from January to June 2001 may have triggered a response at Merapi as expressed by increased activity. The Mw 5.4 earthquake located 214 km southwest of Merapi occurred 7 days before the first PDC-producing eruption. The daily number of PDC-seismic events doubled one day following the Mw 6.0 earthquake on 16 February 2001, located 768 km to the east of Merapi. Based on stress field modeling this earthquake caused a fluctuation of compression and decompression change at >1 Hz, with the peak-to-peak pressure change of about 10 kPa (Walter et al., 2007). Dynamic changes of stress caused by the 25 May 2001 earthquake with Mw 6.3 increased by about 30°C in the temperature of fumaroles located 200 m southeast of the Merapi crater (Walter et al., 2007). This earthquake did not produce a change in the cumulative power and volume data (Fig. 6.7B), possibly because MODVOLC was unable to detect fumarolic activity. However, the 25 May 2001 earthquake was followed by a small-volume PDC the following day (Fig. 6.7B).

During January to June 2001, at least two relatively small earthquakes likely triggered a response from Merapi by producing PDCs two days after the event. The first earthquake on 5 April 2001 with (mb 3.5) was located 31 km WNW of Merapi at a depth of 33 km, and the second one (mb 3.7) on 10 May 2001 was located 68 km north of Merapi at a depth of 100 km. Stress field model of Walter et al., (2007) also suggested that inflation

of Merapi during the crisis could have increased the static stress at proximal seismogenic faults. Therefore, these small earthquakes may be triggered by the deformation or intrusion at Merapi during the 2001 eruption. This also could be similar to the hypothesis for distal VT events proposed by White and McCausland (in review).

10 May - 14 June 2006

Harris and Ripepe (2007) published results that indicate the Mw 6.3 earthquake on 26 May 2006 induced a response from Merapi that was characterized by an increase in the heat and volume flux, which began three days after the event and lasted nine days (Fig. 6.8A). Three phases of Merapi activity during the period 10 May to 14 June 2006 were identified on the basis of heat and volume flux (Fig. 6.8A). They suggested that the three days lag time between the event and Merapi response reflected the time it took for the change felt by magma residing at deeper level to be transmitted to the surface. In this 2006 case, change in the static and/or dynamic stress (the effect of the earthquake) and the increase in erupted volume flux was transient and short-lived (nine days).

We compare the heat and volume flux of Merapi with daily numbers of PDCs recorded by seismometers (Fig. 6.8). We also identify three phases of Merapi activity based on daily numbers of PDC events and a sudden increase in seismic data shortly after the earthquake (Fig. 6.8B). Before the earthquake, the average number of PDC was 35 events per day, but one day after the earthquake, this number increased to 159 events per day (Fig. 6.8B). The number of PDCs decreased over the two following days and then increased again during the second phase beginning four days after the earthquake. High number of PDC during the second phase reached 115 events per day on average and lasted for ten days. The number of PDC decreased during the third phase to a lower activity with an average of 26 events per day.

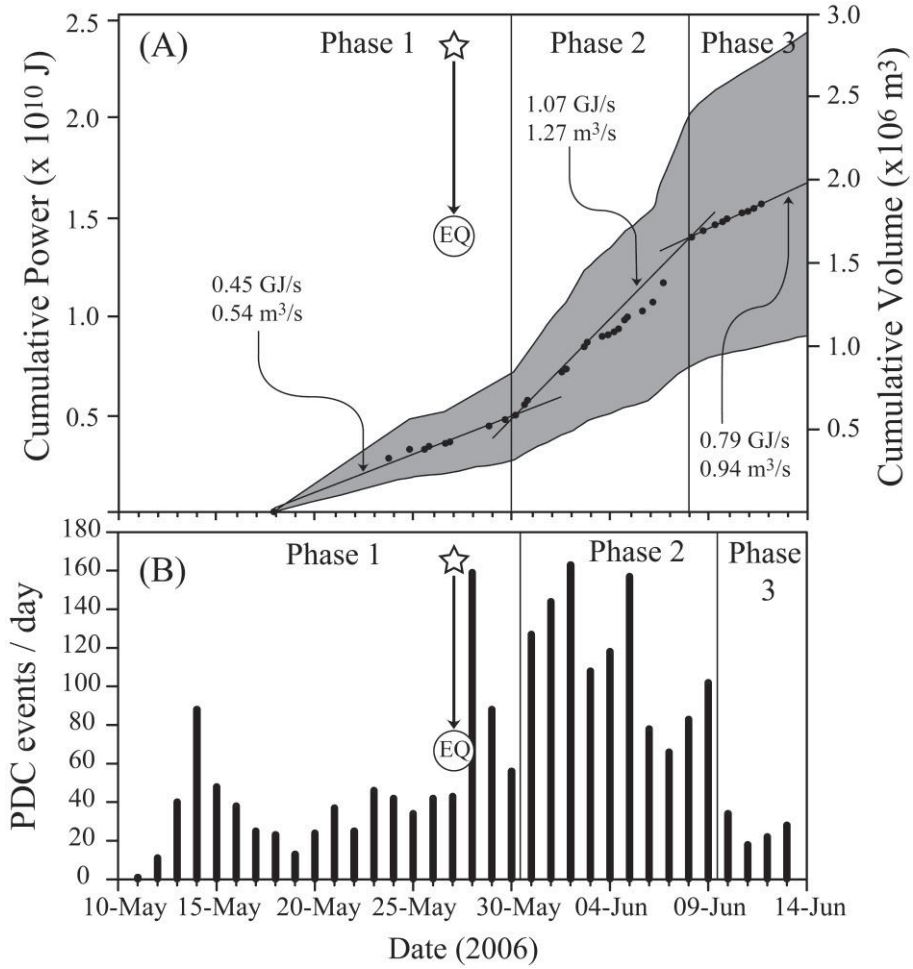

Figure 6.8. (A) Envelope of cumulative power and volume (gray zone) for Merapi (Harris & Ripepe, 2007) compared with **(B)** daily numbers of PDC events during the period 10 May to 14 June 2006.

January 2009 – March 2011

The 2010 eruption is the first large (VEI 4) explosive eruption of Merapi that has been instrumentally observed. The precursory unrest preceding the 2010 eruption was marked by VT swarms detected on 31 October 2009, 6 December 2009, 1 February 2010, and 10 June 2010 (Surono et al., 2012; Budi-Santoso et al., 2013). The level of seismicity began to increase in early September 2010, one and half months before the first eruption on 26 October 2010. The eruption process and deposits have been discussed in previous studies (e.g., the special issue of the 2010 Merapi eruption in Journal of Volcanology and Geothermal Research, volume 261, in 2013) as well as Chapters 4 and 5 of this thesis.

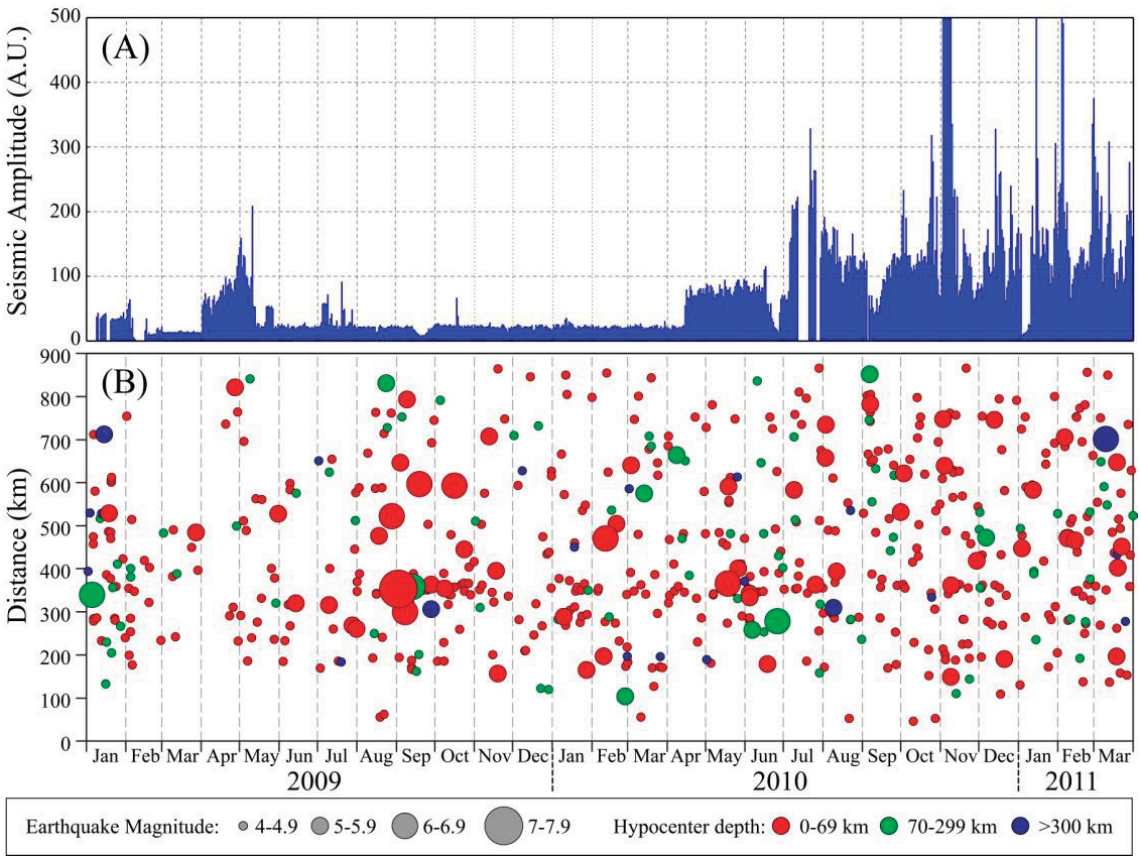

Figure 6.9. A. Daily data of seismic spectral amplitude measurement (SSAM) of Merapi in the frequency range of 0.3-25 Hz, during the period from January 2009 to March 2011. Note that maximum amplitude during the climactic eruption on 5 November 2010 is 5124 arbitrary units (A.U.). **B.** Time distribution of regional tectonic earthquakes and their distance to Merapi.

Heavy cloud cover during the 2010 eruption prevented hot spot detection by Terra and Aqua satellites, so only four hot spots are detected by an overpass of Aqua on 29 October 2010. We used the seismic data represented in SSAM values to see the variations of Merapi activity during the period January 2009 to March 2011 (Fig. 6.9). SSAM calculates the amplitude of every recorded seismic event in the frequency range of 0.3 to 25 Hz, including deep, shallow and surface volcanic activities as well as tectonic earthquakes. Some identified tectonic earthquakes have affected the activity of Merapi based on SSAM, with a lag time in the range of 1 to 7 days. More details (in shorter period of time) of SSAM data, cumulative energy of VT and MP events are shown in Figure 6.10, together with the relatively large (≥ Mw 5.0) earthquakes and smaller but closes to the volcano (< 100 km). Based on this data set, large earthquakes do not systematically influence Merapi behavior, for example there is no significant change of SSAM after the Mw 7.0 earthquake on 2 September 2009 (number 1 in Fig. 6.10A). Proximal small earthquakes sometimes seems to increased Merapi seismicity, such as

the M_L 3.9 earthquake on 4 July 2010 and M_L 2.5 earthquake on 25 October 2010 (number 15 and 23, respectively, in Fig. 6.10B-C). However, these small earthquake may also associated with distal VT's produced by changes in stress along nearby faults as a consequence of intrusion (White & McCausland, in review)

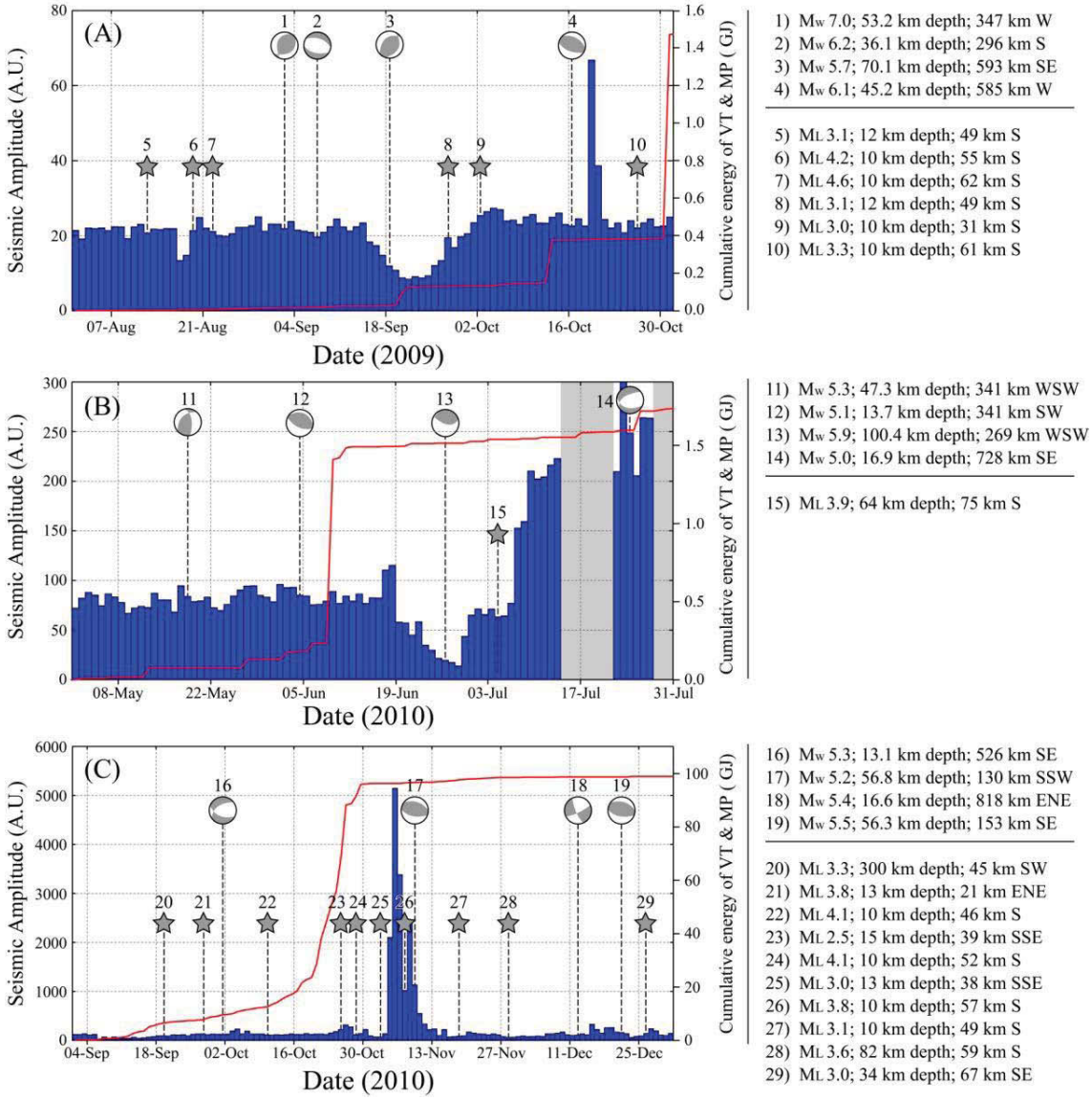

Figure 6.10. Daily SSAM data of Merapi in the frequency range of 0.3-25 Hz (blue bars) and cumulative energy of VT and MP events (red solid line) overlain by the occurrence date of regional tectonic earthquakes marked by their focal mechanism (for ≥ Mw 5.0) or gray stars (any magnitude but located <100 km to the volcano), over the period of August-October 2009 **(A)**, May-July 2010 **(B)**, and September-December 2010 **(C)**. The earthquake parameters (magnitude, depth, distance) are indicated to the right hand side of the graphs.

As noted above, large earthquake are not systematically followed by an increase in Merapi activity. SSAM of Merapi decreased 3 and 7 days before the occurrence of two

large earthquakes. The first earthquake with Mw 5.7, located 593 km ESE of Merapi at a depth of 70.1 km (number 3 in Fig. 6.10A), was associated with activity in the subduction zone south of Java. The second one is the intraplate earthquake with Mw 5.9 located 269 km SW of Merapi at a depth of 100.4 km. It is unclear, if any correlation exists or if these decreases are a coincidence. As mentioned earlier, interaction between tectonic earthquake and volcanic activity can also work inversely; an earthquake can be triggered by the eruptive activity. Very high activity of Merapi during the 2010 crisis (end of October to mid-November) probably induced stress change at the crustal faults around the volcano. This is indicated by the occurrence of several proximal small earthquakes at shallow depth (< 20 km) during the crisis period (Fig. 6.10C).

January 2012 – May 2014

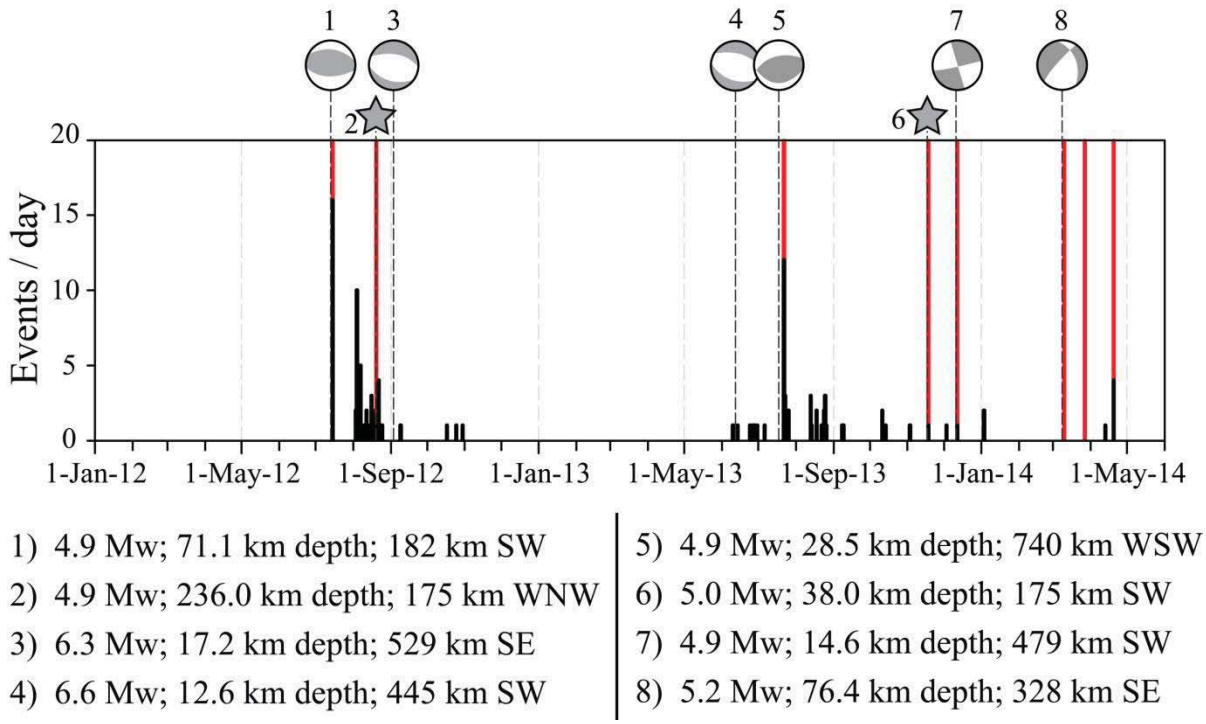

Figure 6.11. Daily numbers of explosions or gas burst events (black bars) during the period from January 2012 to June 2014 overlain by the occurrence of short explosive (phreatic) events (red solid line) and tectonic earthquakes (gray dashed lines with focal mechanism or stars). The earthquake parameters (magnitude, depth, distance) are indicated below the graph.

Merapi eruptions after the 2010 were characterized by short, low magnitude (VEI 1-2) explosive events producing a few hundred meters to several km-high ash plumes. As many as eight major explosive events occurred on 15 July 2012, 20 August 2012, 22 July 2013, 18 November 2013, 12 December 2013, 10 March 2014, 27 March 2014 and 20

April 2014. Six explosions were preceded by regional tectonic earthquakes that occurred a few hours to two days earlier (Fig 6.11). Some earthquakes also indicated to increase number of gas bursts one day later. There are no specific earthquake parameters that indicated the potential to trigger explosion. Merapi volcano observatory (MVO) reported that eruptive activity consists of phreatic eruptions or gas burst from fumaroles and did not involve juvenile magma at depth. This indicates that during the period between January 2012 and May 2014, seismic waves from the earthquake disproportionately affected and increased the stress in the Merapi hydrothermal system rather than the magma chamber, and/or the magma chamber was in a state of "relaxation" after the VEI 4 eruption in 2010, as >70 Mm^3 of material were erupted (Solikhin et al., 2015b).

Table 6.1. List of tectonic earthquakes during the period 2000-2014 inferred to have exerted some influence to the activity at Merapi volcano.

Time (UTC)	Magnitude	Depth in km	Distance to Merapi in km (direction)	Focal mechanism	Volcano response
07/01/2001 (12:55)	Mw 5.4	33.0	214 (SW)		First PDC of the Merapi 2001 eruption occurred 7 days after the earthquake.
16/02/2001 (05:59)	Mw 6.0	515.0	768 (E)		The daily number of PDC-seismic events has doubled one day after the earthquake.
05/04/2001 (20:51)	mb 3.5 ~Mw 4.0	33.0	31 (WNWW)	-	A PDC occurred two days after the earthquake.
10/05/2001 (13:17)	mb 3.5 ~Mw 4.0	100.0	68 (N)	-	Two PDCs occurred two days after the earthquake.
25/05/2001 (05:06)	Mw 6.3	131.3	50 (SW)		~30°C increase in the fumaroles temperature (Walter et al., 2007).
26/05/2006 (22:54)	Mw 6.4	21.7	48 (SSE)		Increases in the heat and volume fluxes beginning 3 days after the earthquake, and lasted 9 days (Harris & Ripepe, 2007).
18/09/2009 (23:06)	Mw 5.7	70.1	593 (SE)		Preceded by a decrease in SSAM 3 days before the earthquake and then 6 days later SSAM increased and lasted for 9 days.
16/10/2009 (09:52)	Mw 6.1	45.2	585 (W)		SSAM increase (~250%) began 3 days after the earthquake and lasted for 2 days.
26/10/2009 (09:57)	ML 3.3 ~Mw 4.1	10.0	61 (S)	-	Increase in energy of VT and MP events began 4 days after the earthquake.

Table 6.1. (continued)

Time (UTC)	Magnitude	Depth in km	Distance to Merapi in km (direction)*	Focal mechanism	Volcano response
04/06/2010 (15:12)	MW 5.1	13.7	341 (SW)		Increase in energy of VT and MP events began 4 days after the earthquake.
26/06/2010 (09:50)	MW 5.9	100.4	269 (WSW)		Preceded by a decrease of SSAM 4 days before the earthquake and then SSAM increased 2 days later.
04/07/2010 (05:13)	ML 3.9 ~Mw 4.3	64.0	75 (S)	-	SSAM increase (~200%) began 2 days after the earthquake.
01/10/2010 (01:24)	MW 5.3	13.1	526 (SE)		SSAM increase (~150%) began 2 days after the earthquake and lasted for 4 days.
25/10/2010 (07:39)	ML 2.5 ~Mw 3.9	15.0	39 (SSE)	-	The earthquake occurred one day before the first eruption of the 2010 Merapi crisis.
02/11/2010 (08:30)	ML 3.0 ~Mw 4.0	13.0	38 (SSE)	-	After the earthquake, activity of Merapi increased and reached the climactic stage of the 2010 eruption on 5 November 2010.
07/11/2010 (16:08)	ML 3.8 ~Mw 4.3	10.0	57 (S)	-	SSAM of Merapi increased one day after the earthquake.
12/12/2010 (15:59)	Mw 5.4	16.6	818 (NE)		SSAM increase (~200%) began 3 days after the earthquake and lasted for 8 days.
13/07/2012 (17:57)	Mw 4.9	71.1	182 (SW)		Earthquake followed by a phreatic eruption at Merapi 2 days later.
20/08/2012 (08:52)	mb 4.5 ~Mw 4.9	236.0	175 (WNW)	-	Earthquake followed by a phreatic eruption at Merapi a few hours later.
18/07/2013 (15:43)	Mw 4.9	28.5	740 (WSW)		Earthquake followed by a phreatic eruption at Merapi 2 days later.
17/11/2003 (21:41)	mb 4.7 ~Mw 5.0	38.0	175 (SW)	-	Earthquake followed by a phreatic eruption at Merapi a few hours later.
11/12/2013 (18:23)	Mw 4.9	14.6	479 (SW)		Earthquake followed by a phreatic eruption at Merapi a few hours later.
09/03/2014 (13:42)	Mw 5.2	76.4	328 (SE)		Earthquake followed by a phreatic eruption at Merapi 11 hours later.

6.4.2. Semeru volcano response to regional earthquakes

February 2002 – January 2003

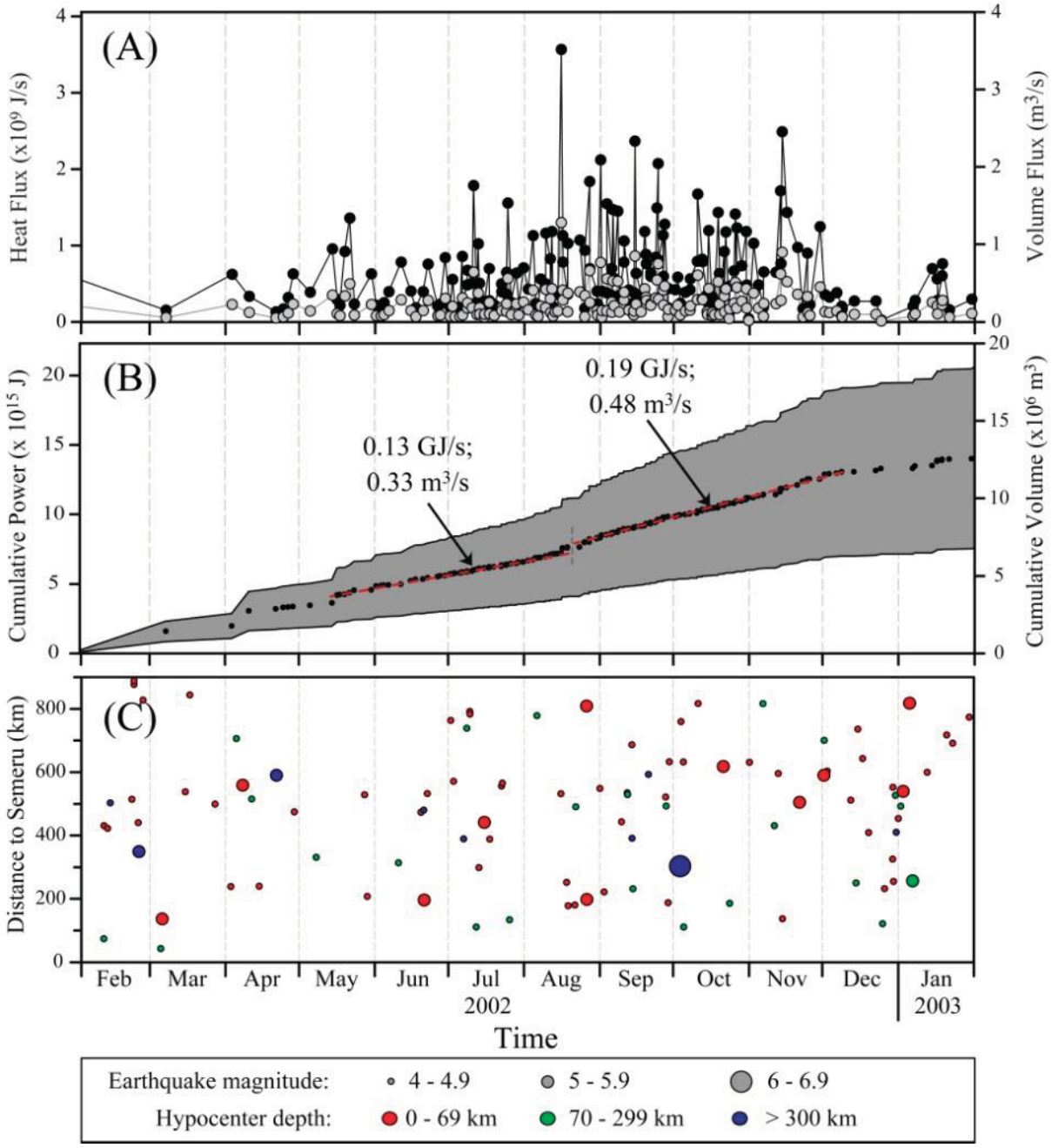

Figure 6.12. (A) Heat and volume flux ranges, where maximum (black circle) and minimum (gray circle) bounds are placed on the heat or volume flux through application of cold and hot models. **(B)** Envelope of cumulative power and volume (gray zone) from integration of heat and volume fluxes. The mean values for heat and volume fluxes for two certain periods (dashed red lines) are also indicated. **(C)** Time distribution of tectonic earthquakes and their distance to Semeru during the period February 2002 to January 2003.

During the period February 2002 to January 2003, MODVOLC detected hot spots at Semeru during 369 Terra and Aqua overpasses, which corresponds to about 12% of total overpasses. However, only a few hot spots were detected during the major eruption in December 2002-January 2003 (Fig. 6.12). Prior to the major eruption (from May to November 2002) the average heat flux of Semeru was ~0.18 GJ/s that is equivalent with the volume flux of ~ 0.46 m^3/s. By integrating the heat flux through time, we obtain a total power released by Semeru for a year of 1.42 ± 0.44 x 10^{16} J. This converts to a total extruded volume for the same period of 12.56 ± 5.82 x 10^6 m^3. During this period some earthquakes (summarized in Table 6.2) appear to have affected the Semeru activity.

January 2004 – December2005

The Mw 9.3 Sumatra-Andaman earthquake on 26 December 2004 was located ~2300 km away from Semeru volcano. Following this large earthquake, the heat flux generated by global volcanic activity, which was already at relatively high level since April 2004, underwent a 300% increase (Delle Donne et al., 2010). During the year 2004 and 2005, MODVOLC detected hot spots in 17 and 21%, respectively, of the total Terra and Aqua overpasses (Fig. 6.13). During the year 2004, we obtain heat fluxes for Semeru in the range of 0.6 to 41.5 x 10^8 J/s, equivalent to volume fluxes in the range 0.04 to 4.12 m^3/s, with a mean of 0.64 m^3/s. In 2005, Semeru showed a wider range of heat fluxes of 0.15 to 58.6 x 10^8 J/s, equivalent to volume fluxes in the range of 0.01 to 5.82 m^3/s and with a mean of 0.72 m^3/s. We also obtained total power released by Semeru for one year periods of 1.94 ± 0.6 x 10^{16} J for 2004 and 2.13 ± 0.66 x 10^{16} J for 2005. This converts to a total extruded volume of 17.23 ± 8 x 10^6 m^3 and 18.89 ± 8.8 x 10^6 m^3 for 2004 and 2005, respectively. Indeed, there is an increase in the average volume fluxes for Semeru during the year following the Sumatra-Andaman earthquake; however, there is no abrupt change in the power distribution associated with the time of the earthquake (Fig. 6.13). In evaluating these data we must also consider the cloud cover that prevented hot spot detection during a large number of days during the two years in question.

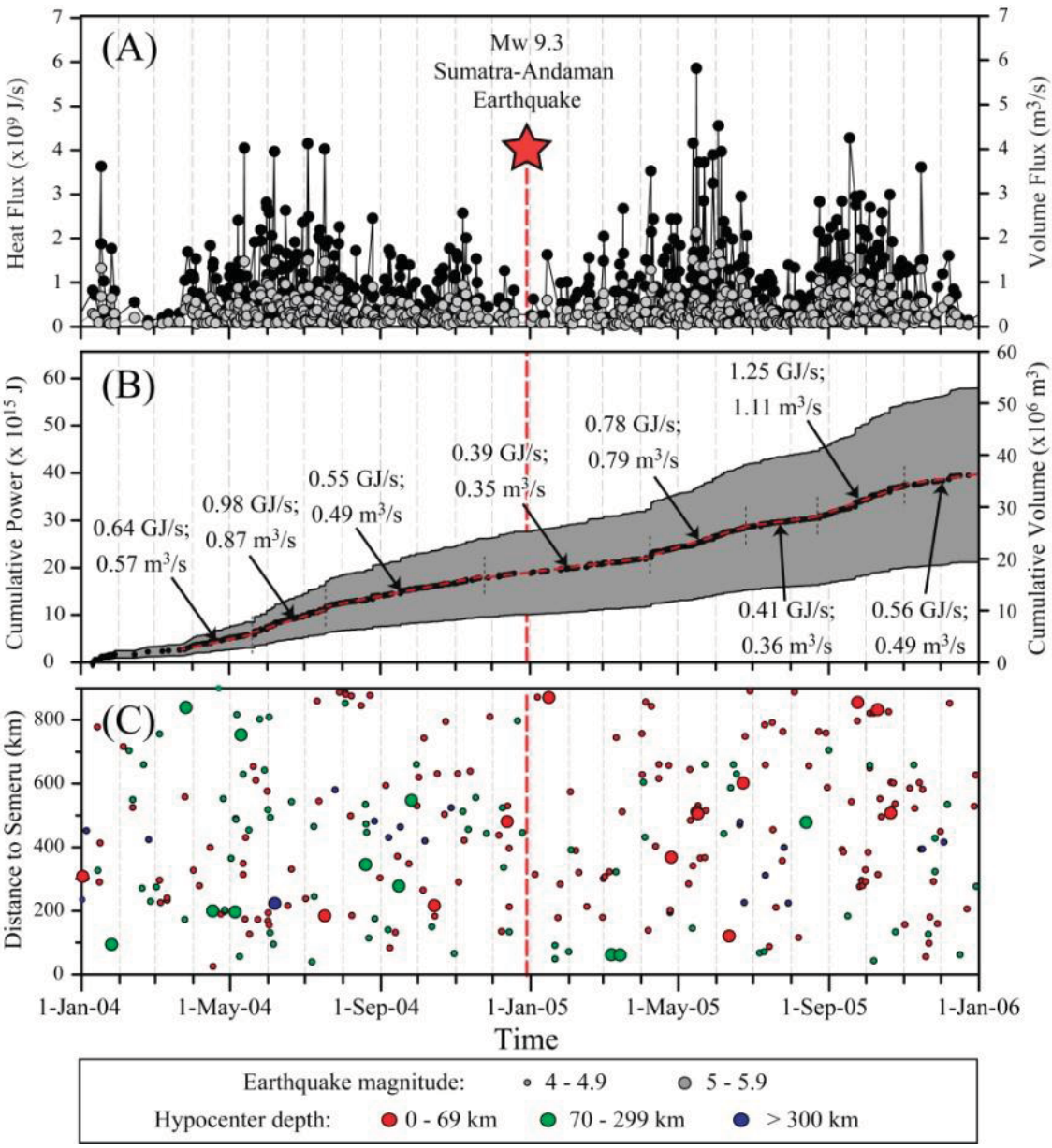

Figure 6.13. (A) Heat and volume flux ranges, where maximum (black circle) and minimum (gray circle) bounds are placed on the heat or volume flux through application of cold and hot models. **(B)** Envelope of cumulative power and volume (gray zone) from integration heat and volume fluxes. The mean values for heat and volume fluxes for certain periods (dashed red lines are also indicated. **(C)** Time distribution of tectonic earthquakes and their distance to Semeru during the two years period 2004-2005. Red star and dashed line indicate the occurrence time of Mw 9.3 Sumatra-Andaman earthquake (26 December 2004).

May - July 2006

As for Merapi during the 2006 Merapi eruption and Java earthquake, we compare the heat and volume fluxes of Semeru (Fig. 6.14A; Harris & Ripepe, 2007) with seismic data, in this case together with daily numbers of explosive events (Fig. 6.14B). The number of

explosive events at Semeru does not seem to have been affected by the Mw 6.3 earthquake on 26 May 2006 (UTC). There is no important variation in the eruptive activity after the earthquake. However, it cannot be concluded that the heat and volume fluxes data are not in accordance with the actual Semeru activity, because each explosive event has a different magnitude. Unfortunately, we do not have information on the magnitude or energy of the explosive events.

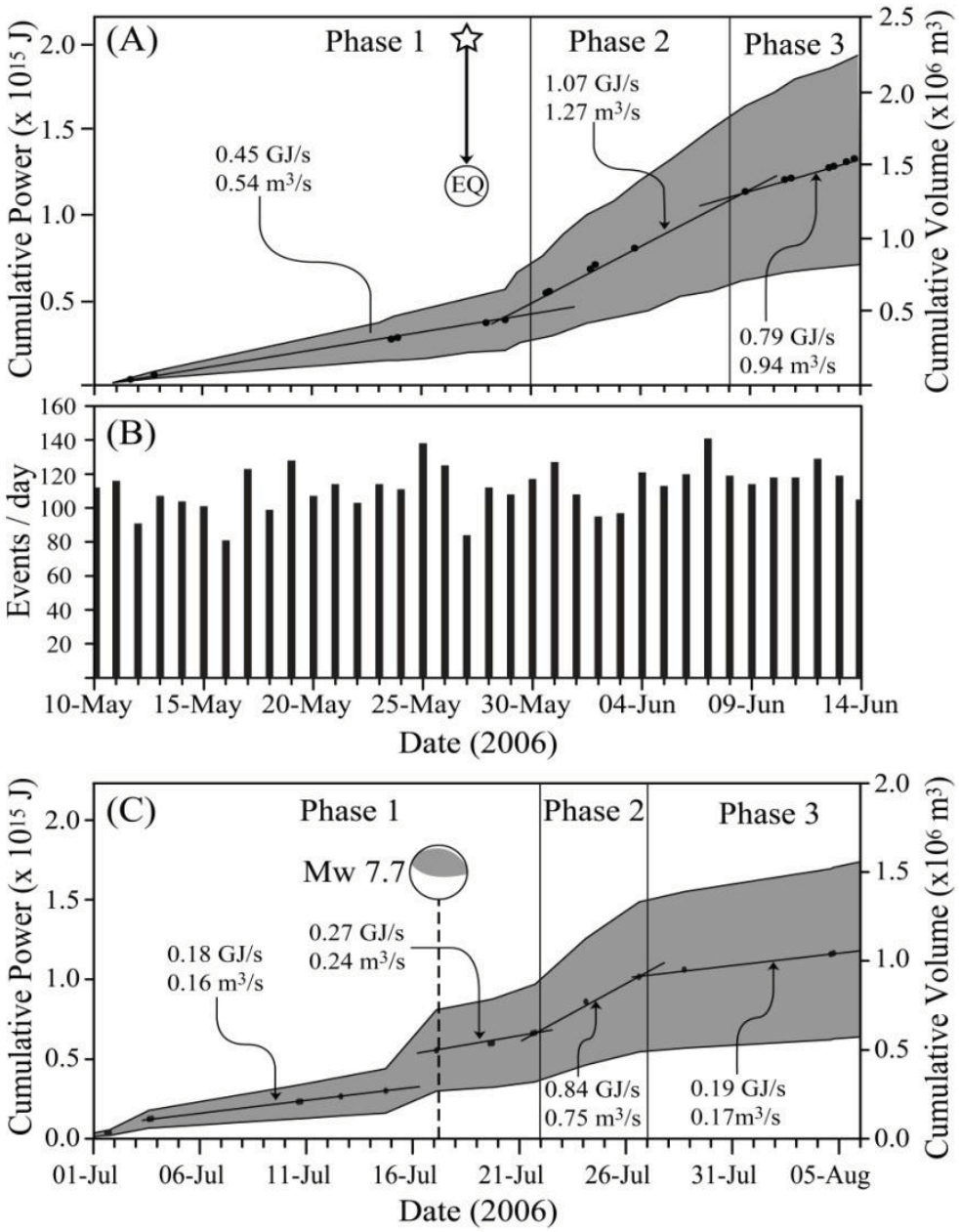

Figure 6.14. (A) Envelope of cumulative power and volume (gray zone) for Semeru (Harris & Ripepe, 2007) compared with **(B)** daily numbers of explosion and gasburst events during the period 10 May to 14 June 2006. **(C)** Envelope of cumulative power and volume (gray zone) for Semeru during the period 1 July-6 August 2006. The position of Mw 7.7 earthquake and three eruption phases are marked in the graph.

In 2006, another large earthquake (Mw 7.7) on 17 July was located offshore near the trench of the Sunda subduction zone south of Java, ~610 km southwest of Semeru volcano. There was no ground motion damage from the earthquake, but there was extensive damage and loss of life from the tsunami along 250 km of the southern coasts of West Java and Central Java. Increases in heat and volume fluxes at Semeru were first recorded 5 days after the earthquake on 22 July and lasted 5 days (Fig. 6.14C). As in the case of May-June 2006 (Harris & Ripepe, 2007), we also identified three phases of Semeru activity on the basis of heat and volume flux for the period 1 July to 6 August 2006. The first phase spanned 3–21 July and was characterized by relatively low heat fluxes of ~2.3 x 10^8 J/s in average. The second phase began on 22 July and was characterized by higher fluxes of ~8.4 x 10^8 J/s or almost fourfold the first phase. During this phase calculated heat and volume fluxes increased by a factor of 3.2, which is almost similar to the increased factor after the 26 May 2006 earthquake. The third phase was marked by a return to lower fluxes of ~1.9 x 10^8 J/s after 27 July.

June – December 2014

The most recent eruptive state of Semeru has been described in chapter 3 of this thesis: essentially lava flows, and dome-coulee and collapse from lava flow fronts characterize the Semeru eruptive activity since 2010. Unfortunately, only a few hot spots were detected by MODVOLC from early 2009 to mid-2014. Since July 2014, the daily number of gas bursts has increased and since September, Strombolian activity associated to lava extrusion was frequently observed in the Jonggring-Seloko crater. During the period June to December 2014, MODVOLC detected hot spots at Semeru during 226 Terra and Aqua overpasses or about 26% of total overpasses (Fig. 6.15). During the period of August to mid-November 2014, Semeru showed an almost constant heat flux of 1.15 GJ/s and a volume flux of 1.02 m^3/s on average. Tectonic earthquakes that could have influenced Semeru activity during this period are summarized in Table 6.2. The relatively constant heat flux suggest that these smaller (all < M6) earthquake either had no affect on the heat flux, or their effects were too small and/or short in duration to be detected, given the low temporal resolution of the MODVOLC observations.

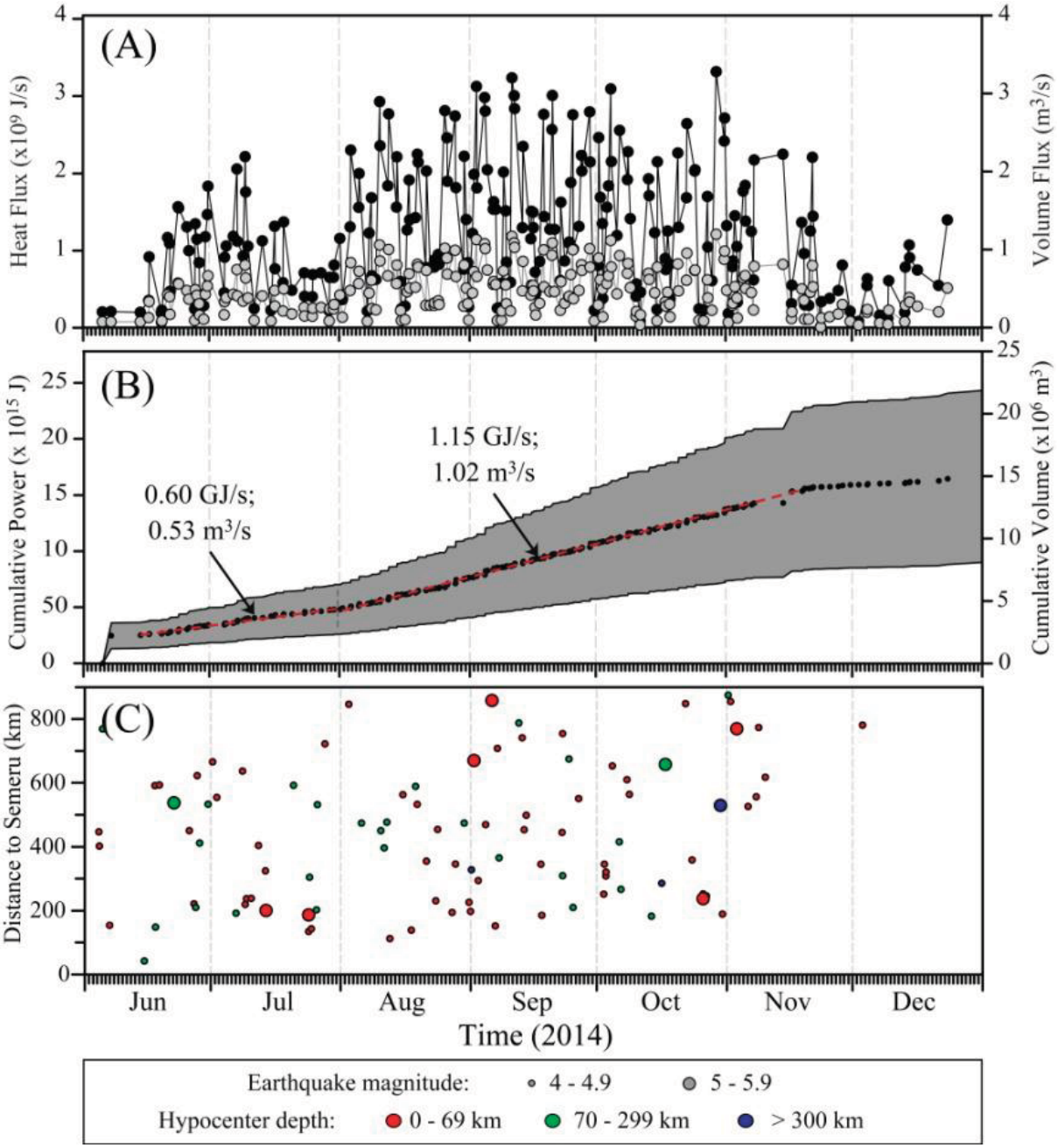

Figure 6.15. (A) Heat and volume flux ranges, **(B)** envelope of cumulative power and volume (gray zone) from integration heat and volume fluxes, and **(C)** tectonic earthquakes time distribution and their distance to Semeru during the period June to December 2014

Table 6.2. List of tectonic earthquakes during the period 2000-2014 inferred to have exerted some influence to the eruptive activity at Semeru volcano.

Time (UTC)	Magnitude	Depth in km	Distance to Semeru in km (direction)	Focal mechanism	Volcano response
21/06/2002 (05:07)	Mw 5.1	45.5	195 (NNE)		Heat and volume fluxes in Semeru increased (~220%) 1 day after the earthquake and lasted for 5 days.
26/08/2002 (17:36)	Mw 5.6	15.1	198 (N)		Heat and volume fluxes in Semeru increased (~198%) 1 day after the earthquake and lasted for 6 days.
03/10/2002 (19:05)	Mw 6.0	316.7	308 (ENE)		Heat and volume fluxes in Semeru increased (~172%) 4 days after the earthquake and lasted for 7 days.
28/05/2003 (01:34)	Mw 5.2	86.3	70 (SW)		Heat and volume fluxes in Semeru increased (~150%) 3 days after the earthquake and lasted for 6 days.
08/09/2003 (06:26)	Mw 5.9	15.0	205 (SW)		Heat and volume fluxes in Semeru suddenly increased (~300%) a few hours after the earthquake.
09/05/2004 (22:25)	Mw 5.1	54.6	758 (SW)		Heat and volume fluxes in Semeru increased (~153%) 2 days after the earthquake and lasted for 4 days.
27/10/2004 (09:45)	ML 4.4 ~Mw 4.6	148.9	54 (S)	-	Heat and volume fluxes in Semeru increased (~120%) 3 days after the earthquake and lasted for 4 days.
08/04/2005 (18:38)	ML 4.8 ~Mw 4.9	33.0	66 (NE)	-	Heat and volume fluxes in Semeru increased (~163%) 1 day after the earthquake and lasted for 2 days.
10/05/2005 (02:32)	ML 4.6 ~Mw 4.7	128.5	74 (SW)	-	Heat and volume fluxes in Semeru increased (~171%) 3 days after the earthquake and lasted for 5 days.
26/05/2006 (22:54)	Mw 6.4	21.7	285 (W)		Increases in heat and volume fluxes began 3 days after the earthquake, and lasted for 9 days (Harris & Ripepe, 2007).
17/07/2006 (08:20)	Mw 7.7	20.0	630 (WSW)		Increases in heat and volume fluxes began 5 days after the earthquake, and lasted for 5 days.

Table 6.2. (Continued)

Time (UTC)	Magnitude	Depth in km	Distance to Semeru in km (direction)	Focal mechanism	Volcano response
27/04/2008 (05:02)	Mw 5.0	68.2	557 (W)		Heat and volume fluxes in Semeru increased (~315%) 5 days after the earthquake and lasted for 9 days.
31/07/2014 (03:34)	ML 4.0 ~Mw 4.4	10.0	93 (S)	-	Heat and volume fluxes in Semeru increased (~220%) 1 days after the earthquake and lasted for 7 days.

6.5. Discussion: MODVOLC data for volcano monitoring

This thesis focuses on the application of remote imaging data to assess the volcano activity and products. For this reason, we highlight the use of MODVOLC thermal radiance data converted into heat and volume fluxes, combined with limited seismic data, in approaching temporal variations of the eruptive activity. MODIS with its two sensors (Terra and Aqua) provides four hot-spot observations per day (morning, afternoon, evening and night). In addition, the detection and publishing of the location of volcanic hot-spot by MODVOLC is rapid, within 12 to 24 hours after data acquisition. Under appropriate conditions (e.g., limited cloud cover), this permits dynamic monitoring of volcanic phenomenon such as active lava flows (Wright et al., 2004). The reliance of MODVOLC on a fixed, globally applicable threshold is adequate to prevent many false alarms but, unfortunately, also results in a lack of sensitivity, which may prevent the detection of low intensity volcanic phenomena. This insensitivity is also a result of the poor spatial resolution of MODIS itself (Vaughan & Hook, 2006). Another limitation is the impact of volcanic ash or meteorological clouds on MODVOLC radiance time-series.

Despite these limitations, for particularly active volcanic phenomena, MODVOLC has provided some useful observations. Wright and Flynn (2003) utilized MODVOLC to acquire a two-year time series of quantitative observations of activity at Nyiragongo (Democratic Republic of Congo) prior to, during and following a 2002 eruptive event. Jay et al. (2013) also used MODVOLC data to examine 150 volcanoes and geothermal areas in the central, southern and austral Andes for thermal anomalies between the years

2000 and 2010. MODVOLC data was also used to produce heat and volume flux time series and obtain a total extruded volume at Merapi that can be compared to ground-based estimates of lava dome volumes. In this study, using the methodology of Harris and Ripepe (2007), we find that MODVOLC data enable monitoring of activity at Merapi and Semeru especially in periods with less cloud cover and during eruptions. It should be noted that the methodology of Harris and Ripepe (2007) was developed and tested for application to lava domes and lava (basaltic and silicic) flows. The methodology is suited for Merapi volcano but not entirely appropriate for Semeru, as its eruptive activity dominated by explosive events rather than lava dome construction, except for the most recent period (2010-2014) of the eruption. Unfortunately, we do not have comparable data from ground-based or other measurements to validate our result at Semeru. Therefore, caution must be applied to values of heat and volume fluxes at Semeru, although their first order variations and trends may be reliable.

6.6. Conclusion and perspectives

The use of MODVOLC thermal radiance data converted into heat and volume fluxes, combined with limited seismic data, has been highlighted in approaching temporal variations of the eruptive activity. In this study, we show that MODVOLC data together with the methodology of Harris and Ripepe (2007) used to evaluate the activity of Merapi and Semeru especially in periods with less cloud cover and during an eruption. The method is best suited for Merapi, but also appears to be appropriate for Semeru, especially during the 2010-2014 eruptive activity.

In this study we propose correlations between several large magnitude (>Mw6) tectonic earthquakes and increases in thermal flux during ongoing eruptions at Merapi and Semeru. In addition, some smaller (Mw4-5) events at Merapi may have induced changes. However, at both volcanoes both larger (e.g., the Mw 9.3 Sumatra-Andaman earthquake and many smaller (Mw <5) regional tectonic earthquakes had little if any effect. Manga and Brodsky (2006) suggested approximately 0.4% of explosive volcanic eruptions occur within a few days of large, distant earthquakes. Given a total of 2450 examined tectonic earthquakes in catalog, we observe 36 events that could have influenced activity of Merapi and Semeru during the period 2000-2014, i.e., 1.5% of the catalog.

Building up on this preliminary study, several points can be emphasized for future research as follows:

1. The process behind seasonal variations of Semeru activity, which in this case are expressed by the VT events, need to be studied in more detail and in a quantitative manner. One of many ways is by modeling the influence of groundwater mass variations in the magmatic and/or hydrothermal system at Semeru. Future work will require the additional information on rainfall, hydrothermal system, and subsurface volcanic structures at Semeru.
2. The mechanism of increased volcanic activity triggered by regional earthquakes is still not clearly defined. Future research to be carried out may include modeling the stress changes induced by earthquakes. A clearer correlation between the parameters of earthquakes (e.g. magnitude, distance, fault orientation, etc.) and the response of the volcano also needs to be improved.
3. Small and proximal earthquakes during high activity of the volcano and a decline of SSAM preceded a given earthquake need to be scrutinized as to whether they are associated with regional tectonic deformation or stress propagation forced by localized magmatic activity. Additional evidence from other volcanoes and accompanied by modeling could help to better understand these phenomena.

Chapter 7 – Concluding remarks

The significance of remote sensing has long been emphasized at active and hazardous volcanoes in order to understand the processes that underlie volcanic activity and to use this understanding in volcanic risk reduction. Indonesia, a tropical country which hosts 127 active volcanoes and approximately 5 million people living on the flanks of 77 persistently active and high risk volcanoes, provides multiple challenges for the value of remote sensing to contribute to volcanic hazard assessment. This thesis presents several studies undertaken using HSR optical (IKONOS, Pleriades, GeoEye, Quickbird and SPOT5), radar (ALOS-PALSAR) and thermal (ASTER and MODIS hot spot) images in association with DEMs and aerial photographs to apply remote sensing techniques for studying two of the most active and densely populated volcanoes in Indonesia, Semeru and Merapi. This research has underlined the importance of remote sensing to perform long-term observations and statistical studies spanning several years by taking advantage of satellite imagery that are available with the same level of noise over all periods of time. This remote sensing study has helped unravel structures, geological features and erupted deposits at both volcanoes and has helped assess hazards from their most recent (post-2001) eruptions. In addition, this research provides a first step toward understanding the possible interactions between regional tectonic earthquakes and the eruptive activity of Merapi and Semeru volcanoes. In sum, this is a summary of the contributions, limitations and perspectives of the results together with a new hazard assessment for both volcanoes.

7.1. Remote sensing contributions

The geophysical, geological and tectonic setting of Java Island, as well as the structure of the edifice and historical activity at Semeru and Merapi volcanoes, are described in Chapter 2. Seismotectonic study of Java shows that the source region of magma interpreted from the aseismic gap in the Wadati-Benioff zone is located at 150-190 km in depth beneath Merapi volcano and at 150-240 km in depth beneath Semeru volcano. The seismically active columns or clusters of earthquake beneath active volcanoes, are observed with a majority of shallow depth (<50 km) earthquakes beneath Merapi and

with deeper (down to 80 km) earthquakes beneath Semeru. A Bouguer gravity anomaly map (Untung & Sato, 1978) shows that the Semeru region has a stronger positive anomaly, which suggests that the Semeru edifice is denser and/or may be older than Merapi. A very strong low-velocity (S-wave) anomaly related to an area with a high content of fluids and melts in the crust has been evidenced for the Merapi region just north of Sumbing, Merapi and Lawu volcanoes (Koulakov et al., 2007).

7.1.1. Semeru Volcano

Mount Semeru is composed of two cones, Mahameru (old Semeru) and young Semeru, which belongs to the Semeru-Tengger volcanic massif, whose eruptive centers lie on a roughly north-south-trending arc. Kinematic analysis of fault data suggests that the principal compressive stress direction in the Semeru region is 005°, which is related to the northward movement of the Indo-Australian plate south of the Semeru edifice. A new structural map of the Semeru-Tengger volcanic massif, based on the interpretation of DEMs, HSR satellite images combined with the drainage network map, the CVGHM geological maps (Zaennudin et al., 1995; Sutawidjaja et al., 1996), and the analysis of earthquake focal mechanisms is presented in Chapters 2 and 3. This map shows four groups of faults orientated 040°, 160°, 075°, and 105° to 140°. Conspicuous structures of the Semeru summit cone may be related to the regional tectonic setting such as the SE-trending horseshoe-shaped scar with boundaries that parallel 160°-trending faults. The Semeru composite cone hosts the currently active Jonggring-Seloko vent. The summit cone is located on, and buttressed against the Mahameru edifice at the head of a large scar, which may reflect a failure plane at shallow depth. This feature suggests that the deformation pattern of Semeru and its large scar may be induced by flank spreading over the weak basal layer of the volcano. It is therefore necessary to consider the potential for flank and summit collapse in the future.

An updated geological map of Semeru based on additional data derived from interpretation of the most recent satellite images, aerial photographs, DEM analysis and fieldwork is presented in Chapter 2. The post-2001 eruptive activity at Semeru, including the larger eruption in 2002-2003 and the uncommon effusive eruptions in 2010-2014, has been described. The 2003 ASTER Surface Kinetic Temperature image combined with two 10 m-pixel images acquired before and after the event has enabled

mapping of the 2002–2003 PDC deposits and assessment of the extent and impact of an estimated volume of 5.45 × 10^6 m^3 of block-and-ash flow and surge deposits. Activity at Semeru during the period 2010-2014, produced several lava flows from the central vent, showing a change in eruption style for the first time since at least 1967 or perhaps since 1941. This significant change in Semeru eruptive behavior may have been caused by changes in conduit geometry and/or in magma composition and physical properties (e.g., vesicularity, volatile content). One of the common Semeru hazards is lava-dome collapse producing relatively large volume of PDCs (3 to 6.5 million m^3). Since at least 1977, PDCs dominantly traveled from the crater towards the south and southeast flanks of Semeru, reaching as far as the city of Pronojiwo (12 km from the summit). The 2010-2014 eruptions also involved the growth of a dome-coulée, with an estimated volume of 2.5 ± 0.5 million m^3 as of September 2014. At the time of writing, a dome-coulee in the Jonggring-Seloko crater continues to grow and will probably collapse to produce large volume PDCs, perhaps exceeding the average (1967-2007) volume range of 3 to 6.5 million m^3.

7.1.2. Merapi Volcano

Merapi volcano belongs to a cross-island range of four composite volcanoes comprising, from north to south, Ungaran, Telemoyo, Merbabu and Merapi, aligned along a regional 165°-trending tectonic lineament. Several studies (see subsection 2.4.1 in Chapter 2) have shown that Merapi is a very young polygenetic edifice, but age information on the older Merapi units has remained scarce and many aspects of the overall volcanological and structural evolution of Merapi continue to be controversial. In addition to differences in the classification of Merapi's stages of growth and chronology, discrepancies in interpretations stem from the significance attributed by authors to geologic deposits and their relation to growth, flank failure(s), and blasts or high-energy surges. Although all authors recognize the occurrence of at least one flank failure at Merapi, their interpretations of the details of deposits, chronology and significance vary, as do interpretations of the extents of past pyroclastic flows, surges and blasts. Thus, this work has focused on the application of remote sensing to better elucidate tectonic structures, summit evolution, and identification of the most recent pyroclastic deposits.

On the basis of previous studies, analysis of DEMs and interpretation of satellite imagery, a geological map of Merapi and its ring plain has been drawn to depict the lithological units and tectonic structures of the region. This map defines five groups of inferred faults with trending clusters at 060°, 090°, 115°, 140°, and 175°. The NW-SE-trending basement structures also appear to control the orientation of 115° dextral strike-slip and 140°-trending reverse faults at the surface. The 175°-trending faults appear to have formed from crustal extension and may act as a weak zone in which the Unggaran-Merapi volcanic range has been formed. The kinematic analysis of fault data in Merapi region reveals that the NE-SW (040°) direction is the principal compressive stress axis.

More than 74 eruptions have been recorded at Merapi since 1548 and at least seventeen of them have caused fatalities. Most events fall within the VEI 2 range, at least once per decade since 1861. Larger in magnitude and more explosive (large Vulcanian to sub-Plinian), the 2010 eruption of Merapi differs from previous eruptions in 1994, 1997, 2001 and 2006. The 26 October-23 November 2010 eruption is Merapi's largest event (VEI 4) in the past 140 years. The interpretation of HSR images shows that due to the explosive eruption, the summit area lost about 10 x 10^6 m^3. The eruption enlarged the SSE-trending Gendol Breach to be 1.3x0.3x0.2 km. The 2010 tephra and pyroclastic density current (PDC) deposits covered about 26 km^2 in the two catchments of Gendol and Opak Rivers on Merapi's south flank, i.e. 60-75% of the total PDC deposit area and a total bulk volume of 45 x 10^6 m^3. The volume of tephra fall deposit from Merapi has been determined using empirical volume calculation methods based on exponential, power-law, and Weibull thinning. The tephra fall deposit covered an area of about 1300 km^2 with a range in volume of 18-21 x 10^6 m^3. Additional high spatial-resolution data are provided to delineate and analyze flooded areas due to lahar activity in 2011-2012 on the south and west flanks. Subsequent overbank lahars impacted selective small areas in the populated ring plain, devastating villages along the Putih River on the southwest flank and along the Gendol-Opak River on the south flank. For the first time, the analysis of geomorphological parameters (channel capacity, longitudinal change in channel confinement, and channel sinuosity) has pointed out where and how lahars can spill over the principal river banks and avulse towards otherwise un-threatened but populated valleys.

7.1.3. Remote sensing-based mapping of pyroclastic deposits

The existence of satellite images of an active volcano acquired before, during and immediately after a paroxysmal event, allowed for mapping and evaluating the area covered by fresh volcanic deposits. The 2010 Merapi pyroclastic and lahar deposits have been identified by applying several methods to high-spatial resolution satellite optical images and synthetic aperture radar (SAR) data. The results show that the ability of remotely sensed data to capture fresh, pristine features and extent of deposits shortly after emplacement and before any reworking, highlights the purpose of using high-spatial resolution imagery and SAR data on persistently active volcanoes, where access for field surveys is often impossible. A comparison of tools and methods for the classification of pyroclastic and lahar deposits is summarized in Table 7.1.

Table 7.1. Comparison of tools and methods for the classification of pyroclastic and lahar deposits

Tools and Methods	Criteria value		
	Good	**Fair**	**Poor**
Classification using GeoEye image: Supervised and object-oriented classification	• High-spatial resolution (<1 m) • Provides detailed map • 16 distinct deposit units		• Cloud cover • Illumination effect
Classification using ALOS-PALSAR dataset: • Single polarization • Dual polarization	• No cloud • Differentiates: reflectivity & roughness	• Lower resolution (23 m) • Distinguish well two to four deposit units • Distinguish well up to seven deposit units	• Foreshortening, lengthening, shadow-ing & layover effect

Identification of pyroclastic deposits, for the first time ever in Indonesia, benefited from the 50-cm resolution of the HSR satellite images, and mapping was conducted by using two supervised and object-oriented methods for classification. Supervised and object-

oriented classification carried out on HSR imagery has enabled detailed mapping of the PDC deposits across the Gendol-Opak catchment. We have delineated sixteen spectrally and/or texturally distinct units of PDC deposits and they compared favorably with previously published results of field studies. In addition, due ti the timing of acquisition, some of the HSR images, they provide a snapshot during the waning phase of the eruption, allowing recognition of: (1) pristine (pre-erosion) landforms and deposits associated with valley-confined and unconfined PDCs, (2) severe PDC impacts on devastated villages and housing, cultivated terraces and forests, (3) mudflows fed by water from rice fields beyond the river banks overrun by PDC deposits, and (4) small features such as flow lobes, levees, tree logs and debris strewn on the top surface of pyroclastic-flow deposits.

For the first time again, pyroclastic deposits have been characterized by using direct-polarized and cross-polarized SAR data and combining the information of amplitude evolution with temporal decorrelation. Changes in amplitude of the radar signal enabled accurate mapping of the pyroclastic density currents (PDCs) and tephra fall deposits. Radar amplitudes in direct (HH) and cross (HV) polarizations decrease where the valley-confined and overbank block-and-ash flow (BAF) deposits are emplaced. Rainfall- and runoff-reworked PDC deposits are characterized by an increase in ground backscattering for HH polarization and a decrease for HV polarization. Ground backscattering transiently increases in both polarizations after pyroclastic surge and tephra fall deposition. We have utilized a supervised classification method based on maximum likelihood to map the deposits. The temporal decorrelation of the radar signal and the amplitude evolution improve the quality of classification results. Classification derived from ALOS-PALSAR images provides a result with 70% classification accuracy for deposits overall. The estimated areas of valley-confined and overbank PDC deposits (either primary or reworked by rainfall and runoff) are consistent with the areas measured by other studies, while the large discrepancy in area estimated for pyroclastic-surge deposits can be partly explained by the strong erosion due to intense rainfall that removed a large part of these thin deposits.

7.1.4. Earthquake-volcano interactions

Chapter 6 of this thesis presents preliminary results that provided some insight into the interactions between regional earthquakes and volcanic activity of Merapi and Semeru, over the period 2000-2014. This work highlights the use of MODVOLC thermal radiance data converted into heat and volume fluxes, combined with limited seismic data, in evaluation of temporal variations of the eruptive activity. Each regional tectonic earthquake within a radius of 1000 km from the volcano was cross-checked with the time series of volcanic heat flux and seismic events searching for a change in volcanic activity following each event. An inventory has been produced which includes events inferred to have triggered a response in the eruptive activity at Merapi and Semeru with various time delays and response duration. Approximately 1.5% of regional tectonic earthquakes during the period 2000-2014 have influenced eruptive activity of Merapi and Semeru. The inventory dataset was then examined in order to determine if there is a clear correlation between the response(s) of volcanoes to the occurrence of regional earthquakes. The volcano response to the regional earthquake is mostly shown by an increase in eruptive activity caused by static and/or dynamic changes in stress field induced by the earthquake. The absence of strong correlation between the response ratio and the distance from the earthquake epicenter to the responding volcano suggests that most of the earthquake-volcano interactions in the data inventory likely involve dynamic stress change rather than static stress change.

7.2. Limitation and research perspectives

In general, remote sensing provides many advantages that can be used for research purposes. However, in order to obtain valid results, remote sensing data should be integrated together with ground-based observations and near real-time measurements. Besides contributions of this research to understanding persistently active volcanoes such as Semeru and Merapi, there remain limitations to be solved, methods to be improved and perspectives for future research projects.

1. The location of the source region of magma and the area of high content of fluids and melts in the crust beneath Merapi and Semeru volcanoes have been interpreted based on previous studies of seismotectonics, seismic tomography and gravimetry.

However, the link between the shallow plumbing system and reservoirs beneath the two volcanoes remains ambiguous. Information on geometry of any reservoir at shallow depth (<10 km) beneath Merapi and Semeru are poorly known. A dense seismic network around Merapi volcano would allow a better knowledge of the plumbing system beneath the volcano. For example using such a network, a "small" shallow magma reservoir was detected at 1.5-2.5 km in depth as indicated by an aseismic zone (Ratdomopurbo & Poupinet, 2000; confirmed by Budi-Santoso et al., 2013). At Semeru, the lack of a dense seismic network prevents us from linking the surface tectonic faults, the main geologic features of Semeru (the SE scar) and the complex behavior as expressed by repeated dome growth and collapse, open system vulcanian-Stombolian explosions and lava flows. A petrological analysis of the tephra, PDC deposits and lava flow will likely become a significant asset towards understanding the complex eruptive behaviour of Semeru.

2. The origin of the Jonggring-Seloko SE-trending scar is not fully understood. Although this scar coincides with one of regional faults, it may be a transient volcanic structure and landform that can be rapidly filled by lava flows as shown by an aerial photograph in 1923 (Fig. 10 in Solikhin et al., 2012). Deformation data are required to understand the structures of the Semeru edifice as well as to support the working hypothesis presented in this thesis concerning an asymmetric deformation pattern induced by flank spreading at Semeru.
3. The eruptive behavior of Semeru may have changed in 2010, as it produced several lava flows from the central vent for the first time since 1967 or 1941. As yet, it has not been possible to ascertain the cause of this change and it remains unclear as to whether the 2010-2014 events herald a major change in behavior of the Semeru system. To better understand this change, the composition and physical characteristics of the new lava flows should be analyzed and a geophysical analysis of Semeru sub-surface structures should be carried out.
4. Radar images that can be acquired at night and in cloudy conditions can complement the HSR multispectral images in the classification of pyroclastic deposits. However, limitations of radar imagery, such as the effects of foreshortening, lengthening, shadowing and layover on steep slopes may reduce the accuracy of classification. This problem may be partly overcome by combining both ascending and descending images. The classification of the 2010 Merapi deposits presented in this thesis is

based on change detection and semi-automated (supervised) classification methods applied to ALOS-PALSAR dual polarization data. It can also be utilized for other active volcanoes with fresh pyroclastic deposits. However, caution should be exercised when applying these methods to other radar data with different wavelengths. It has been shown that the change in amplitude images due to PDC deposition observed in L-band radar images is different from the amplitude change detected in X-band radar images (Solikhin et al., 2015a).

5. The use of MODVOLC thermal radiance data converted into heat and volume fluxes, combined with limited seismic data, has been highlighted in approaching temporal variations of the eruptive activity. This study highlights that MODVOLC data together with the methodology of Harris and Ripepe (2007) are reliable to approach the activity of Merapi and Semeru especially in periods with less cloud cover and during an eruption. The methods was developed and tested for application to lava domes and lava flows, thus, it is suited for Merapi and may be appropriate for Semeru, especially during the 2010-2014 eruptive activity. However, additional data from ground-based or remotely sensed measurements are required to validate the result of the methodology at Semeru volcano.
6. Many questions remain after this study related to the response of Semeru and Merapi volcanoes to external factors, especially tectonic earthquakes. First, the process behind the seasonal variations of Semeru activity, as expressed by the VT event variations, is still unknown. This may be solved by modeling the influence of groundwater mass variation on the magmatic and/or hydrothermal system at Semeru. Second, the mechanism of increased volcanic activity triggered by regional earthquakes is still not clearly defined. Future research to be carried out requires modeling the stress changes induced by earthquakes. Third, small and proximal earthquakes during heightened activity of the volcano need to be scrutinized as to whether or not they are associated with inflation or stress propagation forced by magmatic activity.

7.3. Hazard assessment

On the basis of the eruptive behavior of Semeru since 2010, this thesis provides a new hazard assessment for the near future, as follows: (1) the fact that the SE scar has been

partially filled by the 2010, 2012 and 2014 lava flows should be taken into account for hazard mitigation during upcoming eruptions. Future PDCs may not travel only farther down the SE scar but during Vulcanian eruptions, or were the SE-scar to be filled, PDC flows could also spill over its rims towards the southwest and east flanks. (2) Time series of HSR imagery can be of great utility in tracking the rapid changes that occur on summit and flank structures and landforms of persistently active volcanic edifices. This should be continuously applied at Semeru as rapid morphological changes occur especially at the summit vent and in the drainage system due to the impact of frequent PDCs and lahars. (3) The Semeru hazard-zone map currently used by CVGHM was published in 1996. It is suggested that this map be updated, considering several studies that have been carried out (Thouret et al., 2007; Solikhin et al., 2012), recent conditions outlined in this thesis, and the results of numerical simulations of PDCs and lahars (e.g., Weningsulistri et al., 2014), or preferably, using new modeling using a new, higher resolution and accurate DEM and integrated with existing and additional detailed geologic field studies.

This study has reappraised the hazard assessment for the south flank of Merapi (Thouret et al., 2000). This new hazard assessment of Merapi volcano after the 2010 eruption indicates the following issues (areas, deposits and processes) at stake in the near future : (1) The new, enlarged and deep summit crater is unstable. Phreatic, phreatomagmatic, or small vulcanian events such as the 22 July 2013, 18 November 2013 and 9 March 2014 eruptions will pose threats to visitors and scientists around the summit area and can weaken the already unstable rims of the summit crater. In addition, the 18 November 2013 explosion divided the 2010 dome into two main parts and left a major NW-SE trending fracture; this may affect the dynamics and the stability of the post-2010 Merapi dome (Walter et al., 2015). (2) The enlarged summit scar and Gendol Breach will act as pathways for future flows, and the high, steep, fractured and hydrothermally altered walls of the Breach are subject to rockfalls and earthquake-triggered landslides. (3) A large amount of sediment accumulated in radial valleys is still susceptible to remobilization by lahars. Field evidence shows that such remobilization is developing at a fast rate. However, mining activity since 2011 has already removed the majority of the PDC deposits within the Gendol channel from distance of 6 km from the summit to the PDC front, located 16 km down valley. (4) Lahar overspill is the most hazardous process acting along the lowermost river courses of Kali Putih towards the

city of Magelang, and along the Gendol-Opak Rivers, which transport material towards the Prambanan temples and the Yogyakarta airport. Lahars currently threaten the area of the iconic Prambanan temple farther down the Opak River. This study pinpoints three locations near the Prambanan temples that are potential for future lahar overbank processes, by applying geometric indices.

Bibliography

A

Abdurachman, E.K., Bourdier, J.L., & Voight, B. (2000). Nuées ardentes of 22 November 1994 at Merapi volcano, Java, Indonesia. *Journal of Volcanology and Geothermal Research, 100*, 345-361.

Albino, F., Pinel, V., & Sigmundsson, F. (2010). Influence of surface load variations on eruption likelihood: application to two Icelandic subglacial volcanoes, Grímsvötn and Katla. *Geophysical Journal International, 181*, 1510–1524.

Allmendinger, R.W., Cardozo, N., & Fisher, D.M. (2012). *Structural geology algorithms: Vectors and tensors*. Cambridge, England: Cambridge University Press.

Andreastuti, S.D., Alloway, B.V., & Smith, I.E.M. (2000). A detailed tephrostratigraphic framework at Merapi Volcano, Central Java, Indonesia: implications for eruption predictions and hazard assessment. *Journal of Volcanology and Geothermal Research, 100*, 51-67.

Andrews, B.J., & Manga, M. (2011). Effects of topography on pyroclastic density current runout and formation of coignimbrites. *Geology, 39*, 1099-1102.

B

Bahar, I. (1984). Contribution à la connaissance du volcanisme Indonésien: Le Merapi (Centre-Java); Cadre structural, pétrologie-géochimie et implications volcanologiques. *PhD dissertation*. Université des Sciences et Techniques du Langue, Montpellier.

BAPPENAS, & BNPB (2011). Rencana aksi rehabilitasi dan rekonstruksi wilayah pasca bencana Gunung Merapi di Provinsi D. I. Yogyakarta dan Provinsi Jawa Tengah 2011-2013 (In Indonesian). BAPPENAS and BNPB, Jakarta, Indonesia.

Bautista, B.C., Bautista, L.P., Stein, R.S., Barcelona, E.S., Punongbayan, R.S., Laguerta, E.P., Rasdas, A.R., Ambubuyog, G., & Amin, A.Q. (1996). Relationship of regional and local structures to Mount Pinatubo activity. In C.G. Newhall, & R.S. Punongbayan (Eds.), *Fire and mud*, University of Washington Press, Seattle, 351–370.

Berthommier, P.C. (1990). Étude volcanologique du Merapi: Téphro-stratigraphie et chronologie, produits éruptifs. *PhD dissertation*. Université Blaise Pascal, Clermont-Ferrand II.

Bignami, C., Ruch, J., Chini, M., Neri, M., Buongiorno, M.F., Hidayati, S., Sayudi, D.S., & Surono (2013). Pyroclastic density current volume estimation after the 2010 Merapi volcano eruption using X-band SAR. *Journal of Volcanology and Geothermal Research, 261*, 236-243.

Blackett, M. (2014). Early Analysis of Landsat-8 Thermal Infrared Sensor Imagery of Volcanic Activity. *Remote Sensing, 6*, 2282-2295.

Blake, S. (1999). Viscoplastic models of lava domes. In, *IAVCEI Proceddings in Volcanology, Vol. 2. Lava flowsand domes*Springer Verlag, Heidelberg , 88-126.

Blom, R.G., Schenck, L.R., & Alley, R.E. (1987). What are the best radar wavelengths, incidence angles, and polarizations for discrimination among lava flows and sedimentary rocks? A statistical approach. *IEEE Transactions Geoscience Remote Sensing, GE-25*, 208-213.

Blong, R.J. (1984). *Volcanic hazards: a sourcebook on the effects of eruptions*. Academic Press, Orlando, Florida.

Boechair, I. (1976). Some considerations of the problem of the shift of Mataram's center of government from Central Java to East Java in the 10th century A.D. *Bulletin of Research Center of Arquaeology of Indonesia, 10*, 1-9.

Bonadonna, C., & Costa, A. (2012). Estimating the volume of tephra deposits: A new simple strategy. *Geology, 40*, 415-418.

Bonadonna, C., & Houghton, B.F. (2005). Total grain-size distribution and volume of tephra-fall deposits. *Bulletin of Volcanology, 67*, 441-456.

Borgia, A. (1994). Dynamic basis of volcanic spreading. *Journal of Geophysical Research, 99*, 17791.

BPS (2010). Kabupaten dalam angka (In Indonesian). Biro Pusat Statistik, Yogyakarta Special Province, Indonesia.

BPS (2011). Penduduk Indonesia menurut desa hasil sensus penduduk 2010 (In Indonesian). Biro Pusat Statistik, Jakarta, Indonesia.

Branney, M.J., & Kokelaar, P. (2002). Pyroclastic density currents and the sedimentation of ignimbrites. *Memoirs, Geological Society of London, 27*, 152 pp.

Brenguier, F., Campillo, M., Takeda, T., Aoki, Y., Shapiro, N.M., Briand, X., Emoto, K., & Miyake, H. (2014). Earthquake dynamics. Mapping pressurized volcanic fluids from induced crustal seismic velocity drops. *Science, 345*, 80-82.

Brodsky, E.E., Sturtevant, B., & Kanamori, H. (1998). Earthquakes, volcanoes, and rectified diffusion. *Journal of Geophysical Research, 103*, 23827.

Bronto, S., Hamidi, S., & Martono, A. (1996). Peta Kawasan Rawan Bencana G. Semeru, Jawa Tengah (Disaster-prone zone map of Semeru volcano, East Java). Direktorat Vulkanologi, Volcanological Survey of Indonesia, Bandung.

Budi-Santoso, A., Lesage, P., Dwiyono, S., Sumarti, S., Subandriyo, Surono, Jousset, P., & Metaxian, J.-P. (2013). Analysis of the seismic activity associated with the 2010 eruption of Merapi Volcano, Java. *Journal of Volcanology and Geothermal Research, 261*, 153-170.

C

Camus, G., Gourgaud, A., Mossand-Berthommier, P.C., & Vincent, P.M. (2000). Merapi (Central Java, Indonesia): An outline of the structural and magmatological evolution, with a special emphasis to the major pyroclastic events. *Journal of Volcanology and Geothermal Research, 100*, 139-163.

Carn, S.A. (1999). Application of synthetic aperture radar (SAR) imagery to volcano mapping in the humid tropics: a case study in East Java, Indonesia. *Bulletin of Volcanology, 61*, 92-105.

Carn, S.A., Krueger, A.J., Bluth, G.J.S., Schaefer, S.J., Krotkov, N.A., Watson, I.M., & Datta, S. (2003). Volcanic eruption detection by the Total Ozone Mapping Spectrometer (TOMS) instruments: a 22-year record of sulfur dioxide and ash emissions. In C. Oppenheimer, D.M. Pyle, & J. Barclay, (Eds.), *Volcanic degassing*, Geological Society, London, 177-202.

Cecchi, E., van Wyk de Vries, B., & Lavest, J.-M. (2004). Flank spreading and collapse of weak-cored volcanoes. *Bulletin of Volcanology, 67*, 72-91.

Charbonnier, S.J., Germa, A., Connor, C.B., Gertisser, R., Preece, K., Komorowski, J.C., Lavigne, F., Dixon, T., & Connor, L. (2013). Evaluation of the impact of the 2010 pyroclastic density currents at Merapi volcano from high-resolution satellite imagery, field investigations and numerical simulations. *Journal of Volcanology and Geothermal Research, 261*, 295-315.

Charbonnier, S.J., & Gertisser, R. (2008). Field observations and surface characteristics of pristine block-and-ash flow deposits from the 2006 eruption of Merapi Volcano, Java, Indonesia. *Journal of Volcanology and Geothermal Research, 177*, 971-982.

Charbonnier, S.J., & Gertisser, R. (2011). Deposit architecture and dynamics of the 2006 block-and-ash flows of Merapi Volcano, Java, Indonesia. *Sedimentology, 58*, 1573-1612.

Charlton, T.R. (2000). Tertiary evolution of the Eastern Indonesia Collision Complex. *Journal of Asian Earth Sciences, 18*, 603-631.

Chaussard, E., Amelung, F., & Aoki, Y. (2013). Characterization of open and closed volcanic systems in Indonesia and Mexico using InSAR time series. *Journal of Geophysical Research: Solid Earth, 118*, 3957-3969.

Chesner, C.A., Rose, W.I., Deino, A., Drake, R., & Westgate, J.A. (1991). Eruptive history of Earth's largest Quaternary caldera (Toba, Indonesia) clarified. *Geology, 19*, 200.

Chorowicz, J., Deffontaines, B., Huaman-Rodrigo, D., Guillande, R., Leguern, F., & Thouret, J.C. (1992). SPOT satellite monitoring of the eruption of Nevado Sabancaya volcano (Southern Peru). *Remote Sensing of Environment, 42*, 43-49.

Cracknell, M.J., & Reading, A.M. (2014). Geological mapping using remote sensing data: A comparison of five machine learning algorithms, their response to variations in the spatial distribution of training data and the use of explicit spatial information. *Computers & Geosciences, 63*, 22-33.

Cronin, S.J., Lube, G., Dayudi, D.S., Sumarti, S., Subrandiyo, S., & Surono (2013). Insights into the October–November 2010 Gunung Merapi eruption (Central Java, Indonesia) from the stratigraphy, volume and characteristics of its pyroclastic deposits. *Journal of Volcanology and Geothermal Research, 261*, 244-259.

Curlander, J.C., & McDonough, R.N. (1991). *Synthetic Aperture Radar: Systems and Signal Processing*. Wiley.

D

Dana, I.N., Wildan, A., Martono, A., Sutresna, D., Triyono, Rochman, & Djuandi (1996). Evaluasi kegiatan G. Semeru, Jawa Timur (assessment of the Mt. Semeru volcanic activity, East Java). Volcanological Survey of Indonesia, Bandung, 44 pp.

de Bélizal, E., Lavigne, F., Hadmoko, D.S., Degeai, J.-P., Dipayana, G.A., Mutaqin, B.W., Marfai, M.A., Coquet, M., Mauff, B.L., Robin, A.-K., Vidal, C., Cholik, N., & Aisyah, N. (2013). Rain-triggered lahars following the 2010 eruption of Merapi volcano, Indonesia: A major risk. *Journal of Volcanology and Geothermal Research, 261*, 330-347.

De Boer, J.Z., & Sanders, D.T. (2002). *Volcanoes in human history: the far-reaching effects of major eruptions*. Princeton University Press.

Del Marmol, M.-A. (1989). The petrology and geochemistry of Merapi volcano, Central Java, Indonesia. In: Johns Hopkins University.

Delle Donne, D., Harris, A.J.L., Ripepe, M., & Wright, R. (2010). Earthquake-induced thermal anomalies at active volcanoes. *Geology, 38*, 771-774.

Dellwig, L.F., & Moore, R.K. (1966). The geological value of simultaneously produced like- and cross-polarized radar imagery. *Journal of Geophysical Research, 71*, 3597-3601.

DeMets, C., Gordon, R.G., Argus, D.F., & Stein, S. (1994). Effect of recent revisions to the geomagnetic reversal time scale on estimates of current plate motions. *Geophysical Research Letters, 21*, 2191-2194.

Dietterich, H.R., Poland, M.P., Schmidt, D.A., Cashman, K.V., Sherrod, D.R., & Espinosa, A.T. (2012). Tracking lava flow emplacement on the east rift zone of Kīlauea, Hawai'i, with synthetic aperture radar coherence. *Geochemistry Geophysics Geosystems, 13.*

Djumarma, A., Bronto, S., Bahar, I., Suparban, F.X., Sukhyar, R., Newhall, C.G., Holcomb, R.T., Banks, N.G., Torley, R., Lockwood, J.P., Tilling, R.I., Rubin, M., & Malingreau, M.A. (1986). Did Merapi volcano (Central Java) erupt catastrophically in 1006 A.D.? In, *International Volcanology Congress IAVCEI* (p. 236). New Zealand.

Doocy, S., Daniels, A., Dooling, S., & Gorokhovich, Y. (2013). The human impact of volcanoes: a historical review of events 1900-2009 and systematic literature review. *PLoS Curr, 5.*

Dziewonski, A., Chou, T.A., & Woodhouse, J. (1981). Determination of earthquake source parameters from waveform data for studies of global and regional seismicity. *Journal of Geophysical Research: Solid Earth (1978–2012), 86*, 2825-2852.

E

Ekström, G., Nettles, M., & Dziewoński, A. (2012). The global CMT project 2004–2010: Centroid-moment tensors for 13,017 earthquakes. *Physics of the Earth and Planetary Interiors, 200*, 1-9.

Endo, E.T., & Murray, T. (1991). Real-time Seismic Amplitude Measurement (RSAM): a volcano monitoring and prediction tool. *Bulletin of Volcanology, 53*, 533-545.

Engdahl, E.R., van der Hilst, R., & Buland, R. (1998). Global teleseismic earthquake relocation with improved travel times and procedures for depth determination. *Bulletin of the Seismological Society of America, 88*, 722-743.

F

Feuillet, N., Cocco, M., Musumeci, C., & Nostro, C. (2006). Stress interaction between seismic and volcanic activity at Mt Etna. *Geophysical Journal International, 164*, 697-718.

Fierstein, J., & Nathenson, M. (1992). Another look at the calculation of fallout tephra volumes. *Bulletin of Volcanology, 54*, 156-167.

Fisher, R.V., & Schmincke, H.U. (1984). *Pyroclastic Rocks*. Springer Berlin Heidelberg.

G

Gaddis, L., Mouginis-Mark, P., Singer, R., & Kaupp, V. (1989). Geologic analyses of Shuttle Imaging Radar (SIR-B) data of Kilauea Volcano, Hawaii. *Geological Society of America Bulletin, 101*, 317-332.

Gaddis, L.R. (1992). Lava-flow characterization at Pisgah volcanic field, California, with multiparameter imaging radar. *Geological Society of America Bulletin, 104*, 695-703.

Garwin, S., Hall, R., & Watanabe, Y. (2005). Tectonic setting, geology, and gold and copper mineralization in Cenozoic magmatic arcs of Southeast Asia and the West Pacific. *Economic Geology 100th anniversary volume*, 891-930.

Gerstenecker, C., Läufer, G., Steineck, D., Tiede, C., & Wrobel, B. (2005). Validation of Digital Elevation Models around Merapi Volcano, Java, Indonesia. *Natural Hazards and Earth System Science, 5*, 863-876.

Gertisser, R., Charbonnier, S.J., Keller, J., & Quidelleur, X. (2012). The geological evolution of Merapi volcano, Central Java, Indonesia. *Bulletin of Volcanology, 74*, 1213-1233.

Gillespie, A.R., Matsunaga, T., Rokugawa, S., & Hook, S.J. (1998). Temperature and emissivity separation from Advance Spaceborne Thermal Emission and Reflection Radiometer (ASTER) images. *IEEE Transactions on Geoscience and Remote Sensing 36*, 1113-1126.

Gomez, C., & Lavigne, F. (2010). Automated block detection in lahars through 3-bands spectral analysis of video images. *Journal of Volcanology and Geothermal Research, 190*, 379-384.

Gutenberg, B., & Richter, C.F. (1956). Earthquake magnitude, intensity, energy, and acceleration: (Second paper). *Bulletin of the Seismological Society of America, 46*, 105-145.

H

Hadisantono, R.D. (1990). The Sukapura and other ignimbrites, in the Sapikerep-Sukapura valley and the relationship to caldera formation of Bromo-Tengger volcanic complex, Probolinggo, East Java, Indonesia. *Master thesis*, Research School of Earth Science, Victoria University of Wellington.

Hall, R. (1995). Plate tectonic reconstructions of the Indonesian region. *Indonesian Petroleum Association, Proceedings 24th Annual Convention, 24*, 71-84.

Hall, R. (2002). Cenozoic geological and plate tectonic evolution of SE Asia and the SW Pacific: computer-based reconstructions, model and animations. *Journal of Asian Earth Sciences, 20*, 353-431.

Hall, R. (2009). Indonesia, Geology. In R. Gillespie, & D. Clague (Eds.), *Encyclopedia of Islands* (pp. 454-460). University of California Press, California.

Hall, R., Clements, B., Smyth, H.R., & Cottam, M.A. (2007). A new interpretation of Java's structure. *Indonesian Petroleum Association, Proceedings 31st Annual Convention*, 63-86.

Hall, R., Cross, L., Clements, B., & Spakman, W. (2009). Neogene subduction beneath Java: slab tearing, arc deformation and arc magmatism, and their causes. In, *Southeast Asian Gateway Evolution Conference (abstract)*. Royal Holloway University of London, United Kingdom.

Hall, R., & Smyth, H.R. (2008). Cenozoic arc processes in Indonesia: Identification of the key influences on the stratigraphic record in active volcanic arcs*, 436*, 27-54.

Hamilton, W. (1979). Tectonics of the Indonesia region. *USGS Proffesional Paper, 1078*, 345 pp.

Hanuš, V., Špičák, A., & Vaněk, J. (1996). Sumatran segment of the Indonesian subduction zone: morphology of the Wadati-Benioff zone and seismotectonic pattern of the continental wedge. *Journal of Southeast Asian Earth Sciences, 13*, 39-60.

Hanuš, V., & Vaněk, J. (1988). Deep structure, volcanism and Wadati-Benioff zone of the northwestern Pacific convergent margin. *Journal of geodynamics, 10*, 25-41.

Harington, C.R. (1992). *The year without a summer?-World climate in 1816*. Canadian Museum of Nature.

Harris, A.J.L., Blake, S., Rothery, D.A., & Stevens, N.F. (1997). A chronology of the 1991 to 1993 Mount Etna eruption using advanced very high resolution radiometer data: Implications for real-time thermal volcano monitoring. *Journal of Geophysical Research, 102*, 7985.

Harris, A.J.L., Flynn, L.P., Dean, K., Pilger, E., Wooster, M., Okubu, C., Mouginis-Mark, P., Gerbeil, H., Thornber, C., De la Cruz-Reyna, S., Rothery, D., & Wright, R. (2000). Real-time satellite monitoring of volcanic hot spots. In P. Mouginis-Mark, J.A. Crisp, & J.H. Fink (Eds.), *Remote sensing of active volcanism*, American Geophysical Union, 139-160.

Harris, A.J.L., & Ripepe, M. (2007). Regional earthquake as a trigger for enhanced volcanic activity: Evidence from MODIS thermal data. *Geophysical Research Letters, 34.*

Hayashi, J.N., & Self, S. (1992). A comparison of pyroclastic flow and debris avalanche mobility. *Journal of Geophysical Research, 97*, 9063.

Head, E.M., Maclean, A.L., & Carn, S.A. (2012). Mapping lava flows from Nyamuragira volcano (1967–2011) with satellite data and automated classification methods. *Geomatics, Natural Hazards and Risk, 4*, 119-144.

Hildreth, W.E.S., & Lanphere, M.A. (1994). Potassium-argon geochronology of a basalt-andesite-dacite arc system: The Mount Adams volcanic field, Cascade Range of southern Washington. *Geological Society of America Bulletin, 106*, 1413-1429.

Hill, D.P., Pollitz, F., & Newhall, C. (2002). Earthquake–volcano interactions. *Physics Today, 55*, 41-47.

Honthaas, C., Maury, R.C., Priadi, B., Bellon, H., & Cotten, J. (1999). The Plio–Quaternary Ambon arc, Eastern Indonesia. *Tectonophysics, 301*, 261-281.

Hooper, A., Prata, F., & Sigmundsson, F. (2012). Remote Sensing of Volcanic Hazards and Their Precursors. *Proceedings of the IEEE, 100*, 2908-2930.

Hora, J.M., Singer, B.S., & Worner, G. (2007). Volcano evolution and eruptive flux on the thick crust of the Andean Central Volcanic Zone: 40Ar/39Ar constraints from Volcan Parinacota, Chile. *Geological Society of America Bulletin, 119*, 343-362.

I

Iguchi, M., Yakiwara, H., Tameguri, T., Hendrasto, M., & Hirabayashi, J.-i. (2008). Mechanism of explosive eruption revealed by geophysical observations at the Sakurajima, Suwanosejima and Semeru volcanoes. *Journal of Volcanology and Geothermal Research, 178*, 1-9.

Irsyam, M., Sengara, I.W., Aldiamar, F., Widiyantoro, S., Triyoso, W., Natawidjaja, D.H., Engkon, K., Meilano, I., Suhardjono, Asrurifak, M., & Ridwan, M. (2010). Ringkasan hasil studi. *Tim revisi peta gempa Indonesia 2010*.

Iverson, R.M. (1997). The physics of debris flows. *Reviews of Geophysics, 35*, 245.

J

Jay, J.A., Welch, M., Pritchard, M.E., Mares, P.J., Mnich, M.E., Melkonian, A.K., Aguilera, F., Naranjo, J.A., Sunagua, M., & Clavero, J. (2013). Volcanic hotspots of the central and southern Andes as seen from space by ASTER and MODVOLC between the years 2000 and 2010. *Geological Society, London, Special Publications, 380*, 161-185.

Jenkins, S., Komorowski, J.C., Baxter, P.J., Spence, R., Picquout, A., Lavigne, F., & Surono (2013). The Merapi 2010 eruption: An interdisciplinary impact assessment methodology for studying pyroclastic density current dynamics. *Journal of Volcanology and Geothermal Research, 261*, 316-329.

Jenkins, S., Magill, C., McAneney, J., & Blong, R. (2012). Regional ash fall hazard I: a probabilistic assessment methodology. *Bulletin of Volcanology, 74*, 1699-1712.

Johnston, M.J.S., & Mauk, F.J. (1972). Earth Tides and the Triggering of Eruptions from Mt Stromboli, Italy. *Nature, 239*, 266-267.

Jousset, P., Pallister, J., & Surono (2013). The 2010 eruption of Merapi volcano. *Journal of Volcanology and Geothermal Research, 261*, 1-6.

Joyce, K.E., Samsonov, S., Manville, V., Jongens, R., Graettinger, A., & Cronin, S.J. (2009). Remote sensing data types and techniques for lahar path detection: A case study at Mt Ruapehu, New Zealand. *Remote Sensing of Environment, 113*, 1778-1786.

K

Kassouk, Z., Thouret, J.-C., Gupta, A., Solikhin, A., & Liew, S.C. (2014). Object-oriented classification of a high-spatial resolution SPOT5 image for mapping geology and landforms of active volcanoes: Semeru case study, Indonesia. *Geomorphology, 221*, 18-33.

Komorowski, J.-C., Jenkins, S., Baxter, P.J., Picquout, A., Lavigne, F., Charbonnier, S., Gertisser, R., Preece, K., Cholik, N., Budi-Santoso, A., & Surono (2013). Paroxysmal dome explosion during the Merapi 2010 eruption: Processes and facies relationships of associated high-energy pyroclastic density currents. *Journal of Volcanology and Geothermal Research, 261*, 260-294.

Koulakov, I., Bohm, M., Asch, G., Lühr, B.G., Manzanares, A., Brotopuspito, K.S., Fauzi, P., Purbawinata, M.A., Puspito, N.T., Ratdomopurbo, A., Kopp, H., Rabbel, W., & Shevkunova, E. (2007). PandSvelocity structure of the crust and the upper mantle beneath central Java from local tomography inversion. *Journal of Geophysical Research, 112.*

Krueger, A.J., Schaefer, S.J., Krotkov, N., Bluth, G., & Barker, S. (2000). Ultraviolet remote sensing of volcanic emissions. In P. Mouginis-Mark, J.A. Crisp, & J.H. Fink (Eds.), *Remote sensing of active volcanism*, American Geophysical Union, 25-43.

Kumagai, H. (2009). Volcano seismic signal, source quantification of. In R.A. Meyers (Ed.), *Encyclopedia of Complexity and Systems Science* (pp. 9899-9932): Springer New York.

L

Lara, L.E., Naranjo, J.A., & Moreno, H. (2004). Rhyodacitic fissure eruption in Southern Andes (Cordón Caulle; 40.5°S) after the 1960 (Mw:9.5) Chilean earthquake: a structural interpretation. *Journal of Volcanology and Geothermal Research, 138*, 127-138.

Lavigne, F., Degeai, J.P., Komorowski, J.C., Guillet, S., Robert, V., Lahitte, P., Oppenheimer, C., Stoffel, M., Vidal, C.M., Surono, Pratomo, I., Wassmer, P., Hajdas, I., Hadmoko, D.S., & de Belizal, E. (2013). Source of the great A.D. 1257 mystery eruption unveiled, Samalas volcano, Rinjani Volcanic Complex, Indonesia. *Proceedings of the National Academy of Science U S A, 110*, 16742-16747.

Lavigne, F., & Suwa, H. (2004). Contrasts between debris flows, hyperconcentrated flows and stream flows at a channel of Mount Semeru, East Java, Indonesia. *Geomorphology, 61*, 41-58.

Lavigne, F., & Thouret, J.-C. (2002). Sediment transportation and deposition by rain-triggered lahars at Merapi Volcano, Central Java, Indonesia. *Geomorphology, 49*, 45-69.

Lavigne, F., Thouret, J.C., Voight, B., Suwa, H., & Sumaryono, A. (2000). Lahars at Merapi volcano, Central Java: an overview. *Journal of Volcanology and Geothermal Research, 100*, 423-456.

Linde, A.T., & Sacks, I.S. (1998). Triggering of volcanic eruptions. *Nature, 395*, 888-890.

Lu, Z., & Dzurisin, D. (2014). InSAR Imaging of Aleutian Volcanoes, 87-345.

Lube, G., Cronin, S.J., Thouret, J.C., & Surono (2011). Kinematic characteristics of pyroclastic density currents at Merapi and controls on their avulsion from natural and engineered channels. *Geological Society of America Bulletin, 123*, 1127-1140.

Luehr, B.-G., Koulakov, I., Rabbel, W., Zschau, J., Ratdomopurbo, A., Brotopuspito, K.S., Fauzi, P., & Sahara, D.P. (2013). Fluid ascent and magma storage beneath Gunung Merapi revealed by multi-scale seismic imaging. *Journal of Volcanology and Geothermal Research, 261*, 7-19

M

MacKay, M.E., & Mouginis-Mark, P.J. (1997). The effect of varying acquisition parameters on the interpretation of SIR-C radar data: The Virunga volcanic chain. *Remote Sensing of Environment, 59*, 321-336.

Manga, M., & Brodsky, E. (2006). Seismic triggering of eruptions in the far field: Volcanoes and Geysers. *Annual Review of Earth and Planetary Sciences, 34*, 263-291.

Manville, V., Segschneider, B., Newton, E., White, J., Houghton, B., & Wilson, C. (2009). Environmental impact of the 1.8 ka Taupo eruption, New Zealand: Landscape responses to a large-scale explosive rhyolite eruption. *Sedimentary Geology, 220*, 318-336.

Marrett, R., & Allmendinger, R.W. (1990). Kinematic analysis of fault-slip data. *Journal of Structural Geology, 12*, 973-986.

Mason, B.G., Pyle, D.M., Dade, W.B., & Jupp, T. (2004). Seasonality of volcanic eruptions. *Journal of Geophysical Research, 109*, B04206.

Massonnet, D., Briole, P., & Arnaud, A. (1995). Deflation of Mount Etna monitored by spaceborne radar interferometry. *Nature, 375*, 567-570.

Massonnet, D., & Sigmundsson, F. (2000). Remote sensing of volcano deformation by radar interferometry from various satellite. In P. Mouginis-Mark, J.A. Crisp, & J.H. Fink (Eds.), *Remote sensing of active volcanism*, American Geophysical Union, Washington DC, 207-221.

Mazzarini, F., & Armienti, P. (2001). Flank Cones at Mount Etna Volcano: Do they have a power-law distribution? *Bulletin of Volcanology, 62*, 420-430.

McAlpin, D., & Meyer, F.J. (2013). Multi-sensor data fusion for remote sensing of post-eruptive deformation and depositional features at Redoubt Volcano. *Journal of Volcanology and Geothermal Research, 259*, 414-423.

McGuire, W.J., Howarth, R.J., Firth, C.R., Solow, A.R., Pullen, A.D., Saunders, S.J., Stewart, I.S., & Vita-Finzi, C. (1997). Correlation between rate of sea-level change and frequency of explosive volcanism in the Mediterranean. *Nature, 389*, 473-476.

Mei, E.T.W., Lavigne, F., Picquout, A., de Bélizal, E., Brunstein, D., Grancher, D., Sartohadi, J., Cholik, N., & Vidal, C. (2013). Lessons learned from the 2010 evacuations at Merapi volcano. *Journal of Volcanology and Geothermal Research, 261*, 348-365.

Miller, V., Ammon, C., Voight, B., & De Angelis, S. (2008). A moving block-and-ash flow of Merapi volcano (Indonesia) and deposit facies as imaged by IKONOS on 16 June 2006. In, *IAVCEI General Assembly*. Reykjavik.

Minakami, T. (1974). Seismology of volcanoes in Japan. In L. Civetta, P. Gasparini, G. Luongo, & A. Rapolla (Eds.), *Physical Volcanology Developments in Solid Earth Geophysics* (pp. p. 1-27): Elsevier Amsterdam.

Minster, J.B., & Jordan, T.H. (1978). Present-day plate motions. *Journal of Geophysical Research, 83*, 5331.

Mouginis-Mark, P.J., Crisp, J.A., & Fink, J.H. (2000). Remote sensing of active volcanism. *Geophysical Monograph Series, 116,* American Geophysical Union, Washington DC.

Mouginis-Mark, P.J., & Domergue-Schmidt, N. (2000). Acquisition of satellite data for volcano studies. In P. Mouginis-Mark, J.A. Crisp, & J.H. Fink (Eds.), *Remote sensing of active volcanism*, American Geophysical Union, 9-24.

Mouginis-Mark, P.J., & Garbeil, H. (2005). Quality of TOPSAR topographic data for volcanology studies at Kilauea Volcano, Hawaii: An assessment using airborne lidar data. *Remote Sensing of Environment, 96*, 149-164.

Müller, R.D., Roest, W.R., Royer, J.-Y., Gahagan, L.M., & Sclater, J.G. (1997). Digital isochrons of the world's ocean floor. *Journal of Geophysical Research, 102*, 3211.

Mulyadi, E. (1992). Le complexe de Bromo-Tengger (Est Java, Indonésie): Etude structural et volcanologique. *Phd dissertation*, Laboratoire Magmas et Volcans, Université Blaise Pascal, Clermont Ferrand II, 135 p.

N

Neuberg, J. (2000). External modulation of volcanic activity. *Geophysical Journal International, 142*, 232-240.

Newhall, C.G., Bronto, S., Alloway, B., Banks, N.G., Bahar, I., del Marmol, M.A., Hadisantono, R.D., Holcomb, R.T., McGeehin, J., Miksic, J.N., Rubin, M., Sayudi, S.D., Sukhyar, R., Andreastuti, S., Tilling, R.I., Torley, R., Trimble, D., & Wirakusumah, A.D. (2000). 10,000Years of explosive eruptions of Merapi Volcano, Central Java: archaeological and modern implications. *Journal of Volcanology and Geothermal Research, 100*, 9-50.

Nishi, K., Hendrasto, M., Mulyana, I., Rosadi, U., & Purbawinata, M.A. (2007). Micro-tilt changes preceding summit explosions at Semeru volcano, Indonesia. *Earth Planets Space, 59*, 151-156.

Nishimura, T., Iguchi, M., Kawaguchi, R., Surono, Hendrasto, M., & Rosadi, U. (2012). Inflations prior to Vulcanian eruptions and gas bursts detected by tilt observations at Semeru Volcano, Indonesia. *Bulletin of Volcanology, 74*, 903-911.

O

Oppenheimer, M. (1998). Global warming and the stability of the West Antarctic Ice Sheet. *Nature, 393*, 325-332.

P

Pallister, J.S., Schneider, D.J., Griswold, J.P., Keeler, R.H., Burton, W.C., Noyles, C., Newhall, C.G., & Ratdomopurbo, A. (2013). Merapi 2010 eruption—Chronology and extrusion rates monitored with satellite radar and used in eruption forecasting. *Journal of Volcanology and Geothermal Research, 261*, 144-152.

Pieri, D., & Abrams, M. (2004). ASTER watches the world's volcanoes: a new paradigm for volcanological observations from orbit. *Journal of Volcanology and Geothermal Research, 135*, 13-28.

Pierson, T.C., & Major, J.J. (2014). Hydrogeomorphic Effects of Explosive Volcanic Eruptions on Drainage Basins. *Annual Review of Earth and Planetary Sciences, 42*, 469-507.

Pinel, V., & Jaupart, C. (2000). The effect of edifice load on magma ascent beneath a volcano. *Philosophical Transactions: Mathematical, Physical and Engineering Sciences, 358*, 1515-1532.

Pinel, V., & Jaupart, C. (2005). Some consequences of volcanic edifice destruction for eruption conditions. *Journal of Volcanology and Geothermal Research, 145*, 68-80.

Pinel, V., Poland, M.P., & Hooper, A. (2014). Volcanology: Lessons learned from Synthetic Aperture Radar imagery. *Journal of Volcanology and Geothermal Research, 289*, 81-113

Pyle, D.M. (1989). The thickness, volume and grainsize of tephra fall deposits. *Bulletin of Volcanology, 51*, 1-15.

Pyle, D.M., Mather, T.A., & Biggs, J. (2013). Remote sensing of volcanoes and volcanic processes: integrating observation and modelling - introduction. *Geological Society, London, Special Publications, 380*, 1-13.

R

Rahardjo, W., Sukandarrumidi, & D., R.H.M. (1995). Geological map of the Yogyakarta sheet, Java (1:100,000). Geological Survey of Indonesia, Ministry of Mines, Bandung.

Ratdomopurbo, A., & Poupinet, G. (2000). An overview of the seismicity of Merapi volcano (Java, Indonesia), 1983–1994. *Journal of Volcanology and Geothermal Research, 100*, 193-214.

Ratdomopurbo, A., Beauducel, F., Subandriyo, J., Agung Nandaka, I.G.M., Newhall, C.G., Suharna, Sayudi, D.S., Suparwaka, H., & Sunarta (2013). Overview of the 2006 eruption of Mt. Merapi. *Journal of Volcanology and Geothermal Research, 261*, 87-97

Richards, J.A., & Jia, X. (1999). *Remote Sensing Digital Image Analysis: An Introduction*. Springer Berlin Heidelberg.

Rosen, P.A., Hensley, S., Peltzer, G., & Simons, M. (2004). Updated repeat orbit interferometry package released. *Eos, Transactions American Geophysical Union, 85*, 47-47.

Rowland, S.K., MacKay, M.E., Garbeil, H., & Mouginis-Mark, P.J. (1999). Topographic analyses of Kilauea Volcano, Hawai'i, from interferometric airborne radar. *Bulletin of Volcanology, 61*, 1-14.

S

Saar, M.O., & Manga, M. (2003). Seismicity induced by seasonal groundwater recharge at Mt. Hood, Oregon. *Earth and Planetary Science Letters, 214*, 605-618.

Sadjiman, Sinulingga, I.K., & Gunawan, H. (1995). Penyebaran dan perhitungan volume awanpanas guguran G. Semeru, Jawa Timur, 20 Juli 1995 (Dispersion and volume calculation of dome-collapse pyroclastic flow at Mt. Semeru, East Java, 20 July 1995). Volcanological Survey of Indonesia, Bandung, 14 p.

Saepuloh, A., Koike, K., & Omura, M. (2012). Applying Bayesian Decision Classification to Pi-SAR Polarimetric Data for Detailed Extraction of the Geomorphologic and Structural Features of an Active Volcano. *IEEE Geoscience and Remote Sensing Letters, 9*, 554-558.

Saepuloh, A., Koike, K., Omura, M., Iguchi, M., & Setiawan, A. (2010). SAR- and gravity change-based characterization of the distribution pattern of pyroclastic flow deposits at Mt. Merapi during the past 10 years. *Bulletin of Volcanology, 72*, 221-232.

Saepuloh, A., Urai, M., Aisyah, N., Sunarta, Widiwijayanti, C., Subandriyo, & Jousset, P. (2013). Interpretation of ground surface changes prior to the 2010 large eruption of Merapi volcano using ALOS/PALSAR, ASTER TIR and gas emission data. *Journal of Volcanology and Geothermal Research, 261*, 130-143.

Sayudi, D.S., Aisyah, N., Juliani, D., & Muzani, M. (2010). Peta Kawasan Rawan Bencana Gunungapi Merapi, Jawa Tengah dan Daerah Istimewa Yogyakarta 2010. In. Bandung: Pusat Vulkanologi dan Mitigasi Bencana Geologi.

Schaber, G.G., Elachi, C., & Farr, T.G. (1980). Remote sensing data of SP Mountain and SP Lava flow in North-Central Arizona. *Remote Sensing of Environment, 9*, 149-170.

Schneider, D., Dean, K., Dehn, J., Miller, T., & Kirianov, V.Y. (2000). Monitoring and analyses of volcanic activity using remote sensing data at the Alaska Volcano Observatory: case study for Kamchatka, Russia, December 1997. In P. Mouginis-Mark, J.A. Crisp, & J.H. Fink (Eds.), *Remote sensing of active volcanism*, American Geophysical Union, 65-85.

Schwarzkopf, L.M., Schmincke, H.-U., & Cronin, S.J. (2005). A conceptual model for block-and-ash flow basal avalanche transport and deposition, based on deposit architecture of 1998 and 1994 Merapi flows. *Journal of Volcanology and Geothermal Research, 139*, 117-134.

Scordilis, E.M. (2006). Empirical Global Relations Converting M S and m b to Moment Magnitude. *Journal of Seismology, 10*, 225-236.

Shelley, I., & Voight, B. (1995). Medical effects of nuée ardente eruptions: the November 1994 eruption at Merapi Volcano, Indonesia. In, *Proceedings of the Merapi Decade Volcano International Workshop, UNESCO/Volcanological Survey of Indonesia, Yogyakarta,* 9 p.

Siebert, L., Simkin, T., & Kimberly, P. (2010). *Volcanoes of the World (3rd edition)* Berkeley: University of California Press, 568 p.

Simandjuntak, T.O., & Barber, A.J. (1996). Contrasting tectonic styles in the Neogene orogenic belts of Indonesia. *Geological Society, London, Special Publications, 106*, 185-201.

Simkin, T., & Siebert, L. (1994). *Volcanoes of the World (2nd edition)*. Tucson, Geoscience Press, 369 p.

Siswowidjoyo, S., Santoso, D., Sudarsono, U., & Surono (1995). Penelitian mekanisme letusan G. Semeru di Jawa Timur dan evaluasi daerah bahayanya. *Laporan Final Riset Unggulan Terpadu,* Dewan Riset Nasional dan Proyek Pusat Pengembangan Ilmu Pengetahuan dan Teknologi, 125 p.

Siswowidjoyo, S., Sudarsono, U., & Wirakusumah, A.D. (1997). The threat of hazards in the Semeru volcano region inEast Java, Indonesia. *Journal of Asian Earth Sciences, 15*, 185-194.

Situmorang, T. (1989). Lahar and pyroclastic flow hazards zoning of Semeru volcano, East Java, Indonesia (using aerial photograph). In, *International Symposium on Erosion and Volcanic Debris Flow Technology*. Yogyakarta, Indonesia.

Situmorang, T. (1992). Mt. Semeru (In Indonesian). *Indonesian Bulletin of Volcanology, 174.*

Situmorang, T., & Modjo, S. (1991). Use of satellite imagery to track volcanic ash clouds in Indonesia: a new possibility for aviation safety. In T.J. Casadevall (Ed.), *First international symposium on volcanic ash and aviation safety*.USGS, Washington, Seattle.

Sjarifudin, M.Z. (1990). G. Bromo. *Berita Berkala Vulkanologi, Edisi Khusus No. 127, Bandung, Indonesia.*

Smith, G.A., & Fritz, W.J. (1989). Volcanic influences on terrestrial sedimentation. *Geology, 17*, 375.

Smyth, H.R., Hall, R., Hamilton, J., & Kinny, P. (2005). East Java: Cenozoic basins, volcanoes and ancient basement. In, *Thirtieth Annual Convention & Exhibition* (pp. 251-266): Proceedings, Indonesian Petroleum Association.

Smyth, H.R., Hall, R., & Nichols, G.J. (2008). Cenozoic volcanic arc history of East Java, Indonesia: The stratigraphic record of eruptions on an active continental margin*, 436*, 199-222.

Solikhin, A. (2009). High-resolution satellite images and remote sensing applied to mapping and examining eruptive activity and evolution of Semeru and Merapi volcanoes (Java, Indonesia). *Master thesis*, Laboratoire Magmas et Volcans, Université Blaise Pascal-Clemont Ferrand II.

Solikhin, A., Pinel, V., Vandemeulebrouck, J., Thouret, J.-C., & Hendrasto, M. (2015a). Mapping the 2010 Merapi pyroclastic deposits using dual-polarization Synthetic Aperture Radar (SAR) data. *Remote Sensing of Environment, 158*, 180-192.

Solikhin, A., Thouret, J.-C., Gupta, A., Harris, A.J.L., & Liew, S.C. (2012). Geology, tectonics, and the 2002–2003 eruption of the Semeru volcano, Indonesia: Interpreted from high-spatial resolution satellite imagery. *Geomorphology, 138*, 364-379.

Solikhin, A., Thouret, J.-C., Liew, S.C., Gupta, A., Sayudi, D.S., Oehler, J.-F., & Kassouk, Z. (2015b). High-spatial resolution imagery helps map deposits of the large (VEI 4) 2010 MErapi Volcano eruption and their impact. *Bulletin of Volcanology, Accepted for publication on 6 February 2015.*

Sparks, R.S., Biggs, J., & Neuberg, J.W. (2012). Geophysics. Monitoring volcanoes. *Science, 335*, 1310-1311.

Sparks, R.S.J. (1981). Triggering of volcanic eruptions by Earth tides. *Nature, 290*, 448-448.

Špičák, A., Hanuš, V., & Vaněk, J. (2002). Seismic activity around and under Krakatau Volcano, Sunda arc: constraints to the source region of island arc volcanics. *Studia Geophysica et Geodaetica, 46*, 545-565.

Sribudiyani, N.M., Ryacudu, R., Kunto, T., Astono, P., Prasetya, I., Sapiie, B., Asikin, S., Harsolumakso, A.H., & Yulianto, I. (2003). The collision of the East Java Microplate and its implication for hydrocarbon occurrences in the East Java Basin. Indonesia Petroleum Association, Proceedings 29th Annual Convention, 335-346

Starheim, C.C.A., Gomez, C., Davies, T., Lavigne, F., & Wassmer, P. (2013). In-flow evolution of lahar deposits from video-imagery with implications for post-event deposit interpretation, Mount Semeru, Indonesia. *Journal of Volcanology and Geothermal Research, 256*, 96-104.

Sukamto, R., & Sukarna, D. (2001). Regional Geological Map of Indonesia. *Pusat Penelitian dan Pengembangan Geologi*, Bandung.

Surjo, I. (1986). G. Semeru (in Indonesian). *Indonesian Bulletin of Volcanology, 111.*

Surono, Jousset, P., Pallister, J., Boichu, M., Buongiorno, M.F., Budisantoso, A., Costa, F., Andreastuti, S., Prata, F., Schneider, D., Clarisse, L., Humaida, H., Sumarti, S., Bignami, C., Griswold, J., Carn, S., Oppenheimer, C., & Lavigne, F. (2012). The 2010 explosive eruption of Java's Merapi volcano—A '100-year' event. *Journal of Volcanology and Geothermal Research, 241-242*, 121-135

Sutawidjaja, I.S., Wahyudin, D., & Kusdinar, E. (1996). Geological map of Semeru volcano, East Java. Direktorat Vulkanologi, VSI, Bandung, Indonesia.

Syahbana, D.K. (2013). Seismological study of volcanic activity at Papandayan volcano, West Java, Indonesia. *PhD dissertation*, Université Libre de Bruxelles, Brussels.

Székely, B., & Karátson, D. (2004). DEM-based morphometry as a tool for reconstructing primary volcanic landforms: examples from the Börzsöny Mountains, Hungary. *Geomorphology, 63*, 25-37.

T

Tanguy, J.C., Ribière, C., Scarth, A., & Tjetjep, W.S. (1998). Victims from volcanic eruptions: a revised database. *Bulletin of Volcanology, 60*, 137-144.

Thaden, R.E., Sumadirja, H., & W., R.P. (1975). Peta Geologi lembar Magelang dan Semarang, Jawa Tengah. Direktorat Geologi, Bandung.

Thouret, J.C. (1999). Volcanic geomorphology—an overview. *Earth-Science Reviews, 47*, 95-131.

Thouret, J.C., Lavigne, F., Kelfoun, K., & Bronto, S. (2000). Toward a revised hazard assessment at Merapi volcano, Central Java. *Journal of Volcanology and Geothermal Research, 100*, 479-502.

Thouret, J.-C., Gupta, A., Lube, G., Liew, S.C., Cronin, S.J., & Surono (2010). The 2006 pyroclastic deposits of Merapi Volcano, Java, Indonesia: High-spatial resolution IKONOS images and complementary ground based observations. *Remote Sensing of Environment, 114*, 1949-1967.

Thouret, J.-C., Lavigne, F., Suwa, H., Sukatja, B., & Surono (2007). Volcanic hazards at Mount Semeru, East Java (Indonesia), with emphasis on lahars. *Bulletin of Volcanology, 70*, 221-244.

Thouret, J.-C., Oehler, J.-F., Gupta, A., Solikhin, A., & Procter, J.N. (2014). Erosion and aggradation on persistently active volcanoes—a case study from Semeru Volcano, Indonesia. *Bulletin of Volcanology, 76.*

Tilling, R.I., Koyanagi, R.Y., Lipman, P.W., Lockwood, J.P., Moore, J.G., & Swanson, D.A. (1976). Earthquake and related catastrophic events, Island of Hawaii, November 29, 1975: A preliminary report. *U.S. Geological Survey Circular, 740*, 33 p.

Toda, S., Stein, R.S., & Sagiya, T. (2002). Evidence from the AD 2000 Izu islands earthquake swarm that stressing rate governs seismicity. *Nature, 419*, 58-61.

Tregoning, P., Brunner, F.K., Bock, Y., Puntodewo, S.S.O., McCaffrey, R., Genrich, J.F., Calais, E., Rais, J., & Subarya, C. (1994). First geodetic measurement of convergence across the Java Trench. *Geophysical Research Letters, 21*, 2135-2138.

Triastuty, H., Haerani, N., Mulyana, I., Loeqman, A., & Adi, S. (2012). Laporan penelitian gunungapi Semeru, Jawa Timur. *Center for Volcanology and Geological Hazard Mitigation*, Bandung, Indonesia.

Tupin, F., Inglada, J., & Mercier, G. (2014). Image Processing Techniques for Remote Sensing In F. Tupin, J. Inglada, & J.-M. Nicolas (Eds.), *Remote Sensing Imagery* (pp. 125-154): Wiley-ISTE

Tupper, A., Carn, S., Davey, J., Kamada, Y. Potts, R., Prata, F., & Tokuno, M., (2004). An evaluation of volcanic cloud detection techniques during recent significant eruptions in the western 'Ring of Fire'. *Remote Sensing of Environment, 91,* 27-46.

Tupper, A., Textor, C., Herzog, M., Graf, H., & Richards, M.S., (2009). Tall clouds from small eruptions: the sensitivity of eruption height and fine ash content to tropospheric instability. *Natural Hazards,* 51, 375-401

U

Untung, M., & Sato, Y. (1978). Gravity and Geological Studies in Java, Indonesia. *Geological Survey of Indonesia and Geological Survey of Japan Special Publication, 6*, 207 p.

V

van Bemmelen, R.W. (1949). The eastern spur of Java and Madura. *Transcription of The Geology of Indonesia.*

van Bemmelen, R.W. (1970). *The Geology of Indonesia. 2nd Edition*. The Hague: Government Printing Office, Nijhoff.

van Gerven, M. (1990). Vulkanologisch-Petrographische chemische Untersuchungen im Bereich der Tengger-Caldera, Java, Indonesien. In, *Geological Institute* (p. 101): University of Tiibingen.

van Gerven, M., & Pichler, H. (1995). Some aspects of the volcanology and geochemistry of the Tengger Caldera, Java, Indonesia: eruption of a K-rich tholeiitic series. *Journal of Southeast Asian Earth Sciences, 11*, 125-133.

van Padang, N.M. (1951). Semeru. Catalogue of the Active Volcanoes of the World Including Solfatara Fields. Part 1. Indonesia. *International Association of Volcanology, Napoli*, p. 271.

Vapnik, V.N. (1998). *Statistical Learning Theory*. New York: Wiley-Interscience.

Vaughan, R.G., & Hook, S.J. (2006). Using satellite data to characterize the temporal thermal behavior of an active volcano: Mount St. Helens, WA. *Geophysical Research Letters, 33.*

Venzke, E. (2003). Report on Semeru (Indonesia). *Bulletin of the Global Volcanism Network, 28.*

Verbeek, R.D.M., & Fennema, R. (1896). *Geologische beschrijving van Java en Madoera.* J.G. Stemler cz, Amsterdam.

Voight, B., Constantine, E.K., Siswowidjoyo, S., & Torley, R. (2000). Historical eruptions of Merapi Volcano, Central Java, Indonesia, 1768–1998. *Journal of Volcanology and Geothermal Research, 100*, 69-138.

W

Wadge, G., Cole, P., Stinton, A., Komorowski, J.C., Stewart, R., Toombs, A.C., & Legendre, Y. (2011). Rapid topographic change measured by high-resolution satellite radar at Soufriere Hills Volcano, Montserrat, 2008–2010. *Journal of Volcanology and Geothermal Research, 199*, 142-152.

Wadge, G., Francis, P.W., & Ramirez, C.F. (1995). The Socompa collapse and avalanche event. *Journal of Volcanology and Geothermal Research, 66*, 309-336.

Wadge, G., Saunders, S., & Itikarai, I. (2012). Pulsatory andesite lava flow at Bagana Volcano. *Geochemistry, Geophysics, Geosystems, 13*, Q11011.

Wadge, G., Scheuchl, B., & Stevens, N.F. (2002). Spaceborne radar measurements of the eruption of Soufriere Hills Volcano, Montserrat. *Geological Society, London, Memoirs, 21*, 583-594.

Wahyudin, D. (1991). Volcanology and petrology of Mt. Semeru volcanic complex, East Java, Indonesia. *Master thesis*, Victoria University of Wellington, New Zealand.

Walter, T.R., & Amelung, F. (2007). Volcanic eruptions following M ≥ 9 megathrust earthquakes: Implications for the Sumatra-Andaman volcanoes. *Geology, 35*, 539.

Walter, T.R., Subandriyo, J., Kirbani, S., Bathke, H., Suryanto, W., Aisyah, N., Darmawan, H., Jousset, P., Luehr, B.G., & Dahm, T. (2015). Volcano-tectonic control of Merapi's lava dome splitting: The November 2013 fracture observed from high resolution TerraSAR-X data. *Tectonophysics, 639*, 23-33.

Walter, T.R., Wang, R., Zimmer, M., Grosser, H., Lühr, B., & Ratdomopurbo, A. (2007). Volcanic activity influenced by tectonic earthquakes: Static and dynamic stress triggering at Mt. Merapi. *Geophysical Research Letters, 34.*

Weningsulistri, Kartadinata, M.N., Kristiawan, Y., Natalias, M.C., Praponco, N.T., Purwanto, B.H., & Syafi'i, M. (2014). Pemodelan bahaya aliran piroklastik dan lahar Gunungapi Semeru, Provinsi Jawa Timur. *CVGHM Report,* Bandung.

White, R., & McCausland, W., (2015). Estimating intrusive volumes and forecasting eruptions using distal volcano-tectonic earthquakes, *Journal of Volcanology and Geothermal Research,* in review.

Widiyantoro, S., Pesicek, J.D., & Thurber, C.H. (2011). Subducting slab structure below the eastern Sunda arc inferred from non-linear seismic tomographic imaging. *Geological Society, London, Special Publications, 355*, 139-155.

Widiyantoro, S., & van der Hilst, R. (1997). Mantle structure beneath Indonesia inferred from high-resolution tomographic imaging. *Geophysical Journal International, 130*, 167-182.

Wilson, T., Kaye, G., Stewart, C., & Cole, J. (2007). Impacts of the 2006 eruption of Merapi volcano, Indonesia, on agriculture and infrastructure. *GNS Science Report 2007/07*, 69p.

Wirakusumah, A.D., Juwarna, H., & Loebis, H. (1989). Geologic map of Merapi volcano, Central Java (1/50 000). Direktorat Vulkanologi, V.S.I., Ministry of Mines and Energy, Bandung.

Wright, R., Flynn, L., Garbeil, H., Harris, A., & Pilger, E. (2002). Automated volcanic eruption detection using MODIS. *Remote Sensing of Environment, 82*, 135-155.

Wright, R., & Flynn, L.P. (2003). On the retrieval of lava-flow surface temperatures from infrared satellite data. *Geology, 31*, 893.

Wright, R., Flynn, L.P., Garbeil, H., Harris, A.J.L., & Pilger, E. (2004). MODVOLC: near-real-time thermal monitoring of global volcanism. *Journal of Volcanology and Geothermal Research, 135*, 29-49.

Wunderman, R. (2001). Report on Merapi (Indonesia). *Bulletin of the Global Volcanism Network, 26.*

Wunderman, R. (2007). Report on Merapi (Indonesia). *Bulletin of the Global Volcanism Network, 32.*

Wunderman, R. (2012). Report on Semeru (Indonesia). *Bulletin of the Global Volcanism Network, 37.*

Y

Yamamoto, T., Takarada, S., & Suto, S. (1993). Pyroclastic flows from the 1991 eruption of Unzen volcano, Japan. *Bulletin of Volcanology, 55*, 166-175.

Yu, T., & Rose, W.I. (2000). Retrieval of sulfate and silicate ash masses in young (1 to 4 days old) eruption clouds using multiband infrared HIRS/2 data. In P. Mouginis-Mark, J.A. Crisp, & J.H. Fink (Eds.), *Remote sensing of active volcanism*, American Geophysical Union, 87-100.

Yulianto, F., Sofan, P., Khomarudin, M.R., & Haidar, M. (2012). Extracting the damaging effects of the 2010 eruption of Merapi volcano in Central Java, Indonesia. *Natural Hazards, 66*, 229-247.

Z

Zaennudin, A. (1990). The stratigraphy and natur of the stratocone of MT. Cemorolawang in the Bromo-Tengger caldera, East Java, Indonesia. *Master thesis*, Research School of Earth Science, Victoria University of Wellington.

Zaennudin, A., Hadisantono, R.D., Erfan, R., & Mulyana, A.R. (1995). Peta Geologi G. Bromo – Tengger. In. Bandung: Direktorat Vulkanologi.

Zaennudin, A., Kristianto, & Saragih, E.L.A. (2012). Eruption model of Bromo Volcano, East Java, in the year 2010 - 2011 (In Indoneisan). *Jurnal Lingkungan dan Bencana Geologi, 3*, 41 – 55.

Zanoni, V.M., & Goward, S.N. (2003). A new direction in Earth observations from space: IKONOS. *Remote Sensing of Environment, 88*, 1-2.

Zebker, H.A., Amelung, F., & Jonsson, S. (2000). Remote sensing of volcano surface and internal processes using radar interferometry*, 116*, 179-205.

Zebker, H.A., Rosen, P., Hensley, S., & Mouginis-Mark, P.J. (1996). Analysis of active lava flows on Kilauea volcano, Hawaii, using SIR-C radar correlation measurements. *Geology, 24*, 495.

Zebker, H.A., van Zyl, J.J., & Held, D.N. (1987). Imaging radar polarimetry from wave synthesis. *Journal of Geophysical Research, 92*, 683.

Appendix A

List of satellite images

Optical images

Satellite sensor; image type	Spatial resolution	Acquisition date	Coverage area	Sources (courtesy of:)	Used in:
GeoEye1; panchromatic	0.41 m	15/11/2010	Merapi	CRISP	Chap. 4
GeoEye1; multispectral	1.65 m	15/11/2010 04/09/2011 16/04/2012	Merapi Merapi Semeru	CRISP CRISP	Chaps. 2; 4; 5 Chaps. 2; 4 Chap. 3
WorldView-2; multispectral	1.84 m	08/06/2011	Semeru	CRISP	Chaps. 2; 3
Pléiades; panchromatic & multispectral	0.5 m & 2 m	29/09/2012 22/10/2012	Merapi Semeru	CNES CNES	Chap. 4 Chap. 3
IKONOS; multispectral	3.2 m	14/11/2002 25/09/2004 16/06/2006 10/04/2008 07/07/2008	Semeru Semeru Semeru Semeru Merapi	CRISP; STIC-ASIA CRISP; STIC-ASIA CRISP; STIC-ASIA CRISP; STIC-ASIA CRISP; STIC-ASIA	Chap. 3 Chap. 3 Chap. 3 Chaps. 2; 3 Chaps. 2; 4
SPOT 5; panchromatic	2.5 m	20/08/2009 24/10/2003 26/09/2004 11/08/2003	Semeru Semeru Semeru Semeru	CRISP; STIC-ASIA CRISP; STIC-ASIA CRISP CRISP; STIC-ASIA	Chaps. 2; 3 Chap. 3 Chap. 2 Chap. 2
SPOT 5; multispectral	10 m	16/05/2006 06/06/2006 26/06/2006 18/05/2008 26/07/2008 15/11/2010 10/06/2011	Merapi Merapi Merapi Merapi Semeru Merapi Merapi	CRISP CRISP CRISP CRISP CRISP; STIC-ASIA CNES CNES	Chap. 2 Chap. 2 Chap. 2 Chap. 2; 4 Chaps. 2; 3 Chaps. 2; 4 Chaps. 2; 4
SPOT 2; multispectral	20 m	11/05/1996	Semeru	CRISP; STIC-ASIA	Chap. 3
SPOT 1; multispectral	20 m	08/08/1997	Semeru	CRISP; STIC-ASIA	Chap. 3

(continued)

Satellite sensor; image type	Spatial resolution	Acquisition date	Coverage area	Sources (courtesy of:)	Used in:
ASTER; multispectral	15 m	26/10/2002	Semeru	http://ava.jpl.nasa.gov	Chap. 3
		23/06/2003	Semeru		Chap. 3
		28/08/2004	Semeru		Chap. 3
		03/11/2005	Semeru		Chap. 3
		30/05/2006	Semeru		Chap. 3
		06/07/2008	Semeru		Chap. 3
		27/09/2009	Semeru		Chap. 3
		13/08/2010	Semeru		Chap. 3
		13/06/2011	Semeru		Chap. 3
		13/06/2012	Merapi		Chaps. 1; 2
		15/06/2012	Semeru		Chaps. 1; 3
		20/07/2013	Semeru		Chap. 3
		05/06/2014	Semeru		Chap. 3
		09/09/2014	Semeru		Chap. 3

Thermal images

Satellite sensor; image type	Spatial resolution	Acquisition date	Coverage area	Used in:
ASTER; TIR Surface Kinetic Temperature	90 m	08/07/2002 08/02/2003 25/09/2003	Semeru	Chap. 3

Radar images

Satellite sensor; image type	Spatial resolution	Acquisition date	Coverage area	Sources (courtesy of:)	Used in:
ALOS-PALSAR; FBD (HH + HV)	28.4 m in azimuth; 33.2 m in ground range.	13/09/2009 16/06/2010 16/09/2010 01/11/2010 01/02/2011	Merapi	• Cooperation RESTEC (Japan) -LAPAN and Geological Agency (Indonesia) • JAXA project no. 1188	Chap. 5
FBS (HH)		17/12/2010			

Appendix B

Supplementary data to the article of Solikhin et al. (2015b) in Chapter 4

High-spatial resolution imagery helps map deposits of the large (VEI 4) 2010 Merapi Volcano eruption and their impact

Akhmad Solikhin, Jean-Claude Thouret, Soo Chin Liew, Avijit Gupta, Dewi Sri Sayudi, Jean-François Oehler, Zeineb Kassouk

Supplementary Material

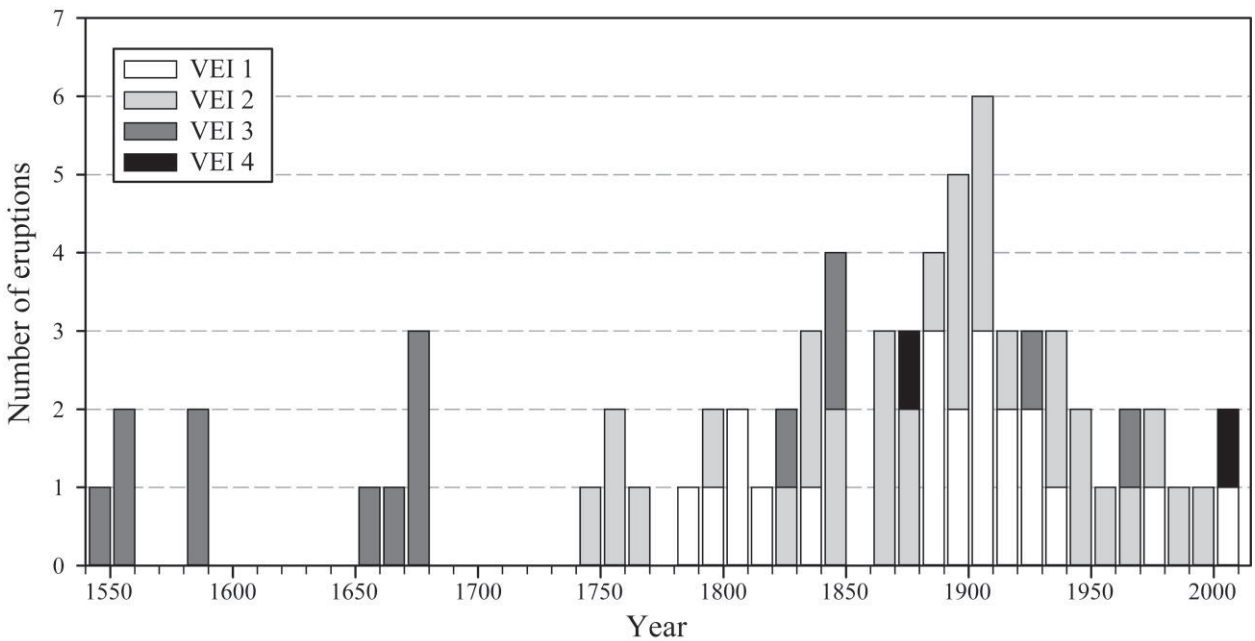

Appendix Figure 1. Historical eruptions of Merapi since 1548 shown as frequency histograms of Volcanic Explosivity Index (VEI) divided by 10-year time intervals. Note that before AD 1700, the number of large eruptions is probably biased with respect to unreported small eruptions.

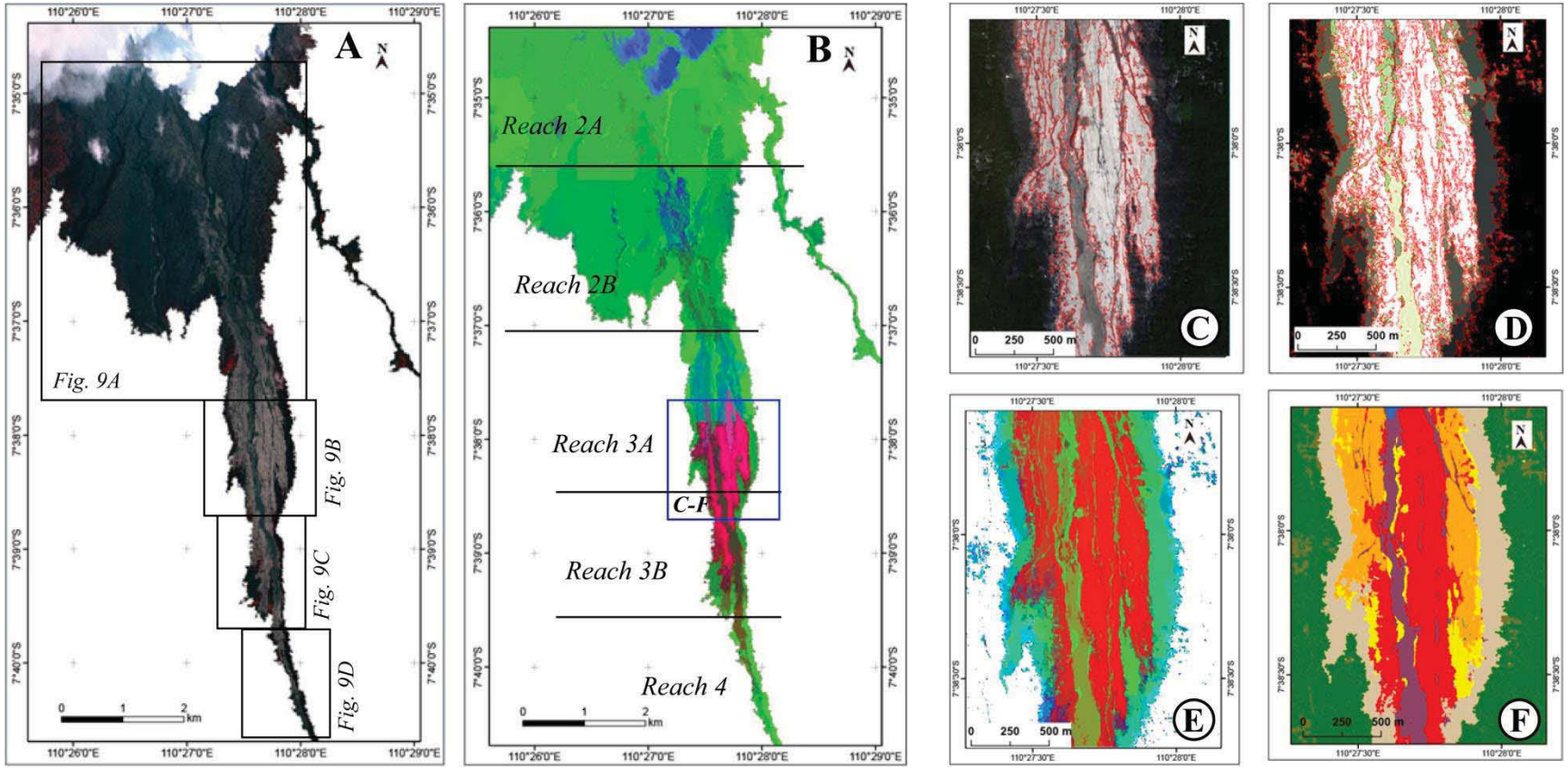

Appendix Figure 2. A. 15 November 2010 GeoEye image and (**B**) intensity, hue and saturation (IHS) image used to breakdown the Gendol catchment into several reaches. Subscene of the GeoEye image of reach 3A show how the object-oriented method has led to: (**C**) compute NDWI, NDVI, and NDRSI, (**D**) segment the image in pixel areas, (**E**) compute attributes for each region, and (**F**) carry out a supervised classification and outline the principal deposit units in valley-confined and un-confined areas.

Appendix C

Supplementary data to the article of Solikhin et al. (2015a) in Chapter 5

Mapping the 2010 Merapi pyroclastic deposits using dual-polarization Synthetic Aperture Radar (SAR) data

Akhmad Solikhin, Virginie Pinel, Jean Vandemeulebrouck, Jean-Claude Thouret, and Muhamad Hendrasto

Supplementary Data

Training and control data for supervised classification

We characterize the 2010 Merapi deposits using direct-polarized and cross-polarized L-band SAR data and by combining the information of amplitude evolution with temporal decorrelation. Changes in amplitude of the radar signal enable us to map the pyroclastic density currents (PDCs) and tephra-fall deposits. Changes in amplitude can be quantified by taking the ratio between the two amplitude images acquired after and before the emplacement of deposits (Fig. S1). We also use a supervised classification method based on Maximum Likelihood Classification (MLC) and the Support Vector Machine (SVM) classification techniques to map four types of deposit. The four deposits are valley-confined and overbank block-and-ash flow (D1), rainfall- runoff- reworked PDC deposits (D2), pyroclastic surge (D3), and tephra fall (D4) deposits.

Training samples and control data play an important role in the supervised classification process of remotely sensed images. Its quality is an important factor affecting the accuracy of image classification. We define training samples based on visual interpretation of optical views and the radar image in the false-color composite representation by referring to field-based data. A set of training samples characterizing seven deposit classes (D1 to D7) and five 'non-deposit' classes (O1 to O5) shown in Figure S1b. The 'non deposit' classes consist of vegetation (O1), agriculture/farm (O2),

settlements and villages (O3), bright pixels corresponding to foreshortening effect (O4) and shadowed areas (O5). We assess the quality of training data before performing the classification by computing the separability value between a pair of training classes using based on Jeffries-Matusita (J-M) distance. Accuracy assessment of the classification is quantitatively performed by comparing the results of MLC and SVM classification with control data (Fig. S1c).

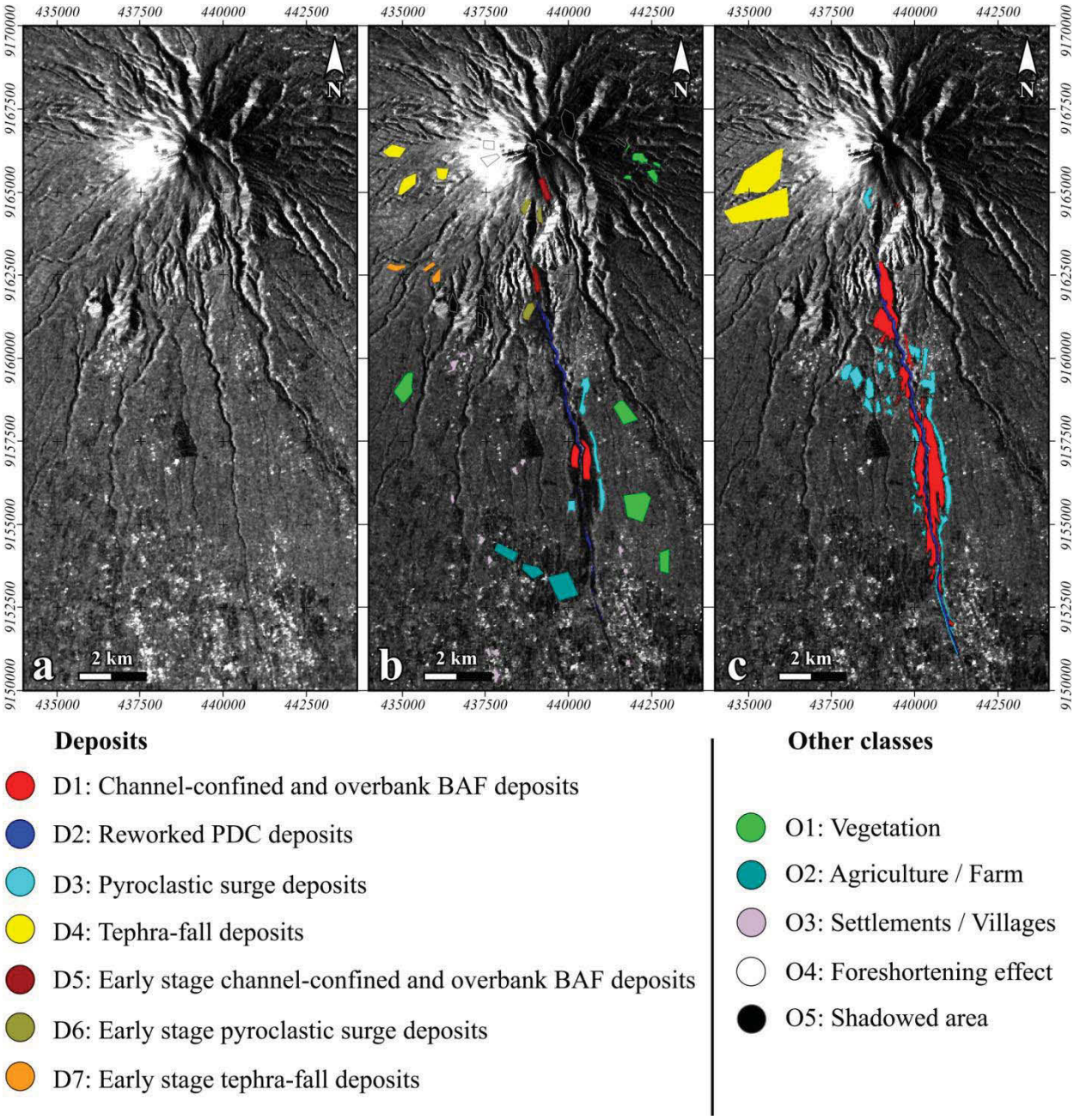

Figure. S1. Georeferenced ALOS-PALSAR amplitude image (four looks) for HH polarization acquired **(a)** before eruption (16 September 2010) and **(b)** after the eruption (17 December 2010) overlain by map of training data and **(c)** map of control data.

Support Vector Machine classification result

In addition to Maximum Likelihood Classification (MLC), the supervised classification based on Support Vector Machine (SVM) has been applied to ALOS-PALSAR data in order to create a map of the 2010 Merapi pyroclastic deposits in a semi-automatic way. This classification aims to categorize all pixels in the radar image into one of several pre-defined deposit or land cover classes. SVM is a supervised classification method derived from statistical learning theory that discriminates the classes with a decision surface (hyperplane) that maximizes the margin between the classes. In this work, the SVM is applied using the radial basis kernel.

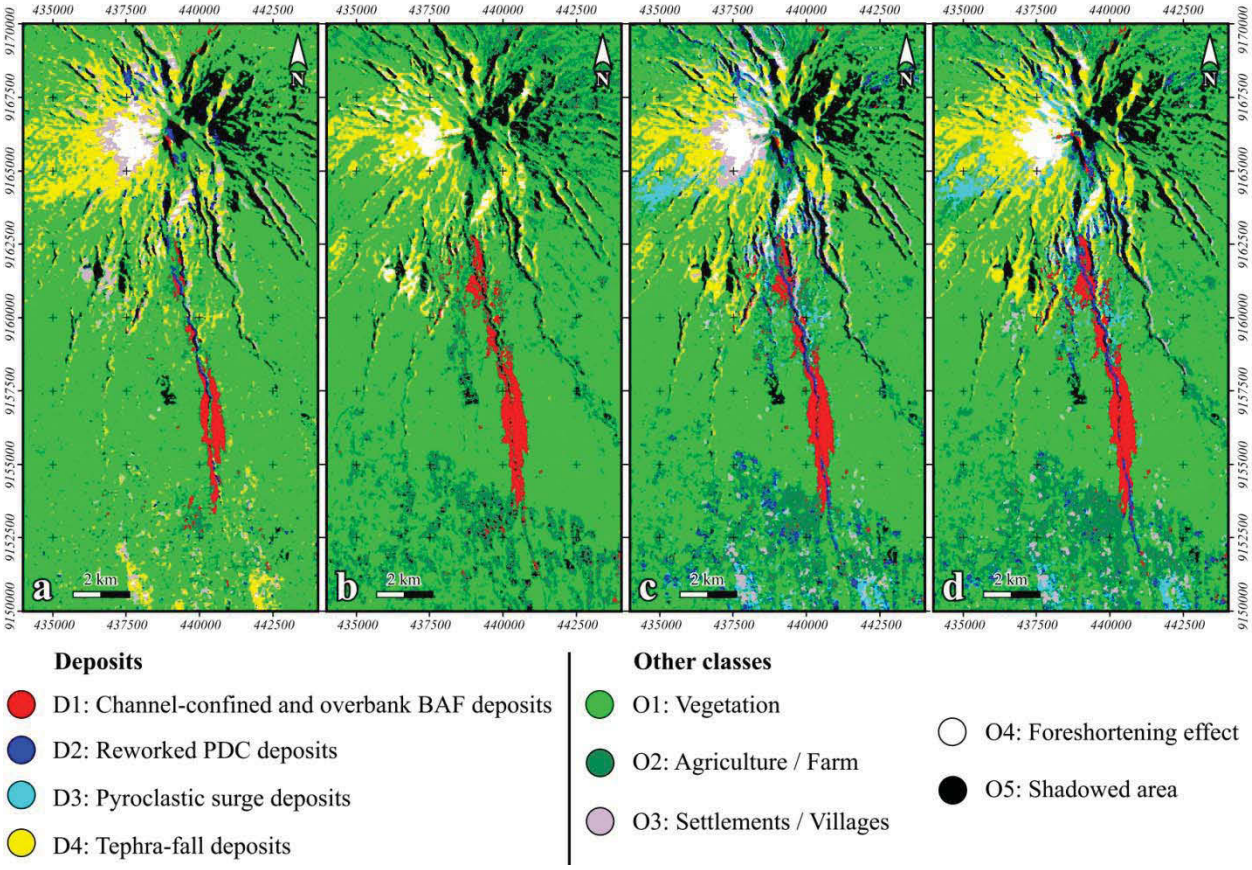

Figure S2. Map of the 2010 Merapi pyroclastic deposits based on the support vector machine (SVM) classification method and using amplitude images acquired before (16 September 2010) and after the eruption (1 February 2011) for **(a)** HH polarization only (two images have been used for this purpose); **(b)** HV polarization only (two images); **(c)** HH and HV polarizations (four images); and **(d)** HH and HV polarizations dates together with the coherence image represented in Fig. 3e (five images).

The map of 2010 Merapi deposits based on SVM using various sets of 16 September 2010 and 1 February 2011 images and nine classes (D1-D4 and O1-O5) of training data

is shown in Figure S2. Similar to MLC result, the SVM result shows that classification using only two images (acquired before and after the eruption) of HH polarization (Fig. S2a) produces better results than using HV polarization images (Fig. S2b). The classification always produces better results when combining both HH and HV images (Fig. 6c) and even better when adding the coherence image (Figs. 6d and 7c) as input. Accuracy assessment of four deposit classes (D1-D3) from the SVM classification is summarized in a confusion matrix (Tables S1). SVM provides 63.97% overall classification accuracy, where 89.83% of D1, 74.41% of D2, 27.29 % of D3 and 54.67% of D4 are correctly classified. SVM is slightly better than MLC in classifying D1 (89.83%) with ~3% different. We also measured the area of the deposits from the SVM and obtained an area of 4.14 km^2 for D1, 1.19 km^2 for D2 and 4.75 km^2 for D3.

Table S1
Cross-validated confusion matrix for Support Vector Machine (SVM) method.

Class	Control Data (%)			
	D1	D2	D3	D4
D1	**89.83**	8.49	2.55	0.08
D2	2.39	**74.41**	2.51	0.35
D3	0.15	2.12	**27.29**	24.66
D4	0.00	0.00	4.11	**54.67**
O1	0.87	0.47	52.84	19.01
O2	6.37	4.25	10.06	1.05
O3	0.00	0.00	0.65	0.03
O4	0.00	0.00	0.00	0.00
O5	0.38	10.26	0.00	0.15

The bold font indicates the percentage of correctly classified pixels of each deposit class.